Technological and design aspects of the processing of composites and nanocomposites

Volume IV

NewEX
H2020-MSCA-RISE-2017

MARIE CURIE ACTIONS

Technical University of Košice
Lublin University of Technology
University of Minho

TECHNOLOGICAL AND DESIGN ASPECTS OF THE PROCESSING OF COMPOSITES AND NANOCOMPOSITES

Volume IV

Monography

edited by

Assoc. Prof. **Ľudmila Dulebová**, Ph.D., D.Sc.
Technical University of Košice

Prof. **Janusz W. Sikora**, Ph.D., D.Sc.
Lublin University of Technology

Košice
Technical University of Košice
2021

Scientific-Practical International Workshop under a Project H2020-MSCA-RISE-2016-734205

This project has received funding from the European Union's Horizon 2020 research and innovation programme under the Marie Skłodowska-Curie grant agreement No 734205–H2020-MSCA-RISE-2016

Reviewed by:
prof. Janette Brezinová, Ph.D., D.Sc., Technical University of Košice, Slovakia
Assoc. Prof. Tomasz Rydzkowski, Ph.D, D.Sc., Koszalin University of Technology, Poland
Assoc. Prof. Mykola Brailo, Ph.D., D.Sc., Kherson State Maritime Academy, Ukraine

© Copyright by Technical University of Košice 2021

All rights reserved.
No part of this work may be reproduced or transmitted in any form or by means, electronic or mechanical, including photocopying and recording, or by any information storage or retrieval systems without permission in writing from Publisher.

Publisher:
Technical University of Kosice, Faculty of Mechanical Engineering,
Letna 1/9 Str., 040 01 Kosice, Slovakia

Production Editor:
Ľudmila Dulebová, Janusz W. Sikora

Printed by:
Technical University of Kosice, Kosice, Slovakia

ISBN 978-80-553-3817-0

PREFACE

We would like to present to the readers another study "*Technological and design aspects of the processing of composites and nanocomposites. Volume IV*". The book contains a selection of issues which - on the basis of such a defined topic - the team describing them found particularly important and interesting. The authors have taken up the presented problems considering them to be extremely up-to-date and relevant to the contemporary international community representing both the industrial and scientific sectors.

The work presented in this monograph relates primarily to the activities carried out in the fifth year of the international project "Investigation and development of a new generation of machines for the processing of composite and nanocomposites materials" with the acronym Newex, for which contract GA 734205 was signed under the Horizon 2020, Research and Innovation programme under the Marie Sklodowska-Curie Actions (H2020-MSCA-RISE-2016). This is the fourth monograph on the project topic.

The period of the pandemic (March 2020 - July 2021) significantly limited the opportunities for knowledge transfer and international exchange within the Newex project, but the enthusiasm accompanying the realization of the project idea and the belief in the further possibility of international cooperation and discovering the undiscovered, contributed to the creation of this monograph.

We dedicate the monograph primarily to internationalists - practitioners and theoreticians, including adepts of science and industry, dealing with issues related to the design of processing machines and tools and new materials, as well as the study of their properties. We think especially warmly of the doctoral students and undergraduates of the Faculty of Mechanical Engineering of Lublin University of Technology, Technical University of Košice and University of Minho, for whom lectures on polymer processing have been given for several years as part of the third, second- and first-degree studies.

The team of persons who wrote this monograph consists of lecturers with decades of scientific and didactic experience as well as of those who are taking their first steps in the field of science. Such a selection of authors allows us to hope that the book is varied, both in terms of style and content, and that it will be of interest to the Reader, thus fulfilling its role well.

Košice, November 2021

Ľudmila Dulebová
Janusz W. Sikora

TABLE OF CONTENT

1. *Karolina Głogowska, Emil Spišák, Marcin Buczaj*: Implementation of the plastication process in an innovative extrusion machine for the processing of composite and nanocomposite materials. Concept and implementation of control system of the extruder. Part I - Motors ………………………….......... 7
2. *Łukasz Majewski, Jan Varga, Andrzej Sumorek*: Implementation of the plastication process in an innovative extrusion machine for the processing of composite and nanocomposite materials. Concept and implementation of control system of the extruder. Part II – Pressure & Temperature System 35
3. *Janusz W. Sikora, Ľudmila Dulebová:* Implementation of the plastication process in an innovative extrusion machine for the processing of composite and nanocomposite materials. Concept and implementation of control system of the extruder. Part III - Data Acquisition & Control System ………………………. 63
4. *Ján Varga, Łukasz Majewski:* The application of CAM system in the production of selected parts of the innovative extruder …………………………………… 119
5. *Ľudmila Dulebová, Janusz W. Sikora, Volodymyr Moravskyi*: The impact of technological parameters of plastics extrusion process on products quality.. 137
6. *Ivan Gajdoš, Emil Spišák, Volodymyr Krasinskyi:* Simulation of extrusion based additive manufacturing technologies…………………………............. 151
7. *António Gaspar-Cunha:* Optimization of conventional and barrier screws …… 165
8. *José A. Covas, Loic Hilliou*: In-line characterization of the dispersion of polymer nanocomposites during melt compounding …………………………. 179
9. *Fernando M. Duarte, Catarina G. Ribeiro, João G. Ferreira, Sílvia A. Forte, José A. Covas*: Using hybrid thermoforming to control the thickness distribution of the parts produced ……………………………………….…….. 195
10. *Volodymyr Krasinskyi, Ivan Gajdoš, Tomasz Jachowicz:* Review on the processing and properties of nanocomposites based on polyvinyl alcohol and intercalated montmorillonite …………………………………………………… 211
11. *Anastasia Kucherenko, Ludmila Dulebova, Volodymyr Moravskyi:* Analysis of processes occurring during processing of metallized polymer granules ……… 229
12. *Oleksandr Grytsenko, Natalia Baran, Bohdan Berezhnyy:* Development of a new technology of obtaining of tubular products based on composite hydrogels 245
13. *Andrii Masyuk, Bozhena Kulish, Khrystyna Kysil, Volodymyr Levytskyi, Diana Katruk, Dmytro Ketchur*: Features of technology, morphology and properties of heat-resistant polylactide composites ………………………………………. 259

Karolina Głogowska[1], Emil Spišák[2], Marcin Buczaj[3]

IMPLEMENTATION OF THE PLASTICATION PROCESS IN AN INNOVATIVE EXTRUSION MACHINE FOR THE PROCESSING OF COMPOSITE AND NANOCOMPOSITE MATERIALS. CONCEPT AND IMPLEMENTATION OF CONTROL SYSTEM OF THE EXTRUDER. PART I - MOTORS

Abstract: *The process of extruding composite and nanocomposite materials is a complicated technological process. The extrusion process requires taking into account many technological factors. Factors that should be considered are the parameters of the composite blend and the process parameters related to the temperature and pressure of the composite during the formation of the final product. The required physical parameters are obtained thanks to the use of appropriate control, measurement and executive systems. The paper presents executive, measurement and control systems used in an innovative extruder for composite and nanocomposite materials.*

Keywords: *innovation technologies of extrusion, extrusion of composites and nanocomposites, pressure and temperature measurement system, control systems.*

1. Introduction

Extrusion is a process that enables the production of semi-finished or finished products during continuously plasticizing a polymeric material and extruding it through a fixed geometry die into the final form. Extrusion of plastic consists in squeezing plasticized material through the extruder die. The shape of the die enables the element to be shaped in desired form. Extrusion technology is now well known. Extrusion technology is widespread in the plastics industry. Forming polymeric materials to the shapes required by finished products is most often an integrated process. The extruder is only one element of the entire technological line in the process of forming materials. Extrusion requires continuous control of the entire technological process. Stable extruder operating parameters are especially required [1, 2, 3, 4, 7].

---

[1] *Lublin University of Technology, Faculty of Mechanical Engineering, Department of Technology and Polymer Processing, ul. Nadbystrzycka 36, 20-618 Lublin, Poland, k.glogowska@pollub.pl.*

[2] *Technical University of Kosice, Faculty of Mechanical Engineering, Department Technologies, Materials and Computer Aided Production, Masiarska 74, 040 01 Kosice, Slovakia, emil.spisak@tuke.sk.*

[3] *Lublin University of Technology, Faculty of Electrical Engineering and Computer Science, Department of Electrical Engineering and Electrotechnologies, ul. Nadbystrzycka 38A, 20-618 Lublin, Poland, m.buczaj@pollub.pl.*

The aim of the extrusion process is to obtain the element in the desired form. Proper mixing and plasticizing the material is the first step in the process of extrusion. The forming process of plastic can be divided into three basic stages: solids conveying, melting and metering. In a next step, the plasticized material is forced through the die of the extrusion head due to the high pressure created in the plasticizing system of the extruder, a properly shaped die gives the molded material the required shape [1, 2, 7].

Single-screw extruders are usually used for the processes of forming homogeneous materials in the form of granules (e.g. pure polymers). Counter-rotating twin-screw extruders or planetary extruders are used for the extrusion of thermally sensitive plastics (e.g. PVC) and for materials in a form other than granules (e.g. powder). Co-rotating twin-screw extruders are used for extrusion of modified plastics and polymer composites [1, 2].

A typical screw extruder (Fig. 1) consists of a plasticizing system (hopper, barrel, screw, heating elements, cooling elements), an extrusion head with a die, a drive system (motor, gears) and a control system [1, 2].

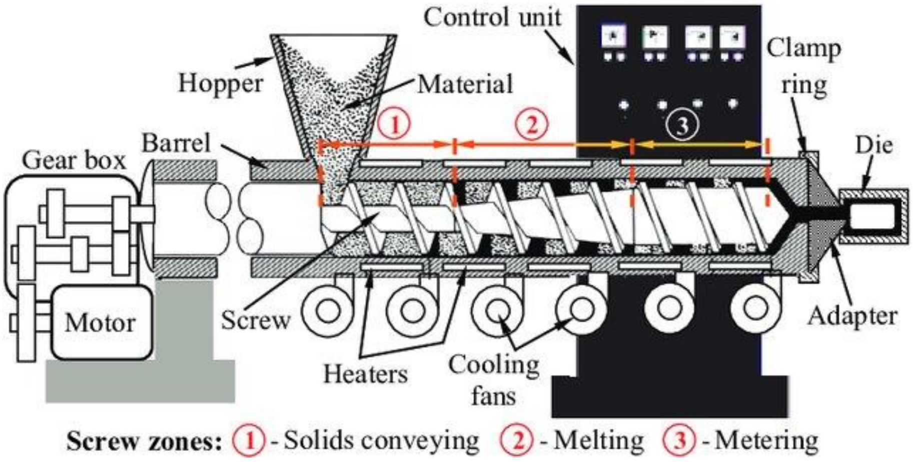

Fig. 1. A screw extruder – schematic diagram [1]

Each stage of the technological extrusion process has an impact on the quality of the final product. Maintaining all technological parameters in line with the design assumptions enables us to obtain valuable products. Incorrect setting or incorrect technological parameters may make the entire process ineffective and the product will not meet the assumed requirements [2, 7].

Full, precise control over the entire plasticization and forming process of products is very difficult in real conditions. In order to effectively produce finished products or semi-finished products of satisfactory quality, it is required to take into account many material, machine, technological and disruptive factors. At the same time, requirements resulting from a number of technical, physical, chemical and environmental criteria must be met. Meeting all the requirements leads to the creation of stable conditions for extrusion processes. Correct design assumptions and the proper course of the technological process give the effect of dimensional repeatability of products and homogeneity of final products. The dimensional repeatability of the final product is often taken as a measure of the stability of the extrusion process [1, 2, 3, 7].

Currently, new design constructions for plasticizing systems are offered. Modern constructions enable greater control over the extrusion process, processing of more demanding and modern polymer materials, including composite and nanocomposite materials [1, 3].

The paper presents the characteristics of electrical equipment used in an innovative extruder for processing composite and nanocomposite materials. The presented technical construction of the extruder was built under the NEWEX project. The work presents the parameters and functional requirements for individual elements of the electrical equipment of the developed extruder. The text describes in detail the electrical systems and elements of the control and steering system used in the extruder.

2. An innovative extruder for processing composite and nanocomposite materials (NEWEX project)

The use of screw extruders, polymeric, composite and nanocomposite materials has been growing significantly for many years. Polymer, composite and nanocomposite materials are commonly used in many different areas of life. The attractiveness of these materials is related to the possibility of any shape, high mechanical strength, resistance to physical, chemical and environmental conditions. Making products from polymeric or composite materials is relatively inexpensive. The extrusion process is used to produce elements in various industrial sectors. Extruded parts can be found in household, automotive, aerospace, marine, construction, electrical and electronics, and medical applications.

Despite a good knowledge of the extrusion processes, there are still factors that have a negative effect on the extrusion process. Due to negative factors, an important aspect during the operation of extruders is constant control and monitoring of temperature and pressure parameters. For the same reasons, it is important to maintain a high quality working parts of extruders.

The scientific and innovative aim of the NEWEX project is to develop the concept, design, manufacture and test the original plasticizing system of a new generation extruder. The NEWEX project also includes the determination of the extruder geometry and technological conditions of the extrusion process in order to increasing the efficiency of the extrusion process. The innovation consists in increasing the flow rate of the polymer, obtaining extruded elements with better mechanical and thermal properties, improving the structure of the material, reducing unit energy consumption and increasing the overall energy efficiency compared to currently used extruders. It is expected that the construction will be better than the current in all aspects at least 10% [5, 6, 8].

Thanks to the use of the new concept of the key parts of the new extruder: the innovative active grooved section (IAGFS), the original rotary barrel segment (ORBS) and the special screw (SS), a completely new breakthrough extrusion technology and plasticizing system design will be obtained.

The extruder will enable the production of products with improved properties. The extruder will enable the processing of materials that could not be processed so far, including food, cosmetic and pharmaceutical materials. Obtaining the assumed effects requires the use of appropriate electrical equipment enabling the implementation of production processes (motors, drives, heating and cooling systems) and control and measurement systems (sensors, controllers, communication interfaces, protection) [8]. The schematic diagram of the innovative extruder is shown in Fig. 2. The view of the prototype of the extruder is shown in Fig. 3.

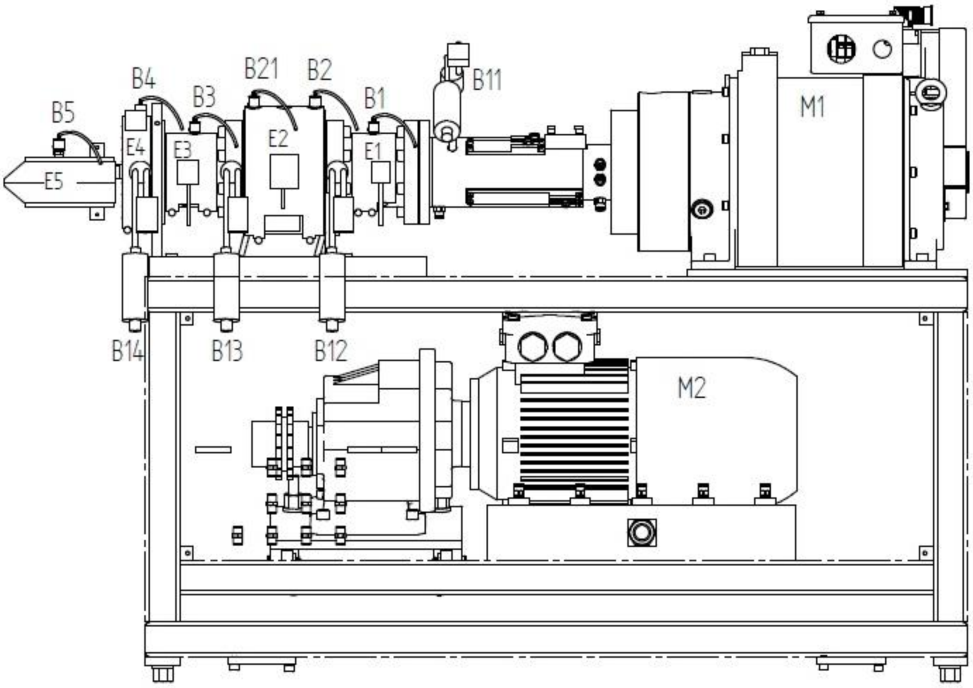

Fig. 2. Schematic diagram of an innovative extruder for use in the processing of composite and nanocomposite materials [5, 8]; M1 – main drive motor; M2 rotary sleeve drive motor; E1, E2, E3, E4, E5 – heaters (elements of the heating system); B1, B2, B3, B4, B5 – temperature sensors; B11, B12, B13, B14 – pressure sensors

The prototype of the extruder for use in the processing of composite and nanocomposite materials is characterized by the following technical parameters: a constant torque independent of the screw speed 250 N·m, the range of rotational speeds of the screw 0÷300 rpm, barrel sleeve rotational speed range 0÷200 rpm, screw diameter 25 mm, L/D = 22, power of screw drive motor 5 kW, power of rotary sleeve drive motor 3,5 kW, 4 heating zones, a flat slot head for tapes, a water-cooled grooved active zone.

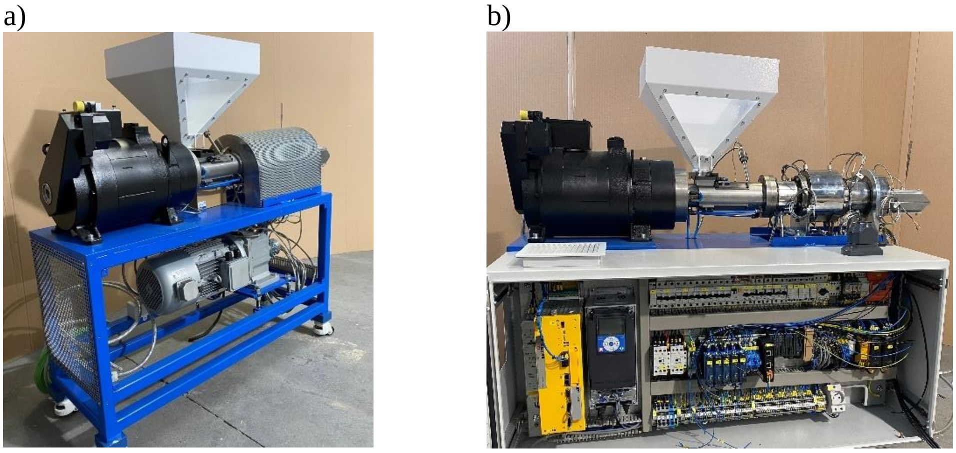

Fig. 3. An innovative extruder for use in the processing of composite and nanocomposite materials [8]; a) main working elements; b) view of the extruder with a control system for a control and measurement processes

3. The selection of the electrical components of the extruder

The correct operation of the extruder is the interaction of mechanical and electrical components. Mechanical elements enable the implementation of working processes (shaping, mixing, forming). On the other hand, electrical equipment enables the correct course of mechanical processes (force, power, temperature, rotational speed).

The following elements were included during the selection of electrical components:

- main drive motor,
- rotary sleeve drive motor,
- elements of the heating system,
- components of the temperature measurement system,
- elements of the pressure measurement system,
- stream control component in the cooling system.

Approximate arrangement of individual electrical components in the extruder is shown in Fig. 4.

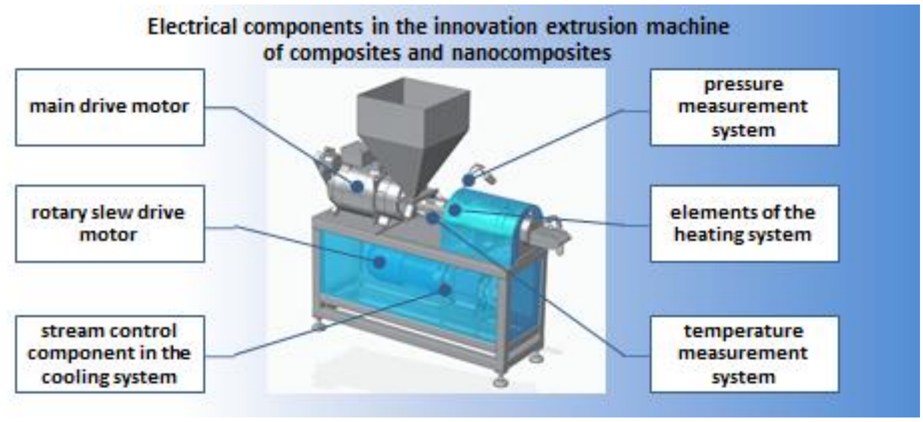
Electrical components in the innovation extrusion machine of composites and nanocomposites
main drive motor
rotary slew drive motor
stream control component in the cooling system
pressure measurement system
elements of the heating system
temperature measurement system

Fig. 4. Electrical components in the innovation extrusion machine of composites and nanocomposites

The main technical requirements for the distinguished basic elements of electrical equipment of the extruder are presented in the tables: Table 1 (main drive motor), Table 2 (rotary sleeve drive motor), Table 3 (temperature measurement system), Table 4 (pressure sensors), Table 5 (stream control components in the cooling system) and Tables 6÷11 (heating element).

Table 1. Basic technical requirements for main drive motor

Requirement (parameter)	Value (feature)
Motor type	synchronous torque motor
Torque	constant torque
Nominal (rated) torque	≥ 265 Nm
Nominal (rated) speed (with speed control up to 200 rpm)	≈ 175 rpm
Rated power	≈ 5,0 kW;
Temperature inspection	built-in temperature inspection
Cooling system	built-in cooling system (preferred water cooling)

Table 2. Basic technical requirements for rotary sleeve drive motor

Requirement (parameter)	Value (feature)
Motor type	undefined
Nominal (rated) torque	≥ 200 Nm
Nominal (rated) speed	≈ 130 rpm
Rated power	≈ 4,0 kW
Temperature inspection	yes
Cooling system	forced ventilation (air forced ventilation)

Table 3. Basic technical requirements for temperature measurement system

Requirement (parameter)	Value (feature)
Temperature range	0÷400°C
Tolerance	class 2 (~±2,5 °C)
Sheath length	≥ 10 mm
Sheath diameter	5÷8 mm
Fitting	bayonet fitting
Lead wire length	≥ 1,5 m

Table 4. Basic technical requirements for pressure sensors

Requirement (parameter)	Value (feature)
Sensor type	Melt pressure
Pressure range	0÷350 bar, 0÷500 bar
Accuracy class	≤ 0.50 % FSO
Maximal work temperature (diaphgram /membrane temp.)	≥ 400 °C
Preferred supply voltage	24 V DC
Output signal	analog
Output signal type	typical current: 4÷20 mA
Integrated temperature sensor	yes
Sensor temperature range	0÷400 °C
Approximated rigid stem length	≥ 100 mm
Approximated flexible stem length	≥ 400 mm

Table 5. Basic technical requirements for cooling system

Requirement (parameter)	Value (feature)
Device type	Electromagnetic valve
Type of valve	undefined
Port connection	G ¼
Membrane /seal material	NBR, EPDM
Nominal (differential) pressure	≥ 4 bar
Flow (Kv value)	undefined
Max. medium (water) temperature	80 °C
Preferred supply voltage	24 V DC

Table 6. Basic technical requirements for heating element – barrel III

Requirement (parameter)	Value (feature)
Type	band heater
Power	750 W
Supply voltage	230 V AC
Working temperature / maximum temperature	300 °C / 450 °C
Insulation of a heating element	micanite
Surface load capacity	app. 4,5W/cm^2
Power cord integrated with the sensor	Yes, dł. 2-3 m, protective of heat
Connector type of cable exit	tangents, planar
Internal diameter of a heater element	ø100 mm
Width of a heater element	65 mm

Table 7. Basic technical requirements for heating element – barrel II

Requirement (parameter)	Value (feature)
Type	band heater
Power	2200 W
Supply voltage	230 V AC
Working temperature / maximum temperature	300 °C / 450 °C
Insulation of a heating element	micanite
Surface load capacity	app. 4,5W/cm^2
Power cord integrated with the sensor	Yes, dł. 2-3 m, protective of heat
Connector type of cable exit	tangents, planar
Internal diameter of a heater element	ø180 mm
Width of a heater element	115 mm

Table 8. Basic technical requirements for heating element – barrel I

Requirement (parameter)	Value (feature)
Type	band heater
Power	800 W
Supply voltage	230 V AC
Working temperature / maximum temperature	300 °C / 450 °C
Insulation of a heating element	micanite
Surface load capacity	app. 4,5W/cm^2
Power cord integrated with the sensor	Yes, dł. 2-3 m, protective of heat
Connector type of cable exit	tangents, planar
Internal diameter of a heater element	ø100 mm
Width of a heater element	75 mm

Table 9. Basic technical requirements for heating element – coupler

Requirement (parameter)	Value (feature)
Type	band heater
Power	650 W
Supply voltage	230 V AC
Working temperature / maximum temperature	300 °C / 450 °C
Insulation of a heating element	micanite
Surface load capacity	app. 4,5W/cm^2
Power cord integrated with the sensor	Yes, dł. 2-3 m, protective of heat
Connector type of cable exit	tangents, planar
Internal diameter of a heater element	ø150 mm
Width of a heater element	40 mm

Table 10. Basic technical requirements for heating element – head I

Requirement (parameter)	Value (feature)
Type	flat heater
Power	650 W
Supply voltage	230 V AC
Working temperature / maximum temperature	300 °C / 450 °C
Insulation of a heating element	micanite
Surface load capacity	app. 4,5W/cm²
Power cord integrated with the sensor	Yes, dł. 2-3 m, protective of heat
Connector type of cable exit	axial, planar (bottom to the right side)
Length of a heater element	125 mm
Width of a heater element	130 mm

Table 11. Basic technical requirements for heating element – head II

Requirement (parameter)	Value (feature)
Type	flat heater
Power	650 W
Supply voltage	230 V AC
Working temperature / maximum temperature	300 °C / 450 °C
Insulation of a heating element	micanite
Surface load capacity	app. 4,5W/cm²
Power cord integrated with the sensor	Yes, dł. 2-3 m, protective of heat
Connector type of cable exit	axial, planar (bottom to the left side)
Length of a heater element	125 mm
Width of a heater element	130 mm

The main drive motor - selection of elements

The main motor of the extruder enables the achievement of appropriate mechanical parameters by the screw system and the achievement of appropriate properties by the plasticizing mixture. The following electrical motors were selected for the final stage of the drive element selection:

- Dyneo 1500 LSRPM 100L 6 IM2031 400V motor by Nidec Motor Corporation;
- TMW204LRA20UFR0001 motor by Parker Hannifin Corporation;
- DST2-135MO54W-017-5-A-DG-6-MTR-O-000 motor by Baumüller GmbH Corporation.

Preliminary technical parameters analysis (electrical and mechanical) of this electrical motors qualified them as devices useful and possible to be used in the extruder drive system.

Characteristics of the Dyneo 1500 LSRPM 100L 6 IM2031 400V motor by Nidec Motor Corporation

Motors type LSRPM - IP 55 are motors with a world-renowned reputation. The description of the basic features and the view of the engine are presented in Fig. 5. The electric motor, designated 1500 LSRPM 100L 6 IM2031 400V, selected from the Nidec Motor Corporation catalog [9], is characterized by the following technical parameters (based on the engine designations):

- 1500 - Speed rate (rpm),
- LSRPM - Aluminum alloy (IP55 protection),
- 100L - Frame size (mm)/ Housing designation and manufacturer code,
- 6 - Rated power in kW (6 kW),
- IM2101 - Mounting arrangements (horizontal shaft, feet on floor),
- 400V: Power supply.

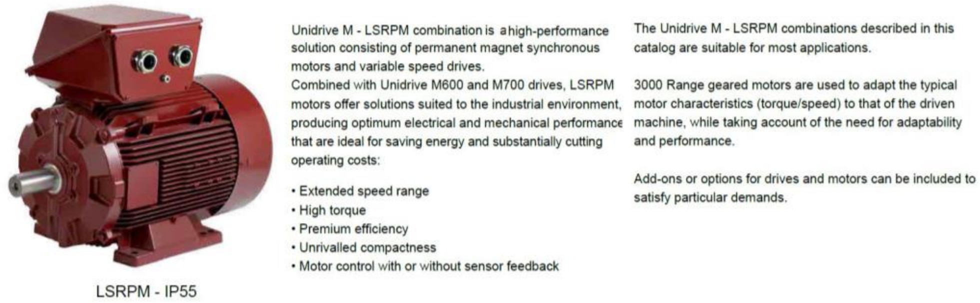

LSRPM - IP55

Unidrive M - LSRPM combination is a high-performance solution consisting of permanent magnet synchronous motors and variable speed drives.
Combined with Unidrive M600 and M700 drives, LSRPM motors offer solutions suited to the industrial environment, producing optimum electrical and mechanical performance that are ideal for saving energy and substantially cutting operating costs:

- Extended speed range
- High torque
- Premium efficiency
- Unrivalled compactness
- Motor control with or without sensor feedback

The Unidrive M - LSRPM combinations described in this catalog are suitable for most applications.

3000 Range geared motors are used to adapt the typical motor characteristics (torque/speed) to that of the driven machine, while taking account of the need for adaptability and performance.

Add-ons or options for drives and motors can be included to satisfy particular demands.

Fig. 5. LSRPM – IP55 motors - description of the basic features

Detailed catalog data of the LSRPM series motors (technical parameters, characteristics and geometrical dimensions) by Nidec Motor Corporation are presented in Fig. 6, Fig. 7 and Fig. 8.

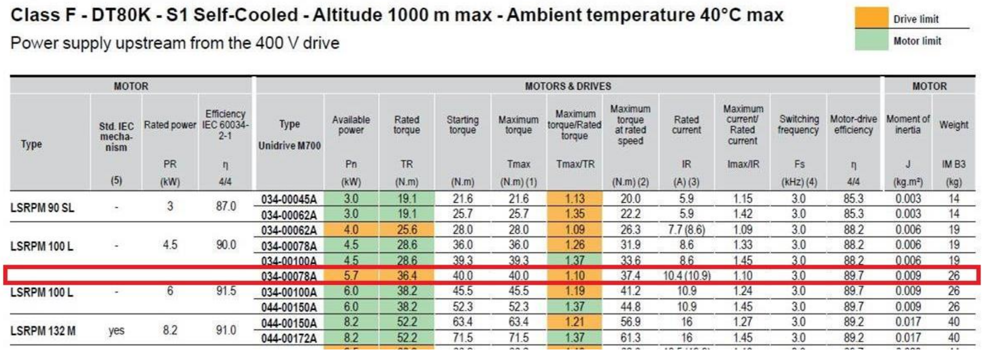

Class F - DT80K - S1 Self-Cooled - Altitude 1000 m max - Ambient temperature 40°C max

Power supply upstream from the 400 V drive

🟧 Drive limit
🟩 Motor limit

MOTOR				MOTORS & DRIVES											MOTOR	
Type	Std. IEC mecha-nism	Rated power	Efficiency IEC 60034-2-1	Type Unidrive M700	Available power	Rated torque	Starting torque	Maximum torque	Maximum torque/Rated torque	Maximum torque at rated speed	Rated current	Maximum current/ Rated current	Switching frequency	Motor-drive efficiency	Moment of inertia	Weight
		PR	η		Pn	TR		Tmax	Tmax/TR		IR	Imax/IR	Fs	η	J	IM B3
	(5)	(kW)	4/4		(kW)	(N.m)	(N.m)	(N.m) (1)		(N.m) (2)	(A) (3)		(kHz) (4)	4/4	(kg.m²)	(kg)
LSRPM 90 SL	-	3	87.0	034-00045A	3.0	19.1	21.6	21.6	1.13	20.0	5.9	1.15	3.0	85.3	0.003	14
				034-00062A	3.0	19.1	25.7	25.7	1.35	22.2	5.9	1.42	3.0	85.3	0.003	14
LSRPM 100 L	-	4.5	90.0	034-00062A	4.0	25.6	28.0	28.0	1.09	26.3	7.7 (8.6)	1.09	3.0	88.2	0.006	19
				034-00078A	4.5	28.6	36.0	36.0	1.26	31.9	8.6	1.33	3.0	88.2	0.006	19
				034-00100A	4.5	28.6	39.3	39.3	1.37	33.6	8.6	1.45	3.0	88.2	0.006	19
LSRPM 100 L	-	6	91.5	034-00078A	5.7	36.4	40.0	40.0	1.10	37.4	10.4 (10.9)	1.10	3.0	89.7	0.009	26
				034-00100A	6.0	38.2	45.5	45.5	1.19	41.2	10.9	1.24	3.0	89.7	0.009	26
				044-00150A	6.0	38.2	52.3	52.3	1.37	44.8	10.9	1.45	3.0	89.7	0.009	26
LSRPM 132 M	yes	8.2	91.0	044-00150A	8.2	52.2	63.4	63.4	1.21	56.9	16	1.27	3.0	89.2	0.017	40
				044-00172A	8.2	52.2	71.5	71.5	1.37	61.3	16	1.45	3.0	89.2	0.017	40

Fig. 6. Basic technical data of the LSRPM series motors

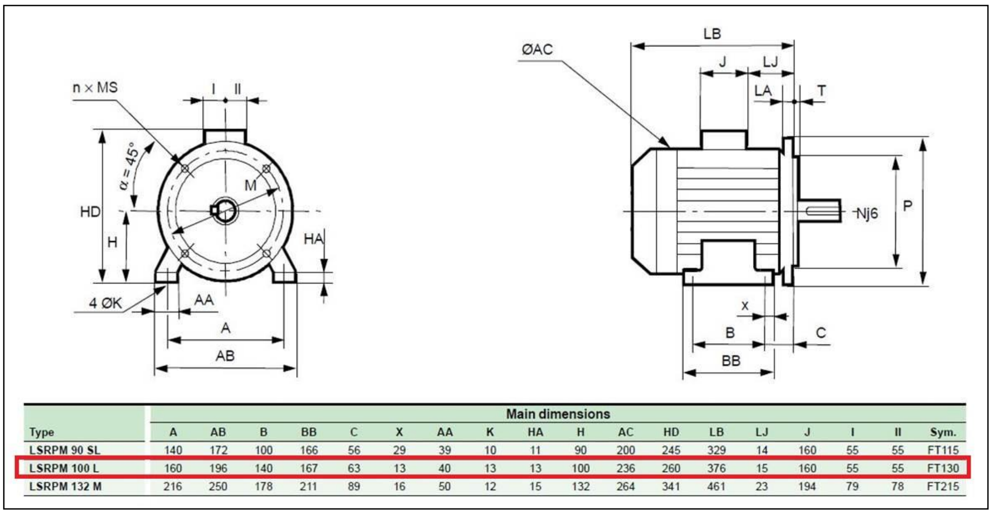

Type	Main dimensions																
	A	AB	B	BB	C	X	AA	K	HA	H	AC	HD	LB	LJ	J	I	II	Sym.
LSRPM 90 SL	140	172	100	166	56	29	39	10	11	90	200	245	329	14	160	55	55	FT115
LSRPM 100 L	160	196	140	167	63	13	40	13	13	100	236	260	376	15	160	55	55	FT130
LSRPM 132 M	216	250	178	211	89	16	50	12	15	132	264	341	461	23	194	79	78	FT215

Fig. 7. Dimensions of the LSRPM series motors

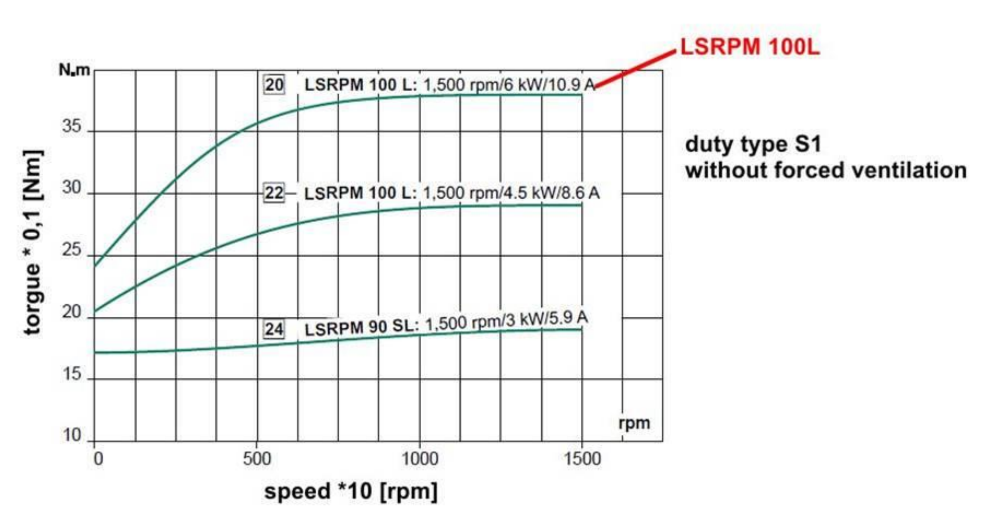

Fig. 8. Mechanical characteristics of the LSRPM series motors

Additional elements of LSRPM motors equipment are shown in Fig. 9 (encoders), Fig. 10 (servo drivers) and Fig. 11 (thermal protection).

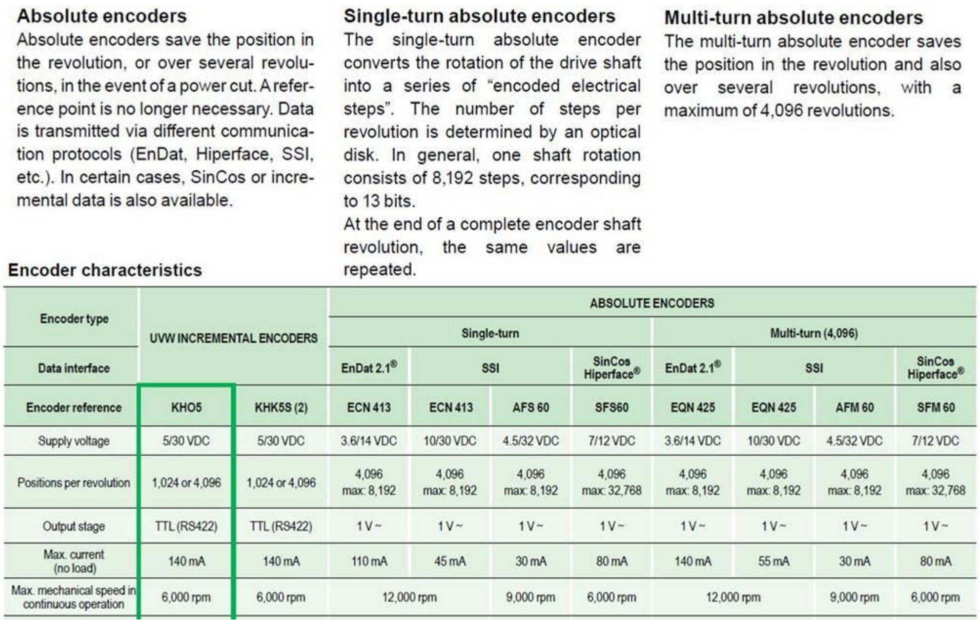

Absolute encoders

Absolute encoders save the position in the revolution, or over several revolutions, in the event of a power cut. A reference point is no longer necessary. Data is transmitted via different communication protocols (EnDat, Hiperface, SSI, etc.). In certain cases, SinCos or incremental data is also available.

Single-turn absolute encoders

The single-turn absolute encoder converts the rotation of the drive shaft into a series of "encoded electrical steps". The number of steps per revolution is determined by an optical disk. In general, one shaft rotation consists of 8,192 steps, corresponding to 13 bits.

At the end of a complete encoder shaft revolution, the same values are repeated.

Multi-turn absolute encoders

The multi-turn absolute encoder saves the position in the revolution and also over several revolutions, with a maximum of 4,096 revolutions.

Encoder characteristics

Encoder type	UVW INCREMENTAL ENCODERS		ABSOLUTE ENCODERS							
			Single-turn				Multi-turn (4,096)			
Data interface			EnDat 2.1®	SSI		SinCos Hiperface®	EnDat 2.1®	SSI		SinCos Hiperface®
Encoder reference	KHO5	KHK5S (2)	ECN 413	ECN 413	AFS 60	SFS60	EQN 425	EQN 425	AFM 60	SFM 60
Supply voltage	5/30 VDC	5/30 VDC	3.6/14 VDC	10/30 VDC	4.5/32 VDC	7/12 VDC	3.6/14 VDC	10/30 VDC	4.5/32 VDC	7/12 VDC
Positions per revolution	1,024 or 4,096	1,024 or 4,096	4,096 max: 8,192	4,096 max: 8,192	4,096 max: 8,192	4,096 max: 32,768	4,096 max: 8,192	4,096 max: 8,192	4,096 max: 8,192	4,096 max: 32,768
Output stage	TTL (RS422)	TTL (RS422)	1 V ~	1 V ~	1 V ~	1 V ~	1 V ~	1 V ~	1 V ~	1 V ~
Max. current (no load)	140 mA	140 mA	110 mA	45 mA	30 mA	80 mA	140 mA	55 mA	30 mA	80 mA
Max. mechanical speed in continuous operation	6,000 rpm	6,000 rpm	12,000 rpm		9,000 rpm	6,000 rpm	12,000 rpm		9,000 rpm	6,000 rpm

Fig. 9. Characteristics of the encoder for LSRPM series motors

Unidrive M is a range of variable speed drives designed for controlling induction, servo or synchronous motors. The Unidrive M700 model can handle Sensorless control but it can in particular be used to control LSRPM motors in closed loop mode with exceptional performance, and guarantees maximum machine productivity thanks to its advanced functions. Unidrive M7000 034-00078A is dedicated to LSRPM 100L motor.

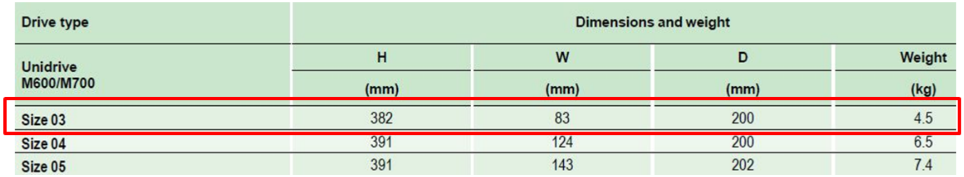

Drive type	Dimensions and weight			
Unidrive M600/M700	H (mm)	W (mm)	D (mm)	Weight (kg)
Size 03	382	83	200	4.5
Size 04	391	124	200	6.5
Size 05	391	143	202	7.4

Fig. 10. Characteristics of servo drivers for LSRPM series motors

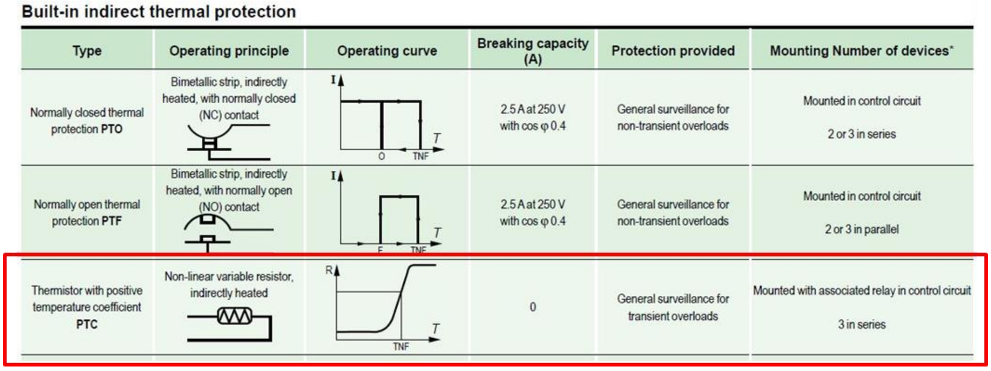

Built-in indirect thermal protection

Type	Operating principle	Operating curve	Breaking capacity (A)	Protection provided	Mounting Number of devices*
Normally closed thermal protection **PTO**	Bimetallic strip, indirectly heated, with normally closed (NC) contact	I T O TNF	2.5 A at 250 V with cos φ 0.4	General surveillance for non-transient overloads	Mounted in control circuit 2 or 3 in series
Normally open thermal protection **PTF**	Bimetallic strip, indirectly heated, with normally open (NO) contact	I T F TNF	2.5 A at 250 V with cos φ 0.4	General surveillance for non-transient overloads	Mounted in control circuit 2 or 3 in parallel
Thermistor with positive temperature coefficient **PTC**	Non-linear variable resistor, indirectly heated	R T TNF	0	General surveillance for transient overloads	Mounted with associated relay in control circuit 3 in series

Fig. 11. Characteristics of thermal protections for motors of the LSRPM series

Characteristics of the TMW204LRA20UFR0001 motor by Parker Hannifin Corporation

TM Torque Motors Series are electrical motors with an established reputation on the market. The description of the basic features and the view of the engine are presented in Fig. 12. The engine marked TMW204LRA20UFR0001 selected from the Parker catalog [10] is characterized by the following technical parameters (based on engine designations):

- TM - Product Series, Torque motor;
- W - Cooling Method, W – Water;
- 20 - Frame Size, Shaft Height, 20 = 200 mm;
- 4LR - Type of motor characteristics, Winding Type, 4LR = 175 rpm;
- A - Feedback Sensor, a = remote Resolver;
- 20 - Bearing Option, 20 = Thurst Bearing;
- U - Terminal Box Option, U= Terminal Box on Top;
- FR – F - Front side extrusion screw cooling; R - Unused character;
- 0 - Shaft End, 0 = Hollow shaft with keyway;
- 001 - Mechanical Interface: 001 - By feet and by flange.

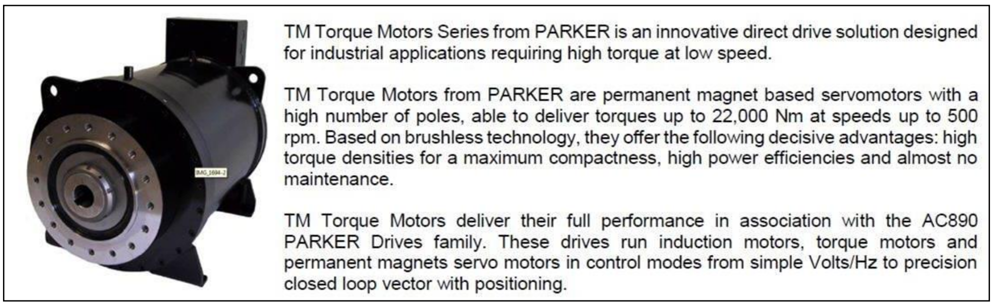

TM Torque Motors Series from PARKER is an innovative direct drive solution designed for industrial applications requiring high torque at low speed.

TM Torque Motors from PARKER are permanent magnet based servomotors with a high number of poles, able to deliver torques up to 22,000 Nm at speeds up to 500 rpm. Based on brushless technology, they offer the following decisive advantages: high torque densities for a maximum compactness, high power efficiencies and almost no maintenance.

TM Torque Motors deliver their full performance in association with the AC890 PARKER Drives family. These drives run induction motors, torque motors and permanent magnets servo motors in control modes from simple Volts/Hz to precision closed loop vector with positioning.

Fig. 12. TM series from Parker - description of the basic features

Detailed catalog data of Parker TM series motor (technical parameters, characteristics and geometrical dimensions) are presented in Fig. 13, Fig. 14 and Fig. 15.

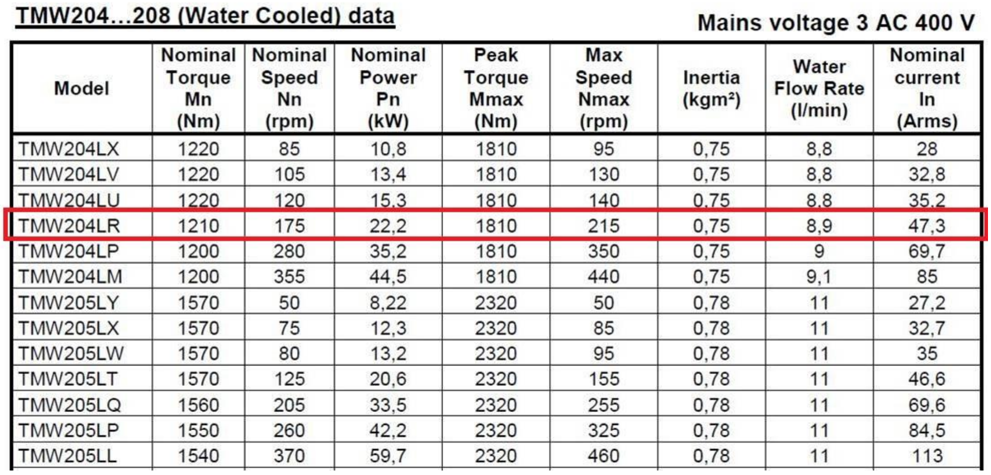

TMW204…208 (Water Cooled) data

Mains voltage 3 AC 400 V

Model	Nominal Torque Mn (Nm)	Nominal Speed Nn (rpm)	Nominal Power Pn (kW)	Peak Torque Mmax (Nm)	Max Speed Nmax (rpm)	Inertia (kgm²)	Water Flow Rate (l/min)	Nominal current In (Arms)
TMW204LX	1220	85	10,8	1810	95	0,75	8,8	28
TMW204LV	1220	105	13,4	1810	130	0,75	8,8	32,8
TMW204LU	1220	120	15,3	1810	140	0,75	8,8	35,2
TMW204LR	1210	175	22,2	1810	215	0,75	8,9	47,3
TMW204LP	1200	280	35,2	1810	350	0,75	9	69,7
TMW204LM	1200	355	44,5	1810	440	0,75	9,1	85
TMW205LY	1570	50	8,22	2320	50	0,78	11	27,2
TMW205LX	1570	75	12,3	2320	85	0,78	11	32,7
TMW205LW	1570	80	13,2	2320	95	0,78	11	35
TMW205LT	1570	125	20,6	2320	155	0,78	11	46,6
TMW205LQ	1560	205	33,5	2320	255	0,78	11	69,6
TMW205LP	1550	260	42,2	2320	325	0,78	11	84,5
TMW205LL	1540	370	59,7	2320	460	0,78	11	113

Fig. 13. Basic technical data of TM series motors

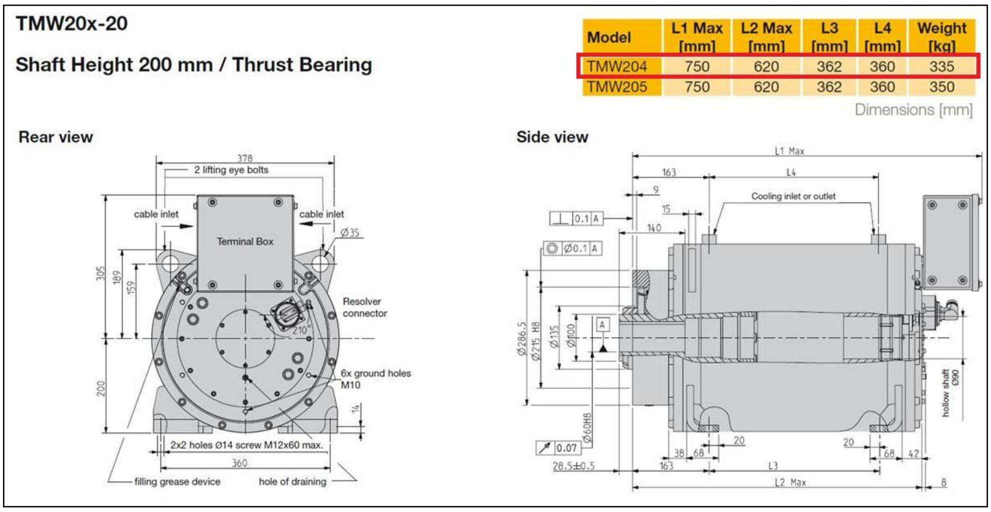

TMW20x-20

Shaft Height 200 mm / Thrust Bearing

Model	L1 Max [mm]	L2 Max [mm]	L3 [mm]	L4 [mm]	Weight [kg]
TMW204	750	620	362	360	335
TMW205	750	620	362	360	350

Dimensions [mm]

Rear view
378
2 lifting eye bolts
cable inlet
cable inlet
Terminal Box
Ø35
305
189
159
Resolver connector
210°
200
6x ground holes M10
14
2x2 holes Ø14 screw M12x60 max.
360
filling grease device
hole of draining
Side view
L1 Max
163
L4
9
Cooling inlet or outlet
15
0.1 A
140
Ø0.1 A
Ø286.5
Ø215 H8
Ø135
Ø100
A
Ø60H8
0.07
hollow shaft Ø90
20
20
38
68
68
42
28.5±0.5
163
L3
L2 Max
8

Fig. 14. Dimensions of TM series motors

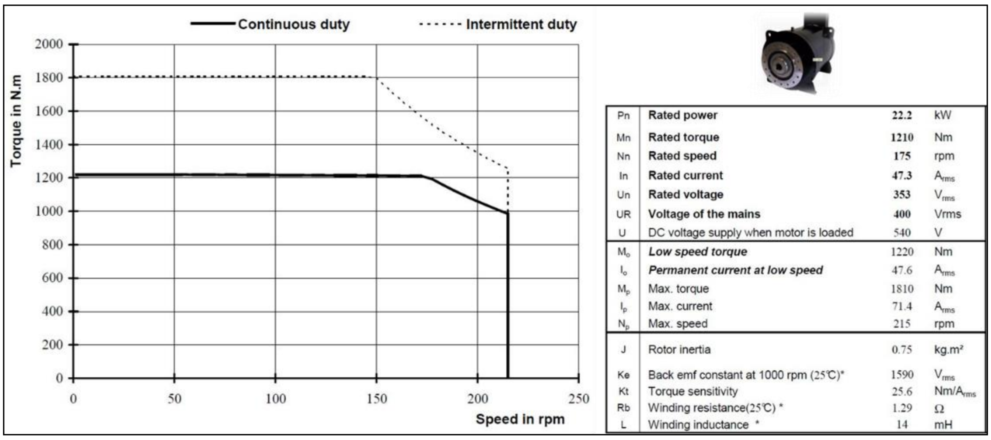

Pn	**Rated power**	**22.2**	kW
Mn	**Rated torque**	**1210**	Nm
Nn	**Rated speed**	**175**	rpm
In	**Rated current**	**47.3**	A_{rms}
Un	**Rated voltage**	**353**	V_{rms}
UR	**Voltage of the mains**	**400**	Vrms
U	DC voltage supply when motor is loaded	540	V
M_o	***Low speed torque***	1220	Nm
I_o	***Permanent current at low speed***	47.6	A_{rms}
M_p	Max. torque	1810	Nm
I_p	Max. current	71.4	A_{rms}
N_p	Max. speed	215	rpm
J	Rotor inertia	0.75	kg.m²
Ke	Back emf constant at 1000 rpm (25℃)*	1590	V_{rms}
Kt	Torque sensitivity	25.6	Nm/A_{rms}
Rb	Winding resistance(25℃) *	1.29	Ω
L	Winding inductance *	14	mH

Fig. 15. Mechanical characteristics of TM series motors

Additional elements of TM motors equipment are presented in Fig. 16 (resolver), Fig. 17 (servo drivers) and Fig. 18 (thermal protection).

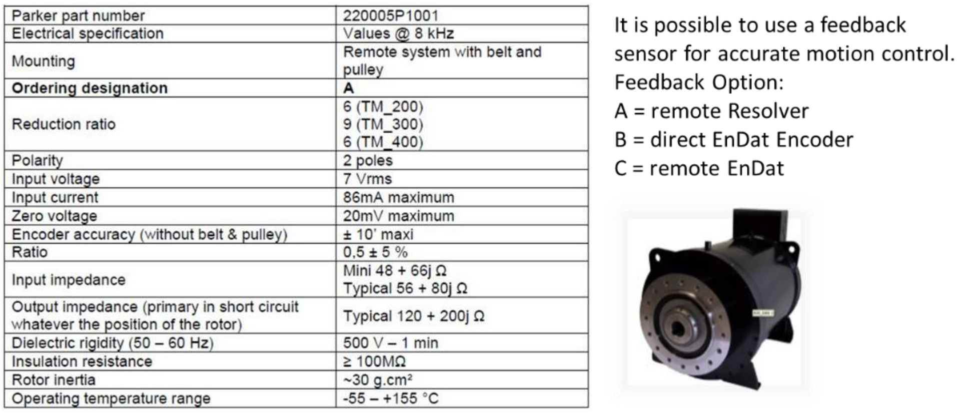

Parker part number	220005P1001
Electrical specification	Values @ 8 kHz
Mounting	Remote system with belt and pulley
Ordering designation	**A**
Reduction ratio	6 (TM_200) 9 (TM_300) 6 (TM_400)
Polarity	2 poles
Input voltage	7 Vrms
Input current	86mA maximum
Zero voltage	20mV maximum
Encoder accuracy (without belt & pulley)	± 10' maxi
Ratio	0,5 ± 5 %
Input impedance	Mini 48 + 66j Ω Typical 56 + 80j Ω
Output impedance (primary in short circuit whatever the position of the rotor)	Typical 120 + 200j Ω
Dielectric rigidity (50 – 60 Hz)	500 V – 1 min
Insulation resistance	≥ 100MΩ
Rotor inertia	~30 g.cm²
Operating temperature range	-55 – +155 °C

It is possible to use a feedback sensor for accurate motion control.
Feedback Option:
A = remote Resolver
B = direct EnDat Encoder
C = remote EnDat

Fig. 16. Characteristics of a resolver for TM series motors

Compax3 servo drive platform is offering a range of high performance single and multi-axis servo drive modules, as well as hydraulic controllers. The 'C3S' series of low/medium power stand-alone single-axis servo drives and servo drive/controllers offer output power ratings from 1 to 25kVA, with input power supply options of 1/3*230VAC to 3*480VAC. Compax3 H050 V4 servo drive can be used with TMW204LRA20UFR0001 motor.

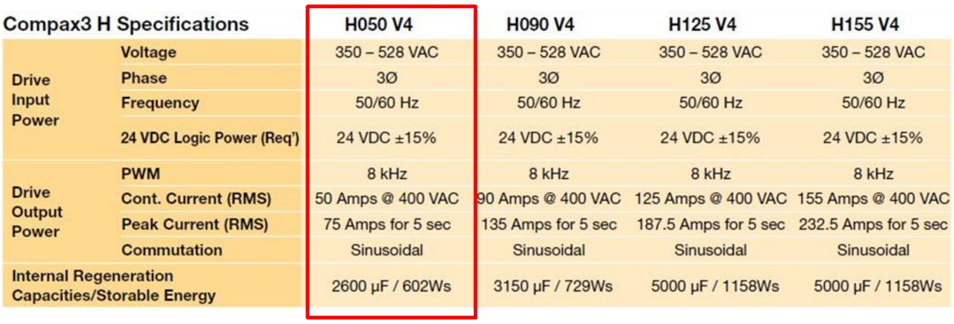

Compax3 H Specifications		H050 V4	H090 V4	H125 V4	H155 V4
Drive Input Power	Voltage	350 – 528 VAC	350 – 528 VAC	350 – 528 VAC	350 – 528 VAC
	Phase	3Ø	3Ø	3Ø	3Ø
	Frequency	50/60 Hz	50/60 Hz	50/60 Hz	50/60 Hz
	24 VDC Logic Power (Req')	24 VDC ±15%	24 VDC ±15%	24 VDC ±15%	24 VDC ±15%
Drive Output Power	PWM	8 kHz	8 kHz	8 kHz	8 kHz
	Cont. Current (RMS)	50 Amps @ 400 VAC	90 Amps @ 400 VAC	125 Amps @ 400 VAC	155 Amps @ 400 VAC
	Peak Current (RMS)	75 Amps for 5 sec	135 Amps for 5 sec	187.5 Amps for 5 sec	232.5 Amps for 5 sec
	Commutation	Sinusoidal	Sinusoidal	Sinusoidal	Sinusoidal
Internal Regeneration Capacities/Storable Energy		2600 µF / 602Ws	3150 µF / 729Ws	5000 µF / 1158Ws	5000 µF / 1158Ws

Fig. 17. Characteristics of servo drivers for TM series motors

Protection against thermal overloading of the motor is provided by 2 x 3 PTC thermistors and one KTY temperature sensor (and one more in case of KTY failure) built into the stator winding as standard. The thermal sensors, due to their thermal inertia, are unable to follow very fast winding temperature variations. They achieve their thermal steady state after a few minutes. Two thermal probes (PTC thermistors) fitted in the servomotor winding trip the electronic system at 140° and 150° +/- 5°C.

Motor temperature can also be continuously monitored by the drive using a KTY 84-130 thermal sensor built in to the stator winding. KTY sensors are semiconductor sensors that change their resistance according to an approximately linear characteristic. The required temperature limits for alarm and tripping can be set in the drive.

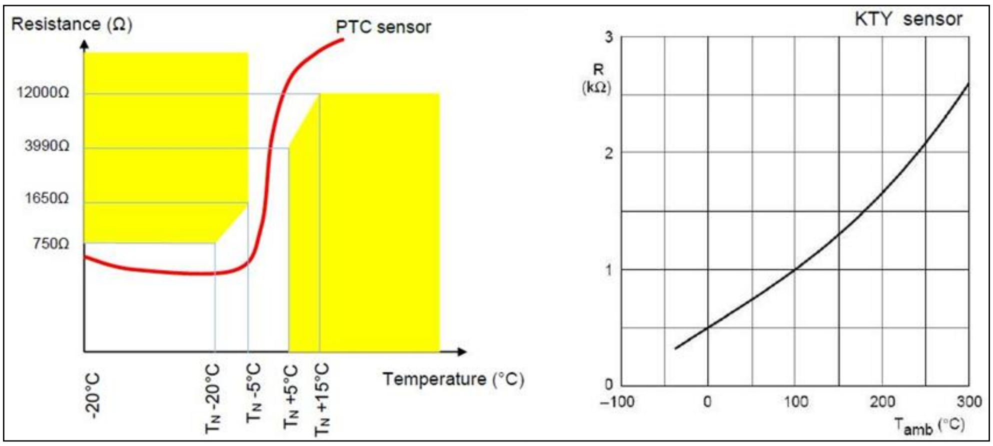

Fig. 18. Thermal protections characteristics for TM series motors

Characteristics of the DST2-135MO54W-017-5-A-DG-6-MTR-O-000 motor by Baumüller GmbH Corporation

DST2 engines are electric motors of one of the most important engine manufacturers in the world. The description of the basic features and the view of the engine are presented in Fig. 19. The engine selected from the Baumüller catalog [11], with the designation DST2-135MO54W-017-5-A-DG-6-MTR-O-000, is characterized by the following technical parameters (on the engine markings):

- DST2 - synchronous torque motor from the DST2 series;
- 135 - Overall size;
- MO - Overall length;
- 54 - Degree of protection IP54;
- W - Cooling type, W - Water cooling;
- 017 - Nominal speed class, 017 - 175 rpm;
- 5 – Voltage Uzk_ DC, 5 = 540 V;
- A - Encoder type, a – Resolver;
- D - Shaft type, D - Thrust bearing;
- G - Shaft options, G - Blind bore with key;
- 6 - Type of construction, 6 - IM B34 - Foot D and N side;
- M - Main connection type: M – terminal box with PT1000;
- T - Position of main connection, T – Top;
- R - Main connection outlet, R - Right with D-side facing towards shaft end;
- O - Relubrication, O - No relubrication;
- 000 - Special design, 000 - No special design.

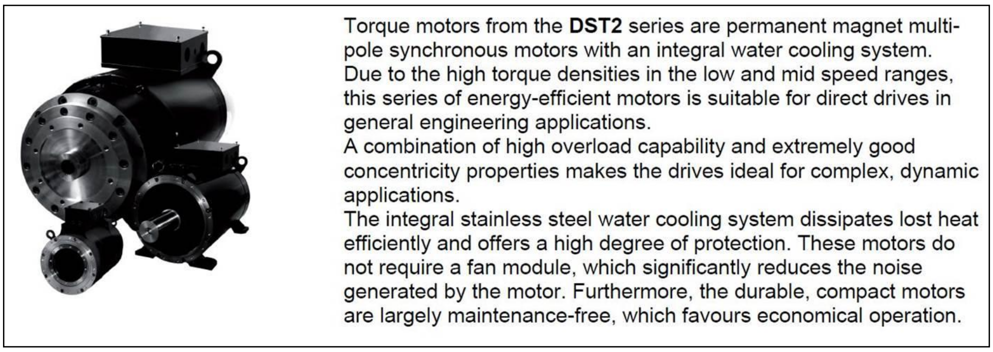

Torque motors from the **DST2** series are permanent magnet multi-pole synchronous motors with an integral water cooling system.
Due to the high torque densities in the low and mid speed ranges, this series of energy-efficient motors is suitable for direct drives in general engineering applications.
A combination of high overload capability and extremely good concentricity properties makes the drives ideal for complex, dynamic applications.
The integral stainless steel water cooling system dissipates lost heat efficiently and offers a high degree of protection. These motors do not require a fan module, which significantly reduces the noise generated by the motor. Furthermore, the durable, compact motors are largely maintenance-free, which favours economical operation.

Fig. 19. DST2 series from Baumüller - description of the basic features

Detailed catalog data of Baumüller DST2 series motors (technical parameters, characteristics and geometrical dimensions) are presented in Fig. 20, Fig. 21 and Fig. 22.

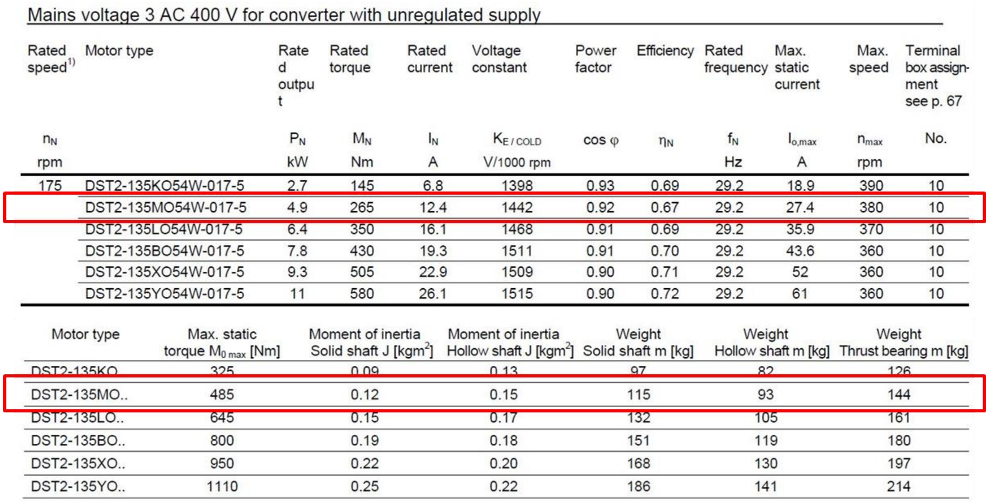

Mains voltage 3 AC 400 V for converter with unregulated supply

Rated speed[1)]	Motor type	Rated output	Rated torque	Rated current	Voltage constant	Power factor	Efficiency	Rated frequency	Max. static current	Max. speed	Terminal box assignment see p. 67
n_N		P_N	M_N	I_N	$K_{E / COLD}$	cos φ	η_N	f_N	$I_{o,max}$	n_{max}	No.
rpm		kW	Nm	A	V/1000 rpm			Hz	A	rpm	
175	DST2-135KO54W-017-5	2.7	145	6.8	1398	0.93	0.69	29.2	18.9	390	10
	DST2-135MO54W-017-5	4.9	265	12.4	1442	0.92	0.67	29.2	27.4	380	10
	DST2-135LO54W-017-5	6.4	350	16.1	1468	0.91	0.69	29.2	35.9	370	10
	DST2-135BO54W-017-5	7.8	430	19.3	1511	0.91	0.70	29.2	43.6	360	10
	DST2-135XO54W-017-5	9.3	505	22.9	1509	0.90	0.71	29.2	52	360	10
	DST2-135YO54W-017-5	11	580	26.1	1515	0.90	0.72	29.2	61	360	10

Motor type	Max. static torque $M_{0\,max}$ [Nm]	Moment of inertia Solid shaft J [kgm^2]	Moment of inertia Hollow shaft J [kgm^2]	Weight Solid shaft m [kg]	Weight Hollow shaft m [kg]	Weight Thrust bearing m [kg]
DST2-135KO..	325	0.09	0.13	97	82	126
DST2-135MO..	485	0.12	0.15	115	93	144
DST2-135LO..	645	0.15	0.17	132	105	161
DST2-135BO..	800	0.19	0.18	151	119	180
DST2-135XO..	950	0.22	0.20	168	130	197
DST2-135YO..	1110	0.25	0.22	186	141	214

Fig. 20. Basic technical data of the DST2 series motors

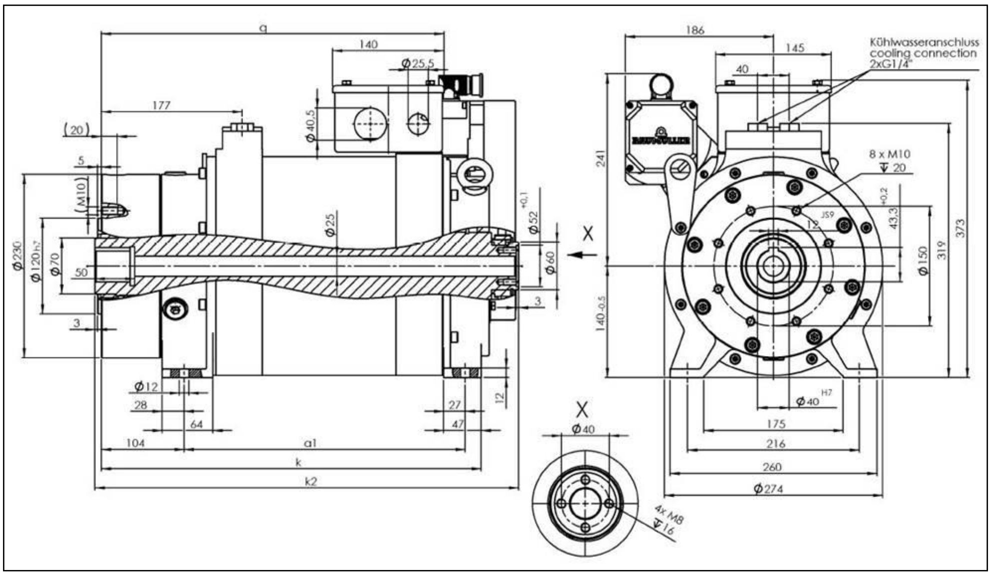
q
140
Ø25,5
177
Ø40,5
(20)
5
(M10)
Ø230
Ø120h7
Ø70
50
3
Ø25
Ø52 +0,1
Ø60
3
X
Ø12
28
64
104
a1
k
k2
27
47
12
186
145
40
Kühlwasseranschluss
cooling connection
2xG1/4"
241
8 x M10
20
JS9
12
43,3 +0,2
Ø150
319
373
140 -0,5
Ø40 H7
175
216
260
Ø274
X
Ø40
4x M8
16

Fig. 21. Dimensions of the DST2 series motors

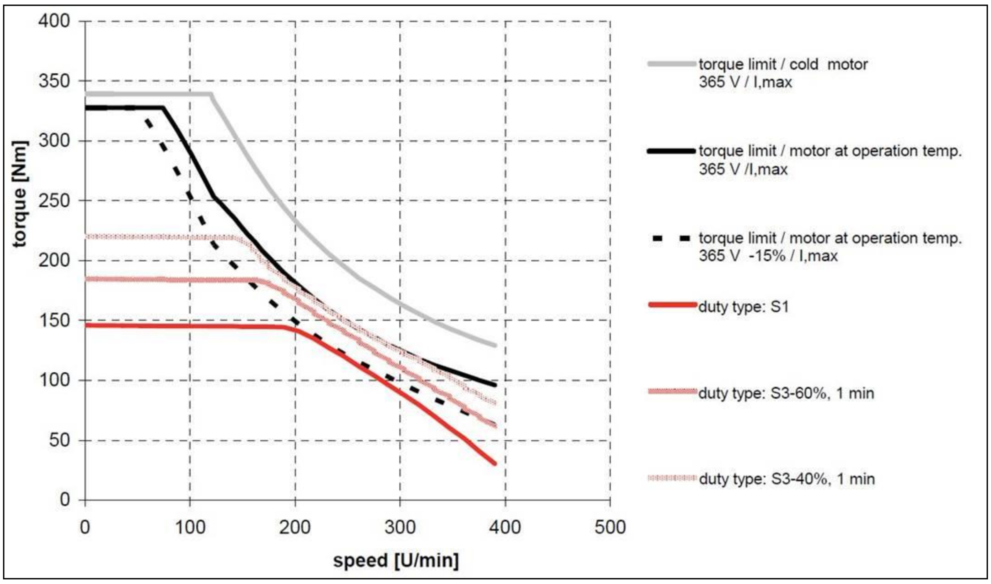

Fig. 22. Mechanical characteristics of DST2 series motors

Additional elements of equipment for DST2 motors are shown in Fig. 23 (resolver), Fig. 24 (servo drivers) and Fig. 25 (thermal protection).

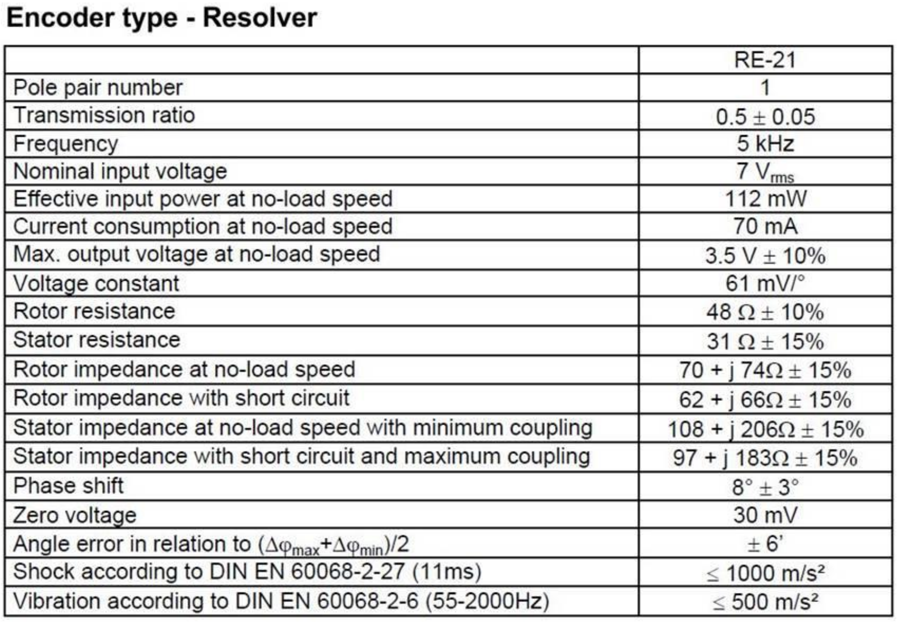

Encoder type - Resolver

	RE-21
Pole pair number	1
Transmission ratio	0.5 ± 0.05
Frequency	5 kHz
Nominal input voltage	$7\ V_{rms}$
Effective input power at no-load speed	112 mW
Current consumption at no-load speed	70 mA
Max. output voltage at no-load speed	3.5 V ± 10%
Voltage constant	61 mV/°
Rotor resistance	48 Ω ± 10%
Stator resistance	31 Ω ± 15%
Rotor impedance at no-load speed	70 + j 74Ω ± 15%
Rotor impedance with short circuit	62 + j 66Ω ± 15%
Stator impedance at no-load speed with minimum coupling	108 + j 206Ω ± 15%
Stator impedance with short circuit and maximum coupling	97 + j 183Ω ± 15%
Phase shift	8° ± 3°
Zero voltage	30 mV
Angle error in relation to $(\Delta\varphi_{max}+\Delta\varphi_{min})/2$	± 6’
Shock according to DIN EN 60068-2-27 (11ms)	≤ 1000 m/s²
Vibration according to DIN EN 60068-2-6 (55-2000Hz)	≤ 500 m/s²

Fig. 23. Characteristics of the encoder for motors of the DST2 series

BmaXX 5500 controller covers a power range of 1.1 kW to 315 kW. All devices contain integrated rectifiers, DC link capacities and power inverters. The 5000 side-by-side converters have been extended to mono units in the 5500 series. Increased safety functions, such as SLS (safely limited speed) and SLP (safely limited position), can be integrated into the servo controller.

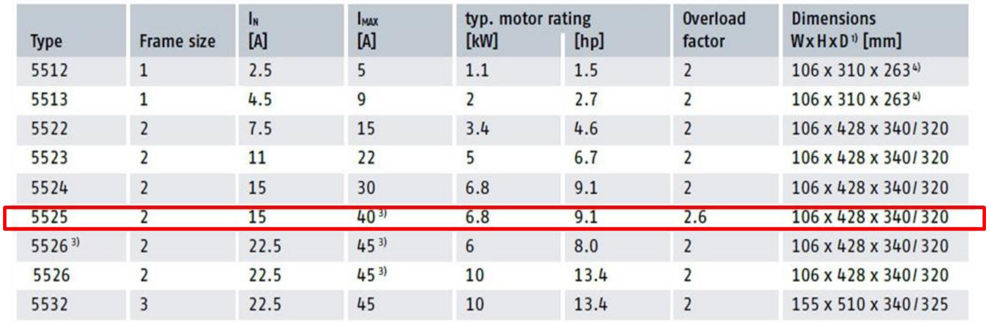

Type	Frame size	I_N [A]	I_{MAX} [A]	typ. motor rating [kW]	[hp]	Overload factor	Dimensions W x H x D[1] [mm]
5512	1	2.5	5	1.1	1.5	2	106 x 310 x 263[4]
5513	1	4.5	9	2	2.7	2	106 x 310 x 263[4]
5522	2	7.5	15	3.4	4.6	2	106 x 428 x 340/ 320
5523	2	11	22	5	6.7	2	106 x 428 x 340/ 320
5524	2	15	30	6.8	9.1	2	106 x 428 x 340/ 320
5525	2	15	40[3]	6.8	9.1	2.6	106 x 428 x 340/ 320
5526[3]	2	22.5	45[3]	6	8.0	2	106 x 428 x 340/ 320
5526	2	22.5	45[3]	10	13.4	2	106 x 428 x 340/ 320
5532	3	22.5	45	10	13.4	2	155 x 510 x 340/ 325

Fig. 24. Characteristics of servo drivers for DST2 series motors

A temperature sensor for performing evaluations in the motor controller is fitted to the stator winding on all motors as standard. Additional PTCs or heat monitors can be installed on request and are connected to the terminal box. The PT1000 temperature sensor monitors the motor temperature continuously.

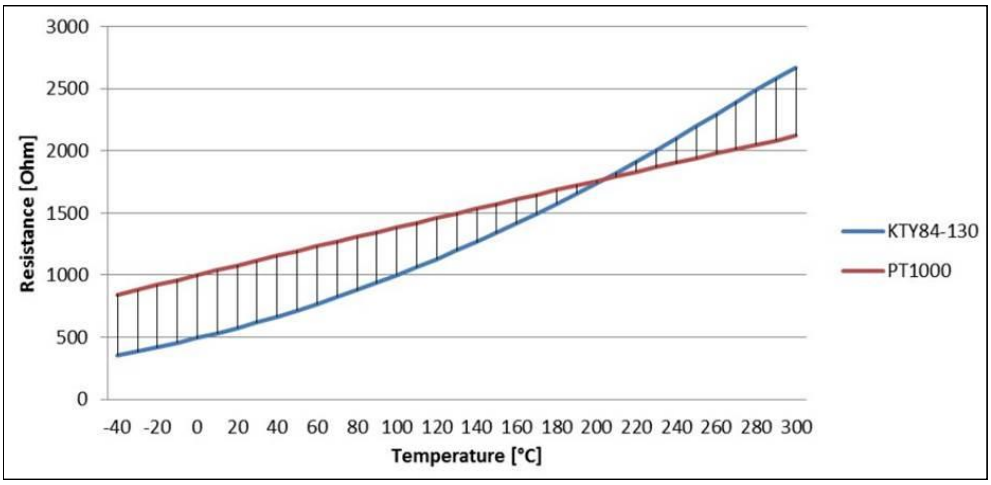

Fig. 25. Thermal protection characteristics for TM series motors

The main drive motor - summary

Based on the available information, the engine DST2-135MO54W-017-5-A-DG-6-MTR-O-000 motor by Baumüller GmbH Corporation was selected as the most suitable device. The results of the data analysis and the comparison of the parameters of the motors are shown in Table 12 and Table 13. According to the data presented, the motor has a suitable power, current, speed and torque range.

Table 12. Main drive motor – comparison of selected parameters

Requirement (parameter)	Value (feature)	Model of motor		
		Dyneo 1500 LSRPM 100L 6 IM2031 400V Nidec Motor Corporation	TMW204LRA20UFR0001 Parker Hannifin Corporation	DST2-135MO54W-017-5-A-DG-6-MTR-O-000 Baumüller GmbH
Power supply	3 phase AC	3 phase AC	3 phase AC	3 phase AC
Voltage value	3 x 400 V	3 x 400 V	3 x 400 V	3 x 400 V
Torque	constant torque	constant torque	constant torque	constant torque
Preferred motor type	synchronous torque motor	synchronous torque motor	synchronous torque motor	synchronous torque motor
Nominal (rated) torque	≥ 265 Nm	36.4 (gearbox required)	1210	265
Starting torque [Nm]		40.0 (gearbox required)	1810	485
Form of characteristic curve	Flat	„Soft" at low speed	„Flat" at low speed	„Flat" at low speed
Speed control	up to 200 rpm	up to 200 and more with gearbox and Unidrive M7000 034-00078A controller	up to 215 rpm via Compax3 H050 V4 servo drive	up to 380 rpm via Bma5525 controller
Nominal (rated) power	≈ 5,0 kW	6.0	22.2	4.9
Nominal (rated) current [A]		10.4	47.3	12.4

Table 13. Main drive motor – the selection summary

Requirement (parameter)	Value (feature)	Model of motor		
		Dyneo 1500 LSRPM 100L 6 IM2031 400V Nidec Motor Corporation	TMW204LRA20UFR0001 Parker Hannifin Corporation	DST2-135MO54W-017-5-A-DG-6-MTR-O-000 Baumüller GmbH
Efficiency [-]		0.86 (with gearbox)	depends on temperature	0.67
Temperature inspection	built-in	PT1000 temperature sensor (standard)	PTC thermistors and one KTY sensor (standard)	PT1000 temperature sensor (standard)
Preferred cooling system	water	air cooling	water cooling	water cooling
Summary		- correct rated power range, - correct rated current, - proper temperature inspection, - gearbox required to obtain the rotational speed, - gearbox required to obtain the required torque, - "soft" characteristic curve, - air cooling dependent on the temperature of the ambient air	- oversized rated power range, - oversized rated current, - proper temperature inspection, - correct rotational speed, - correct torque, - "flat" characteristic curve, - water cooling (easy controlled by the fluid flow value)	- correct rated power range, - correct rated current, - proper temperature inspection, - correct rotational speed, - correct torque, - "flat" characteristic curve, - water cooling (easy controlled by the fluid flow value)

The rotary sleeve drive motor - selection of elements

The extruder barrel sleeve motor enables the extruder barrel to achieve the appropriate mechanical parameters.

The most common electric motors are three-phase induction motors. The widespread use of three-phase induction motors is due to their: simple construction, high reliability and low production costs. Typical rotational speed of synchronous motors is about 2800, 1400, 950, 700 rpm.

The selection of the electric motor was made on the basis of the technical data of the real gearbox presented later in this study.

The following electrical motors were selected for the final stage of the drive element selection:

- TCA-1 112M-4 by TEC Electric Motors Ltd.;
- T112A by Neri Motori S.R.L.;
- CHT 112 M4 B5 IE2 4.0 KW + 3xPTC by CHIARAVALLI.

Preliminary technical parameters analysis (electrical and mechanical) of electrical motors qualified them as devices useful and possible to be used in the extruder drive system.

Characteristics of the TCA-1 112M-4 motor by TEC Electric Motors Ltd

TCA type motors are motors with an internationally recognized reputation. The description of the basic features and the view of the engine are presented in Fig. 26 and Fig. 27. The motor with the designation 1 TCA-1 112M-4 selected from the TEC Electric Motors Ltd. catalog [12] is characterized by the following technical parameters (based on the engine designations):

- TC - manufacturer name, TC=TEC Electric Motors,
- A - Aluminium Housing Three-Phase Multi-Mount Asynchronous Motor,
- 1 - efficiency class for IEC line motors 1=IE1,
- 112M – type/model of motor (mounting dimension),
- 4 - type of motor (number of poles).

TEC® "ECOL" Motors

FEATURES

- Energy savings, high efficiency
- High starting torque, lower starting current
- Versatile and easy to modify design adapts to a variety of applications
- Option of integrated or removable feet
- Option of aluminum housing up to frame size 200
- Option of terminal box location (top, left or right)
- Full use of the magnetization properties of cold rolled silicone steel in which the stator laminations are magnetized evenly to reduce temperature rise

APPLICATIONS

- Pumps
- Waste water treatment plants
- Air compressors, fans
- Gear reducers and power transmission
- Pulp and paper mills
- Steel mill
- Conveyors, elevators
- Material handling equipment
- Agricultural application
- Mining equipment
- Hydraulic equipment

Fig. 26. TCA motors - description of the basic features

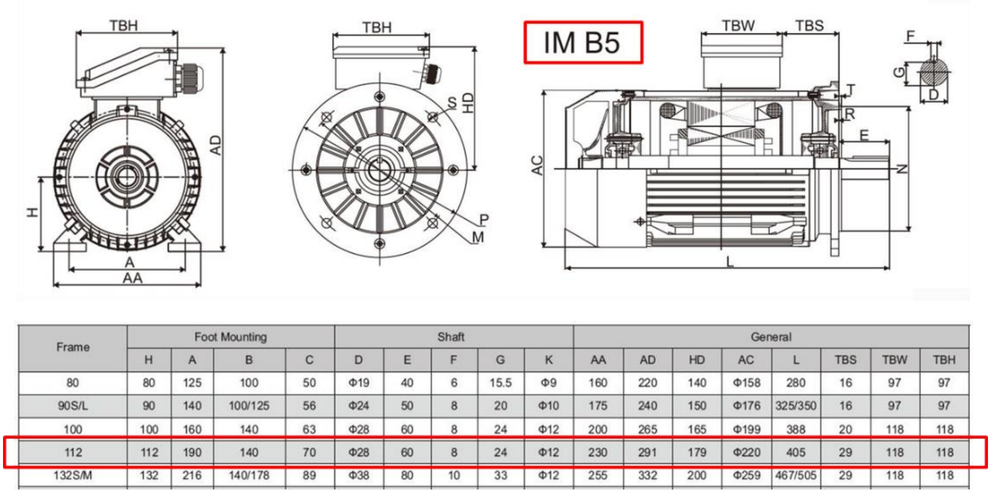

Frame	Foot Mounting				Shaft					General							
	H	A	B	C	D	E	F	G	K	AA	AD	HD	AC	L	TBS	TBW	TBH
80	80	125	100	50	Φ19	40	6	15.5	Φ9	160	220	140	Φ158	280	16	97	97
90S/L	90	140	100/125	56	Φ24	50	8	20	Φ10	175	240	150	Φ176	325/350	16	97	97
100	100	160	140	63	Φ28	60	8	24	Φ12	200	265	165	Φ199	388	20	118	118
112	112	190	140	70	Φ28	60	8	24	Φ12	230	291	179	Φ220	405	29	118	118
132S/M	132	216	140/178	89	Φ38	80	10	33	Φ12	255	332	200	Φ259	467/505	29	118	118

Fig. 27. Dimensions of the TCA series motors

Characteristics of the T112A motor by Neri Motori S.R.L.

T112 type electrical motors are motors with good technical parameters. The description of the basic features and the view of the engine are presented in Fig. 28 and Fig. 29. Selected from the catalog of Neri Motori S.R.L. [13] engine with the T112A designation has the following technical parameters (based on engine designations):

- T - serie T (Three-phase induction motors),
- 112 – type/model of motor (mounting dimension),
- A - anti-condensation holes,
- Flange mounted motor B5 (IM 3001 (IM B5),
- P3 - Motor with 3 thermistors PTC.

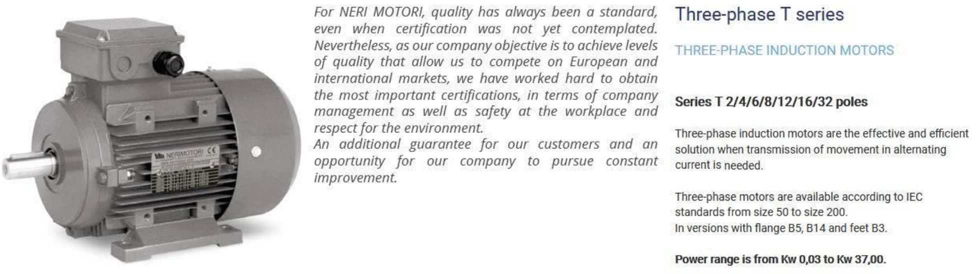

For NERI MOTORI, quality has always been a standard, even when certification was not yet contemplated. Nevertheless, as our company objective is to achieve levels of quality that allow us to compete on European and international markets, we have worked hard to obtain the most important certifications, in terms of company management as well as safety at the workplace and respect for the environment.
An additional guarantee for our customers and an opportunity for our company to pursue constant improvement.

Three-phase T series

THREE-PHASE INDUCTION MOTORS

Series T 2/4/6/8/12/16/32 poles

Three-phase induction motors are the effective and efficient solution when transmission of movement in alternating current is needed.

Three-phase motors are available according to IEC standards from size 50 to size 200.
In versions with flange B5, B14 and feet B3.

Power range is from Kw 0,03 to Kw 37,00.

Fig. 28. T112 motors - description of the basic features

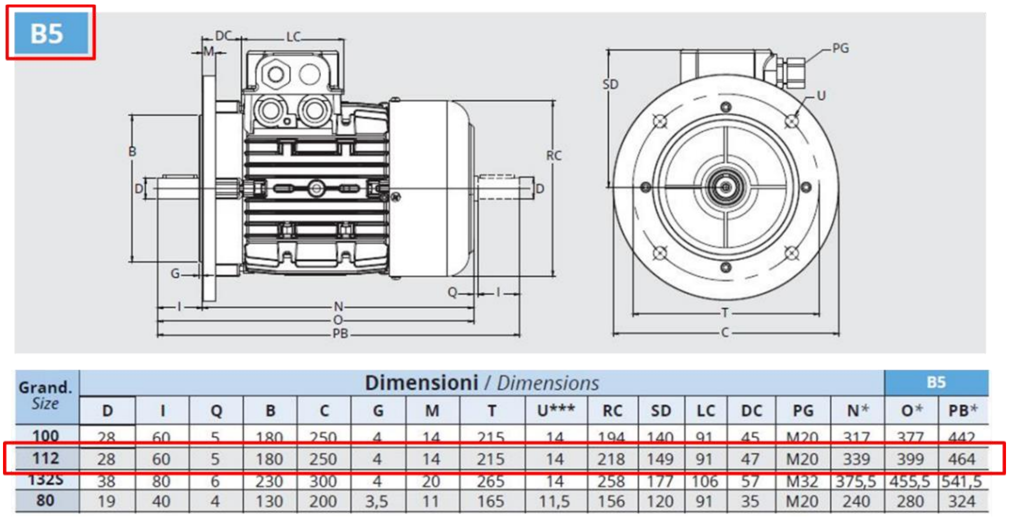

Grand. *Size*	Dimensioni / *Dimensions*															B5	
	D	I	Q	B	C	G	M	T	U***	RC	SD	LC	DC	PG	N*	O*	PB*
100	28	60	5	180	250	4	14	215	14	194	140	91	45	M20	317	377	442
112	28	60	5	180	250	4	14	215	14	218	149	91	47	M20	339	399	464
132S	38	80	6	230	300	4	20	265	14	258	177	106	57	M32	375,5	455,5	541,5
80	19	40	4	130	200	3,5	11	165	11,5	156	120	91	35	M20	240	280	324

Fig. 29. Dimensions of the T112 series motors

Characteristics of the CHT 112 M4B5 IE2 4.0KW+3xPTC motors by CHIARAVALLI

CHT type motors are electrical motors of a recognized manufacturer. The description of the basic features and the view of the engine are presented in Fig. 30 and Fig. 31. The engine selected from the Chiaravalli catalog [14], with the designation CHT 112 M4 B5 IE2 4.0 KW + 3xPTC, is characterized by the following technical parameters (based on the engine designations):

- CHT - series motors have been produced to be mounted on gearboxes,
- 112 – type/model of motor,
- M4 - type of motor (number of poles),
- B5 - type of mounting position and terminal box orientation,
- IE2 - efficiency class for IEC line motors (IE2 = High Efficiency),
- 4.0 kW - rated power (4.0 kW),
- 3xPTC - 3 PTC thermistors (sensors with a positive temperature coefficient),
- GR112 - forced ventilation kit, model 112.

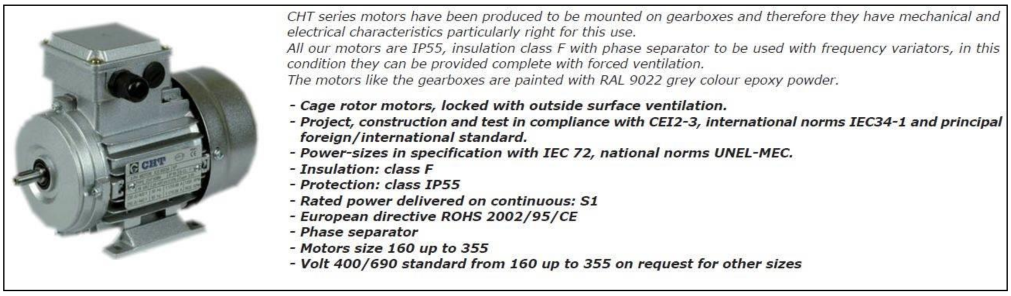

CHT series motors have been produced to be mounted on gearboxes and therefore they have mechanical and electrical characteristics particularly right for this use.
All our motors are IP55, insulation class F with phase separator to be used with frequency variators, in this condition they can be provided complete with forced ventilation.
The motors like the gearboxes are painted with RAL 9022 grey colour epoxy powder.

- ***Cage rotor motors, locked with outside surface ventilation.***
- ***Project, construction and test in compliance with CEI2-3, international norms IEC34-1 and principal foreign/international standard.***
- ***Power-sizes in specification with IEC 72, national norms UNEL-MEC.***
- ***Insulation: class F***
- ***Protection: class IP55***
- ***Rated power delivered on continuous: S1***
- ***European directive ROHS 2002/95/CE***
- ***Phase separator***
- ***Motors size 160 up to 355***
- ***Volt 400/690 standard from 160 up to 355 on request for other sizes***

Fig. 30. CHT motors - description of the basic features

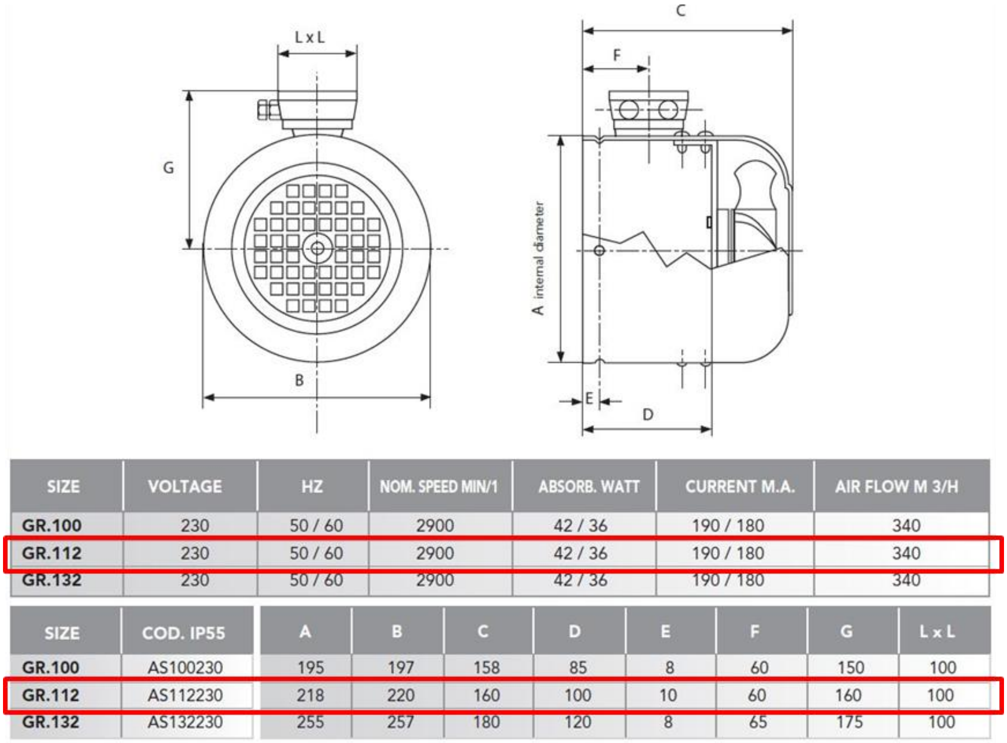

SIZE	VOLTAGE	HZ	NOM. SPEED MIN/1	ABSORB. WATT	CURRENT M.A.	AIR FLOW M 3/H
GR.100	230	50 / 60	2900	42 / 36	190 / 180	340
GR.112	230	50 / 60	2900	42 / 36	190 / 180	340
GR.132	230	50 / 60	2900	42 / 36	190 / 180	340

SIZE	COD. IP55	A	B	C	D	E	F	G	L x L
GR.100	AS100230	195	197	158	85	8	60	150	100
GR.112	AS112230	218	220	160	100	10	60	160	100
GR.132	AS132230	255	257	180	120	8	65	175	100

Fig. 31. CHT series motors dimensions

The rotary sleeve drive motor - summary

Based on the available information, the CHT 112 M4 B5 IE2 4.0 KW + 3xPTC motor CHIARAVALLI was selected as the most suitable device. The results of the data analysis and the comparison of the engine parameters are presented in Table 14 and Table 15. The rated parameters of the selected engine are the closest to the assumed operating ranges of the device.

Table 14. The rotary sleeve drive motor – comparison of selected parameters

Requirement (parameter)	**Value (feature)**	**Model of motor**		
		TCA-1 112M-4 (TEC Electric Motors Ltd.)	T112A (Neri Motori S.R.L.)	CHT 112 M4 B5 IE2 4.0 KW + 3xPTC (CHIARAVALLI SpA)
Power supply	3 phase AC	3 phase AC	3 phase AC	3 phase AC
Voltage value	3 x 400 V	3 x 400 V	3 x 400 V	3 x 400 V
Preferred motor type	Asynchronous three-phase motor	Asynchronous three-phase motor	Asynchronous three-phase motor	Asynchronous three-phase motor
Nominal (rated) torque [Nm]	≥ 26.9 Nm	26.8 (gearbox required)	26.8 (gearbox required)	26.7 (gearbox required)
Gear unit	-	External manufacturer	External manufacturer	Delivered by manufacturer of motor – type CHC40
Form of characteristic curve	Typical	Typical	Typical	Typical
Nominal (rated) rotational speed [rpm]	1417 rpm	1425	1440	1420
Nominal (rated) power	≈ 4.0 kW	4.0	4.0	4.0
Nominal (rated) current [A]		8.47	8.20	8.26
Efficiency [-]	-	0.831	0.844	0.836
Power factor [-]	-	0.820	0.840	0.840

Table 15. The rotary sleeve drive motor – the selection summary

Requirement (parameter)	**Value (feature)**	**Model of motor**		
		TCA-1 112M-4 (TEC Electric Motors Ltd.)	T112A (Neri Motori S.R.L.)	CHT 112 M4 B5 IE2 4.0 KW + 3xPTC (CHIARAVALLI SpA)
Temperature inspection	built-in	PTC 130°C temperature sensor	3 x PTC thermistors (temperature sensors - standard)	3 x PTC thermistors (temperature sensors - standard)
Preferred cooling system	air cooling	Forced ventilation kit - Forcevent-112A	Forced ventilation kit - KS11SW08	Forced ventilation kit – GR 112
Air cooling system performance	m^3/min	229	5.2	340
Summary		- correct rated power range, - the biggest rated current, - the worst efficiency and power factor, - correct temperature inspection, - correct air cooling system performance, - rotational speed to high, - gearbox from an external manufacturer required.	- correct rated power range, - correct rated current, - proper efficiency and power factor, - correct temperature inspection, - the worst air cooling system performance, - correct rotational speed, - gearbox from an external manufacturer required.	- correct rated power range, - correct rated current, - proper efficiency and power factor, - correct temperature inspection, - air cooling system with maximal performance, - the most desirable rotational speed, - gearbox from a native manufacturer required.

4. Conclusions

Making a prototype of a new device requires taking into account many material, process and construction factors. Appropriate selection of individual elements of the machine enables its proper operation. One of the essential elements of the devices are power supply systems and control and measurement systems. The individual elements shown in the work met the expectations of the creators and constructors of the machine.

The preliminary tests carried out have shown that the operating systems in the form of two electrical motors works with a power and current lower than nominal power and nominal current. This solution guarantees obtaining appropriate operating parameters and correctly and uninterrupted works.

Acknowledgements

This project has received funding from the European Union's Horizon 2020 research and innovation programme under the Marie Skłodowska-Curie grant agreement No. 734205 – H2020-MSCA-RISE-2016.

References

[1] Abeykoon Ch, Li K., McAfee M., Martin P. J., Irwin G. W., Extruder Melt Temperature Control with Fuzzy Logic. Preprints of the 18th IFAC World Congress Milano (Italy) August 28 - September 2, 2011, p. 8577-8582.
[2] Giles H. F. Jr., Wagner J. R. Jr., Mount E. M., Extrusion: The Definitive Processing Guide and Handbook. William Andrew Publishing, New York 2005.
[3] Głogowska K., Majewski Ł., Studies of extrusion of polyethylene with the addition of halloysite nanotubes. Part 1. Characteristics of the extrusion. Przemysł chemiczny, no. 98/8 (2019), p. 1313-1315.
[4] Mościcki L., van Zuilichem D. J., Extrusion-Cooking and Related Technique, Extrusion-Cooking Techniques: Applications, Theory and Sustainability. Wainheim 2011.
[5] Sikora J.W., Projekt NEWEX – wytłaczarka nowej generacji. Tworzywa sztuczne w przemyśle, no. 3/2019, p. 128-130.
[6] Sikora J. W., Wysmulski P., Varga J., New concepts of a special screw for a new generation extruder. W: Technological and design aspects of the processing of composites and nanocomposites: monography. Vol. 2. Wyd. Politechniki Lubelskiej, Lublin 2019.
[7] Stasiek J., Wytłaczanie tworzyw polimerowych. Zagadnienia wybrane, Wyd. Uczelniane Uniwersytetu Technologiczno - Przyrodniczego, Bydgoszcz 2007.
[8] http://newex.pollub.pl
[9] https://acim.nidec.com/motors
[10] https://ph.parker.com/us/17607/en/direct-drive-torque-motors-tmw-tma-series
[11] https://www.baumueller.com/de/produkte/motoren/high-torque
[12] https://tecmotors.co.uk/products/
[13] https://www.nerimotori.com/en/prodotti/series-of-motors/three-phase/three-phase-t
[14] https://chiaravalli.pl/oferta/napedy/silniki-asynchroniczne/silniki-elektryczne-asynchroniczne

Łukasz Majewski[1], Ján Varga[2] , Andrzej Sumorek [3]

IMPLEMENTATION OF THE PLASTICATION PROCESS IN AN INNOVATIVE EXTRUSION MACHINE FOR THE PROCESSING OF COMPOSITE AND NANOCOMPOSITE MATERIALS. CONCEPT AND IMPLEMENTATION OF CONTROL SYSTEM OF THE EXTRUDER. PART II – PRESSURE & TEMPERATURE SYSTEM

Abstract: *The process of extruding composite and nanocomposite materials is a complicated technological process. The extrusion process requires taking into account many technological factors. Factors that should be considered are the parameters of the composite blend and the process parameters related to the temperature and pressure of the composite during the formation of the final product. The required physical parameters are obtained thanks to the use of appropriate control, measurement and executive systems. The paper presents executive, measurement and control systems used in an innovative extruder for composite and nanocomposite materials.*

Keywords: *innovation technologies of extrusion, extrusion of composites and nanocomposites, pressure and temperature measurement system, control systems.*

1. Introduction

Pressure and temperature measurements are components of almost all measurements used in engineering practice, including the processing of polymeric and nanocomposite materials, in single- and twin-screw extruders. Modern extruders allow for very high repeatability of the manufactured products, and their control makes it possible to constantly monitor the extrusion process, its control and immediate reaction to noticed changes. To make it possible, it is necessary to properly select the control elements of the extrusion process, and above all, to select the pressure and temperature sensors of the processed material and thermocouples that fix and monitor the temperature distribution of the barrel and the extrusion head along the extruder length.

---

[1] *Lublin University of Technology, Faculty of Mechanical Engineering, Department of Technology and Polymer Processing, ul. Nadbystrzycka 36, 20-618 Lublin, Poland, l.majewski@pollub.pl.*

[2] *Technical University of Kosice, Faculty of Mechanical Engineering, Department Technologies, Materials and Computer Aided Production, Masiarska 74, 040 01 Kosice, Slovakia, jan.varga@tuke.sk.*

[3] *Lublin University of Technology, Faculty of Civil Engineering and Architecture, Department of Structural Mechanics, ul. Nadbystrzycka 40, 20-618 Lublin, Poland, a.sumorek@pollub.pl.*

The paper presents the selection of elements of the temperature and pressure control system, i.e. heaters, temperature and pressure sensors and thermocouples used in the construction of a new generation extruder.

2. Elements of the heating system - selection of elements

The heating system is a system of six elements arranged around the working elements of the extruder: including the plasticizing system and the extruder head. Heating elements of various parameters and shapes enable proper heating of the components of composite and nanocomposite materials subjected to heating processes and the correct course of the plasticization process. Due to the characteristic stages of the heating, mixing and plasticizing process, heating systems must have different parameters of power, temperature and band. There are two basic types of heating elements: flat and strip. The arrangement of heating elements in the extruder is shown in Fig. 1. Fig. 2 and Fig. 3 show an image of flat and band heaters.

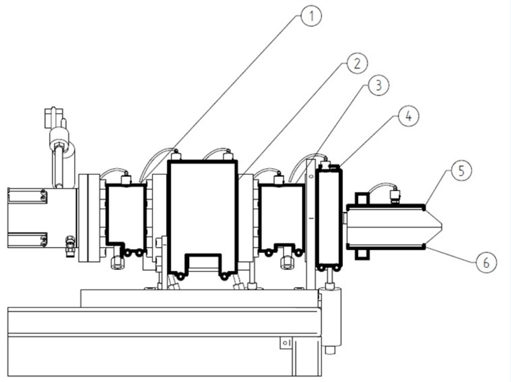

The heating system elements of the extruder
1 - The heating element of cylinder III
2 - The heating element of cylinder II
3 - The heating element of cylinder I
4 - The heating element of coupler
5 - The heating element of head I
6 - The heating element of head II

Fig. 1. The arrangement of the heating system elements

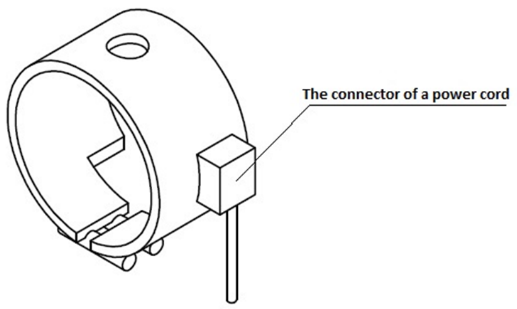

The heating system elements of the extruder
The heating element of cylinder III
The heating element of cylinder II
The heating element of cylinder I
The heating element of coupler

Fig. 2. The model of a band heater

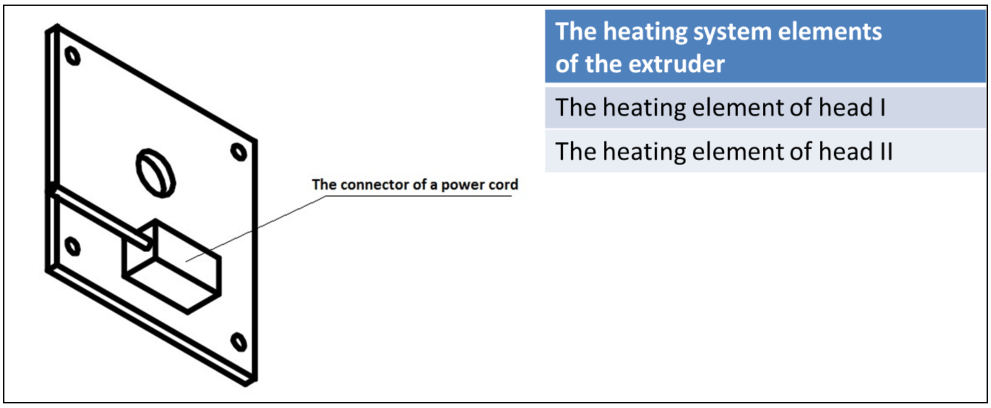
The connector of a power cord
The heating system elements of the extruder
The heating element of head I
The heating element of head II

Fig. 3. The model of a flat heater

Due to the specific requirements regarding the shape, power and temperature range of the heating elements, the following manufacturers of heating elements were selected for the final selection stage:

- Limatherm;
- Selfa;
- Termik;
- Centrotherm.

Preliminary analysis of their technical parameters qualified them as devices useful and possible to be used in the heating system of the innovation extruder.

Characteristics of Limatherm heating elements

Fig. 4, Fig. 5 and Fig. 6 show the most important information about the heating elements offered by Limatherm [1].

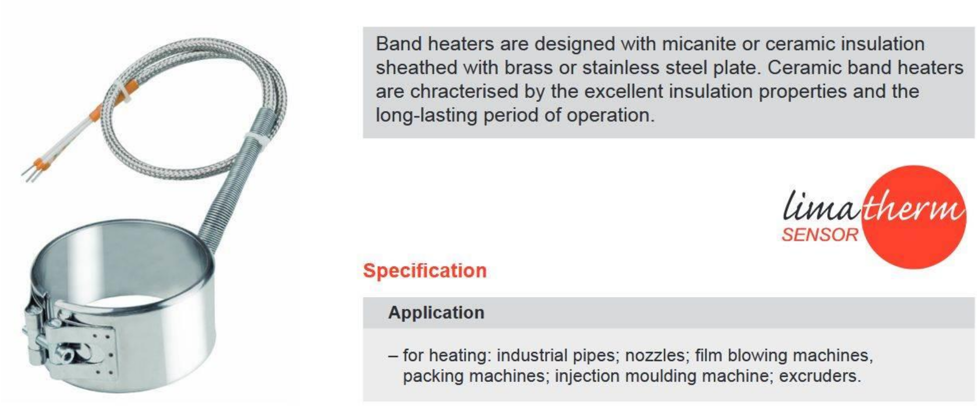

Band heaters are designed with micanite or ceramic insulation sheathed with brass or stainless steel plate. Ceramic band heaters are chracterised by the excellent insulation properties and the long-lasting period of operation.

limatherm
SENSOR

Specification

Application

– for heating: industrial pipes; nozzles; film blowing machines, packing machines; injection moulding machine; excruders.

Fig. 4. Characteristics of Limatherm heating elements

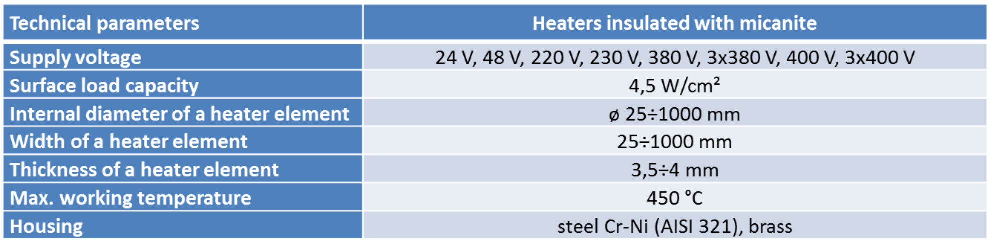

Technical parameters	Heaters insulated with micanite
Supply voltage	24 V, 48 V, 220 V, 230 V, 380 V, 3x380 V, 400 V, 3x400 V
Surface load capacity	4,5 W/cm²
Internal diameter of a heater element	ø 25÷1000 mm
Width of a heater element	25÷1000 mm
Thickness of a heater element	3,5÷4 mm
Max. working temperature	450 °C
Housing	steel Cr-Ni (AISI 321), brass

Fig. 5. Technical parameters of heating elements

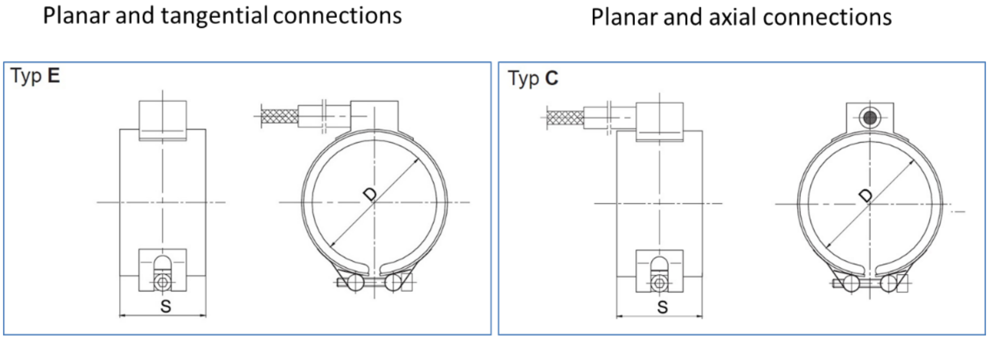
Planar and tangential connections
Planar and axial connections
Typ E
S
D
Typ C
S
D

Fig. 6. The connector type of a cable connection

Characteristics of Selfa heating elements

Fig. 7, Fig. 8 and Fig. 9 show the most important information about the heating elements offered by Selfa [2].

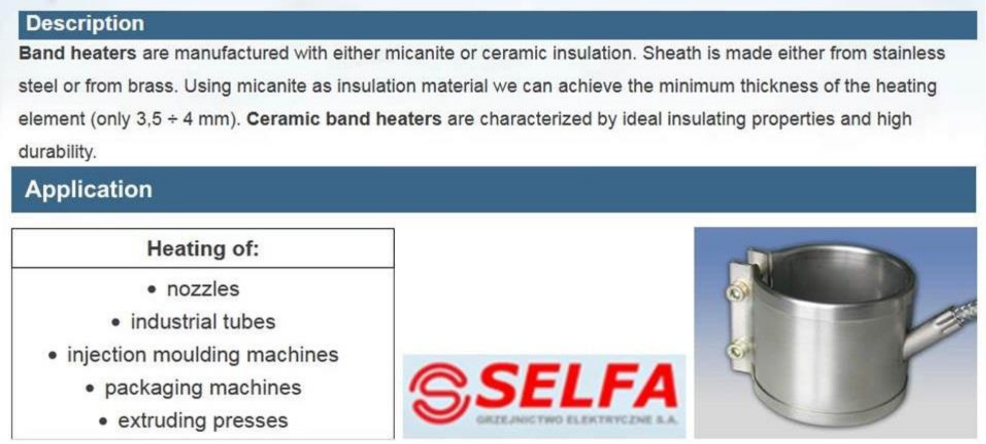

Description

Band heaters are manufactured with either micanite or ceramic insulation. Sheath is made either from stainless steel or from brass. Using micanite as insulation material we can achieve the minimum thickness of the heating element (only 3,5 ÷ 4 mm). **Ceramic band heaters** are characterized by ideal insulating properties and high durability.

Application

Heating of:

- nozzles
- industrial tubes
- injection moulding machines
- packaging machines
- extruding presses

Fig. 7. Characteristics of Selfa heating elements

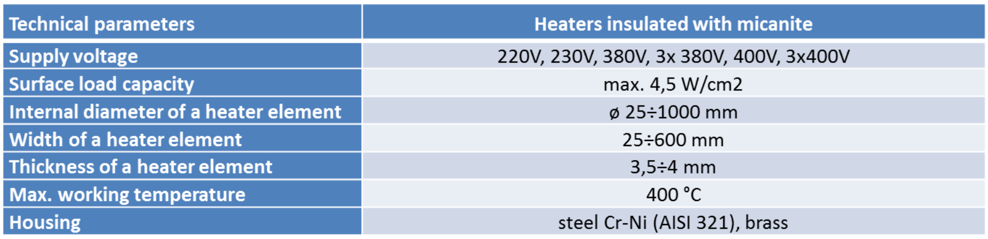

Technical parameters	Heaters insulated with micanite
Supply voltage	220V, 230V, 380V, 3x 380V, 400V, 3x400V
Surface load capacity	max. 4,5 W/cm2
Internal diameter of a heater element	ø 25÷1000 mm
Width of a heater element	25÷600 mm
Thickness of a heater element	3,5÷4 mm
Max. working temperature	400 °C
Housing	steel Cr-Ni (AISI 321), brass

Fig. 8. Technical parameters of heating elements

Planar and tangential connections

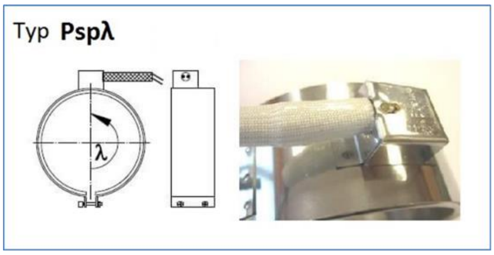

Planar and axial connections

NO ITEMS

Fig. 9. The connector type of a cable connection

Characteristics of Termik heating elements

Fig. 10, Fig. 11 and Fig. 12 show the most important information about the heating elements offered by Termik [3].

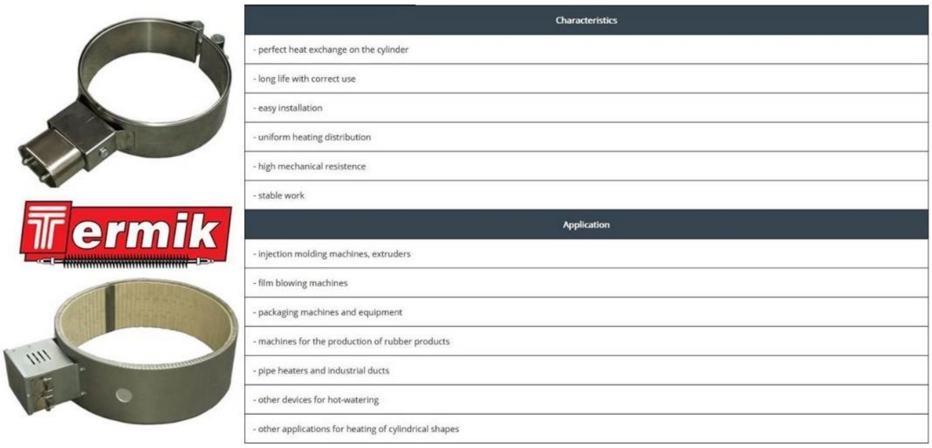

Characteristics
- perfect heat exchange on the cylinder
- long life with correct use
- easy installation
- uniform heating distribution
- high mechanical resistence
- stable work
Application
- injection molding machines, extruders
- film blowing machines
- packaging machines and equipment
- machines for the production of rubber products
- pipe heaters and industrial ducts
- other devices for hot-watering
- other applications for heating of cylindrical shapes

Fig. 10. Characteristics of Termik heating elements

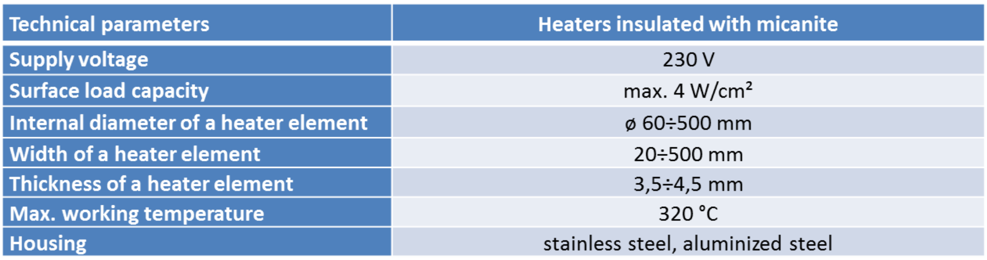

Technical parameters	Heaters insulated with micanite
Supply voltage	230 V
Surface load capacity	max. 4 W/cm²
Internal diameter of a heater element	ø 60÷500 mm
Width of a heater element	20÷500 mm
Thickness of a heater element	3,5÷4,5 mm
Max. working temperature	320 °C
Housing	stainless steel, aluminized steel

Fig. 11. Technical parameters of heating elements

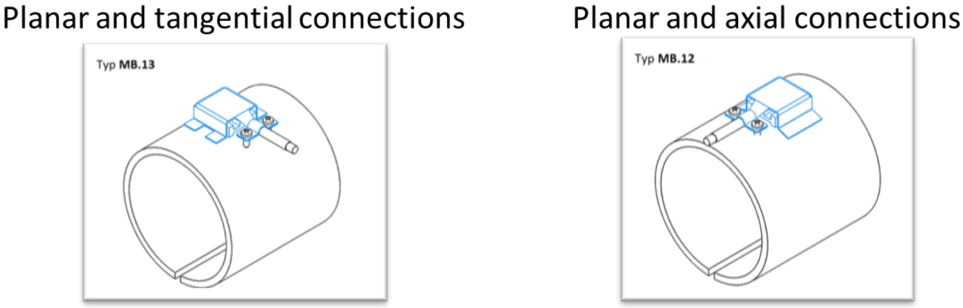

Planar and tangential connections

Planar and axial connections

Fig. 12. The connector type of a cable connection

Characteristics of Centrotherm heating elements

Fig. 13, Fig. 14 and Fig. 15 present the most important information about the heating elements offered by Centrotherm [4].

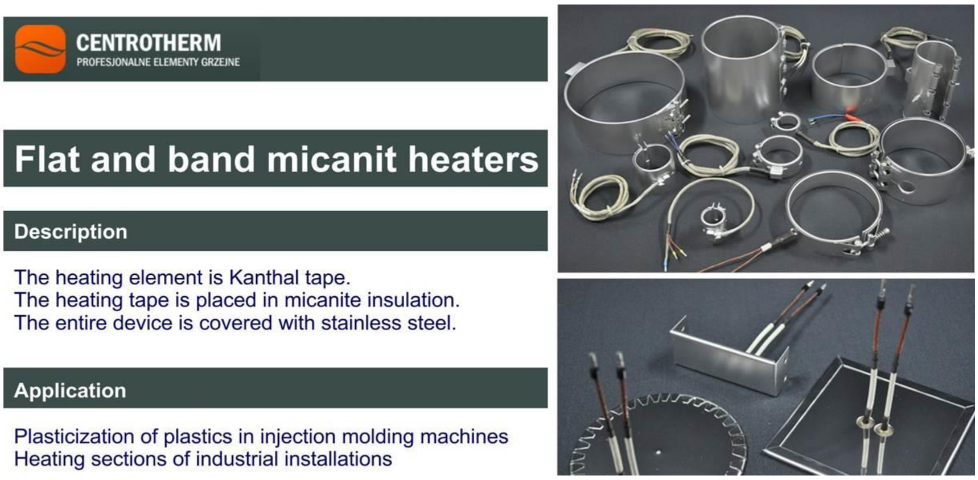

CENTROTHERM
PROFESJONALNE ELEMENTY GRZEJNE

Flat and band micanit heaters

Description

The heating element is Kanthal tape.
The heating tape is placed in micanite insulation.
The entire device is covered with stainless steel.

Application

Plasticization of plastics in injection molding machines
Heating sections of industrial installations

Fig. 13. Characteristics of Centrotherm heating elements

Technical parameters	Heaters insulated with micanite
Supply voltage	220V, 230V, 380V, 3x 380V, 400V, 3x400V
Surface load capacity	max. 4,5 W/cm²
Internal diameter of a heater element	ø 20÷900 mm
Width of a heater element	15÷800 mm
Thickness of a heater element	4 mm
Max. working temperature	450 °C
Housing	steel Cr-Ni

Fig. 14. Technical parameters of heating elements

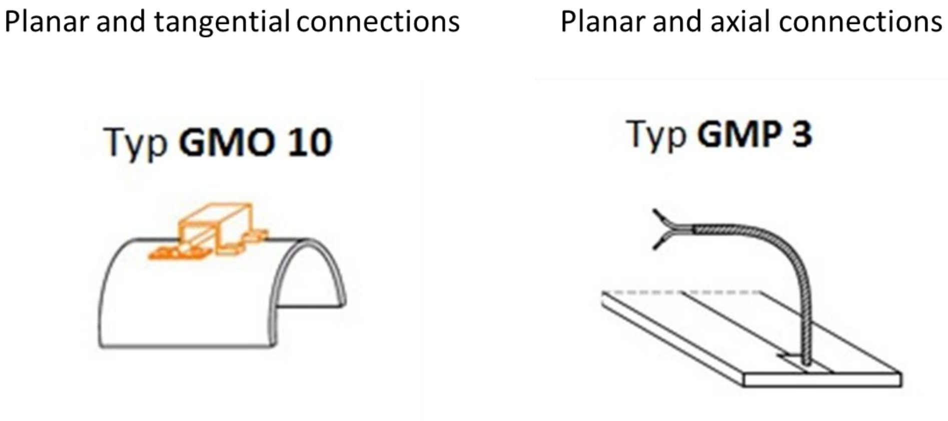
Planar and tangential connections
Planar and axial connections

Fig. 15. The connector type of a cable connection

Elements of the heating system - summary

Based on the collected information, Limatherm heating elements were selected as the most suitable for use in the extruder. The Limatherm company offers heating elements that fit all heating points in the extruder. This feature made the choice of Limatherm heating elements. The results of the data analysis and the comparison of the parameters of the heating elements are presented in the following tables: Table 1 and Table 2, Table 3, Table 4, Table 5 and Table 6.

Table 1. The heating element of barrel III – Summary. Comparison of selected parameters

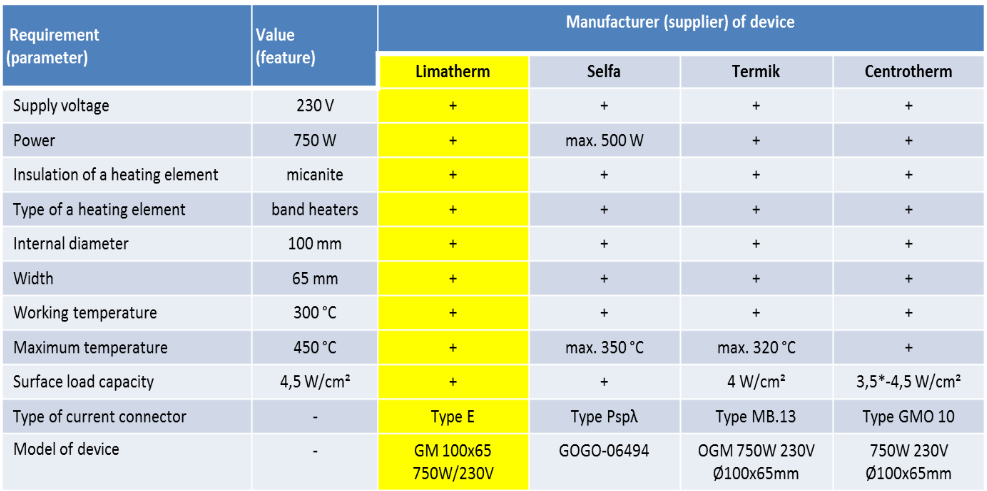

Requirement (parameter)	Value (feature)	Manufacturer (supplier) of device			
		Limatherm	Selfa	Termik	Centrotherm
Supply voltage	230 V	+	+	+	+
Power	750 W	+	max. 500 W	+	+
Insulation of a heating element	micanite	+	+	+	+
Type of a heating element	band heaters	+	+	+	+
Internal diameter	100 mm	+	+	+	+
Width	65 mm	+	+	+	+
Working temperature	300 °C	+	+	+	+
Maximum temperature	450 °C	+	max. 350 °C	max. 320 °C	+
Surface load capacity	4,5 W/cm²	+	+	4 W/cm²	3,5*-4,5 W/cm²
Type of current connector	-	Type E	Type Pspλ	Type MB.13	Type GMO 10
Model of device	-	GM 100x65 750W/230V	GOGO-06494	OGM 750W 230V Ø100x65mm	750W 230V Ø100x65mm

Table 2. The heating element of barrel II – Summary. Comparison of selected parameters

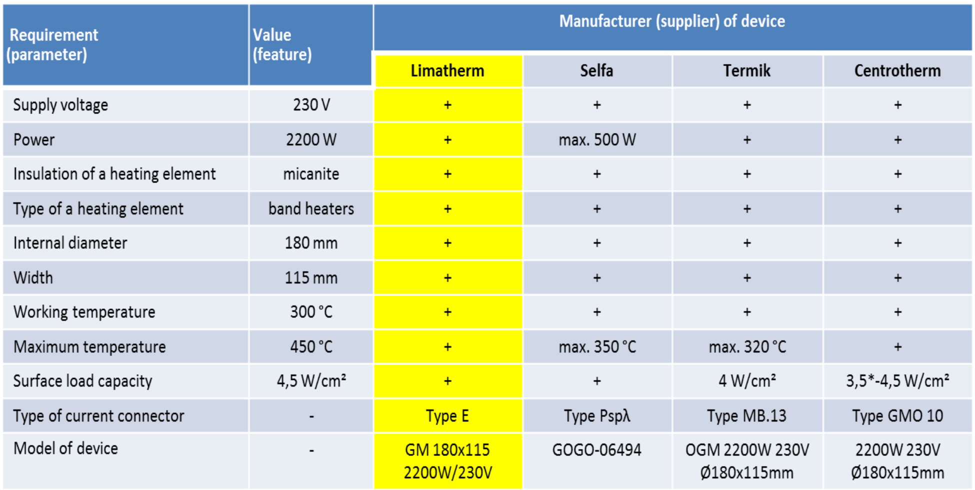

Requirement (parameter)	Value (feature)	Manufacturer (supplier) of device			
		Limatherm	Selfa	Termik	Centrotherm
Supply voltage	230 V	+	+	+	+
Power	2200 W	+	max. 500 W	+	+
Insulation of a heating element	micanite	+	+	+	+
Type of a heating element	band heaters	+	+	+	+
Internal diameter	180 mm	+	+	+	+
Width	115 mm	+	+	+	+
Working temperature	300 °C	+	+	+	+
Maximum temperature	450 °C	+	max. 350 °C	max. 320 °C	+
Surface load capacity	4,5 W/cm²	+	+	4 W/cm²	3,5*-4,5 W/cm²
Type of current connector	-	Type E	Type Pspλ	Type MB.13	Type GMO 10
Model of device	-	GM 180x115 2200W/230V	GOGO-06494	OGM 2200W 230V Ø180x115mm	2200W 230V Ø180x115mm

Table 3. The heating element of barrel I – Summary. Comparison of selected parameters

Requirement (parameter)	Value (feature)	Manufacturer (supplier) of device			
		Limatherm	Selfa	Termik	Centrotherm
Supply voltage	230 V	+	+	+	+
Power	800 W	+	max. 500 W	+	+
Insulation of a heating element	micanite	+	+	+	+
Type of a heating element	band heaters	+	+	+	+
Internal diameter	100 mm	+	+	+	+
Width	75 mm	+	+	+	+
Working temperature	300 °C	+	+	+	+
Maximum temperature	450 °C	+	max. 350 °C	max. 320 °C	+
Surface load capacity	4,5 W/cm²	+	+	4 W/cm²	3,5*-4,5 W/cm²
Type of current connector	-	Type E	Type Pspλ	Type MB.13	Type GMO 10
Model of device	-	GM 100x75 800W/230V	GOGO-06494	OGM 800W 230V Ø100x75mm	800W 230V Ø100x75mm

Table 4. The heating element of coupler – Summary. Comparison of selected parameters

Requirement (parameter)	Value (feature)	Manufacturer (supplier) of device			
		Limatherm	Selfa	Termik	Centrotherm
Supply voltage	230 V	+	+	+	+
Power	650 W	+	max. 500 W	+	+
Insulation of a heating element	micanite	+	+	+	+
Type of a heating element	band heaters	+	+	+	+
Internal diameter	150 mm	+	+	+	+
Width	40 mm	+	+	+	+
Working temperature	300 °C	+	+	+	+
Maximum temperature	450 °C	+	max. 350 °C	max. 320 °C	+
Surface load capacity	4,5 W/cm²	+	+	4 W/cm²	3,5*-4,5 W/cm²
Type of current connector	-	Type E	Type Pspλ	Type MB.13	Type GMO 10
Model of device		GM 150x40 650W/230V	GOGO-06494	OGM 650W 230V Ø150x40mm	650W 230V Ø150x40mm

Table 5. *The heating element of head I – Summary. Comparison of selected parameters*

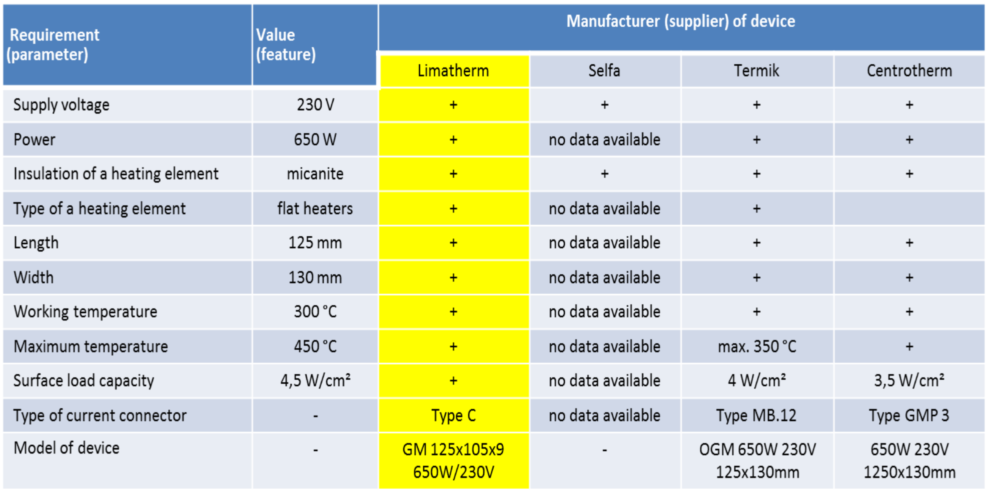

Requirement (parameter)	Value (feature)	Manufacturer (supplier) of device			
		Limatherm	Selfa	Termik	Centrotherm
Supply voltage	230 V	+	+	+	+
Power	650 W	+	no data available	+	+
Insulation of a heating element	micanite	+	+	+	+
Type of a heating element	flat heaters	+	no data available	+	
Length	125 mm	+	no data available	+	+
Width	130 mm	+	no data available	+	+
Working temperature	300 °C	+	no data available	+	+
Maximum temperature	450 °C	+	no data available	max. 350 °C	+
Surface load capacity	4,5 W/cm²	+	no data available	4 W/cm²	3,5 W/cm²
Type of current connector	-	Type C	no data available	Type MB.12	Type GMP 3
Model of device	-	GM 125x105x9 650W/230V	-	OGM 650W 230V 125x130mm	650W 230V 1250x130mm

Table 6. *The heating element of head II – Summary. Comparison of selected parameters*

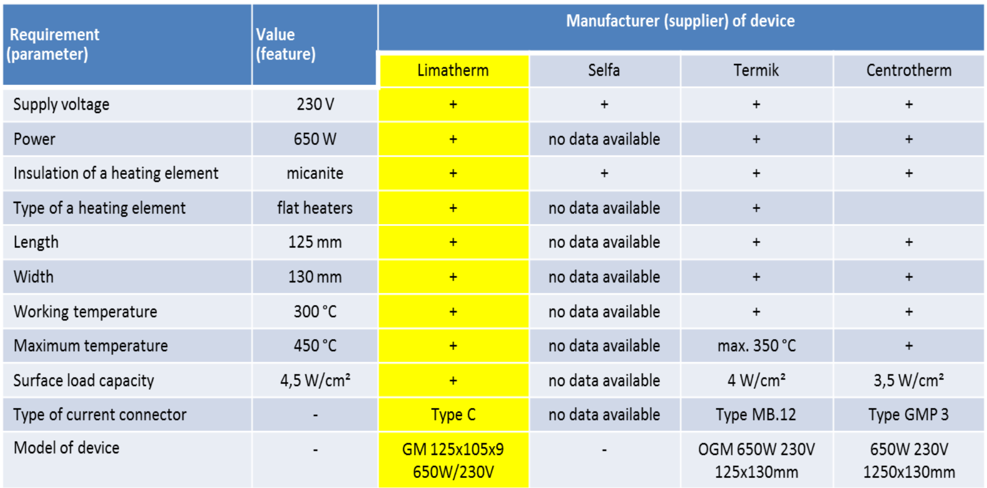

Requirement (parameter)	Value (feature)	Manufacturer (supplier) of device			
		Limatherm	Selfa	Termik	Centrotherm
Supply voltage	230 V	+	+	+	+
Power	650 W	+	no data available	+	+
Insulation of a heating element	micanite	+	+	+	+
Type of a heating element	flat heaters	+	no data available	+	
Length	125 mm	+	no data available	+	+
Width	130 mm	+	no data available	+	+
Working temperature	300 °C	+	no data available	+	+
Maximum temperature	450 °C	+	no data available	max. 350 °C	+
Surface load capacity	4,5 W/cm²	+	no data available	4 W/cm²	3,5 W/cm²
Type of current connector	-	Type C	no data available	Type MB.12	Type GMP 3
Model of device	-	GM 125x105x9 650W/230V	-	OGM 650W 230V 125x130mm	650W 230V 1250x130mm

Components of the temperature measurement system - selection of elements

The extrusion process requires proper preparation of the material. Temperature sensors were used for continuous temperature control in selected zones. Their task is to control the heating elements to ensure the required working conditions.

Due to the difficult working conditions, these elements must be resistant to unfavorable factors. The following temperature sensors were selected for the final stage of the selection:

- 902190/20-397-1003-2-6-85-11-1500 (2000)/317 firmy JUMO GmbH & Co. KG;
- 04-Pt100-A-Z1-KS2-30-1500 (2000) - TW204-B5/KS121 firmy Czah-pomiar Sp. z o.o.;
- TTJE-26-S-10-6-M12x1-SP-2-1,5m (2,0m) firm Limatherm Sensor Sp. z o.o.

Initial analysis of their technical parameters qualified them as useful and applicable elements for temperature control in the extruder heating system.

Characteristics of Jumo temperature sensors

Fig. 16, Fig. 17, Fig. 18 and Fig. 19 show the most important information about the Jumo 902190 / 20-397-1003-2-6-85-11-1500 (2000) / 317 temperature sensors [5].

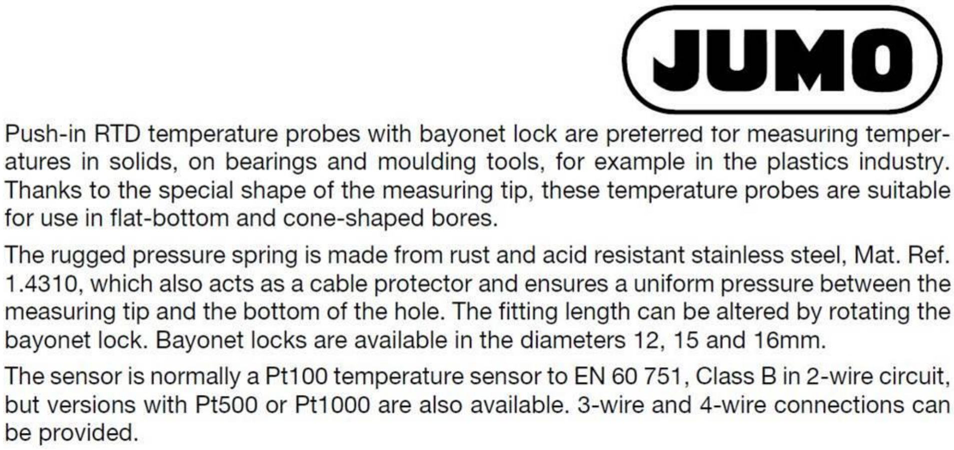

JUMO

Push-in RTD temperature probes with bayonet lock are preferred for measuring temperatures in solids, on bearings and moulding tools, for example in the plastics industry. Thanks to the special shape of the measuring tip, these temperature probes are suitable for use in flat-bottom and cone-shaped bores.

The rugged pressure spring is made from rust and acid resistant stainless steel, Mat. Ref. 1.4310, which also acts as a cable protector and ensures a uniform pressure between the measuring tip and the bottom of the hole. The fitting length can be altered by rotating the bayonet lock. Bayonet locks are available in the diameters 12, 15 and 16mm.

The sensor is normally a Pt100 temperature sensor to EN 60 751, Class B in 2-wire circuit, but versions with Pt500 or Pt1000 are also available. 3-wire and 4-wire connections can be provided.

Fig. 16. Jumo temperature sensors - General description

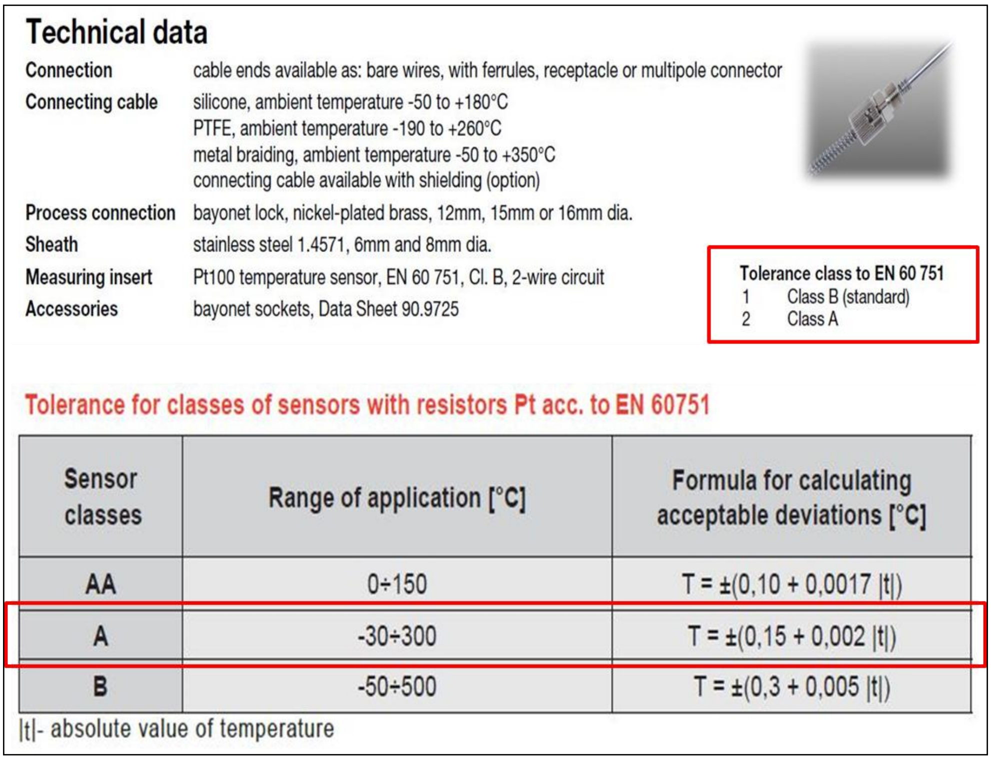

Technical data

Connection	cable ends available as: bare wires, with ferrules, receptacle or multipole connector
Connecting cable	silicone, ambient temperature -50 to +180°C PTFE, ambient temperature -190 to +260°C metal braiding, ambient temperature -50 to +350°C connecting cable available with shielding (option)
Process connection	bayonet lock, nickel-plated brass, 12mm, 15mm or 16mm dia.
Sheath	stainless steel 1.4571, 6mm and 8mm dia.
Measuring insert	Pt100 temperature sensor, EN 60 751, Cl. B, 2-wire circuit
Accessories	bayonet sockets, Data Sheet 90.9725

Tolerance class to EN 60 751

1	Class B (standard)
2	Class A

Tolerance for classes of sensors with resistors Pt acc. to EN 60751

Sensor classes	Range of application [°C]	Formula for calculating acceptable deviations [°C]
AA	0÷150	T = ±(0,10 + 0,0017 |t|)
A	-30÷300	T = ±(0,15 + 0,002 |t|)
B	-50÷500	T = ±(0,3 + 0,005 |t|)

|t|- absolute value of temperature

Fig. 17. Jumo temperature sensors - Technical data

902190/20-397-1003-2-6-85-11-1500 (2000)/317

902190/20 - Push-in RTD temperature probe, sheath in stainless steel, Mat. Ref. 1.4571, measuring tip (120°) ceramic, KER 221; bayonet lock: 12mm diameter

397 - Operating temperature in °C / connecting cable; -50 to +350°C /metal braiding

1003 - Measuring insert: 1 x Pt100 in 2-wire circuit

2 - Tolerance class to EN 60751; 2 - Class A

6 - Sheath diameter D in mm; 6 = 6 mm

85 - Fitting length EL in mm; 85 = 20 - 85mm

11 - Connecting cable end; 11 = ferrules to DIN 46 228 Part 4

1500 (2000) - Connecting cable length AL in mm: 1500 = 1500 mm (2000 = 2000 mm)

317 - Extra code: 317 = shielded connecting cable

Fig. 18. Jumo temperature sensors - Sensor type

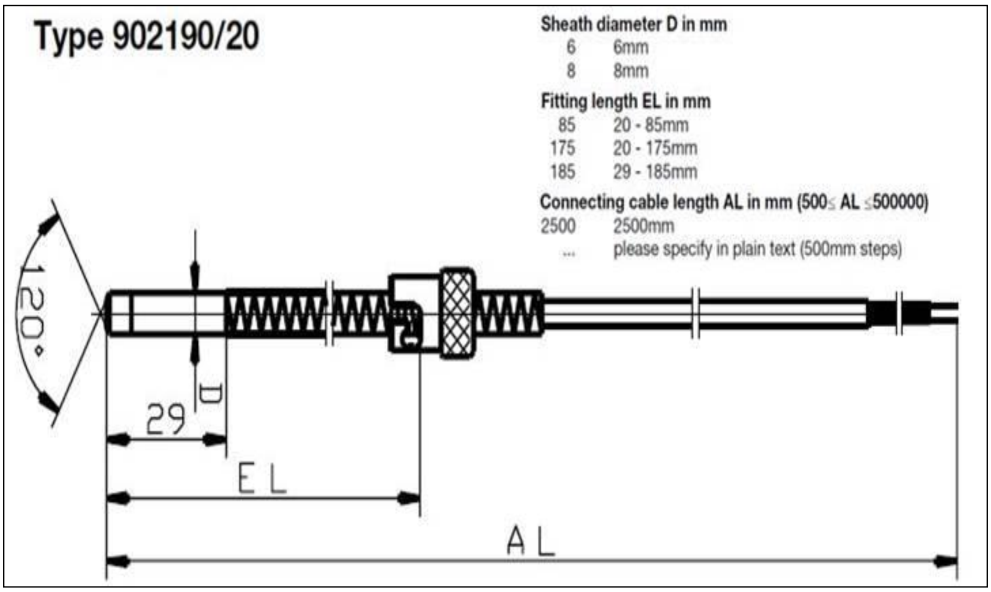
Type 902190/20
Sheath diameter D in mm
6 6mm
8 8mm
Fitting length EL in mm
85 20 - 85mm
175 20 - 175mm
185 29 - 185mm
Connecting cable length AL in mm (500≤ AL ≤500000)
2500 2500mm
... please specify in plain text (500mm steps)
120°
D
29
EL
AL

Fig. 19. Jumo temperature sensors - Dimensions

Characteristics of Czah-pomiar Sp. z o.o temperature sensors

Fig. 20, Fig. 21, Fig. 22 and Fig. 23 show the most important information about the 04-Pt100-A-Z1-KS2-30-1500 (2000) - TW204-B5 / KS121 temperature sensors from Czah-Pomiar Sp. z o.o. [6].

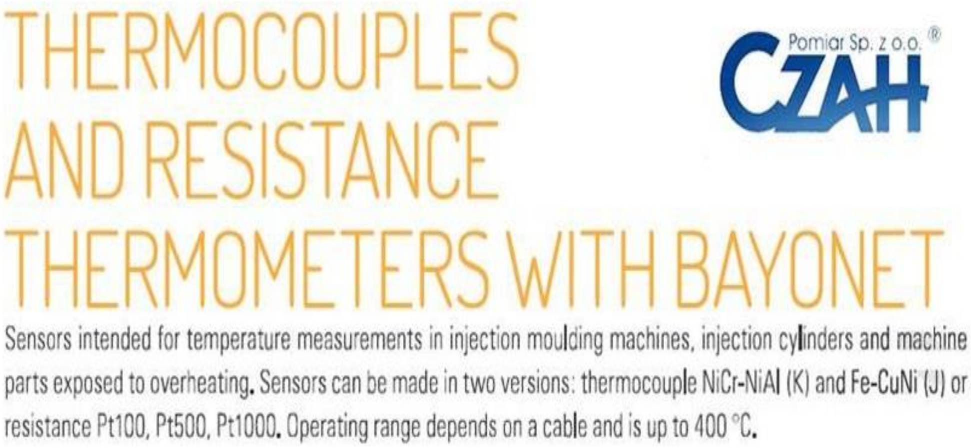

THERMOCOUPLES AND RESISTANCE THERMOMETERS WITH BAYONET

CZAH Pomiar Sp. z o.o.®

Sensors intended for temperature measurements in injection moulding machines, injection cylinders and machine parts exposed to overheating. Sensors can be made in two versions: thermocouple NiCr-NiAl (K) and Fe-CuNi (J) or resistance Pt100, Pt500, Pt1000. Operating range depends on a cable and is up to 400 °C.

Fig. 20. Czah-pomiar Sp. z o.o temperature sensors - General description

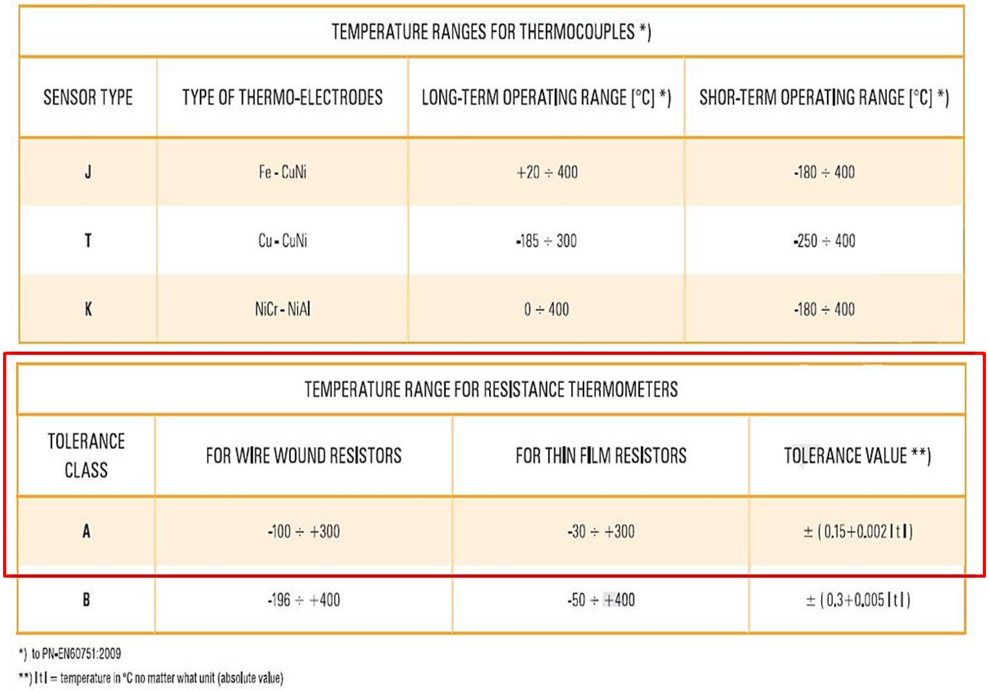

TEMPERATURE RANGES FOR THERMOCOUPLES *)			
SENSOR TYPE	TYPE OF THERMO-ELECTRODES	LONG-TERM OPERATING RANGE [°C] *)	SHOR-TERM OPERATING RANGE [°C] *)
J	Fe - CuNi	+20 ÷ 400	-180 ÷ 400
T	Cu - CuNi	-185 ÷ 300	-250 ÷ 400
K	NiCr - NiAl	0 ÷ 400	-180 ÷ 400

TEMPERATURE RANGE FOR RESISTANCE THERMOMETERS			
TOLERANCE CLASS	FOR WIRE WOUND RESISTORS	FOR THIN FILM RESISTORS	TOLERANCE VALUE **)
A	-100 ÷ +300	-30 ÷ +300	± (0.15+0.002 | t |)
B	-196 ÷ +400	-50 ÷ +400	± (0.3+0.005 | t |)

*) to PN-EN60751:2009

**) | t | = temperature in °C no matter what unit (absolute value)

Fig. 21. Czah-pomiar Sp. z o.o temperature sensors - Technical data

04-Pt100-A-Z1-KS2-30-1500-TW204-B5/KS121

04 - temperature sensor
Pt100 - sensor type Pt100
A - accuracy class, class A
Z1 - grounded junction
KS2 - conical tip with spring diameter 6 mm
30 - length of measuring tip, length=30 mm,
1500 (2000) - cable length, 1500=1500 mmm
TT201- cable 2x0.22 mm2, teflon insulated
B5 - bayonet connection, B5 = spring diameter 6 mm, length 18 mm,
KS121 - connection, KS121 = stainless steel, process connection, metric thread M12x1

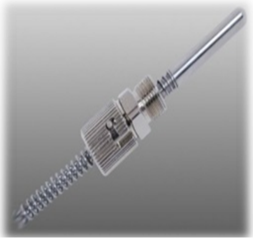

Fig. 22. Czah-pomiar Sp. z o.o temperature sensors - Sensor type

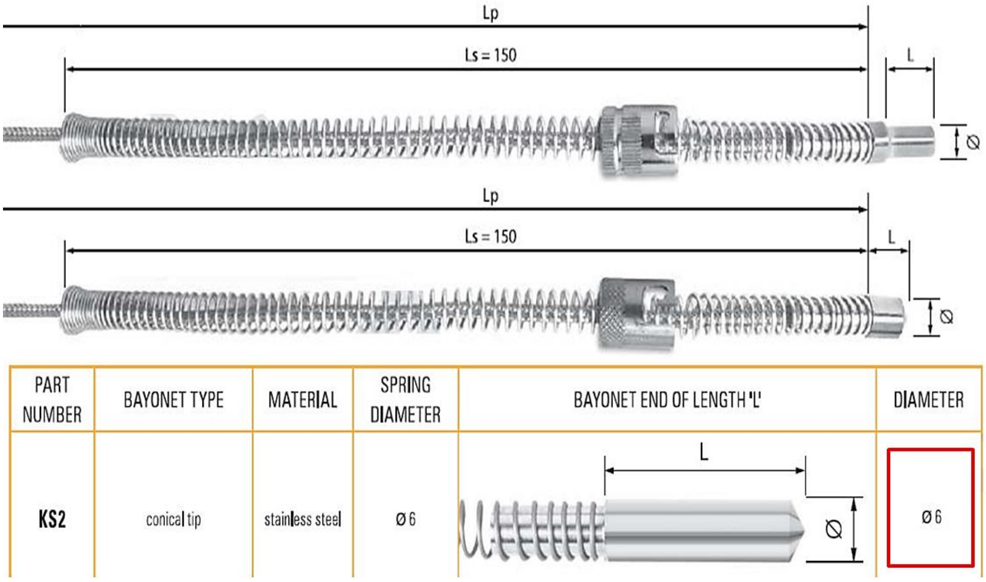

PART NUMBER	BAYONET TYPE	MATERIAL	SPRING DIAMETER	BAYONET END OF LENGTH 'L'	DIAMETER
KS2	conical tip	stainless steel	Ø 6		Ø 6

Fig. 23. Czah-pomiar Sp. z o.o temperature sensors - Dimensions

Characteristics of Limatherm temperature sensors

Fig. 24, Fig. 25, Fig. 26 and Fig. 27 show the most important information about the TTJE-26-S-10-6-M12x1-SP-2-1.5m (2.0m) temperature sensors by Limatherm Sensor Sp. z o.o. [7].

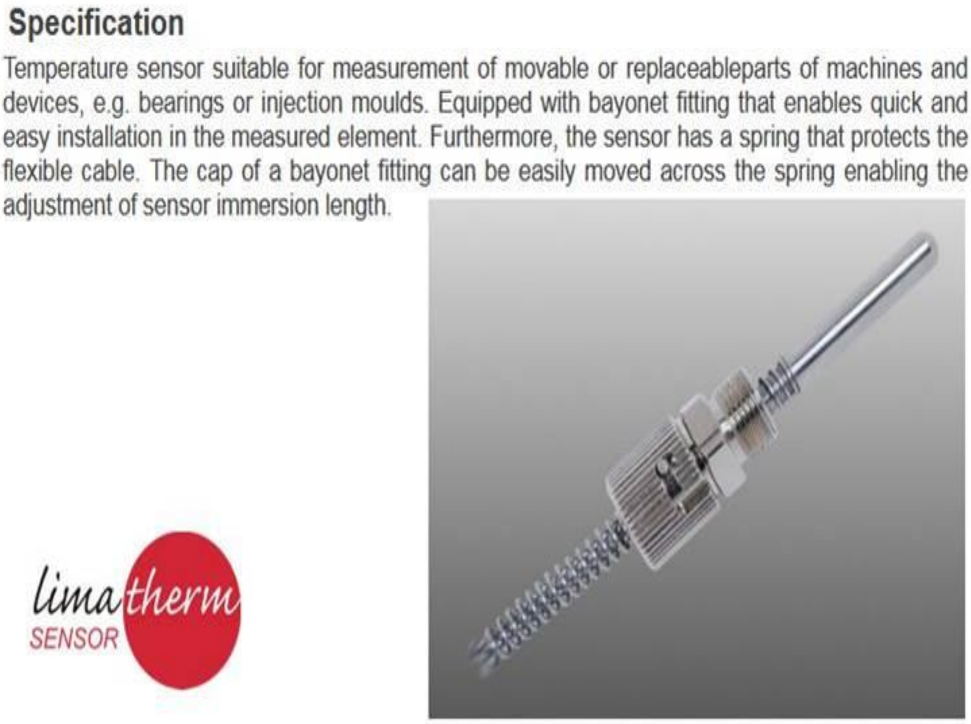

Specification

Temperature sensor suitable for measurement of movable or replaceableparts of machines and devices, e.g. bearings or injection moulds. Equipped with bayonet fitting that enables quick and easy installation in the measured element. Furthermore, the sensor has a spring that protects the flexible cable. The cap of a bayonet fitting can be easily moved across the spring enabling the adjustment of sensor immersion length.

Fig. 24. Limatherm Sensor Sp. z o.o. temperature sensors - General description

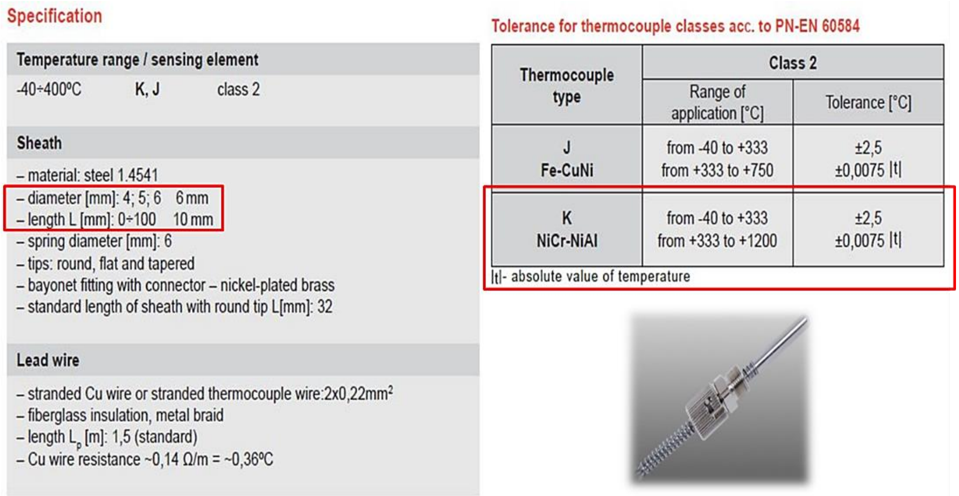

Specification

Temperature range / sensing element

-40÷400ºC K, J class 2

Sheath

– material: steel 1.4541
– diameter [mm]: 4; 5; 6 6 mm
– length L [mm]: 0÷100 10 mm
– spring diameter [mm]: 6
– tips: round, flat and tapered
– bayonet fitting with connector – nickel-plated brass
– standard length of sheath with round tip L[mm]: 32

Lead wire

– stranded Cu wire or stranded thermocouple wire:2x0,22mm^2
– fiberglass insulation, metal braid
– length L_p [m]: 1,5 (standard)
– Cu wire resistance ~0,14 Ω/m = ~0,36ºC

Tolerance for thermocouple classes acc. to PN-EN 60584

Thermocouple type	Class 2	
	Range of application [°C]	Tolerance [°C]
J **Fe-CuNi**	from -40 to +333 from +333 to +750	±2,5 ±0,0075 |t|
K **NiCr-NiAl**	from -40 to +333 from +333 to +1200	±2,5 ±0,0075 |t|

|t|- absolute value of temperature

Fig. 25. Limatherm Sensor Sp. z o.o. temperature sensors - Technical data

TTJE-26-S-10-6-M12x1-SP-2-1,5m (2,0m)

TXXE - sensors family

TJ - Sensing element: TJ thermocouple Fe-CuNi (J)

26 - sensors family

S - Measuring tip type: S tapered

10 – Sheath length 10 mm

6 - Sheath diameter 6 mm

M12x1 - Dimension of process connection thread, M12x1 = metric thread M12x1

SP - hot junction type for thermocouple, SP = grounded hot junction

2 – Accuracy: 2% for thermocouple

1,5 - Lead wire length, 1.5=1.5m; 2.0=2.0m. Thermocouple wire insulations: Ws-fiberglass - 60÷400°C)

Fig. 26. Limatherm Sensor Sp. z o.o. temperature sensors - Sensor type

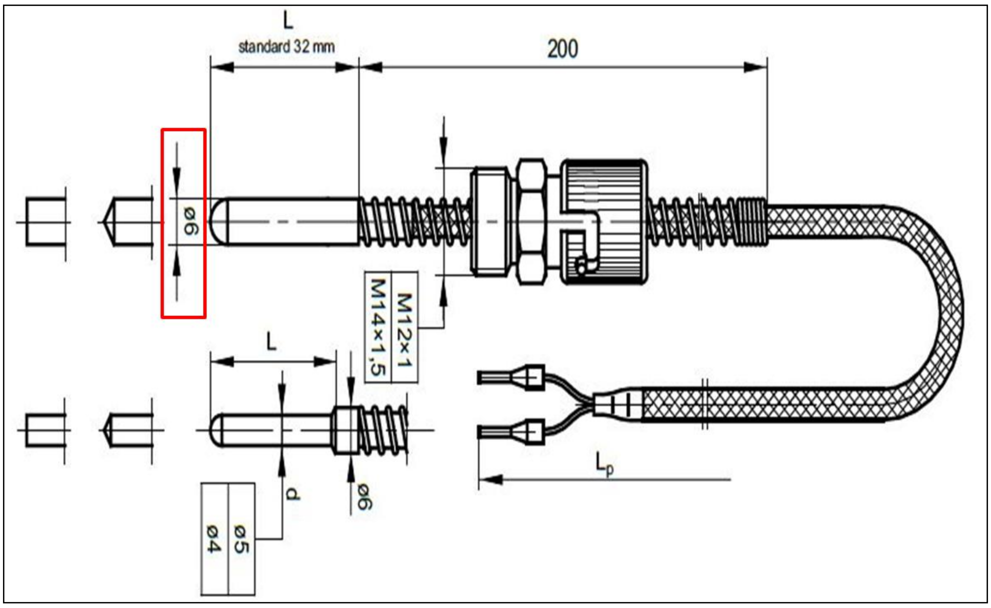

Fig. 27. Limatherm Sensor Sp. z o.o. temperature sensors - Dimensions

Components of the temperature measurement system - summary

Based on the collected information, the Limatherm temperature sensors were selected as the most suitable for use in the extruder. The results of the data analysis and the comparison of the parameters of the temperature sensors are presented in Table 7 and Table 8.

Table 7. Temperature sensors – Comparison of selected parameters

Requirement (parameter)	Value (feature)	Model of sensor		
		902190/20-397-1003-2-6-85-11-1500 (2000)/317 (JUMO GmbH & Co. KG)	04-Pt100-A-Z1-KS2-30-1500 (2000) -TW204-B5/KS121 (Czah-pomiar Sp. z o.o.)	TTJE-26-S-10-6-M12x1-SP-2-1,5m (2,0m) (Limatherm Sensor Sp. z o.o)
Sensor type	Undefined	Resistance thermometer	Resistance thermometer	Thermocouple
Sensor tip	Conical (preferred)	Conical	Conical	Conical
Temperature range:	0÷400 °C	-50÷350 °C	-30÷300(400) °C	-40÷400 °C
Minimal tolerance: Class 2	Class 2	Class A ((± .15± 0.002·temp) for -30÷300 °C)	Class A ((± .15± 0.002·temp) for -30÷300 °C)	Class 2 (± 2.5°C for -40÷333 °C; ± 0.0075·temp for -333÷1200 °C)
Minimal sheath length	10 mm	20	18	10
Sheath diameter:	5~8 mm,	6	6	6
Fitting	bayonet fitting	bayonet fitting	bayonet fitting	bayonet fitting
Lead wire length:	≥ 1.5 m	1.5 (2.0) m	1.5 (2.0) m	1.5 (2.0) m

Table 8. Temperature sensors – Summary

Requirement (parameter)	Value (feature)	Model of sensor		
		902190/20-397-1003-2-6-85-11-1500 (2000)/317 (JUMO GmbH & Co. KG)	04-Pt100-A-Z1-KS2-30-1500 (2000) -TW204-B5/KS121 (Czah-pomiar Sp. z o.o.)	TTJE-26-S-10-6-M12x1-SP-2-1,5m (2,0m) (Limatherm Sensor Sp. z o.o)
Summary	-	- correct shape of sensor tip, - temperature range similar to the required, temperature range limited by properties of sensor and class of sensor, - accuracy better than required, - correct dimensions and wire length, - correct kind of fitting (bayonet).	- correct shape of sensor tip, - temperature range similar to the required, temperature range limited by the teflon insulated cable (operating temperature 50÷200 °C), - accuracy better than required, - correct dimensions and wire length, - correct kind of fitting (bayonet).	- correct shape of sensor tip, - correct temperature range, - correct accuracy, - correct dimensions and wire length, - correct kind of fitting (bayonet).

3. Elements of the pressure measurement system - selection of elements

The extrusion process requires proper preparation of the material. Pressure sensors were used for continuous pressure control at selected points in the operating system. Their task is to control the process of mixing and plasticization of the material.

The following pressure sensors were selected for the final stage of the selection:

- IE2S-6-H-B35D(B05C)-1-4-D-0 firm GEFRAN spa;
- ECHO-MA4-BAR-R21(22)-UNF-6PN-S06-F18-TCJ firmy Dynisco Europe;
- MKJ4-P5(3.5) BND firm MPI Melt Pressure.

Preliminary analysis of their technical parameters qualified them as elements useful and possible to use to control the pressure in the mixing and plasticizing system.

Characteristics of Gefran pressure sensors

Fig. 28, Fig. 29, Fig. 30 and Fig. 31 show the most important information about the Gefran IE2S-6-H-B35D (B05C)-1-4-D-0 pressure sensors [8].

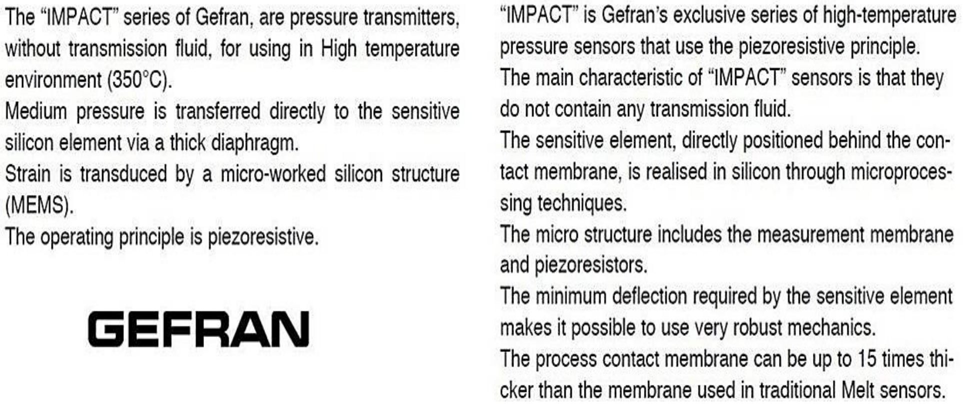

The "IMPACT" series of Gefran, are pressure transmitters, without transmission fluid, for using in High temperature environment (350°C).
Medium pressure is transferred directly to the sensitive silicon element via a thick diaphragm.
Strain is transduced by a micro-worked silicon structure (MEMS).
The operating principle is piezoresistive.

GEFRAN

"IMPACT" is Gefran's exclusive series of high-temperature pressure sensors that use the piezoresistive principle.
The main characteristic of "IMPACT" sensors is that they do not contain any transmission fluid.
The sensitive element, directly positioned behind the contact membrane, is realised in silicon through microprocessing techniques.
The micro structure includes the measurement membrane and piezoresistors.
The minimum deflection required by the sensitive element makes it possible to use very robust mechanics.
The process contact membrane can be up to 15 times thicker than the membrane used in traditional Melt sensors.

Fig. 28. Gefran pressure sensors - General description

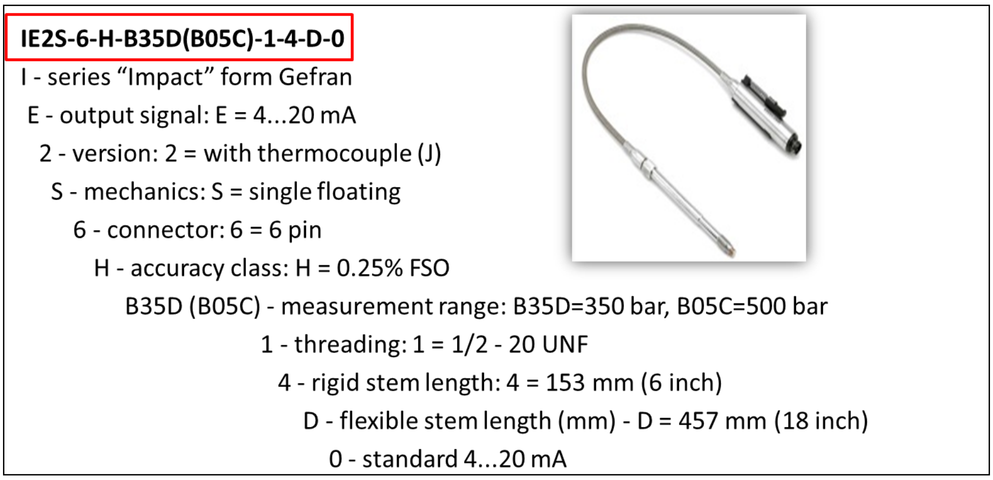

IE2S-6-H-B35D(B05C)-1-4-D-0
I - series "Impact" form Gefran
E - output signal: E = 4...20 mA
2 - version: 2 = with thermocouple (J)
S - mechanics: S = single floating
6 - connector: 6 = 6 pin
H - accuracy class: H = 0.25% FSO
B35D (B05C) - measurement range: B35D=350 bar, B05C=500 bar
1 - threading: 1 = 1/2 - 20 UNF
4 - rigid stem length: 4 = 153 mm (6 inch)
D - flexible stem length (mm) - D = 457 mm (18 inch)
0 - standard 4...20 mA

Fig. 29. Gefran pressure sensors - Sensor type

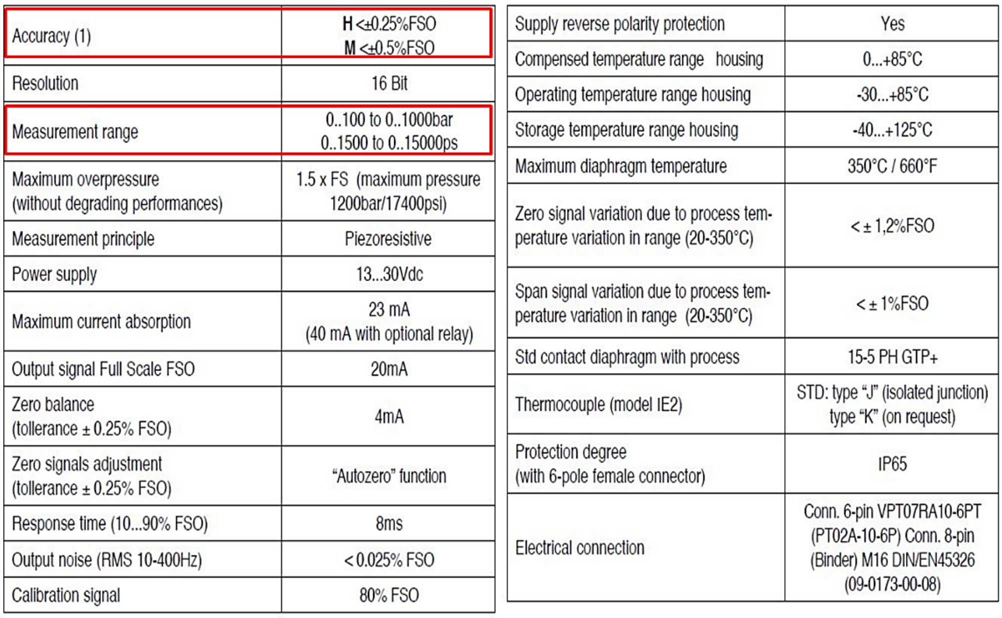

Accuracy (1)	**H** <±0.25%FSO **M** <±0.5%FSO
Resolution	16 Bit
Measurement range	0..100 to 0..1000bar 0..1500 to 0..15000ps
Maximum overpressure (without degrading performances)	1.5 x FS (maximum pressure 1200bar/17400psi)
Measurement principle	Piezoresistive
Power supply	13...30Vdc
Maximum current absorption	23 mA (40 mA with optional relay)
Output signal Full Scale FSO	20mA
Zero balance (tollerance ± 0.25% FSO)	4mA
Zero signals adjustment (tollerance ± 0.25% FSO)	"Autozero" function
Response time (10...90% FSO)	8ms
Output noise (RMS 10-400Hz)	< 0.025% FSO
Calibration signal	80% FSO

Supply reverse polarity protection	Yes
Compensed temperature range housing	0...+85°C
Operating temperature range housing	-30...+85°C
Storage temperature range housing	-40...+125°C
Maximum diaphragm temperature	350°C / 660°F
Zero signal variation due to process temperature variation in range (20-350°C)	< ± 1,2%FSO
Span signal variation due to process temperature variation in range (20-350°C)	< ± 1%FSO
Std contact diaphragm with process	15-5 PH GTP+
Thermocouple (model IE2)	STD: type "J" (isolated junction) type "K" (on request)
Protection degree (with 6-pole female connector)	IP65
Electrical connection	Conn. 6-pin VPT07RA10-6PT (PT02A-10-6P) Conn. 8-pin (Binder) M16 DIN/EN45326 (09-0173-00-08)

Fig. 30. Gefran pressure sensors - Technical data

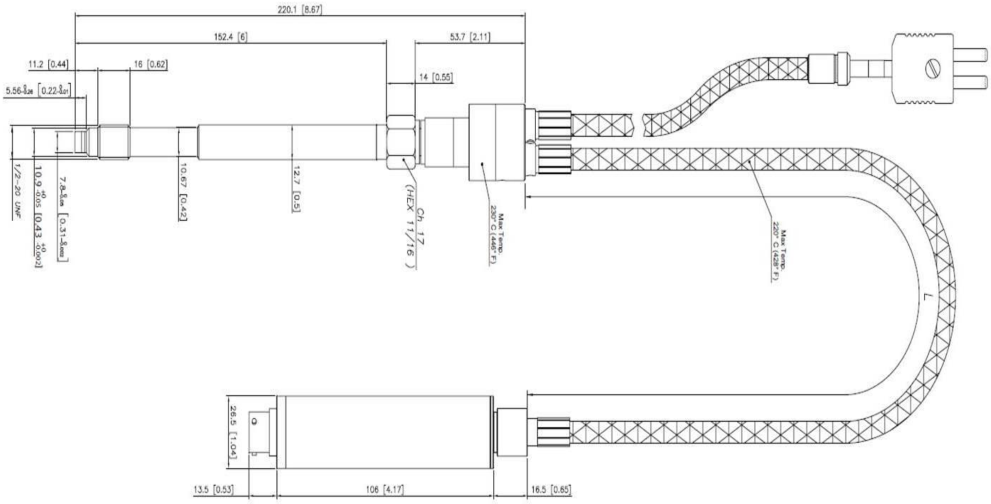
220.1 [8.67]
152.4 [6]
53.7 [2.11]
11.2 [0.44]
16 [0.62]
14 [0.55]
5.56-0.26 [0.22-0.01]
1/2-20 UNF
10.9 +0 -0.05 [0.43 +0 -0.002]
7.8-0.05 [0.31-0.002]
10.67 [0.42]
12.7 [0.5]
Ch. 17 (HEX 11/16)
Max Temp. 230° C (446° F)
Max Temp. 220° C (428° F)
L
26.5 [1.04]
13.5 [0.53]
106 [4.17]
16.5 [0.65]

Fig. 31. Gefran pressure sensors - Dimensions

Characteristics of Dynisco Europe pressure sensors

Fig. 32, Fig. 33, Fig. 34 and Fig. 35 show the most important information about the Dynisco Europe ECHO-MA4-BAR-R21 (22) -UNF-6PN-S06-F18-TCJ pressure sensors [9].

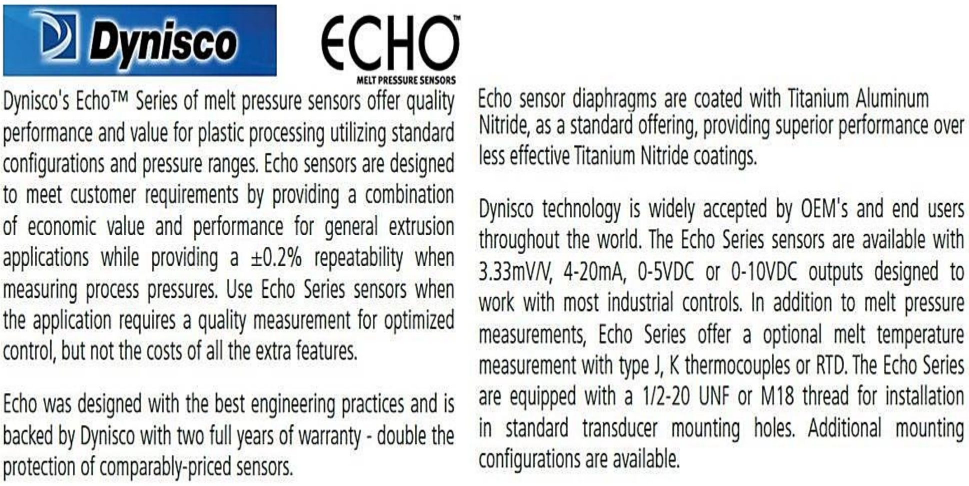

Dynisco ECHO™ MELT PRESSURE SENSORS

Dynisco's Echo™ Series of melt pressure sensors offer quality performance and value for plastic processing utilizing standard configurations and pressure ranges. Echo sensors are designed to meet customer requirements by providing a combination of economic value and performance for general extrusion applications while providing a ±0.2% repeatability when measuring process pressures. Use Echo Series sensors when the application requires a quality measurement for optimized control, but not the costs of all the extra features.

Echo was designed with the best engineering practices and is backed by Dynisco with two full years of warranty - double the protection of comparably-priced sensors.

Echo sensor diaphragms are coated with Titanium Aluminum Nitride, as a standard offering, providing superior performance over less effective Titanium Nitride coatings.

Dynisco technology is widely accepted by OEM's and end users throughout the world. The Echo Series sensors are available with 3.33mV/V, 4-20mA, 0-5VDC or 0-10VDC outputs designed to work with most industrial controls. In addition to melt pressure measurements, Echo Series offer a optional melt temperature measurement with type J, K thermocouples or RTD. The Echo Series are equipped with a 1/2-20 UNF or M18 thread for installation in standard transducer mounting holes. Additional mounting configurations are available.

Fig. 32. Dynisco Europe pressure sensors - General description

ECHO-MA4-BAR-R21(22)-UNF-6PN-S06-F18-TCJ

ECHO - Dynisco's Echo Series of melt pressure sensors

MA4 - Output: MA4 = 4-20mA

BAR - Units of Measure: BAR = Bar

R - Pressure Range: R21 = 5M psi; 350Kg/cm2 350 Bar; 35MPa: R22 = 7.5M psi; 500Kg/cm2 500 Bar; 50MPa

UNF - Process Connection: UNF = 1/2-20 UNF

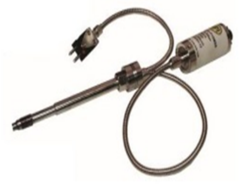

6PN - Electrical Connection: 6PN = 6 pin connector

S06 - Snout Length: S06 = 6 inch (15.2 cm)

F18 - Flexible Length: F18 = 18 inches (45.7 cm)

TCJ - Thermocouple: TCJ = Thermocouple J-type with 3 inch flex

Fig. 33. Dynisco Europe pressure sensors - Sensor type

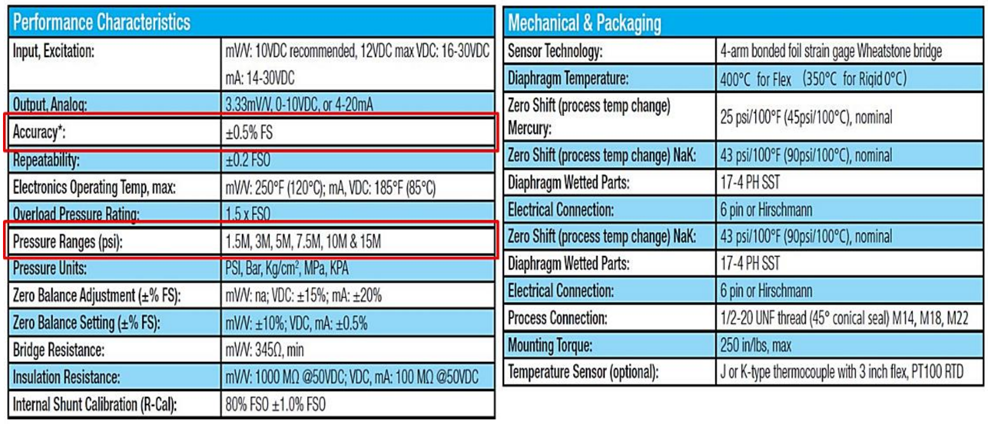

Performance Characteristics	
Input, Excitation:	mV/V: 10VDC recommended, 12VDC max VDC: 16-30VDC mA: 14-30VDC
Output, Analog:	3.33mV/V, 0-10VDC, or 4-20mA
Accuracy*:	±0.5% FS
Repeatability:	±0.2 FSO
Electronics Operating Temp, max:	mV/V: 250°F (120°C); mA, VDC: 185°F (85°C)
Overload Pressure Rating:	1.5 x FSO
Pressure Ranges (psi):	1.5M, 3M, 5M, 7.5M, 10M & 15M
Pressure Units:	PSI, Bar, Kg/cm², MPa, KPA
Zero Balance Adjustment (±% FS):	mV/V: na; VDC: ±15%; mA: ±20%
Zero Balance Setting (±% FS):	mV/V: ±10%; VDC, mA: ±0.5%
Bridge Resistance:	mV/V: 345Ω, min
Insulation Resistance:	mV/V: 1000 MΩ @50VDC; VDC, mA: 100 MΩ @50VDC
Internal Shunt Calibration (R-Cal):	80% FSO ±1.0% FSO

Mechanical & Packaging	
Sensor Technology:	4-arm bonded foil strain gage Wheatstone bridge
Diaphragm Temperature:	400°C for Flex (350°C for Rigid 0°C)
Zero Shift (process temp change) Mercury:	25 psi/100°F (45psi/100°C), nominal
Zero Shift (process temp change) NaK:	43 psi/100°F (90psi/100°C), nominal
Diaphragm Wetted Parts:	17-4 PH SST
Electrical Connection:	6 pin or Hirschmann
Zero Shift (process temp change) NaK:	43 psi/100°F (90psi/100°C), nominal
Diaphragm Wetted Parts:	17-4 PH SST
Electrical Connection:	6 pin or Hirschmann
Process Connection:	1/2-20 UNF thread (45° conical seal) M14, M18, M22
Mounting Torque:	250 in/lbs, max
Temperature Sensor (optional):	J or K-type thermocouple with 3 inch flex, PT100 RTD

Fig. 34. Dynisco Europe pressure sensors - Technical data

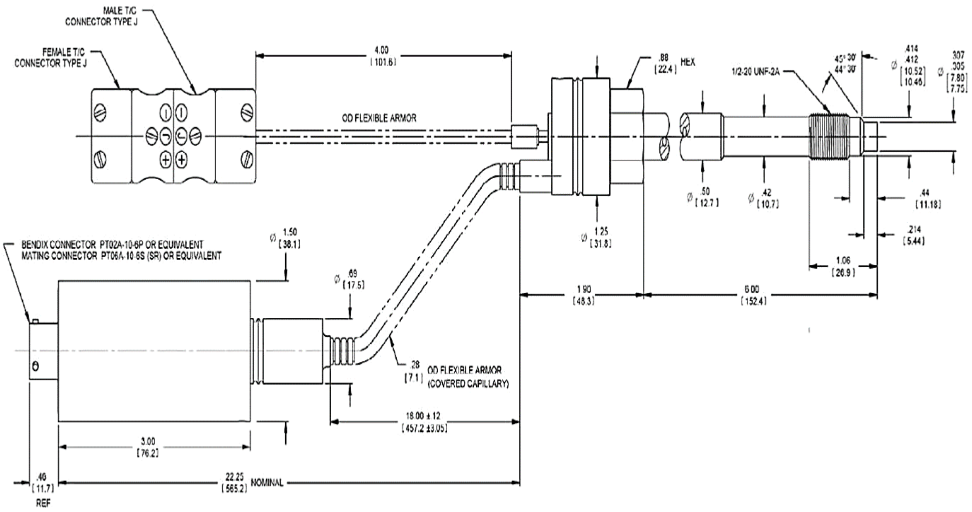
MALE T/C
CONNECTOR TYPE J
FEMALE T/C
CONNECTOR TYPE J
4.00
[101.6]
OD FLEXIBLE ARMOR
.88
[22.4] HEX
1/2-20 UNF-2A
45° 30'
44° 30'
Ø .414
.412
[10.52]
[10.46]
Ø .307
.305
[7.80]
[7.75]
Ø .50
[12.7]
Ø .42
[10.7]
.44
[11.18]
.214
[5.44]
Ø 1.25
[31.8]
1.06
[26.9]
1.90
[48.3]
6.00
[152.4]
BENDIX CONNECTOR PT02A-10-6P OR EQUIVALENT
MATING CONNECTOR PT06A-10-6S (SR) OR EQUIVALENT
Ø 1.50
[38.1]
Ø .69
[17.5]
.28
[7.1]
OD FLEXIBLE ARMOR
(COVERED CAPILLARY)
18.00 ± .12
[457.2 ±3.05]
3.00
[76.2]
.46
[11.7]
REF
22.25
[565.2] NOMINAL

Fig. 35. Dynisco Europe pressure sensors - Dimensions

Characteristics of MPI Melt pressure sensors

Fig. 36, Fig. 37, Fig. 38 and Fig. 39 shows the most important information about the pressure sensors MKJ4-P5 (3.5) BND from MPI Melt Pressure [10].

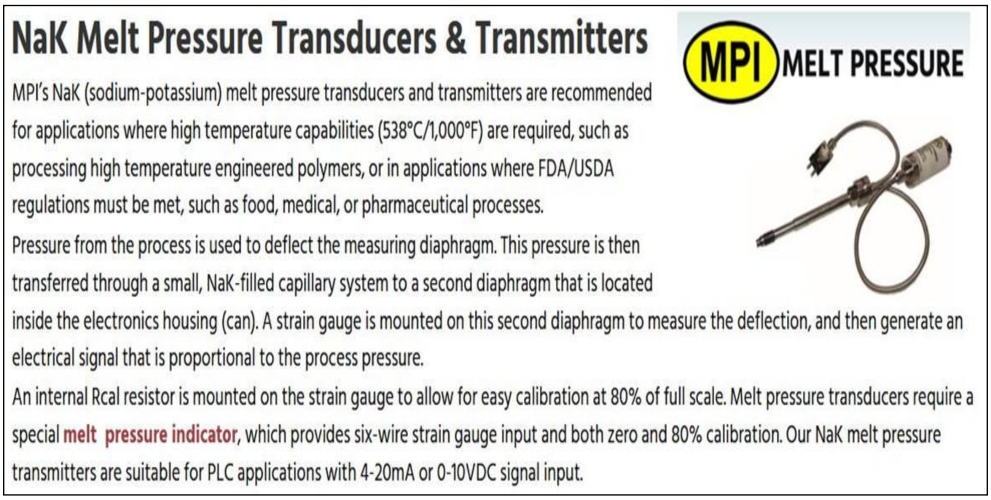

NaK Melt Pressure Transducers & Transmitters

MPI MELT PRESSURE

MPI's NaK (sodium-potassium) melt pressure transducers and transmitters are recommended for applications where high temperature capabilities (538°C/1,000°F) are required, such as processing high temperature engineered polymers, or in applications where FDA/USDA regulations must be met, such as food, medical, or pharmaceutical processes.

Pressure from the process is used to deflect the measuring diaphragm. This pressure is then transferred through a small, NaK-filled capillary system to a second diaphragm that is located inside the electronics housing (can). A strain gauge is mounted on this second diaphragm to measure the deflection, and then generate an electrical signal that is proportional to the process pressure.

An internal Rcal resistor is mounted on the strain gauge to allow for easy calibration at 80% of full scale. Melt pressure transducers require a special **melt pressure indicator**, which provides six-wire strain gauge input and both zero and 80% calibration. Our NaK melt pressure transmitters are suitable for PLC applications with 4-20mA or 0-10VDC signal input.

Fig. 36. MPI Melt pressure sensors - General description

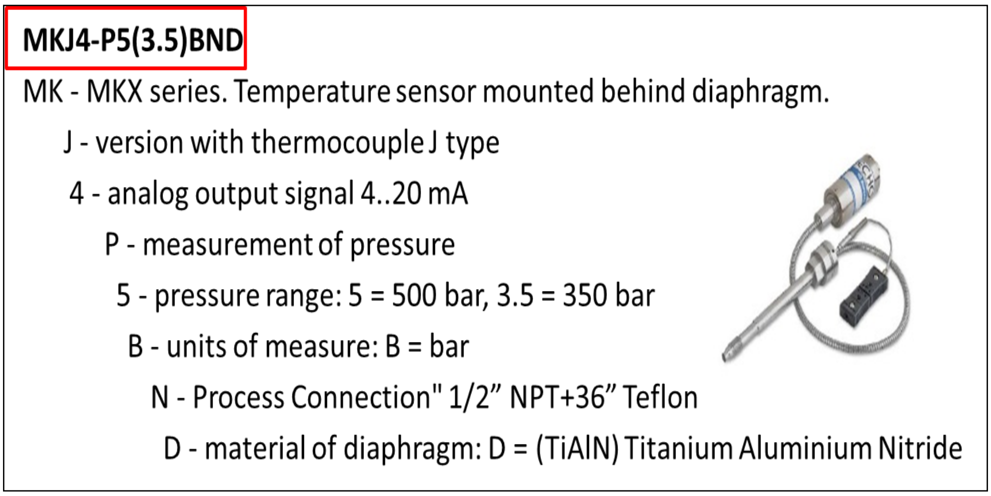

MKJ4-P5(3.5)BND

MK - MKX series. Temperature sensor mounted behind diaphragm.
J - version with thermocouple J type
4 - analog output signal 4..20 mA
P - measurement of pressure
5 - pressure range: 5 = 500 bar, 3.5 = 350 bar
B - units of measure: B = bar
N - Process Connection" 1/2" NPT+36" Teflon
D - material of diaphragm: D = (TiAlN) Titanium Aluminium Nitride

Fig. 37. MPI Melt pressure sensors - Sensor type

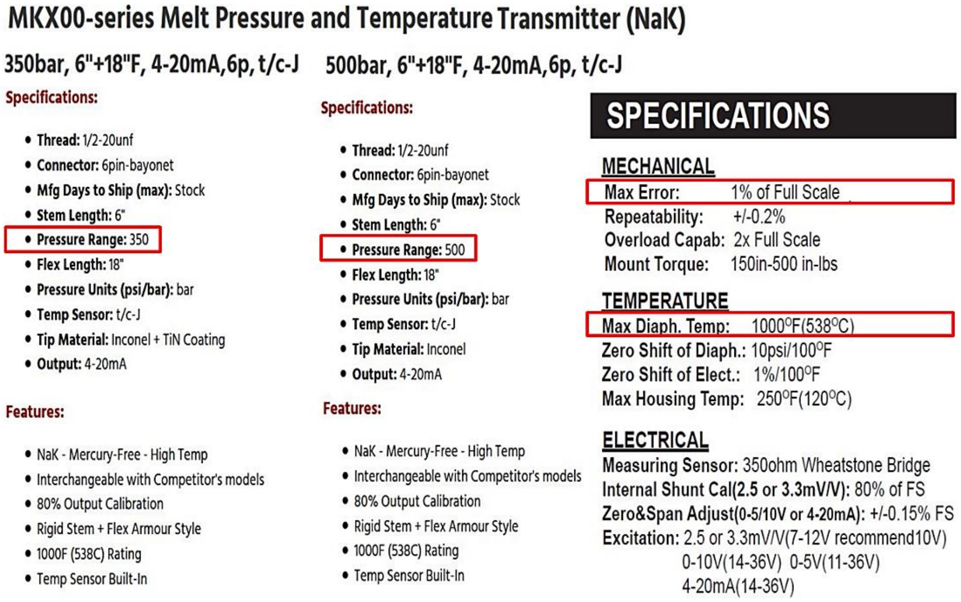

MKX00-series Melt Pressure and Temperature Transmitter (NaK)

350bar, 6"+18"F, 4-20mA,6p, t/c-J

Specifications:

- **Thread:** 1/2-20unf
- **Connector:** 6pin-bayonet
- **Mfg Days to Ship (max):** Stock
- **Stem Length:** 6"
- **Pressure Range:** 350
- **Flex Length:** 18"
- **Pressure Units (psi/bar):** bar
- **Temp Sensor:** t/c-J
- **Tip Material:** Inconel + TiN Coating
- **Output:** 4-20mA

Features:

- NaK - Mercury-Free - High Temp
- Interchangeable with Competitor's models
- 80% Output Calibration
- Rigid Stem + Flex Armour Style
- 1000F (538C) Rating
- Temp Sensor Built-In

500bar, 6"+18"F, 4-20mA,6p, t/c-J

Specifications:

- **Thread:** 1/2-20unf
- **Connector:** 6pin-bayonet
- **Mfg Days to Ship (max):** Stock
- **Stem Length:** 6"
- **Pressure Range:** 500
- **Flex Length:** 18"
- **Pressure Units (psi/bar):** bar
- **Temp Sensor:** t/c-J
- **Tip Material:** Inconel
- **Output:** 4-20mA

Features:

- NaK - Mercury-Free - High Temp
- Interchangeable with Competitor's models
- 80% Output Calibration
- Rigid Stem + Flex Armour Style
- 1000F (538C) Rating
- Temp Sensor Built-In

SPECIFICATIONS

MECHANICAL

Max Error:	1% of Full Scale
Repeatability:	+/-0.2%
Overload Capab:	2x Full Scale
Mount Torque:	150in-500 in-lbs

TEMPERATURE

Max Diaph. Temp:	1000°F(538°C)
Zero Shift of Diaph.:	10psi/100°F
Zero Shift of Elect.:	1%/100°F
Max Housing Temp:	250°F(120°C)

ELECTRICAL

Measuring Sensor:	350ohm Wheatstone Bridge
Internal Shunt Cal(2.5 or 3.3mV/V):	80% of FS
Zero&Span Adjust(0-5/10V or 4-20mA):	+/-0.15% FS
Excitation:	2.5 or 3.3mV/V(7-12V recommend10V) 0-10V(14-36V) 0-5V(11-36V) 4-20mA(14-36V)

Fig. 38. MPI Melt pressure sensors - Technical data

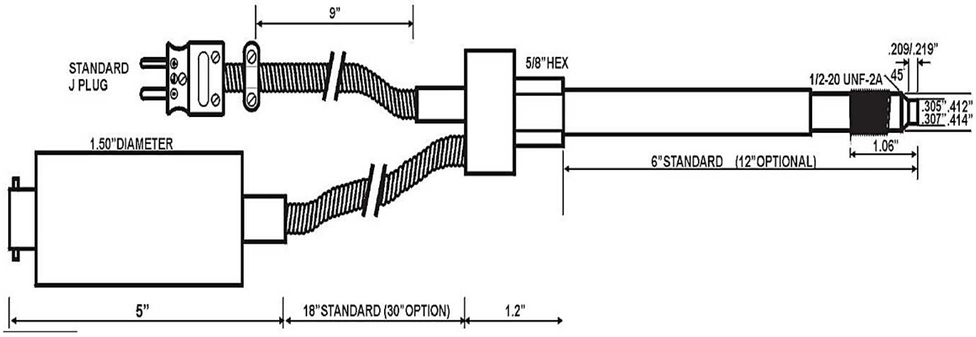

Fig. 39. MPI Melt pressure sensors - Dimensions

Elements of the pressure measurement system - summary

Based on the collected information, pressure sensors from Dynisco Europe were selected as the most suitable for use in the extruder. All technical parameters of Dynisco Europe pressure sensors are within the reference ranges Results of data analysis and comparison of pressure sensors in Table 9 and Table 10.

Table 9. Pressure sensors – Comparison of selected parameters

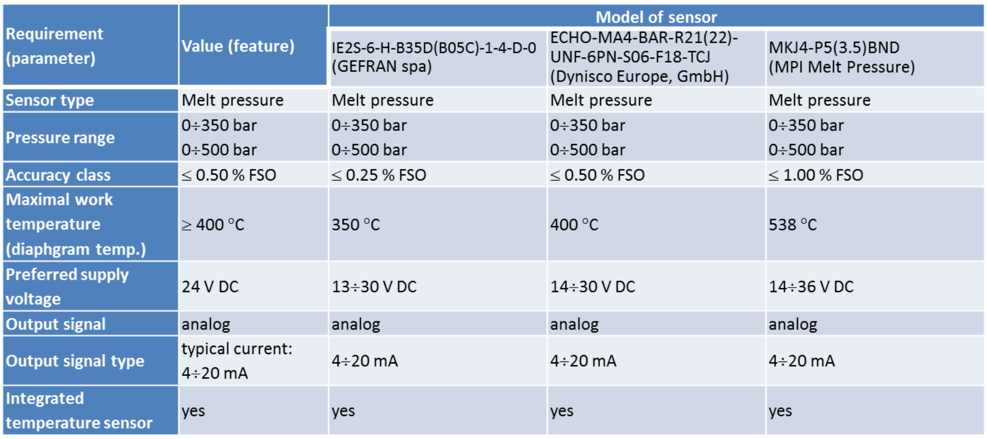

Requirement (parameter)	Value (feature)	Model of sensor		
		IE2S-6-H-B35D(B05C)-1-4-D-0 (GEFRAN spa)	ECHO-MA4-BAR-R21(22)-UNF-6PN-S06-F18-TCJ (Dynisco Europe, GmbH)	MKJ4-P5(3.5)BND (MPI Melt Pressure)
Sensor type	Melt pressure	Melt pressure	Melt pressure	Melt pressure
Pressure range	0÷350 bar 0÷500 bar	0÷350 bar 0÷500 bar	0÷350 bar 0÷500 bar	0÷350 bar 0÷500 bar
Accuracy class	≤ 0.50 % FSO	≤ 0.25 % FSO	≤ 0.50 % FSO	≤ 1.00 % FSO
Maximal work temperature (diaphgram temp.)	≥ 400 °C	350 °C	400 °C	538 °C
Preferred supply voltage	24 V DC	13÷30 V DC	14÷30 V DC	14÷36 V DC
Output signal	analog	analog	analog	analog
Output signal type	typical current: 4÷20 mA	4÷20 mA	4÷20 mA	4÷20 mA
Integrated temperature sensor	yes	yes	yes	yes

Table 10. Pressure sensors – Summary

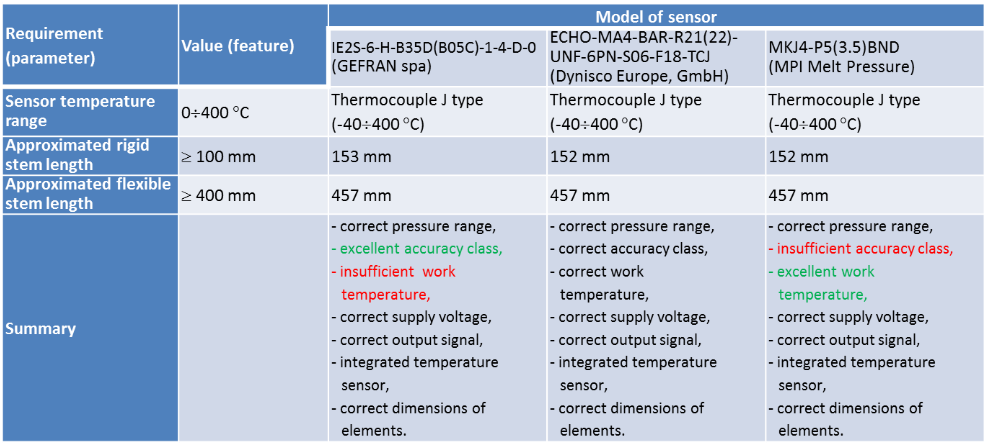

Requirement (parameter)	Value (feature)	Model of sensor		
		IE2S-6-H-B35D(B05C)-1-4-D-0 (GEFRAN spa)	ECHO-MA4-BAR-R21(22)-UNF-6PN-S06-F18-TCJ (Dynisco Europe, GmbH)	MKJ4-P5(3.5)BND (MPI Melt Pressure)
Sensor temperature range	0÷400 °C	Thermocouple J type (-40÷400 °C)	Thermocouple J type (-40÷400 °C)	Thermocouple J type (-40÷400 °C)
Approximated rigid stem length	≥ 100 mm	153 mm	152 mm	152 mm
Approximated flexible stem length	≥ 400 mm	457 mm	457 mm	457 mm
Summary		- correct pressure range, - excellent accuracy class, - insufficient work temperature, - correct supply voltage, - correct output signal, - integrated temperature sensor, - correct dimensions of elements.	- correct pressure range, - correct accuracy class, - correct work temperature, - correct supply voltage, - correct output signal, - integrated temperature sensor, - correct dimensions of elements.	- correct pressure range, - insufficient accuracy class, - excellent work temperature, - correct supply voltage, - correct output signal, - integrated temperature sensor, - correct dimensions of elements.

The selection of the electrical components of the extruder - summary

The selection of elements of electrical equipment (Fig. 40) included the following elements:

- main drive motor,
- rotary sleeve drive motor,
- elements of the heating system,
- components of the temperature measurement system,
- elements of the pressure measurement system,
- stream control component in the cooling system.

The selection of the electrical components of the extruder is shown in Table 11.

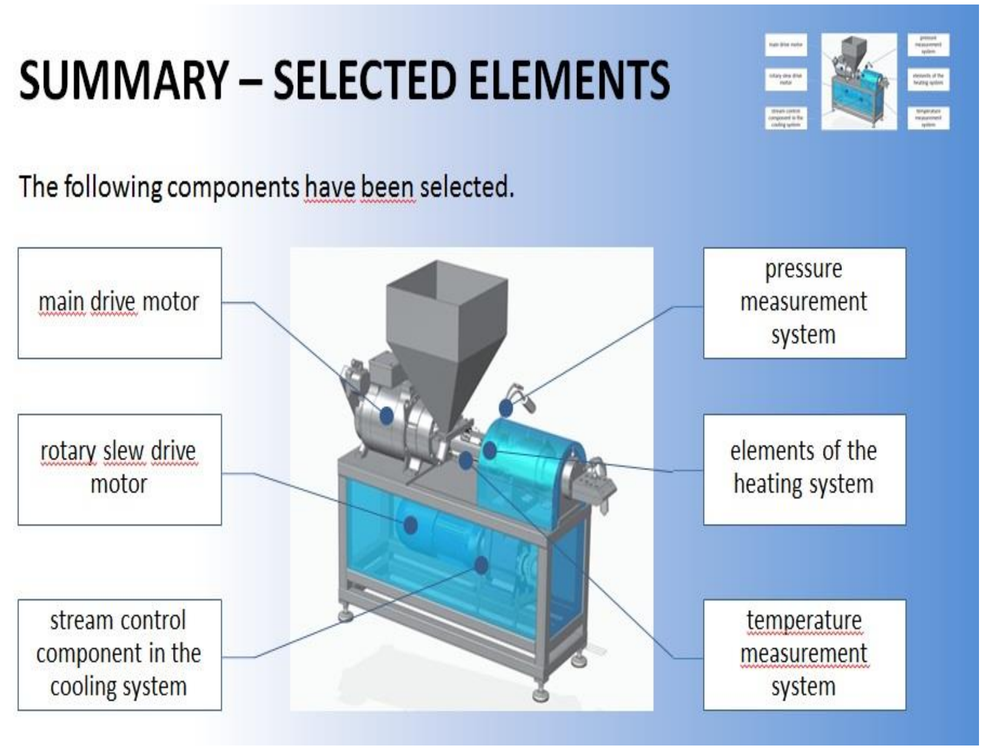

SUMMARY – SELECTED ELEMENTS

The following components have been selected.

main drive motor

rotary slew drive motor

stream control component in the cooling system

pressure measurement system

elements of the heating system

temperature measurement system

Fig. 40. The list of electrical equipment selected to work with the extruder working systems

Table 11. The selection of the electrical components of the extruder - summary

System/Destination	Model/type of device	Manufacturer/Dustributor
Main drive	DST2-135MO54W-017-5-A-DG-6-MTR-O-000	Baumüller GmbH
	BmaXX 5525 servo controller	
Rotary slew drive	CHT 112 M4 B5 IE2 4.0 KW + 3xPTC	Chiaravalli SpA
	CHC40 gear unit	
Temperature measurement system	TTJE-26-S-10-6-M12x1-SP-2-1,5m	Limatherm Sensor Sp. z o.o
	TTJE-26-S-10-6-M12x1-SP-2-2,0 m	
Pressure measurement system	ECHO-MA4-BAR-R21-UNF-6PN-S06-F18-TCJ	Dynisco Europe GmbH
	ECHO-MA4-BAR-R22-UNF-6PN-S06-F18-TCJ	
Heating system	GM 100x65 750W/230V	Limatherm Sensor Sp. z o.o
	GM 180x115 2200W/230V	
	GM 100x75 800W/230V	
	GM 150x40 650W/230V	
	GM 125x105x9 650W/230V	
Stream control in the cooling system	CFB-D22G-R1-B83 (distributor code CFB-2M08-1/4)	Camozzi Automation S.p.A.

4. Conclusions

Making a prototype of a new device requires taking into account many material, process and construction factors. Appropriate selection of individual elements of the machine enables its proper operation. One of the important elements of the devices are power supply systems as well as control and measurement systems, including heating elements as well as temperature and pressure sensors. The individual elements shown in the work met the expectations of the creators and constructors of the machine.

The applied heating elements, temperature and pressure sensors of the material as well as elements of the temperature measurement and control system along the length of the plasticizing system make it possible to achieve the assumed temperatures and maintain the operating temperature within the prescribed range. The material pressure sensors used enable the measurement of this value with the appropriate accuracy. Thanks to this, the processes of mixing and plasticizing the composites proceed according to the plan.

Acknowledgements

This project has received funding from the European Union's Horizon 2020 research and innovation programme under the Marie Skłodowska-Curie grant agreement No. 734205 – H2020-MSCA-RISE-2016.

References

[1] https://www.limathermsensor.pl/products/category/grzalki-elektryczne/48
[2] https://selfa.pl/katalog/grzalki-elektryczne-promienniki-i-kable-grzejne/opaskowe/
[3] http://termik.pl/katalog
[4] http://www.centro-therm.pl/
[5] https://www.jumo.pl/web/products/temperature
[6] https://czah.pl/pl/i/Katalog-produktow/15
[7] https://www.limathermsensor.pl/products/category/czujniki-temperatury/19
[8] https://gefran.pl/gefran-polska/czujniki/
[9] http://www.dynisco.com/sensors-and-measurement/sensors/Melt-Pressure-Transducers/Echo-Series
[10] https://www.mpipressure.com/melt-pressure-transducers-melt-pressure-transmitters

Janusz Sikora[1], Ľudmila Dulebová[2]

IMPLEMENTATION OF THE PLASTICATION PROCESS IN AN INNOVATIVE EXTRUSION MACHINE FOR THE PROCESSING OF COMPOSITE AND NANOCOMPOSITE MATERIALS. CONCEPT AND IMPLEMENTATION OF CONTROL SYSTEM OF THE EXTRUDER. PART III - DATA ACQUISITION & CONTROL SYSTEM

Abstract: *The process of extruding composite and nanocomposite materials is a complicated technological process. The extrusion process requires taking into account many technological factors. Factors that should be considered are the parameters of the composite blend and the process parameters related to the temperature and pressure of the composite during the formation of the final product. The required physical parameters are obtained thanks to the use of appropriate control, measurement and executive systems. The paper presents executive, measurement and control systems used in an innovative extruder for composite and nanocomposite materials.*

Keywords: *innovation technologies of extrusion, extrusion of composites and nanocomposites, pressure and temperature measurement system, control systems.*

1. Introduction

In processing processes, data acquisition, control and monitoring are extremely important, including monitoring of operating parameters, e.g. of an extruder. Data collection allows manufacturers to monitor production lines in real time, maintain product performance and quality, and process data to make smarter decisions. In order for this system to work efficiently, correctly and efficiently, it is necessary to select appropriate elements for it to ensure proper measurement, transmission, collection and visualization of information directly from the extruder.

The article presents the methodology of selecting the elements of the data acquisition and control system that will be implemented in a new generation extruder.

---

[1] *Lublin University of Technology, Faculty of Mechanical Engineering, Department of Technology and Polymer Processing, ul. Nadbystrzycka 36, 20-618 Lublin, Poland, janusz.sikora@pollub.pl.*

[2] *Technical University of Kosice, Faculty of Mechanical Engineering, Department Technologies, Materials and Computer Aided Production, Masiarska 74, 040 01 Kosice, Slovakia, ludmila.dulebova@tuke.sk.*

2. The selection of components of data acquisition and control system

In order to ensure the correct extrusion process, it is important to maintain strictly defined technical parameters. This is especially important in the case of prototype machines. Such a prototype machine with great potential for innovation is an extruder for processing composite and nanocomposite materials. The composite and nanocomposite materials require precise working conditions and maintaining set temperature and pressure values. In order to ensure such precise settings, the executive and working systems must be supervised by modern controllers that enable the implementation of regulatory processes, information exchange, and collection and archiving of measurement data.

The following functions and tasks were defined for the extruder system to be performed by the control system:

Basic tasks to be carried out by the control system:

1. Main (motor) drive:
    - Switching on and off;
    - Rotational speed control;
    - Rotational speed measurement;
    - Measurement of energy consumption (power).
    - Electrical protection
2. Rotary faucet drive:
    - Switching on and off;
    - Rotational speed control;
    - Rotational speed measurement;
    - Measurement of energy consumption;
    - Electrical protection.
3. Pressure and temperature sensors:
    - Pressure measurement in 4 zones (4 analog 4÷20 mA signals);
    - Temperature measurement in 4 zones (4 thermocouple signals).
4. Temperature sensors:
    - Temperature measurement in 6 points (6 thermocouple signals)
5. Heaters:
    - Switching on and off in 5 zones (5 digital outputs);
    - Measurement of heater current in the 5 zones (5 analog inputs).
6. Cooling system:
    - Switching on and off of solenoid valves of the cooling system (3 digital outputs);
    - Thermal monitoring the state of the solenoid valves (3 digital inputs).
7. Main controller:
    - Input data acquisition from expansion modules;
    - Safety devices signals acquisition;
    - Collecting data from the operator panel;
    - Execution of the control algorithm;
    - Transmission of control data to output modules;

- Generating safety signals;
- Displaying data on the operator panel;
- Registration of process data (temperature, power, energy, rotational speed).

Safety and support tasks to be carried out by the control system:

- Cooling of the control system housing;
- Fan thermal protection of cooling of the control system housing;
- The correct phase sequence verification;
- Overcurrent protection of the phase sequence sensor;
- Energy meter overcurrent protection;
- Switching the main drive on and off (main drive contactor);
- Main drive overcurrent protection;
- Switching the rotary faucet drive on and off (faucet drive contactor);
- Rotary faucet drive overcurrent protection;
- Low DC power supply (220VAC / 24VDC power supplies);
- Powering up the heaters (solid state relays);
- Overcurrent protection of power circuits of heaters;
- Powering up the electrovalves (solenoid valves) (solid state relays);
- Overcurrent protection of supply circuits of electrovalves;
- Electrical protection of the entire circuit of power and control system;
- Measurement of electrical energy consumption;
- Mechanical shield of power and control system.

The general scheme of the control system is presented in Fig. 1.

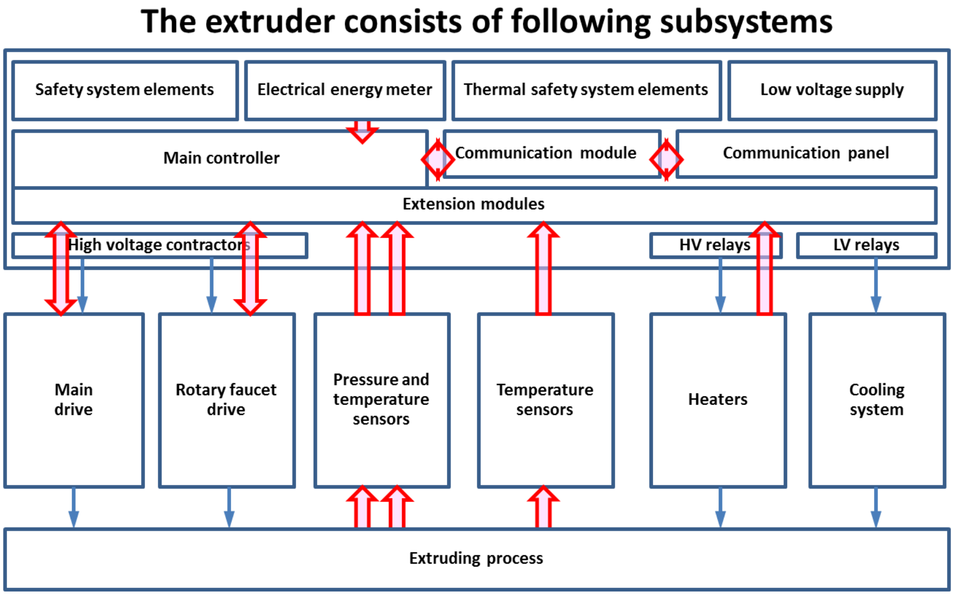
The extruder consists of following subsystems
Safety system elements
Electrical energy meter
Thermal safety system elements
Low voltage supply
Main controller
Communication module
Communication panel
Extension modules
High voltage contractors
HV relays
LV relays
Main drive
Rotary faucet drive
Pressure and temperature sensors
Temperature sensors
Heaters
Cooling system
Extruding process

Fig. 1. General diagram of the extruder controls system

Fig. 2, Fig. 3, Fig. 4, Fig. 5, Fig. 6 and Fig. 7 show the list of electrical devices of the extruder and the signal connections of inputs and outputs with the extruder control system.

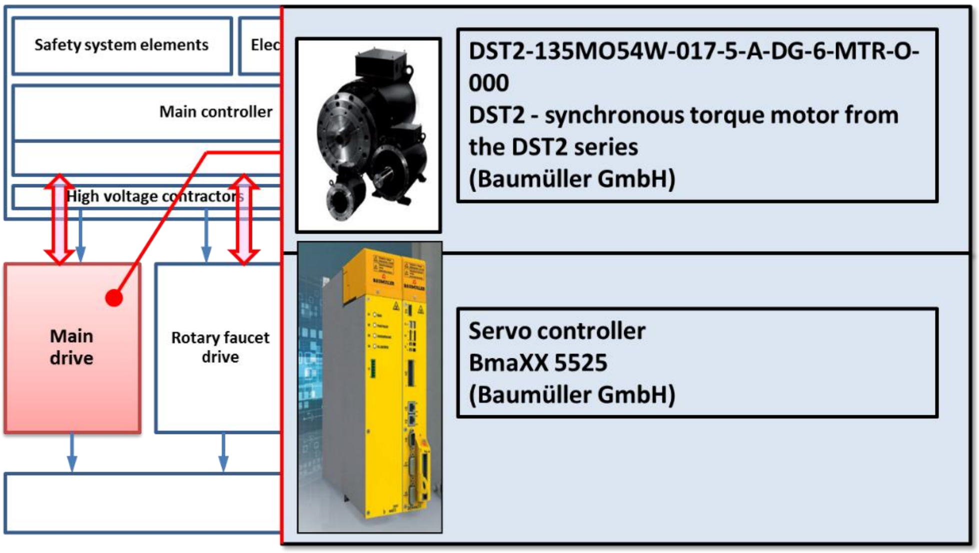
Safety system elements
Elec
Main controller
High voltage contractors
Main drive
Rotary faucet drive
DST2-135MO54W-017-5-A-DG-6-MTR-O-000
DST2 - synchronous torque motor from the DST2 series
(Baumüller GmbH)
Servo controller
BmaXX 5525
(Baumüller GmbH)

Fig. 2. Main drive - output and input signals in control system

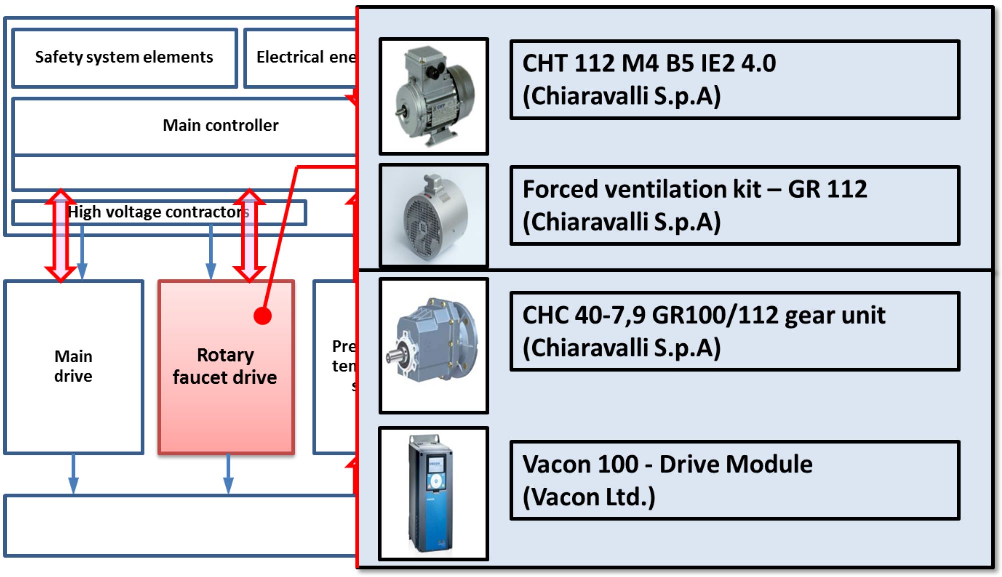
Safety system elements
Electrical ene
Main controller
High voltage contractors
Main drive
Rotary faucet drive
Pre
ten
CHT 112 M4 B5 IE2 4.0
(Chiaravalli S.p.A)
Forced ventilation kit – GR 112
(Chiaravalli S.p.A)
CHC 40-7,9 GR100/112 gear unit
(Chiaravalli S.p.A)
Vacon 100 - Drive Module
(Vacon Ltd.)

Fig. 3. Rotary faucet drive - output and input signals in control system

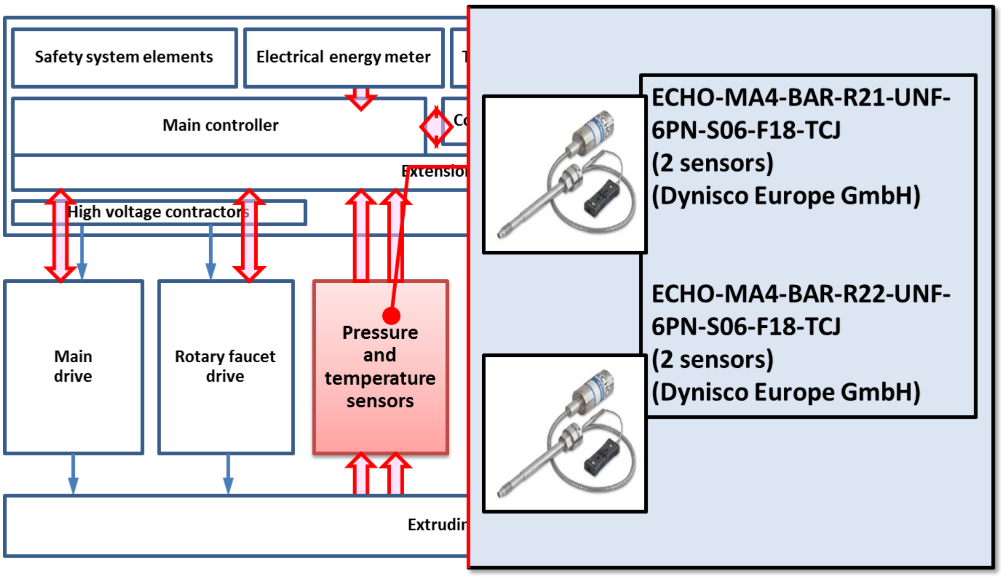
Safety system elements
Electrical energy meter
T
Main controller
Co
Extension
High voltage contractors
Main drive
Rotary faucet drive
Pressure and temperature sensors
Extrudin
ECHO-MA4-BAR-R21-UNF-6PN-S06-F18-TCJ
(2 sensors)
(Dynisco Europe GmbH)
ECHO-MA4-BAR-R22-UNF-6PN-S06-F18-TCJ
(2 sensors)
(Dynisco Europe GmbH)

Fig. 4. Pressure and temperature sensors - output and input signals in control system

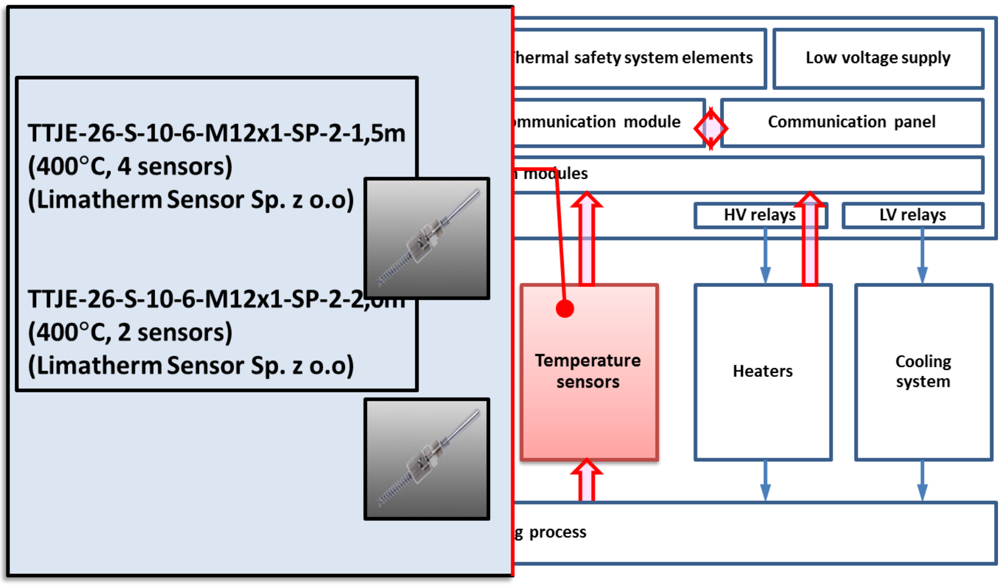
TTJE-26-S-10-6-M12x1-SP-2-1,5m
(400°C, 4 sensors)
(Limatherm Sensor Sp. z o.o)
TTJE-26-S-10-6-M12x1-SP-2-2,
(400°C, 2 sensors)
(Limatherm Sensor Sp. z o.o)
hermal safety system elements
Low voltage supply
mmunication module
Communication panel
modules
HV relays
LV relays
Temperature sensors
Heaters
Cooling system
g process

Fig. 5. Temperature sensors - output and input signals in control system

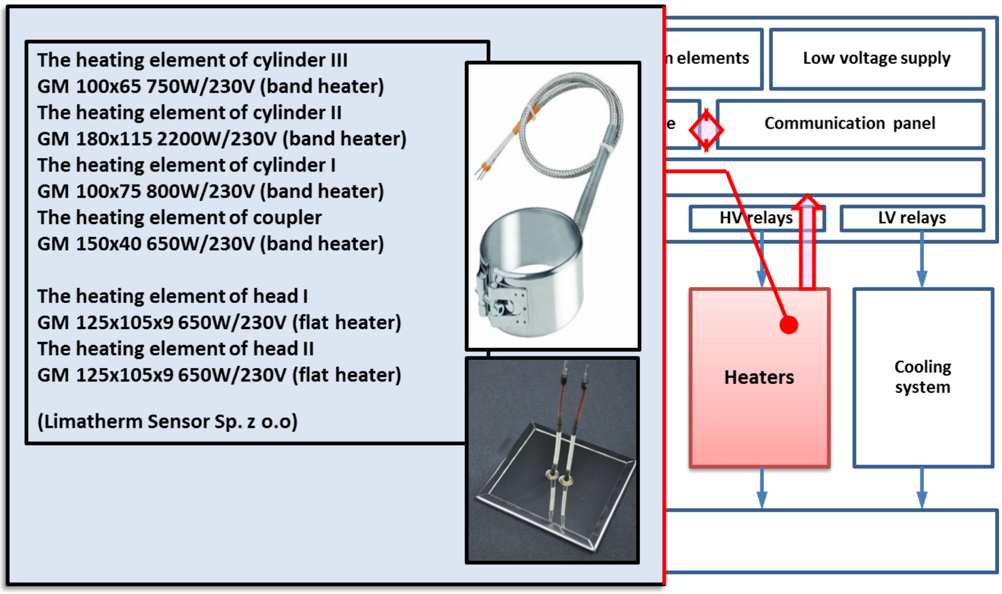

The heating element of cylinder III
GM 100x65 750W/230V (band heater)
The heating element of cylinder II
GM 180x115 2200W/230V (band heater)
The heating element of cylinder I
GM 100x75 800W/230V (band heater)
The heating element of coupler
GM 150x40 650W/230V (band heater)

The heating element of head I
GM 125x105x9 650W/230V (flat heater)
The heating element of head II
GM 125x105x9 650W/230V (flat heater)

(Limatherm Sensor Sp. z o.o)

n elements
Low voltage supply
e
Communication panel
HV relays
LV relays
Heaters
Cooling system

Fig. 6. Heating system - output and input signals in control system

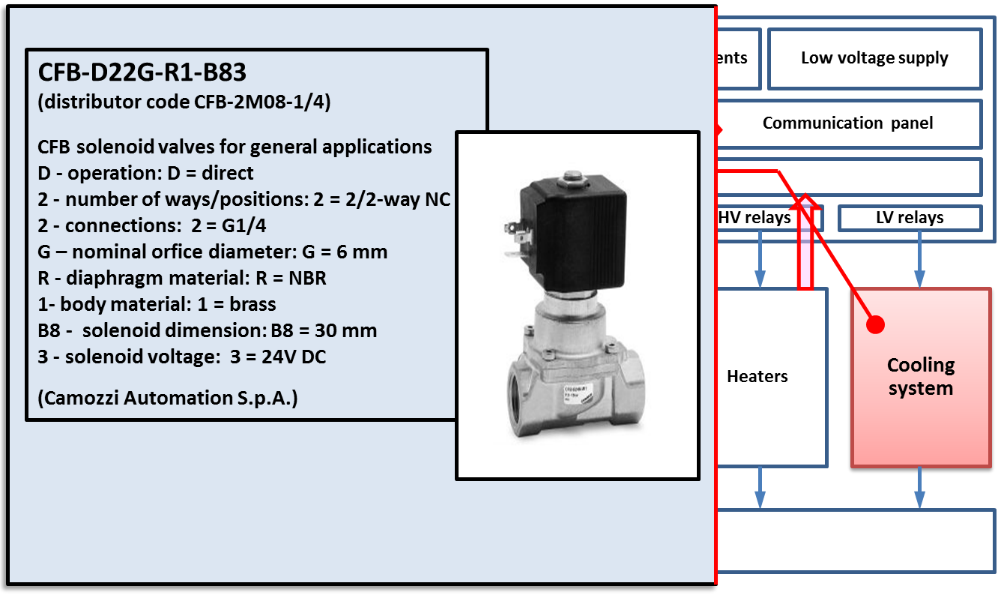

CFB-D22G-R1-B83
(distributor code CFB-2M08-1/4)

CFB solenoid valves for general applications
D - operation: D = direct
2 - number of ways/positions: 2 = 2/2-way NC
2 - connections: 2 = G1/4
G – nominal orfice diameter: G = 6 mm
R - diaphragm material: R = NBR
1- body material: 1 = brass
B8 - solenoid dimension: B8 = 30 mm
3 - solenoid voltage: 3 = 24V DC

(Camozzi Automation S.p.A.)

ents
Low voltage supply
Communication panel
HV relays
LV relays
Heaters
Cooling system

Fig. 7. Cooling system - output and input signals in control system

Components of data acquisition and control system - selection of elements

The implementation of data processing processes for the presented structure of the extruder elements is possible only by specialized control systems. Control systems must be built of proven devices, using modern microprocessor systems and a PLC controller.

The selection of the control system was made on the basis of the technical data of the real components.

The following elements were included during the selection of components of control system:

1. Extension modules:
    - analog input modules,
    - analog output modules,
    - temperature input modules,
    - digital input modules,
    - digital output modules.
2. Main controller (CPU).
3. Communication module.
4. Operator panel.

The following industrial controller manufacturers' solutions were selected for the final stage of the selection of the control system:

- Siemens - SIMATIC S7-1200 system – option no 1 [25];
- B&R - X20 system – option no 2 [26];
- EATON - XC200 system – option no 3 [27].

Preliminary analysis of their technical parameters qualified them as systems useful and possible to use as control and data acquisition systems for the extruder.

Characteristics of SIMATIC S7-1200 control system by Siemens

The Fig. 8 (general description of system), Figs. 9-12 (description of analog inputs modules), Figs. 13-16 (description of analog outputs modules), Figs. 17-20 (description of temperature inputs modules), Figs. 21-24 (description of digital inputs modules), Figs. 25-28 (description of digital outputs modules), Figs. 29-30 (description of HMI panel), Figs. 31-33 (description of communication modules), Fig. 34 (description of PLC main block module) and Fig. 35 (description of power supply module) shows the most important information about the elements and components of the Siemens SIMATIC S7-1200 system [25].

The presented elements can be used in the control and measurement process control system in the extruder.

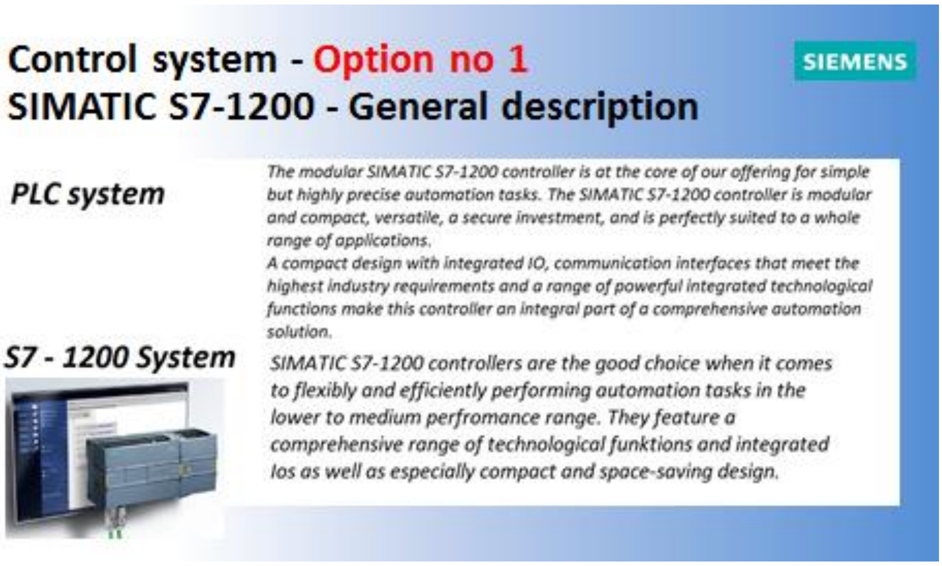

Control system - Option no 1
SIMATIC S7-1200 - General description

SIEMENS

PLC system

The modular SIMATIC S7-1200 controller is at the core of our offering for simple but highly precise automation tasks. The SIMATIC S7-1200 controller is modular and compact, versatile, a secure investment, and is perfectly suited to a whole range of applications.

A compact design with integrated IO, communication interfaces that meet the highest industry requirements and a range of powerful integrated technological functions make this controller an integral part of a comprehensive automation solution.

S7 - 1200 System

SIMATIC S7-1200 controllers are the good choice when it comes to flexibly and efficiently performing automation tasks in the lower to medium perfromance range. They feature a comprehensive range of technological funktions and integrated Ios as well as especially compact and space-saving design.

Fig. 8. SIMATIC S7-1200 system – general description

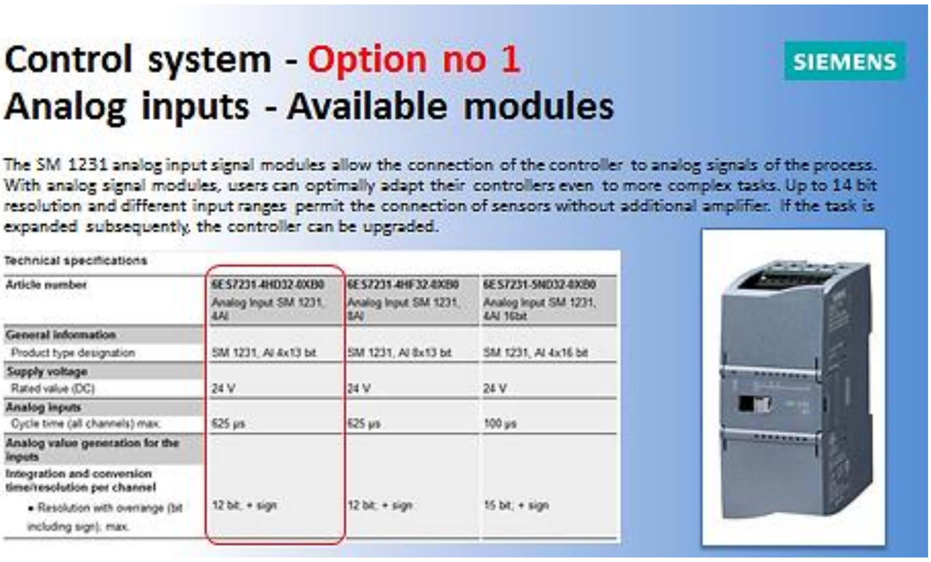

Control system - Option no 1
Analog inputs - Available modules

SIEMENS

The SM 1231 analog input signal modules allow the connection of the controller to analog signals of the process. With analog signal modules, users can optimally adapt their controllers even to more complex tasks. Up to 14 bit resolution and different input ranges permit the connection of sensors without additional amplifier. If the task is expanded subsequently, the controller can be upgraded.

Technical specifications

Article number	6ES7231-4HD32-0XB0 Analog Input SM 1231, 4AI	6ES7231-4HF32-0XB0 Analog Input SM 1231, 8AI	6ES7231-5ND32-0XB0 Analog Input SM 1231, 4AI 16bit
General information			
Product type designation	SM 1231, AI 4x13 bit	SM 1231, AI 8x13 bit	SM 1231, AI 4x16 bit
Supply voltage			
Rated value (DC)	24 V	24 V	24 V
Analog inputs			
Cycle time (all channels) max.	625 μs	625 μs	100 μs
Analog value generation for the inputs			
Integration and conversion time/resolution per channel			
• Resolution with overrange (bit including sign), max.	12 bit; + sign	12 bit; + sign	15 bit; + sign

Fig. 9. SIMATIC S7-1200 system – analog input - available modules

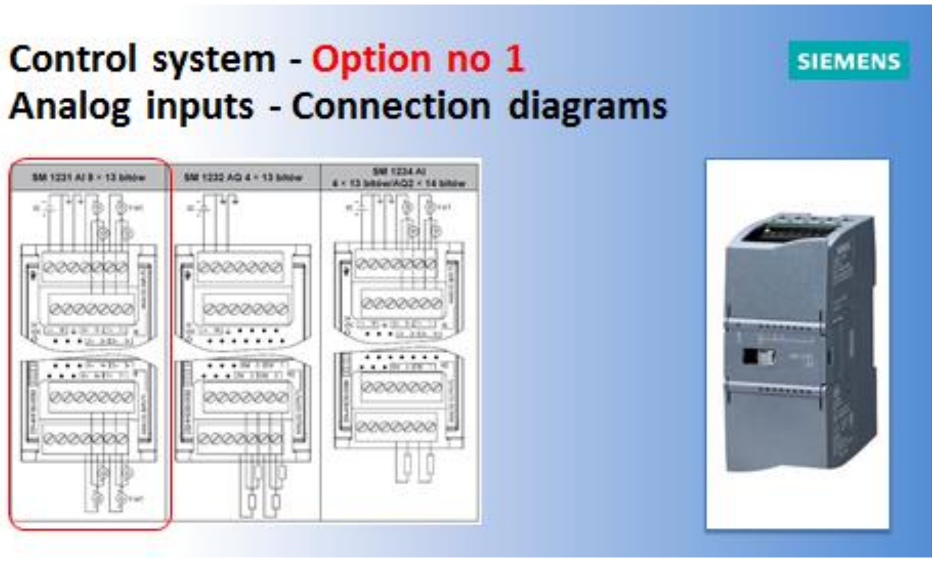

Control system - Option no 1
Analog inputs - Connection diagrams

Fig. 10. SIMATIC S7-1200 system – analog inputs – connection diagrams

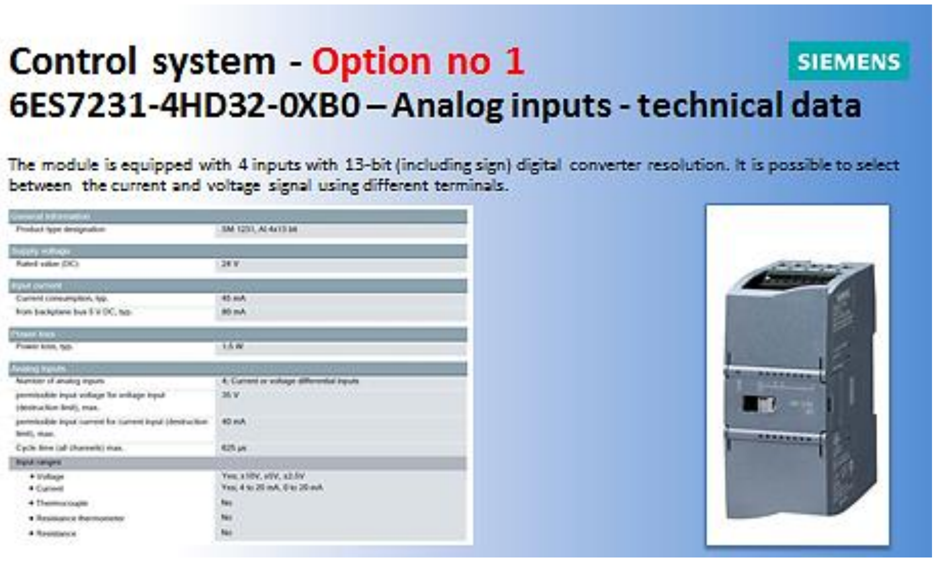

Control system - Option no 1
6ES7231-4HD32-0XB0 – Analog inputs - technical data

The module is equipped with 4 inputs with 13-bit (including sign) digital converter resolution. It is possible to select between the current and voltage signal using different terminals.

General information	
Product type designation	SM 1231, AI 4x13 bit
Supply voltage	
Rated value (DC)	24 V
Input current	
Current consumption, typ.	45 mA
from backplane bus 5 V DC, typ.	80 mA
Power loss	
Power loss, typ.	1.5 W
Analog inputs	
Number of analog inputs	4; Current or voltage differential inputs
permissible input voltage for voltage input (destruction limit), max.	35 V
permissible input current for current input (destruction limit), max.	40 mA
Cycle time (all channels) max.	625 µs
Input ranges	
• Voltage	Yes; ±10V, ±5V, ±2.5V
• Current	Yes; 4 to 20 mA, 0 to 20 mA
• Thermocouple	No
• Resistance thermometer	No
• Resistance	No

Fig. 11. SIMATIC S7-1200 system – analog inputs – technical data of module

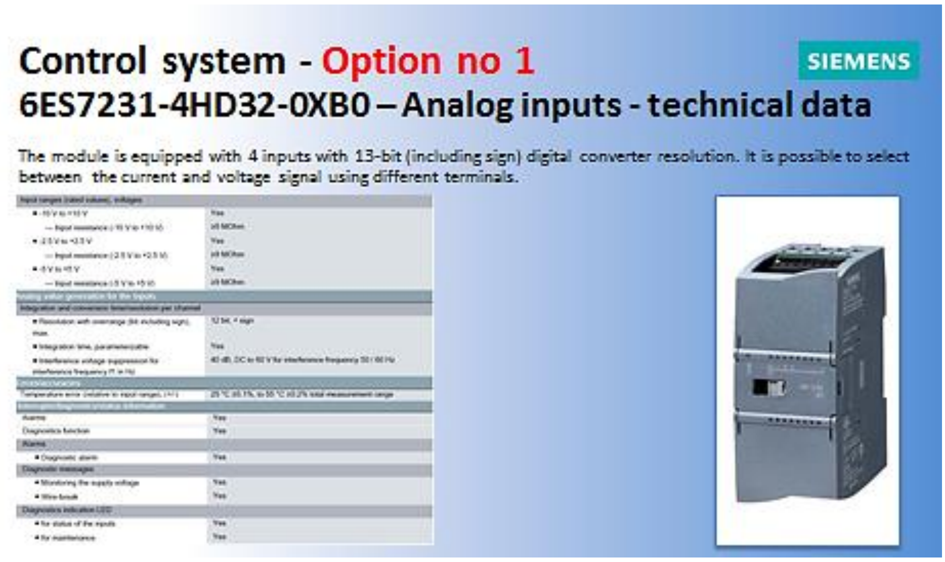

Control system - Option no 1

6ES7231-4HD32-0XB0 – Analog inputs - technical data

The module is equipped with 4 inputs with 13-bit (including sign) digital converter resolution. It is possible to select between the current and voltage signal using different terminals.

Fig. 12. SIMATIC S7-1200 system – analog inputs – technical data of module

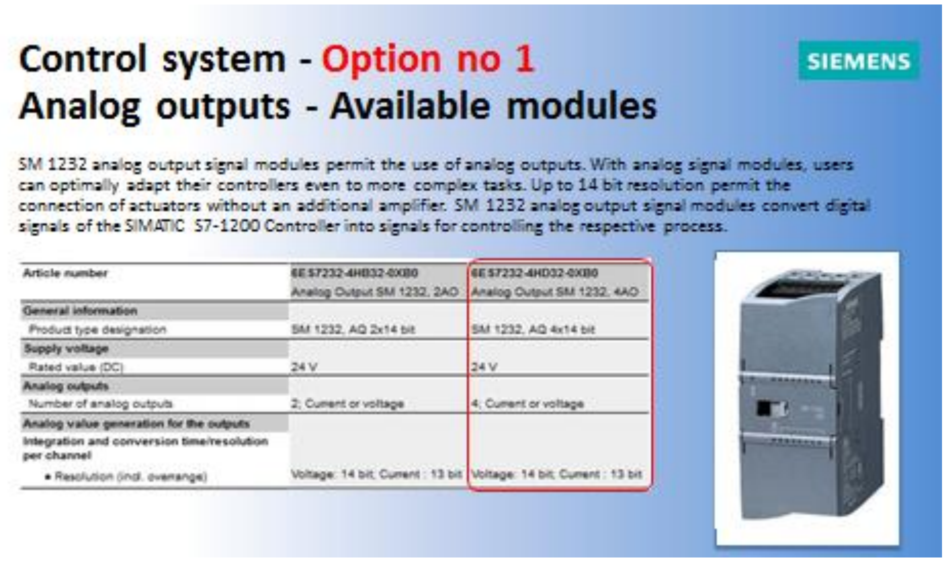

Control system - Option no 1

Analog outputs - Available modules

SM 1232 analog output signal modules permit the use of analog outputs. With analog signal modules, users can optimally adapt their controllers even to more complex tasks. Up to 14 bit resolution permit the connection of actuators without an additional amplifier. SM 1232 analog output signal modules convert digital signals of the SIMATIC S7-1200 Controller into signals for controlling the respective process.

Article number	6ES7232-4HB32-0XB0 Analog Output SM 1232, 2AO	6ES7232-4HD32-0XB0 Analog Output SM 1232, 4AO
General information		
Product type designation	SM 1232, AQ 2x14 bit	SM 1232, AQ 4x14 bit
Supply voltage		
Rated value (DC)	24 V	24 V
Analog outputs		
Number of analog outputs	2; Current or voltage	4; Current or voltage
Analog value generation for the outputs		
Integration and conversion time/resolution per channel		
• Resolution (incl. overrange)	Voltage: 14 bit; Current : 13 bit	Voltage: 14 bit; Current : 13 bit

Fig. 13. SIMATIC S7-1200 system – analog output – available modules

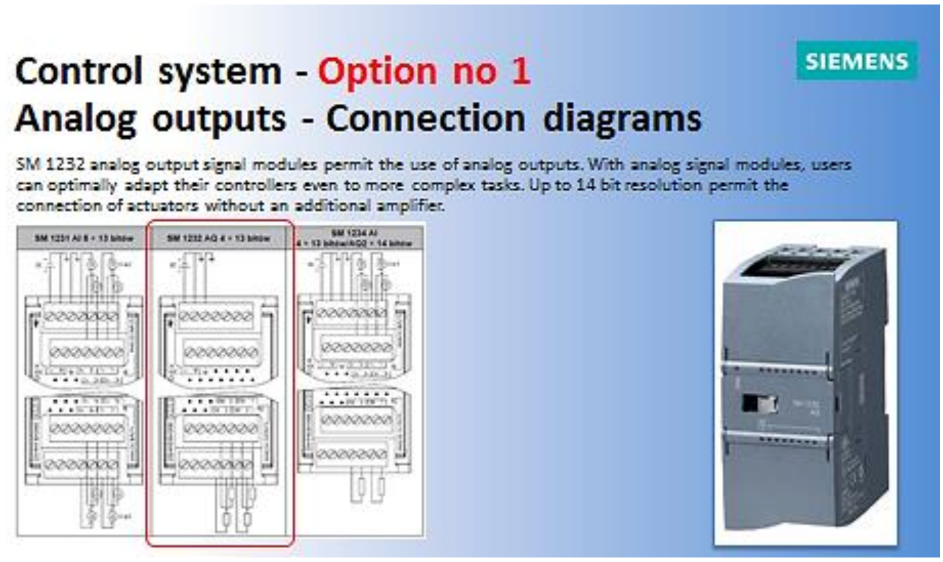

Control system - Option no 1
Analog outputs - Connection diagrams

SIEMENS

SM 1232 analog output signal modules permit the use of analog outputs. With analog signal modules, users can optimally adapt their controllers even to more complex tasks. Up to 14 bit resolution permit the connection of actuators without an additional amplifier.

Fig. 14. SIMATIC S7-1200 system – analog outputs – connection diagram

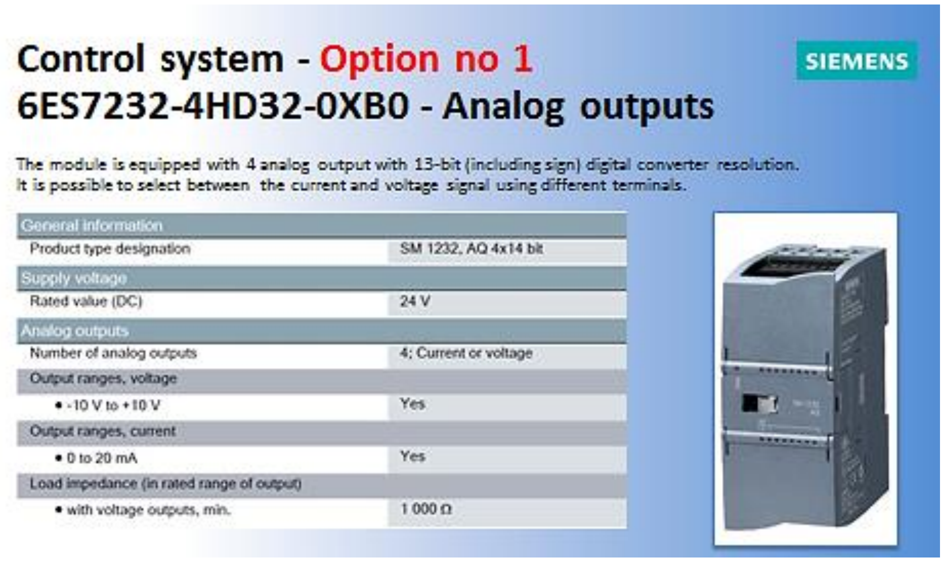

Control system - Option no 1
6ES7232-4HD32-0XB0 - Analog outputs

SIEMENS

The module is equipped with 4 analog output with 13-bit (including sign) digital converter resolution. It is possible to select between the current and voltage signal using different terminals.

General information	
Product type designation	SM 1232, AQ 4x14 bit
Supply voltage	
Rated value (DC)	24 V
Analog outputs	
Number of analog outputs	4; Current or voltage
Output ranges, voltage	
• -10 V to +10 V	Yes
Output ranges, current	
• 0 to 20 mA	Yes
Load impedance (in rated range of output)	
• with voltage outputs, min.	1 000 Ω

Fig. 15. SIMATIC S7-1200 system – analog outputs – technical data of module

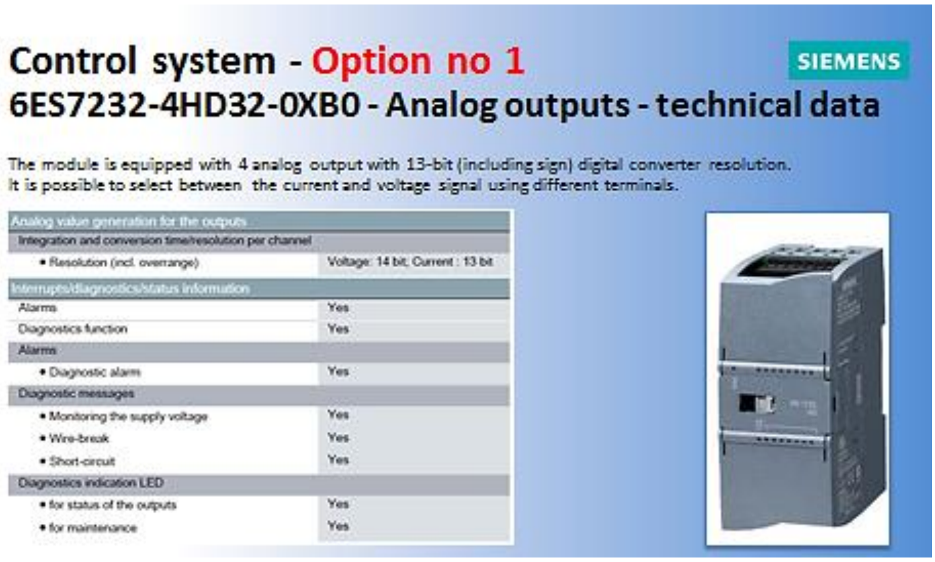

Control system - Option no 1
6ES7232-4HD32-0XB0 - Analog outputs - technical data

The module is equipped with 4 analog output with 13-bit (including sign) digital converter resolution.
It is possible to select between the current and voltage signal using different terminals.

Analog value generation for the outputs	
Integration and conversion time/resolution per channel	
• Resolution (incl. overrange)	Voltage: 14 bit; Current : 13 bit
Interrupts/diagnostics/status information	
Alarms	Yes
Diagnostics function	Yes
Alarms	
• Diagnostic alarm	Yes
Diagnostic messages	
• Monitoring the supply voltage	Yes
• Wire-break	Yes
• Short-circuit	Yes
Diagnostics indication LED	
• for status of the outputs	Yes
• for maintenance	Yes

Fig. 16. SIMATIC S7-1200 system – analog outputs – technical data of module

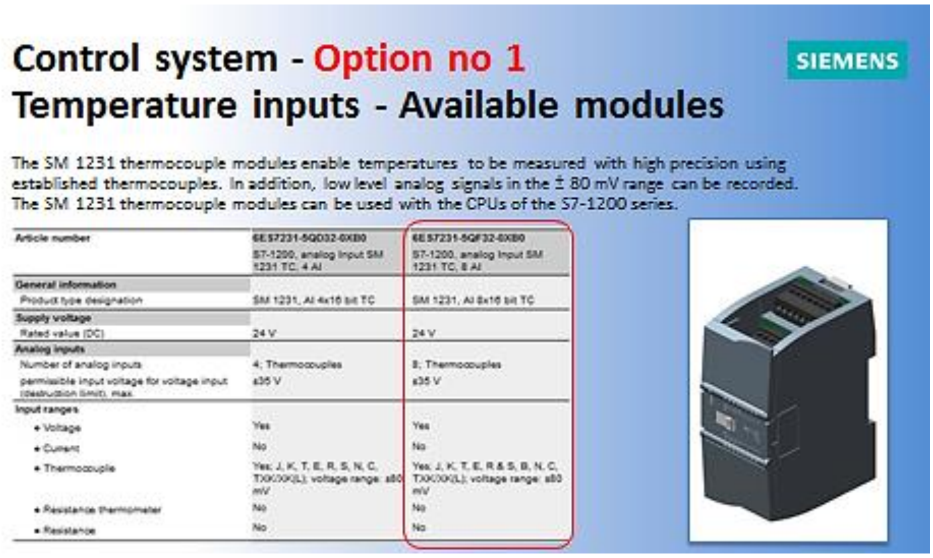

Control system - Option no 1
Temperature inputs - Available modules

The SM 1231 thermocouple modules enable temperatures to be measured with high precision using established thermocouples. In addition, low level analog signals in the ± 80 mV range can be recorded. The SM 1231 thermocouple modules can be used with the CPUs of the S7-1200 series.

Article number	6ES7231-5QD32-0XB0 S7-1200, analog Input SM 1231 TC, 4 AI	6ES7231-5QF32-0XB0 S7-1200, analog Input SM 1231 TC, 8 AI
General information		
Product type designation	SM 1231, AI 4x16 bit TC	SM 1231, AI 8x16 bit TC
Supply voltage		
Rated value (DC)	24 V	24 V
Analog inputs		
Number of analog inputs	4; Thermocouples	8; Thermocouples
permissible input voltage for voltage input (destruction limit), max.	≤35 V	≤35 V
Input ranges		
• Voltage	Yes	Yes
• Current	No	No
• Thermocouple	Yes; J, K, T, E, R, S, N, C, TXK/XK(L); voltage range: ±80 mV	Yes; J, K, T, E, R & S, B, N, C, TXK/XK(L); voltage range: ±80 mV
• Resistance thermometer	No	No
• Resistance	No	No

Fig. 17. SIMATIC S7-1200 system – temperature inputs – available modules

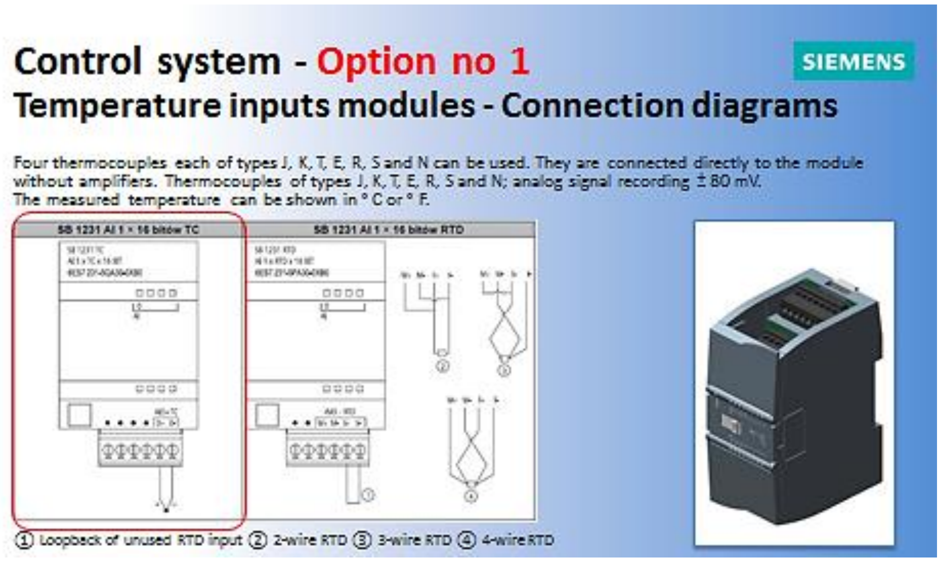

Control system - Option no 1

Temperature inputs modules - Connection diagrams

SIEMENS

Four thermocouples each of types J, K, T, E, R, S and N can be used. They are connected directly to the module without amplifiers. Thermocouples of types J, K, T, E, R, S and N; analog signal recording ± 80 mV.
The measured temperature can be shown in ° C or ° F.

① Loopback of unused RTD input ② 2-wire RTD ③ 3-wire RTD ④ 4-wire RTD

Fig. 18. SIMATIC S7-1200 system – temperature inputs – connection diagrams

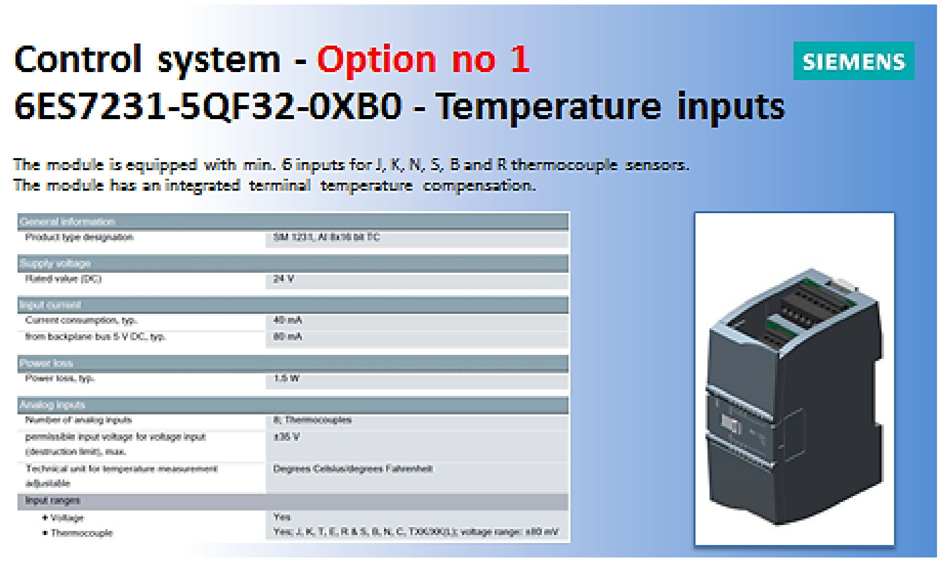

Control system - Option no 1

6ES7231-5QF32-0XB0 - Temperature inputs

SIEMENS

The module is equipped with min. 6 inputs for J, K, N, S, B and R thermocouple sensors.
The module has an integrated terminal temperature compensation.

General information	
Product type designation	SM 1231, AI 8x16 bit TC
Supply voltage	
Rated value (DC)	24 V
Input current	
Current consumption, typ.	40 mA
from backplane bus 5 V DC, typ.	80 mA
Power loss	
Power loss, typ.	1.5 W
Analog inputs	
Number of analog inputs	8; Thermocouples
permissible input voltage for voltage input (destruction limit), max.	±35 V
Technical unit for temperature measurement adjustable	Degrees Celsius/degrees Fahrenheit
Input ranges	
• Voltage	Yes
• Thermocouple	Yes; J, K, T, E, R & S, B, N, C, TXK/XK(L); voltage range: ±80 mV

Fig. 19. SIMATIC S7-1200 system – temperature inputs – connection diagrams

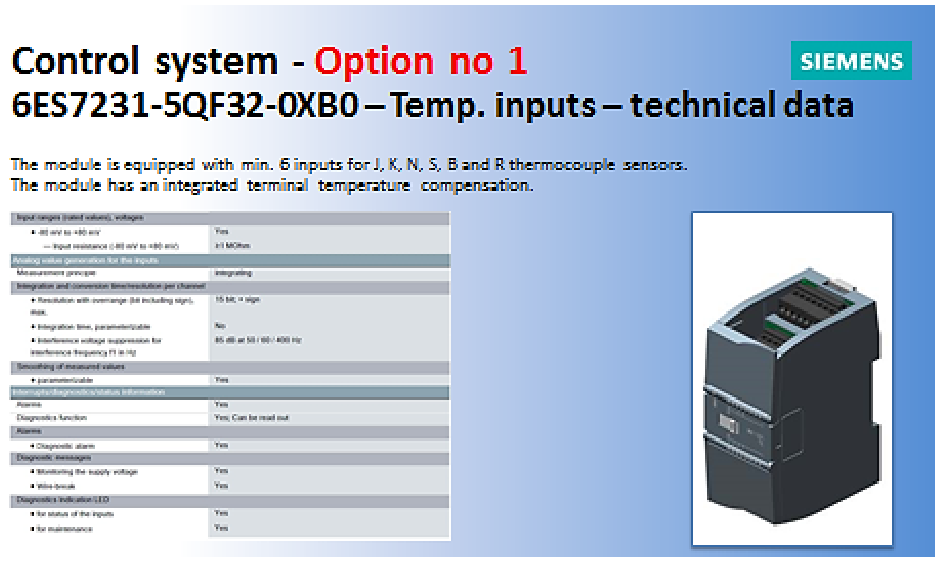

Control system - Option no 1 SIEMENS

6ES7231-5QF32-0XB0 – Temp. inputs – technical data

The module is equipped with min. 6 inputs for J, K, N, S, B and R thermocouple sensors.
The module has an integrated terminal temperature compensation.

Input ranges (rated values), voltages	
• -80 mV to +80 mV	Yes
— Input resistance (-80 mV to +80 mV)	≥1 MOhm
Analog value generation for the inputs	
Measurement principle	integrating
Integration and conversion time/resolution per channel	
• Resolution with overrange (bit including sign), max.	15 bit; + sign
• Integration time, parameterizable	No
• Interference voltage suppression for interference frequency f1 in Hz	85 dB at 50 / 60 / 400 Hz
Smoothing of measured values	
• parameterizable	Yes
Interrupts/diagnostics/status information	
Alarms	Yes
Diagnostics function	Yes; Can be read out
Alarms	
• Diagnostic alarm	Yes
Diagnostic messages	
• Monitoring the supply voltage	Yes
• Wire-break	Yes
Diagnostics indication LED	
• for status of the inputs	Yes
• for maintenance	Yes

Fig. 20. SIMATIC S7-1200 system – temperature inputs – technical data of module

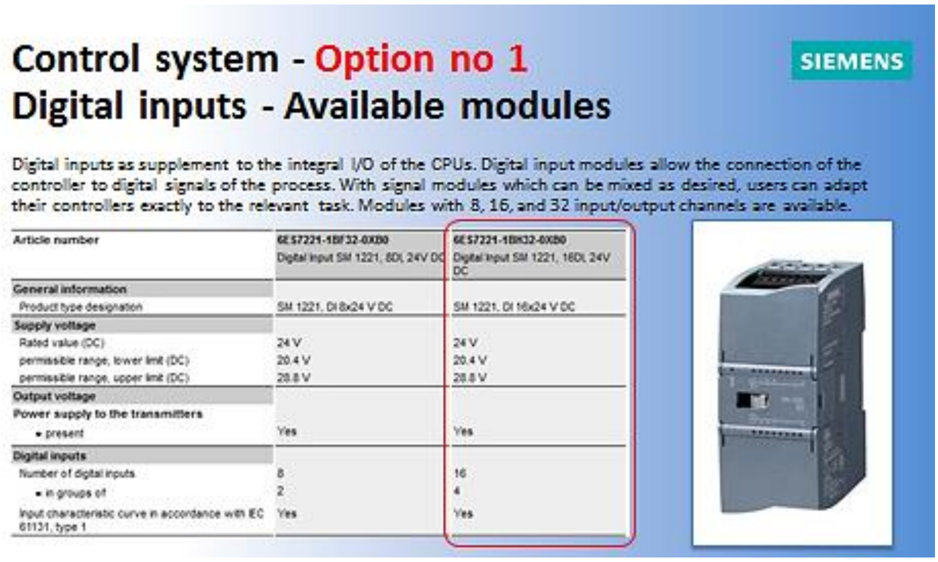

Control system - Option no 1 SIEMENS

Digital inputs - Available modules

Digital inputs as supplement to the integral I/O of the CPUs. Digital input modules allow the connection of the controller to digital signals of the process. With signal modules which can be mixed as desired, users can adapt their controllers exactly to the relevant task. Modules with 8, 16, and 32 input/output channels are available.

Article number	**6ES7221-1BF32-0XB0** Digital input SM 1221, 8DI, 24V DC	**6ES7221-1BH32-0XB0** Digital input SM 1221, 16DI, 24V DC
General information		
Product type designation	SM 1221, DI 8x24 V DC	SM 1221, DI 16x24 V DC
Supply voltage		
Rated value (DC)	24 V	24 V
permissible range, lower limit (DC)	20.4 V	20.4 V
permissible range, upper limit (DC)	28.8 V	28.8 V
Output voltage		
Power supply to the transmitters		
• present	Yes	Yes
Digital inputs		
Number of digital inputs	8	16
• in groups of	2	4
Input characteristic curve in accordance with IEC 61131, type 1	Yes	Yes

Fig. 21. SIMATIC S7-1200 system – digital inputs – available modules

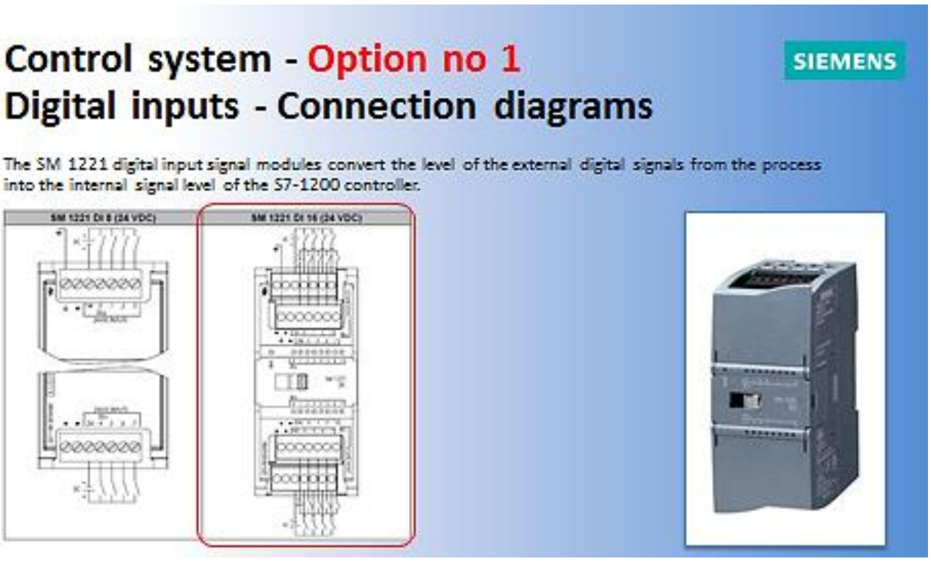

Control system - Option no 1

Digital inputs - Connection diagrams

SIEMENS

The SM 1221 digital input signal modules convert the level of the external digital signals from the process into the internal signal level of the S7-1200 controller.

Fig. 22. SIMATIC S7-1200 system – digital inputs – connection diagram

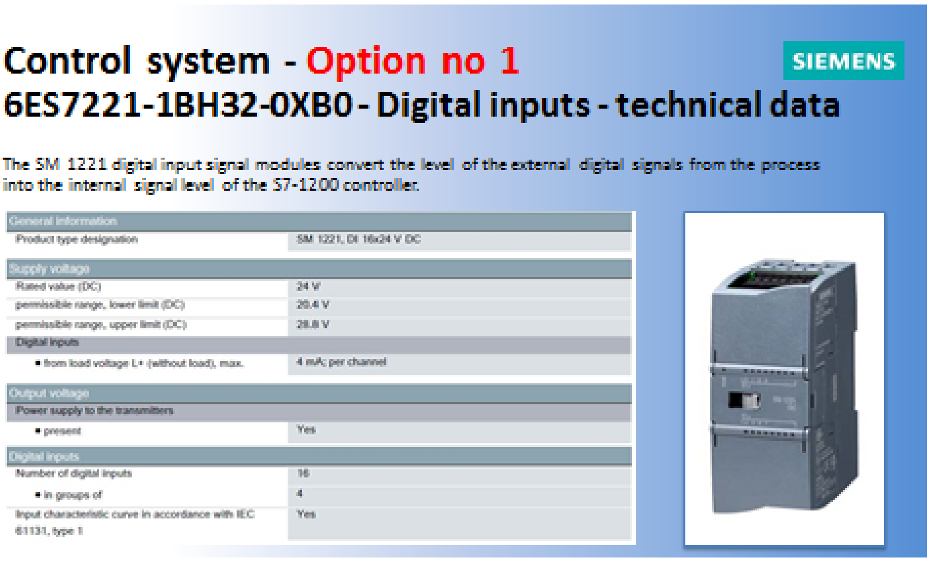

Control system - Option no 1

6ES7221-1BH32-0XB0 - Digital inputs - technical data

SIEMENS

The SM 1221 digital input signal modules convert the level of the external digital signals from the process into the internal signal level of the S7-1200 controller.

General information	
Product type designation	SM 1221, DI 16x24 V DC
Supply voltage	
Rated value (DC)	24 V
permissible range, lower limit (DC)	20.4 V
permissible range, upper limit (DC)	28.8 V
Digital inputs	
▪ from load voltage L+ (without load), max.	4 mA; per channel
Output voltage	
Power supply to the transmitters	
▪ present	Yes
Digital inputs	
Number of digital inputs	16
▪ in groups of	4
Input characteristic curve in accordance with IEC 61131, type 1	Yes

Fig. 23. SIMATIC S7-1200 system – digital inputs – technical data of module

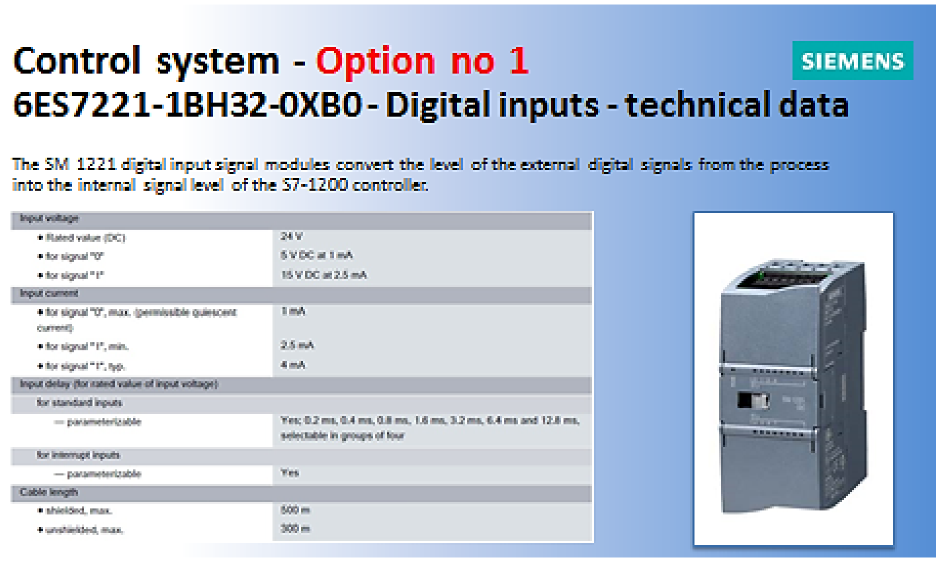

Control system - Option no 1

6ES7221-1BH32-0XB0 - Digital inputs - technical data

SIEMENS

The SM 1221 digital input signal modules convert the level of the external digital signals from the process into the internal signal level of the S7-1200 controller.

Input voltage	
• Rated value (DC)	24 V
• for signal "0"	5 V DC at 1 mA
• for signal "1"	15 V DC at 2.5 mA
Input current	
• for signal "0", max. (permissible quiescent current)	1 mA
• for signal "1", min.	2.5 mA
• for signal "1", typ.	4 mA
Input delay (for rated value of input voltage)	
for standard inputs	
— parameterizable	Yes; 0.2 ms, 0.4 ms, 0.8 ms, 1.6 ms, 3.2 ms, 6.4 ms and 12.8 ms, selectable in groups of four
for interrupt inputs	
— parameterizable	Yes
Cable length	
• shielded, max.	500 m
• unshielded, max.	300 m

Fig. 24. SIMATIC S7-1200 system – digital inputs – technical data of module

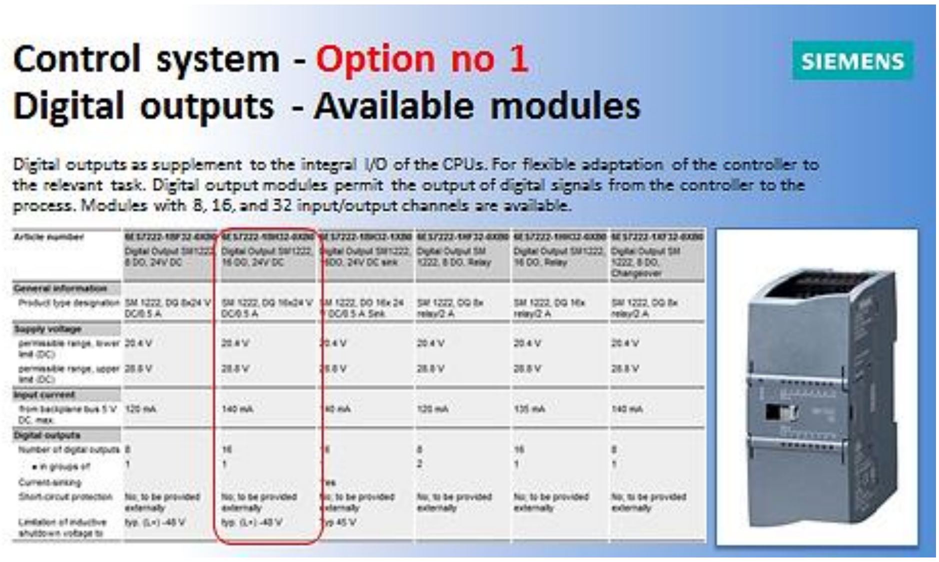

Control system - Option no 1

Digital outputs - Available modules

SIEMENS

Digital outputs as supplement to the integral I/O of the CPUs. For flexible adaptation of the controller to the relevant task. Digital output modules permit the output of digital signals from the controller to the process. Modules with 8, 16, and 32 input/output channels are available.

Article number	6ES7222-1BF32-0XB0 Digital Output SM1222, 8 DO, 24V DC	6ES7222-1BH32-0XB0 Digital Output SM1222, 16 DO, 24V DC	ES7222-1BH32-1XB0 igital Output SM1222, 16DO, 24V DC sink	6ES7222-1HF32-0XB0 Digital Output SM 1222, 8 DO, Relay	6ES7222-1HH32-0XB0 Digital Output SM1222, 16 DO, Relay	6ES7222-1XF32-0XB0 Digital Output SM 1222, 8 DO, Changeover
General information						
Product type designation	SM 1222, DQ 8x24 V DC/0.5 A	SM 1222, DQ 16x24 V DC/0.5 A	M 1222, DQ 16x 24 V DC/0.5 A Sink	SM 1222, DQ 8x relay/2 A	SM 1222, DQ 16x relay/2 A	SM 1222, DQ 8x relay/2 A
Supply voltage						
permissible range, lower limit (DC)	20.4 V	20.4 V	0.4 V	20.4 V	20.4 V	20.4 V
permissible range, upper limit (DC)	28.8 V	28.8 V	8.8 V	28.8 V	28.8 V	28.8 V
Input current						
from backplane bus 5 V DC, max.	120 mA	140 mA	40 mA	120 mA	135 mA	140 mA
Digital outputs						
Number of digital outputs	8	16	6	8	16	8
• in groups of	1	1	1	2	1	1
Current-sinking			es			
Short-circuit protection	No; to be provided externally	No; to be provided externally	o; to be provided xternally	No; to be provided externally	No; to be provided externally	No; to be provided externally
Limitation of inductive shutdown voltage to	typ. (L+) -48 V	typ. (L+) -48 V	yp 45 V			

Fig. 25. SIMATIC S7-1200 system – digital outputs – available modules

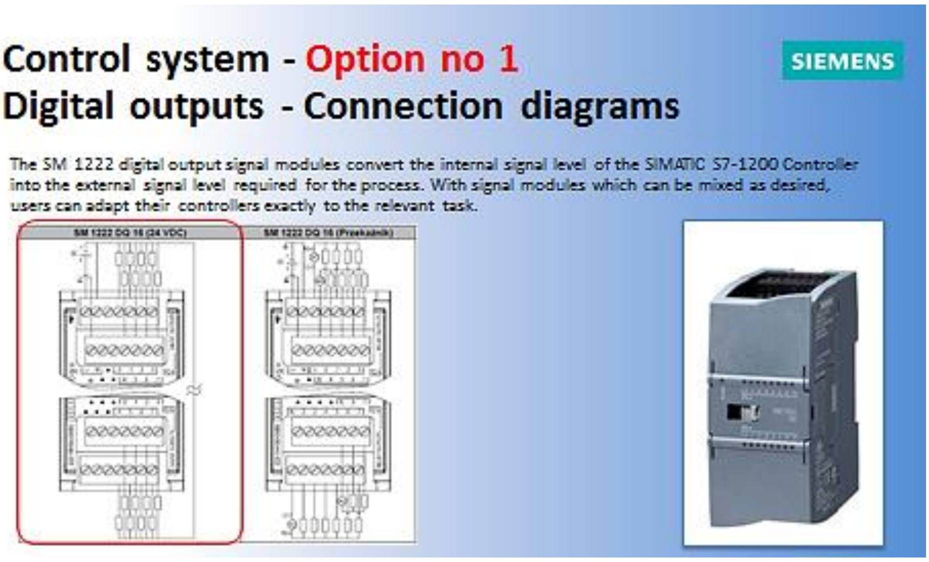

Control system - Option no 1
Digital outputs - Connection diagrams

The SM 1222 digital output signal modules convert the internal signal level of the SIMATIC S7-1200 Controller into the external signal level required for the process. With signal modules which can be mixed as desired, users can adapt their controllers exactly to the relevant task.

Fig. 26. SIMATIC S7-1200 system – digital outputs – connection diagrams

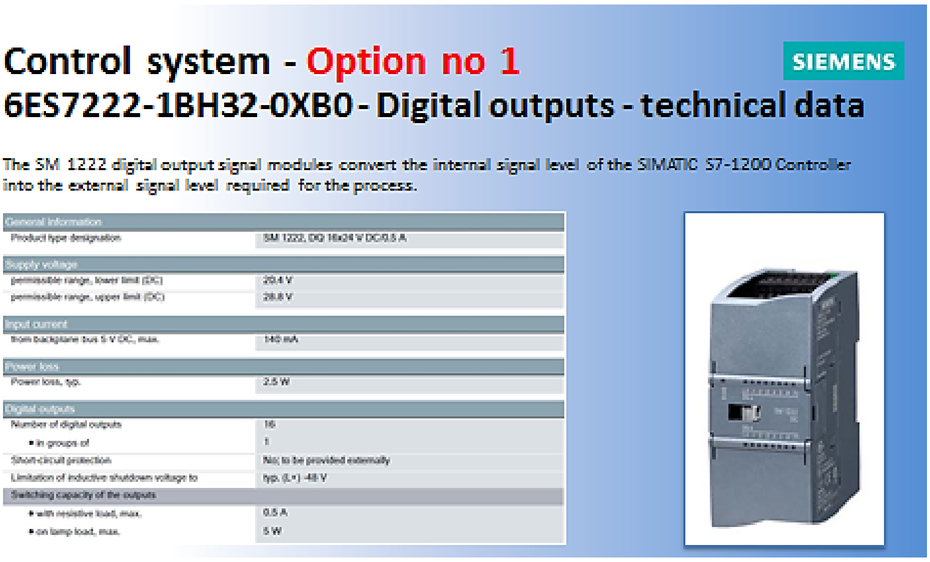

Control system - Option no 1
6ES7222-1BH32-0XB0 - Digital outputs - technical data

The SM 1222 digital output signal modules convert the internal signal level of the SIMATIC S7-1200 Controller into the external signal level required for the process.

General information	
Product type designation	SM 1222, DQ 16x24 V DC/0.5 A
Supply voltage	
permissible range, lower limit (DC)	20.4 V
permissible range, upper limit (DC)	28.8 V
Input current	
from backplane bus 5 V DC, max.	140 mA
Power loss	
Power loss, typ.	2.5 W
Digital outputs	
Number of digital outputs	16
• in groups of	1
Short-circuit protection	No; to be provided externally
Limitation of inductive shutdown voltage to	typ. (L+) -48 V
Switching capacity of the outputs	
• with resistive load, max.	0.5 A
• on lamp load, max.	5 W

Fig. 27. SIMATIC S7-1200 system – digital outputs – technical data of module

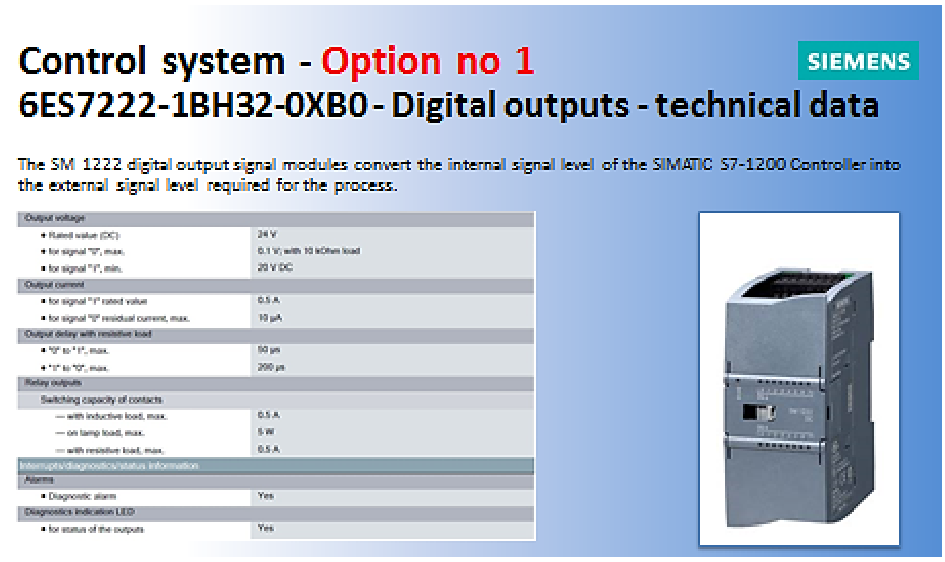

Control system - Option no 1

6ES7222-1BH32-0XB0 - Digital outputs - technical data

The SM 1222 digital output signal modules convert the internal signal level of the SIMATIC S7-1200 Controller into the external signal level required for the process.

Output voltage	
• Rated value (DC)	24 V
• for signal "0", max.	0.1 V; with 10 kOhm load
• for signal "1", min.	20 V DC
Output current	
• for signal "1" rated value	0.5 A
• for signal "0" residual current, max.	10 µA
Output delay with resistive load	
• "0" to "1", max.	50 µs
• "1" to "0", max.	200 µs
Relay outputs	
Switching capacity of contacts	
— with inductive load, max.	0.5 A
— on lamp load, max.	5 W
— with resistive load, max.	0.5 A
Interrupts/diagnostics/status information	
Alarms	
• Diagnostic alarm	Yes
Diagnostics indication LED	
• for status of the outputs	Yes

Fig. 28. SIMATIC S7-1200 system – digital outputs – technical data of module

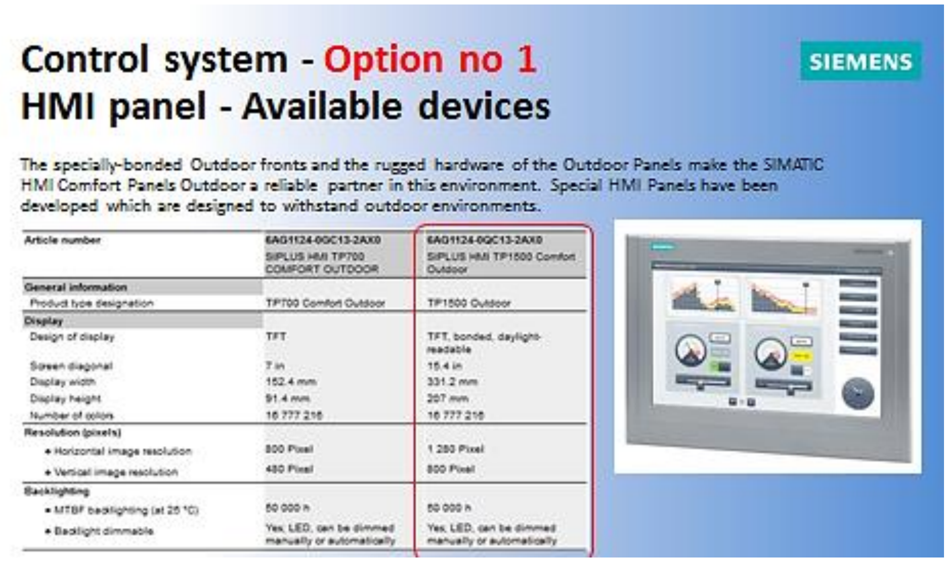

Control system - Option no 1

HMI panel - Available devices

The specially-bonded Outdoor fronts and the rugged hardware of the Outdoor Panels make the SIMATIC HMI Comfort Panels Outdoor a reliable partner in this environment. Special HMI Panels have been developed which are designed to withstand outdoor environments.

Article number	6AG1124-0GC13-2AX0 SIPLUS HMI TP700 COMFORT OUTDOOR	6AG1124-0QC13-2AX0 SIPLUS HMI TP1500 Comfort Outdoor
General information		
Product type designation	TP700 Comfort Outdoor	TP1500 Outdoor
Display		
Design of display	TFT	TFT, bonded, daylight-readable
Screen diagonal	7 in	15.4 in
Display width	152.4 mm	331.2 mm
Display height	91.4 mm	207 mm
Number of colors	16 777 216	16 777 216
Resolution (pixels)		
• Horizontal image resolution	800 Pixel	1 280 Pixel
• Vertical image resolution	480 Pixel	800 Pixel
Backlighting		
• MTBF backlighting (at 25 °C)	80 000 h	80 000 h
• Backlight dimmable	Yes, LED, can be dimmed manually or automatically	Yes, LED, can be dimmed manually or automatically

Fig. 29. SIMATIC S7-1200 system – HMI panel – available devices

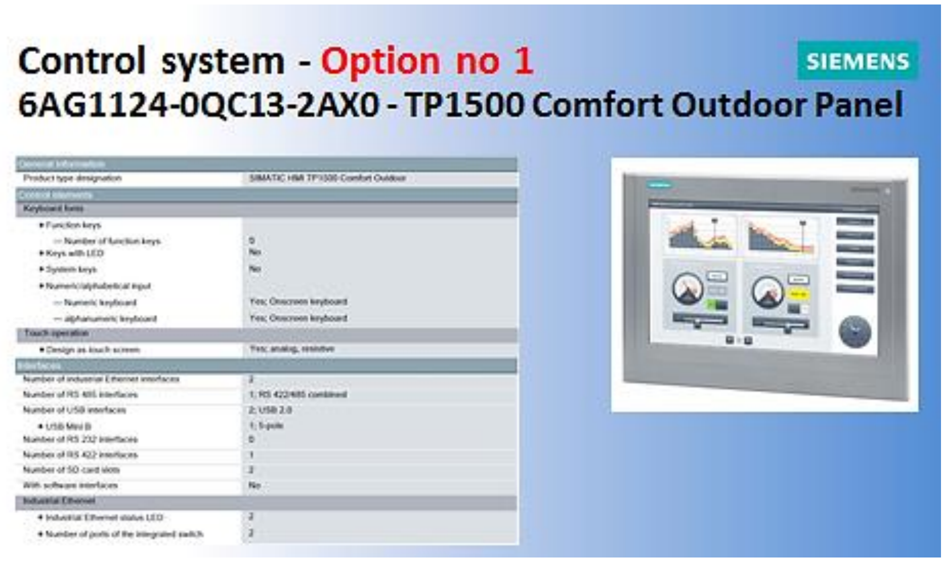

Control system - Option no 1

6AG1124-0QC13-2AX0 - TP1500 Comfort Outdoor Panel

SIEMENS

General information	
Product type designation	SIMATIC HMI TP1500 Comfort Outdoor
Control elements	
Keyboard fonts	
• Function keys	
— Number of function keys	0
• Keys with LED	No
• System keys	No
• Numeric/alphabetical input	
— Numeric keyboard	Yes; Onscreen keyboard
— alphanumeric keyboard	Yes; Onscreen keyboard
Touch operation	
• Design as touch screen	Yes; analog, resistive
Interfaces	
Number of industrial Ethernet interfaces	2
Number of RS 485 interfaces	1; RS 422/485 combined
Number of USB interfaces	2; USB 2.0
• USB Mini B	1; 5-pole
Number of RS 232 interfaces	0
Number of RS 422 interfaces	1
Number of SD card slots	2
With software interfaces	No
Industrial Ethernet	
• Industrial Ethernet status LED	2
• Number of ports of the integrated switch	2

Fig. 30. SIMATIC S7-1200 system – HMI panel – technical data of module

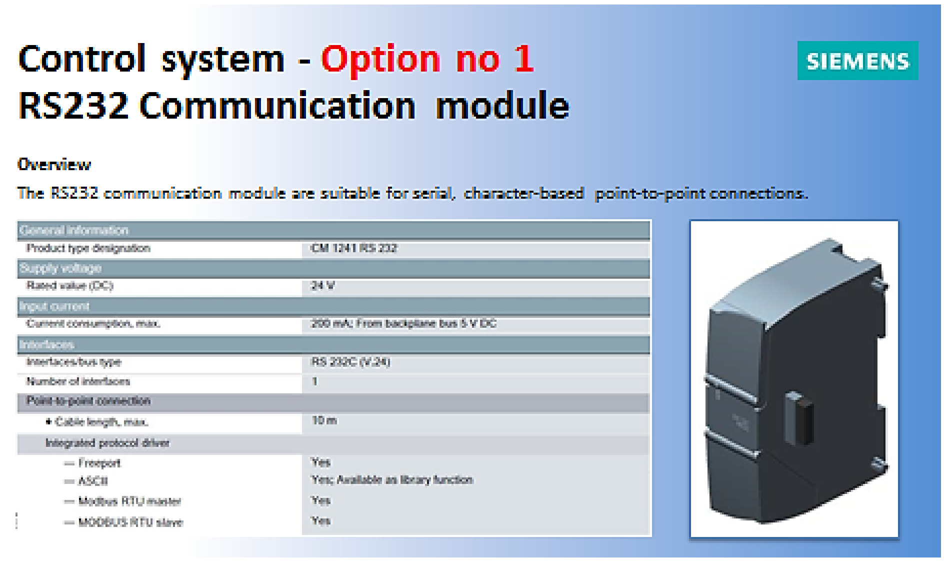

Control system - Option no 1

RS232 Communication module

SIEMENS

Overview

The RS232 communication module are suitable for serial, character-based point-to-point connections.

General information	
Product type designation	CM 1241 RS 232
Supply voltage	
Rated value (DC)	24 V
Input current	
Current consumption, max.	200 mA; From backplane bus 5 V DC
Interfaces	
Interfaces/bus type	RS 232C (V.24)
Number of interfaces	1
Point-to-point connection	
• Cable length, max.	10 m
Integrated protocol driver	
— Freeport	Yes
— ASCII	Yes; Available as library function
— Modbus RTU master	Yes
— MODBUS RTU slave	Yes

Fig. 31. SIMATIC S7-1200 system
– technical data of RS232 communication module

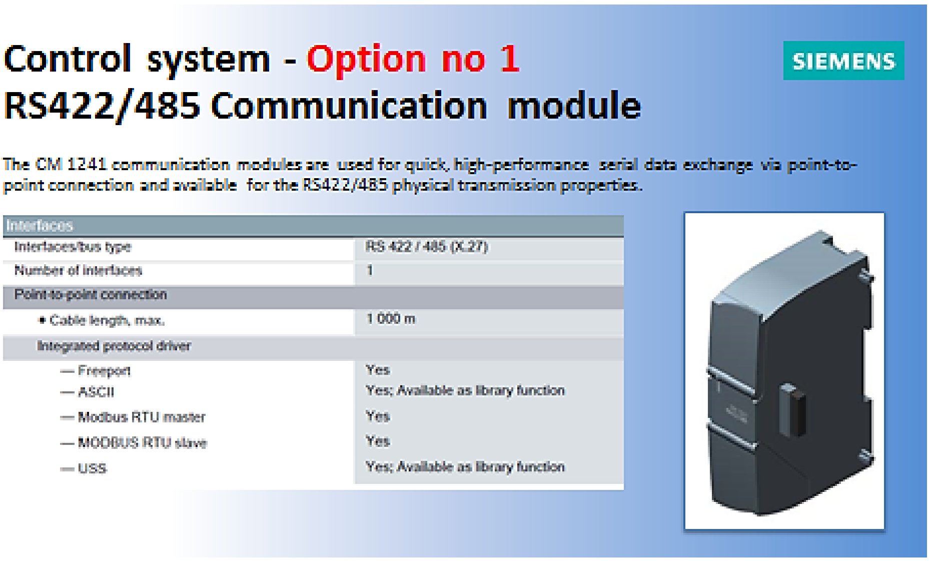

Control system - Option no 1
RS422/485 Communication module

SIEMENS

The CM 1241 communication modules are used for quick, high-performance serial data exchange via point-to-point connection and available for the RS422/485 physical transmission properties.

Interfaces	
Interfaces/bus type	RS 422 / 485 (X.27)
Number of interfaces	1
Point-to-point connection	
• Cable length, max.	1 000 m
Integrated protocol driver	
— Freeport	Yes
— ASCII	Yes; Available as library function
— Modbus RTU master	Yes
— MODBUS RTU slave	Yes
— USS	Yes; Available as library function

Fig. 32. SIMATIC S7-1200 system
– technical data of RS422/485 communication module

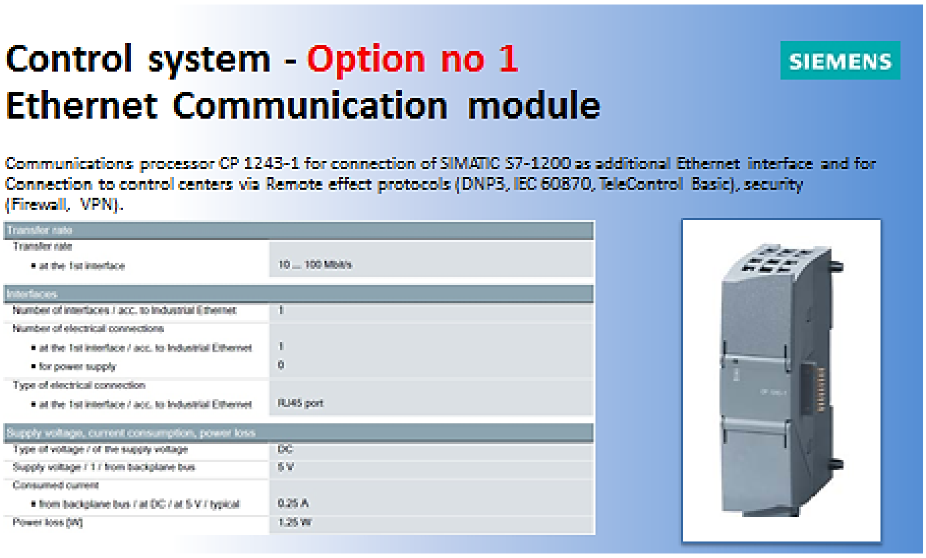

Control system - Option no 1
Ethernet Communication module

SIEMENS

Communications processor CP 1243-1 for connection of SIMATIC S7-1200 as additional Ethernet interface and for Connection to control centers via Remote effect protocols (DNP3, IEC 60870, TeleControl Basic), security (Firewall, VPN).

Transfer rate	
Transfer rate	
• at the 1st interface	10 ... 100 Mbit/s
Interfaces	
Number of interfaces / acc. to Industrial Ethernet	1
Number of electrical connections	
• at the 1st interface / acc. to Industrial Ethernet	1
• for power supply	0
Type of electrical connection	
• at the 1st interface / acc. to Industrial Ethernet	RJ45 port
Supply voltage, current consumption, power loss	
Type of voltage / of the supply voltage	DC
Supply voltage / 1 / from backplane bus	5 V
Consumed current	
• from backplane bus / at DC / at 5 V / typical	0.25 A
Power loss [W]	1.25 W

Fig. 33. SIMATIC S7-1200 system
– technical data of Ethernet communication module

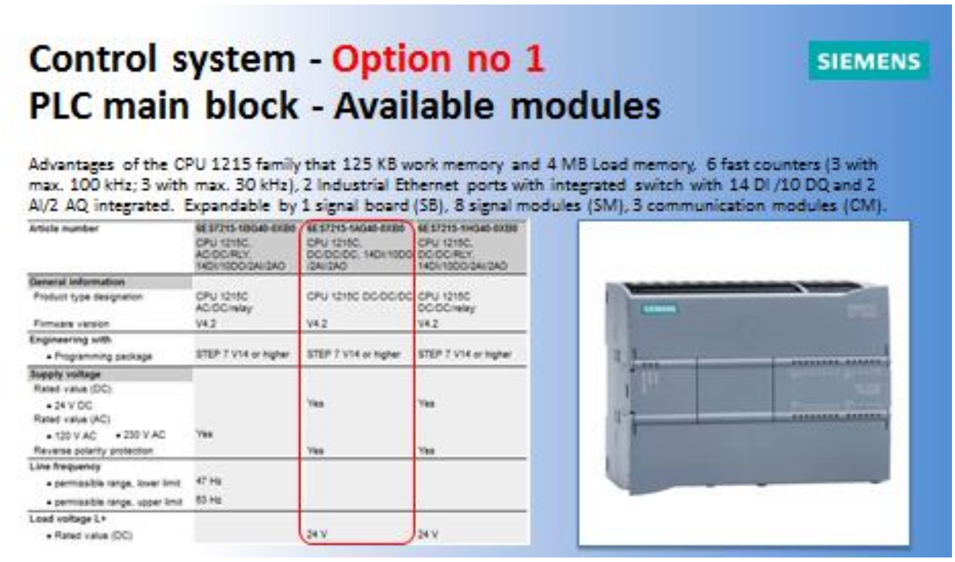

Control system - Option no 1
PLC main block - Available modules

SIEMENS

Advantages of the CPU 1215 family that 125 KB work memory and 4 MB Load memory, 6 fast counters (3 with max. 100 kHz; 3 with max. 30 kHz), 2 Industrial Ethernet ports with integrated switch with 14 DI /10 DQ and 2 AI/2 AQ integrated. Expandable by 1 signal board (SB), 8 signal modules (SM), 3 communication modules (CM).

Article number	6ES7215-1BG40-0XB0 CPU 1215C, AC/DC/RLY, 14DI/10DO/2AI/2AO	6ES7215-1AG40-0XB0 CPU 1215C, DC/DC/DC, 14DI/10DO/2AI/2AO	6ES7215-1HG40-0XB0 CPU 1215C, DC/DC/RLY, 14DI/10DO/2AI/2AO
General information			
Product type designation	CPU 1215C AC/DC/relay	CPU 1215C DC/DC/DC	CPU 1215C DC/DC/relay
Firmware version	V4.2	V4.2	V4.2
Engineering with			
• Programming package	STEP 7 V14 or higher	STEP 7 V14 or higher	STEP 7 V14 or higher
Supply voltage			
Rated value (DC)			
• 24 V DC		Yes	Yes
Rated value (AC)			
• 120 V AC • 230 V AC	Yes		
Reverse polarity protection		Yes	Yes
Line frequency			
• permissible range, lower limit	47 Hz		
• permissible range, upper limit	63 Hz		
Load voltage L+			
• Rated value (DC)		24 V	24 V

Fig. 34. SIMATIC S7-1200 system – PLC main block – available modules

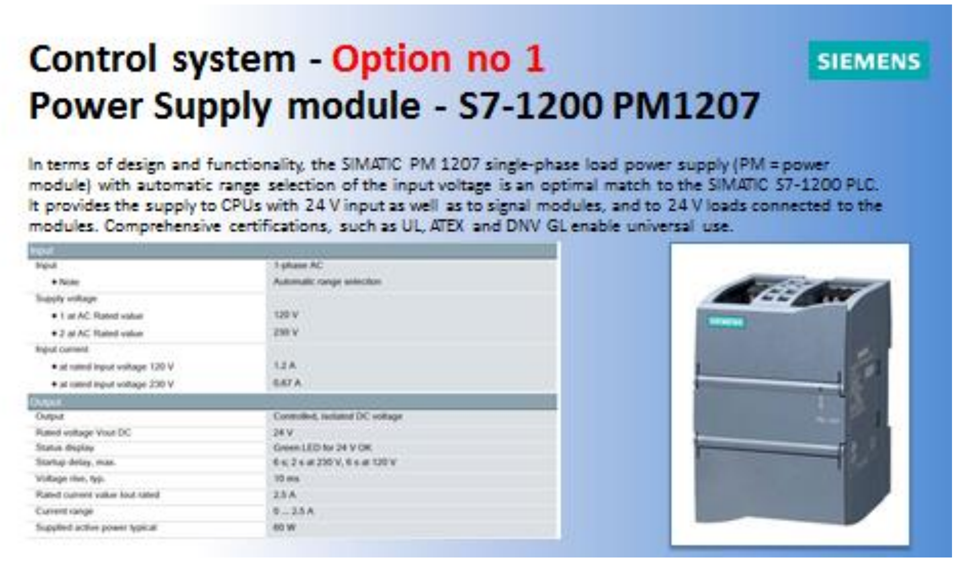

Control system - Option no 1
Power Supply module - S7-1200 PM1207

SIEMENS

In terms of design and functionality, the SIMATIC PM 1207 single-phase load power supply (PM = power module) with automatic range selection of the input voltage is an optimal match to the SIMATIC S7-1200 PLC. It provides the supply to CPUs with 24 V input as well as to signal modules, and to 24 V loads connected to the modules. Comprehensive certifications, such as UL, ATEX and DNV GL enable universal use.

Input	
Input	1-phase AC
• Note	Automatic range selection
Supply voltage	
• 1 at AC Rated value	120 V
• 2 at AC Rated value	230 V
Input current	
• at rated input voltage 120 V	1.2 A
• at rated input voltage 230 V	0.67 A
Output	
Output	Controlled, isolated DC voltage
Rated voltage Vout DC	24 V
Status display	Green LED for 24 V OK
Startup delay, max.	6 s; 2 s at 230 V, 6 s at 120 V
Voltage rise, typ.	10 ms
Rated current value Iout rated	2.5 A
Current range	0 ... 2.5 A
Supplied active power typical	60 W

Fig. 35. SIMATIC S7-1200 system – Power Supply module

Characteristics of X20 control system by B&R

The Fig. 36 (general description of system), Figs. 37-40 (description of analog inputs modules), Figs. 41-44 (description of analog outputs modules), Figs. 45-48 (description of temperature inputs modules), Figs. 49-52 (description of digital inputs modules), Figs. 53-56 (description of digital outputs modules), Figs. 57-59 (description of HMI panel), Fig. 60-61 (description of communication modules) and Figs. 62-67 (description of CPU main block module) shows the most important information about the elements and components of the B&R X20 system [26].

The presented elements can be used in the control and measurement process control system in the extruder.

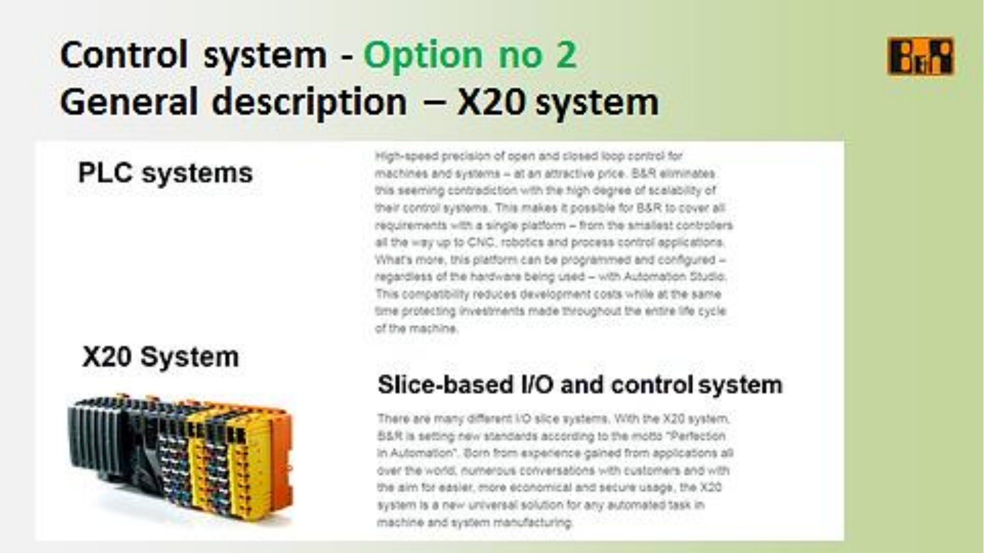

Control system - Option no 2
General description – X20 system

PLC systems

High-speed precision of open and closed loop control for machines and systems – at an attractive price. B&R eliminates this seeming contradiction with the high degree of scalability of their control systems. This makes it possible for B&R to cover all requirements with a single platform – from the smallest controllers all the way up to CNC, robotics and process control applications. What's more, this platform can be programmed and configured – regardless of the hardware being used – with Automation Studio. This compatibility reduces development costs while at the same time protecting investments made throughout the entire life cycle of the machine.

X20 System

Slice-based I/O and control system

There are many different I/O slice systems. With the X20 system, B&R is setting new standards according to the motto "Perfection in Automation". Born from experience gained from applications all over the world, numerous conversations with customers and with the aim for easier, more economical and secure usage, the X20 system is a new universal solution for any automated task in machine and system manufacturing.

Fig. 36. B&R X20 system – general description

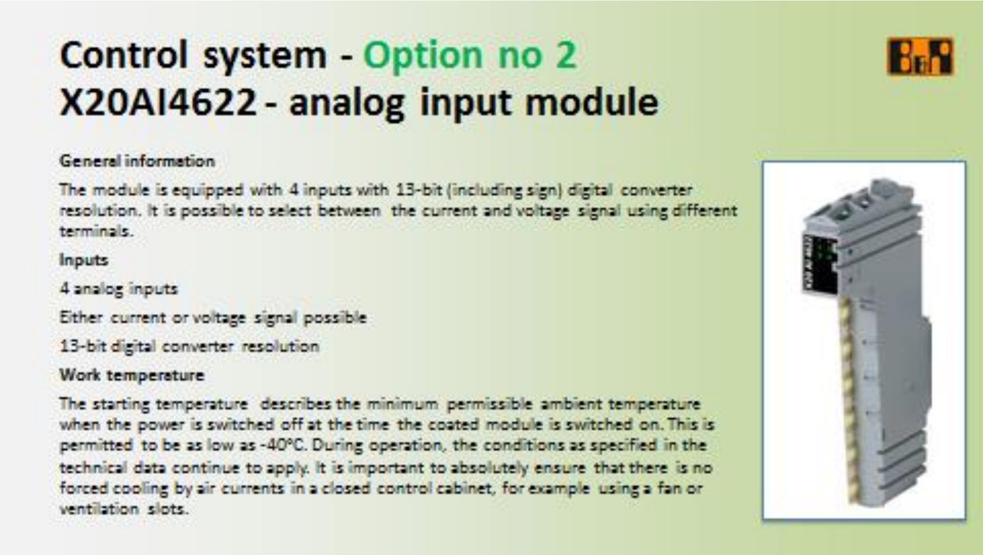

Control system - Option no 2
X20AI4622 - analog input module

General information

The module is equipped with 4 inputs with 13-bit (including sign) digital converter resolution. It is possible to select between the current and voltage signal using different terminals.

Inputs

4 analog inputs

Either current or voltage signal possible

13-bit digital converter resolution

Work temperature

The starting temperature describes the minimum permissible ambient temperature when the power is switched off at the time the coated module is switched on. This is permitted to be as low as -40°C. During operation, the conditions as specified in the technical data continue to apply. It is important to absolutely ensure that there is no forced cooling by air currents in a closed control cabinet, for example using a fan or ventilation slots.

Fig. 37. B&R X20 system – analog input – description of module

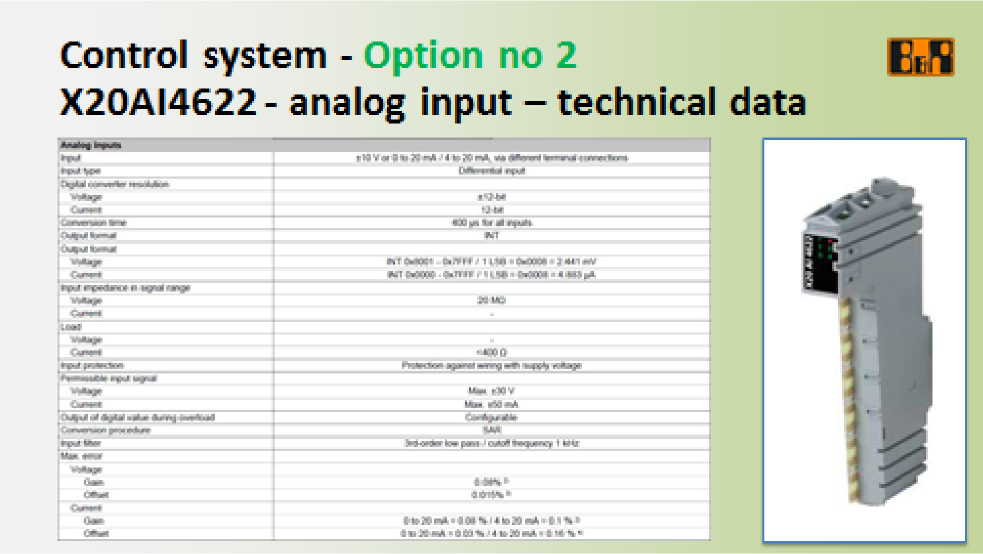

Control system - Option no 2
X20AI4622 - analog input – technical data

Analog inputs	
Input	±10 V or 0 to 20 mA / 4 to 20 mA, via different terminal connections
Input type	Differential input
Digital converter resolution	
Voltage	±12-bit
Current	12-bit
Conversion time	400 µs for all inputs
Output format	INT
Output format	
Voltage	INT 0x8001 - 0x7FFF / 1 LSB = 0x0008 = 2.441 mV
Current	INT 0x0000 - 0x7FFF / 1 LSB = 0x0008 = 4.883 µA
Input impedance in signal range	
Voltage	20 MΩ
Current	-
Load	
Voltage	-
Current	<400 Ω
Input protection	Protection against wiring with supply voltage
Permissible input signal	
Voltage	Max. ±30 V
Current	Max. ±50 mA
Output of digital value during overload	Configurable
Conversion procedure	SAR
Input filter	3rd-order low pass / cutoff frequency 1 kHz
Max. error	
Voltage	
Gain	0.08% [1]
Offset	0.015% [1]
Current	
Gain	0 to 20 mA = 0.08 % / 4 to 20 mA = 0.1 % [1]
Offset	0 to 20 mA = 0.03 % / 4 to 20 mA = 0.16 % [1]

Fig. 38. B&R X20 system – analog inputs – technical data of module

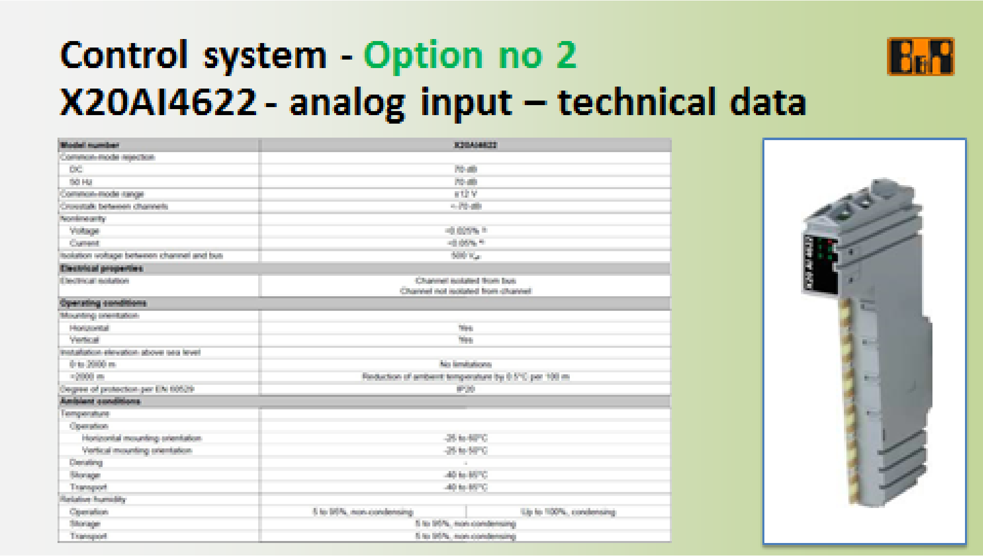

Control system - Option no 2
X20AI4622 - analog input – technical data

Model number	X20AI4622
Common-mode rejection	
DC	70 dB
50 Hz	70 dB
Common-mode range	±12 V
Crosstalk between channels	<-70 dB
Nonlinearity	
Voltage	<0.025% 1)
Current	<0.05% 1)
Isolation voltage between channel and bus	500 V_{eff}
Electrical properties	
Electrical isolation	Channel isolated from bus Channel not isolated from channel
Operating conditions	
Mounting orientation	
Horizontal	Yes
Vertical	Yes
Installation elevation above sea level	
0 to 2000 m	No limitations
>2000 m	Reduction of ambient temperature by 0.5°C per 100 m
Degree of protection per EN 60529	IP20
Ambient conditions	
Temperature	
Operation	
Horizontal mounting orientation	-25 to 60°C
Vertical mounting orientation	-25 to 50°C
Derating	-
Storage	-40 to 85°C
Transport	-40 to 85°C
Relative humidity	
Operation	5 to 95%, non-condensing Up to 100%, condensing
Storage	5 to 95%, non-condensing
Transport	5 to 95%, non-condensing

Fig. 39. B&R X20 system – analog inputs – technical data of module

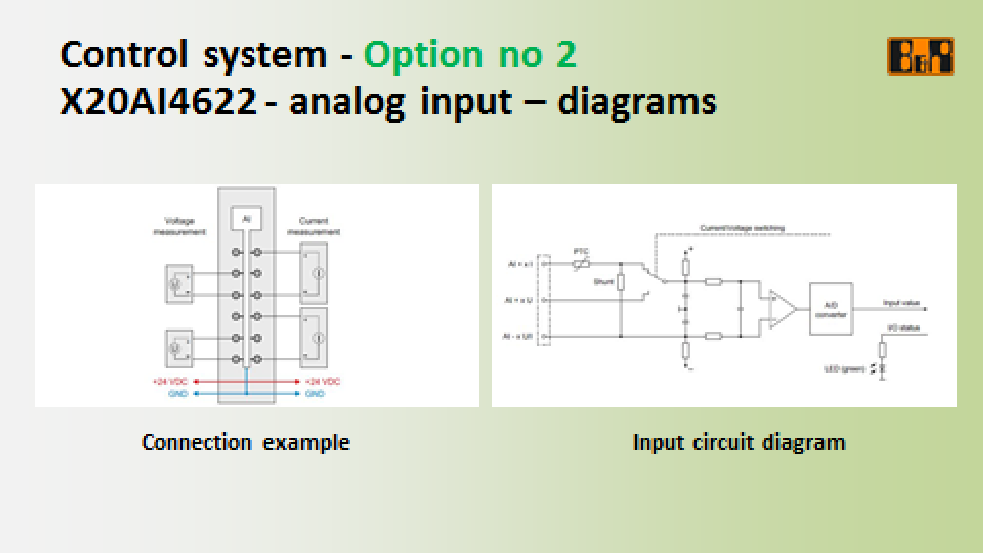

Control system - Option no 2
X20AI4622 - analog input – diagrams

Voltage measurement
AI
Current measurement
+24 VDC
GND
+24 VDC
GND
Current/Voltage switching
PTC
Shunt
AI + x I
AI + x U
AI - x U/I
A/D converter
Input value
I/O status
LED (green)

Connection example

Input circuit diagram

Fig. 40. B&R X20 system – analog inputs – connection diagrams

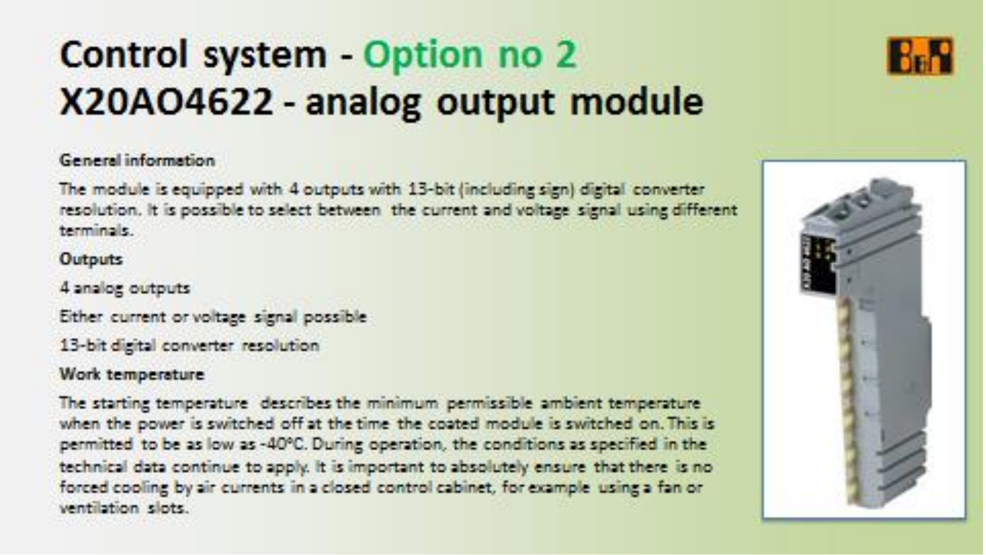

Control system - Option no 2
X20AO4622 - analog output module

General information

The module is equipped with 4 outputs with 13-bit (including sign) digital converter resolution. It is possible to select between the current and voltage signal using different terminals.

Outputs

4 analog outputs

Either current or voltage signal possible

13-bit digital converter resolution

Work temperature

The starting temperature describes the minimum permissible ambient temperature when the power is switched off at the time the coated module is switched on. This is permitted to be as low as -40°C. During operation, the conditions as specified in the technical data continue to apply. It is important to absolutely ensure that there is no forced cooling by air currents in a closed control cabinet, for example using a fan or ventilation slots.

Fig. 41. B&R X20 system – analog outputs – description of module

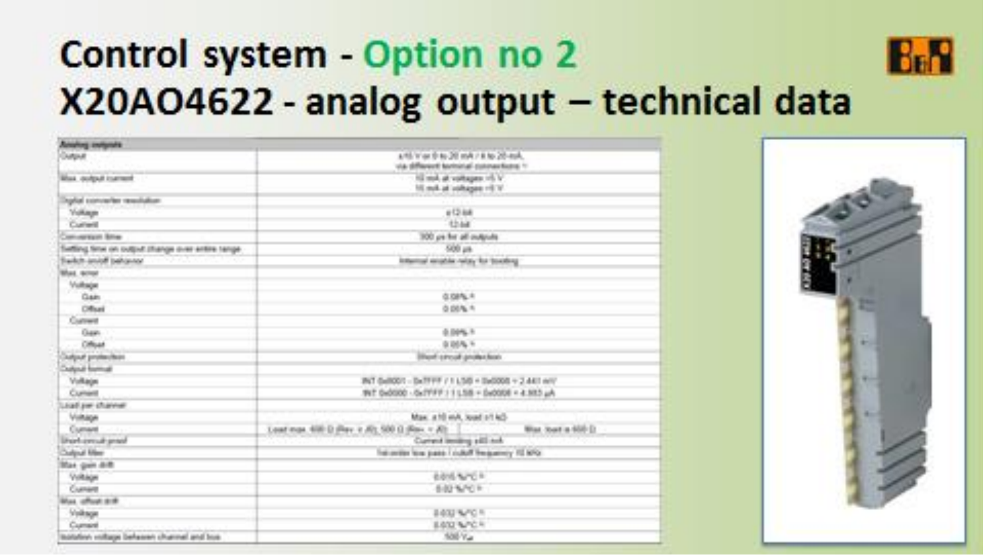

Control system - Option no 2
X20AO4622 - analog output – technical data

Analog outputs	
Output	±10 V or 0 to 20 mA / 4 to 20 mA, via different terminal connections 1)
Max. output current	10 mA at voltages >5 V 15 mA at voltages <5 V
Digital converter resolution	
Voltage	±12-bit
Current	12-bit
Conversion time	300 µs for all outputs
Settling time on output change over entire range	500 µs
Switch on/off behavior	Internal enable relay for booting
Max. error	
Voltage	
Gain	0.08% 2)
Offset	0.05% 3)
Current	
Gain	0.09% 2)
Offset	0.05% 3)
Output protection	Short circuit protection
Output format	
Voltage	INT 0x8001 - 0x7FFF / 1 LSB = 0x0008 = 2.441 mV
Current	INT 0x0000 - 0x7FFF / 1 LSB = 0x0008 = 4.883 µA
Load per channel	
Voltage	Max. ±10 mA, load ≥1 kΩ
Current	Load max. 400 Ω (Rev. ≤ J0), 500 Ω (Rev. ≥ J0) Max. load ≤ 600 Ω
Short-circuit proof	Current limiting ±40 mA
Output filter	1st-order low pass / cutoff frequency 10 kHz
Max. gain drift	
Voltage	0.015 %/°C 2)
Current	0.02 %/°C 2)
Max. offset drift	
Voltage	0.032 %/°C 3)
Current	0.032 %/°C 3)
Isolation voltage between channel and bus	500 V_{eff}

Fig. 42. B&R X20 system – analog outputs – technical data of module

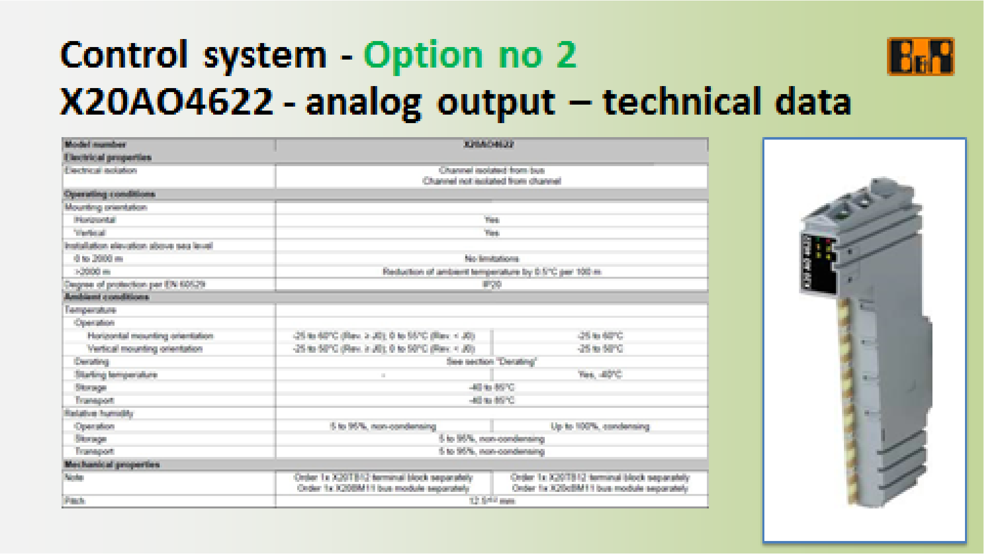

Control system - Option no 2
X20AO4622 - analog output – technical data

Model number	X20AO4622	
Electrical properties		
Electrical isolation	Channel isolated from bus Channel not isolated from channel	
Operating conditions		
Mounting orientation		
Horizontal	Yes	
Vertical	Yes	
Installation elevation above sea level		
0 to 2000 m	No limitations	
>2000 m	Reduction of ambient temperature by 0.5°C per 100 m	
Degree of protection per EN 60529	IP20	
Ambient conditions		
Temperature		
Operation		
Horizontal mounting orientation	-25 to 60°C (Rev. ≥ J0); 0 to 55°C (Rev. < J0)	-25 to 60°C
Vertical mounting orientation	-25 to 50°C (Rev. ≥ J0); 0 to 50°C (Rev. < J0)	-25 to 50°C
Derating	See section "Derating"	
Starting temperature	-	Yes, -40°C
Storage	-40 to 85°C	
Transport	-40 to 85°C	
Relative humidity		
Operation	5 to 95%, non-condensing	Up to 100%, condensing
Storage	5 to 95%, non-condensing	
Transport	5 to 95%, non-condensing	
Mechanical properties		
Note	Order 1x X20TB12 terminal block separately Order 1x X20BM11 bus module separately	Order 1x X20TB12 terminal block separately Order 1x X20cBM11 bus module separately
Pitch	12.5$^{+0.2}$ mm	

Fig. 43. B&R X20 system – analog outputs – technical data of module

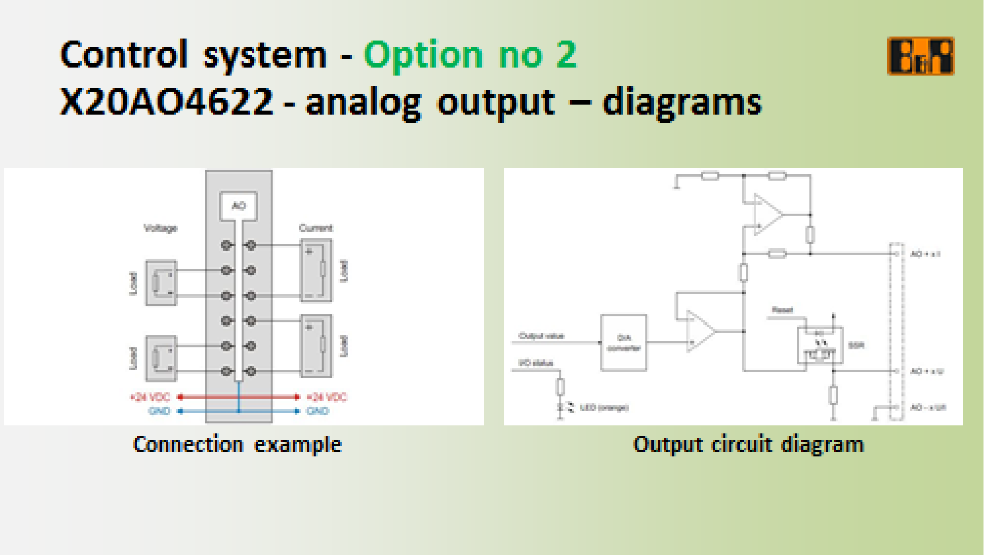

Control system - Option no 2
X20AO4622 - analog output – diagrams

Connection example

Output circuit diagram

Fig. 44. B&R X20 system – analog outputs – connection diagrams

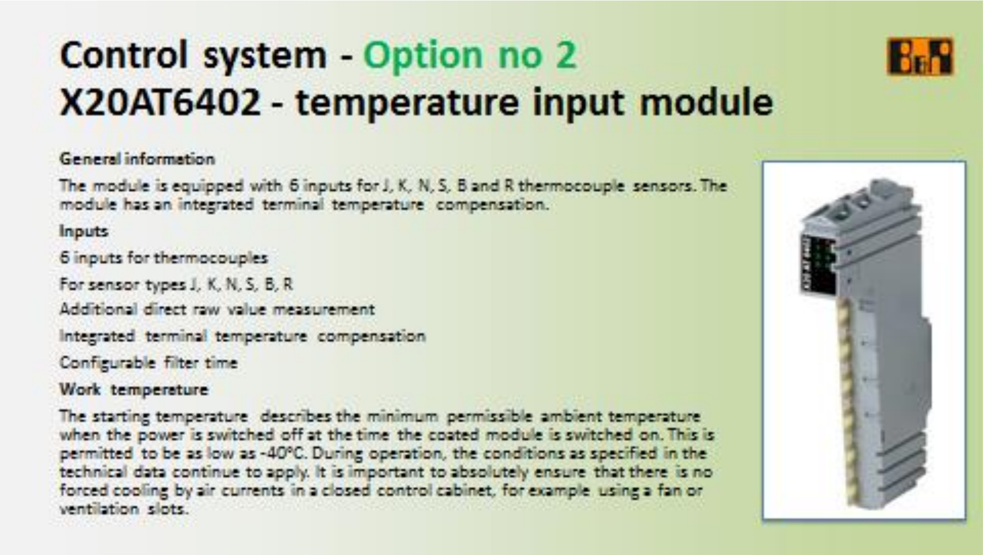

Control system - Option no 2
X20AT6402 - temperature input module

General information

The module is equipped with 6 inputs for J, K, N, S, B and R thermocouple sensors. The module has an integrated terminal temperature compensation.

Inputs

6 inputs for thermocouples

For sensor types J, K, N, S, B, R

Additional direct raw value measurement

Integrated terminal temperature compensation

Configurable filter time

Work temperature

The starting temperature describes the minimum permissible ambient temperature when the power is switched off at the time the coated module is switched on. This is permitted to be as low as -40°C. During operation, the conditions as specified in the technical data continue to apply. It is important to absolutely ensure that there is no forced cooling by air currents in a closed control cabinet, for example using a fan or ventilation slots.

Fig. 45. B&R X20 system – temperature inputs – description of module

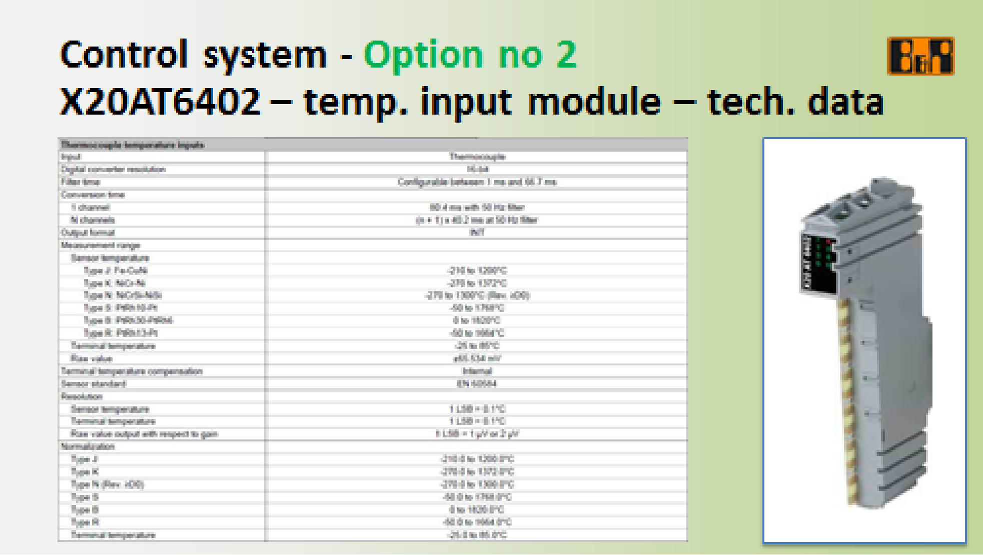

Control system - Option no 2
X20AT6402 – temp. input module – tech. data

Thermocouple temperature inputs	
Input	Thermocouple
Digital converter resolution	16-bit
Filter time	Configurable between 1 ms and 66.7 ms
Conversion time	
1 channel	80.4 ms with 50 Hz filter
N channels	(n + 1) x 40.2 ms at 50 Hz filter
Output format	INT
Measurement range	
Sensor temperature	
Type J: Fe-CuNi	-210 to 1200°C
Type K: NiCr-Ni	-270 to 1372°C
Type N: NiCrSi-NiSi	-270 to 1300°C (Rev. ≥D0)
Type S: PtRh10-Pt	-50 to 1768°C
Type B: PtRh30-PtRh6	0 to 1820°C
Type R: PtRh13-Pt	-50 to 1664°C
Terminal temperature	-25 to 85°C
Raw value	±65.534 mV
Terminal temperature compensation	Internal
Sensor standard	EN 60584
Resolution	
Sensor temperature	1 LSB = 0.1°C
Terminal temperature	1 LSB = 0.1°C
Raw value output with respect to gain	1 LSB = 1 µV or 2 µV
Normalization	
Type J	-210.0 to 1200.0°C
Type K	-270.0 to 1372.0°C
Type N (Rev. ≥D0)	-270.0 to 1300.0°C
Type S	-50.0 to 1768.0°C
Type B	0 to 1820.0°C
Type R	-50.0 to 1664.0°C
Terminal temperature	-25.0 to 85.0°C

Fig. 46. B&R X20 system – temperature inputs – technical date of module

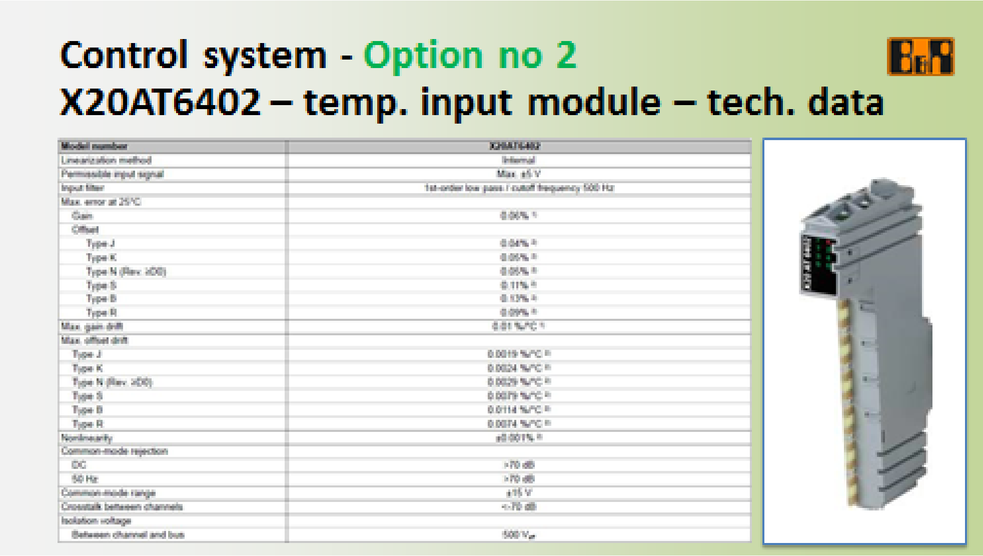

Control system - Option no 2
X20AT6402 – temp. input module – tech. data

Model number	X20AT6402
Linearization method	Internal
Permissible input signal	Max. ±5 V
Input filter	1st-order low pass / cutoff frequency 500 Hz
Max. error at 25°C	
Gain	0.06% 1)
Offset	
Type J	0.04% 2)
Type K	0.05% 2)
Type N (Rev. ≥D0)	0.05% 2)
Type S	0.11% 2)
Type B	0.13% 2)
Type R	0.09% 2)
Max. gain drift	0.01 %/°C 1)
Max. offset drift	
Type J	0.0019 %/°C 2)
Type K	0.0024 %/°C 2)
Type N (Rev. ≥D0)	0.0029 %/°C 2)
Type S	0.0079 %/°C 2)
Type B	0.0114 %/°C 2)
Type R	0.0074 %/°C 2)
Nonlinearity	±0.001% 2)
Common-mode rejection	
DC	>70 dB
50 Hz	>70 dB
Common-mode range	±15 V
Crosstalk between channels	<-70 dB
Isolation voltage	
Between channel and bus	500 V_{eff}

Fig. 47. B&R X20 system – temperature inputs – technical date of module

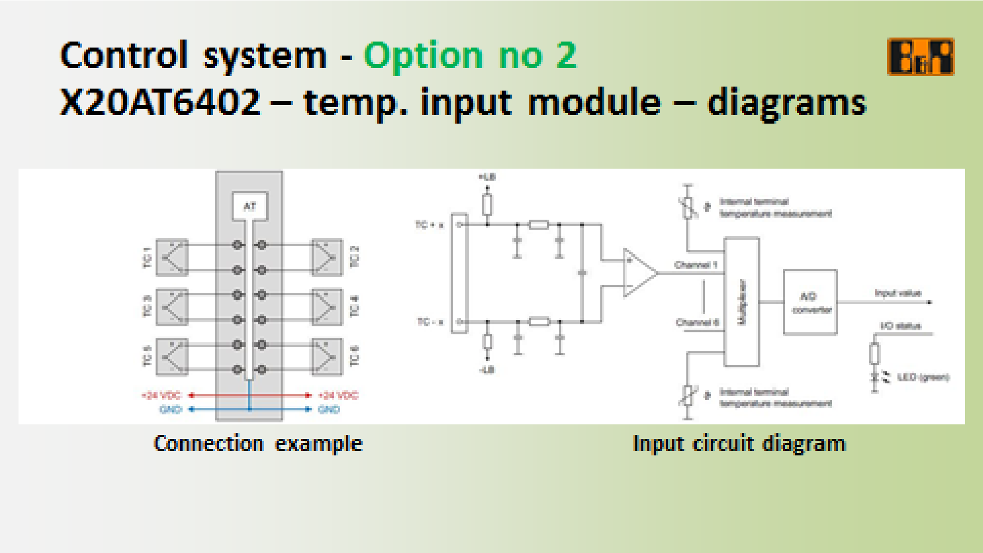

Control system - Option no 2
X20AT6402 – temp. input module – diagrams

AT
TC 1
TC 2
TC 3
TC 4
TC 5
TC 6
+24 VDC
GND
+24 VDC
GND
+UB
TC + x
TC - x
-UB
Internal terminal temperature measurement
Channel 1
Channel 6
Multiplexer
A/D converter
Input value
I/O status
LED (green)
Internal terminal temperature measurement

Connection example

Input circuit diagram

Fig. 48. B&R X20 system – temperature inputs – connection diagrams

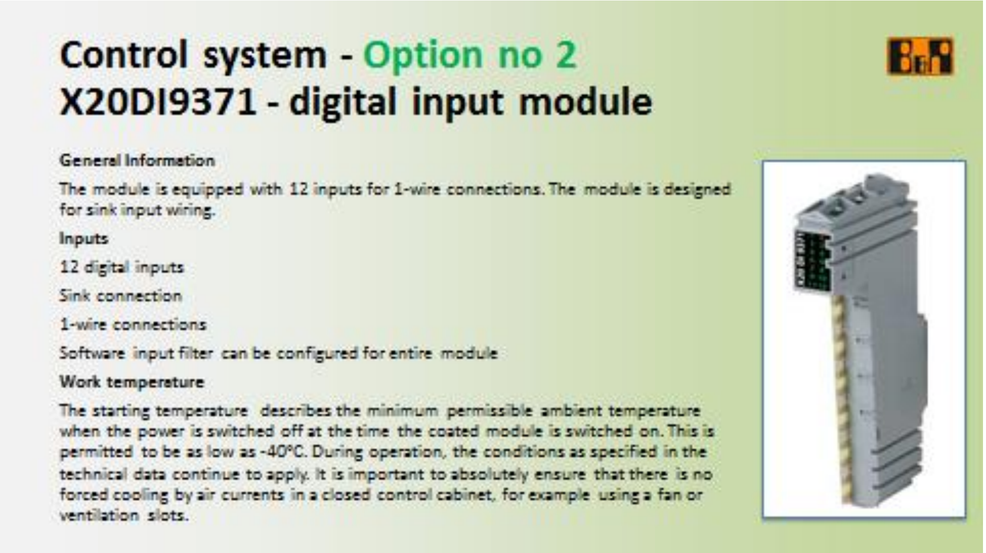

Control system - Option no 2
X20DI9371 - digital input module

General Information

The module is equipped with 12 inputs for 1-wire connections. The module is designed for sink input wiring.

Inputs

12 digital inputs

Sink connection

1-wire connections

Software input filter can be configured for entire module

Work temperature

The starting temperature describes the minimum permissible ambient temperature when the power is switched off at the time the coated module is switched on. This is permitted to be as low as -40°C. During operation, the conditions as specified in the technical data continue to apply. It is important to absolutely ensure that there is no forced cooling by air currents in a closed control cabinet, for example using a fan or ventilation slots.

Fig. 49. B&R X20 system – digital inputs – description of module

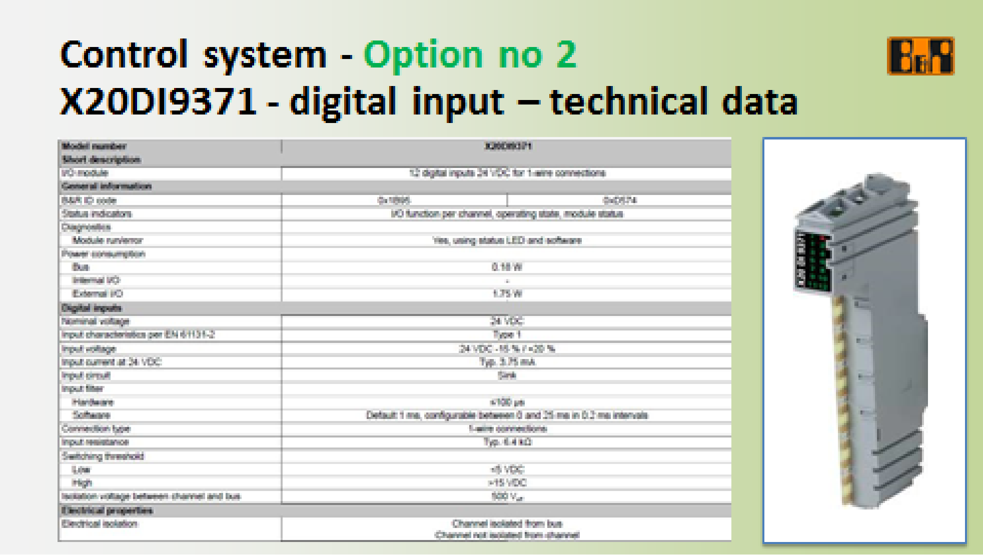

Control system - Option no 2
X20DI9371 - digital input – technical data

Model number	**X20DI9371**	
Short description		
I/O module	12 digital inputs 24 VDC for 1-wire connections	
General information		
B&R ID code	0x1B95	0xD574
Status indicators	I/O function per channel, operating state, module status	
Diagnostics		
Module run/error	Yes, using status LED and software	
Power consumption		
Bus	0.18 W	
Internal I/O	-	
External I/O	1.75 W	
Digital inputs		
Nominal voltage	24 VDC	
Input characteristics per EN 61131-2	Type 1	
Input voltage	24 VDC -15 % / +20 %	
Input current at 24 VDC	Typ. 3.75 mA	
Input circuit	Sink	
Input filter		
Hardware	≤100 µs	
Software	Default 1 ms, configurable between 0 and 25 ms in 0.2 ms intervals	
Connection type	1-wire connections	
Input resistance	Typ. 6.4 kΩ	
Switching threshold		
Low	<5 VDC	
High	>15 VDC	
Isolation voltage between channel and bus	$500\ V_{eff}$	
Electrical properties		
Electrical isolation	Channel isolated from bus Channel not isolated from channel	

Fig. 50. B&R X20 system – digital inputs – technical data of module

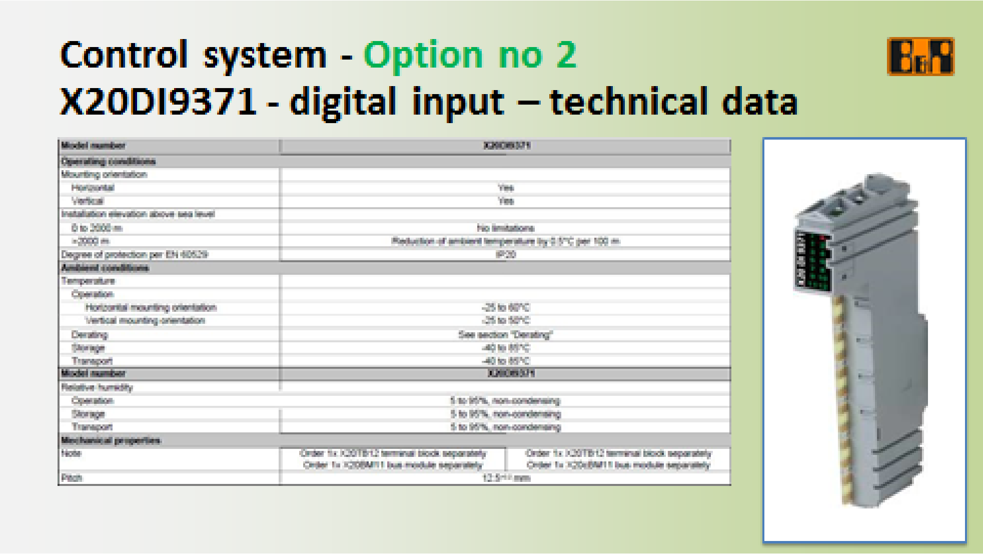

Control system - Option no 2
X20DI9371 - digital input – technical data

Model number	X20DI9371	
Operating conditions		
Mounting orientation		
Horizontal	Yes	
Vertical	Yes	
Installation elevation above sea level		
0 to 2000 m	No limitations	
>2000 m	Reduction of ambient temperature by 0.5°C per 100 m	
Degree of protection per EN 60529	IP20	
Ambient conditions		
Temperature		
Operation		
Horizontal mounting orientation	-25 to 60°C	
Vertical mounting orientation	-25 to 50°C	
Derating	See section "Derating"	
Storage	-40 to 85°C	
Transport	-40 to 85°C	
Model number	X20DI9371	
Relative humidity		
Operation	5 to 95%, non-condensing	
Storage	5 to 95%, non-condensing	
Transport	5 to 95%, non-condensing	
Mechanical properties		
Note	Order 1x X20TB12 terminal block separately Order 1x X20BM11 bus module separately	Order 1x X20TB12 terminal block separately Order 1x X20cBM11 bus module separately
Pitch	$12.5^{+0.2}$ mm	

Fig. 51. B&R X20 system – digital inputs – technical data of module

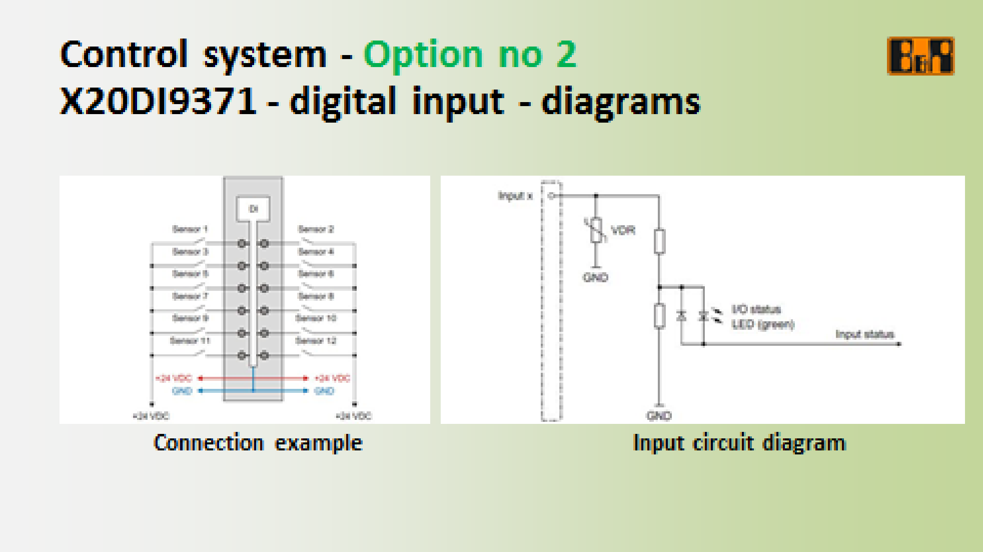

Control system - Option no 2
X20DI9371 - digital input - diagrams

DI
Sensor 1
Sensor 2
Sensor 3
Sensor 4
Sensor 5
Sensor 6
Sensor 7
Sensor 8
Sensor 9
Sensor 10
Sensor 11
Sensor 12
+24 VDC
GND
+24 VDC
GND
+24 VDC
+24 VDC
Input x
VDR
GND
I/O status
LED (green)
Input status
GND

Connection example

Input circuit diagram

Fig. 52. B&R X20 system – digital inputs – connection diagrams

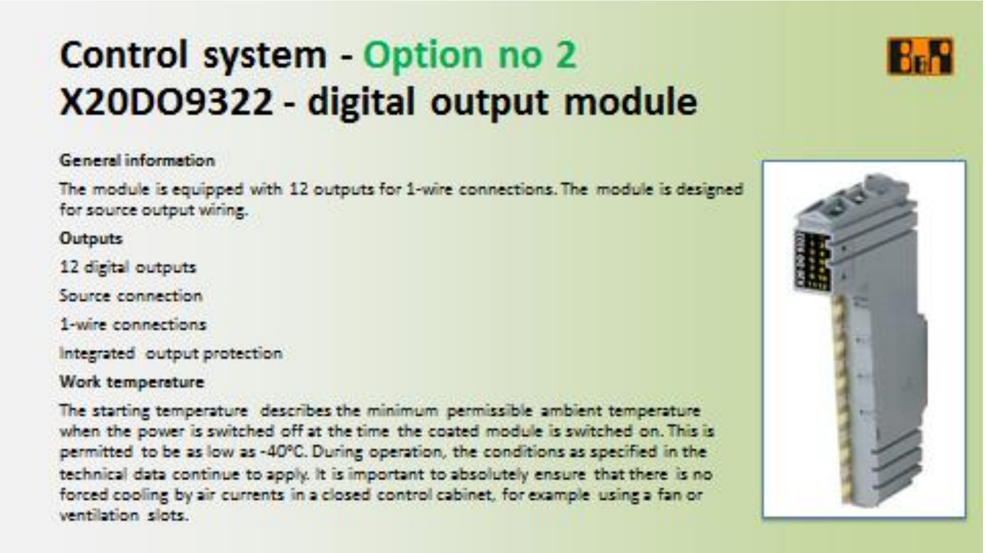

Control system - Option no 2
X20DO9322 - digital output module

General information

The module is equipped with 12 outputs for 1-wire connections. The module is designed for source output wiring.

Outputs

12 digital outputs

Source connection

1-wire connections

Integrated output protection

Work temperature

The starting temperature describes the minimum permissible ambient temperature when the power is switched off at the time the coated module is switched on. This is permitted to be as low as -40°C. During operation, the conditions as specified in the technical data continue to apply. It is important to absolutely ensure that there is no forced cooling by air currents in a closed control cabinet, for example using a fan or ventilation slots.

Fig. 53. B&R X20 system – digital outputs – description of module

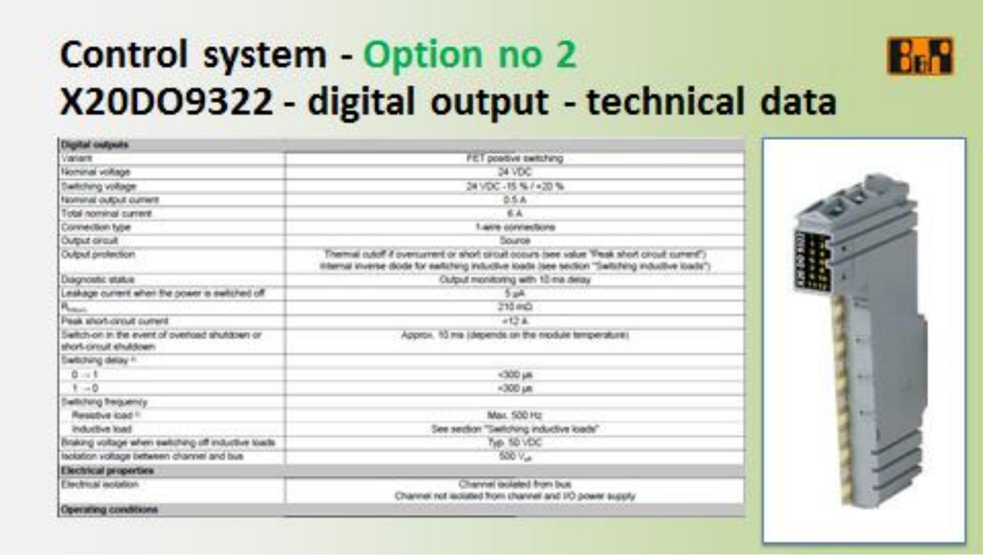

Control system - Option no 2
X20DO9322 - digital output - technical data

Digital outputs	
Variant	FET positive switching
Nominal voltage	24 VDC
Switching voltage	24 VDC -15 % / +20 %
Nominal output current	0.5 A
Total nominal current	6 A
Connection type	1-wire connections
Output circuit	Source
Output protection	Thermal cutoff if overcurrent or short circuit occurs (see value "Peak short circuit current") Internal inverse diode for switching inductive loads (see section "Switching inductive loads")
Diagnostic status	Output monitoring with 10 ms delay
Leakage current when the power is switched off	5 µA
$R_{DS(on)}$	210 mΩ
Peak short-circuit current	<12 A
Switch-on in the event of overload shutdown or short-circuit shutdown	Approx. 10 ms (depends on the module temperature)
Switching delay 1)	
0 → 1	<300 µs
1 → 0	<300 µs
Switching frequency	
Resistive load 1)	Max. 500 Hz
Inductive load	See section "Switching inductive loads"
Braking voltage when switching off inductive loads	Typ. 50 VDC
Isolation voltage between channel and bus	500 V_{eff}
Electrical properties	
Electrical isolation	Channel isolated from bus Channel not isolated from channel and I/O power supply
Operating conditions	

Fig. 54. B&R X20 system – digital outputs – technical data of module

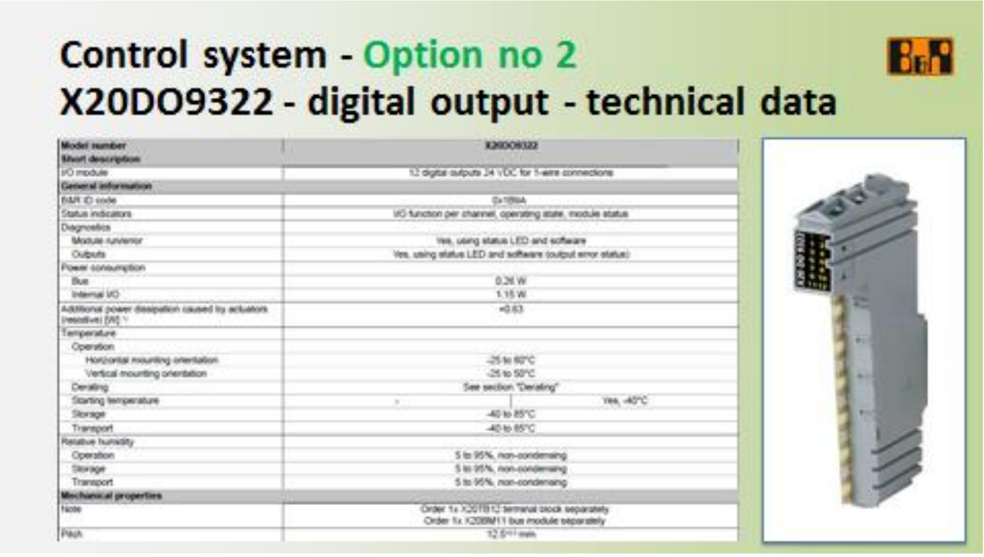

Control system - Option no 2
X20DO9322 - digital output - technical data

Model number	X20DO9322
Short description	
I/O module	12 digital outputs 24 VDC for 1-wire connections
General information	
B&R ID code	0x1B9A
Status indicators	I/O function per channel, operating state, module status
Diagnostics	
Module run/error	Yes, using status LED and software
Outputs	Yes, using status LED and software (output error status)
Power consumption	
Bus	0.26 W
Internal I/O	1.15 W
Additional power dissipation caused by actuators (resistive) [W] 1)	+0.63
Temperature	
Operation	
Horizontal mounting orientation	-25 to 60°C
Vertical mounting orientation	-25 to 50°C
Derating	See section "Derating"
Starting temperature	- Yes, -40°C
Storage	-40 to 85°C
Transport	-40 to 85°C
Relative humidity	
Operation	5 to 95%, non-condensing
Storage	5 to 95%, non-condensing
Transport	5 to 95%, non-condensing
Mechanical properties	
Note	Order 1x X20TB12 terminal block separately Order 1x X20BM11 bus module separately
Pitch	$12.5^{+0.2}$ mm

Fig. 55. B&R X20 system – digital outputs – technical data of module

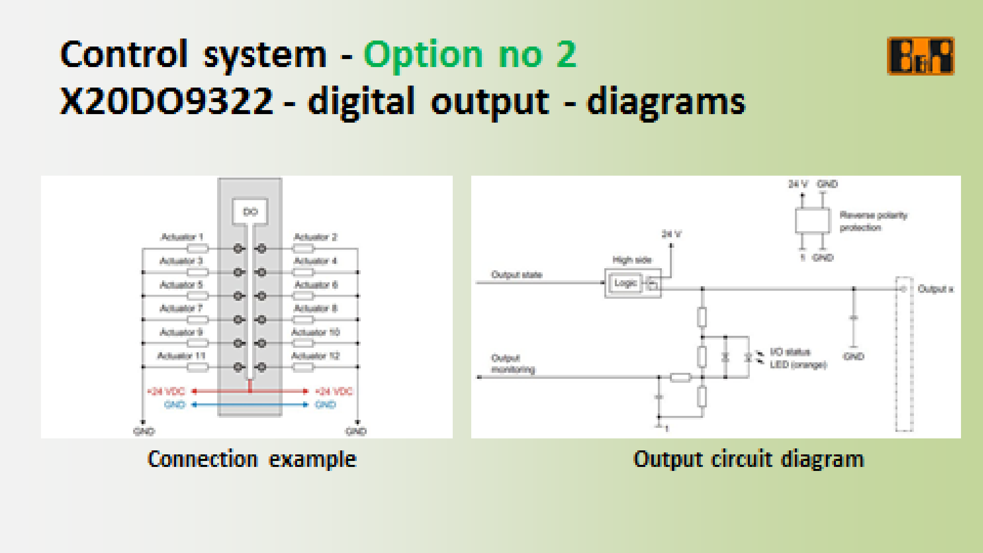

Control system - Option no 2
X20DO9322 - digital output - diagrams

DO
Actuator 1
Actuator 2
Actuator 3
Actuator 4
Actuator 5
Actuator 6
Actuator 7
Actuator 8
Actuator 9
Actuator 10
Actuator 11
Actuator 12
+24 VDC
+24 VDC
GND
GND
GND
GND
24 V
GND
Reverse polarity protection
24 V
High side
Output state
Logic
Output x
I/O status LED (orange)
Output monitoring
GND

Connection example

Output circuit diagram

Fig. 56. B&R X20 system – digital outputs – connection diagrams

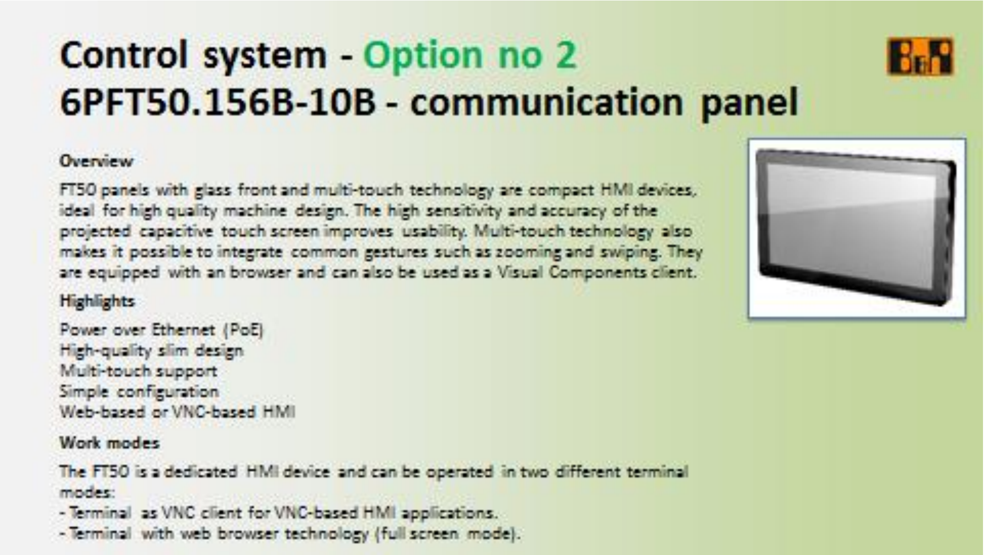

Control system - Option no 2
6PFT50.156B-10B - communication panel

Overview

FT50 panels with glass front and multi-touch technology are compact HMI devices, ideal for high quality machine design. The high sensitivity and accuracy of the projected capacitive touch screen improves usability. Multi-touch technology also makes it possible to integrate common gestures such as zooming and swiping. They are equipped with an browser and can also be used as a Visual Components client.

Highlights

Power over Ethernet (PoE)
High-quality slim design
Multi-touch support
Simple configuration
Web-based or VNC-based HMI

Work modes

The FT50 is a dedicated HMI device and can be operated in two different terminal modes:
- Terminal as VNC client for VNC-based HMI applications.
- Terminal with web browser technology (full screen mode).

Fig. 57. B&R X20 system – HMI communication panel – description of module

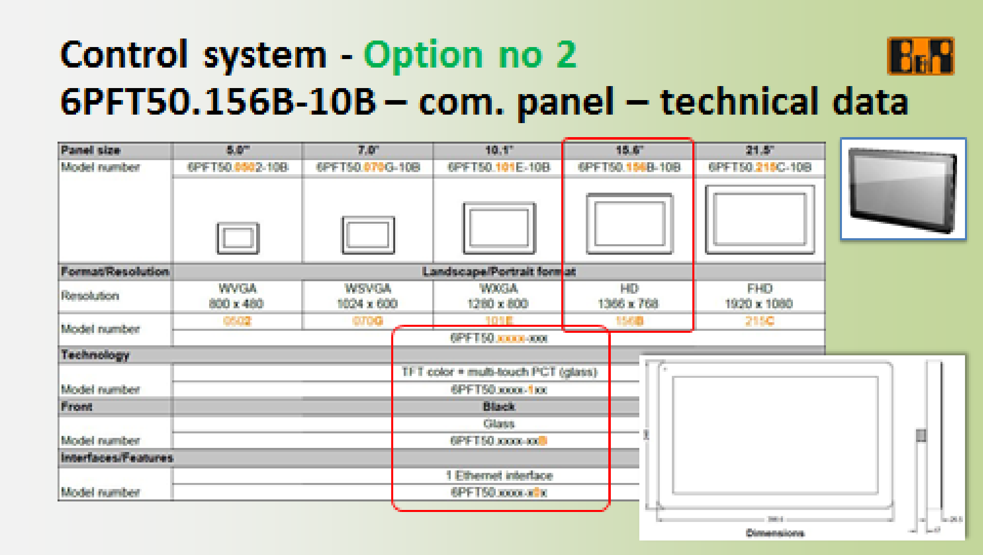

Control system - Option no 2
6PFT50.156B-10B – com. panel – technical data

Panel size	5.0"	7.0"	10.1"	15.6"	21.5"
Model number	6PFT50.0502-10B	6PFT50.070G-10B	6PFT50.101E-10B	6PFT50.156B-10B	6PFT50.215C-10B
Format/Resolution	Landscape/Portrait format				
Resolution	WVGA 800 x 480	WSVGA 1024 x 600	WXGA 1280 x 800	HD 1366 x 768	FHD 1920 x 1080
Model number	0502	070G	101E	156B	215C
	6PFT50.xxxx-xxx				
Technology					
	TFT color + multi-touch PCT (glass)				
Model number	6PFT50.xxxx-1xx				
Front	Black				
	Glass				
Model number	6PFT50.xxxx-xxB				
Interfaces/Features					
	1 Ethernet interface				
Model number	6PFT50.xxxx-x0x				

Fig. 58. B&R X20 system – HMI communication panel – technical data of modules

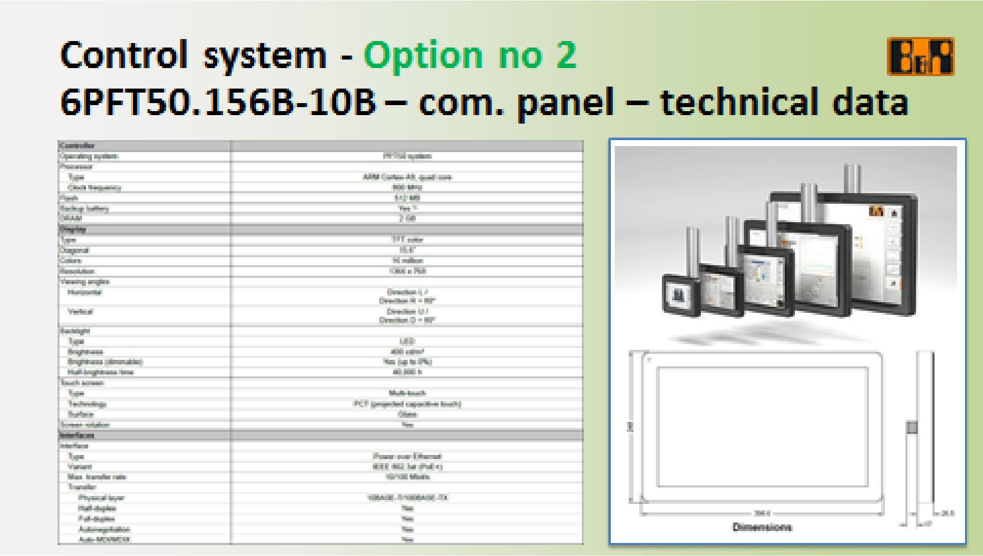

Control system - Option no 2

6PFT50.156B-10B – com. panel – technical data

Dimensions

Fig. 59. B&R X20 system – HMI communication panel – technical data of modules

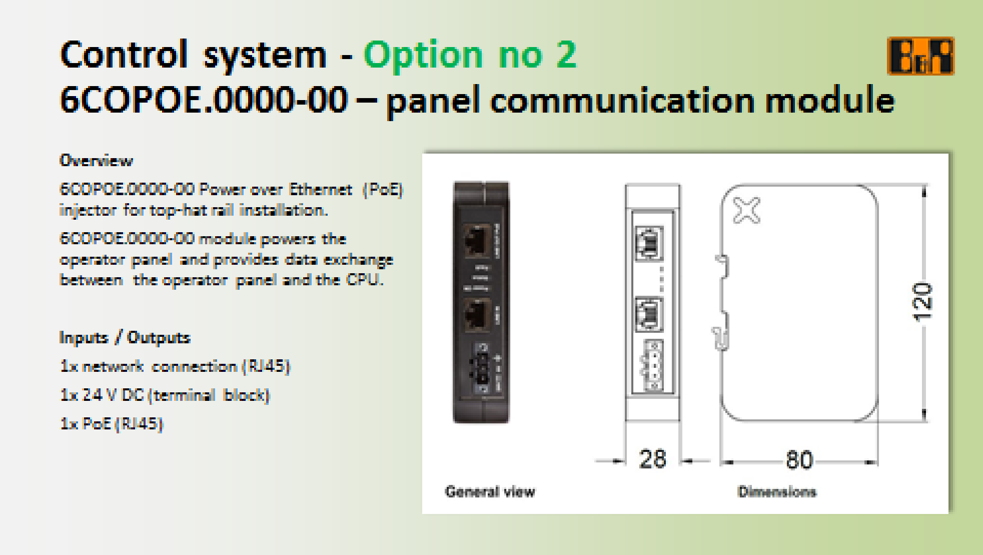

Control system - Option no 2

6COPOE.0000-00 – panel communication module

Overview

6COPOE.0000-00 Power over Ethernet (PoE) injector for top-hat rail installation.

6COPOE.0000-00 module powers the operator panel and provides data exchange between the operator panel and the CPU.

Inputs / Outputs

1x network connection (RJ45)

1x 24 V DC (terminal block)

1x PoE (RJ45)

28
80
120
General view
Dimensions

Fig. 60. B&R X20 system – communication module – description of module

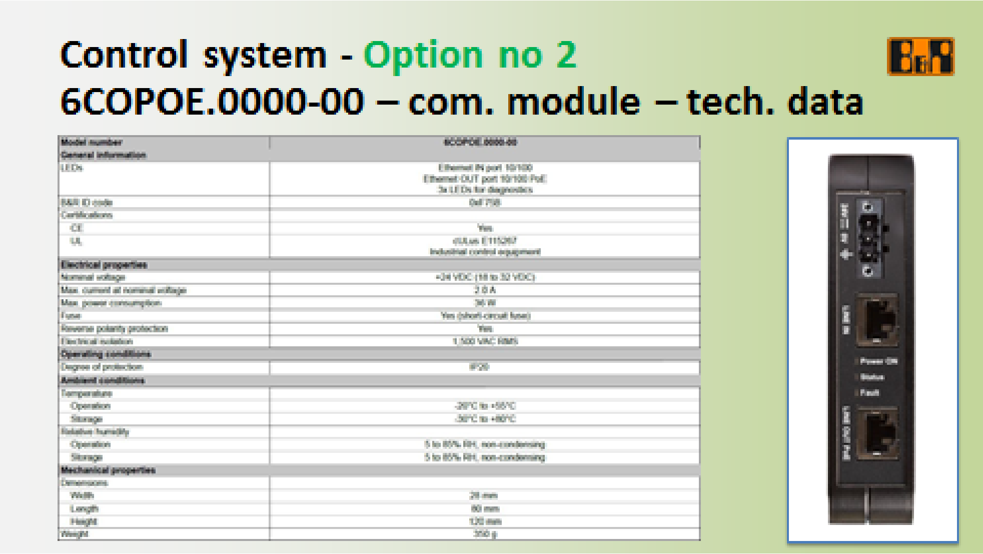

Control system - Option no 2
6COPOE.0000-00 – com. module – tech. data

Model number	6COPOE.0000-00
General information	
LEDs	Ethernet IN port 10/100 Ethernet OUT port 10/100 PoE 3x LEDs for diagnostics
B&R ID code	0xF75B
Certifications	
CE	Yes
UL	cULus E115267 Industrial control equipment
Electrical properties	
Nominal voltage	+24 VDC (18 to 32 VDC)
Max. current at nominal voltage	2.0 A
Max. power consumption	36 W
Fuse	Yes (short-circuit fuse)
Reverse polarity protection	Yes
Electrical isolation	1,500 VAC RMS
Operating conditions	
Degree of protection	IP20
Ambient conditions	
Temperature	
Operation	-20°C to +55°C
Storage	-30°C to +80°C
Relative humidity	
Operation	5 to 85% RH, non-condensing
Storage	5 to 85% RH, non-condensing
Mechanical properties	
Dimensions	
Width	28 mm
Length	80 mm
Height	120 mm
Weight	350 g

24V
0V
LINE IN
Power ON
Status
Fault
LINE OUT PoE

Fig. 61. B&R X20 system – communication module – technical data of module

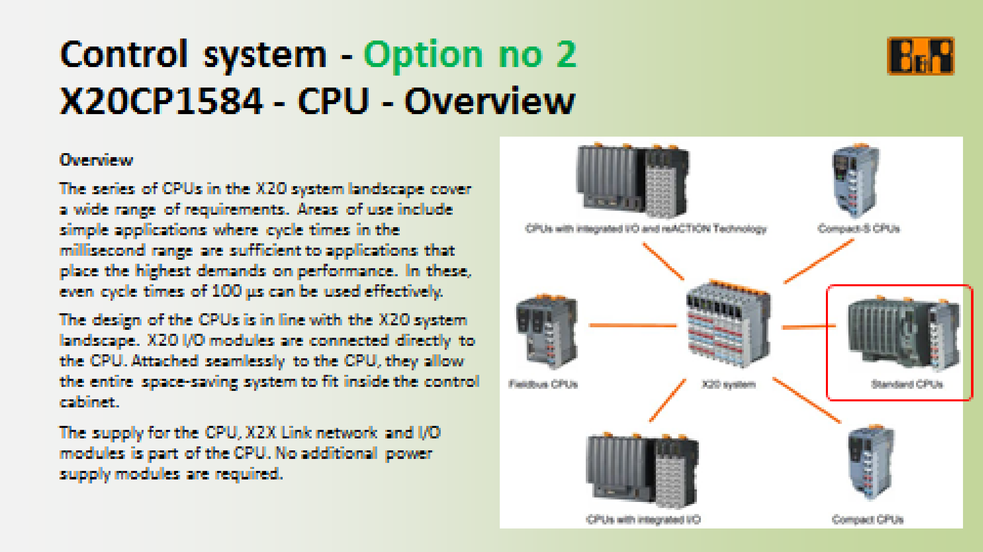

Control system - Option no 2
X20CP1584 - CPU - Overview

Overview

The series of CPUs in the X20 system landscape cover a wide range of requirements. Areas of use include simple applications where cycle times in the millisecond range are sufficient to applications that place the highest demands on performance. In these, even cycle times of 100 µs can be used effectively.

The design of the CPUs is in line with the X20 system landscape. X20 I/O modules are connected directly to the CPU. Attached seamlessly to the CPU, they allow the entire space-saving system to fit inside the control cabinet.

The supply for the CPU, X2X Link network and I/O modules is part of the CPU. No additional power supply modules are required.

CPUs with integrated I/O and reACTION Technology
Compact-S CPUs
Fieldbus CPUs
X20 system
Standard CPUs
CPUs with integrated I/O
Compact CPUs

Fig. 62. B&R X20 system – CPU module – description of module

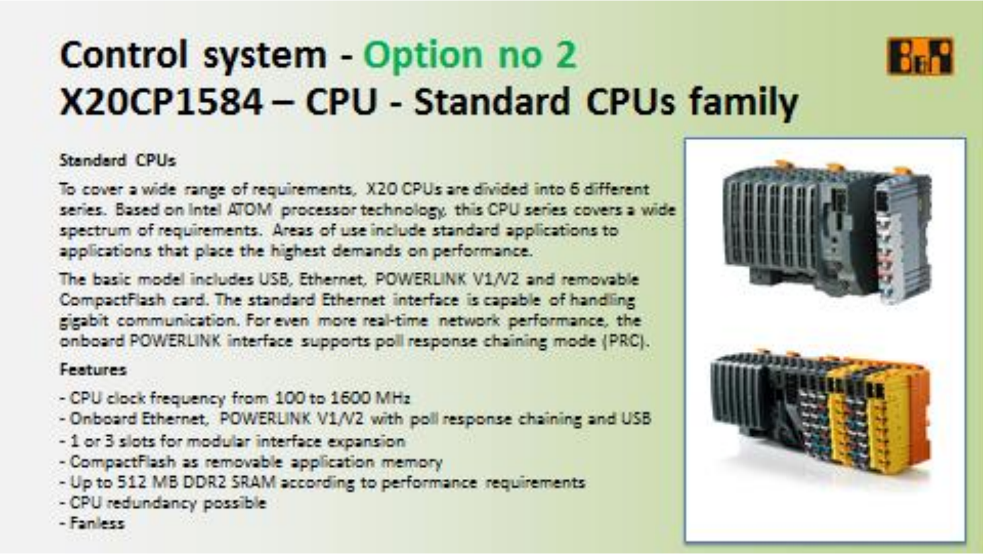

Control system - Option no 2
X20CP1584 – CPU - Standard CPUs family

Standard CPUs

To cover a wide range of requirements, X20 CPUs are divided into 6 different series. Based on Intel ATOM processor technology, this CPU series covers a wide spectrum of requirements. Areas of use include standard applications to applications that place the highest demands on performance.

The basic model includes USB, Ethernet, POWERLINK V1/V2 and removable CompactFlash card. The standard Ethernet interface is capable of handling gigabit communication. For even more real-time network performance, the onboard POWERLINK interface supports poll response chaining mode (PRC).

Features

- CPU clock frequency from 100 to 1600 MHz
- Onboard Ethernet, POWERLINK V1/V2 with poll response chaining and USB
- 1 or 3 slots for modular interface expansion
- CompactFlash as removable application memory
- Up to 512 MB DDR2 SRAM according to performance requirements
- CPU redundancy possible
- Fanless

Fig. 63. B&R X20 system – CPU module – description of module

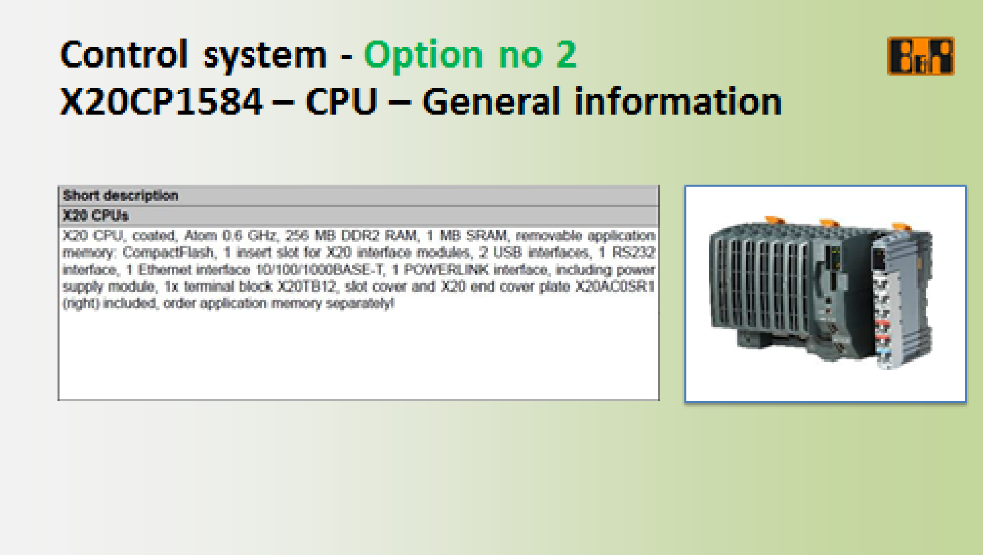

Control system - Option no 2
X20CP1584 – CPU – General information

Short description
X20 CPUs
X20 CPU, coated, Atom 0.6 GHz, 256 MB DDR2 RAM, 1 MB SRAM, removable application memory: CompactFlash, 1 insert slot for X20 interface modules, 2 USB interfaces, 1 RS232 interface, 1 Ethernet interface 10/100/1000BASE-T, 1 POWERLINK interface, including power supply module, 1x terminal block X20TB12, slot cover and X20 end cover plate X20AC0SR1 (right) included, order application memory separately!

Fig. 64. B&R X20 system – CPU module – general information of module

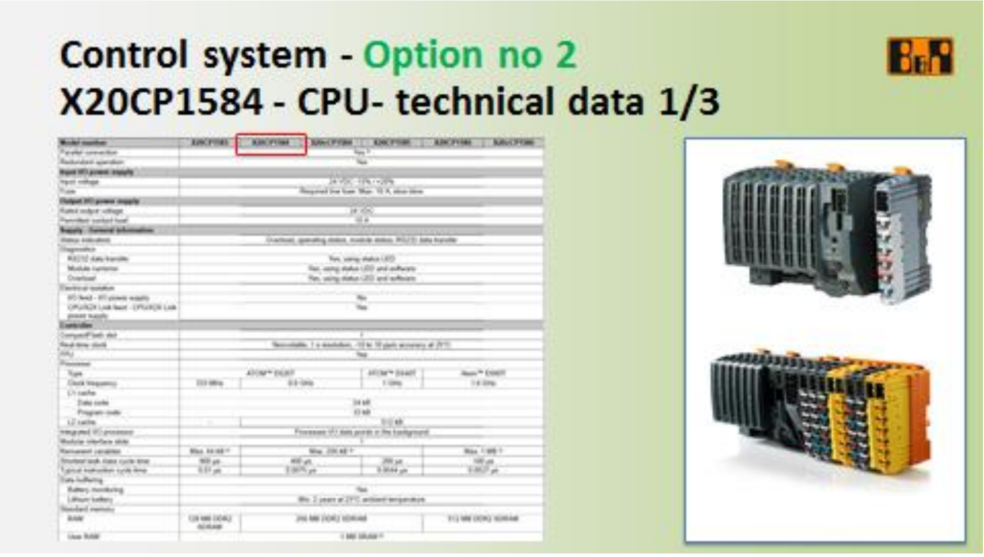

Control system - Option no 2

X20CP1584 - CPU- technical data 1/3

Fig. 65. B&R X20 system – CPU module – technical data of modules

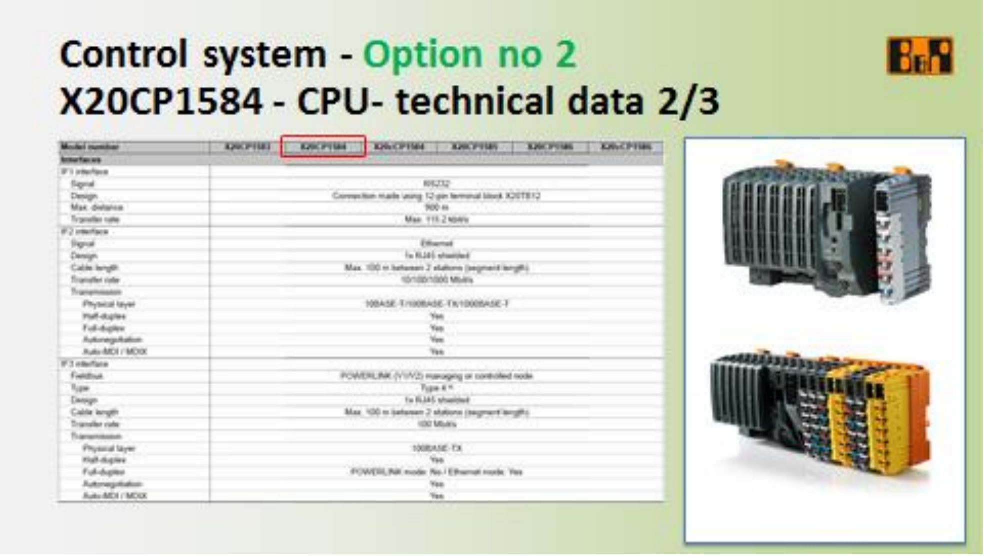

Control system - Option no 2

X20CP1584 - CPU- technical data 2/3

Fig. 66. B&R X20 system – CPU module – technical data of modules

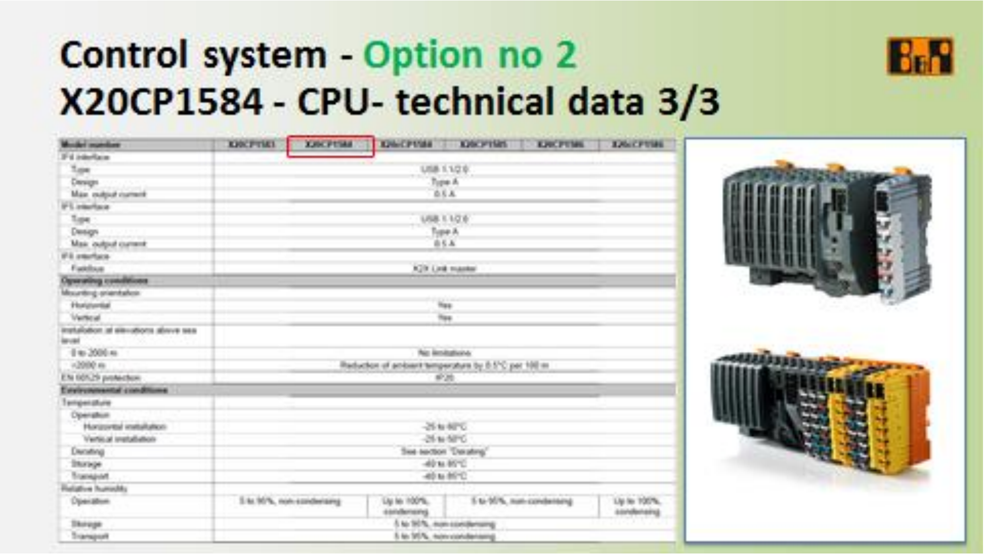

Control system - Option no 2

X20CP1584 - CPU- technical data 3/3

Model number	X20CP1583	X20CP1584	X20cCP1584	X20CP1585	X20CP1586	X20cCP1586
IF4 interface						
Type	USB 1.1/2.0					
Design	Type A					
Max. output current	0.5 A					
IF5 interface						
Type	USB 1.1/2.0					
Design	Type A					
Max. output current	0.5 A					
IF6 interface						
Fieldbus	X2X Link master					
Operating conditions						
Mounting orientation						
Horizontal	Yes					
Vertical	Yes					
Installation at elevations above sea level						
0 to 2000 m	No limitations					
>2000 m	Reduction of ambient temperature by 0.5°C per 100 m					
EN 60529 protection	IP20					
Environmental conditions						
Temperature						
Operation						
Horizontal installation	-25 to 60°C					
Vertical installation	-25 to 50°C					
Derating	See section "Derating"					
Storage	-40 to 85°C					
Transport	-40 to 85°C					
Relative humidity						
Operation	5 to 95%, non-condensing		Up to 100%, condensing	5 to 95%, non-condensing		Up to 100%, condensing
Storage	5 to 95%, non-condensing					
Transport	5 to 95%, non-condensing					

Fig. 67. B&R X20 system – CPU module – technical data of modules

Characteristics of XC200 control system by Eaton

The Fig. 68 (general description of system), Figs. 69-71 (description of analog inputs modules), Figs. 72-74 (description of analog outputs modules), Figs. 75-77 (description of temperature inputs modules), Fig. 78-80 (description of digital inputs modules), Figs. 82-83 (description of digital outputs modules), Fig. 84 (description of HMI panel), Figs. 85-87 (description of communication modules) and Figs. 88-92 (description of CPU main block module) shows the most important information about the elements and components of the EATON XC200 system [27].

The presented elements can be used in the control and measurement process control system in the extruder.

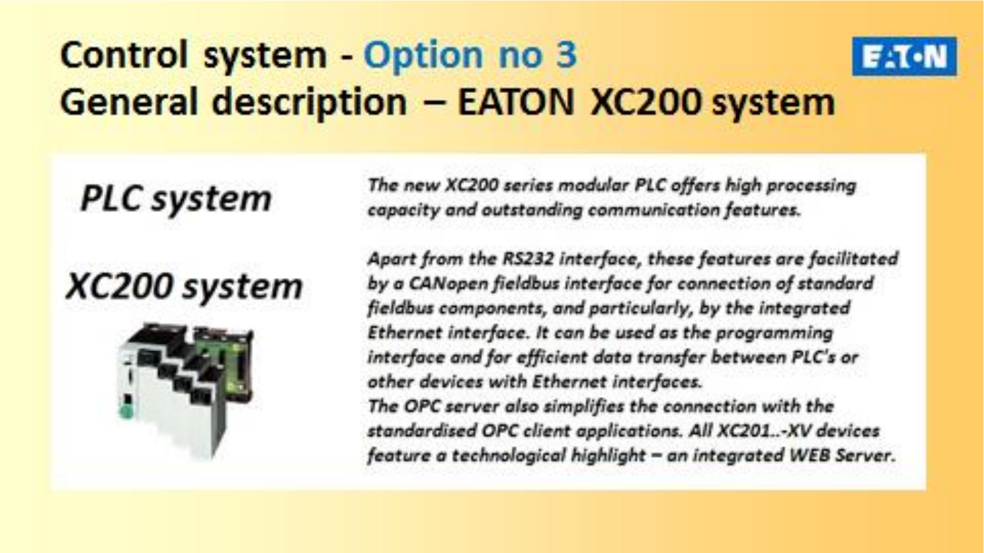

Control system - Option no 3
General description – EATON XC200 system

PLC system

XC200 system

The new XC200 series modular PLC offers high processing capacity and outstanding communication features.

Apart from the RS232 interface, these features are facilitated by a CANopen fieldbus interface for connection of standard fieldbus components, and particularly, by the integrated Ethernet interface. It can be used as the programming interface and for efficient data transfer between PLC's or other devices with Ethernet interfaces.
The OPC server also simplifies the connection with the standardised OPC client applications. All XC201..-XV devices feature a technological highlight – an integrated WEB Server.

Fig. 68. EATON XC200 system – general description

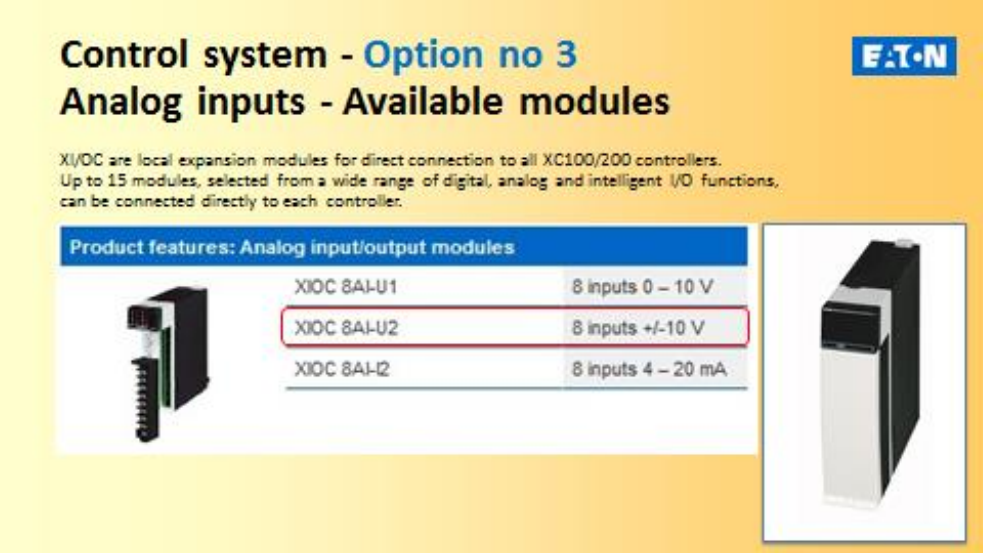

Control system - Option no 3
Analog inputs - Available modules

XI/OC are local expansion modules for direct connection to all XC100/200 controllers.
Up to 15 modules, selected from a wide range of digital, analog and intelligent I/O functions, can be connected directly to each controller.

Product features: Analog input/output modules	
XIOC 8AI-U1	8 inputs 0 – 10 V
XIOC 8AI-U2	8 inputs +/-10 V
XIOC 8AI-I2	8 inputs 4 – 20 mA

Fig. 69. EATON XC200 system – analog input – available modules

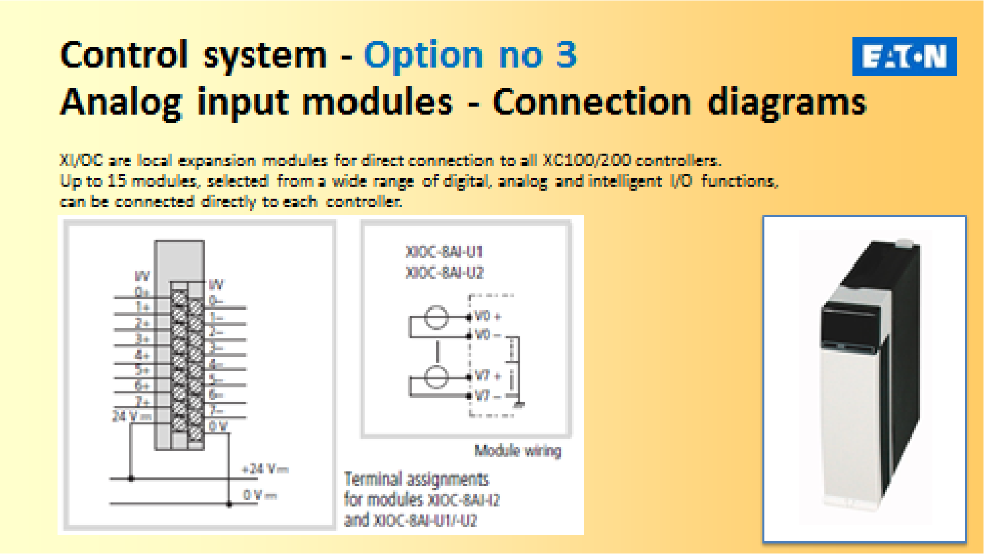

Control system - Option no 3
Analog input modules - Connection diagrams

XI/OC are local expansion modules for direct connection to all XC100/200 controllers.
Up to 15 modules, selected from a wide range of digital, analog and intelligent I/O functions, can be connected directly to each controller.

Terminal assignments for modules XIOC-8AI-I2 and XIOC-8AI-U1/-U2

Fig. 70. EATON XC200 system – analog input – connection diagrams

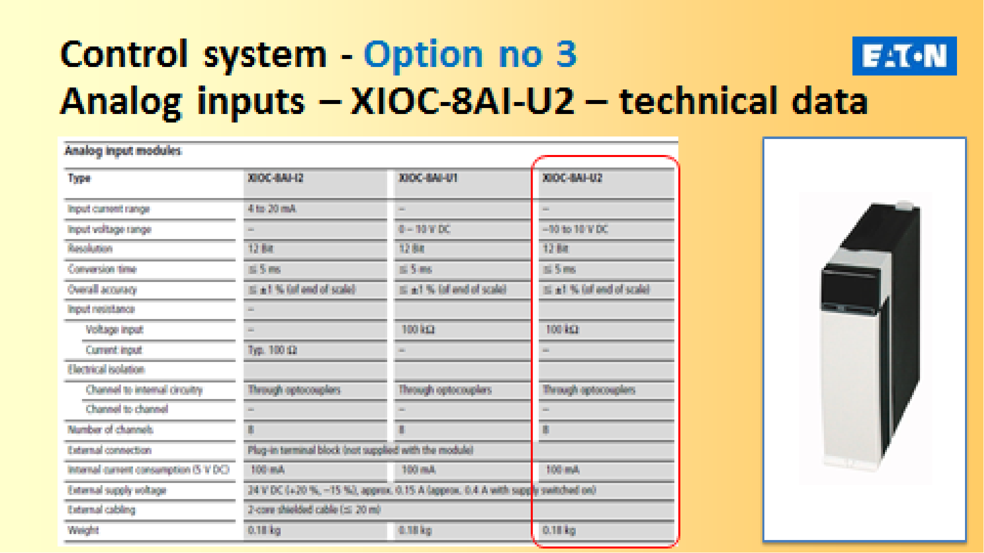

Control system - Option no 3
Analog inputs – XIOC-8AI-U2 – technical data

Analog input modules

Type	XIOC-8AI-I2	XIOC-8AI-U1	XIOC-8AI-U2
Input current range	4 to 20 mA	–	–
Input voltage range	–	0 – 10 V DC	–10 to 10 V DC
Resolution	12 Bit	12 Bit	12 Bit
Conversion time	≦ 5 ms	≦ 5 ms	≦ 5 ms
Overall accuracy	≦ ±1 % (of end of scale)	≦ ±1 % (of end of scale)	≦ ±1 % (of end of scale)
Input resistance	–		
Voltage input	–	100 kΩ	100 kΩ
Current input	Typ. 100 Ω	–	–
Electrical isolation			
Channel to internal circuitry	Through optocouplers	Through optocouplers	Through optocouplers
Channel to channel	–	–	–
Number of channels	8	8	8
External connection	Plug-in terminal block (not supplied with the module)		
Internal current consumption (5 V DC)	100 mA	100 mA	100 mA
External supply voltage	24 V DC (+20 %, –15 %), approx. 0.15 A (approx. 0.4 A with supply switched on)		
External cabling	2-core shielded cable (≦ 20 m)		
Weight	0.18 kg	0.18 kg	0.18 kg

Fig. 71. EATON XC200 system – analog input – technical data of modules

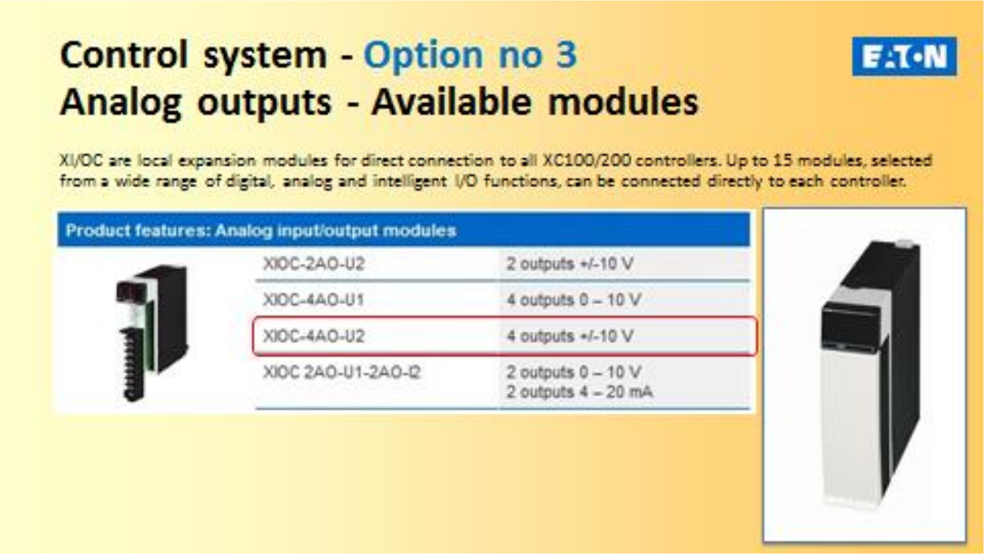

Control system - Option no 3

Analog outputs - Available modules

XI/OC are local expansion modules for direct connection to all XC100/200 controllers. Up to 15 modules, selected from a wide range of digital, analog and intelligent I/O functions, can be connected directly to each controller.

Product features: Analog input/output modules	
XIOC-2AO-U2	2 outputs +/-10 V
XIOC-4AO-U1	4 outputs 0 – 10 V
XIOC-4AO-U2	4 outputs +/-10 V
XIOC 2AO-U1-2AO-I2	2 outputs 0 – 10 V 2 outputs 4 – 20 mA

Fig. 72. EATON XC200 system – analog outputs – available modules

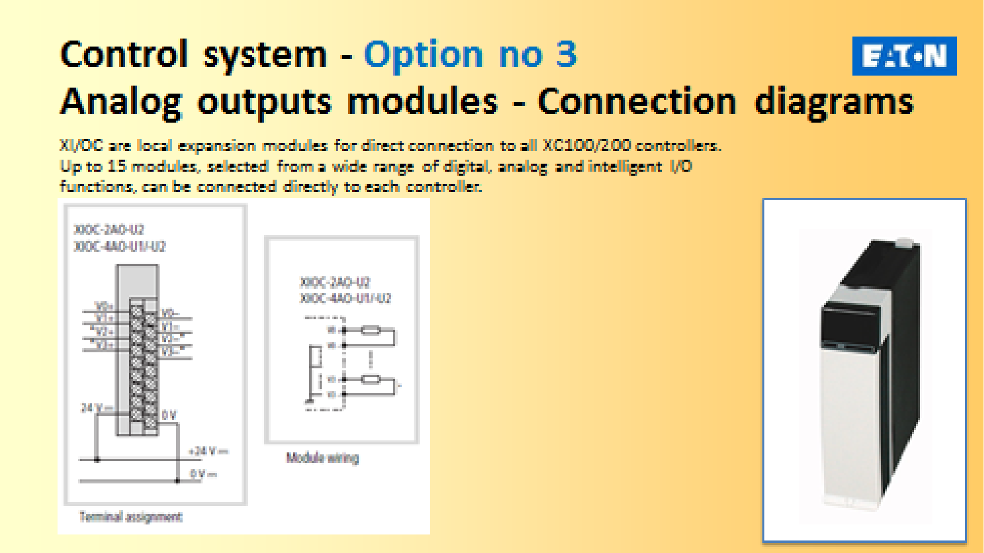

Control system - Option no 3

Analog outputs modules - Connection diagrams

XI/OC are local expansion modules for direct connection to all XC100/200 controllers.
Up to 15 modules, selected from a wide range of digital, analog and intelligent I/O functions, can be connected directly to each controller.

XIOC-2AO-U2
XIOC-4AO-U1/-U2
V0+
V1+
V2+
V3+
V0–
V1–
V2–
V3–
24 V ⎓
0 V
+24 V ⎓
0 V ⎓
Terminal assignment
XIOC-2AO-U2
XIOC-4AO-U1/-U2
Module wiring

Fig. 73. EATON XC200 system – analog outputs – connection diagrams

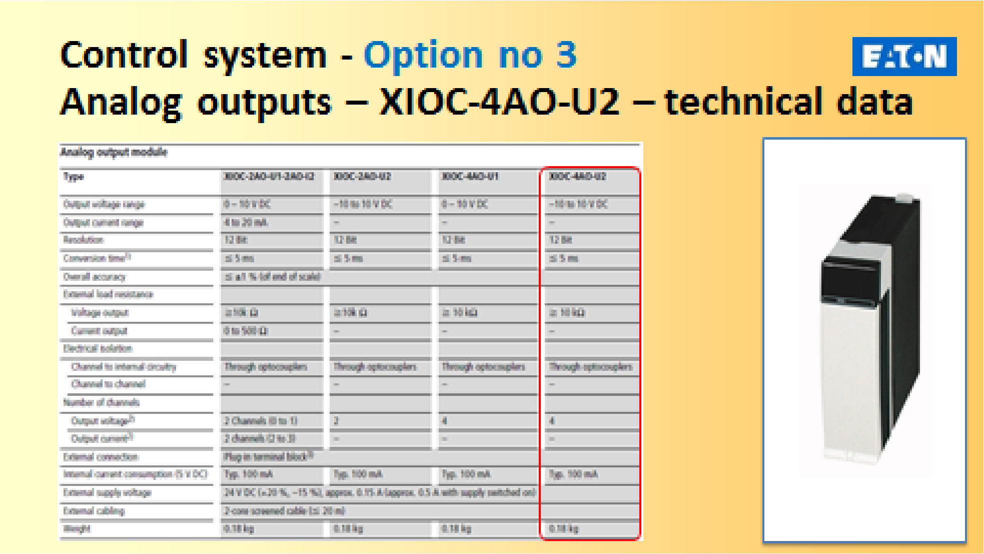

Control system - Option no 3
Analog outputs – XIOC-4AO-U2 – technical data

Analog output module

Type	XIOC-2AO-U1-2AO-I2	XIOC-2AO-U2	XIOC-4AO-U1	XIOC-4AO-U2
Output voltage range	0 – 10 V DC	−10 to 10 V DC	0 – 10 V DC	−10 to 10 V DC
Output current range	4 to 20 mA	–	–	–
Resolution	12 Bit	12 Bit	12 Bit	12 Bit
Conversion time[1]	≤ 5 ms	≤ 5 ms	≤ 5 ms	≤ 5 ms
Overall accuracy	≤ ±1 % (of end of scale)			
External load resistance				
Voltage output	≥10k Ω	≥10k Ω	≥ 10 kΩ	≥ 10 kΩ
Current output	0 to 500 Ω	–	–	–
Electrical isolation				
Channel to internal circuitry	Through optocouplers	Through optocouplers	Through optocouplers	Through optocouplers
Channel to channel	–	–	–	–
Number of channels				
Output voltage[2]	2 Channels (0 to 1)	2	4	4
Output current[2]	2 channels (2 to 3)	–	–	–
External connection	Plug in terminal block[3]			
Internal current consumption (5 V DC)	Typ. 100 mA	Typ. 100 mA	Typ. 100 mA	Typ. 100 mA
External supply voltage	24 V DC (+20 %, −15 %), approx. 0.15 A (approx. 0.5 A with supply switched on)			
External cabling	2-core screened cable (≤ 20 m)			
Weight	0.18 kg	0.18 kg	0.18 kg	0.18 kg

Fig. 74. EATON XC200 system – analog outputs – technical data of modules

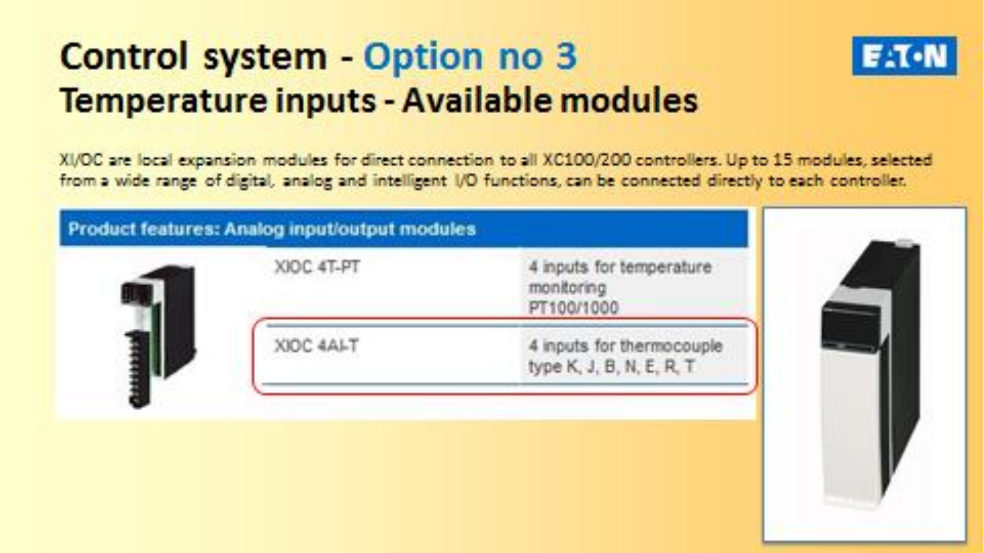

Control system - Option no 3
Temperature inputs - Available modules

XI/OC are local expansion modules for direct connection to all XC100/200 controllers. Up to 15 modules, selected from a wide range of digital, analog and intelligent I/O functions, can be connected directly to each controller.

Product features: Analog input/output modules

XIOC 4T-PT	4 inputs for temperature monitoring PT100/1000
XIOC 4AI-T	4 inputs for thermocouple type K, J, B, N, E, R, T

Fig. 75. EATON XC200 system – temperature inputs – available modules

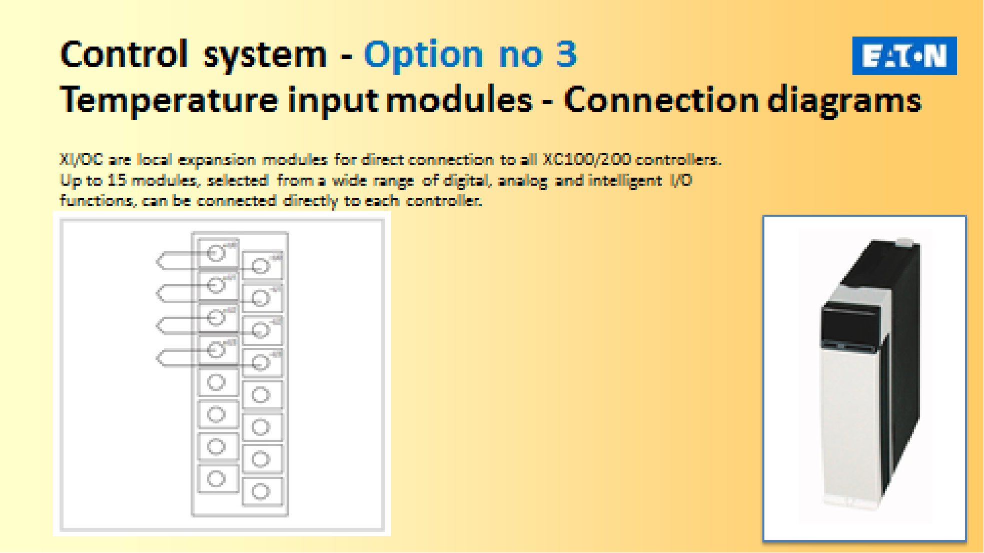

Control system - Option no 3

Temperature input modules - Connection diagrams

XI/OC are local expansion modules for direct connection to all XC100/200 controllers.
Up to 15 modules, selected from a wide range of digital, analog and intelligent I/O functions, can be connected directly to each controller.

Fig. 76. EATON XC200 system – temperature inputs – connection diagrams

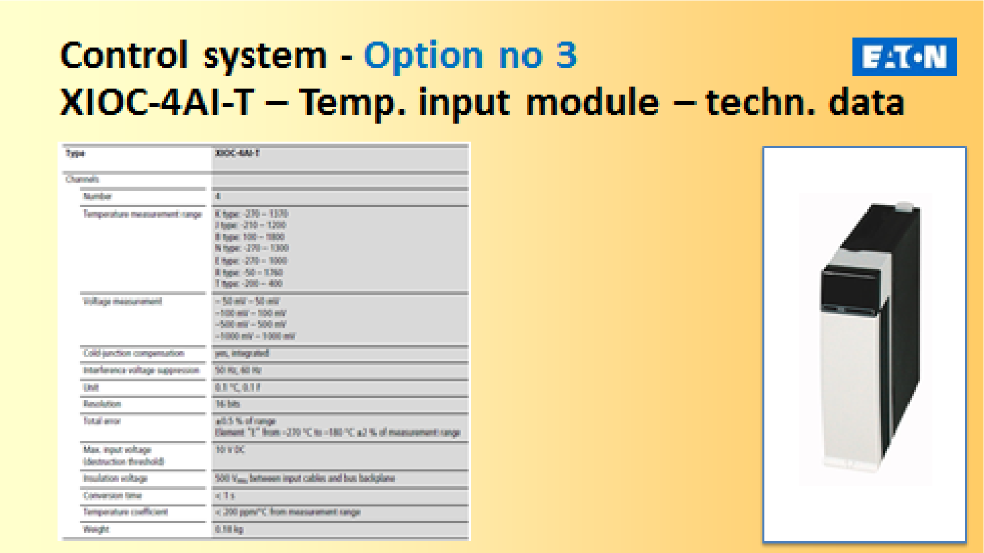

Control system - Option no 3

XIOC-4AI-T – Temp. input module – techn. data

Type	XIOC-4AI-T
Channels	
Number	4
Temperature measurement range	K type: -270 – 1370 J type: -210 – 1200 B type: 100 – 1800 N type: -270 – 1300 E type: -270 – 1000 R type: -50 – 1760 T type: -200 – 400
Voltage measurement	−50 mV – 50 mV −100 mV – 100 mV −500 mV – 500 mV −1000 mV – 1000 mV
Cold-junction compensation	yes, integrated
Interference voltage suppression	50 Hz, 60 Hz
Unit	0.1 °C, 0.1 F
Resolution	16 bits
Total error	±0.5 % of range Element "T" from -270 °C to -180 °C ±2 % of measurement range
Max. input voltage (destruction threshold)	10 V DC
Insulation voltage	500 V_{rms} between input cables and bus backplane
Conversion time	< 1 s
Temperature coefficient	< 200 ppm/°C from measurement range
Weight	0.18 kg

Fig. 77. EATON XC200 system – temperature inputs – technical data of modules

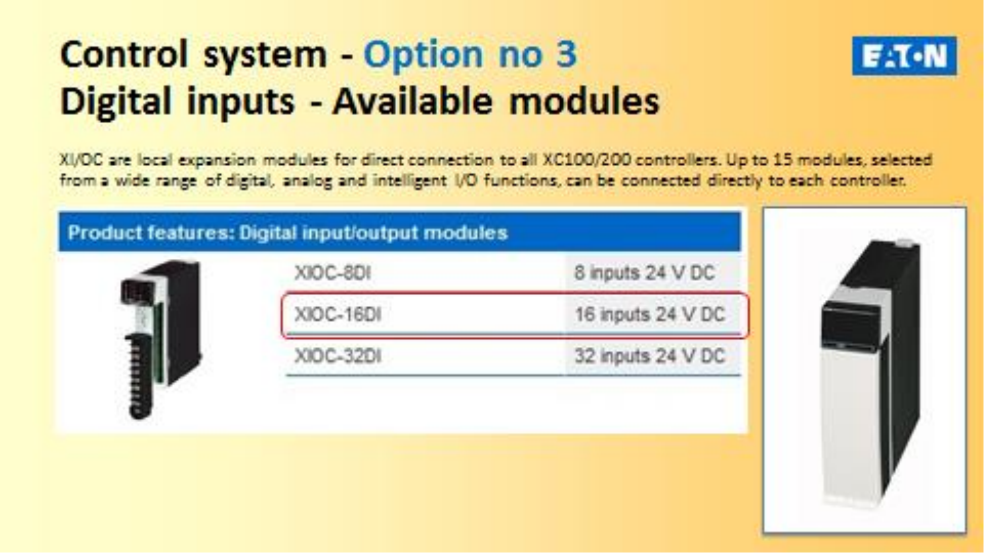

Control system - Option no 3
Digital inputs - Available modules

XI/OC are local expansion modules for direct connection to all XC100/200 controllers. Up to 15 modules, selected from a wide range of digital, analog and intelligent I/O functions, can be connected directly to each controller.

Product features: Digital input/output modules

XIOC-8DI	8 inputs 24 V DC
XIOC-16DI	16 inputs 24 V DC
XIOC-32DI	32 inputs 24 V DC

Fig. 78. EATON XC200 system – digital inputs – available modules

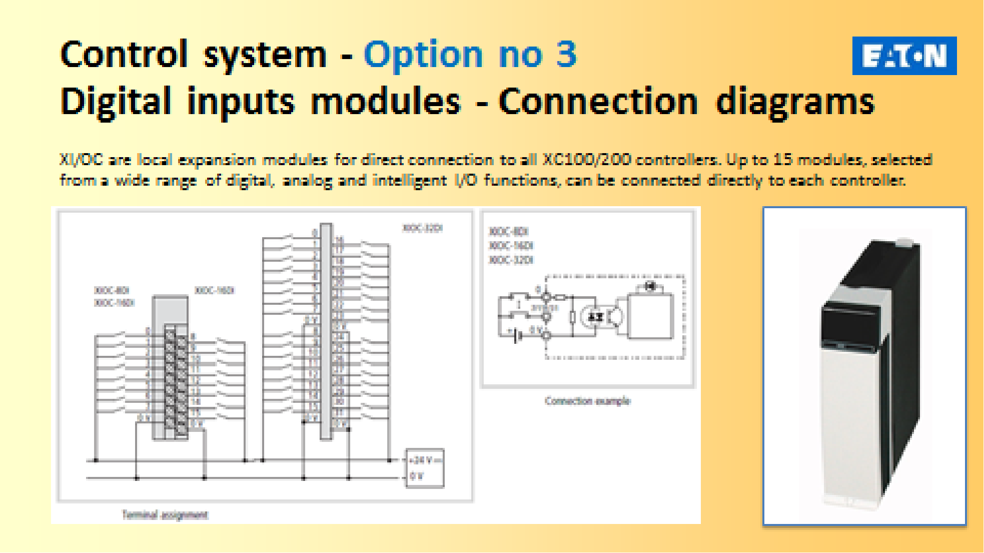

Control system - Option no 3
Digital inputs modules - Connection diagrams

XI/OC are local expansion modules for direct connection to all XC100/200 controllers. Up to 15 modules, selected from a wide range of digital, analog and intelligent I/O functions, can be connected directly to each controller.

XIOC-8DI
XIOC-16DI
XIOC-16DI
XIOC-32DI
0 V
+24 V
0 V
Terminal assignment
XIOC-8DI
XIOC-16DI
XIOC-32DI
0 V
Connection example

Fig. 79. EATON XC200 system – digital inputs – connection diagrams

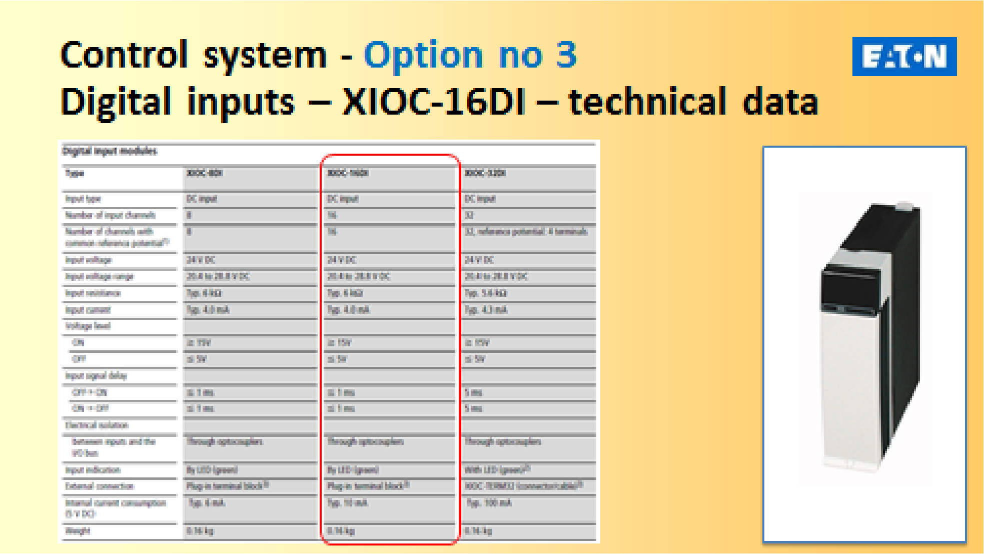

Control system - Option no 3
Digital inputs – XIOC-16DI – technical data

Digital input modules

Type	XIOC-8DI	XIOC-16DI	XIOC-32DI
Input type	DC input	DC input	DC input
Number of input channels	8	16	32
Number of channels with common reference potential1)	8	16	32, reference potential: 4 terminals
Input voltage	24 V DC	24 V DC	24 V DC
Input voltage range	20.4 to 28.8 V DC	20.4 to 28.8 V DC	20.4 to 28.8 V DC
Input resistance	Typ. 6 kΩ	Typ. 6 kΩ	Typ. 5.6 kΩ
Input current	Typ. 4.0 mA	Typ. 4.0 mA	Typ. 4.3 mA
Voltage level			
ON	≥ 15V	≥ 15V	≥ 15V
OFF	≤ 5V	≤ 5V	≤ 5V
Input signal delay			
OFF → ON	≤ 1 ms	≤ 1 ms	5 ms
ON → OFF	≤ 1 ms	≤ 1 ms	5 ms
Electrical isolation			
Between inputs and the I/O bus	Through optocouplers	Through optocouplers	Through optocouplers
Input indication	By LED (green)	By LED (green)	With LED (green)2)
External connection	Plug-in terminal block3)	Plug-in terminal block3)	XIOC-TERM32 (connector/cable)3)
Internal current consumption (5 V DC)	Typ. 6 mA	Typ. 10 mA	Typ. 100 mA
Weight	0.16 kg	0.16 kg	0.16 kg

Fig. 80. EATON XC200 system – digital inputs – technical data of modules

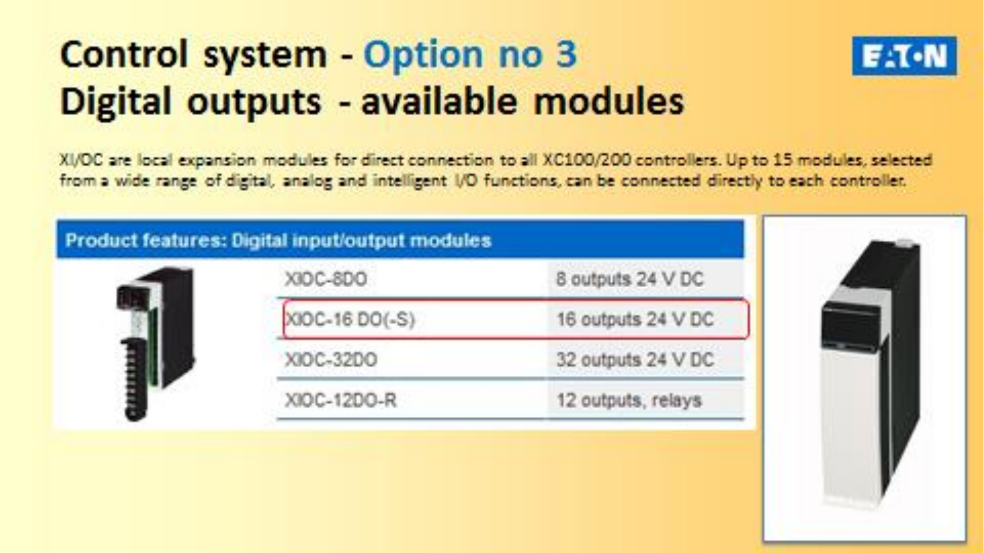

Control system - Option no 3
Digital outputs - available modules

XI/OC are local expansion modules for direct connection to all XC100/200 controllers. Up to 15 modules, selected from a wide range of digital, analog and intelligent I/O functions, can be connected directly to each controller.

Product features: Digital input/output modules

XIOC-8DO	8 outputs 24 V DC
XIOC-16 DO(-S)	16 outputs 24 V DC
XIOC-32DO	32 outputs 24 V DC
XIOC-12DO-R	12 outputs, relays

Fig. 81. EATON XC200 system – digital outputs – available modules

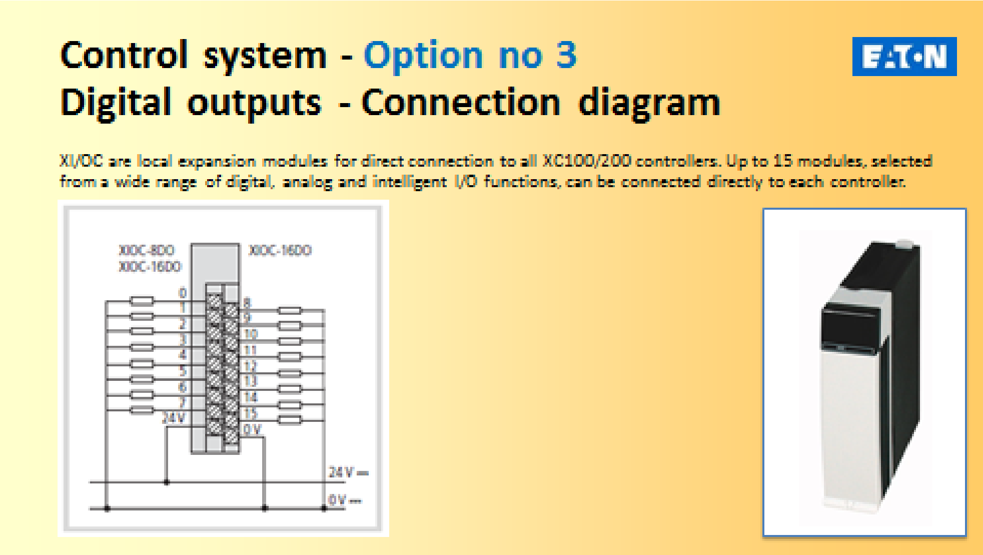

Control system - Option no 3
Digital outputs - Connection diagram

XI/OC are local expansion modules for direct connection to all XC100/200 controllers. Up to 15 modules, selected from a wide range of digital, analog and intelligent I/O functions, can be connected directly to each controller.

Fig. 82. EATON XC200 system – digital outputs – connection diagram

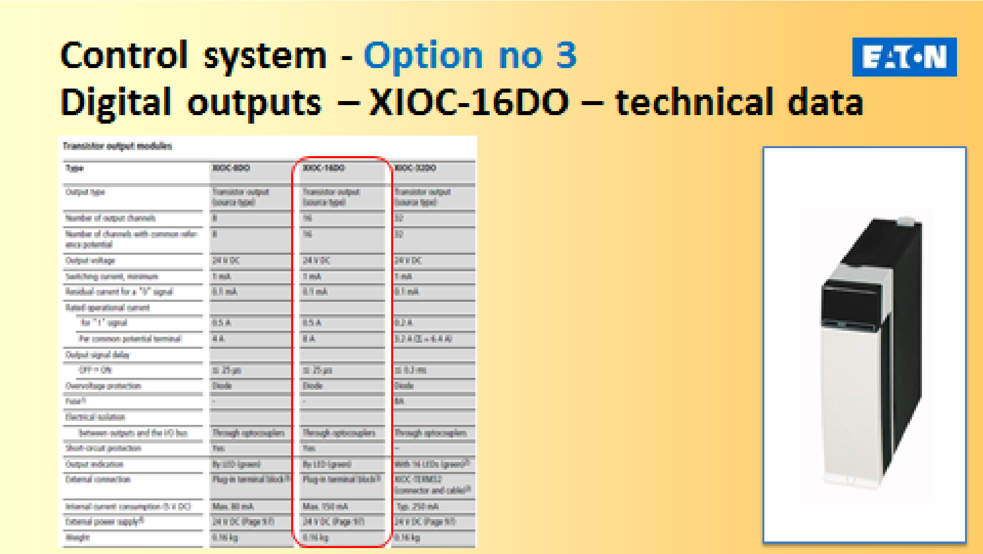

Control system - Option no 3
Digital outputs – XIOC-16DO – technical data

Transistor output modules

Type	XIOC-8DO	XIOC-16DO	XIOC-32DO
Output type	Transistor output (source type)	Transistor output (source type)	Transistor output (source type)
Number of output channels	8	16	32
Number of channels with common reference potential	8	16	32
Output voltage	24 V DC	24 V DC	24 V DC
Switching current, minimum	1 mA	1 mA	1 mA
Residual current for a "0" signal	0.1 mA	0.1 mA	0.1 mA
Rated operational current			
for "1" signal	0.5 A	0.5 A	0.2 A
Per common potential terminal	4 A	8 A	3.2 A (Σ = 6.4 A)
Output signal delay			
OFF → ON	≤ 25 µs	≤ 25 µs	≤ 0.3 ms
Overvoltage protection	Diode	Diode	Diode
Fuse[1]	-	-	8A
Electrical isolation			
Between outputs and the I/O bus	Through optocouplers	Through optocouplers	Through optocouplers
Short-circuit protection	Yes	Yes	–
Output indication	By LED (green)	By LED (green)	With 16 LEDs (green)[2]
External connection	Plug-in terminal block[3]	Plug-in terminal block[3]	XIOC-TERM32 (connector and cable)[4]
Internal current consumption (5 V DC)	Max. 80 mA	Max. 150 mA	Typ. 250 mA
External power supply[5]	24 V DC (Page 97)	24 V DC (Page 97)	24 V DC (Page 97)
Weight	0.16 kg	0.16 kg	0.16 kg

Fig. 83. EATON XC200 system – digital outputs – technical data of modules

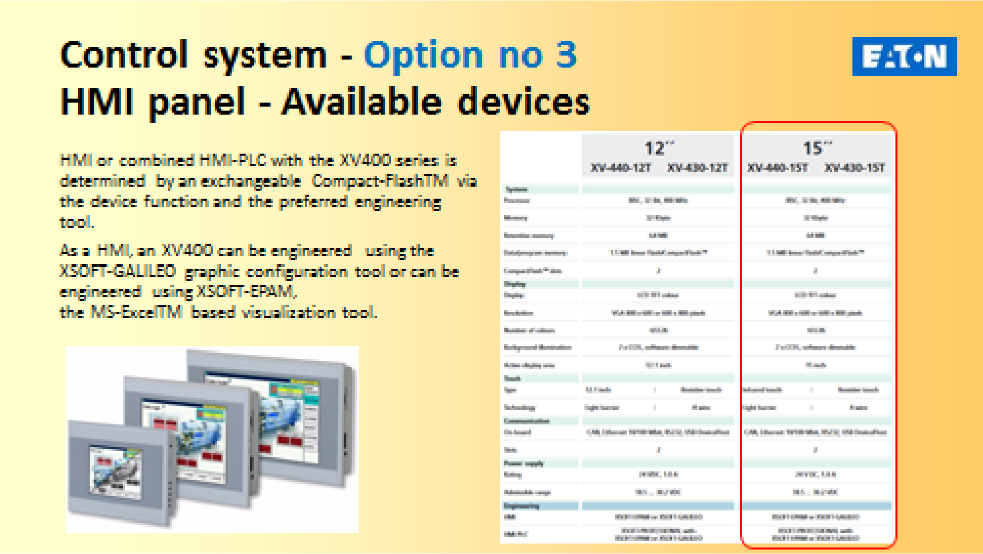

Control system - Option no 3
HMI panel - Available devices

HMI or combined HMI-PLC with the XV400 series is determined by an exchangeable Compact-FlashTM via the device function and the preferred engineering tool.

As a HMI, an XV400 can be engineered using the XSOFT-GALILEO graphic configuration tool or can be engineered using XSOFT-EPAM, the MS-ExcelTM based visualization tool.

Fig. 84. EATON XC200 system – HMI panels – available modules

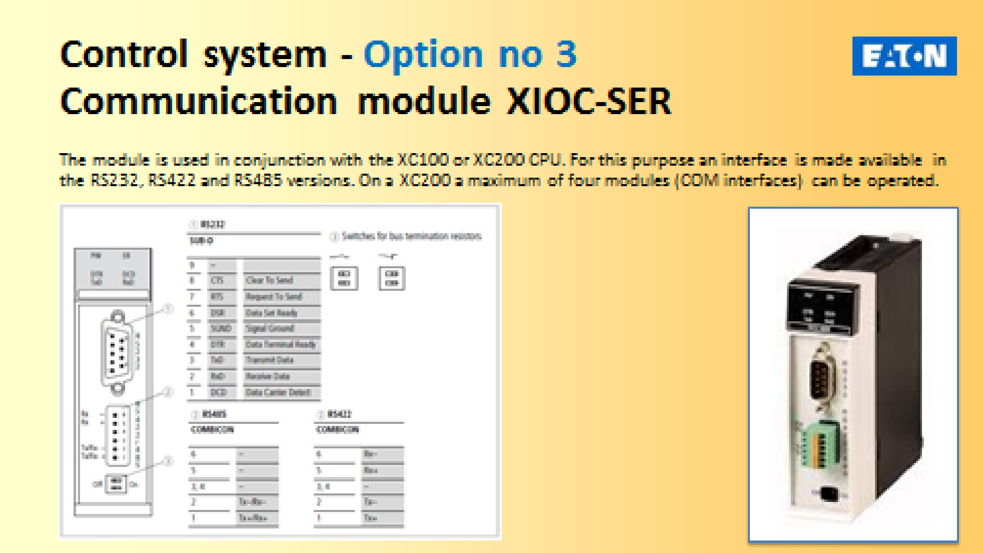

Control system - Option no 3
Communication module XIOC-SER

The module is used in conjunction with the XC100 or XC200 CPU. For this purpose an interface is made available in the RS232, RS422 and RS485 versions. On a XC200 a maximum of four modules (COM interfaces) can be operated.

① RS232

SUB-D		
9	–	
8	CTS	Clear To Send
7	RTS	Request To Send
6	DSR	Data Set Ready
5	SGND	Signal Ground
4	DTR	Data Terminal Ready
3	TxD	Transmit Data
2	RxD	Receive Data
1	DCD	Data Carrier Detect

② RS485

COMBICON	
6	–
5	–
3, 4	–
2	Tx-/Rx-
1	Tx+/Rx+

② RS422

COMBICON	
6	Rx-
5	Rx+
3, 4	–
2	Tx-
1	Tx+

③ Switches for bus termination resistors

Fig. 85. EATON XC200 system – communications module – technical data

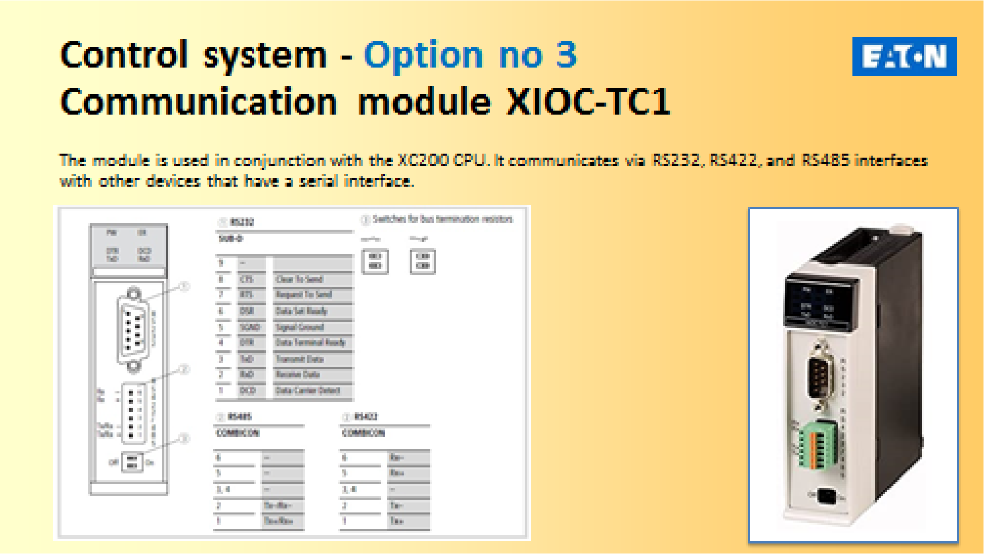

Control system - Option no 3
Communication module XIOC-TC1

The module is used in conjunction with the XC200 CPU. It communicates via RS232, RS422, and RS485 interfaces with other devices that have a serial interface.

① RS232

SUB-D

9	–	
8	CTS	Clear To Send
7	RTS	Request To Send
6	DSR	Data Set Ready
5	SGND	Signal Ground
4	DTR	Data Terminal Ready
3	TxD	Transmit Data
2	RxD	Receive Data
1	DCD	Data Carrier Detect

③ Switches for bus termination resistors

② RS485

COMBICON

6	–
5	–
3, 4	–
2	Tx-/Rx-
1	Tx+/Rx+

② RS422

COMBICON

6	Rx-
5	Rx+
3, 4	–
2	Tx-
1	Tx+

Fig. 86. EATON XC200 system – communications module – technical data

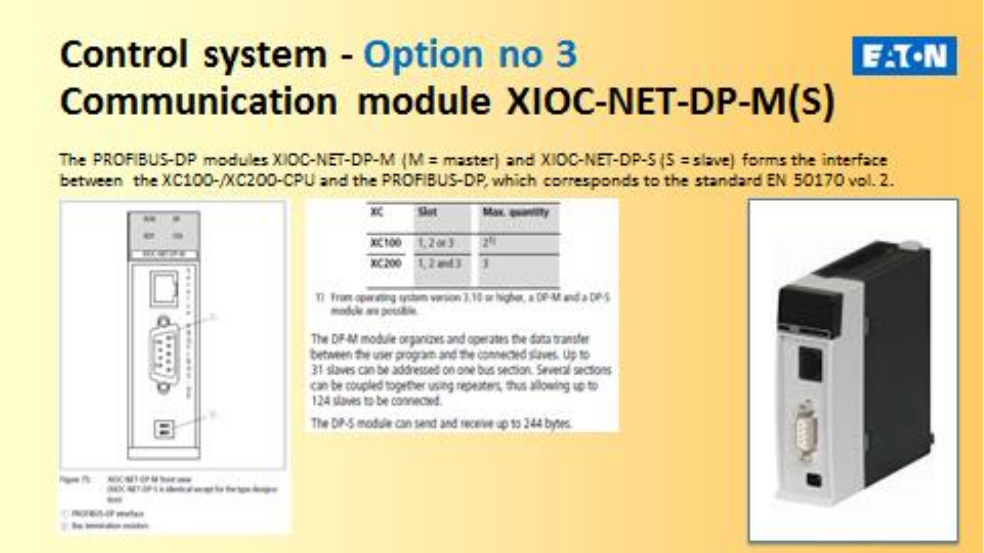

Control system - Option no 3
Communication module XIOC-NET-DP-M(S)

The PROFIBUS-DP modules XIOC-NET-DP-M (M = master) and XIOC-NET-DP-S (S = slave) forms the interface between the XC100-/XC200-CPU and the PROFIBUS-DP, which corresponds to the standard EN 50170 vol. 2.

XC	Slot	Max. quantity
XC100	1, 2 or 3	2[1]
XC200	1, 2 and 3	3

[1] From operating system version 3.10 or higher, a DP-M and a DP-S module are possible.

The DP-M module organizes and operates the data transfer between the user program and the connected slaves. Up to 31 slaves can be addressed on one bus section. Several sections can be coupled together using repeaters, thus allowing up to 124 slaves to be connected.

The DP-S module can send and receive up to 244 bytes.

Fig. 87. EATON XC200 system – communications module – technical data

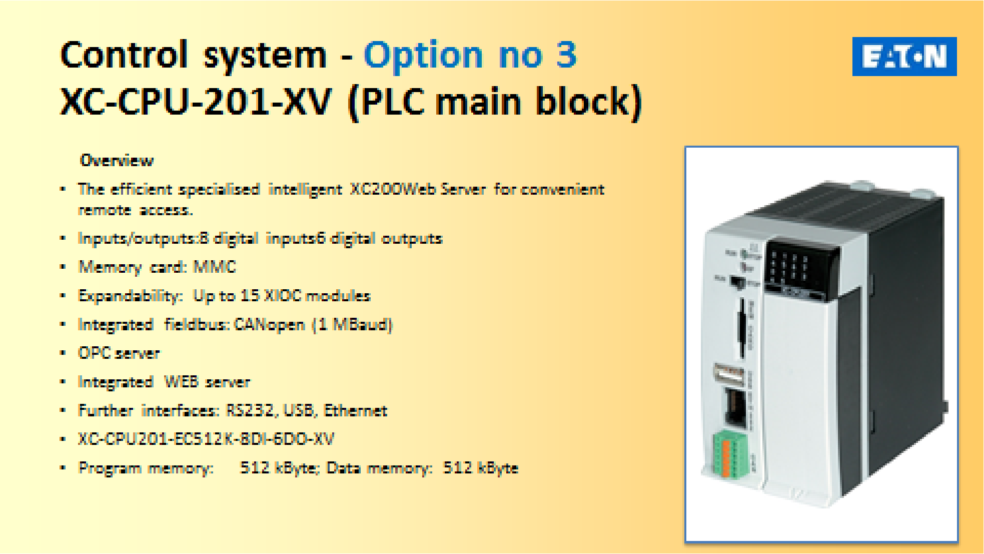

Control system - Option no 3
XC-CPU-201-XV (PLC main block)

Overview

- The efficient specialised intelligent XC200Web Server for convenient remote access.
- Inputs/outputs:8 digital inputs6 digital outputs
- Memory card: MMC
- Expandability: Up to 15 XIOC modules
- Integrated fieldbus: CANopen (1 MBaud)
- OPC server
- Integrated WEB server
- Further interfaces: RS232, USB, Ethernet
- XC-CPU201-EC512K-8DI-6DO-XV
- Program memory: 512 kByte; Data memory: 512 kByte

Fig. 88. EATON XC200 system – PLC main block module – general data

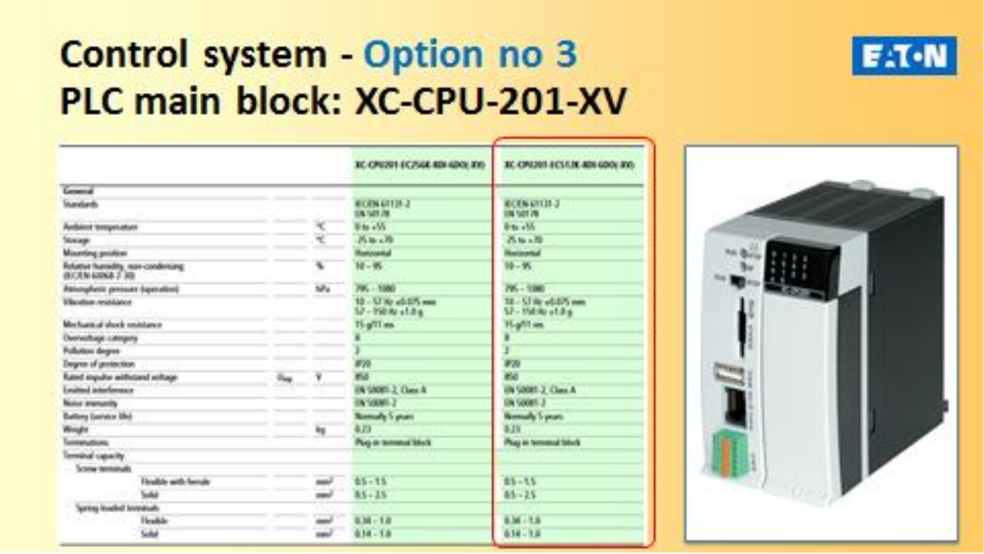

Control system - Option no 3
PLC main block: XC-CPU-201-XV

			XC-CPU201-EC256K-8DI-6DO(-XV)	XC-CPU201-EC512K-8DI-6DO(-XV)
General				
Standards			IEC/EN 61131-2 EN 50178	IEC/EN 61131-2 EN 50178
Ambient temperature		°C	0 to +55	0 to +55
Storage		°C	-25 to +70	-25 to +70
Mounting position			Horizontal	Horizontal
Relative humidity, non-condensing (IEC/EN 60068-2-30)		%	10 – 95	10 – 95
Atmospheric pressure (operation)		hPa	795 – 1080	795 – 1080
Vibration resistance			10 – 57 Hz ±0.075 mm 57 – 150 Hz ±1.0 g	10 – 57 Hz ±0.075 mm 57 – 150 Hz ±1.0 g
Mechanical shock resistance			15 g/11 ms	15 g/11 ms
Overvoltage category			II	II
Pollution degree			2	2
Degree of protection			IP20	IP20
Rated impulse withstand voltage	U_{imp}	V	850	850
Emitted interference			EN 50081-2, Class A	EN 50081-2, Class A
Noise immunity			EN 50082-2	EN 50082-2
Battery (service life)			Normally 5 years	Normally 5 years
Weight		kg	0.23	0.23
Terminations			Plug-in terminal block	Plug-in terminal block
Terminal capacity				
Screw terminals				
Flexible with ferrule		mm²	0.5 – 1.5	0.5 – 1.5
Solid		mm²	0.5 – 2.5	0.5 – 2.5
Spring-loaded terminals				
Flexible		mm²	0.38 – 1.0	0.38 – 1.0
Solid		mm²	0.14 – 1.0	0.14 – 1.0

Fig. 89. EATON XC200 system – PLC main block module – technical data

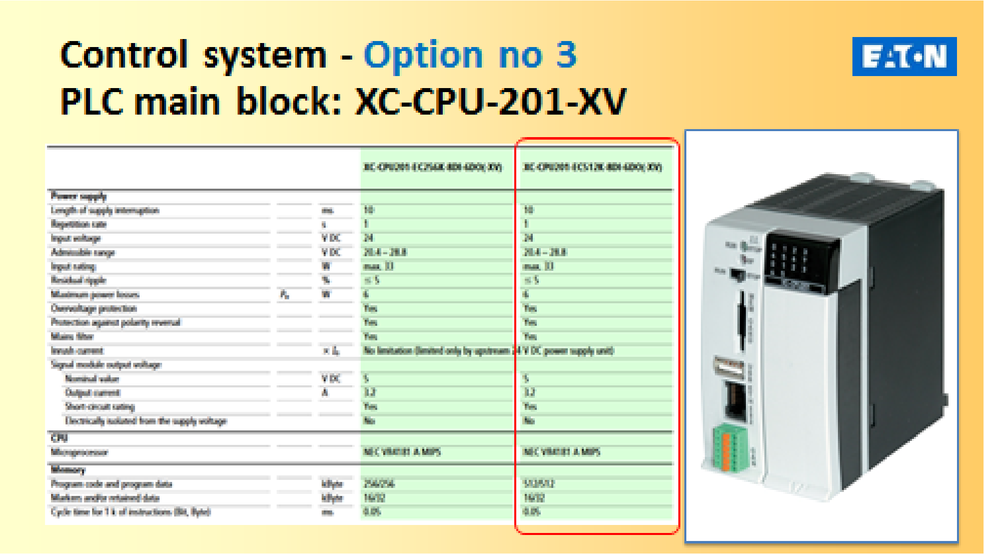

Control system - Option no 3
PLC main block: XC-CPU-201-XV

			XC-CPU201-EC256K-8DI-6DO(-XV)	XC-CPU201-EC512K-8DI-6DO(-XV)
Power supply				
Length of supply interruption		ms	10	10
Repetition rate		s	1	1
Input voltage		V DC	24	24
Admissible range		V DC	20.4 – 28.8	20.4 – 28.8
Input rating		W	max. 33	max. 33
Residual ripple		%	≤ 5	≤ 5
Maximum power losses	P_v	W	6	6
Overvoltage protection			Yes	Yes
Protection against polarity reversal			Yes	Yes
Mains filter			Yes	Yes
Inrush current		× I_n	No limitation (limited only by upstream 24 V DC power supply unit)	
Signal module output voltage				
Nominal value		V DC	5	5
Output current		A	3.2	3.2
Short-circuit rating			Yes	Yes
Electrically isolated from the supply voltage			No	No
CPU				
Microprocessor			NEC VR4181 A MIPS	NEC VR4181 A MIPS
Memory				
Program code and program data		kByte	256/256	512/512
Markers and/or retained data		kByte	16/32	16/32
Cycle time for 1 k of instructions (Bit, Byte)		ms	0.05	0.05

Fig. 90. EATON XC200 system – PLC main block module – technical data

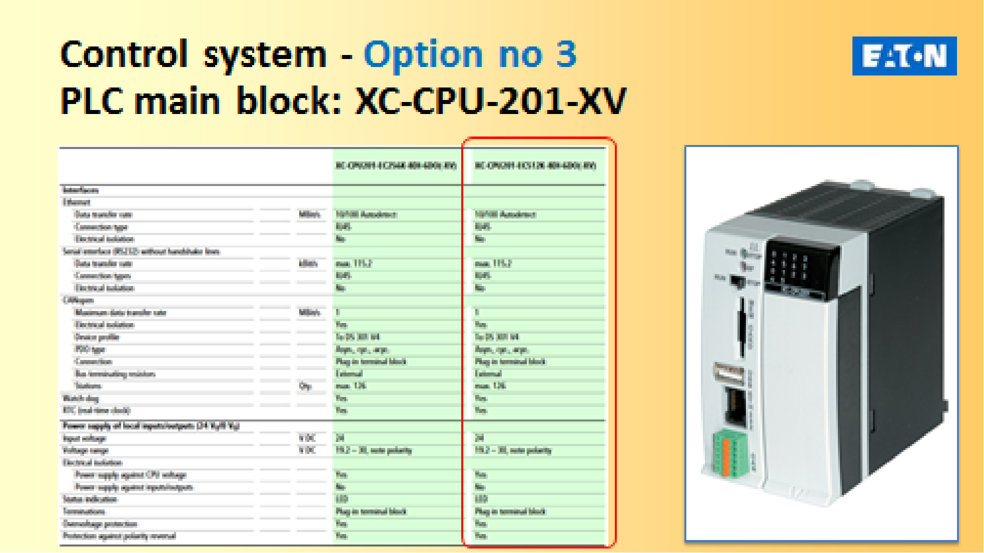

Control system - Option no 3
PLC main block: XC-CPU-201-XV

		XC-CPU201-EC256K-8DI-6DO(-XV)	XC-CPU201-EC512K-8DI-6DO(-XV)
Interfaces			
Ethernet			
Data transfer rate	MBit/s	10/100 Autodetect	10/100 Autodetect
Connection type		RJ45	RJ45
Electrical isolation		No	No
Serial interface (RS232) without handshake lines			
Data transfer rate	kBit/s	max. 115.2	max. 115.2
Connection types		RJ45	RJ45
Electrical isolation		No	No
CANopen			
Maximum data transfer rate	MBit/s	1	1
Electrical isolation		Yes	Yes
Device profile		To DS 301 V4	To DS 301 V4
PDO type		Async., cyc., acyc.	Async., cyc., acyc.
Connection		Plug in terminal block	Plug in terminal block
Bus terminating resistors		External	External
Stations	Qty.	max. 126	max. 126
Watch dog		Yes	Yes
RTC (real time clock)		Yes	Yes
Power supply of local inputs/outputs (24 V_Q/0 V_Q)			
Input voltage	V DC	24	24
Voltage range	V DC	19.2 – 30, note polarity	19.2 – 30, note polarity
Electrical isolation			
Power supply against CPU voltage		Yes	Yes
Power supply against inputs/outputs		No	No
Status indication		LED	LED
Terminations		Plug in terminal block	Plug in terminal block
Overvoltage protection		Yes	Yes
Protection against polarity reversal		Yes	Yes

Fig. 91. EATON XC200 system – PLC main block module – technical data

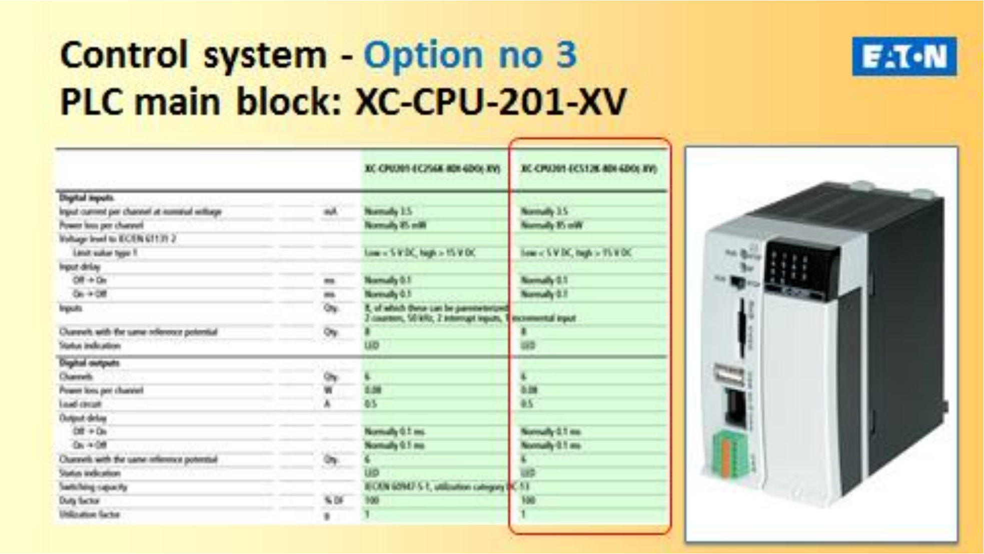

Control system - Option no 3

PLC main block: XC-CPU-201-XV

		XC-CPU201-EC256K-8DI-6DO(-XV)	XC-CPU201-EC512K-8DI-6DO(-XV)
Digital inputs			
Input current per channel at nominal voltage	mA	Normally 3.5	Normally 3.5
Power loss per channel		Normally 85 mW	Normally 85 mW
Voltage level to IEC/EN 61131-2			
Limit value type 1		Low < 5 V DC, high > 15 V DC	Low < 5 V DC, high > 15 V DC
Input delay			
Off → On	ms	Normally 0.1	Normally 0.1
On → Off	ms	Normally 0.1	Normally 0.1
Inputs	Qty.	8, of which these can be parameterized: 2 counters, 50 kHz, 2 interrupt inputs, 1 incremental input	
Channels with the same reference potential	Qty.	8	8
Status indication		LED	LED
Digital outputs			
Channels	Qty.	6	6
Power loss per channel	W	0.08	0.08
Load circuit	A	0.5	0.5
Output delay			
Off → On		Normally 0.1 ms	Normally 0.1 ms
On → Off		Normally 0.1 ms	Normally 0.1 ms
Channels with the same reference potential	Qty.	6	6
Status indication		LED	LED
Switching capacity		IEC/EN 60947-5-1, utilization category DC-13	
Duty factor	% DF	100	100
Utilization factor	g	1	1

Fig. 92. EATON XC200 system – PLC main block module – technical data

Components of data acquisition and control system - summary

The selection of the control system was made on the basis of the technical data of the real components. The following elements were included during the selection of components of control system:

1. Extension modules:
   - analog input modules,
   - analog output modules,
   - temperature input modules,
   - digital input modules,
   - digital output modules.
2. Main controller (CPU).
3. Communication module.
4. Operator panel.

Based on the collected information, a system composed of the components of the B&R X20 system was selected as the most suitable for use in the extruder. The list and comparison of the available modules for each of the analyzed systems are presented in the following tables: Table 1, Table 2, Table 3, Table 4, Table 5, Table 6 and Table 7.

Table 1. Analog inputs – Comparison of selected parameters

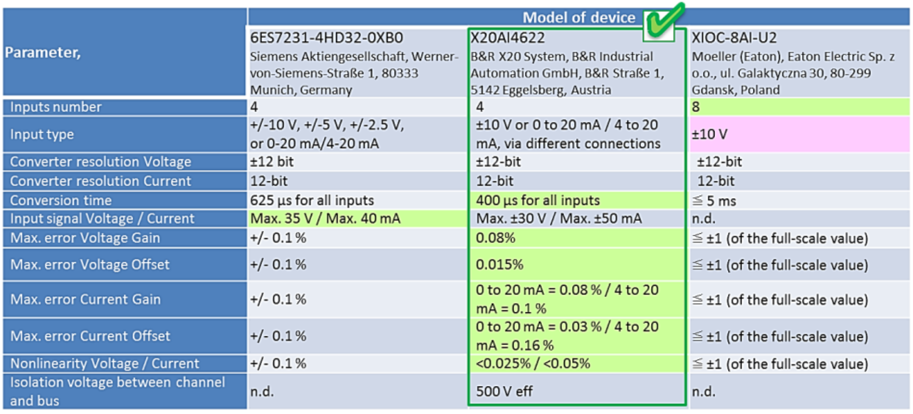

Parameter,	Model of device		
	6ES7231-4HD32-0XB0 Siemens Aktiengesellschaft, Werner-von-Siemens-Straße 1, 80333 Munich, Germany	✓ X20AI4622 B&R X20 System, B&R Industrial Automation GmbH, B&R Straße 1, 5142 Eggelsberg, Austria	XIOC-8AI-U2 Moeller (Eaton), Eaton Electric Sp. z o.o., ul. Galaktyczna 30, 80-299 Gdansk, Poland
Inputs number	4	4	8
Input type	+/-10 V, +/-5 V, +/-2.5 V, or 0-20 mA/4-20 mA	±10 V or 0 to 20 mA / 4 to 20 mA, via different connections	±10 V
Converter resolution Voltage	±12 bit	±12-bit	±12-bit
Converter resolution Current	12-bit	12-bit	12-bit
Conversion time	625 µs for all inputs	400 µs for all inputs	≦ 5 ms
Input signal Voltage / Current	Max. 35 V / Max. 40 mA	Max. ±30 V / Max. ±50 mA	n.d.
Max. error Voltage Gain	+/- 0.1 %	0.08%	≦ ±1 (of the full-scale value)
Max. error Voltage Offset	+/- 0.1 %	0.015%	≦ ±1 (of the full-scale value)
Max. error Current Gain	+/- 0.1 %	0 to 20 mA = 0.08 % / 4 to 20 mA = 0.1 %	≦ ±1 (of the full-scale value)
Max. error Current Offset	+/- 0.1 %	0 to 20 mA = 0.03 % / 4 to 20 mA = 0.16 %	≦ ±1 (of the full-scale value)
Nonlinearity Voltage / Current	+/- 0.1 %	<0.025% / <0.05%	≦ ±1 (of the full-scale value)
Isolation voltage between channel and bus	n.d.	500 V eff	n.d.

Table 2. Analog outputs – Comparison of selected parameters

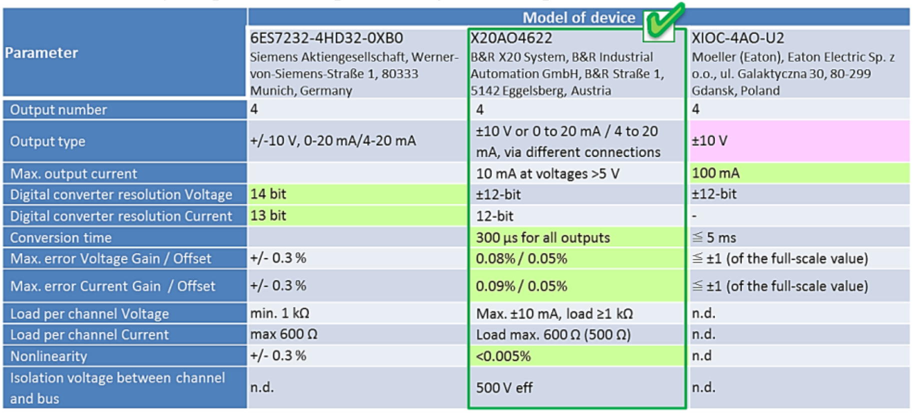

Parameter	Model of device		
	6ES7232-4HD32-0XB0 Siemens Aktiengesellschaft, Werner-von-Siemens-Straße 1, 80333 Munich, Germany	✓ X20AO4622 B&R X20 System, B&R Industrial Automation GmbH, B&R Straße 1, 5142 Eggelsberg, Austria	XIOC-4AO-U2 Moeller (Eaton), Eaton Electric Sp. z o.o., ul. Galaktyczna 30, 80-299 Gdansk, Poland
Output number	4	4	4
Output type	+/-10 V, 0-20 mA/4-20 mA	±10 V or 0 to 20 mA / 4 to 20 mA, via different connections	±10 V
Max. output current		10 mA at voltages >5 V	100 mA
Digital converter resolution Voltage	14 bit	±12-bit	±12-bit
Digital converter resolution Current	13 bit	12-bit	-
Conversion time		300 µs for all outputs	≦ 5 ms
Max. error Voltage Gain / Offset	+/- 0.3 %	0.08% / 0.05%	≦ ±1 (of the full-scale value)
Max. error Current Gain / Offset	+/- 0.3 %	0.09% / 0.05%	≦ ±1 (of the full-scale value)
Load per channel Voltage	min. 1 kΩ	Max. ±10 mA, load ≥1 kΩ	n.d.
Load per channel Current	max 600 Ω	Load max. 600 Ω (500 Ω)	n.d.
Nonlinearity	+/- 0.3 %	<0.005%	n.d
Isolation voltage between channel and bus	n.d.	500 V eff	n.d.

Table 3. Temperature inputs – Comparison of selected parameters

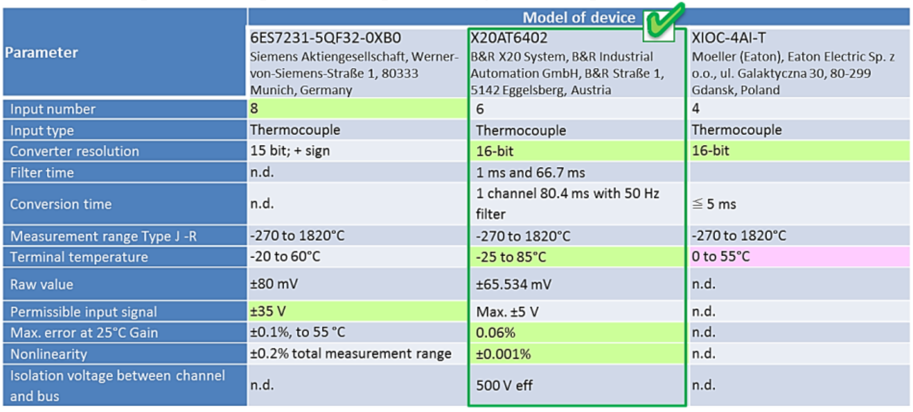

Parameter	Model of device		
	6ES7231-5QF32-0XB0 Siemens Aktiengesellschaft, Werner-von-Siemens-Straße 1, 80333 Munich, Germany	✓ X20AT6402 B&R X20 System, B&R Industrial Automation GmbH, B&R Straße 1, 5142 Eggelsberg, Austria	XIOC-4AI-T Moeller (Eaton), Eaton Electric Sp. z o.o., ul. Galaktyczna 30, 80-299 Gdansk, Poland
Input number	8	6	4
Input type	Thermocouple	Thermocouple	Thermocouple
Converter resolution	15 bit; + sign	16-bit	16-bit
Filter time	n.d.	1 ms and 66.7 ms	
Conversion time	n.d.	1 channel 80.4 ms with 50 Hz filter	≦ 5 ms
Measurement range Type J -R	-270 to 1820°C	-270 to 1820°C	-270 to 1820°C
Terminal temperature	-20 to 60°C	-25 to 85°C	0 to 55°C
Raw value	±80 mV	±65.534 mV	n.d.
Permissible input signal	±35 V	Max. ±5 V	n.d.
Max. error at 25°C Gain	±0.1%, to 55 °C	0.06%	n.d.
Nonlinearity	±0.2% total measurement range	±0.001%	n.d.
Isolation voltage between channel and bus	n.d.	500 V eff	n.d.

Table 4. Digital inputs – Comparison of selected parameters

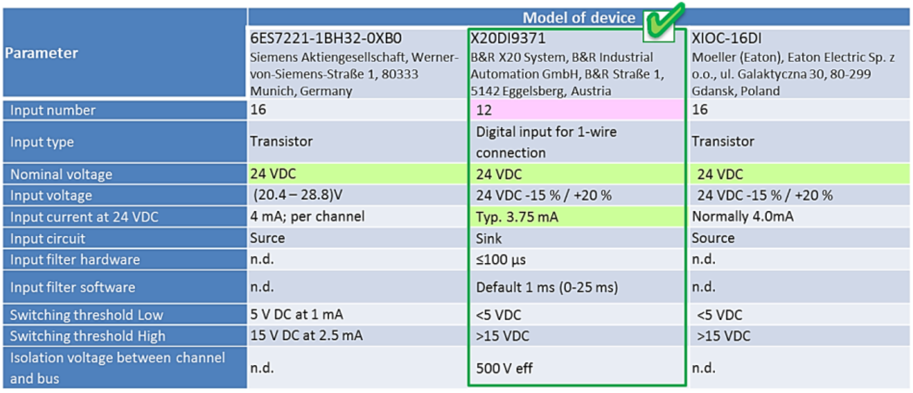

Parameter	Model of device		
	6ES7221-1BH32-0XB0 Siemens Aktiengesellschaft, Werner-von-Siemens-Straße 1, 80333 Munich, Germany	X20DI9371 ✓ B&R X20 System, B&R Industrial Automation GmbH, B&R Straße 1, 5142 Eggelsberg, Austria	XIOC-16DI Moeller (Eaton), Eaton Electric Sp. z o.o., ul. Galaktyczna 30, 80-299 Gdansk, Poland
Input number	16	12	16
Input type	Transistor	Digital input for 1-wire connection	Transistor
Nominal voltage	24 VDC	24 VDC	24 VDC
Input voltage	(20.4 – 28.8)V	24 VDC -15 % / +20 %	24 VDC -15 % / +20 %
Input current at 24 VDC	4 mA; per channel	Typ. 3.75 mA	Normally 4.0mA
Input circuit	Surce	Sink	Source
Input filter hardware	n.d.	≤100 µs	n.d.
Input filter software	n.d.	Default 1 ms (0-25 ms)	n.d.
Switching threshold Low	5 V DC at 1 mA	<5 VDC	<5 VDC
Switching threshold High	15 V DC at 2.5 mA	>15 VDC	>15 VDC
Isolation voltage between channel and bus	n.d.	500 V eff	n.d.

Table 5. Digital outputs – Comparison of selected parameters

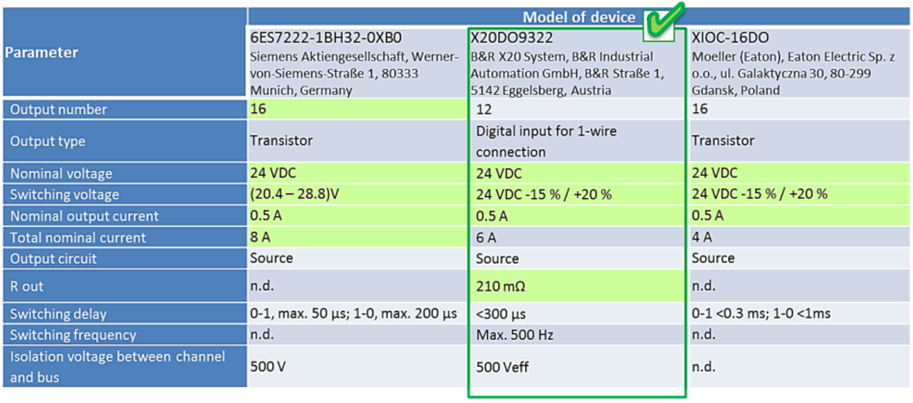

Parameter	Model of device		
	6ES7222-1BH32-0XB0 Siemens Aktiengesellschaft, Werner-von-Siemens-Straße 1, 80333 Munich, Germany	X20DO9322 ✓ B&R X20 System, B&R Industrial Automation GmbH, B&R Straße 1, 5142 Eggelsberg, Austria	XIOC-16DO Moeller (Eaton), Eaton Electric Sp. z o.o., ul. Galaktyczna 30, 80-299 Gdansk, Poland
Output number	16	12	16
Output type	Transistor	Digital input for 1-wire connection	Transistor
Nominal voltage	24 VDC	24 VDC	24 VDC
Switching voltage	(20.4 – 28.8)V	24 VDC -15 % / +20 %	24 VDC -15 % / +20 %
Nominal output current	0.5 A	0.5 A	0.5 A
Total nominal current	8 A	6 A	4 A
Output circuit	Source	Source	Source
R out	n.d.	210 mΩ	n.d.
Switching delay	0-1, max. 50 µs; 1-0, max. 200 µs	<300 µs	0-1 <0.3 ms; 1-0 <1ms
Switching frequency	n.d.	Max. 500 Hz	n.d.
Isolation voltage between channel and bus	500 V	500 Veff	n.d.

Table 6. Communication panel– Comparison of selected parameters

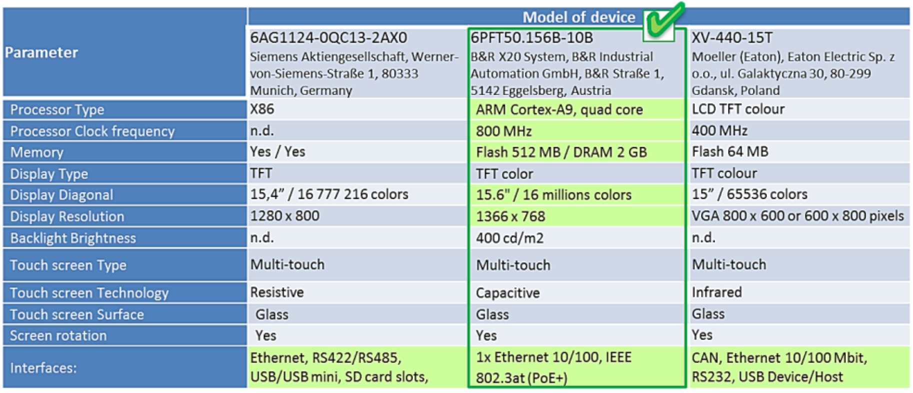

Parameter	Model of device		
	6AG1124-0QC13-2AX0 Siemens Aktiengesellschaft, Werner-von-Siemens-Straße 1, 80333 Munich, Germany	6PFT50.156B-10B ✓ B&R X20 System, B&R Industrial Automation GmbH, B&R Straße 1, 5142 Eggelsberg, Austria	XV-440-15T Moeller (Eaton), Eaton Electric Sp. z o.o., ul. Galaktyczna 30, 80-299 Gdansk, Poland
Processor Type	X86	ARM Cortex-A9, quad core	LCD TFT colour
Processor Clock frequency	n.d.	800 MHz	400 MHz
Memory	Yes / Yes	Flash 512 MB / DRAM 2 GB	Flash 64 MB
Display Type	TFT	TFT color	TFT colour
Display Diagonal	15,4" / 16 777 216 colors	15.6" / 16 millions colors	15" / 65536 colors
Display Resolution	1280 x 800	1366 x 768	VGA 800 x 600 or 600 x 800 pixels
Backlight Brightness	n.d.	400 cd/m2	n.d.
Touch screen Type	Multi-touch	Multi-touch	Multi-touch
Touch screen Technology	Resistive	Capacitive	Infrared
Touch screen Surface	Glass	Glass	Glass
Screen rotation	Yes	Yes	Yes
Interfaces:	Ethernet, RS422/RS485, USB/USB mini, SD card slots,	1x Ethernet 10/100, IEEE 802.3at (PoE+)	CAN, Ethernet 10/100 Mbit, RS232, USB Device/Host

Table 7. CPU (PLC main block) – Comparison of selected parameters

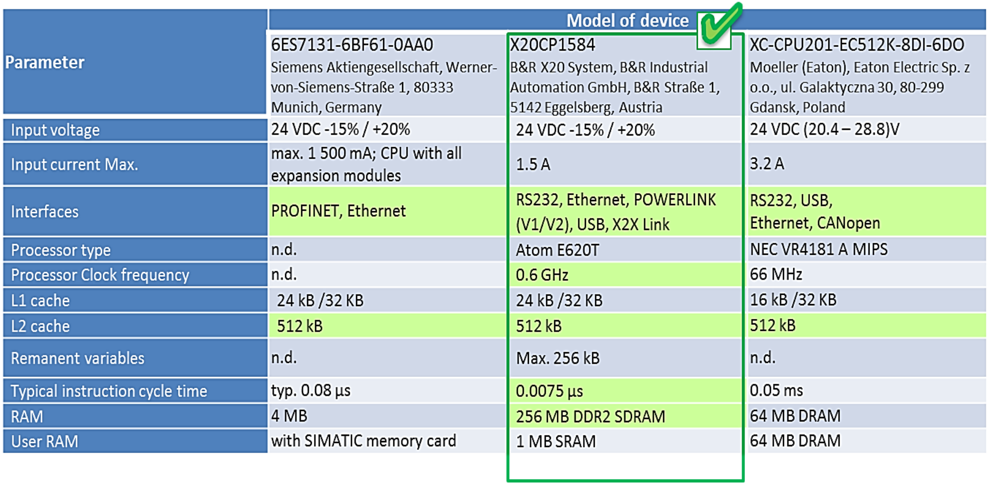

Parameter	Model of device		
	6ES7131-6BF61-0AA0 Siemens Aktiengesellschaft, Werner-von-Siemens-Straße 1, 80333 Munich, Germany	X20CP1584 B&R X20 System, B&R Industrial Automation GmbH, B&R Straße 1, 5142 Eggelsberg, Austria	XC-CPU201-EC512K-8DI-6DO Moeller (Eaton), Eaton Electric Sp. z o.o., ul. Galaktyczna 30, 80-299 Gdansk, Poland
Input voltage	24 VDC -15% / +20%	24 VDC -15% / +20%	24 VDC (20.4 – 28.8)V
Input current Max.	max. 1 500 mA; CPU with all expansion modules	1.5 A	3.2 A
Interfaces	PROFINET, Ethernet	RS232, Ethernet, POWERLINK (V1/V2), USB, X2X Link	RS232, USB, Ethernet, CANopen
Processor type	n.d.	Atom E620T	NEC VR4181 A MIPS
Processor Clock frequency	n.d.	0.6 GHz	66 MHz
L1 cache	24 kB /32 KB	24 kB /32 KB	16 kB /32 KB
L2 cache	512 kB	512 kB	512 kB
Remanent variables	n.d.	Max. 256 kB	n.d.
Typical instruction cycle time	typ. 0.08 µs	0.0075 µs	0.05 ms
RAM	4 MB	256 MB DDR2 SDRAM	64 MB DRAM
User RAM	with SIMATIC memory card	1 MB SRAM	64 MB DRAM

Table 8 presented selected devices for realization of main tasks of data acquisition and control system

Table 8. Selected devices for realization of main tasks of data acquisition and control system

Application	Model of device		Additional information
Input /output (extension) modules			**Slice-based I/O and control system X20** B&R Industrial Automation GmbH B&R Straße 1 5142 Eggelsberg Austria
- analog input	**X20AI4622**	**(x2)**	
- analog output	**X20AO4622**	**(x1)**	
- temperature input	**X20AT6402**	**(x2)**	
- digital input	**X20DI9371**	**(x1)**	
- digital output	**X20DO932**	**(x2)**	
Main controller (CPU)	**X20CP1584**	**(x1)**	
Operator panel	**6PFT50.156B-10B**	**(x1)**	
Communication module	**6COPOE.0000-00**	**(x1)**	

Supplemental devices for safety and support tasks - summary

Important and necessary elements of the equipment of every electrical device are elements of electrical protection, controls and supporting systems. The list of these elements is presented in Table 9.

Fig. 93 shows a diagram of all elements included in the extruder control system and devices for the implementation of tasks related to safety and support of the control and measurement process.

Table 9. Additional electrical equipment of the extruder device (protections, controls, power supplies)

Function	Device /element
The correct phase sequence verification	(F&F) Three-phase asymmetry and sequence monitor CKF-B
Overcurrent protection of the phase sequence sensor	(Eaton) Miniature Circuit Breaker CLS6-B6/3
Energy meter overcurrent protection	(Eaton) Miniature Circuit Breaker CLS6-C16/3
Switching the main drive on and off (main drive contactor)	(Eaton) Contractor DL M17-10-EA
Main drive overcurrent protection	(Eaton) Miniature Circuit Breaker CLS6-C16/3
Switching the rotary faucet drive on and off (faucet drive contactor)	(Eaton) Contractor DL M17-10-EA
Rotary faucet drive overcurrent protection	(Eaton) Miniature Circuit Breaker CLS6-C16/3
Low DC power supply	(Omron) S8VK-C12024 Power Supply
Powering up the heaters (solid state relays)	(Celduc) SAL963460 Solid-State Relay (25A 600V AC)
Overcurrent protection of power circuits of heaters	(Eaton) Fuse disconnector Z-SH/1 (16 A)
Powering up the electrovalves (solenoid valves) (solid state relays)	(Celduc) SPD03505 Solid-State Relay (5A 24V DC)
Overcurrent protection of supply circuits of electrovalves	(Eaton) Miniature Circuit Breaker, CLS6-C2
Electrical protection of the entire circuit of power and control system	(Eaton) Safety relay emergency stop ESR5-NO-41-24VAC-DC
Measurement of electrical energy consumption	(Simet) Three-phase 4-module digital electricity meter LS-3F (230V /400V AC; 10A / 100A AC)
Mechanical shield of power and control system	(Rittal) enclosure system (800 x 1800 x 500 - 2 doors)

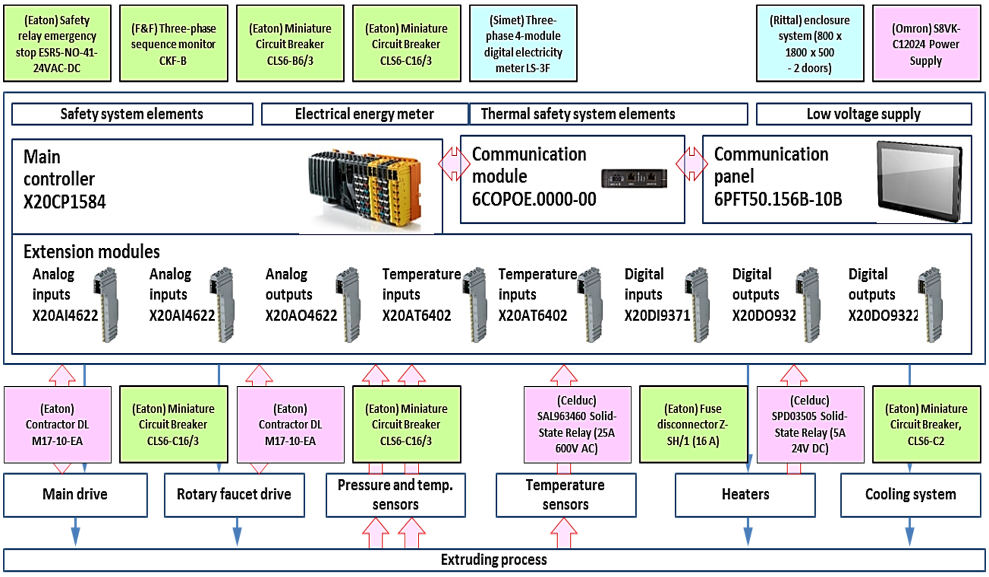
(Eaton) Safety relay emergency stop ESR5-NO-41-24VAC-DC
(F&F) Three-phase sequence monitor CKF-B
(Eaton) Miniature Circuit Breaker CLS6-B6/3
(Eaton) Miniature Circuit Breaker CLS6-C16/3
(Simet) Three-phase 4-module digital electricity meter LS-3F
(Rittal) enclosure system (800 x 1800 x 500 - 2 doors)
(Omron) S8VK-C12024 Power Supply
Safety system elements
Electrical energy meter
Thermal safety system elements
Low voltage supply
Main controller X20CP1584
Communication module 6COPOE.0000-00
Communication panel 6PFT50.156B-10B
Extension modules
Analog inputs X20AI4622
Analog inputs X20AI4622
Analog outputs X20AO4622
Temperature inputs X20AT6402
Temperature inputs X20AT6402
Digital inputs X20DI9371
Digital outputs X20DO932
Digital outputs X20DO9322
(Eaton) Contractor DL M17-10-EA
(Eaton) Miniature Circuit Breaker CLS6-C16/3
(Eaton) Contractor DL M17-10-EA
(Eaton) Miniature Circuit Breaker CLS6-C16/3
(Celduc) SAL963460 Solid-State Relay (25A 600V AC)
(Eaton) Fuse disconnector Z-SH/1 (16 A)
(Celduc) SPD03505 Solid-State Relay (5A 24V DC)
(Eaton) Miniature Circuit Breaker, CLS6-C2
Main drive
Rotary faucet drive
Pressure and temp. sensors
Temperature sensors
Heaters
Cooling system
Extruding process

Fig. 93. General diagram of all devices of controls system of the extruder

3. Conclusions

Making a prototype of a new generation extruder requires taking into account many material, process and construction factors. Appropriate selection of individual elements of the extruder enables its proper operation. One of the important elements of the devices are power supply systems and control and measurement systems, the selection of which determines the proper course of the extrusion process and obtaining a high-quality product with appropriate efficiency.

The applied control and measurement systems confirmed the correct course of the extrusion processes with their readings.

The use of modern control systems with the use of PLC drivers showed their good cooperation with working and control-measurement systems as well as the correct implementation of regulatory processes. The individual elements shown in the work met the expectations of the creators and constructors of the machine.

Acknowledgements

This project has received funding from the European Union's Horizon 2020 research and innovation programme under the Marie Skłodowska-Curie grant agreement No. 734205 – H2020-MSCA-RISE-2016.

References

- [1] https://new.siemens.com/global/en/products/automation/systems/industrial/plc/s7-1200.html
- [2] https://www.br-automation.com/pl/produkty/io-systems/x20-system/
- [3] https://www.eaton.com/pl/pl-pl/catalog/industrial-control--drives--automation--sensors/xc100-200-modular-plcs.html

Ján Varga[1], Łukasz Majewski [2]

THE APPLICATION OF CAM SYSTEM IN THE PRODUCTION OF SELECTED PARTS OF THE INNOVATIVE EXTRUDER

Abstract: *Each machine consists of several components, which use CNC machines due to their efficiency and accuracy in achieving the required dimensions. The paper deals with the application of CAD/CAM systems in the production of four parts, which are part of a new extruder design. When programming CNC machines, various CAM systems are used, which allow to choose suitable strategies for machining the required surfaces of the part. One of the most important factors for surface quality is milling strategy. For production of extruder parts DMG machines were used. The aim was to apply different CAM systems to the manufacturing process in the production of individual parts for the extruder.*

Keywords*: CNC programming, milling strategies, CAM system, tool path*

1. Introduction

An extruder is a machine that processes material by conveying it along a screw and pushing it through a die at a certain pressure. It is thus a known process throughout the manufacturing industry and is used to obtain a product of the desired shape and size with a specific cross-sectional area. The main advantage of this method is that we can produce a product of any cross-section from an existing product without using any new material.

Mechanical parts with sculptured surfaces used in the manufacture of molds, dies …etc. are machined on CNC milling machines in three stages, roughing, semi-finishing and finishing from their continuous or discrete models. CNC milling is today the most effective, productive, and flexible manufacturing method for machining of different surfaces [1]. For CNC milling are important differently milling strategies, which allows optimization of milling tool motion during milling process and by this motion obtain required surface properties mainly accuracy [2]. The strategy chosen to generate the tool path can influence by important parameters (machining time, cutting forces, length of the tool path, surface roughness).

---

1) *Technical University of Kosice, Faculty of Mechanical Engineering, Department of Technology, Materials and Computer Aided Production, Masiarska 74, 040 01 Kosice, Slovakia, jan.varga@tuke.sk.*

2) *Lublin University of Technology, Faculty of Mechanical Engineering, Department of Technology and Polymer Processing, ul. Nadbystrzycka 36, 20-618 Lublin, Poland, l.majewski@pollub.pl.*

This machining strategy requires selection of tools dimensions, identification of valid plunging positions, determination of tools plunge depths and the minimum tool length avoiding collisions. The complex geometry of parts with sculptured surfaces makes the determination of these parameters and the generation of a valid tool path a very difficult task. To optimize this strategy, to reduce the costs and to increase the productivity, it is indispensable to use several tools and to select the optimum combination of tools maximizing the removed volume and minimizing the machining time [3].

The tool movement during milling consists of three types of movements. The first is the movement of the tool during machining, also called the working movement. During this type of movement, the material is removed. Three-axis milling also involves moving the work table. The second is the movement of the tool into and out of the frame. The third is the movement of the stroke and the movement out of the working plane in order to quickly move the tool to the next working movement of the tool. By various combinations of these movements, it is possible to optimize working time, which significantly affects production costs. Especially in the production of shaped surfaces, there is the potential for a combination of movements in order to speed up production while maintaining the achieved product quality [4].

Computer-aided manufacturing (CAM) also known as Computer-aided Modelling or Computer-aided Machining is the use of software to control machine tools and related ones in the manufacturing of work pieces. CAM software for programming CNC milling machine tools provides the ability to define different toolpaths to achieve the desired part shape [5]. The basic sign of CAM is to minimize human intervention during the production process by the exploitation of computer data processed in the main elements of activities [6]. Choice of tool path is very critical for efficient application of the milling process. The tool path determines the axial depth of cut thereby controlling the maximum cutting force while machining. The definition of the tool path controls the productivity by way of cycle time, and it is usually handled by computer aided manufacturing (CAM) system.

For practical application of CAD/CAM systems is characteristic constructing of virtual 3D models, as it can see in the authors research [7], of parts which are designed in CAD (Computer Aided Design) system. SolidCAM has been used for virtual surface comparison of parts with a really machined surface. The main goal of the article was to apply CAM systems to produce selected parts for a newly designed extruder machine.

2. Parts production

This article describes the manufacture process of the four parts Body, Head connector, Sensor housing and Base plate, which are part of a new extruder design. Some simple shapes of parts were programmed directly on the machine in control system Sinumerik, but for complex shapes like part type of body CAM system SolidCAM, or CATIA were used. The machining of parts was carried out on the following's machines:

- DMG MORI ECOTURN 510 CNC turning milling center (Fig.1) with control system Siemens 840D, max. workpiece diameter: ø465 mm, max. workpiece length: 1050 mm, max. workpiece weight: 1200 kg, positioning accuracy X / Z: 8/8 µm, number of driven tools: 6

Fig.1. CNC turning milling center

- DMG MORI ECOMILL 50: 5 axis CNC milling machine (Fig.2) with control system Siemens 840D, working range X, Y, Z: 500 x 450 x 400 mm, working axis B: 5 / + 110 °, working axis C: 360 °, workpiece weight 200 kg

Fig.2. 5 axis CNC milling machine

- Wire cutting machine Accutech AU 500l (Fig.3) with program Accutex 500, table travel in X and Y axes: 750 x 450mm, Z axis travel: 300 mm, max. cutting angle: 22.5 °, max. workpiece size: 990 x 560 x 265 mm, max. workpiece weight: 400 kg

AccuteX
AccuteX AU-500i

Fig. 3. Wire cutting machine Accutech AU 500l

2.1 Production of the Body part

The material of this part was 40HM (1.7225). It is a CrMo-alloyed steel, engineering steel supplied in hardened and tempered conditions with a good machinability. Its used for components with high requirements on toughness, e.g. gear wheels, pinions, connecting rods, and parts for mechanical engineering. The first side of the Body CAD model in Solidworks (Fig.4a) and the second side is shown in Fig.4b.

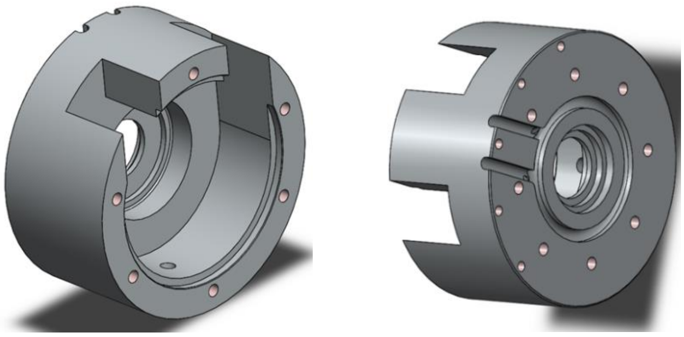

a) *b)*

Fig.4. First side of Body CAD model (a) Second side of Body CAD model (b)

For produce of this Body part CAM system SolidCAM, turning milling center and 5-axis CNC milling machine were used. We used four clamping positions on different machines. For the first clamping all toolpath of the tool in CAM system SolidCAM were programmed. The production process will be described in a few steps and supplemented with pictures from programming in the CAM system SolidCAM.

- The first clamping – turning milling center

The manufacturing process of the Body is nearly describing in following steps:

1. Turning front face – operation, Tool Sandvik DCLNL 2525M-12. Toolpath of the tool (Fig. 5a), and rest material after this operation is shown in Fig. 5b.

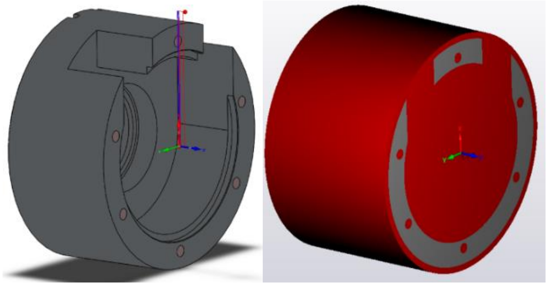

a) b)

Fig.5. Toolpath of the tool (a) Rest material after the turning front face (b)

2. Roughing and finishing of cylindrical face – operation, Tool Sandvik DCLNL 2525M-12. Tool path of the tool (Fig. 6a), rest material after roughing operation (Fig. 6b) and rest material after finishing is shown in Fig. 6c.

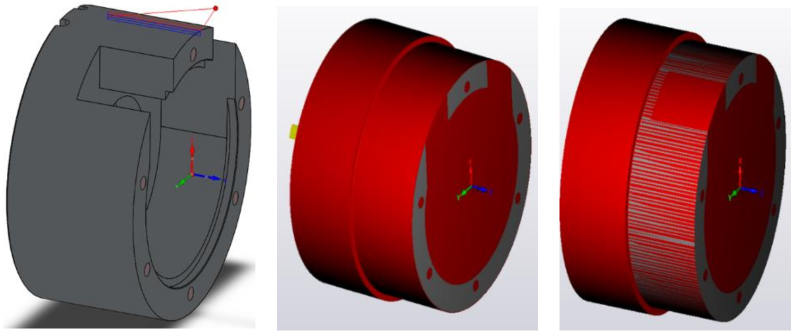

a) b) c)

Fig.6. Toolpath of the tool in 2nd operation (a) Rest material after roughing (b) Rest material after finishing (b)

3. Drilling central hole – operation, Tool drilling Ø 35mm.
4. Inside roughing, finishing of the hole Ø70 and chamfering in Fig.7 – operations, Inside Iscar Tool A25R PWLNL

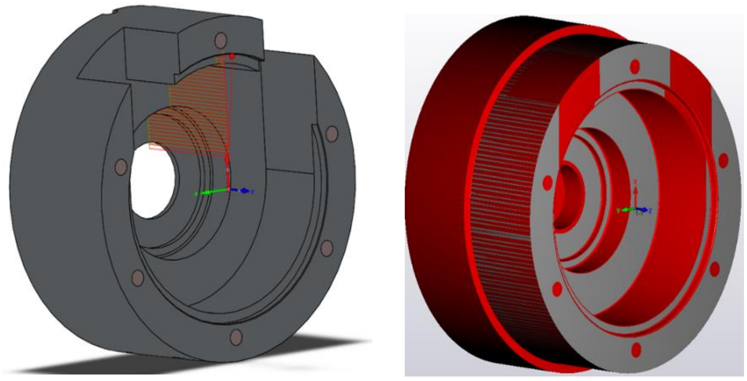

a) *b)*

Fig.7. Toolpath of the inside roughing of the hole Ø70 (a) Rest material after the inside finishing of the hole Ø70 (b)

5. Inside roughing and finishing of the diameter Ø140 in Fig.8– operation, Tool monolit Ø 16mm

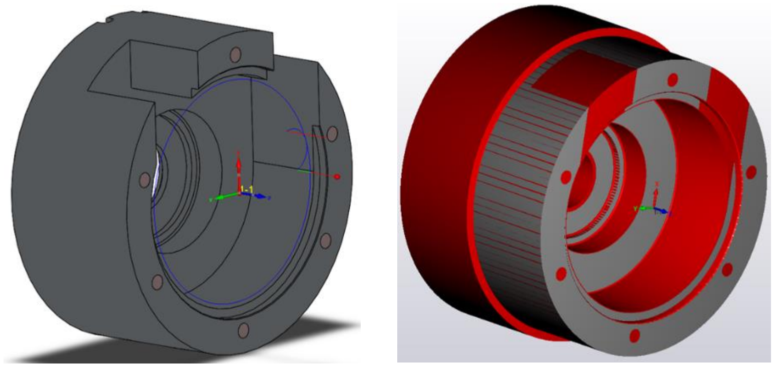

a) *b)*

Fig.8. Toolpath of the inside roughing of the hole Ø140 (a) Rest material after the inside finishing of the hole Ø140 (b)

6. Inside roughing and finishing Ø80 in Fig.9 – operation, Tool monolit Ø 16mm – roughing and Tool Iscar HM90 E90A-D16-2-C16 for finishing

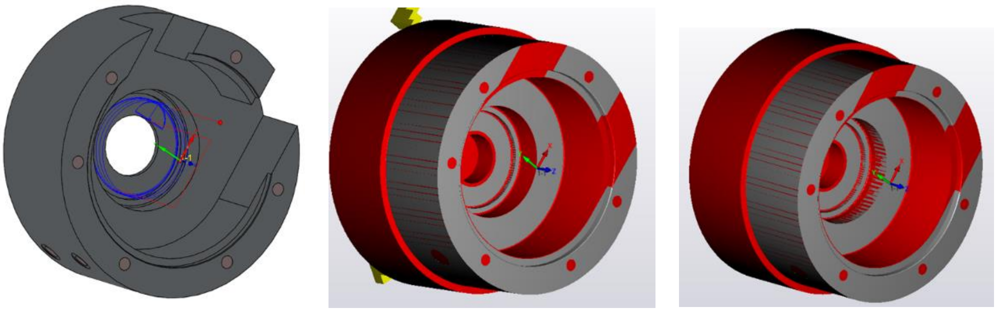

a) b) c)

Fig.9. Toolpath of the roughing operation (a) Rest material after roughing (b) and after finishing operation (c)

7. Inside milling, inside side in Fig.10 - operation, Tool Iscar HM90 E90A-D16-2-C16. Toolpath of the tool (Fig.10a) and rest material after inside milling is shown in Fig.10b.

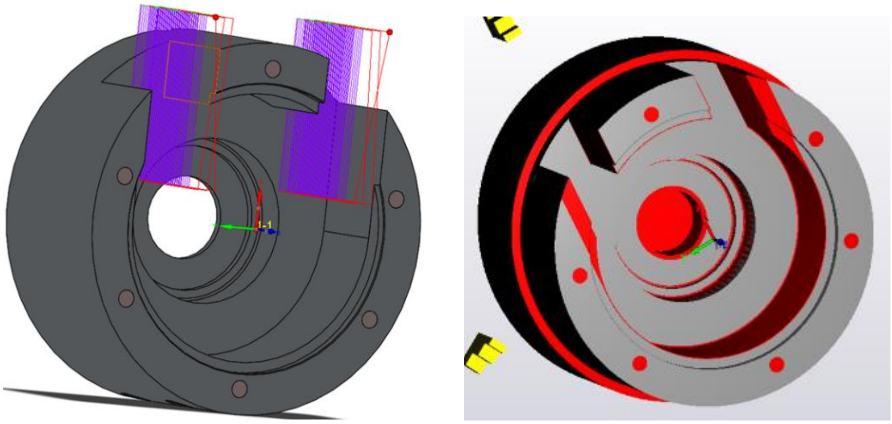

a) b)

Fig.10. Toolpath of the tool in inside milling of inside side (a) Rest material after the inside milling of inside side(b)

8. Inside milling, outside side in Fig.11 - operation, Tool Iscar HM90 E90A-D16-2-C16

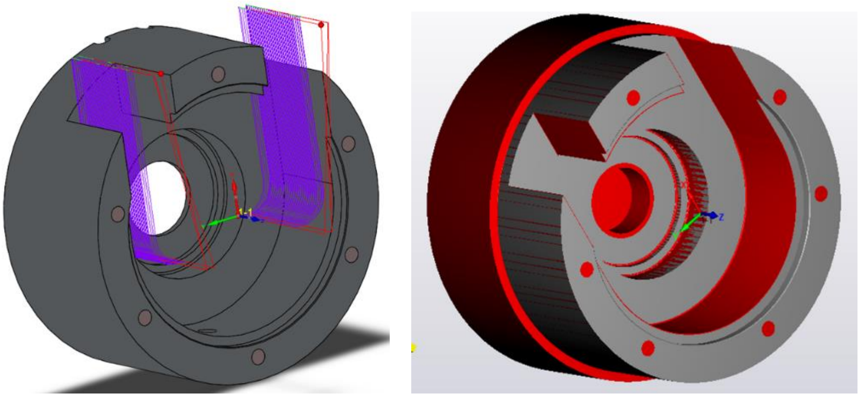

a) *b)*

Fig.11. Toolpath of the tool in inside milling of outside side (a) Rest material after the inside milling of outside side(b)

9. Hole perimeter in Fig.12 - operation, Tool monolit Ø 16mm

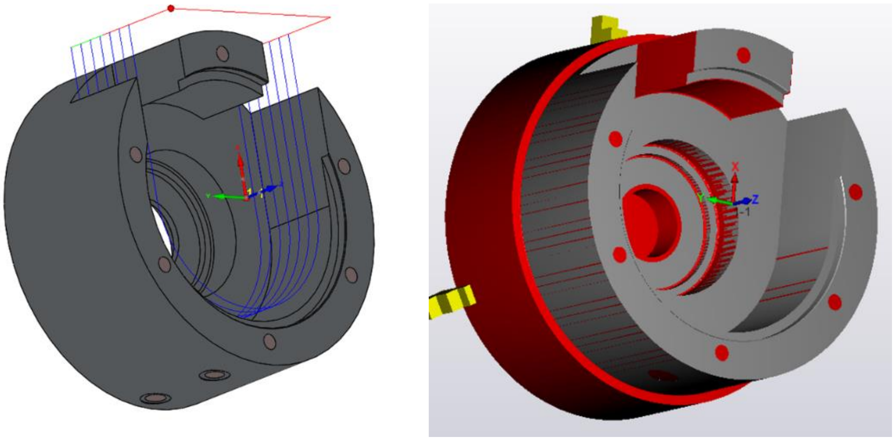

a) *b)*

Fig.12. Toolpath of the tool for hole perimeter produce (a) Rest material after the finish of hole perimeter (b)

10. Rest material perimeter in Fig.13 - operation, Tool monolit Ø 16mm

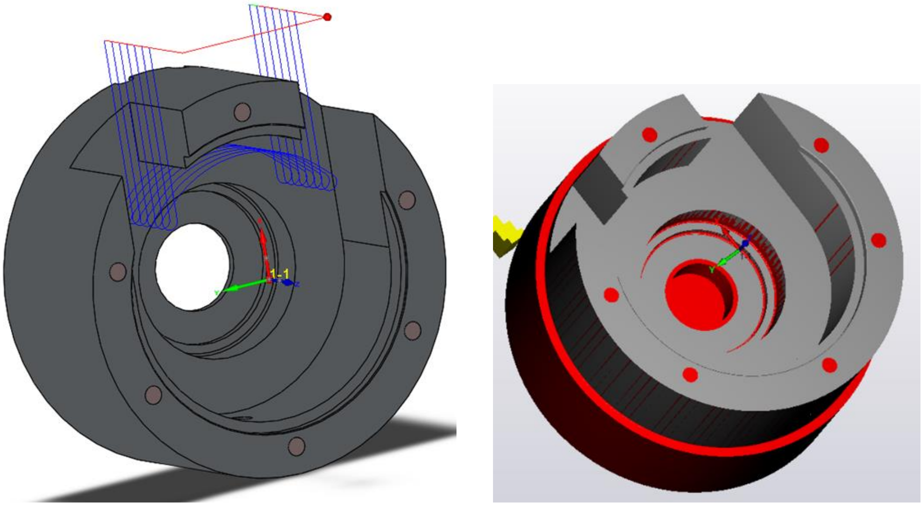

a) *b)*

Fig.13. Toolpath of the tool for rest material perimeter produce (a) Rest material after the operation in CAM system SolidCAM (b)

11. Central hole - operation, Tool central drill Ø 1mm
12. Drilling operation in Fig.14, Tool dril Ø 8,5 mm

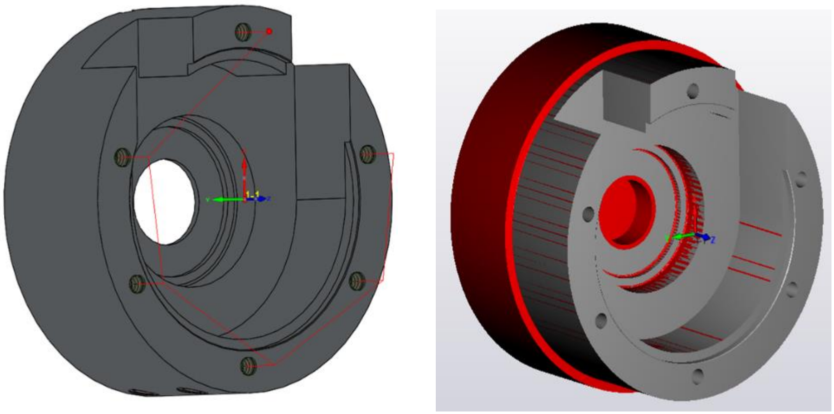

a) *b)*

Fig.14. Toolpath for drilling operation (a) Rest material after holes drilling (b)

13. Threads 6 x M10- operation, Tool thread M10
14. Radial surfaces in Fig.15 - operation, Tool monolit Ø 16mm. In this operation setting of the 2nd zero point for radial holes was necessary.
15. Drilling under threads M12 - operation, Tool drill Ø 10,2 mm

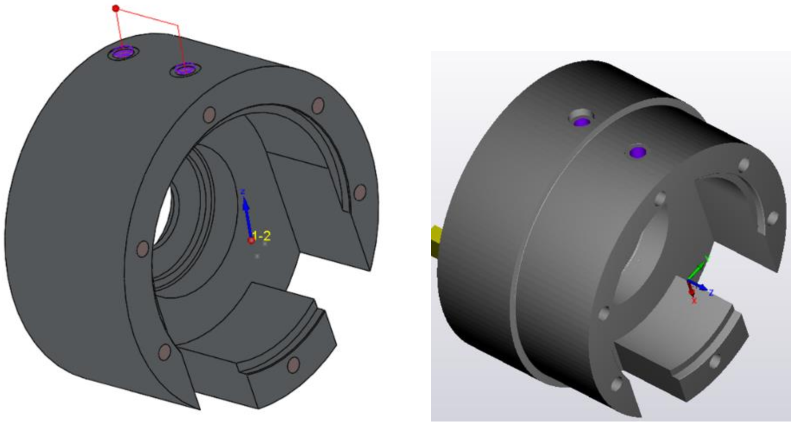

a) b)

Fig.15. Toolpath of the tool for radial surfaces produce (a) Rest material after the radial surfaces produce (b)

16. Hole drilling and threads M12x1 in Fig.16 - operation, Tool drill Ø 6,2 mm, Tool Thread M12

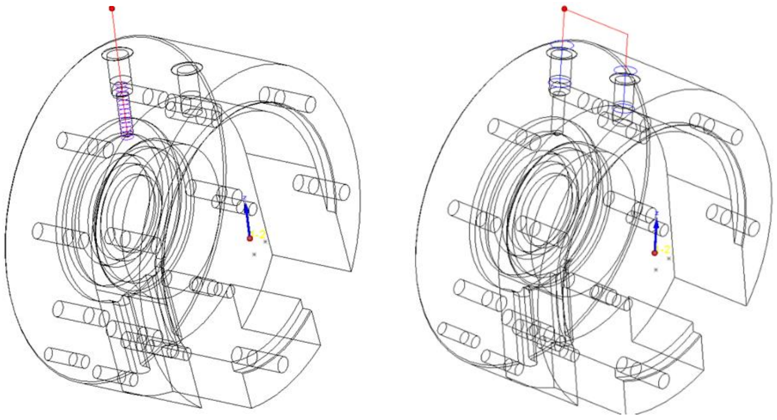

a) b)

Fig.16. Toolpath of the tool for hole drilling (a) Toolpath of the tool for threads produce (b)

- The second clamping – 5 axis CNC milling machine

For this clamping CAM system CATIA was used as is shown in Fig.17. The manufacturing process from the second clamping describe following steps:

1. Finishing of the bottom surface, Tool monolit Ø 16 mm
2. Inside radius milling by linear strategy
3. Chamfers

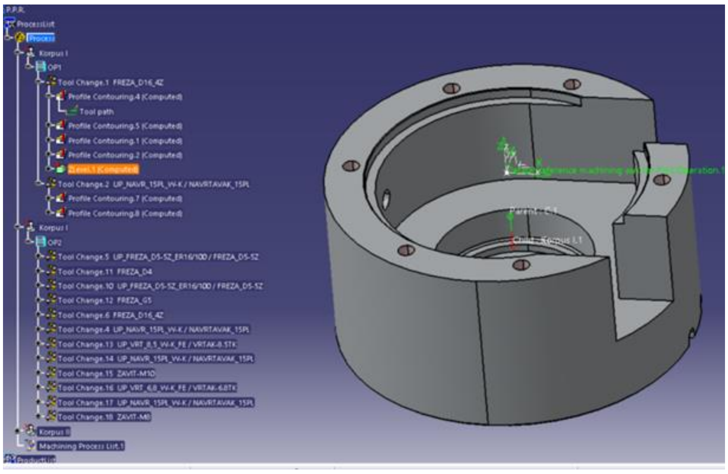
P.P.R.
ProcessList
Process
Korpus I
OP1
Tool Change.1 FREZA_D16_4Z
Profile Contouring.4 (Computed)
Tool path
Profile Contouring.5 (Computed)
Profile Contouring.1 (Computed)
Profile Contouring.2 (Computed)
ZLevel.1 (Computed)
Tool Change.2 UP_NAVR_15PL_W-K / NAVRTAVAK_15PL
Profile Contouring.7 (Computed)
Profile Contouring.8 (Computed)
Korpus I
OP2
Tool Change.5 UP_FREZA_D5-SZ_ER16/100 / FREZA_D5-SZ
Tool Change.11 FREZA_D4
Tool Change.10 UP_FREZA_D5-SZ_ER16/100 / FREZA_D5-SZ
Tool Change.12 FREZA_G5
Tool Change.6 FREZA_D16_4Z
Tool Change.4 UP_NAVR_15PL_W-K / NAVRTAVAK_15PL
Tool Change.13 UP_VRT_8,5_W-K_FE / VRTAK-8.5TK
Tool Change.14 UP_NAVR_15PL_W-K / NAVRTAVAK_15PL
Tool Change.15 ZAVIT-M10
Tool Change.16 UP_VRT_6,8_W-K_FE / VRTAK-6.8TK
Tool Change.17 UP_NAVR_15PL_W-K / NAVRTAVAK_15PL
Tool Change.18 ZAVIT-M8
Korpus II
Machining Process List.1
ProductList

Fig.17. CAD model and its operations in CAM system CATIA for second clamping

- The third clamping – 5 axis CNC milling machine

The manufacturing process from the third clamping describe following steps:

1. Slot roughing, Tool monolit Ø 5mm in CAM system CATIA (Fig.18)
2. Slot semifinish, Tool monolit Ø 4mm
3. Slot finish, Tool ball nose monolit Ø 4mm
4. Pockets milling, Tool monolit Ø 16mm
5. Chamfers of pockets
6. Holes drilling, Tool drill Ø 8,5 mm
7. Chamfers
8. Threads M10
9. Holes drilling, Tool drill Ø 6,8 mm
10. Chamfers
11. Threads 5 x M8

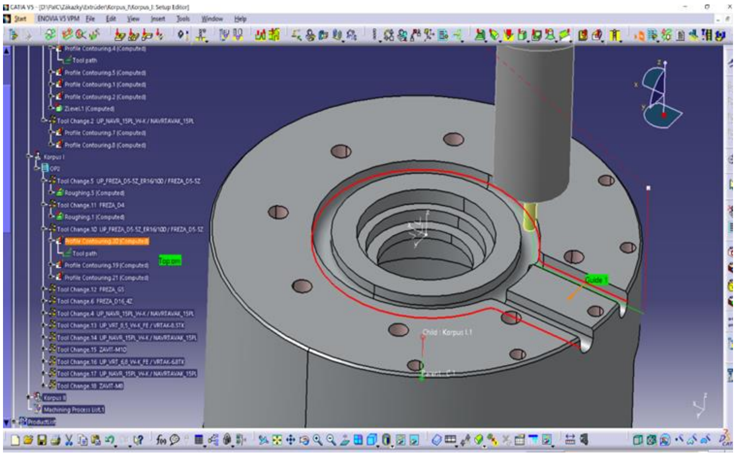
CATIA V5 - [D:\PalC\Zákazky\Extrúder\Korpus_I\Korpus_I: Setup Editor]
Start
ENOVIA V5 VPM
File
Edit
View
Insert
Tools
Window
Help
Profile Contouring.4 (Computed)
Tool path
Profile Contouring.5 (Computed)
Profile Contouring.1 (Computed)
Profile Contouring.2 (Computed)
ZLevel.1 (Computed)
Tool Change.2 UP_NAVR_15PL_W-K / NAVRTAVAK_15PL
Profile Contouring.7 (Computed)
Profile Contouring.8 (Computed)
Korpus I
OP2
Tool Change.5 UP_FREZA_D5-5Z_ER16/100 / FREZA_D5-5Z
Roughing.5 (Computed)
Tool Change.11 FREZA_D4
Roughing.1 (Computed)
Tool Change.10 UP_FREZA_D5-5Z_ER16/100 / FREZA_D5-5Z
Profile Contouring.20 (Computed)
Tool path
Top om
Profile Contouring.19 (Computed)
Profile Contouring.21 (Computed)
Tool Change.12 FREZA_G5
Tool Change.6 FREZA_D16_4Z
Tool Change.4 UP_NAVR_15PL_W-K / NAVRTAVAK_15PL
Tool Change.13 UP_VRT_8,5_W-K_FE / VRTAK-8.5TK
Tool Change.14 UP_NAVR_15PL_W-K / NAVRTAVAK_15PL
Tool Change.15 ZAVIT-M10
Tool Change.16 UP_VRT_6,8_W-K_FE / VRTAK-6,8TK
Tool Change.17 UP_NAVR_15PL_W-K / NAVRTAVAK_15PL
Tool Change.18 ZAVIT-M8
Korpus II
Machining Process List.1
ProductList
Guide
Child : Korpus I.1

Fig.18. CAD model and its operations in CAM system CATIA for third clamping

The final shape of the Body part with the required dimension after third clamping is shown in Fig.19.

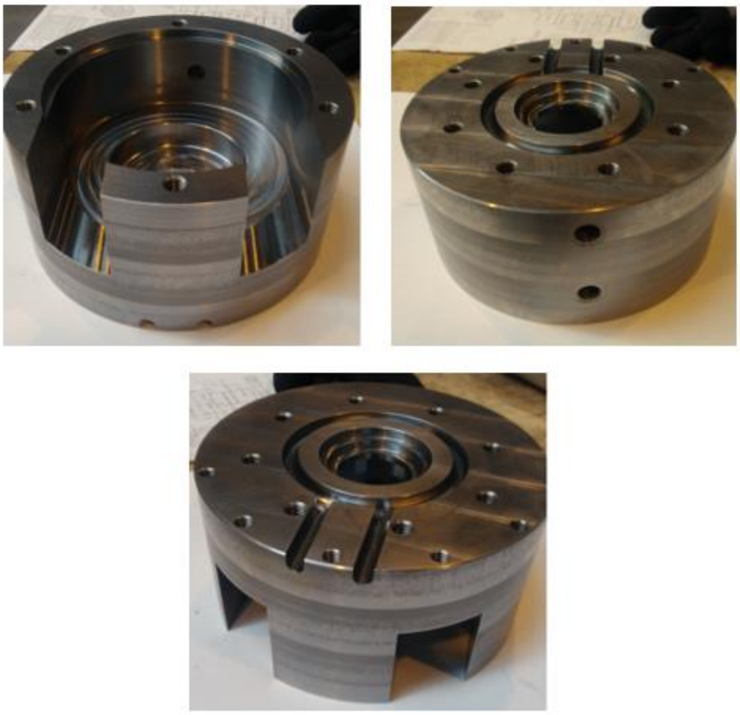

Fig.19. Final shape of the part of Body

2.2 Production of the Head connector

The material of this part was 40HM (1.7225). It is a CrMo-alloyed steel, engineering steel supplied in hardened and tempered conditions with a good machinability. Its used for components with high requirements on toughness, e.g. gear wheels, pinions, connecting rods, and parts for mechanical engineering. The first side of the Head connector CAD model in Solidworks (Fig.20a) and the second side is shown in Fig.20b.

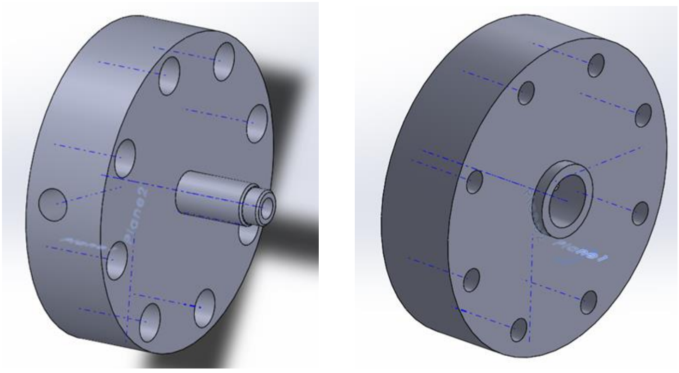

a) *b)*

Fig.20. First side of Body CAD model (a) Second side of Body CAD model (b)

For produce of this segment CAM system SolidCAM and three different machines were used. The production process described in more detail will be described below.

- The first clamping - turning milling center

For the 1st half of the stock two operations were realized:

1. Face turning - finishing
2. Turning cylindrical face – finishing

- The second clamping - turning milling center

For the 2nd half of the stock five operations were realized:

1. Face turning - finishing
2. Turning cylindrical face – finishing
3. Turning face – offset
4. Central hole
5. Milling inside shape by CAM system SolidCAM

Clamping of the stock into the three jaws (Fig.21a) and part after turning cylindrical face is shown in Fig.21b.

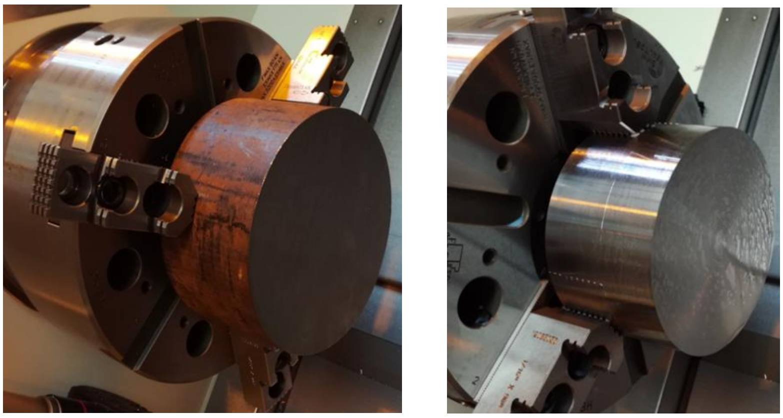

a) b)

Fig.21. Clamping of the stock (a) Part after turning cylindrical face (b)

- The third clamping - turning milling center

For the third clamping turning milling center was used again. In this clamping were realized following operations:

1. Turning on the shape for thread M 20
2. Thread M 20, Thread tool SEL 2525 M 16 Iscar
3. Holes drilling 8 x Ø 11 mm
4. Chamfers

- The four clamping - 5 axis CNC milling machine

The operations used in this clamping is nearly describing in following steps:

1. Drilling of radial holes – Tool drill Ø 6,2mm
2. Drilling under threads M12, Tool drill Ø 10,2 mm
3. Thread ½ 20 UNF

- The five clamping – Wire cutting machine.

Wire cutting machine includes a program Accutex 500 and for cutting was used wire thickness 0,25 mm. In this clamping only one operation was used. We used this machine to achieve the required dimension - – Final hole x Ø 10 $_{-0,05}$. Followings pictures describes finally shape of the part (Fig.22) from both sides.

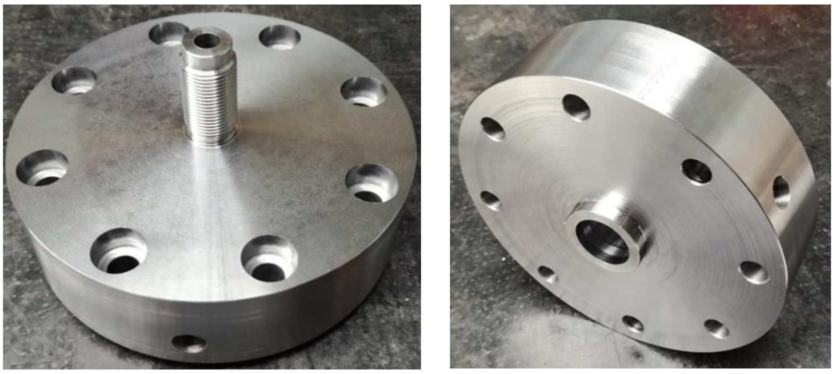

Fig.22. Final shape of the part Head connector

2.3 Production of the Sensor Housing

The material of this part was C45 (1.0503) steel is carbon steel, also called unalloyed, of higher quality. Due to the general availability, C45 steel can be purchased in many forms, among which the most popular are rods with various profiles and shapes, plates, plates, and pipes. This material can be use for the following applications: screws, forgings, shafts, sickles, axes, knives, wood working drills, etc.

For the manufacturing process turning milling center and workshop programming directly on the machine was used.

The production of the part names Sensor Housing was realized in following steps:

- The first clamping - turning milling center

1. Face turning – roughing
2. Turning cylindrical face – finishing
3. Hole drilling D 6,5 m through all
4. Frilling by Tool D 10 mm
5. Hole extension by milling to dimension 11 mm
6. Thread M12x1
7. Cahmfer 1x45°

During operations was made control checking of some dimensions by simulation mode in workshop program Sinumerik 840D as is shown in Fig. 23.

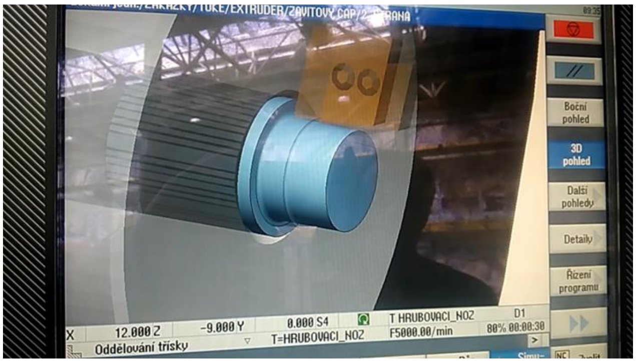
/ZAKAZKY/TUKE/EXTRUDER/ZAVITOVY CAP/2. STRANA
Boční pohled
3D pohled
Další pohledy
Detaily
Řízení programu
X 12.000 Z -9.000 Y 0.000 S4
T HRUBOVACI_NOZ
D1
F5000.00/min
80% 00:00:30
Oddělování třísky
T=HRUBOVACI_NOZ

Fig.23. Display of the simulation before the production of the part in Sinumerik 840D

- The second clamping - turning milling center

1. Face turning – finishing
2. Roughing and finishing of cylindrical to tolerance dimension
3. Finishing inside hole to dimension 6,6 mm

Obtained shape of the part Sensor Housing is shown in Fig. 24.

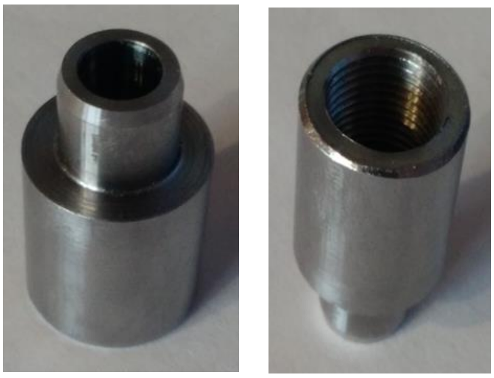

Fig.24. Final part of the Sensor Housing

2.4 Production of the Base plate for the Hopper

The material of this part was 18G2A (1.0562), which is high strength alloy steel suitable for weldable. It has following mechanical properties:

- Hardness under 220 HB softened condition
- Tensile strength Rm 490 - 630 MPa
- Yield strength Re 335 MPa

An illustration of the parts required for production is shown in Fig. 25.

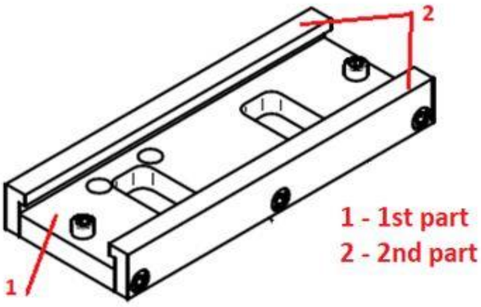

Fig.25. The Base plate

Both parts were produced on the 3-axis CNC milling machine. The production of the part involved the following operations:

1. Face milling operation, depth cut 1 mm, Tool D80 mm, ISCAR
2. Contour roughing, finishing and chamfer of edges
3. Hole's drilling 4x Ø 6,6 mm and 2x Ø 5,2 mm
4. Pockets roughing Ø 11 mm to depth 9,4 mm, Tool Ø 8mm, allowance 0,2 mm
5. Pockets finishing
6. Chamfers of edges for pockets
7. Threads 2x M6, chamfers
8. Roughing of rectangle pockets, Tool Ø 16 mm / allowance 0,3 mm
9. Finishing of rectangle pockets, chamfers

The 2nd part includes only three steps. For the first step it was necessary to make face milling operation by Tool D80 mm, from producer ISCAR and following was realized shape L milling by Tool D80 mm. Finishing of the surface was achieved by the same tool. Finally, holes and pockets were made. Finally, part of the Hopper Guide is shown in Fig. 26.

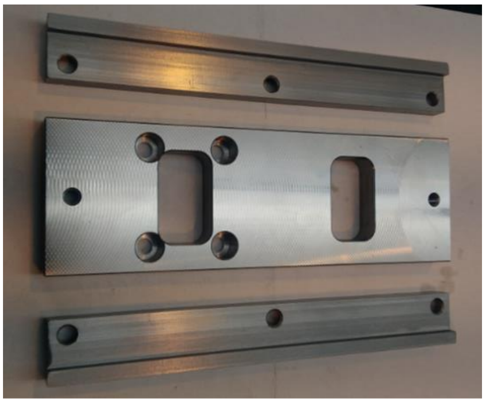

Fig.26. Final shape of the Base plate

3. Conclusion

The paper deals with the application of CAD/CAM systems in the production of four parts, which are part of a new extruder design. The main objective of the authors was implemented CAD/CAM systems in the production process of four parts from the beginning to the end. To produce these parts various CNC machines were used.

In the production process, it was necessary to consider the method of clamping individual parts, the choice of suitable strategies for milling, turning, the choice of suitable tools and cutting conditions the required material and shape. The programs creation was based on drawing documentation and CAD models. Some operations were programmed on the machine in control system Sinumerik and complex shaped surfaces in CAM systems CATIA and SolidCAM. The result was finished parts that are part of the equipment, the extruder.

Acknowledgements

This project has received funding from the European Union's Horizon 2020 research and innovation programme under the Marie Skłodowska-Curie grant agreement No. 734205 – H2020-MSCA-RISE-2016.

References

[1] Ižol P., Beňo J., Mikó B., Precision and Surface Roughness When Free–Form–Surface Milling. Výrobné inžinierstvo, 2011, 10(1), pp 7073. ISSN 1335-7972.

[2] Ižol P., Varga J., Porovnanie CAM stratégií obrábania pri 2.5D frézovaní. Transfer inovácií, 2011, No.19., pp 1021053. ISSN 1337-7094.

[3] M. Bey M., Tchantchane Z., Optimum Combination of Cutting Tools for Roughing Complex Parts Using Plunge Milling Machining Strategy, EMP, Bordj El Bahri, April, (2014) p.15-16.

[4] Fabian M., Ižol P., Tomáš M., Kupec,F., Kopas M., Use of CAM Strategies for Tool Movement in Machining Surfaces of Various Shapes, Acta Mechanica Slovaca 2020, 24(3), p. 40-48.

[5] Ižol P., Tomáš M., Beňo J., Milling strategies evaluation when simulating the forming dies' functional surfaces production. Open Engineering. 2016, 6(1), pp 98105. ISSN 2391-5439.

[6] Peterka J., Pokorny P., Vaclav S., CAM Strategies and Surfaces Accuracy. Ann. DAAAM Proc. 2008, 19, 1061–1063.

[7] Yu T., Zhang X., Liang W., W. Wang W., A web based virtual system for turn milling center, International Journal of Advanced Manufacturing Technology, 67 (2013) pp. 2395-2407.

Ľudmila Dulebová[1], Janusz W. Sikora[2], Volodymyr Moravskyi[3]

THE IMPACT OF TECHNOLOGICAL PARAMETERS OF PLASTICS EXTRUSION PROCESS ON PRODUCTS QUALITY

Abstract: *Extrusion is by far the most important and probably the oldest transformation and shaping process of thermoplastic polymers. To ensure a quality through extrusion process during manufacturing, it is essential to discover, control, and monitor all quality parameters to ensure product quality. Some of the important parameters are based on the condition of equipment used in process, operating conditions, temperatures, pressures, dies quality, and used materials. The aim of this paper was to focus to analyze the various defects in the extrusion process, to describe impact of technological parameters on the product quality and to suggest the mitigation and remedies for the improvement of extrusion process for better product quality and life.*

Keywords*: plastic, extrusion process, defects in extrusion process, product quality*

1. Introduction

Polymers have many advantages as they are light in weight, provide design flexibility, offer electrical insulation, and have relatively low overall and manufacturing cost. Hence the advantages of synthetic polymers are over competent than other materials like metals, it is reasonable to predict that polymers will take an even greater allocation of the total material market in the future [1]. Polymers caused dynamic growth of production and use in everyday life. They are produced by various processing technologies, one of these technologies is extrusion.

Extrusion is by far the most important and probably the oldest transformation and shaping process of thermoplastic polymers. After synthesis (polymerization) up until the formulation and production of the finished or semi-finished product, this process is almost entirely concerned with synthetic polymers, but different applications and processes exist. The development of the single-screw extrusion, which is directly derived from the Archimedean screw principle, began during the 1880s, initially with rubber and then with polymers around 1940. Nowadays, it is primarily used to make finished or semi-finished products that will undergo a second transformation (e.g., the extrusion of sheets that will then be thermoformed for use in packaging). This process essentially involves the melting and homogenization of the raw materials before

---

1) *Technical University of Kosice, Faculty of Mechanical Engineering, Department of Technologies, Material and Computer Aided Production, Masiarska 74, 040 01 Kosice, Slovakia, ludmila.dulebova@tuke.sk.*

2) *Lublin University of Technology, Department of Technology and Polymer Processing, 36 Nadbystrzycka St., 20-618 Lublin, Poland, janusz.sikora@pollub.pl.*

3) *National University Lviv Polytechnic, Department of Plastics Engineering, st. S. Bandera, 12, 79013 Lviv, Ukraine, vmoravsky@gmail.com.*

pumping the molten polymer through a die (continuous process) or into a mold (in the case of injection, a cyclic process). Globally, more than 90 million tons of thermoplastics are transformed in this way each year [2].

2. Extrusion Process

One of the main goals of extrusion is the improvement of quality of extruded parts besides the reduction of cycle time, and lower production cost. Plastic extrusion is a challenging process for many manufacturers and researchers to produce products meeting requirements at the lowest cost. The complexity of extrusion process and the enormous amount of process parameters involved make it difficult to keep the process under control. Solving problems related to quality has a direct effect on the expected profit for companies manufacturing plastic products. Quality characteristics in extrusion process are mechanical properties, dimensions or measurable characteristics, and attributes. In general, some of the main causes of quality problems are material related defects, process related problems, packing and cooling related defects, and post extrusion related defects. Factors that affect the quality of an extruded part can be classified into four categories: part design, die design, machine performance and processing conditions. The part and die design are assumed as established and fixed. During production, quality characteristics may deviate by processing conditions caused by machine wear, environmental change, or operator fatigue. Good quality of extrusion is ideally carried out under the design condition of constant screw rotational speed and temperature and uniform composition. Poor extradite quality for a given designed extruder can be related to the inappropriate setting of processing conditions [3,4].

The extrusion process converts a solid plastic feedstock material into a molten viscous fluid, and then to a finished solid or flexible product for practical use. Extrusion is a continuous process, as opposed to moulding, which is a cyclic process. Extrusion is suitable for many types of continuous plastic products that have a uniform outside shape and can be coiled, cut, or wound. The transformation of a solid plastic feedstock material into a molten viscous fluid takes place in the extruder barrel, through the mechanical shearing action of a rotating screw and the heat provided by electrical resistance heaters clamped to the outside of the extruder barrel and die. The combination of the mechanical, rotating shearing action of the screw and the heat of the electrical heaters causes the solid plastic feedstock to change into a hot molten material [5].

The functional zones of a conventional single screw extruder are shown in Fig. 1.:

- *feed hopper*, this zone is designed to operate under gravity flow, and it feeds the granules or the particulate solids into the extruder,
- *solids conveying zone*, this zone is designed to transport and to slightly compress the granules or the particulate solids,
- *plasticating zone*, polymer melting takes place in this zone due to viscous dissipation and heat transfer by conduction from the extruder barrel,

- *melt conveying zone* (or metering zone), this zone is intended to transport the molten polymeric material and to achieve pressure build up,
- *mixing zone*, this zone is designed to improve melt homogeneity by means of shear mixing elements, such as distributive, dispersive, or elongational mixers,
- *die forming*, the forming or shaping of the extrudate takes place in this zone for subsequent post-extrusion processes, such as calibration, cooling, winding, or cutting, among others,
- *venting*, this zone is only present in two-stage screw extruders or vented extruders and is used to remove any residual moisture or volatiles from the polymer melt.

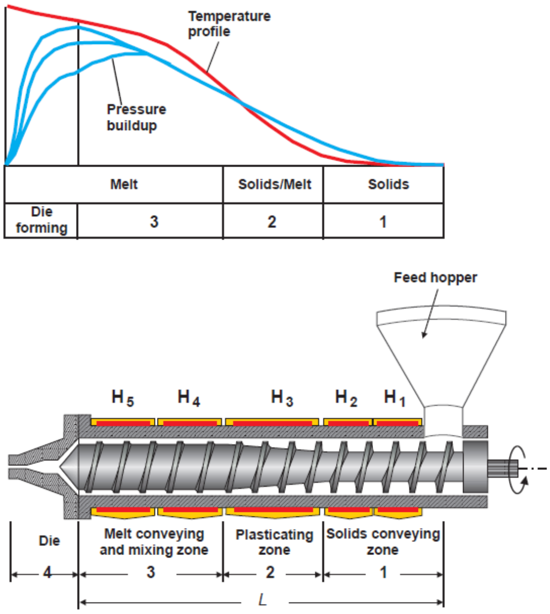
Temperature profile
Pressure buildup
Melt
Solids/Melt
Solids
Die forming
3
2
1
Feed hopper
H_5
H_4
H_3
H_2
H_1
Die
Melt conveying and mixing zone
Plasticating zone
Solids conveying zone
4
3
2
1
L

Fig. 1. Functional zones in a single screw extruder [6]

3. Defects influencing on product quality in extrusion process

The ultimate goal of the extrusion process is to use polymer material in order to cheaply, quickly, and effectively obtain a product, eliminating any waste and meeting the appropriate requirements regarding the product`s parameters and quality while maintaining the assumed processing parameters. Settings and parameters are mostly determined through experiments, by trial and error. Improperly selected processing parameters lead to extruded products with defects, reducing their quality and functional properties. To ensure successful extrusion manufacturing, every parameter must be identified, controlled, and monitored [8].

Defect is any form of deviation of the product’s characteristic from the specification set up by the manufacturing process. It can be caused by a single source or the cumulative effect of several factors, which may arise at any stage of the processing [5].

The melt flow plays a very important role in the extrusion process. In Newtonian fluid mechanics the transition from rectilinear flow (laminar) to chaotic flow (turbulent) is the most important and most frequently studied instability. However, instabilities do occur in polymer extrusion, and they appear above a critical wall shear stress in the range of 0.1 to 0.5 MPa, which is actually the range for flow through dies in many industrial extrusion operations. The extrusion instabilities are related to wall slip and viscoelasticity, with manifestations ranging from surface irregularities to gross extrudate distortions. The most common flow instabilities are usually observed with a naked eye on the extrudate emerging from a capillary viscometer. These extrusion instabilities/defects are usually investigated in conjunction with the corresponding flow curve. A flow curve is a plot of shear stress as a function of the apparent shear rate. The shear stress is obtained from the pressure drop and the capillary length to the radius ratio $\tau=\Delta p/2(L/R)$. The apparent shear rate is obtained from the volume rate of flow and the radius, $\dot{\gamma}=4Q/\pi R^3$. The onset of extrusion defects is manifested, for some polymers, by mild to steep slope changes of the flow curve as shown in Fig.2, where shear stress is as a function of shear rate. The flow in the stick-slip region oscillates with the average values shown by symbol “x”. Wavy flow corresponds to gross melt fracture [9, 10, 11].

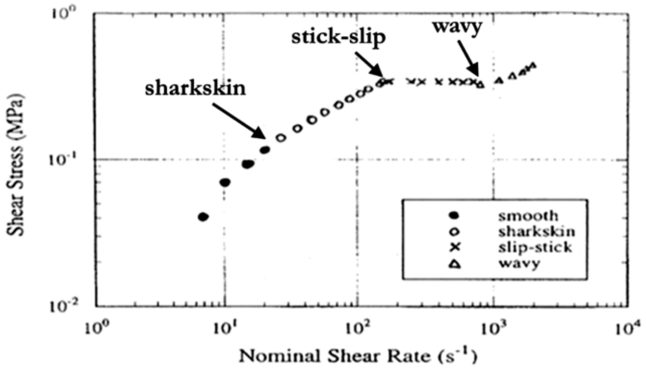

Fig. 2. Flow curve for a material Unipol LLDPE at 155°C with determination of extrusion defects [11]

In many cases, the instabilities occur during the processing and these instabilities causes some defects that can be found in extruded parts such as: warpage, voids, sharkskin, sink mark, residual stress, air trap, weld line, sink marks, low gloss, gels, melt fracture, uneven surface gloss, spotted surface, rough surface, thickness variation, uneven wall thickness. In extrusion products, defects due to processing also include poor understanding of the processing method, use of inadequate or old machines, lack of trained staff, machine break down, and inappropriate working environments [4, 5].

3.1 Voids

Voids are rather common problem in extrusion (Fig. 3). It is caused by air being dragged in with particulate material from the feed hopper. Under normal conditions, the compression of the solid particulate material in the feed section will force the air out of the solid bed. However, under some circumstances the air cannot escape back to the feed hopper and travels with the polymer until it exits from the die. As the air pockets exit from the extruder, the sudden exposure to a much lower ambient pressure may cause the compressed air bubbles to burst in an explosive manner. However, even without the bursting of the air bubbles, the extrudate is generally rendered unacceptable because of the air inclusion. It should be noted that bubbles in the extrudate are not only a sign of air entrapment, but it may also be an indication of moisture, surface agents, volatile species in the polymer itself, or degradation [12, 15].

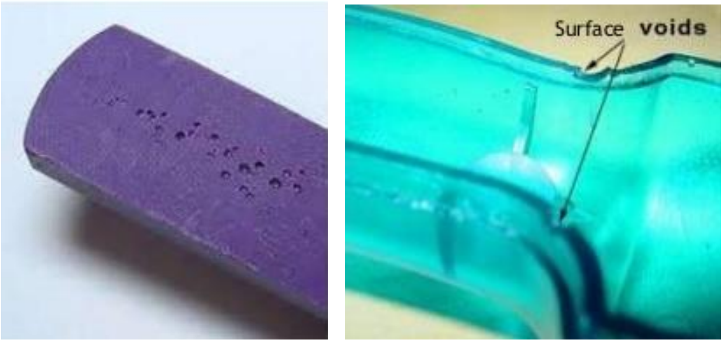

Fig. 3. Typical voids on an extrudate [12]

3.2 Gels

Gels are generally defined as small, round defects in extruded products with a distinct boundary that can be observed by simple visual inspection. This includes discolored specks, contamination, cross-linked polymer droplets, etc. The material making up the gel particle is basically the same as the polymer of the surrounding film. Therefore, a gel particle is different from contamination and in many cases has no discoloration. Gels are an unsightly but common problem in single-screw extrusion. They can be large or small, hollow or solid, clear or discolored. They appear in sudden "showers," discrete stripes, or randomly dispersed. Large, hollow gels, or lensing, are caused by moisture trapped in the melt (Fig.4). To prevent this phenomenon is to pay more attention to material storage and drying [13, 15].

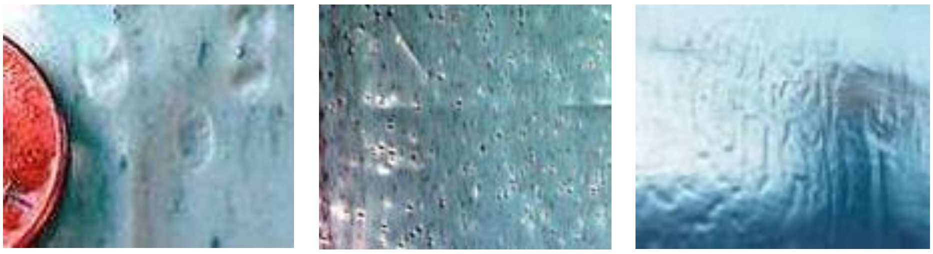

Fig. 4. Defects - gels in the shape of a lens, in the shape of an arrowhead and applesauce [13]

If gels are randomly dispersed, they usually come from the raw material or the extruder. Raw-material problems that produce gels include contamination, too much recycled or reclaimed material, and insufficient antioxidant. If gels form in lanes in the machine direction, alternating with lanes free of gels, the problem is usually downstream from the extruder in the die or die block. When large quantities of gels repeatedly appear and disappear, the phenomenon is called gel showers. They may be caused by improper processing conditions and are common when materials with very different melting rates are blended. Pigment masterbatches, for example, are designed to melt quickly to maximize mixing time in the extruder. But if the feed zone is too hot, pigment granules melt too quickly and become encrusted on the screw. Encrusted granules then break off occasionally, resulting in a sudden cascade of gels the same color as the pigment masterbatch. They aren't burnt gels, just heavily pigmented unmelts. Extruder motor amps will rise because the sudden increase in pigment concentration adds more friction to the transition zone. The preferred solution is to lower the temperature slightly in both the feed and transition zones to delay melting of the masterbatch. [13].

Possible corrective actions to improve gels are raise melt temperature, streamline die to prevent stagnation and increase screen pack mesh to filter out [14].

3.3 Specks

Discoloured specks are a common problem in extrusion (Fig. 5). This problem is like the defect, which is the problem of gels. Like gels, discoloured specks are formed not only in extrusion and molding at the processor but also in polymerization at the resin producer (p-speck) and a speck also formed in extrusion (e-speck). The simplest solution to the problem is that processors first need to figure out how many specks are in the incoming raw material (p-specks). Then they need to minimize specks caused during the extrusion process, or e-specks [15, 16].

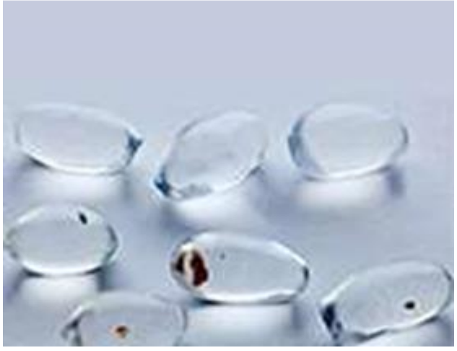

Fig. 5. Pellet with black and discolored specks [15]

3.4 Sharkskin

Sharkskin manifests itself as a regular ridged surface distortion, with the ridges running perpendicular to the extrusion direction A less severe form of sharkskin is the occurrence of maintenance of the surface, where the glossy surface cannot be maintained [16]. Shark skin is generally thought to be formed in the die land or at the exit and it is dependent primarily on the temperature and the linear extrusion speed - Fig.6, (note the formation of ridges perpendicular to flow direction). Sharkskin defect may be described as the appearance of ridges perpendicular to the flow direction, visible to the naked eye. The onset of sharkskin occurs at a critical wall shear stress usually quoted as $\tau_w \approx 0.14$ MPa for HDPE and it is associated with stick-slip phenomena at the die exit [10]. The sharkskin phenomenon is shown with high detail in Fig.7 [17].

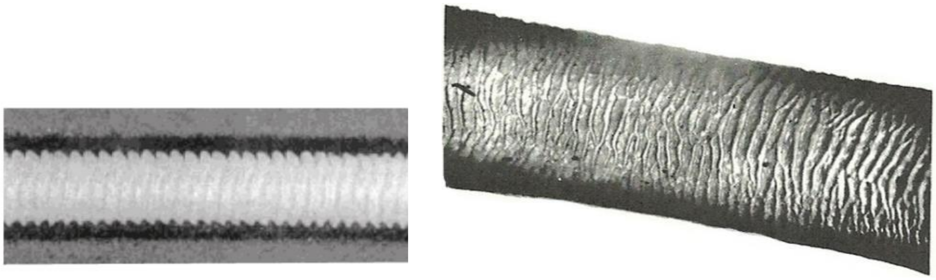

Fig. 6. Sharkskin on an extrudate HDPE of about a 2 mm, (exaggerated due to the enlargement)[10]

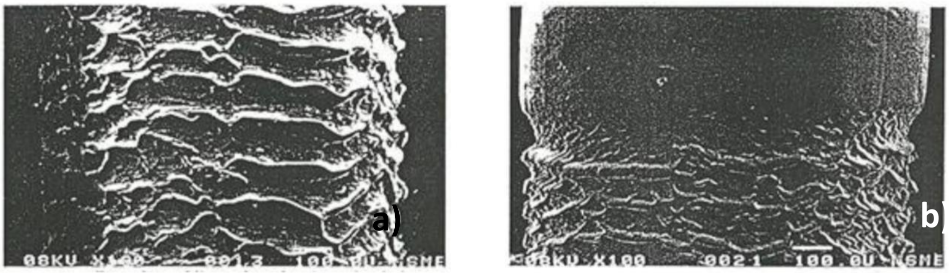

Fig. 7. Extrudates of linear low-density polyethylene (LLDPE) exhibiting sharkskin (a) and alternating sharkskin and somewhat smooth surface in the stick-slip regime (b) [17]

Very pronounced sharkskin is usually observed in linear polymers with a narrow molecular weight distribution (i.e. low polydispersity) and a high molecular weight such as HDPE and LLDPE. These types of polymers tend to have a lower melt strength than polymers with long chain branching, like LDPE. In branched polyolefins, sharkskin and stick-slip phenomena are almost non-existent. Branched polymers like LDPE possess a high melt strength. Therefore, the skin can stretch and subsequently relax without exceeding a critical tensile stress that may cause rupture [18].

The sharkskin effect can be reduced by lowering the shear rate, streamlining the die, slowing the extruder rate, reducing the melt viscosity, and increasing the die temperature [19].

3.5 Melt fracture

Melt fracture is a volumetric gross flow instability that originates at the die entry or in the die land. The term “fracture” is really a misnomer, considering that there is no breaking of anything involved [10]. Molten polyethylene flowing out of a pipe visible at the top is in Fig.8. The flow rate increases from left to right. In the two leftmost photographs the extrudates are nice and smooth, while in the middle one undulations start to develop. As the flow rate increases even further towards the right, the amplitude of the undulations gets stronger. When the flow rate is enhanced even more, the extrudate can break. Hence the name "melt fracture". Melt fracture defects of biodegradable PLA are shown in Fig. 9 [20].

Industrial extrusions usually do not go beyond the shear rate for the onset of sharkskin. However, in the production of pellets (frequently of about 3 mm in diameter) the melt is extruded through numerous holes and extrudates are water cooled and cut by moving knives. At high output rates the critical stress for the onset of melt fracture can easily be exceeded. Cutting of highly distorted polymer strands usually results in production of fine particles, together with the pellets, which are an impediment to subsequent handling operations and feeding of extruders. Thus, melt fracture is not only of scientific interest, but also of practical importance. For some polymers, melt fracture is apparently related to entry flow instabilities [10]. It is most common with polyethylene and can be eliminated by running the melt or the die lips hotter, using a longer or more streamlined die, or trying a different grade or source of material. Additives may help greatly in this regard [10].

The melt fracture effect can be reduced by lowering the shear rate, raising the temperature, using the material of lower molecular weight, using the correct additives and maintaining the speed of extruder [19].

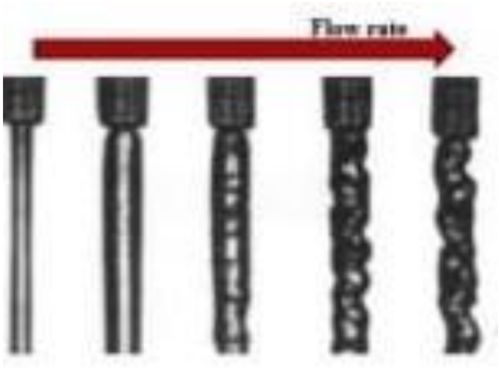

Fig.8. Melt fracture defect of material polyethylene depending on flow rate [12]

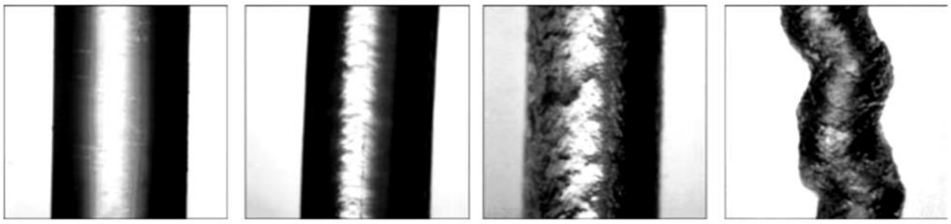

Fig. 9. PLA 4042D extrudates at different shear rates and wall shear stresses. From left to right the values of γ_{app} are 100, 200, 600 and 2500 s^{-1}, while the corresponding values of τ_w are 0.16, 0.22, 0.33 and 0.45 MPa [20]

3.6 Weld Lines

Lines in the extruded product can result from weld lines. These form when the polymer melt is split and recombined in the die or even before the die. Weld lines are also called knit lines; they can form in tubing and pipe dies where a mandrel is held in place by spider supports. The polymer melt is split at the start of the spider leg and flows together again behind (downstream) the spider support. Because of the limited mobility of long polymer molecules, it takes a certain amount of time for the molecules to re-entangle. This re-entanglement process is also called a “healing” process. Longer molecules take longer to re-entangle. As a result, high molecular weight (high viscosity) polymers are more susceptible to weld lines than low molecular weight (low viscosity) polymers. If the residence time is longer than the healing time, the weld line will disappear inside the die and not cause a problem in the extruded product. However, if the residence time is shorter than the healing time, the weld line will not disappear inside the die and the weld line will cause a problem in the extruded product. The weld line problem can be reduced or eliminated by increasing the residence time in the die or reducing the healing time of the polymer melt [16].

In polymer processing, weld lines can be formed by joining two different fluid fronts or when a fluid breaks up due to the presence of an obstacle, then re-joins downstream. Figure 10 shows how a weld line forms in a die.

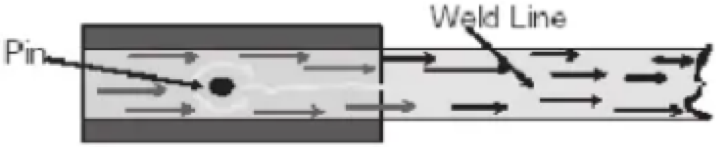

Fig.10. Weld or knit line formation [21]

Possible corrective actions to improve weld line strength are raise barrel temperature, remove any foreign material or contaminate from die, increase the time the flow fronts, increase flow restriction in the die, change the die design to incorporate mixing after the flow fronts, increase pressure on molecules forcing them together [20, 21].

3.7 Warpage

Warpage is a type of distortion where the surface of part does not follow intended shape of design [22]. Warpage is caused by the differential or nonuniform shrinkage in the extrudate cross section. This is often referred to as internal stresses in the part resulting from the molecular orientation, molecular relaxation outside the die, or molecular orientation induced in the final product by drawing. [19, 23].

Proper part cooling is critical to produce warpage free parts with the acceptable dimensions and performance. Part warpage is caused by differential shrinkage. To minimize differential shrinkage, the part must be cooled uniformly on all sides. If one side or area of the extrudate solidifies before another, the part will warp, bending toward the side that solidified last. If one side of the extrudate is dragged over an object in the cooling operation, molecular orientation is induced on that side, causing it to shrink differently from the other side, leading to warpage [23].

Pressure exerted by the puller must be sufficient to prevent product slippage in the puller, but low enough to prevent part distortion or marks on the product surface. Extreme puller pressure can crush the final part, rendering it useless. The puller may be a long distance from the extruder; however, it must be properly aligned with the extruder to prevent the part from being pulled in one direction or another, inducing molecular orientation that may lead to warpage [19,23].

The warpage effect can be reduced by properly aligning the puller with the extruder and balancing the melt temperature [19].

3.8 Sink

Sink is defined as an indentation in the surface opposite a rib or boss. This is generally a problem only in profile extrusion. Sink is caused by shrinkage. Where a flat area intersects with a rib, there is more material present in the cross section. As the material cools, more shrinkage occurs in the thicker section, causing a surface indentation opposite the rib. Indentation is minimized by decreasing the rib width and rib width and the radius going into the rib. However, a very narrow rib compared to the part's main thickness can lead to warpage due to the rib cooling and shrinking faster versus the rest of the part [23]. Possible corrective actions to improve sink is change the part design.

4. Minimizing defects in extrusion process

In many cases, the production of defect product can be minimized if the operator makes basic checks before, and/or during, production. For example, operator must check that the extruder appears to be functioning correctly and that the machine is set correctly. The material fed to the machine must be carefully checked.

4.1 Feedstock Checks

Regarding the feedstock, the operator must check that the:

- Correct types of material are being used
- Correct grade of materials is being used
- Correct level of materials (such as masterbatch and regrind) are being used
- Material is free of contamination
- Material is dry and free from an excessive concentration of fines

4.2 Temperature-Related Settings

Temperature-related settings or parameters cause many problems. The operator must check that the:

- Thermocouples are not loose in their mounting holes
- Thermocouples are of the correct type
- The feed throat is at the correct temperature
- The hopper is at the correct temperature
- The barrel and die are at the correct temperatures
- The melt is at the correct temperatures (in order to be accurate, the melt temperature must be measured with an immersion thermocouple)
- The specified volumes of water are circulating through the feed throat and rolls, so they are at the required temperatures

4.3 Speed Settings

Check that the rotational speed of the screw (in rpm) is being correctly measured and displayed, and that the draw down, or haul off, speed of the rolls (in rpm) is being correctly measured and displayed.

4.4 Die and Ancillary Equipment Checks

With regard to the die, the operator must check that:

- The die lips are clean and polished
- The die is properly set
- Any adjustable parts of the die function smoothly and correctly
- The correct screen pack has been fitted
- The ancillary equipment is properly set and that all the parts function smoothly and correctly
- All parts of the die and the ancillary equipment are at the correct temperature [23]

5. Conclusion

Extrusion is a high-volume processing method in which plastic material is melted with the application of heat and extruded through die into desired shape. A cylindrical rotating screw is placed inside the barrel which forces out molten metal plastic material through a die. Significant parameters affecting the quality of products includes take off speed, temperature of transition and metering zone. Analysis of the various defects in the extrusion process is necessary to minimize the causes of their occurrence in the extrusion product. The task of the manufacturers is to produce the best possible extrusion product. Quality problems (causes) become mainly inappropriate setting of operating parameters. Applying the above remedies would improve the percentage of product losses and increase the quality of extruded products.

Acknowledgements

This project has received funding from the European Union's Horizon 2020 research and innovation programme under the Marie Skłodowska-Curie grant agreement No. 734205 – H2020-MSCA-RISE-2016.

References

[1] Belofsky H., Plastics: Product design and process engineering, Hanser Publishers, 1995, pp. 631, ISBN: 978-1-56990-142-7.

[2] Lafleur P.G., Vergnes B., Polymer Extrusion, ISTE Ltd., London, pp.337, ISBN 978-84821-650-1.

[3] Raju G., Sharma M. L., Meena M. L., Recent Methods for Optimization of Plastic Extrusion Process: A Literature Review, International Journal of Advanced Mechanical Engineering, 2014, 4 (6), 583 -588.

[4] Narasimha M., Rejikumar R., Plastic pipe defects minimization, International Journal of Innovative Research & Development, 2013, 2 (5), 1337-1351.

[5] Khan J.G., Dalu R. S., Gadekar S.S., Defects in extrusion process and their impact on product quality, International Journal of Mechanical Engineering and Robotics Research, 2014, 3 (3), 187-194.

[6] Pilar Noriega E. M., Rauwendaal Ch., Troubleshooting the Extrusion Process: A Systematic Approach to Solving Plastic Extrusion Problems, 2nd Edition, Hanser Publishers, Munich, 2001, pp. 158, ISBNs 978-1-56990-470-1.

[7] Rauwendaal Ch., Understanding Extrusion, 2nd Edition, Hanser Publishers, Munich,2010, pp.231, ISBNs 978-1-56990-453-4.

[8] Sikora J.W., Samujlo B., Impact of feed opening width and position on PVC extrusion process effectiveness, International Polymer processing, 2013, 28 (3), 291-299.

[9] Agassant J.-F., Arda D.R., Combeaud C., Merten A., Münstedt H., Mackley M.R., Robert L., Vergnes B., Polymer Processing Extrusion Instabilities and Methods for their Elimination or Minimization, International Polymer Processing, 2006, 21 (3), 239-255.

[10] Vlachopoulos J., Polychronopoulos N., D., Understanding Rheology and Technology of Polymer Extrusion, First Edition, Polydynamics Inc, Dundas, ON, Canada, 2019, ISBN 978-0-9952407-3-5.

[11] Denn M.M., Polymer Flow Instabilities, Chemical Engineering Education, 162 (summer 1994).

[12] https://www.slideshare.net/HanyAmer4/polymer-extrusion-problems-defects

[13] https://www.ptonline.com/articles/stop-those-gels

[14] Kumar S., Rao P.S., Impact of extrusion process on product quality, International Research Journal of Engineering and Technology, 2019, 6 (1), 115- 124.

[15] https://www.ptonline.com/articles/extrusion-without-discolored-specks

[16] Pawar S. B., Quadri S. A., Dolas D., Root cause analysis of extrusion process defects in PVC pipe manufacturing, Journal of Emerging Technologies and Innovative Research, 2019, 6 (3), 246-250.

[17] Pudjijanto S., Denn M.M., A Stable "Island" in the Slip-Stick region of Linear Low-Density Polyethylene, Journal of Rheology, 1994, 38 (6), 1735.

[18] Miller E., Rothstein J.P., Control of the Sharkskin Instability in the Extrusion of Polymer Melts Using Induced Temperature Gradients, Rheologica Acta, 2004, 44, 160 - 173.

[19] Patil P. M., Sadaphale D.B., A Study of Plastic Extrusion Process and its Defects, International Journal of Latest Technology in Engineering, Management & Applied Science, 2018, VII (IX), 13-20.

[20] Kanev D., Takacs E., Vlachopoulos J., Rheological Evaluation and Observations of Extrusion Instabilities of Biodegradable Polyesters, International Polymer Processing Journal of the Polymer Processing Society, 2007, 22 (5), 395 - 401.
[21] Giles H., F. Jr., Wagner J.R. Jr., Mount E.M., Extrusion: The Definitive Processing Guide and Handbook, William Andrew publishing, NY, 2005, 560 pp., ISBN 0 8155 1473 5.
[22] Keleshian N., Kyser R., Rodriguez J., Cueva C., Vega V., Lee E.W., Ogren J., Es-said O.S., On the Distortion and Warpage of 7249 Aluminum Alloy After Quenching and Machining, Journal of Materials Engineering and Performance, 2011, 20(7), 1230-1234.
[23] Giles H.F., Wagner J.R., Jr. Mount E.M., Extrusion: The Definitive Processing Guide and Handbook, William Andrew publication, 2005, ISBN: 0-8155-1473-5.
[24] Goff J., Whelan T., The Dynisco Extrusion Processors Handbook, Dynisco company. 1988.

Ivan Gajdoš[1], Emil Spišák[1], Volodymyr Krasinskyi[2]

SIMULATION OF EXTRUSION BASED ADDITIVE MANUFACTRUING TECHNOLOGIES

Abstract: *To unlock the full value additive manufacturing has to offer, simulation tools are needed to predict and mitigate part warpage as well as realize the impact of design decisions on the manufacturing process before the part is printed. Several challenges face the development of this process simulation. The complex thermomechanical loadings that occur during the layer-by-layer deposition of the material and the successive cooling of the part. The position of bead deposition creates specific microstructures based on the printing toolpath pattern, which drives the macroscopic mechanical behavior – typically inducing anisotropy. The thermal history of the material deposition generates differential shrinkage between adjacent beads or layers that affects the end tolerances of the part. Presented treaties describes issues connected with simulation of extrusion based additive manufacturing and simulation workflow of Fused Filament Fabrication (FFF) 3D printing with Digimat-AM including results interpretation and cost estimating.*

Keywords*: additive manufacturing, Fused Filament Fabrication, Digimat-AM*

1. Introduction

Todays' major challenge is the shift from metal to composite to bring significant weight saving in the design. This paradigm however requires a dedicated tool for composite design to consider the specific composite behavior. Classical design tools are not able to describe accurately the local composite material behavior, leading to introduction of safety factors and lack of confidence in the design. CAE simulation software provides design tools that give the user confidence in their composite's products thanks to an accurate description of the local composite behavior. Accurate material modeling allows one to reduce the "factor of safety" - allowing composite materials to used close to 100% of their potential, maximizing their competitiveness against metal and leading to substantial weight reduction. CAE tools are commonly integrated within the current FEA process, bridging the gap between manufacturing process and structural analysis [1,2].

Simulating the fabrication process is slowly becoming part of the 3D Printing workflow [3]. 3D printing simulations help to understand and visualize the complex

---

(1) *Technical University of Košice, Faculty of Mechanical Engineering, Department of Technologies, Materials and Computer Aided Production, Masiarska 74, 040 01, Košice, Slovakia, ivan.gajdos@tuke.sk, emil.spisak@tuke.sk.*

(2) *Lviv Polytechnic National University, Department of Chemical Technology of Plastics, 12 S. Bandera, 79013, Lviv, Ukraine, vkrasinsky82@gmail.com.*

thermo-mechanical phenomena taking place during manufacturing, resulting in the production of high-quality, high-accuracy parts.

This is especially important for high-value components fabricated using state-of-the-art 3D printing process, where design iterations (discarding a defective print) are very expensive in terms of both material cost and manufacturing time.

Simulations of the 3D printing process should not be confused with the more common mechanical FEA simulations: The latter helps evaluate the mechanical performance of a part under certain conditions related to its function (load, deformation, temperature etc.), while the former helps predict the result of the 3D printing manufacturing process, layer-by-layer and under certain process parameters.

For Additive Manufacturing to make a successful transition to a standard production technique, dedicated design and engineering tools are required. By enabling as-manufactured part performance predictions – and therefore design optimization, integrative simulation is certainly a must. By accounting for the printing direction and the effects of defects, customers are now able to perform accurate structural analyzes and bring more confidence in the design validation of Plastic and Composite parts.

Simulating the 3D printing process is very valuable, because it helps to avoid print failures and parts rejected for geometric issues, saving time, and reducing overall cost. Simulation of 3D printing enables production risk evaluation, understand the physics of the manufacturing process, predict the microstructural characteristics of the end part, optimize production to improve manufacturing speed, reduce post-processing operations or improve accuracy by reducing the part and support deformation [2].

The simulation can be applied in the pre-processing stage, on model with or without support structures. Before support generation, simulation results help identify critical areas of significant deformation or internal stress during manufacturing. The designer can then add adapted support structures to minimize the deformation, change the print orientation to change the areas of heat accumulation or modify the geometry of the 3D model to improve the quality of the result [4].

After support generation, simulations help minimize the risk of production failure (for example due to recoater interference), ensure that the dimensions of the final part lie within a specified tolerance range and evaluate the impact of different print parameters (for example, by comparing parameters optimized for production versus parameters optimized for accuracy).

In both cases, simulations aid in reducing the risk associated with high-value manufacturing and to improve the productivity of high-volume 3D printing, saving weeks of production time and thousands of dollars in development and production costs [5].

MSC DIGIMAT-AM

Digimat-AM™ is a solution of Digimat Software™ that simulates the printing process and helps printer manufacturers and end-users to identify manufacturing issues. It also optimizes printing parameters for productivity and final part performance prior to printing the first part. The use of numerical simulation allows you to turn hundreds of trials and errors into a couple of clicks in Digimat-AM.

Digimat-AM provide process simulation solutions [6]:

- Simulate the FFF, FDM, SLS and CFF processes of unfilled and reinforced materials.
- Predict the as-printed part warpage, residual stresses and process-induced microstructure.
- Analyze the coupled thermal-structural response of the process for unfilled and reinforced polymers.
- Set up the right manufacturing parameters for high precision printing and further bridge the gap between printing process, material and part performances.
- Digimat-AM simulation solution for Additive Manufacturing allows to:
- Choose additive manufacturing process.
- Select the printer from a dedicated database with predefined parameters or specify user-defined parameters.
- Select the material grade (reinforced or unfilled polymer) and the associated material model from Digimat-MX database.
- Create the voxel mesh of the part.
- Solve the thermo-mechanical or thermal finite element analysis simulating the printing process
- Post-process and export the results of the process simulation (stress/strain fields (Fig.1), warped part shape, …).

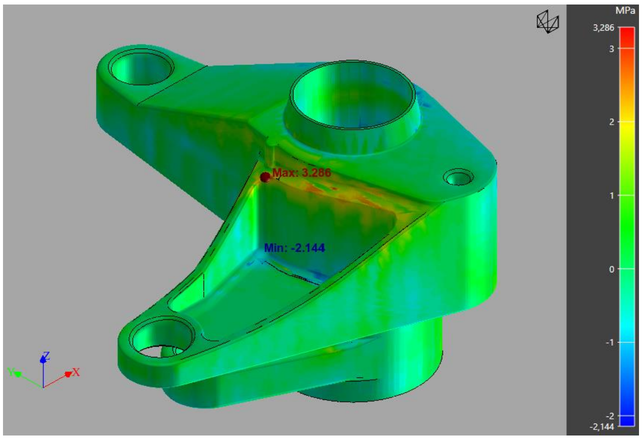

Fig. 1. Residual stress prediction in Digimat-AM [6]

Digimat-AM introduces a 4-step guided workflow to predict and optimize the additive manufacturing process of polymers and composites. These four steps they consist of:

- Definition: this first step allows to select the desired printing process, a specific printer, as well as to describe the component to manufacture. The latter is defined by its geometry (which can be obtained by topology optimization for instance) and its material (unfilled or reinforced polymer).
- Manufacturing: this second step enables to describe how the component is manufactured. This consists of various inputs, such as the positioning, the slicing (Selective Laser Sintering), the toolpath (Fused Filament Fabrication - FFF and Fused Deposition Modeling - FDM), the warpage compensation strategy, the manufacturing steps order and other general process parameters which depend on the process type. By the end of this section, the manufacturing of the part is completely described, and ready to be simulated.
- Simulation: this third step translates the Definition and Manufacturing in an actual FEA simulation. Voxel meshing of the geometry is proposed, solution methods can be chosen, as material model parameters adjusted. Finally, once the simulation model is ready, it can be submitted and monitored until job completion.
- Results: Post-process of the simulation results, such as field visualization of displacement and stresses, analysis of warpage indicator, visualization of warped shape and cut models, history plot, custom reference planes and export of simulation results (warped geometry, residual stresses, ...)

Those four steps allow in a generic way to solve the multiscale thermomechanical simulation problem of additive manufacturing of polymers and composites.

1.1 FFF printing process analysis workflow

Comprehensive analysis and optimization of the additive manufacturing process FFF can be performed through various approaches.

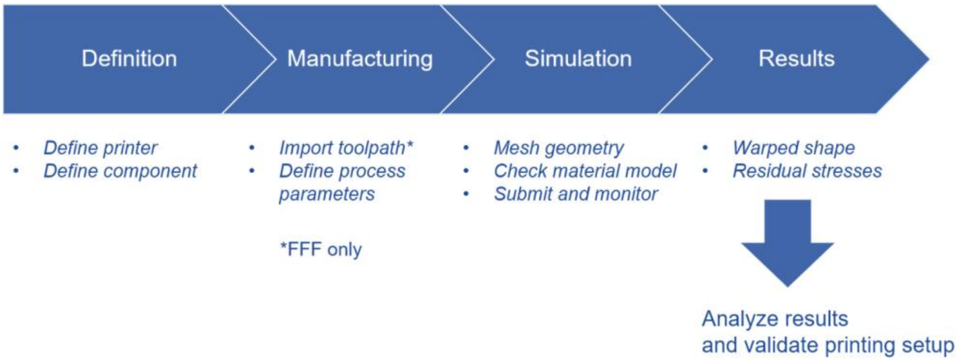
Definition
Manufacturing
Simulation
Results
• Define printer
• Define component
• Import toolpath*
• Define process parameters
*FFF only
• Mesh geometry
• Check material model
• Submit and monitor
• Warped shape
• Residual stresses
Analyze results and validate printing setup

Fig. 2. Workflow to predict warpage and residual stresses in 3D printed part [1]

Predict warpage and residual stresses of a component: this linear workflow (Fig.2) is the basic application allowing to analyze the warpage and residual stresses that result from the additive manufacturing process, as the combination of process parameters and material choice. It allows to validate that a part can be printed physically with a mastered level of warpage and residual stresses.

Optimize process settings (Fig.3): while the linear workflow described above gives a static picture of the consequence of process setting choices, it is also possible to identify what process settings could be optimized to meet a given objective (minimized warpage, minimized residual stresses, minimized printing time, ...). This workflow requires iterations over Digimat-AM manufacturing step parameters. For each process setting change (process parameter and/or toolpath for FFF), a new simulation can be run and results compared with baseline results. By the end of this workflow, process settings for the physical printing can be adapted based on the conclusion of the optimization performed via Digimat-AM usage.

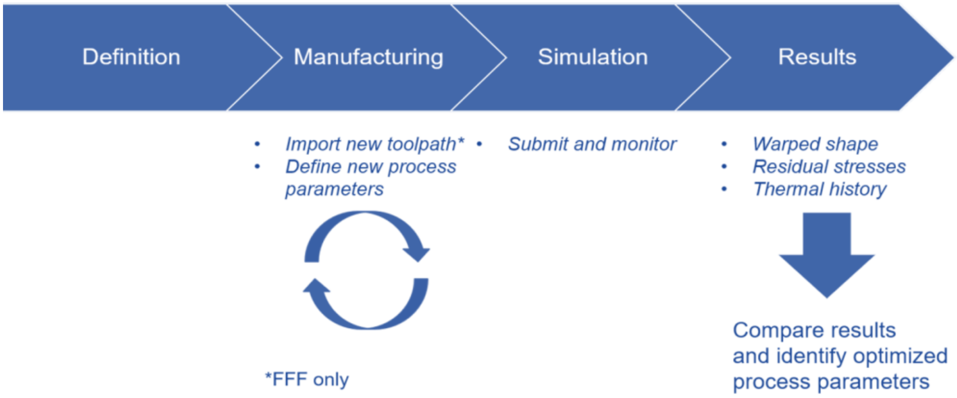
Definition
Manufacturing
Simulation
Results
• Import new toolpath*
• Define new process parameters
• Submit and monitor
• Warped shape
• Residual stresses
• Thermal history
Compare results and identify optimized process parameters
*FFF only

Fig. 3. Optimization of processing parameters workflow

Optimize material choice (Fig.4): another possibility of optimization workflow consists of identifying which material provides the best manufacturing performance. This workflow requires iteration over the material definition of the component in Digimat-AM. This material change can target a slight change of material properties, a complete change of resin, or the exploration of the addition of fillers (bead or fiber) to the polymer resin. Once the material definition is updated, it can then be required to adjust process parameters, accordingly check the material model definition and finally run a new process simulation. Once all material candidates have been tested, the optimized material choice can be performed, and final material selection for optimal physical printing can be achieved.

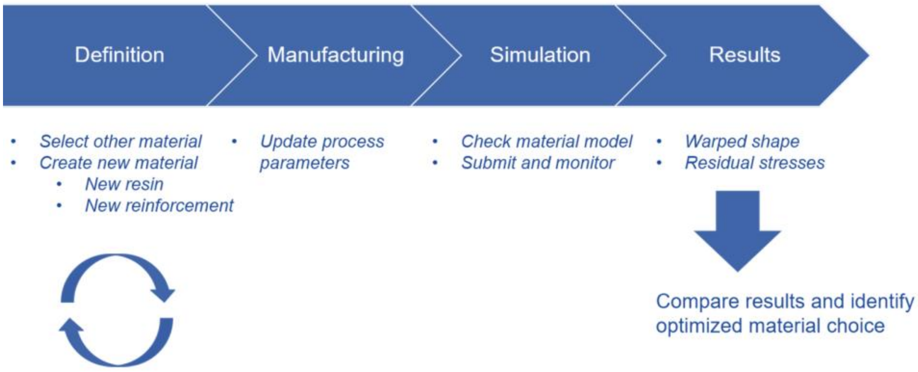
Definition
Manufacturing
Simulation
Results
Select other material
Create new material
New resin
New reinforcement
Update process parameters
Check material model
Submit and monitor
Warped shape
Residual stresses
Compare results and identify optimized material choice

Fig. 4. Optimization of material selection process

Compensate for warpage (Fig.5): a common additive manufacturing issue concerns warpage. The as-printed geometry is usually not corresponding to the as-designed geometry, because of the complex thermomechanical loadings that occur during the layer-by-layer deposition of the material and the cooling of the part once it is printed. A solution to circumvent this situation consists of compensating the geometry to be printed, by specifying it such that after warpage, the as-printed geometry is sufficiently close to the as-designed geometry. Digimat-AM provides an efficient workflow for warpage compensation by allowing. to export a counter-warped shape from the result step, and then using it in the manufacturing step as a compensated geometry (alternatively, a simple anisotropic scale factor can also be applied on the as-designed geometry). By running a new simulation using compensated geometry, it can be checked that the as-printed geometry becomes like the as-designed geometry. If needed, several iterations of counter-warped shape export followed by simulation run on compensated geometry can be performed. By the end of this workflow, the geometry to send to the physical printer is identified, such that physical printing will yield the right as-printed geometry.

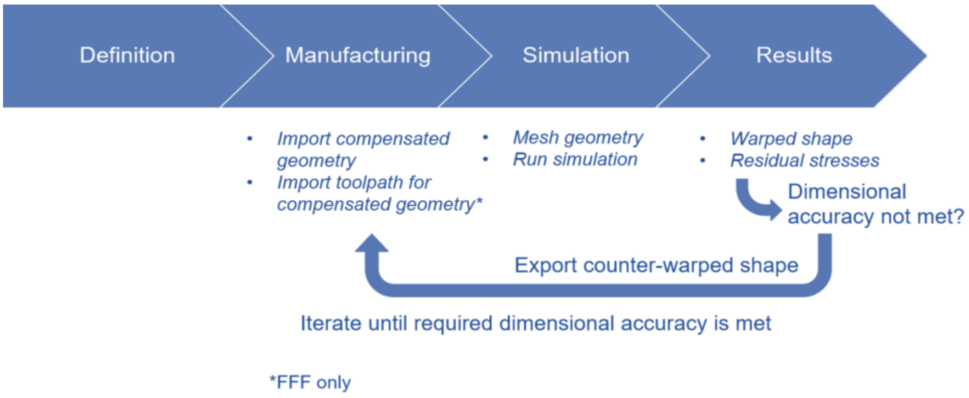
Definition
Manufacturing
Simulation
Results
Import compensated geometry
Import toolpath for compensated geometry*
Mesh geometry
Run simulation
Warped shape
Residual stresses
Dimensional accuracy not met?
Export counter-warped shape
Iterate until required dimensional accuracy is met
*FFF only

Fig. 5. Steps for warpage compensation of printed model

FFF MANUFACTRUING SIMULATION

The Simulation step turns the input from Definition and Manufacturing into an actual advanced finite element analysis. The simulation approach in Digimat-AM is either based on a multiscale workflow or a full transient simulation. In the multiscale workflow, a highly coupled thermomechanical analysis is first performed at the micro-level, allowing to identify the warpage behavior of the material for some given process conditions. This warpage behavior, described by inherent strain values, is then used during a macro-level mechanical layer-bylayer FEA, thereby significantly reducing the computational cost of the macro part analysis. In the full transient workflow, layers or chunks of filament (for FFF/FDM) are incrementally activated while observing the real printing process deposition speed.

Full transient simulation (thermomechanical or thermal) requires temporal discretization strategy [6]:

- Filament: the printing process is closely simulated by incrementally adding chunks of deposited filament. The amount of newly added filament is precomputed based on the user specified time increment.
- Layer-by-layer: In the layer-by-layer method, finite element layers are activated rather than chunk of filament for the filament discretization.

For the Layer-by-layer deposition, the voxel size is suggested for several meshing strategies (Fig.6):

- coarse: mesh size corresponds to 10 times the printed layer thickness
- medium: mesh size corresponds to 5 times the printed layer thickness
- fine: mesh size corresponds to 2 times the printed layer thickness

For the Filament deposition method (transient FFF or FDM only), the mesh size is imposed as the layer thickness.

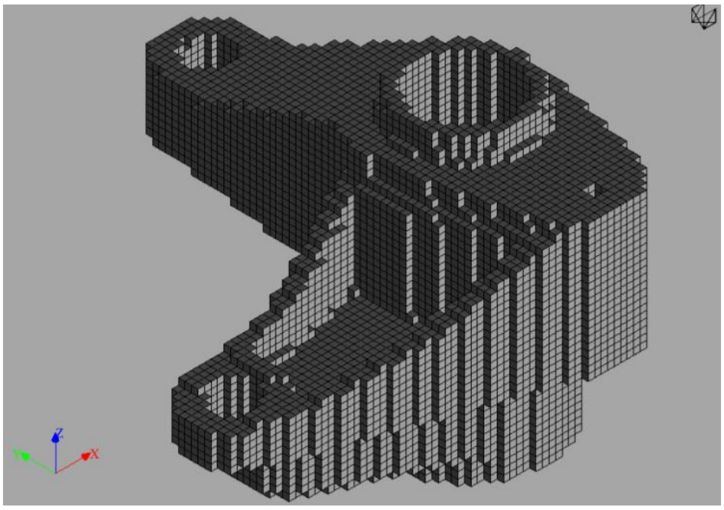

Fig. 6. Voxel mesh of printed model

The mesh size will have an influence on the prediction of the residual stresses, but a rather minor influence on the displacement results (warpage). The mesh size should also be chosen as a function of the component geometry. If very thin walls are present, the mesh size should be reduced to represent these dimensions accurately. However, the mesh size cannot be smaller than the layer thickness. A too coarse voxel mesh could lead to a finite element model which does not represent the geometry sufficiently accurately.

RESULTS POSTPROCESSING

When a simulation is complete, results automatically become available and can be used for result interpretation. The available result fields in Digimat-AM 2021.1 are:

- **Stresses** (Fig.7): All stress components and von Mises stress are available. These fields indicate what are the residual stresses that build up during and by the end of the manufacturing.

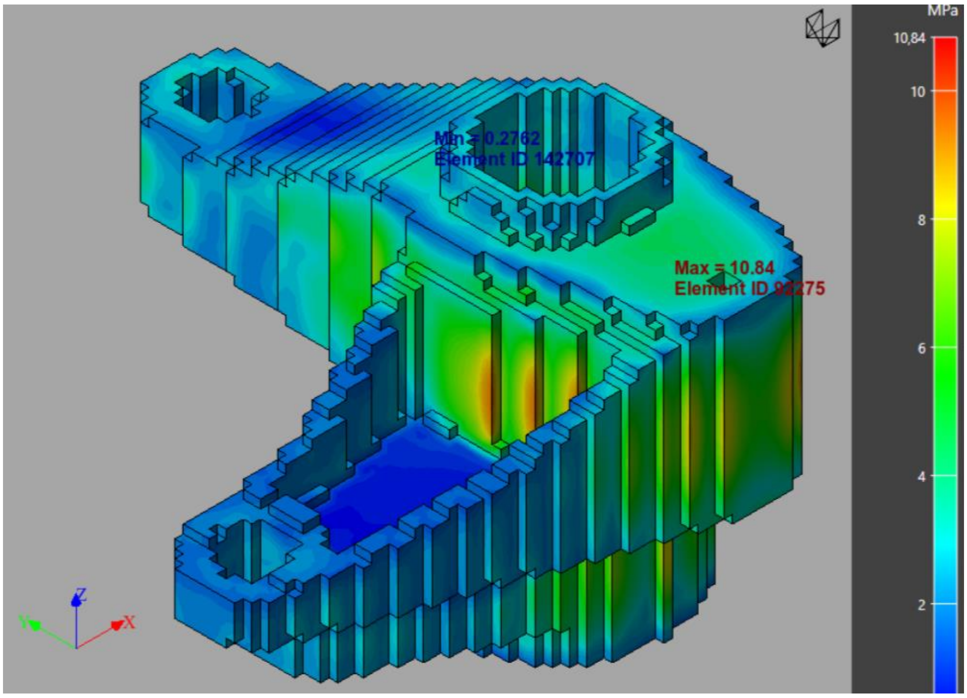

Fig. 7. Distribution of residual stresses at the end of the manufacturing (von Mises stress field) [6]

- **Deflections** (Fig.8): All deflection components and deflection norm are available. These fields show the change of geometry that occurs along the full manufacturing cycle, which are to be used to analyze the warpage.

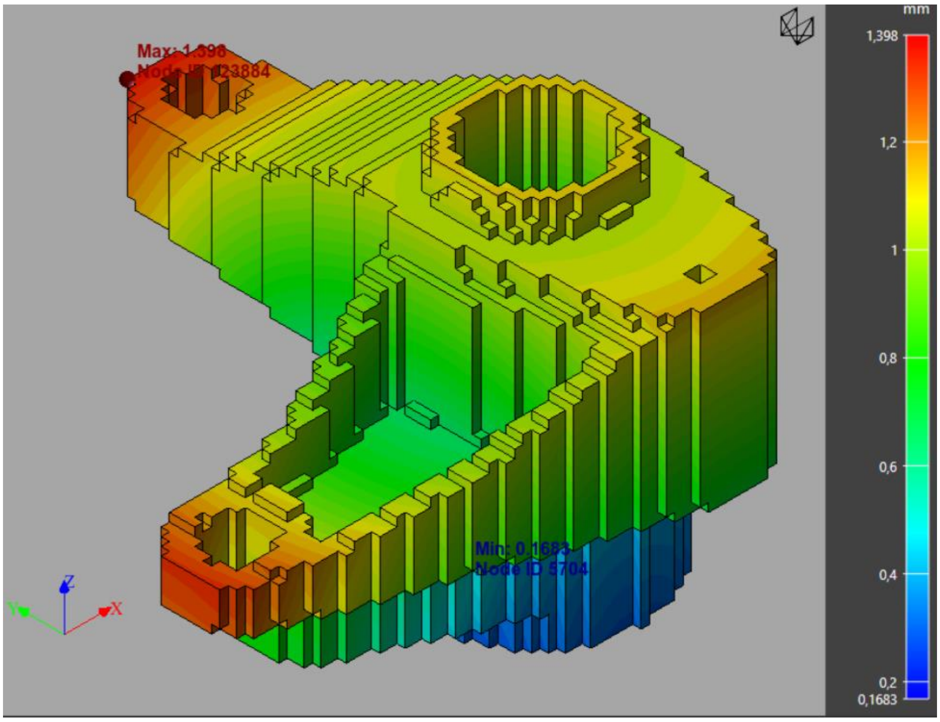

Fig. 8. Plot of deflection (deflection norm field) [6]

- **Warpage indicator** (Fig.9): The warpage indicator allows to check which regions on a part respect a user defined dimensional tolerance. Two warpage indicators are available:

– The total warpage indicator.

– The warpage indicator without shrinkage. This field is available for warpage analyses based on inherent strains when support removal precedes cooling in the manufacturing steps.

There are three possible colors for the warpage indicator, which depend on the user-defined warpage critical value:

– green: shows regions that have a local warpage less than a user-defined percentage of the warpage critical value (by default 80%). These regions thus fully respect the required dimensional accuracy defined by the warpage critical value.

– yellow: shows regions that have a local warpage higher than the green region, and smaller than a user-defined percentage of the warpage critical value (by default

120%). These regions can show a slightly higher warpage than the acceptable one. They should be treated with care.

- red: shows regions that have a local warpage higher than the yellow region: these regions show too much warpage, which usually means that process conditions must be revised to reduce the warpage.

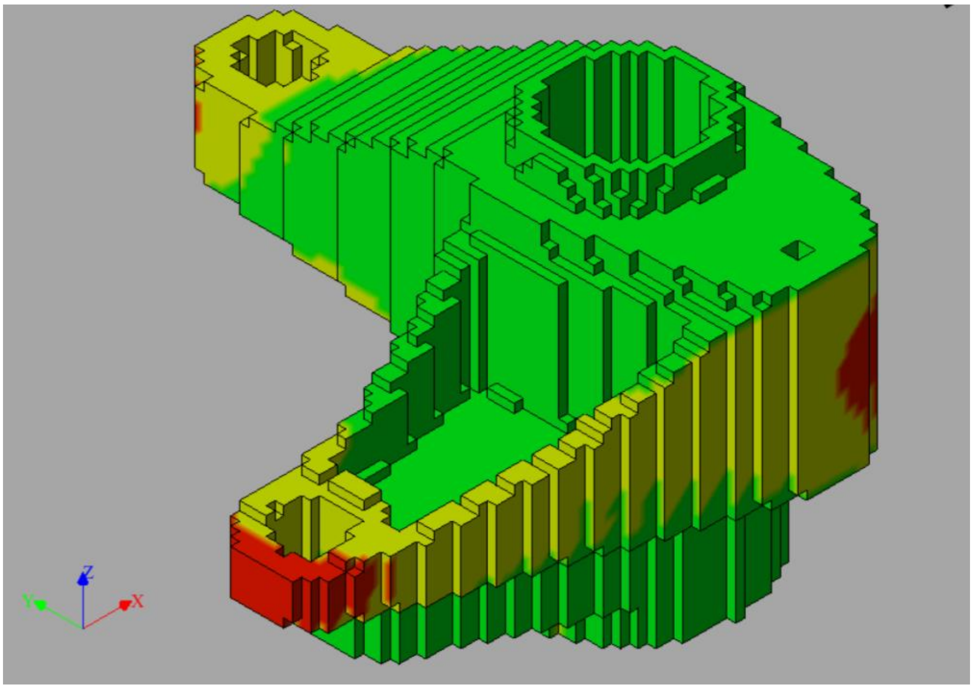

Fig. 9. Warpage indicator result [6]

- Temperature: The temperature field is available.
- Breaking index: When enabled, for FFF and FDM, the breaking index of the support failure criterion is available. When its value is higher than 1, this indicates a risk of decohesion from the support plate.
- Degree of crystallinity: For semi-crystalline materials, the degree of crystallinity is available when using a crystallization kinetics model.
- Porosity: For FFF and FDM, thermal and thermomechanical procedures, a local porosity is computed based on the amount of material really printed in each voxel. This local porosity is introduced in the simulation to compute the local effective material property and achieve accurate predictions for coarser voxel sizes.
- Shape tolerance (Fig.10): The shape tolerance field provides the maximum normal distance to the reference surface. The reference geometry can be the imported model or the simulated deformed geometry when comparing to a

dimensional scan. The shape tolerance allows to compare geometries in a similar way to a dimensional control of manufactured part. This allows a consistent comparison between part design, simulation results and, when available, a part scan.

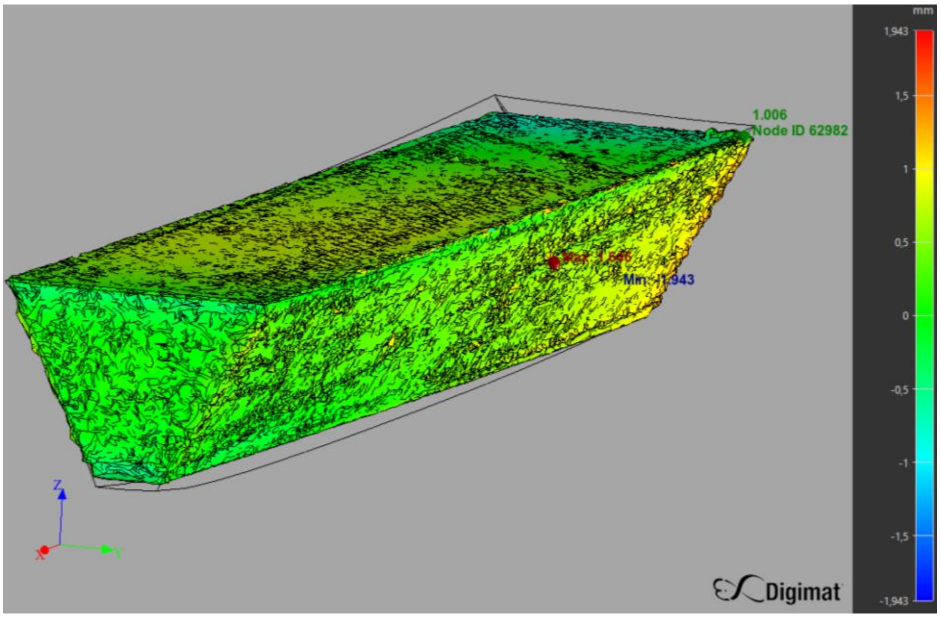

Fig. 10. Comparison between the deformed geometry and a scan geometry [6]

COST ANALYSIS

Tool integrated into Digimat-AM allows to estimate the cost of the printed model with current printing setup. To calculate the price of the printed model these factor is taken into account:

- Material cost: for considering the cost of the material usage in printing, some inputs asked as: the price of material for part and support. The mass of part and support can be computed in AM automatically
- Machine cost: the depreciation cost of printer machine can be considered here with the cost of the printer in purchase and maintenance per year, total service time of the printer in plan, printer taken time in each batch contains setup time, preheating time, printing time, cooling time, removing/clean time and some idling time when the printer is assigned to the project but not really used.
- Labor cost: the cost of labor on the whole printing period, which can be computed with the labor price and the taken time as printer.
- Post processing cost: the cost on the post processing treatment for each part after printing, which can be estimated with

– The cost for post-processing material by mass
– The mass to be treated in each part
– The labor time for post-processing each part

- Energy cost: the electricity cost during the printing period which can be computed with the electricity price and the power of the printer when preheating, printing and cooling
- Design cost: design cost can be considered with the design time and labor price of the design engineer
- Other cost: some additional cost not covered above can be considered here on time or on batch

As output, the cost and percentage for each section can be provided as total cost, average cost per batch or average cost per part (Fig.11). What should be mentioned that the cost for design will be considered in labor cost here. Several plots can be presented for analyzing the effect of parts number per batch on average cost.

- Average cost per part vs Total number of parts
- Average time per part vs Number of parts per batch
- Cost category contribution per part vs Total number of parts
- Total cost per part vs variable: single parameter sensitivity analysis can be plotted when the variable is input as V1;V2;V3;. . .

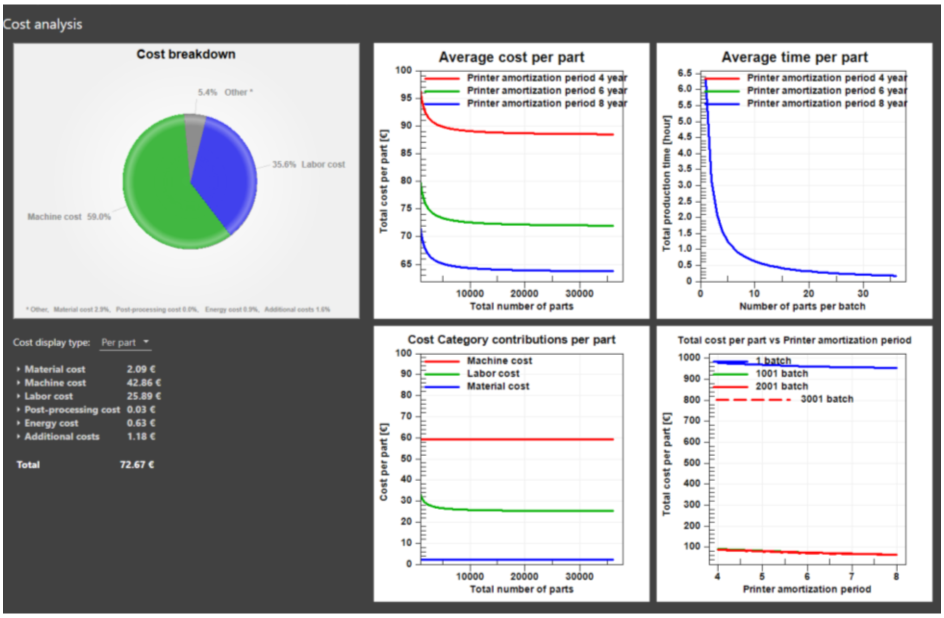
Cost analysis
Cost breakdown
5.4% Other *
35.6% Labor cost
Machine cost 59.0%
* Other, Material cost 2.9%, Post-processing cost 0.0%, Energy cost 0.9%, Additional costs 1.6%
Average cost per part
Printer amortization period 4 year
Printer amortization period 6 year
Printer amortization period 8 year
Total cost per part [€]
100
95
90
85
80
75
70
65
10000
20000
30000
Total number of parts
Average time per part
Printer amortization period 4 year
Printer amortization period 6 year
Printer amortization period 8 year
Total production time [hour]
6.5
6.0
5.5
5.0
4.5
4.0
3.5
3.0
2.5
2.0
1.5
1.0
0.5
0
0
10
20
30
Number of parts per batch
Cost Category contributions per part
Machine cost
Labor cost
Material cost
Cost per part [€]
100
90
80
70
60
50
40
30
20
10
0
10000
20000
30000
Total number of parts
Total cost per part vs Printer amortization period
1 batch
1001 batch
2001 batch
3001 batch
Total cost per part [€]
1000
900
800
700
600
500
400
300
200
100
4
5
6
7
8
Printer amortization period

Cost display type: Per part

Material cost	2.09 €
Machine cost	42.86 €
Labor cost	25.89 €
Post-processing cost	0.03 €
Energy cost	0.63 €
Additional costs	1.18 €
Total	**72.67 €**

Fig. 11. Cost analysis report

6. SUMMARY

It is very challenging to simulate and analyze phenomena occurring during model 3D printing with FFF technology. Some of the issues can be solved with Digimat-AM, which provides simulation and closer insight into whole process. Overall, modeling the printing process requires considering the material state evolution, to model the stress build-up as well as the stress relaxation over time. Numerical predictions of warpage need to account for the process parameters, the material characteristics, and the printing strategy.

Acknowledgements

This project has received funding from the European Union's Horizon 2020 research and innovation programme under the Marie Skłodowska-Curie grant agreement No. 734205 – H2020-MSCA-RISE-2016.

The authors gratefully acknowledge the financial support of the project IVG-21-03.

References

[1] Adam L., Assaker R., Hébert P., Lietaer O., Mathieu S., Additive manufacturing simulation solution as enabler for confident lightweight automotive design, CAMX Conference Proceedings. Dallas, TX, October 15-18, 2018, ISBN978-1-5231-2695-8
[2] Zhang Y., Chou Y.K., 17th Solid Freeform Fabrication Symposium, (2006).
[3] www.hubs.com/knowledge-base/simulations-3d-printing/ (1997)
[4] Schmitz G.J., Prahl U., Handbook of Software Solutions for ICME
[5] Dasappa P., Elleithy R., Ly K., 3D printing process simulations and their applications, ANTEC® 2018 - Proceedings of the Technical Conference & Exhibition, Orlando, FL, May 7-10, 2018, ISBN 978-1-5231-2650-7
[6] Digimat User´s Manual, Release 2021.1- December 2020

António Gaspar-Cunha[3]

OPTIMIZATION OF CONVENTIONAL AND BARRIER SCREWS

Abstract: *In this chapter results of the simultaneous optimization of conventional and Maillefer barrier for single screw extruder are presented and discussed. A multi-objective evolutionary algorithm was used to optimize the relevant geometrical parameters of both type of screws and its performance was evaluated using some important process performance measures, such as output, length of screw required for melting, melt temperature at die exit, mechanical power consumption, mixing degree and viscous dissipation. Two different polymers were studied, a low density polyethylene and a polypropylene. The results obtained allows to conclude that, depending on the particular situation, both screws perform well, being able to process the polymer in the desired conditions. Some dependence on operating conditions was also observed.*

Keywords: *single-screw extrusion, barrier screws, optimization, evolutionary algorithms*

1. Introduction

A considerable percentage of plastics are processed using extrusion-based techniques, of which single-screw extrusion is the most important one, mainly due to their lower cost and ease of operation. The employment of technological improvements in the plasticizing system, such as grooved barrel sections, mixing sections and barrier compression zones, with the aim to increase output, melting efficiency and the extrudate's homogeneity, makes this process much more flexible. The aim of this work is to apply multi-objective optimization techniques in the optimization of barrier screws and compare its performance with optimized conventional screws.

The main function of a barrier screw is to allow that the extruder melt the polymer within a certain screw length. For this purpose, a second screw flight is introduced at the beginning of the melting zone inducing the formation of two independent channels. Thus, the solids were maintained in the initial channel and, as the melting progress, the melted material is forced to move progressively to the secondary channel. In this way, the solids will never surpass the length defined to the barrier. The first barrier screw was patented by Maillefer in 1959 [1], then, other solutions, such as those proposed by Dray and Lawrence in 1970 [2], by Barr in 1971 [3], by Kim in 1972 [4] and by Ingen Housz in 1977 [5], were proposed.

---

[3] *Department of Polymer Engineering, Institute for Polymer and Composites, University of Minho, Guimarães, Portugal, agc@dep.uminho.pt.*

In a previous work (Gaspar-Cunha and Covas [6]) the barrier screws plasticizing system was modeled taking into account the thermomechanical phenomena occurring inside the barrel. For that purpose, the geometry of the barrier section was considered in such a way that most of the existing solutions can be accommodated. The model implemented in computer included solids conveying in hopper and in the first turns of the screw, delay in melting, melting, and melt conveying and, with the aim to consider the influence of the melting phase in the barrier section and to decouple the beginning and length of melting from the geometrical profile of the barrier. This is important, since, for example, if the screw speed increase the output decreases to accommodate melting before the end of the barrier section. In this way, it was possible to compute most of the important performance measures, such as output, mechanical power consumption, length for melting, melt temperature, degree of mixing and viscous dissipation. This computer model was assessed experimentally for Maillefer screws using different operating conditions and two different polymers [7].

Although the advance of the modelling and computer capacities, the design of barrier screws is still a based on trial-and-error using empirical knowledge and no recent efforts were made in order to design screws scientifically, even taking into account the importance of barrier screws [8, 9]. This only can be accomplished by coupling a modelling routine, able to predict the effect of relevant geometrical, material and operating parameters, and an optimization strategy, involving an optimization algorithm and a way of taking into account the multi-objective nature of the problem.

The present paper reports the development and implementation of a Multi-Objective Optimization (MOP) strategy using Evolutionary Algorithms (EA), to design barrier screws. The aim is to design simultaneously Conventional Screws (CS) and Maillefer Barrier Screws (MBS) in order to determine the conditions in which one of this type of screws performs better than the other.

This paper is organized as follows: in section two the geometry and the modelling of barrier screws is described; in section three the Multi-Objective Evolutionary Algorithm (MOEA) used is presented; in section four the results obtained are presented and discussed; and in section five the conclusion is stated.

2. Modelling

2.1 Maillefer barrier screw geometry

Figure 1 shows the geometry of the extruder used in the optimization process. The operating conditions, screw speed (N) and barrel and die temperature profile (T_{b1}, T_{b2}, T_{b3}, T_{b4}, T_{b5}, T_{die}) are kept constant, the aim being to define the geometrical parameters of the screws. For that purpose, the screws were unrolled and transformed in a rectangular channel. Figure 2 shows a schematic representation of the CS and MBS. As can be seen, CS is represented by a rectangular channel that decreases linearly its height in the compression zone, while the MBS has two channels that separates the solids from the melt, but also decrease its height. CS is characterized geometrically by: length of feed, compression and metering zones, external diameter, internal diameter in the feed and metering zones, pitch, flight clearance and thickness of the flight channel. The MBS has an additional flight in the compression zone with a different thickness and a higher flight clearance, thus the width of the solids and channels changes linearly The aim is that the melted polymer be able to cross from the solids channel to the melt channel thought this higher clearance. The solid bed profile in the CS depends on the operating conditions and the specify screw geometry and is usually non-linear. More details concerning MBS geometry are given elsewhere [6].

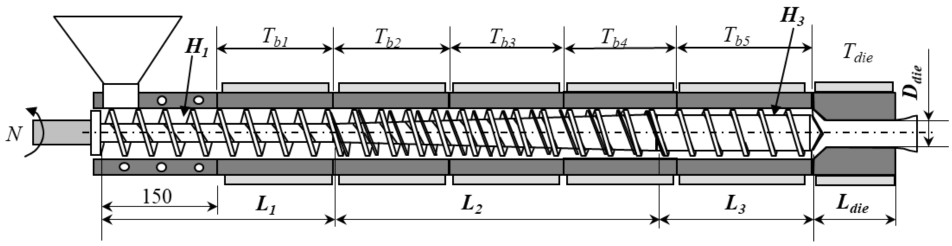

Fig. 1. Geometry of the extruder used in the optimization process: L_1 *–length of feed zone;* L_2 *–length of compression zone;* L_3 *–length of metering zone;* L_{die} *– die length;* H_1 *– channel height of feed zone;* H_3 *– channel height of metering zone*

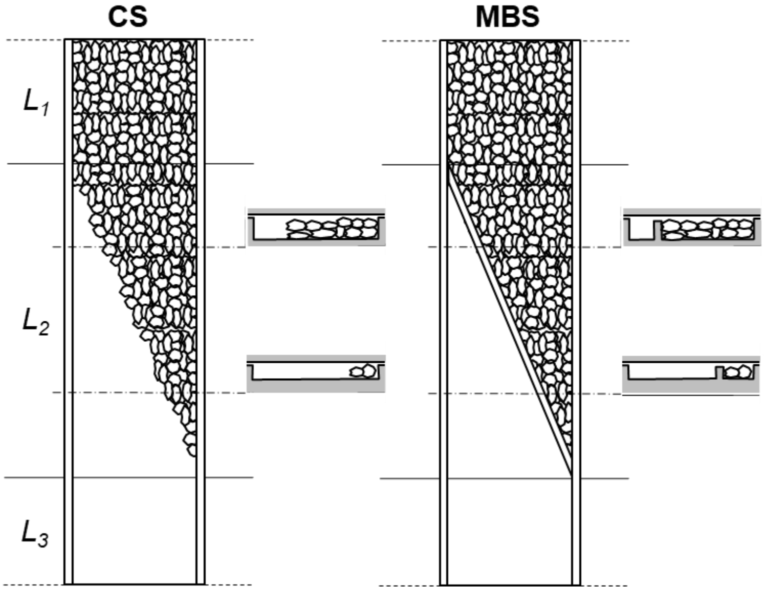

Fig. 2. Representation of CS and MBS

2.2 Modelling of barrier screws

In this work the computer modelling routine developed by Gaspar-Cunha and Covas [6] was adopted, which involves the following typical sequence of physical phenomena developing along the extruder:

i) - gravity conveying of the solid material in the hopper;

ii) - solids conveying in the first screw turns, due to the friction forces acting on the solid plug surfaces;

iii) - delay, characterized by the development of a thin film of melted material separating the solids from the surrounding metallic wall(s);

iv) - melting of the solids, with physical separation of the solids from the melt given that the freshly molten material flows through the flight clearance:

v) - melt conveying;

vi) - pressure flow through the die.

Most of these individual process stages have been studied systematically in the literature and global models linking coherently these steps were made available [10, 11, 12, 13]. However, the model used here was able to generalize the working of barrier screws by separating the thermomechanical phenomena taking place from the screw geometry, *i.e.*, from the location of the barrier [6]. In this way, depending on the operating conditions and on the material properties: i) melting can start before the barrier; ii) the melt pool can be developed, also, in solids channel; and iii) melting can finish before the end of the barrier. Please, see reference [6] for more details.

3. Optimization methodology

3.1 Multi-objective evolutionary algorithms

As stated above, most real optimization problems are multiobjective, since it is necessary to satisfy simultaneously several performance objectives, often conflicting. Mathematically, a multiobjective optimization problem can be de-fined as [14, 15]:

$$\begin{array}{lll} \text{maximise} & f_m(x_i) & i = 1,\ldots,N; \quad m = 1,\ldots,M \\ \text{subject to} & g_j(x_i) = 0 & j = 1,\ldots,J \\ & h_k(x_i) \geq 0 & k = 1,\ldots,K \end{array} \qquad (1)$$

where f is the objective function of the N parameters x_i, M is the number of objectives, g_j are the J ($J\geq 0$) inequality constraints and h_k are the K ($K\geq 0$) equality constraints. A straightforward way to tackle this problem consists in defining the relative importance of the objectives and using aggregation functions, *e.g.*, weighted sum, to obtain a single objective that can be solved by traditional single-objective methodologies.

However, solving more scientifically a multi-objective optimization problem involves the knowledge and use of the concept of non-dominance [14, 15]. This is illustrated in figure 3, where some solutions in the objectives space are represented taking into account that both objectives (f_1 and f_2) are to be maximized. Solution 2 is better than solution 3 in both objectives, thus solution 3 is dominated by solution 1. The same does not happen when comparing solutions 1 and 2, as none of these solutions dominates the other. The set of non-dominated solutions is designate as Pareto set, solutions about which it is not possible to say that one is better than the other in all objectives simultaneously, *i.e.*, they are incomparable.

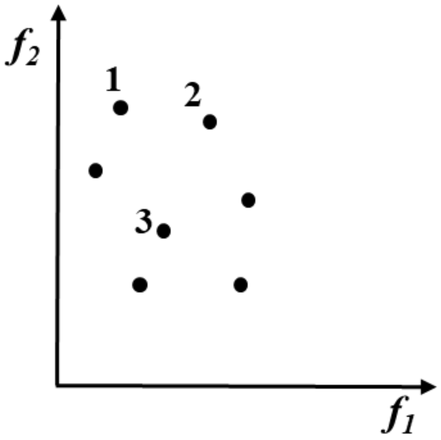

Fig. 3. Concept of non-dominance

Taking into account the advantage of the EAs of working with a population of solutions, a Multi-Objective Evolutionary Algorithm (MOEA) was adopted here. The algorithms selected was the S Metric Selection Evolutionary Multiobjective Optimization Algorithm (SMS-EMOA) proposed by Beume *et al.* [16], which is based on the use of hypervolume indicator, a measure of the contribution of each solution individually to the global performance of the population of solutions.

An EA mimics the process of natural selection and involves several steps: i) a population of solutions is generated randomly; ii) these solutions are evaluated using the modelling routine; iii) the solutions are classified accordingly with its degree of non-dominance; iv) the better solutions are selected with an high degree of probability to be parents of the next generation; v) offspring are generated based on crossover and mutation operators; vi) this process is repeated until a completion criteria is meet. In order to accommodate the multi-objective nature of the problems, step iii) above must be modified, which in the present case the hypervolume metric is used accordingly with the procedure of the SMS-EMOA [16], more specifically, the variation of SMS-EMOA described in paper [17].

4. Optimization results and discussion

4.1 Case studies

The use of the above MOEA optimization methodology, in designing screws for polymer extrusion, must take into account the different number of parameters necessary to optimize the CS and MBS screws simultaneously.

Two different polymers were selected based on the modelling and experimental results obtained previously [6, 7]. Table 1 presents the properties of a Low Density Polyethylene (Lupolen 33FM, from BASELL) and a Polypropylene (ISPLEN 030G1E, from Repsol YPF) that will be used in the optimization. The viscosity was determined in a Rosand RH8 Dual Capillary Rheometer taking into account both Bagley and Rabinowistch corrections, from which the Carreau-Yasuda parameters were obtained. Thermal properties (specific heat, melting heat and melting temperature) were obtained using a Perkin Elmer DSC 7 and the remaining properties were taken from the literature.

The extruder used has a diameter (*D*) of 30 mm and a ratio *L*/*D* of 30. Figure 1 illustrates the extruder geometry and the localization of the heater bands. Table 2 presents the range of variation of the geometrical parameters to be optimized, *i.e.*, the design variables, which include for CS and MBS: L_1, length of feed zone; L_2, length of compression zone; D_1, internal diameter of feed zone; D_3, internal diameter of metering zone; *Pitch*; pitch and, *e*, flight thickness. Two additional parameters are required for the MBS: W_f, clearance between secondary flight and barrel and, H_f, secondary flight width. In both cases the length of the metering zone (L_3) is defined as the difference between the total screw length (900 mm) and the sum of the lengths of feed and compression zones.

In order to accommodate the simultaneous optimization of both screws, an additional decision variable, ranging in the interval [1-100], was defined, this is, if its value is below 50 the screw considered in the calculations is the CS, while in the opposite case is the MBS. This decision variable is optimized together with the remaining 14 decision variables, 6 from the CS and 8 from the MBS.

Table 3 shows the objectives used in the optimization. At this phase, only two objectives are optimized simultaneously by combining the following pairs (*Q*, *L*), (*Q*, *T*), (*Q*, *P*), (*Q*, *WATS*) and (*Q*, *ViscousD*), which implies five optimization runs for each case considered.

As shown in Table 4, during each optimization run the operating conditions were kept constant for each optimization run and for each material and the barrel temperature profile is dependent of the polymer. Therefore, five optimization runs were performed for each combination of operating conditions and material, being the total number of optimization runs equal to 10.

Table 1. Physical, thermal and rheological properties of polymers: LDPE - LUPOLEN 33FM, by Basell; PP - ISPLEN 030G1E, by Repsol YPF

Property			**LDPE**	**PP**	**Unity**
Density	Solids	ρ_s	495	691	$kg.m^{-3}$
	Melt	ρ_m	854.4	902	
Thermal Conductivity	Solids	k_s	0.141	0.50	$W.m^{-1.}{}^{o}C^{-1}$
	Melt	k_m	0.078	0.30	
Specific Heat	Solids	C_s	1345	0.45	$J.kg^{-1}$
	Melt	C_m	1591	0.25	
Melting	Heat	H	115.00x10^3	0.210	$J.kg^{-1}$
	Temperature	T_m	105	0.180	^{o}C
Viscosity, Carreau-Yasuda law: $\eta = \eta_0\, a_T \left(1+\left(\lambda\, a_T\, \dot{y}\right)^a\right)^{\frac{n-1}{a}}$ $a_T = \exp\left(\frac{E}{R}\left(\frac{1}{T}-\frac{1}{T_0}\right)\right)$		η_0	10000.00	3041.5	$Pa.s$
		E/R	7500.00	4023.3	K
		$\hat{\lambda}$	1.80	0.17	s
		a	1,50	1.82	
		n	0.45	0.35	
		T_0	473.15	533.15	K

Table 2. Range of variation for the optimization of CS and MBS geometries used in the study (Db = 30 mm)

Screw	L_1 **(mm)**	L_2 **(mm)**	D_1 **(mm)**	D_3 **(mm)**	***Pitch*** **(mm)**	***e (mm)***	W_f **(mm)**	H_f **(mm)**
CS	100-400	170-400	20-26	26-32	30-42	3-4	--	--
MBS	100-400	170-400	20-26	26-32	30-42	3-4	0.5-0.7	2-4

Table 3. Optimization objectives, aim of optimization and range of variation for single screw extrusion

Objectives	**Aim**	X_{min}	X_{max}
Output – Q (kg/hr)	Maximize	1	20
Length for melting – L (m)	Minimize	0.1	0.9
Melt temperature – T (ºC)	Minimize	150	230
Power consumption – P (W)	Minimize	0	1200
WATS	Maximize	0	1000
Viscous dissipation (T/T_b) - *ViscousD*	Minimize	0.9	1.1

Table 4.Operating conditions used in this study

Runs	**Polymer**	**N (rpm)**	**Tb1 (ºC)**	**Tb2 (ºC)**	**Tb3 (ºC)**	**Tb4 (ºC)**	**Tb5 (ºC)**	**Tdie (ºC)**
Run 1 to 5	HDPE	80	140	150	150	160	160	160
Run 6 to 10	PP	80	200	210	210	220	220	220

4.2 Results and discussion

Figure 4 presents the optimal Pareto curves for runs 1 to 5 using LDPE, while Figure 5 presents the results for runs 6 to 10 using PP. For each one of the points shown in these figures there is a corresponding screw in the decision variables domain, the screw geometry.

In order to understand better these results, let us concentrate in the graph of Figure 4-A, the case where output (Q) and the length required for melting (L) are optimized simultaneously. Since the aim is to maximize Q and minimize L, the better solutions are the ones located in the bottom-right corner, the place where in fact the Pareto solutions obtained are located.

This graph has some important characteristics: i) the two types of screws, CS and MBS, are present in the optimal Pareto solutions; ii) the different types of screws are interleaved, with the MBS screws, which are located preferably in the middle; and iii) there are some gaps in the Pareto curve.

Therefore, it was possible to conclude that in this case the better single solution to be chosen can be either a CS or a MBS, depending on the preferences of a decision maker, which depends on the degree of importance attributed to each one of the objectives. Anyway, the screw identified by number 1 is the one that minimizes (improves) objective L, while screw number 8 is the one that maximize (improves) objective Q. A more equilibrated screw must be located in between these two, and can be one of the CS 2, 5, 6 or 7, or one of the MBS 3 or 4. Also, screw 6 have a particular characteristic, *i.e.*, it has a relatively big output, but without deteriorating the length required for melting, because the next screw, 7, has identical Q but L changes considerably. The selection of a solution form this set of optimal solutions is not an easy task and different aspects to be considered [18].

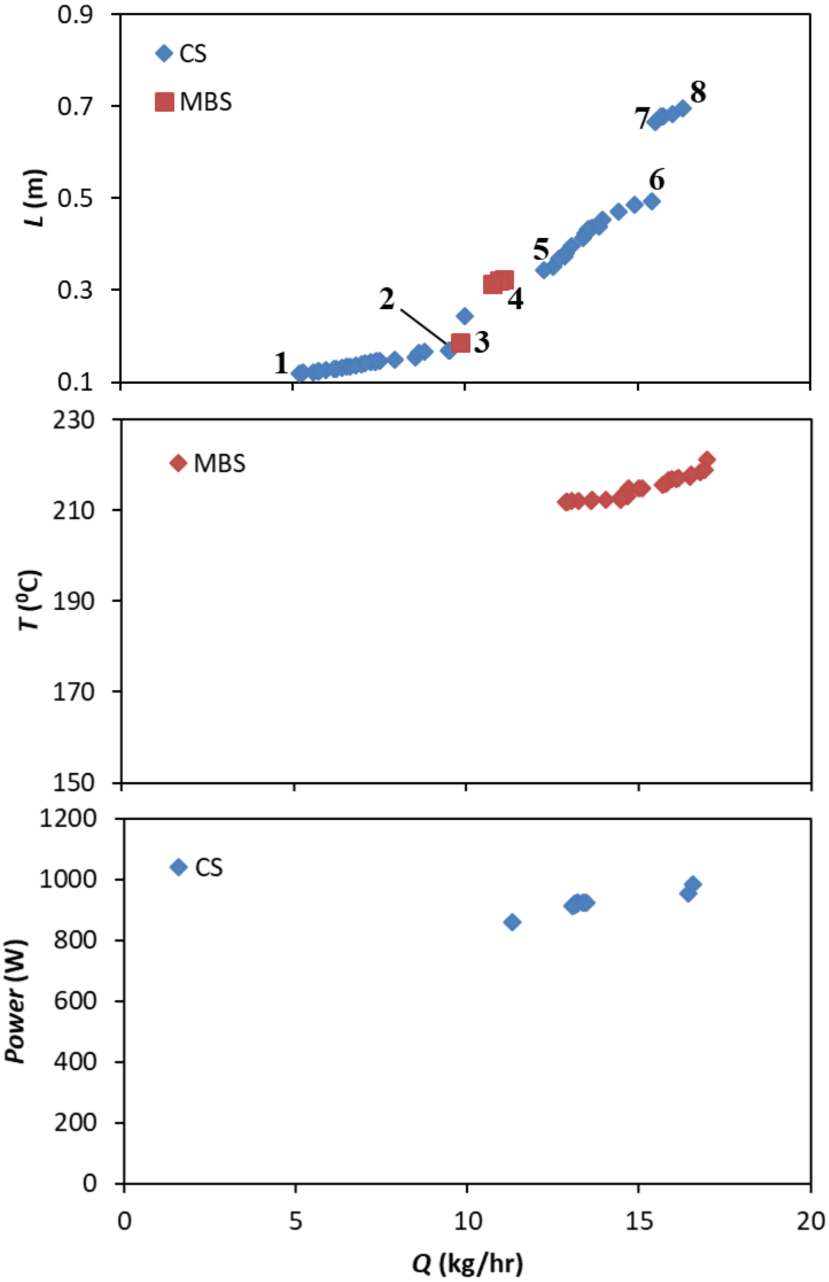

Fig. 4. Pareto curves for runs 1 to 5 using LDPE

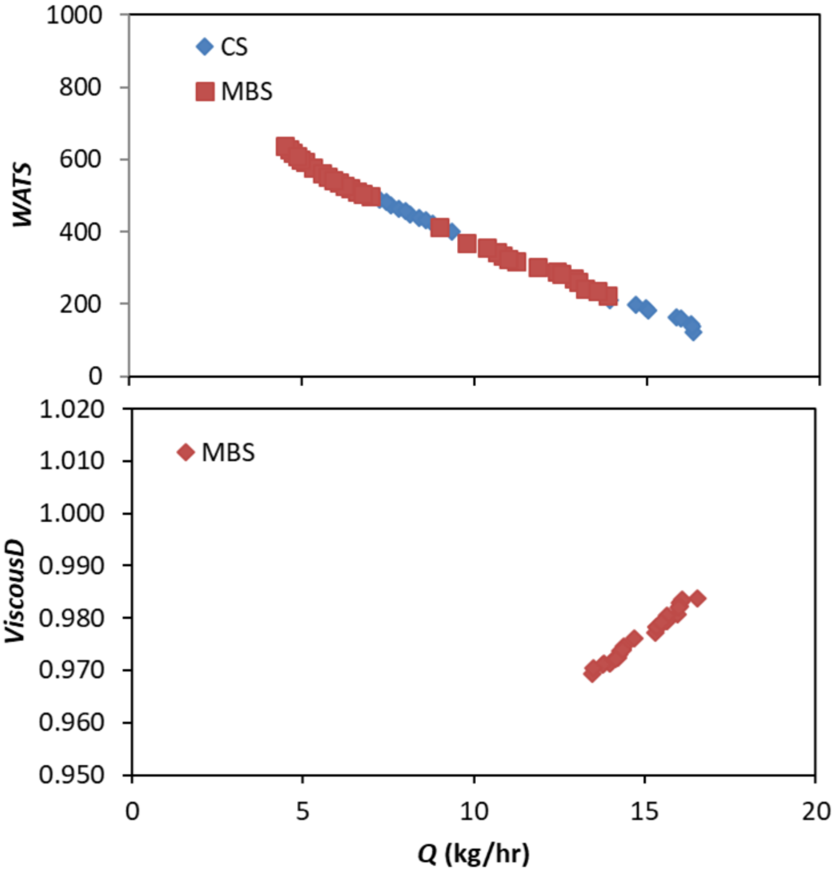

Fig. 4. Pareto curves for runs 1 to 5 using LDPE - continuation

Table 5 shows the geometrical parameters of screw 1 to 8 represented in Figure 4-A. As can be seen, the geometry of the screws changes as moving from screw 1 to 8, but there is no specific regular change that can be determined without a further study.

The results presented in Figure 4-D represent the optimal Pareto curve for optimizing simultaneously Q and WATS (mixing degree), both to maximize. Thus, the aim is to approach the top-right corner. Like in the previous case, both types of screws are present, CS ad MBS. An analysis of the remaining results, Figures 4-B, 4-C and 4-E, allow to conclude that in this situation only a type of screw is able to accomplish better the optimization of the corresponding objectives.

Finally, Figure 5 presents identical results (runs 6 to 10) using PP. It is important to note here that the barrel temperature used was different, as the melting temperature is different for both polymers, and, thus, the results cannot be directly compared. As can be observed, only in the case of the simultaneously optimization of *Q* and viscous dissipation both types of screws were obtained.

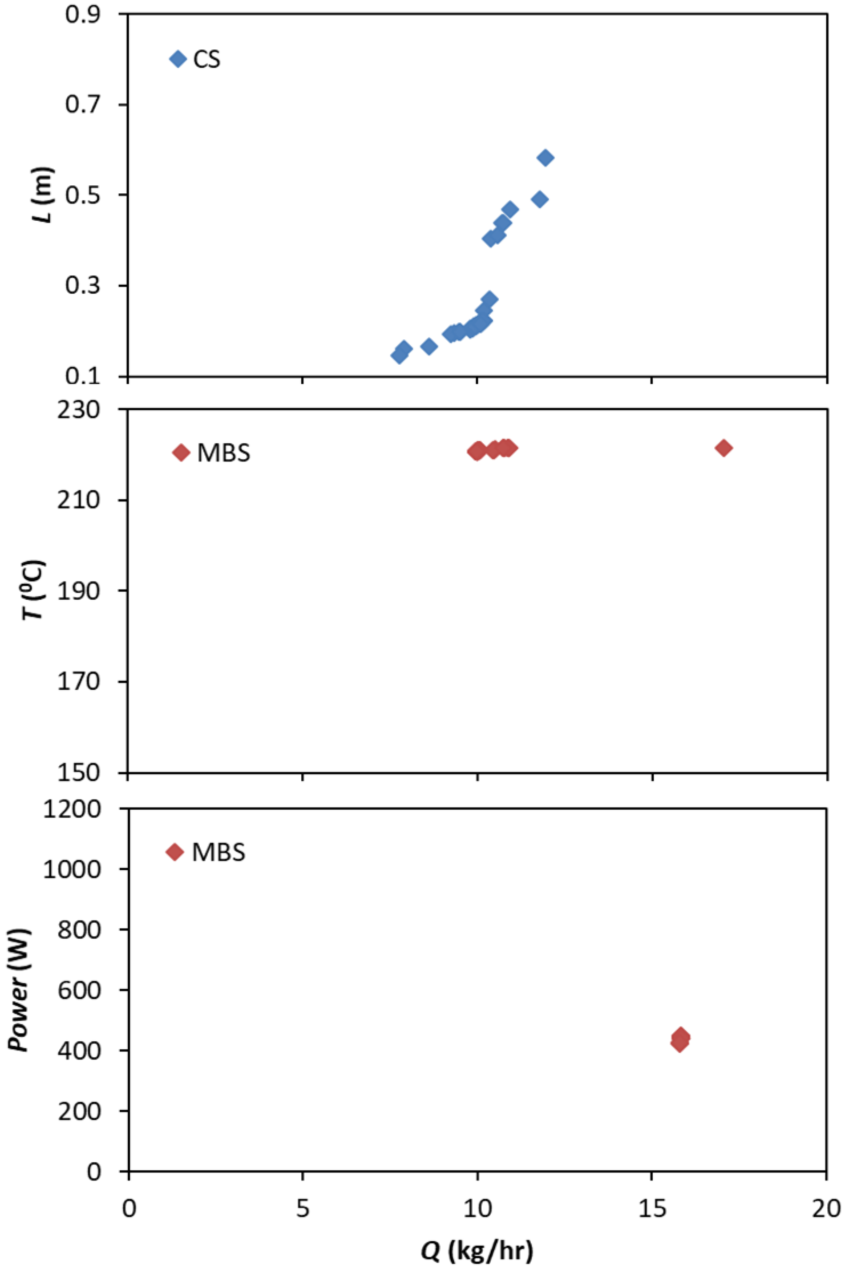

Fig. 5. Pareto curves for runs 6 to 10 using PP

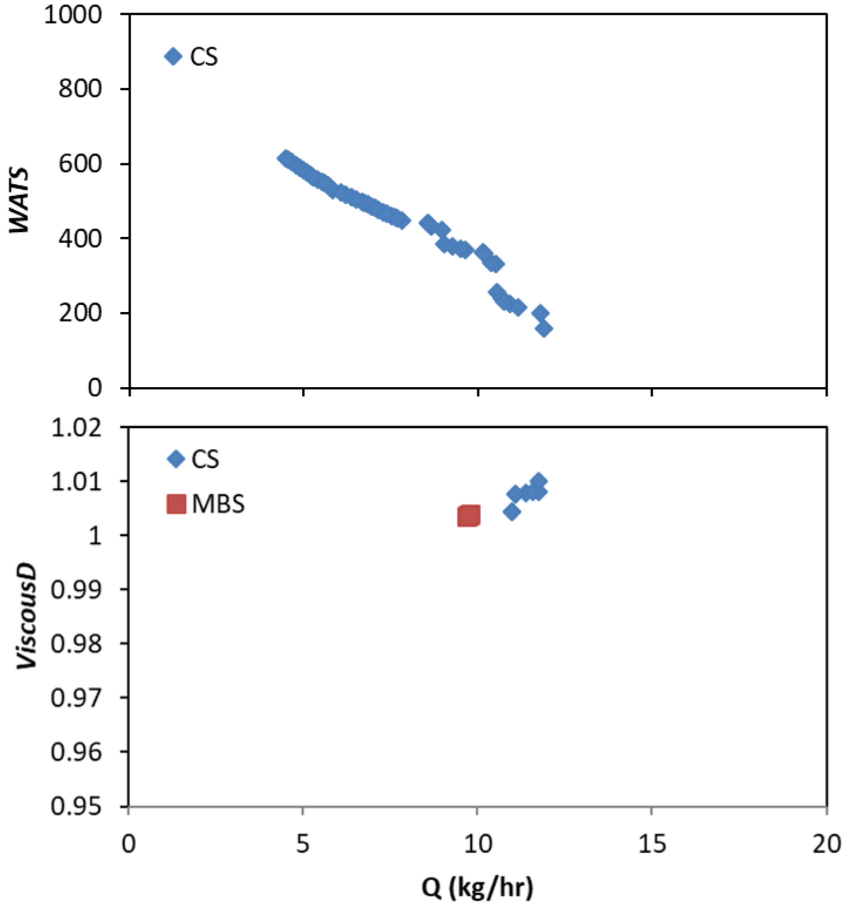

Fig. 5. Pareto curves for runs 6 to 10 using PP - continuation

Table 5. Range of variation for the optimization of CS and MBS

Number	**Screw**	***L_1* (mm)**	***L_2* (mm)**	***D_1* (mm)**	***D_3* (mm)**	***Pitch* (mm)**	***e* (*mm*)**	***W_f* (mm)**	***H_f* (mm)**
1	CS	202.9	178.1	20.1	25.4	25.0	3.28		
2	CS	201.2	209.6	21.5	22.5	33.8	3.01		
3	MBS	400.0	196.7	19.0	22.6	34.4	3.90	0.601	3.00
4	MBS	170.0	193.8	22.0	22.6	32.0	3.00	0.600	3.01
5	CS	204.2	278.1	20.6	22.1	34.6	3.02		
6	CS	203.5	282.5	21.5	22.0	34.6	3.00		
7	CS	204.2	188.4	21.5	22.6	33.5	3.00		
8	CS	197.8	184.9	21.5	22.6	33.5	3.00		

5. Conclusions

A multi-objective optimization methodology based on MOEA was used in the simultaneous design of conventional and barrier screws for single screw extrusion. The performance used in this process allowed to obtain results with physical meaning which can be justified in the thermomechanical environment present inside the barrel.

The bi-objective results obtained allows us to conclude that, and depending on the operating conditions and on the polymer processed, in some cases the CS is better than the MBS, *i.e.*, these results show that is not possible to conclude that the barrier screw is the best. This revels that the use of a multi-objective optimization methodology, like the suggested here, is a key process in defining the better geometry to use in a particular situation.

However, more studies are needed in order to understand better the influence of the operating conditions and to study the performance of the screws obtained against changes in important parameters, namely the operating conditions and the material, *i.e.*, the final solution must be robust.

Acknowledgements

This project has received funding from the European Union's Horizon 2020 research and innovation programme under the Marie Skłodowska-Curie grant agreement No. 734205 – H2020-MSCA-RISE-2016.

References

[1] Maillefer, C., Swiss Pat. 363,149 (1959).

[2] Dray, R.F., Lawrence, D.L., U.S. Pat. 3,650,652 (1970).

[3] Barr, R., U.S. Pat. 3,698,541 (1971).

[4] Kim, H.T., U.S. Pat. 3,867,079 (1972).

[5] Ingen Housz, J.F., U.S. Pat. 4,218,146 (1980).

[6] Gaspar-Cunha A., Covas J. A., The Plasticating Sequence in Barrier Extrusion Screws Part I: Modeling. Polymer Engineering and Science, 2014, 54(8), 1791–1803. http://onlinelibrary.wiley.com/doi/10.1002/pen.23722/full

[7] Gaspar-Cunha A., Covas J.A., The Plasticating Sequence in Barrier Extrusion Screws Part II: Experimental Assessment, Polymer-Plastics Technology and Engineering, 2014, 53:14, 1456-1466, DOI: 10.1080/03602559.2014.909482

[8] Potente H., Bastian M., Flecke J., Design of a Compounding Extruder by means of the SIGMA Simulation Software, Adv. Polym. Technol., 1999, 18, p. 147.

[9] Potente H., Stenzel H., Theoretical Principles Governing the Design of Barrier Sections in Extruders, Int. Polym. Process., 1991, 6, pp. 126-135.

[10] Amellal K., Elbirli B., Performance Study of Barrier Screws in the Transition Zone, Polym. Eng. Sci., 1988, 28, pp. 311-320.

[11] Elbirli B., Lindt J.T., Gottgetreu S.R., Baba S.M., Mathematical Modeling of Melting of Polymers in Barrier-Screw Extruders, Polym. Eng. Sci., 1983, 23, pp. 86-94.
[12] Han C.D., Lee K.Y., Wheeler N., A Study on the Performance of Barrier-Screw Extruders, Polym. Eng. Sci., 1991, 31, pp. 831-841.
[13] Potente H., Stenzel H., Theoretical Principles Governing the Design of Barrier Sections in Extruders, Int. Polym. Process., 1991, 6, pp. 126-135.
[14] Deb K., Multi-Objective Optimization using Evolutionary Algorithms, Wiley, New York, 2001.
[15] Carlos Coello Coello, Gary B. Lamont, David A. van Veldhuizen, Evolutionary Algorithms for Solving Multi-Objective Problems, 2nd Edition, Springer, New York, 2007.
[16] Beume N., Naujoks B., Emmerich, M., SMS-EMOA: Multiobjective selection based on dominated hypervolume. Eur. J. Oper. Res., 2007, 181 (3), 1653–1669.
[17] Quintana D., Denysiuk R., Garcia-rodriguez S., Gaspar-Cunha, A., Portfolio Implementation Risk Management Using Evolutionary Multiobjective Optimization. Applied Sciences, 2017, 10(7). https://doi.org/10.3390/app7101079
[18] Denysiuk R., Recio G., Covas J. A., Gaspar-Cunha, A., Using multiobjective optimization algorithms and decision making support to solve polymer extrusion problems. Polymer Engineering and Science, 2018, 58(4). https://doi.org/https://doi.org/10.1002/pen.24732

José A. Covas[1] , Loic Hilliou[1]

IN-LINE CHARACTERIZATION OF THE DISPERSION OF POLYMER NANOCOMPOSITES DURING MELT COMPOUNDING

Abstract: *In-line rheo-optical investigation of filler dispersion during twin-screw extrusion of a model polymer/organoclay nanocomposite is carried out with the aim of establishing relationships between stresses, residence time, and levels of clay dispersion. Polymer intercalation, particle erosion and break-up contribute simultaneously to dispersion. It is shown that the experimental set-up used here is an ideal toolbox for developing new nanocomposites and/or setting/optimizing the compounding conditions.*

Keywords: *nanocomposites, melt mixing, dispersion, in-line monitoring*

1. Introduction

The practical performance of polymer nanocomposites depends on the interplay between the characteristics of the constituents, the morphology generated and the processing conditions utilized. In general, better dispersion of the filler in the matrix is associated to better properties, but the level of dispersion attained depends, among other parameters, on the preparation method. Melt mixing is generally adopted at practical industrial scale, as it does not involve the use of solvents and can be performed in conventional polymer processing equipment with high yields. However, melt mixing is less efficient than solvent intercalation or in situ polymerization methods, the resulting materials exhibiting structures with sizes ranging from nanometers to micrometers [1,2].

The extent of the dispersion of fillers in thermoplastic polymer matrices by melt mixing is influenced by the filler and polymer properties, as well as by compounding and processing parameters (Figure 1). Indeed, the type, dimensions, cohesion of the original agglomerates, purity and affinity of the filler with the polymer matrix will influence its dispersibility. For example, Socher et al [3] used several commercial carbon nanotubes (CNT) and carbon black to prepare composites with polyamide12 and obtained different correlations between volume electrical conductivity and filler content, and quite distinct filler content at the threshold for electrical conductivity. Bauhofer and Kovacs [4] analyzed the data published between 1998 and 2007 on the loading of CNT necessary to reach maximum conductivity of nanocomposites with different matrices and observed a significant scatter, preannouncing a strong influence of the filler characteristics on dispersibility.

---

[1] *Institute for Polymer and Composites/LASI, Department of Polymer Engineering, University of Minho, Guimarães 4804-533, Portugal, jcovas@dep.uminho.pt.*

During compounding and/or processing, the morphology of the polymer nanocomposite, namely its dispersion and distribution, is determined by the thermomechanical stresses created, by the corresponding residence time and the flow patterns developed. Therefore, the type and geometry of the mixing/processing equipment, and the corresponding processing conditions, are also key factors for dispersion (Figure 1).

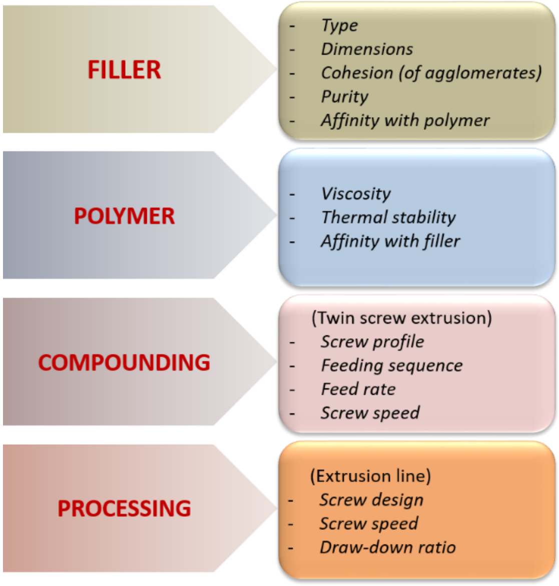
FILLER
- Type
- Dimensions
- Cohesion (of agglomerates)
- Purity
- Affinity with polymer
POLYMER
- Viscosity
- Thermal stability
- Affinity with filler
COMPOUNDING
(Twin screw extrusion)
- Screw profile
- Feeding sequence
- Feed rate
- Screw speed
PROCESSING
(Extrusion line)
- Screw design
- Screw speed
- Draw-down ratio

Fig. 1. Main parameters affecting the dispersion of fillers in thermoplastic polymer matrices by melt mixing

Given the above, it is not surprising that during the last decades many researchers attempted to unveil the dispersion mechanisms of major fillers. In the case of layered clays, which will be the focus of this chapter, both a general mechanism and the effect of processing conditions, were established [5,7]. Nevertheless, a number of reported experimental findings could not be readily explained by the accepted mechanisms. Degradation of the clay surfactant and, eventually, of the polymer matrix, decreased the polymer-clay affinity, enabling easier diffusion of polymer chains out of the clay galleries, which could collapse and re-aggregate [8]. These observations were made possible through the use of in-process characterization methods. Indeed, conventional sampling methods may alter the characteristics of the material to be analysed, yielding misleading conclusions about its properties and morphology. Samples collected along the screws after cooling the extruder and extracting the screw may evidence premature melting and larger particles sizes, as the material stays hot for a long time, favouring coalescence/re-agglomeration. Similarly, collecting a sample from the extrudate and taking it to the laboratory for subsequent characterization often involves reheating the material (to prepare a specimen/making a test), which again may cause degradation, coalescence/re-agglomeration, or even chemical reactions to proceed, these significantly altering the characteristics of the material as collected.

In-line and on-line process characterization circumvent these limitations, as either the material in the flow channel, or a portion of material deviated from the main flow channel, respectively, are directly characterized in the melt state. Several in-process methodologies have been successively developed and used by the author to follow along the axis of an extruder the evolution the peroxide-induced degradation of PP by on-line capillary rheometry [9] and the dispersion of a PP/organoclay nanocomposite with on-line oscillatory rheometry [10], to assess the quality/consistency of PP/clay nanocomposites during compounding at pilot scale [11], to track the evolution of dispersion of polymer/graphite nanoplates nanocomposites during compounding and subsequent screw extrusion [12], and to monitor polymer (PP) melting using on-line turbidity and birefringence [13].

This chapter aims at demonstrating the practical usefulness of an innovative extrusion/compounding system fitted with in-line measuring capabilities, by studying in detail the dispersion of a model polymer-organoclay system. The experimental set-up is presented first, followed by the data collected during the preparation of the nanocomposite. Keeping constant both clay content and feed rate, the effects of screw speed and barrel temperature on the nanocomposite viscosity curves, average particle radii, and corresponding volume fraction, are measured in-line.

2. Experimental set-up

The experimental set-up is schematized in Figure 2. It comprises an extruder, a rheo-optical slit and optical train for the in-situ measurement of flow curves, SALS patterns, and turbidity during extrusion.

The modular small scale intermeshing co-rotating twin-screw extruder used has a diameter *D* of 13 mm and a screw length/diameter ratio of 27. The various barrel modules are equipped with a feed port (which can be tapped) and three sampling devices. These enable the fast collection of small amounts of material from the screw channel along the barrel, without stopping the process, for subsequent characterization, or fast readings of local temperature.

Most rheo-optical dies use a slit-shaped flow channel fitted with melt pressure transducers and optical windows. Coupling the slit die to an extruder and measuring both the resulting throughput and pressure drop will yield a single point of the flow curve. To generate various points (i.e., shear rates), the feed rate must be changed. However, this action will alter the thermomechanical environment in the extruder (i.e., the stresses and the residence time) and, consequently, may change the morphology and degree of mixing of the material. Thus, points of the viscosity curve at different shear rates may correspond to the behavior of materials with distinct characteristics. To avoid this problem, the rheo-optical die used here contains two slit channels, one of which is fitted with melt pressure transducers and optical windows. Both channels are equipped with valves at the entrance to allow for the independent control of material outputs in each channel, while maintaining constant inlet pressure, i.e., constant extruder screw speed and feed rate (Figure 3). The description of the die and of its operation has been done elsewhere [14]. As illustrated in Figure 4, the lower surface of the measuring slit contains a recess in order to apply the *hole pressure method* and thus estimate the first normal stress difference (N_1) (see [15] for details on the method and its application). In practice, N_1 is directly calculated from $P_2 - P_1$, while P_3-P_1 is used for determining the shear viscosity.

The optical windows enable small-angle light scattering (SALS) and turbidity measurements for the assessment of the average radius R and volume fraction ϕ of particles scattering the light (a comprehensive explanation of the optical train used for SALS and turbidimetry can be found in [16]).

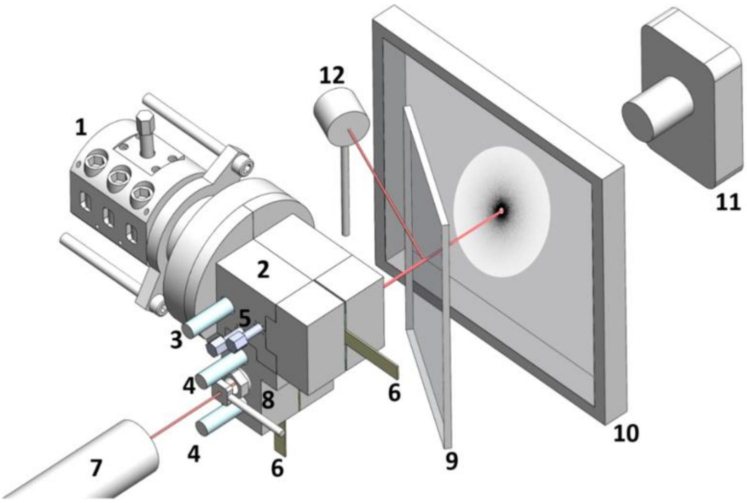

Fig. 2. Extruder, rheo-optical slit and optical train for the in-situ measurement of flow curves, SALS patterns, and turbidity during extrusion. (1) Extruder; (2) rheo-optical die; (3) pressure transducer at die entry; (4) pressure transducers along the measuring channel; 5) valves for control of material output; (6) extrudate; (7) HeNe laser; (8) pinhole; (9) beam splitter; (10) screen; (11) CDD camera; (12) photodetector

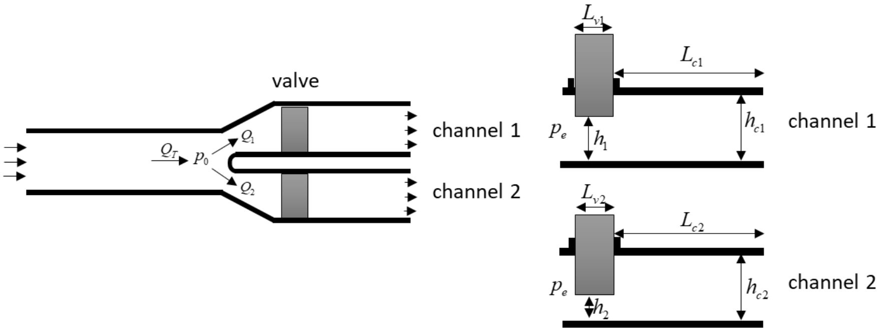

Fig. 3 The double-slit die. The inlet channel is sub-divided into two channels (1, 2) equipped with valves (dark rectangles) at the entrance. The distribution of the inlet flow (Q_T) through the two slits (Q_1, Q_2) is controlled by vertically moving the two valves in opposite directions (changing the heights h_1 and h_2 of the channel entrance), while maintaining constant the pressure at the entrance (p_0), which corresponds to keeping constant the extruder screw speed and feed rate.

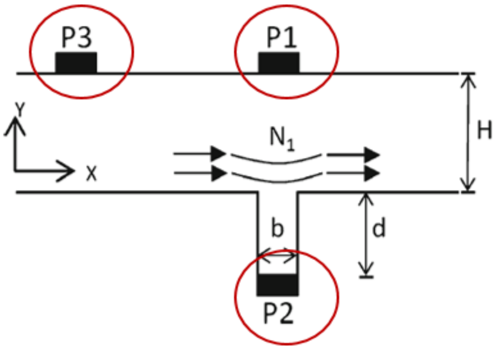

Fig. 4. Concept of the hole pressure method applied to flow in a slit die. P1, P2 and P3 are melt pressure readings. H is the channel height; b and d are the recess width and height, respectively

3. Dispersion of organoclay in a polymer matrix

Practical polymer—clay nanocomposites contain structures with sizes ranging from nanometers to micrometers. This is because breaking and exfoliating the high cohesive clay platelets by melt mixing requires the creation of high thermomechanical stresses that would also cause significant polymer degradation. As represented in Fig. 5, a stepwise dispersion mechanism is commonly accepted to explain the development of this multiscale structure along the extruder. Clay dispersion in the polymer melt involves the diffusion of polymer chains within the clay interlayer spacing of the tactoids (intercalation step) and the delamination of the individual platelets (exfoliation step) [17,18]. In modified clays (known as organoclays), hydrated inorganic cations are often exchanged with organic ones bearing aliphatic chains, thus facilitating melt intercalation. Large stresses first promote the disruption of the initial agglomerates of clay tactoids into single tactoids, which are subsequently ruptured into smaller platelet stacks. Low viscosity and lower stresses should then facilitate polymer diffusion into the clay galleries, thus increasing platelet-to-platelet distance. Large stresses will eventually lead to tactoid rupture. Simultaneously, platelet-by-platelet peeling of tactoids (an erosion process) may develop [7,18].

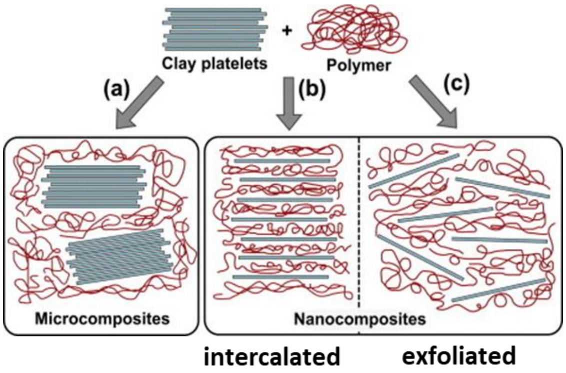

Fig. 5. Stepwise dispersion mechanism for polymer-organoclay nanocomposites

This sequential break-up/peeling mechanism can be questioned. The opposing need of low viscosity for melt intercalation and of large viscosity for tactoid break-up and complete platelet exfoliation has been highlighted [19,20]. Also, several authors obtained results that do not fit in the dispersion mechanism and/or in the expected processing parameters–clay dispersion relationships. It has been shown that thermal degradation of the organic clay modifier due to large viscous heating and/or longer residence times, or of the polymer (especially when processing thermally sensitive matrices) have an effect on clay dispersion (for a review on this topic, see [8,21]). Also, sample collection, preparation and testing may modify the nanocomposite characteristics and yield misleading data.

The study reported here adopts simultaneously three innovative approaches:

- The *in situ* characterization of the nanocomposite using a rheo-optical die and in-line measurements avoids all the concerns related to morphological rearrangements, e.g., particle re-agglomeration;
- The use of a model system, consisting of an organo-modified montmorillonite (Dellite 72 T, Laviosa Chi. Mine., Livorno, Italy) and a polydimethylsiloxane (PDMS) (AK 1,000,000, Wacker-Chemie GmbH, Munich, Germany) enables processing at ambient or low temperatures (up to 100ºC), which are well below the onset for their degradation;

- Processing this system avoids the superposition of polymer melting and mixing (which occurs upon processing of most thermoplastic matrices), thus isolating mixing from other phenomena.

Figure 6 shows the flow curves of the PDMS at different temperatures. The polymer behaves basically as a Newtonian fluid in the range of shear rates tested with the rheo-optical die (with the onset for shear-thinning shifting to larger shear rates with increasing temperature). This is advantageous for the study, since it minimizes the effect of shear thinning on the viscosity that would result from a growth in shear rate due to an increase in screw speed. Moreover, the temperature follows an Arrhenius dependence with the zero shear viscosity (η_0), as shown by the fit to the data included in Figure 6.

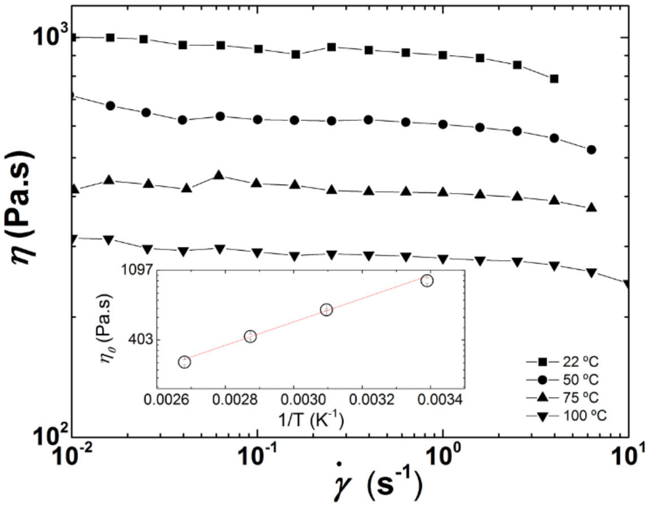

Fig. 6. PDMS flow curves measured off-line at different temperatures. The inset is an Arrhenius fit to the thermal dependence of the zero shear viscosity η_0

The flow curves of the nanocomposite measured in-line at four different screw speeds (between 20 and 80 rpm) are shown in Figure 7. The solid line represents a Cross equation fit to the PDMS data. As expected, the viscosity of the composites is higher than that of the polymer. In the lower shear rate range, the curves shift upwards as the screw speed decreases, whereas at the higher shear rate range they tend to converge. The SALS patterns obtained are isotropic, which is indicative of the absence of eventual flow orientation effects. Also, local temperature sensing did not pick up any significant viscous dissipation. This type of data is not frequently reported, as most rheological measurements on nanocomposites are performed with oscillatory rheometry, as flow in the capillary/slit may alter the morphology of the material during testing. Consequently, although the relative position of the individual flow curves seems to be the opposite of that usually reported for oscillatory data (increase in yield stress and in shear thinning with clay exfoliation [7], any conclusions concerning the extent of clay dispersion from the flow curves should be taken cautiously. Instead, the *in situ* morphological information retrieved from both SALS patterns and turbidimetry can be used for that purpose, since the average clay particle radius (R) can be estimated from the light intensity profiles extracted from the circular average of the isotropic SALS patterns, and the volume fraction (ϕ) of clay particles with radius R is obtained from the measured turbidity [21].

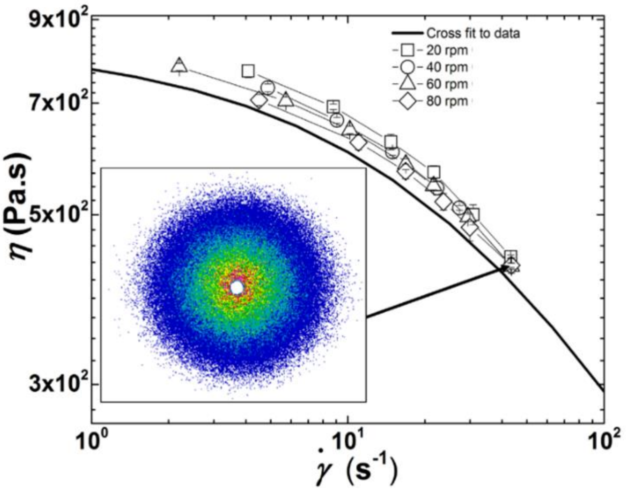

Fig. 7. Flow curves measured in-line for different screw speeds (no barrel heating). The line is the Cross equation fit to the PDMS flow curve. The inset presents a SALS pattern at the highest screw speed and shear rate

Figure 8 presents the variation of R and ϕ with shear rate for the various screw speeds utilized in the experiments. As the screw speed increases, R reduces (from 0.74 μm at 20 rpm to 0.60 μm at 80 rpm) and more particles with a smaller size are generated (from 1.0% at lower shear rates and 20 rpm to 1.4% at larger shear rates and 80 rpm). Both R and ϕ show shear rate dependence for the lower screw speeds. As discussed above, the break-up of particle agglomerates is associated with the development of sufficiently high stresses, this being a relatively fast process, whereas erosion can develop under lower stresses, but requires longer times [22,23]. The data of Figure 8 seem to indicate that higher screw speeds (and thus higher stresses) promote the break-up of clay agglomerates/tactoids into smaller ones, whereas lower screw speeds should favour the erosion of the clay tactoids. In both cases, there is a progressive generation of smaller objects suspended in the melt, with gradual effects on the rheological properties.

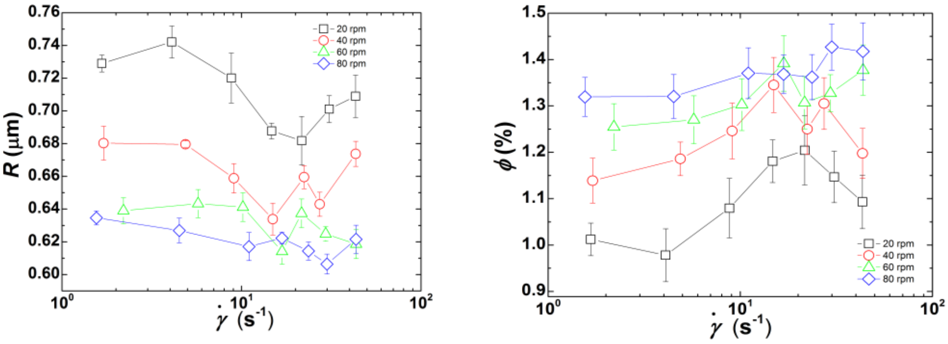

Fig. 8. Clay particle radius R computed from the analysis of SALS patterns (left) and volume fraction ϕ of clay particles of size R computed from turbidimetry (right)

In order to test this assumption, the values measured at the smallest shear rate applied in the rheo-optical slit were compared with the predictions of models describing the kinetics of particle dispersion. Assuming erosion, Rwei et al. [24] proposed the following equation:

$$\ln R(t) = \ln R_0 - C\, \dot{\gamma}_{av}\, t \qquad (1)$$

where R_0 is the initial particle size of the clay, C is a constant and t is the average residence time of the clay particles in the extruder, which is operated at a screw speed inducing $\dot{\gamma}_{av}$. Collin et al [25] proposed a relationship valid for negligible cohesive strength of the clay particles:

$$R(t)^3 = R^3_0 - C_1\, \sigma_{av}\, \dot{\gamma}_{av}\, t \qquad (2)$$

where C_1 is a constant and σ_{av} is the average stress applied on the clay particles, which is computed from:

$$\sigma_{av} = \eta(\dot{\gamma}_{av})\, \dot{\gamma}_{av} \qquad (3)$$

Figure 9 displays a graphical representation of equations (1) and (2), using the values of R reported in Figure 8, and those of t were measured experimentally. The figure depicts linear relationships when processing at lower screw speeds (equivalent to lower stresses). This means that the two models are at least qualitatively valid, signifying that clay particle erosion takes place. The R value measured at the highest screw speed (80 rpm) departs significantly from the linear trend, suggesting a change in dispersion mode, from particle erosion to rupture.

Use of a fragmentation number (Fa), balancing the hydrodynamic stress σ with the cohesive strength σ_c of the filler, has been proposed to estimate the threshold conditions for dispersion, as well as the dispersion route [22,23]. For silica agglomerates of various densities suspended in low molecular weight polymers with different viscosities, Scurati et al. [21] confirmed that the critical stress for erosion is smaller than that for break-up, and concluded that erosion takes place when $2 \leq Fa < 5$, while break-up develops quickly when $Fa \geq 5$. Given the lack of data for other systems, but assuming that these relationships hold for the organoclay and polymer used here, the cohesive strength σ_c can be computed from the average and maximum stresses estimated at 20 rpm and $Fa = 2$, which yields $3.3 < \sigma_c < 26.9$ kPa. On the other hand, since rupture most likely occurred at 80 rpm (as presumed above from the information conveyed in Figure 8), σ_c can also be appraised from the average and maximum stresses calculated at 80 rpm, but now assuming that Fa is at least 5. This produces $3.6 < \sigma_c < 19$ kPa, which is quite similar to the first estimated value range. The higher values calculated are of the same order of magnitude of the reported range of stresses needed to peel off a 1 μm clay tactoid into two halves, for tactoids with stacking defects allowing peeling angles larger than 3° [19]. Remarkably, the values are also within the scale of the predicted cohesive strengths of graphite nanoplates and CNT [26,27], which are well known for their high cohesion and poor dispersibility in polymers due to van der Waals interactions between the individual tubes or platelets and chemical inertia.

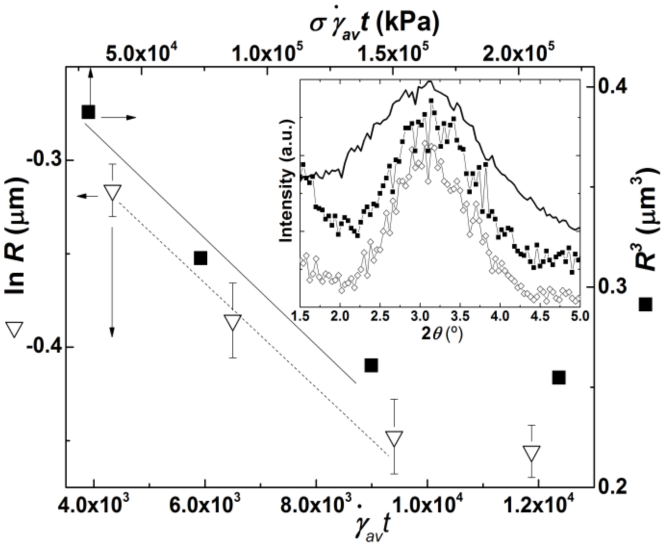

Fig. 9. Graphical representation of equation (1) (open triangles) and equation (2) (solid squares). Solid and dotted lines are guides to the eyes. Inset: WAXD spectra of clay powder (line) and of extrudates collected during experiments performed with a screw speed of 40 rpm (solid squares) and 80 rpm (empty diamonds)

The inset in Figure 9 compares the WAXD spectra of extrudate samples of nanocomposites produced at 40 and 80 rpm. Since the three diffraction peaks are in essence similar, they demonstrate that little or no PDMS intercalation within the organoclay galleries took place despite of the dispersion levels attained.

Thus, the data presented demonstrates that distinct clay dispersion levels are achieved with different screw speeds, but they are not directly linked to progressively higher PDMS intercalation and higher clay exfoliation with increasing screw speed. Instead, an interaction between lower stress and longer residence time induces predominant erosion of the tactoids at lower screw speeds, whereas break-up is more likely to occur at larger screw speeds, due to the higher stress levels. This result is only in partial agreement with the classical sequential dispersion mechanism, which presumes polymer diffusion into the clay galleries before achieving dispersion.

As discussed above, in order to achieve more extensive dispersion, it has been suggested first to mix clay and matrix under mild shearing conditions (to facilitate the diffusion of polymer chains into the confined space between the galleries, i.e., intercalation), followed by a high level of shearing (for break-up of the tactoids, i.e., exfoliation) [18,28]. To test this procedure with the model system adopted here, the viscosity of PDMS was lowered in the feed and first mixing zones of the extruder by heating the barrel in these zones. No heating was used downstream, in order to increase the viscosity and generate higher stresses for break-up.

Figure 10a presents the evolution along the barrel of the temperature of the nanocomposite for the various screw speeds selected, as measured by a fast response thermocouple inserted into samples of material collected using the sampling ports. Figure 10b shows the corresponding axial shear stress profile, calculated taking into consideration the data in Figure 6. The temperature almost attains the barrel set temperature of 100ºC in the first half of the screw, but it decreases with increasing screw speed due to corresponding reduction of the local residence time (necessary for the conduction heat transfer). Inversely, but for the same reason, heat relaxation along the barrel is less efficient at larger screw speeds. The melt temperature evolution influences the average axial shear stress profile as plotted in Figure 10b, with low values in the first part of the extruder and then an increase of about 50% downstream (the latter being the value attained for the experiments performed without barrel heating).

Table 1 compares the morphology of the nanocomposite in terms of particles average radii R and corresponding volume fraction ϕ for three shear rate values, and for three screw speeds (extrusion at 20 rpm with barrel heating could not reach steady state due to the low pressures generated), when prepared without heating and locally heating the barrel. Heating the first half of the barrel enables achieving a greater number of smaller clay particles for screw speeds of 40 and 60 rpm (except for the data measured at 43 s^{-1} with N = 60 rpm). No improvement of clay dispersion with heating is observed at 80 rpm. These results seem to confirm that low melt viscosities are useful in the initial stages of dispersion, most probably because they ease melt intercalation which, in later stages, will facilitate exfoliation even in the presence of lower stresses. At 80 rpm, it appears that the effect of any eventual intercalation is masked by that resulting from the higher intensity of the stresses generated.

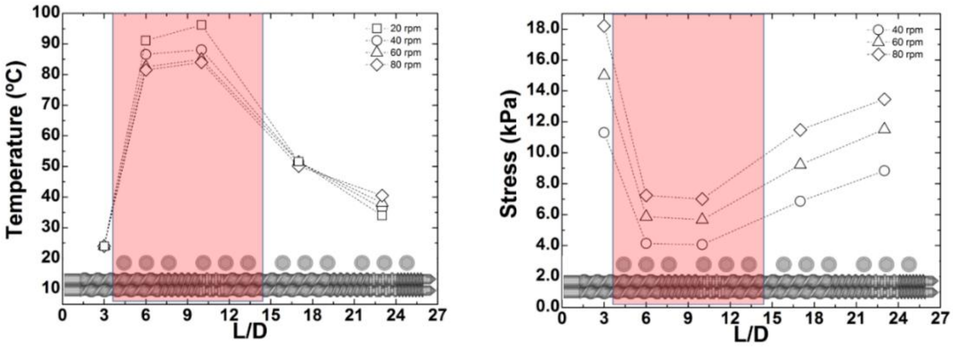

a) b)

Fig. 10. Measured temperature and computed shear stress profiles along the barrel of the extruder with barrel heating set to 100 ºC at the feed and first mixing zones (shaded region)

Table 1. Clay particles radii R and corresponding volume fraction ϕ measured in the rheo-optical die, at three constant shear rates (4, 10, and 43 s^{-1}) during extrusion runs with various screw speeds N (40, 60, and 80 rpm), performed without barrel heating and with partial barrel heating.

N = 40 rpm	**$\dot{\gamma} = 4\ s^{-1}$**		**$\dot{\gamma} = 10\ s^{-1}$**		**$\dot{\gamma} = 43\ s^{-1}$**	
	R (μm)	**ϕ (%)**	**R (μm)**	**ϕ (%)**	**R (μm)**	**ϕ (%)**
No heating	0.68 ± 0.01	1.18 ± 0.05	0.66 ± 0.01	1.24 ± 0.06	0.67 ± 0.01	1.20 ± 0.05
Heating	0.58 ± 0.01	1.42 ± 0.04	0.58 ± 0.01	1.39 ± 0.03	0.61 ± 0.01	1.32 ± 0.05
N = 60 rpm	**$\dot{\gamma} = 4\ s^{-1}$**		**$\dot{\gamma} = 10\ s^{-1}$**		**$\dot{\gamma} = 43\ s^{-1}$**	
	R (μm)	**ϕ (%)**	**R (μm)**	**ϕ (%)**	**R (μm)**	**ϕ (%)**
No heating	0.64 ± 0.01	1.26 ± 0.05	0.64 ± 0.01	1.30 ± 0.06	0.62 ± 0.01	1.38 ± 0.05
Heating	0.58 ± 0.01	1.35 ± 0.03	0.58 ± 0.01	1.45 ± 0.05	0.63 ± 0.01	1.30 ± 0.06
N = 80 rpm	**$\dot{\gamma} = 4\ s^{-1}$**		**$\dot{\gamma} = 10\ s^{-1}$**		**$\dot{\gamma} = 43\ s^{-1}$**	
	R (μm)	**ϕ (%)**	**R (μm)**	**ϕ (%)**	**R (μm)**	**ϕ (%)**
No heating	0.63 ± 0.01	1.32 ± 0.04	0.62 ± 0.01	1.27 ± 0.05	0.62 ± 0.01	1.42 ± 0.06
Heating	0.63 ± 0.01	1.23 ± 0.04	0.63 ± 0.01	1.25 ± 0.03	0.63 ± 0.01	1.31 ± 0.03

A careful analysis of the experimental data obtained for the various compounding experiments shows that two sets of extrusion trials allow to isolate the effects of the average residence time t and of the average mechanical power ($\eta\dot{\gamma}^{2}$) on the level of clay dispersion. The experiments carried out at N = 40 rpm, with and without partial barrel heating, generated nearly the same level of $\eta\dot{\gamma}^{2}$ (250 $\text{kPa}\cdot\text{s}^{-1}$) but the average residence times were quite different (t = 318 and t = 287 s, respectively). The experiments performed at N = 80 rpm involved similar average residence times (t = 263 ± 1 s) and distinct mechanical power (512 $\text{kPa}\cdot\text{s}^{-1}$and 825 $\text{kPa}\cdot\text{s}^{-1}$ for partial barrel heating and no heating, respectively).

The viscosity curves of the nanocomposite, average clay particles radii R and corresponding volume fraction ϕ for the two sets of experiments are compared in Figure 11. As anticipated, increasing the average residence time favors dispersion (see the relative magnitude of radii and volume fraction), also shifting upwards the shear viscosity curves. However, increasing $\eta\dot{\gamma}^2$ approximately by 60% had a minor effect on clay dispersion, although a careful analysis reveals a slightly smaller R and a higher ϕ for higher $\eta\dot{\gamma}^2$, but nearly identical viscosities. Figure 9 suggested that for experiments performed at 80 rpm without heating, dispersion could involve both break-up and erosion.

Thus, the almost similar level of dispersion probed probably means that at $N = 80$ rpm the average residence time in the first part of the extruder is insufficient to allow for significant intercalation, the higher stresses downstream playing the dominant role in dispersion.

4. Conclusions

The research reported and discussed in this chapter showed that monitoring *in situ* (i.e., using in-line and/or on-line sensing techniques) the development of the relevant physical and rheological phenomena along the axis of an extruder is important to better understand the underlying mechanisms and its influencing factors, as well as optimize compounding operations, such as the preparation of polymer-clay nanocomposites. In-process measurements can quickly provide information at different length scales, and thus contribute to establish correlations between rheological response, process-induced material structure/morphology and product properties.

In the case of the model nanocomposite studied here, consisting of an organoclay dispersed in PDMS, it was observed that applying larger stresses (e.g., increasing the screw speed) does not directly translate into better clay dispersion, whereas longer residence times do, but only if sufficient stresses are applied. Although a polymer melt intercalation step was not always identified, processing conditions facilitating it attained higher dispersion levels.

Acknowledgements

This project has received funding from the European Union's Horizon 2020 research and innovation programme under the Marie Skłodowska-Curie grant agreement No. 734205 – H2020-MSCA-RISE-2016.

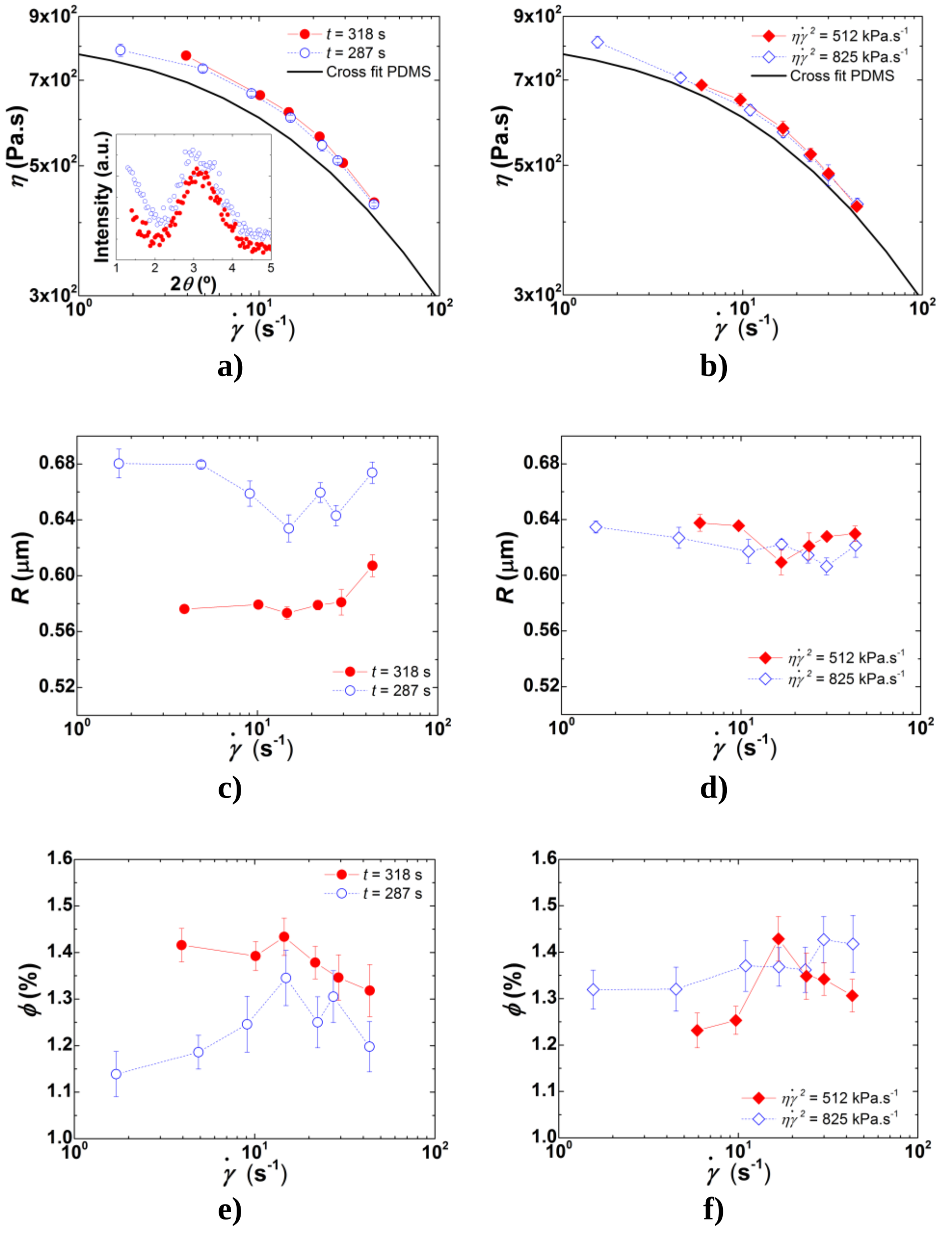

Fig. 11. Shear rate ($\dot{\gamma}$) dependence of shear viscosity η (a,b), clay particles radii R (c,d), and corresponding volume fraction ϕ (e,f); a),c) and e): Experiments with similar stress levels but different residence times (40 rpm, with and without partial barrel heating); b),d) and f): Experiments with similar residence times but different stress levels (80 rpm, with and without partial barrel heating)

References

1. Kim H., Kobayashi S., AbdurRahim M. A., Zhang M. J., Khusainova A., Hillmyer M. A., Abdala A. A., Macosko C. W., Graphene/Polyethylene Nanocomposites: Effect of Polyethylene Functionalization and Blending Methods. Polymer, 52: 1837-1846, 2011.
2. Alexandre. M., Dubois, P., Polymer-layered silicate nanocomposites: Preparation, properties and uses of a new class of materials. Mat. Sci. Eng. R., 28: 1–63, 2000.
3. Socher R., Krause B., Boldt R., Hermasch S., Wursche R., Potschke P., Melt mixed nano composites of PA12 with MWNTs: Influence of MWNTand matrix properties on macrodispersion and electrical properties. Compos. Sci. Technol., 71: 306-314, 2011.
4. Bauhofer W., Kovacs J. Z., A review and analysis of electrical percolation in carbon nanotube polymer composites. Comp. Sci. Technol., 69: 1486-1498, 2009.
5. Mittal V., Polymer Layered Silicate Nanocomposites: A Review. Materials, 2: 992-1057, 2009.
6. Lertwimolnun W., Vergnes B., Effects of processing conditions on the formation of polypropylene/organoclay nanocomposites in a twin screw extruder. Polym. Eng. Sci, 46*:* 314–323, 2006.
7. Vergnes B., Influence of processing conditions on the preparation of clay-based nanocomposites by twin-screw extrusion. Int. Polym. Proc, XXXIV: 482-501, 2019.
8. Barbas J. M., Machado A.V., Covas J.A., Processing conditions effects on dispersion evolution in a twin-screw extruder: Polypropylene-clay nanocomposites. Chem. Eng. Technol., 37: 257–266, 2014.
9. Covas J. A., Nóbrega J. M., Maia J. M., Rheological measurements along an extruder with an on-line capillary rheometer. Polym. Testing, 19: 165-176, 2000.
10. Mould S., Barbas J., Machado A. V., Nóbrega J. M., Covas J. A., Measuring the rheological properties of polymer melts with on-line rotational rheometry. Polym. Testing, 30: 602–610, 2010.
11. Mould S., Barbas J., Machado A. V., Nóbrega J. M., Covas J. A., Preparation of polymer-clay nanocomposites by melt mixing in a twin screw extruder: using on-line SAOS rheometry to assess the level of dispersion. Int. Polym. Proc., XXIX: 63-70, 2014.
12. Rodrigues P., Santos R. M., Paiva M. C., Covas J. A., Development of dispersion during compounding and extrusion of Polypropylene/Graphite Nanoplates Composites. Int. Polym. Proc., XXXII: 614-622, 2017.
13. Bicalho L. A., Covas J. A., Canevarolo S. V., On-line optical monitoring of polymer melting in a twin-screw extruder. Polym. Eng. Sci., 60: 2163–2175, 2020.
14. Teixeira P. F., Ferrás L. L., Hilliou L., Covas J. A., A new double-slit rheometrical die for in-process characterization and extrusion of thermo-mechanically sensitive polymer systems. Polym. Test., 66: 137–145, 2018.
15. Teixeira P. F., Hilliou L., Covas J. A., Maia J. M., Assessing the practical utility of the hole-pressure method for the in-line rheological characterization of polymer melts. Rheol. Acta, 52: 661-672, 2013.

16. Teixeira P.F, Sutera F., Scaffaro R., Covas J.A., Hilliou L., Multi-parameter in-process monitoring of clay dispersion during melt compounding with PLA, eXPRESS Polym. Lett.,13: 276–285, 2019.
17. Dennis H.R., Hunter D.L., Chang D., Kim S., White J.L., Paul D.R., Effect of melt processing conditions on the extent of exfoliation in organoclay-based nanocomposites. Polymer, 42: 9513–9522, 2019.
18. Bousmina M., Study of intercalation and exfoliation processes in polymer nanocomposites. Macromolecules, 39*:* 4259–4263, 2006.
19. Borse N.K., Kamal M.R., Estimation of stresses required for exfoliation of clay particles in polymer nanocomposites. Polym. Eng. Sci., 49: 641–650, 2009**.**
20. Reyna-Valencia A., Deyrail Y., Bousmina M., In situ follow-up of the intercalation process in a clay/polymer nanocomposite model system by rheo-XRD analysis. Macromolecules, 43: 354–361, 2010.
21. Teixeira P. F., Covas J. A., Hilliou L., In-line rheo-optical investigation of the dispersion of organoclay in a polymer matrix during twin-screw compounding, Polymers, 13: 2128, 2021.
22. Scurati A., Feke D.L., Manas-Zloczower I., Analysis of the kinetics of agglomerate erosion in simple shear flows. Chem. Eng. Sci.**,** 60: 6564–6573, 2005.
23. Domingues N., Gaspar-Cunha A., Covas J.A., Camesasca M., Kaufman M., Manas-Zloczower I., Dynamics of filler size and spatial distribution in a plasticating single screw extruder-modelling and experimental observations. Int. Polym. Process., XXV: 188–198, 2010.
24. Rwei S.P., Manas-Zloczower I., Feke D.L., Characterization of agglomerate dispersion by erosion in shear flows. Polym. Eng. Sci., 31, 558–562, 1991,
25. Collin V., Boudimbou I., Peuvrel-Disdier E., New insights in dispersion mechanisms of carbon black in a polymer matrix under shear by rheo-optics. J. Appl. Polym. Sci., 127: 2121–2131, 2013.
26. Ferrás L.L., Fernandes C., Semyonov D., Nóbrega J.M., Covas J.A., Dispersion of grafite nanoplates in polypropylene by melt mixing: The effects of hydrodynamic stresses and residence time. Polymers, 13: 102, 2021.
27. Matsumoto, K., Tanaka, T., Basic Study of Extensional Flow Mixing for the Dispersion of Carbon Nanotubes, Intern. Polymer Process., XXXVI: 379-387, 2021.
28. Yamada H., Manas-Zloczower I., Feke D. L., Influence of matrix infiltration on the dispersion kinetics of carbon black agglomerates. Powder Technol.**,** 92: 163–169, 1997.

Fernando M. Duarte[1], Catarina G. Ribeiro[1], João G. Ferreira[1], Sílvia A. Forte[1], José A. Covas[1]

USING HYBRID THERMOFORMING TO CONTROL THE THICKNESS DISTRIBUTION OF THE PARTS PRODUCED

Abstract: *The concept of hybrid thermoforming is introduced, with the aim of controlling the thickness gradient of thermoformed parts, and thus increase their performance and/or reduce their weight. The approach consists in producing sheets with non-uniform thickness by removing material by* CO_2 *ablation and/or adding an over-thickness by additive manufacturing at specific locations of sheets previously extruded, which are subsequently thermoformed. The usefulness of this novel methodology is demonstrated experimentally for a case study involving the production of a truncated conical cup. The conventional thickness distribution obtained for this type of geometry is significantly changed with the new strategy and can be tuned by selecting the locations and amount of material do be removed and/or added.*

Keywords: *thermoforming, thickness distribution, additive manufacturing;* CO_2 *laser ablation*

1. Introduction

Thermoforming is a processing technique whereby a previously extruded thermoplastic sheet is heated above its softening temperature and forced against the contours of a female or male mold, by applying pressure or vacuum to the sheet surface, eventually assisted by a direct mechanical load. The combined effect of the formation of a free bubble in the initial deformation stages, followed by the progressive contact of the hot sheet with the cold surface of the mold, which prevents it from undertaking any further deformation, causes a thickness gradient in the final part (Figure 1). Moreover, the bottom corner is always the last portion of the sheet to touch the mold, hence becoming the thinnest region of the part This thickness distribution is generally quite unfavorable in terms of mechanical performance (particularly to lateral and vertical compression, and impact resistance).

---

1) *Department of Polymer Engineering, Institute for Polymer and Composites, University of Minho, Guimarães, Portugal, fduarte@dep.uminho.pt; catarinafgribeiro@gmail.com; jpgferreira00@gmail.com; silvia-araujof@hotmail.com; jcovas@dep.uminho.pt.*

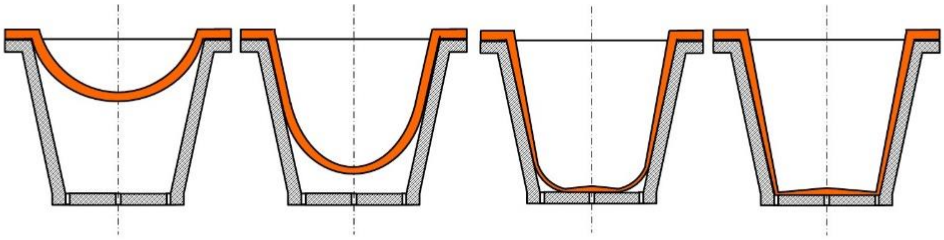

Fig. 1. Sheet deformation sequence during conventional vacuum thermoforming using a female mold. Typically, the thickness of the lateral wall of the part decreases from the top downwards, reaching a minimum value at the bottom corner

In order to circumvent this limitation, various thermoforming variants have been proposed over the years, which were progressively adopted in industry [1] For example, bubble thermoforming consists in inflating the hot sheet with compressed air, followed by the application of vacuum to shape the part usually using a male mold, whereas in plug-assisted thermoforming the hot sheet is initially stretched vertically downwards by mechanical means and then the application of vacuum pushes it against the contours of a female mold [1, 2-7]. Despite of these ingenious solutions, the presence of a thickness gradient in the parts produced is intrinsic to the existing thermoforming technologies.

Since the deformability of the sheet is temperature dependent, the thickness distribution of a thermoformed part can be altered somewhat by tuning locally the temperature of the heating elements, and thus create a more advantageous sheet temperature field at the end of the heating stage. This approach has been the focus of some research [8-15], but it often faces practical implementation difficulties in existing processing equipment. Anyway, the use of an appropriate thermoforming technique, together with an optimal set-up of the operating parameters and, if possible, the correct design of the part geometry, can minimize thickness gradients and ensure that the part has a minimum local thickness, and therefore, exhibits the required mechanical performance. As a matter of fact, it is not obvious that a thermoformed part should have uniform thickness for better properties under service.

The actual control of the thickness of a thermoformed part requires a novel approach to the process. This chapter presents and discusses a concept that could be used to control thickness distribution, by combining thermoforming with other manufacturing technologies. Specifically, the thickness of previously extruded sheets is changed locally, defining thickness variations both in the length and width directions, are then they are subjected a thermoforming stage. In the following sections, this hybrid thermoforming concept is first presented, and then the options of removing and adding material to the extruded sheet are discussed using experimental data.

2. The concept of hybrid thermoforming

When vacuum forming a truncated conical cup-like geometry, the resulting thickness gradient is that represented in Fig.1., i.e., the base of the cup is thinner than the lateral wall, the bottom corner is the thinnest, whereas the top is over thick. This is a consequence of the deformation mechanism also depicted in Fig. 1, whereby the free bubble progresses vertically downwards, freezing as it touches the lateral wall and finally touches the base, where it induces a radial thickness gradient. Consequently, the cup tends to be too thin at the base (and also at the lateral wall near the base), and maybe too thick at the top for most practical applications. This outcome could be corrected either by using a more complex thermoforming variant, but also by changing the thickness of the sheet to be formed at strategic locations, for example (Fig.2):

i) Removing material near to the sheet periphery (Fig.2a), so that at the end of the forming stage the thickness of the lateral wall is smaller and comparable to the average lateral thickness. This has also the added advantage of making the part lighter (and the material removed could be recycled). Of course, both the width and the depth of the ring to be removed will depend on the geometry of the part and on the targeted thickness gradient;

ii) Adding material in the center of the sheet (Fig.2b), so that upon forming this thicker region of the sheet will give rise to the base of the cup. In doing so, the extruded sheet could be thinner, hence thermoformed parts could also be lighter. With this methodology, the diameter and thickness of the material added must be carefully defined.

A combined solution would also be feasible, depending on the geometrical complexity of the part to be produced. The first example involves the hybridization of thermoforming with CO_2 laser ablation. The second possibility can be achieved by hybridizing thermoforming with 3D printing, namely Fused Filament Fabrication, FFF, a technique that uses continuous filaments of thermoplastic materials to gradually build 3D parts layer by layer.

As represented in Fig.2c, in both cases it is necessary to adequately define the geometry of the material to be removed/added. This can be done either empirically on a trial and error basis, or using available process modeling software capable of predicting the part thickness gradient produced from a pre-defined sheet thickness, or by coupling an optimization algorithm to a process modelling routine and find the geometries to add/remove that create, as much as possible, the target thickness gradient [16].

3. Experimental

Fig. 3 presents the geometry and dimensions of the female mold to be fixed in the vacuum thermoforming machine (Formech HD750, UK) used in this study. 1 mm thick extruded sheets of a blend of 50% Polystyrene (PS Laquerene 1540, manufactured by Total Petrochemicals) with 50% impact modified Polystyrene (HIPS

Laquerene 7240, also manufactured by Total Petrochemicals) were kindly supplied by Intraplás (Santo Tirso, Portugal) and cut into 250x250mm squares.

The removal / addition of material followed the procedures described in detail in sections 4 and 5, respectively.

For thermoforming purposes, the oven temperature and heating time were adjusted in order to assure a uniform sheet temperature of 140°C, which is the usual forming temperature for PS/HIPS. As schematized in Figure 4, after thermoforming the parts were cut into four slices, and the thicknesses along the arc length, from the center to the periphery, were measured with a digital caliper. At least five parts were produced under the same conditions and tested.

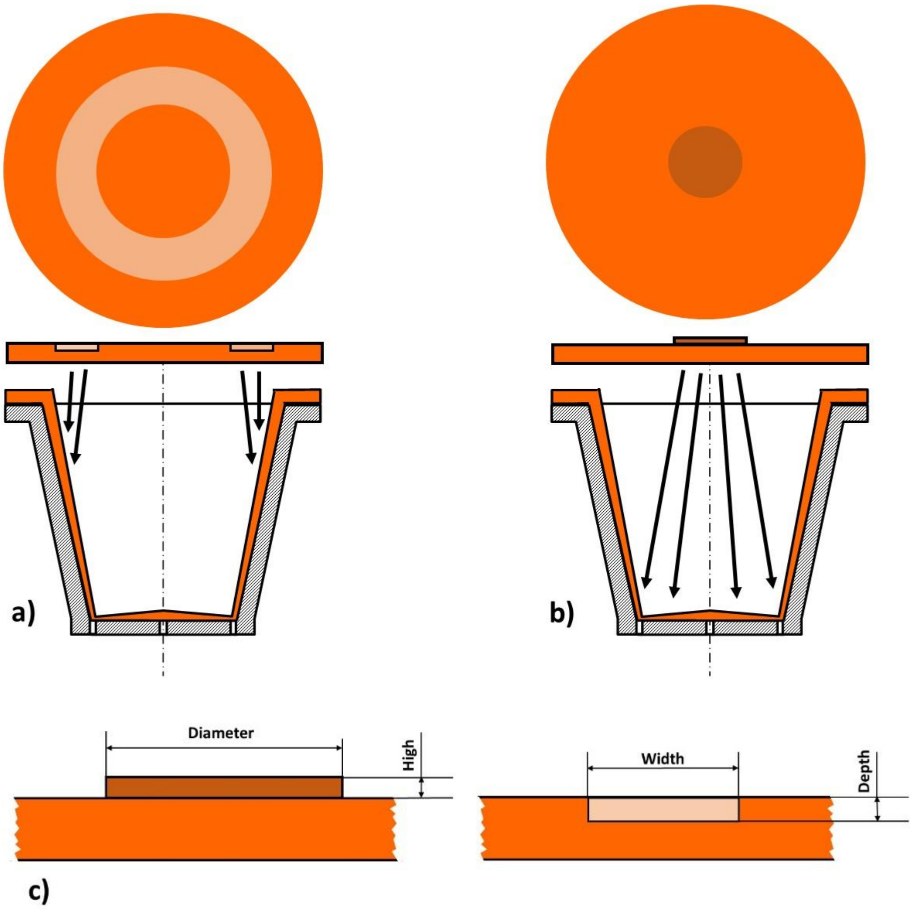

Fig. 2. The concept of hybrid thermoforming. Extruded sheets are subjected to a) material ablation, or b) material deposition to create localized thickness differences, and then thermoformed to obtain more favorable thickness gradients in the part. The geometry of the material to be removed/added (c) must be carefully defined

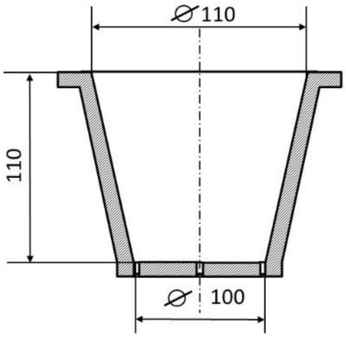

Fig. 3. Geometry and dimensions of the female mold used in this work

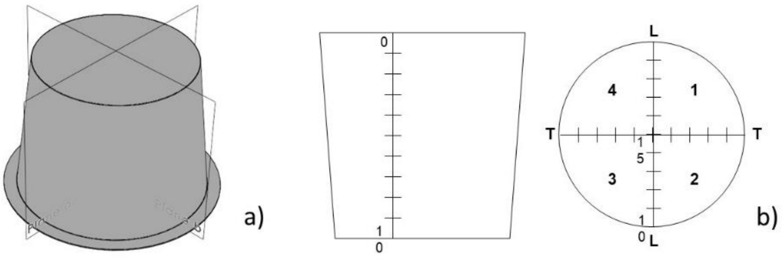

Fig. 4. Thickness measurement. a) Division the part into four identical slices. b) Identification of points along the arc length

4. Removing material approach

4.1 CO_2 laser ablation

Before using the 100W CO_2 laser (Thunder Laser CO_2 manufactured by Dongguan Thunder Laser Equipment Co., Ltd.), it is necessary to select the processing parameters (power and velocity) that assure the removal of the required amount of material, but without degrading the sheet. Thus, correlations between laser operating parameters and percentage of removed material were established assuming as objective a square area of 20x20mm (in order to estimate the reproducibility of the procedure, five squares were removed per laser operating condition). For that purpose, each sample was observed with a digital Leica DMS1000 microscope and the remaining sheet thickness was measured at 10 different points along the cutting line (see Figure 5).

Figure 6 presents the percentage of removed material depth relative to the initial 1 mm thickness as a function of laser power and velocity. Each experimental point is the mean value of 50 measurements (5 samples x 10 measurements). As expected, at constant power the removed material depth decreases with increasing speed. For example, at 30% of power and 150mm/s, the removed material is approximately 40%, while for 450 mm/s the removed material decreases to approximately 11%. The trends are not exactly linear, although the standard deviation is lower than 4.5%, and even lower for smaller removed depths. This phenomenon is not entirely clear, but may be related to unavoidable sheet heating under conditions inducing higher material removal.

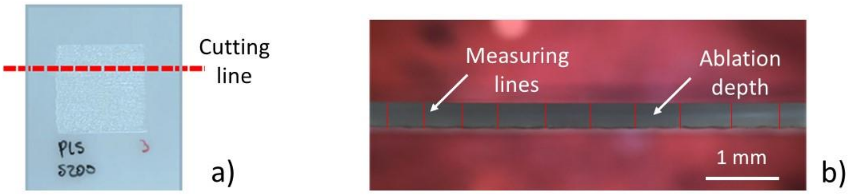

Fig. 5. Establishing a correlation between laser power/velocity and percentage of removed material. a) area with removed material; b) thickness measurements

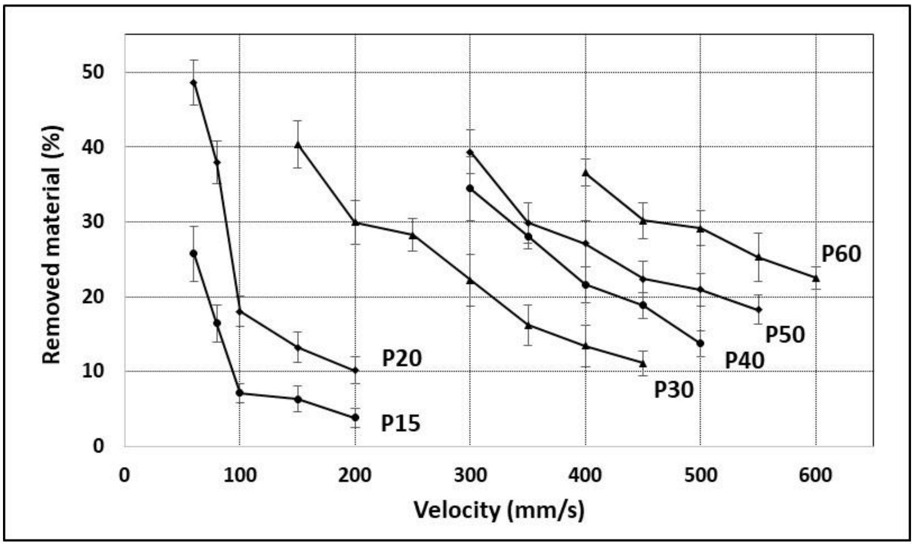

Fig. 6. Removed material depth for various CO_2 laser operation conditions (PXX refers to laser power)

Given the results obtained, sheets with different depths of removed material were obtained and subsequently thermoformed (Table 1). As shown, distinct combinations of power/speed conditions yield approximately the same removed material depth.

Table 1. Removal material depth for various laser operating conditions

Approximate removed material depth (%)	Power (W)	Velocity (mm/s)
10%	20	200
10%	30	450
20%	50	500
20%	40	400
30%	50	530
30%	30	200
30%	60	450
40%	50	300

4.2 Thickness distribution

Figures 7 and 8 depict the thickness distribution of thermoformed parts made using the mold presented in Fig. 3, from sheets containing a thinner annulus near the periphery, with a width of 10 and 15 mm, respectively, for a removal material depth of 10% and 30%. The reference line represents the thickness distribution along the arc length of a vacuum thermoformed part from a sheet with uniform thickness of 1mm. The other two lines in each figure denote the thickness distribution using different laser conditions (power/velocity) producing the same depth removal (see also Table 1).

The figures clearly demonstrate the significant role of removing material on the thickness distribution of the part. As expected (Figs. 7a and 8a), the removal of some material near to the periphery of the sheet affects mostly the thickness distribution near to the top of the cup, which becomes thinner. However, if more material is removed (i.e., keeping the width of the annulus but increasing the depth of material removed), the effect on the thickness distribution extends to the remaining regions of the arc length, including the base of the cup. This results from the fact that thinner regions of the sheet will become hotter than the thicker ones during the heating stage, and this affects the progress of the deformation mechanism during forming. Figs. 7b and 8b present interesting thickness distributions, with less thickness differences along the arc length, a thicker base and a thicker bottom corner – and a lighter cup than that obtained with the conventional uniform sheet.

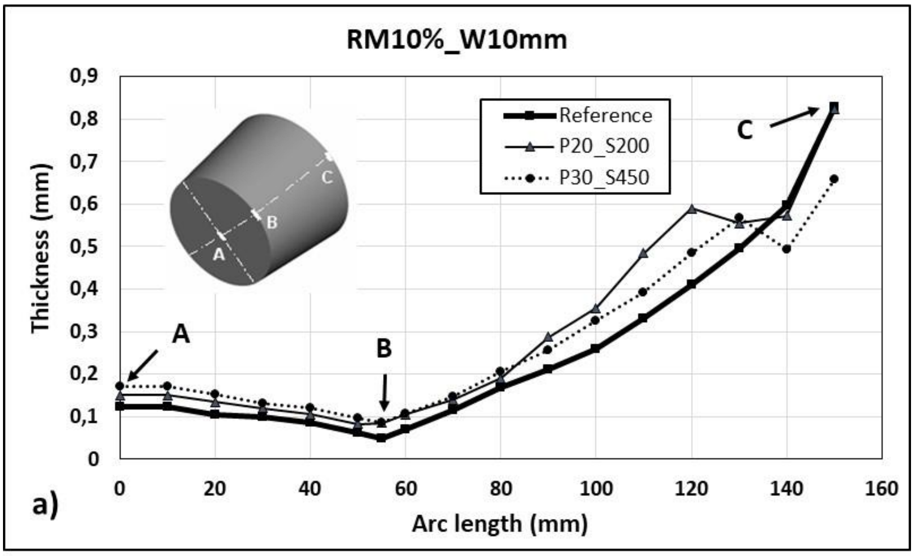

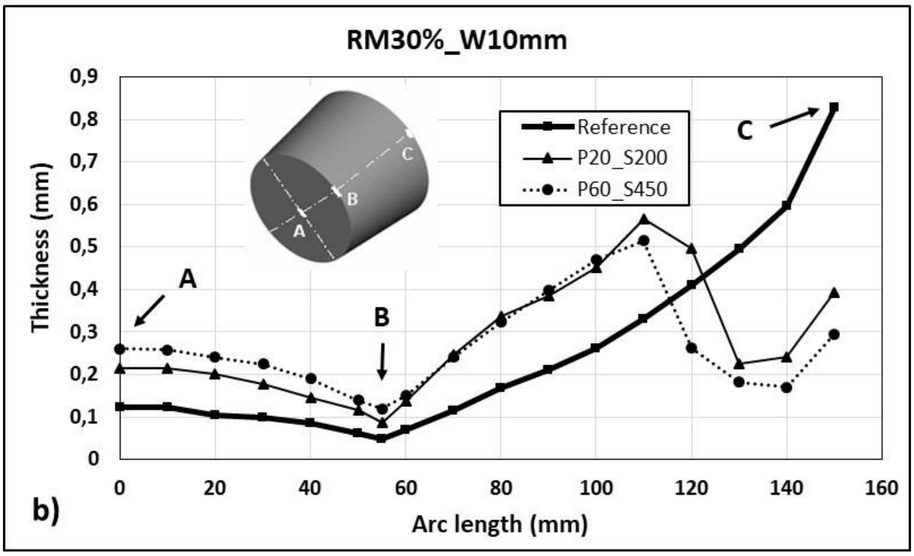

Fig. 7. Thickness distribution of a vacuum-formed part from a sheet containing a thinner annulus with a width of 10 mm with a) a removed material depth of 10%. b) a removed material depth of 30%. The reference line represents the thickness distribution along the arc length of a vacuum thermoformed part from a sheet with uniform thickness of 1mm. The thinner lines represent the thickness distribution using different laser conditions producing the same depth removal

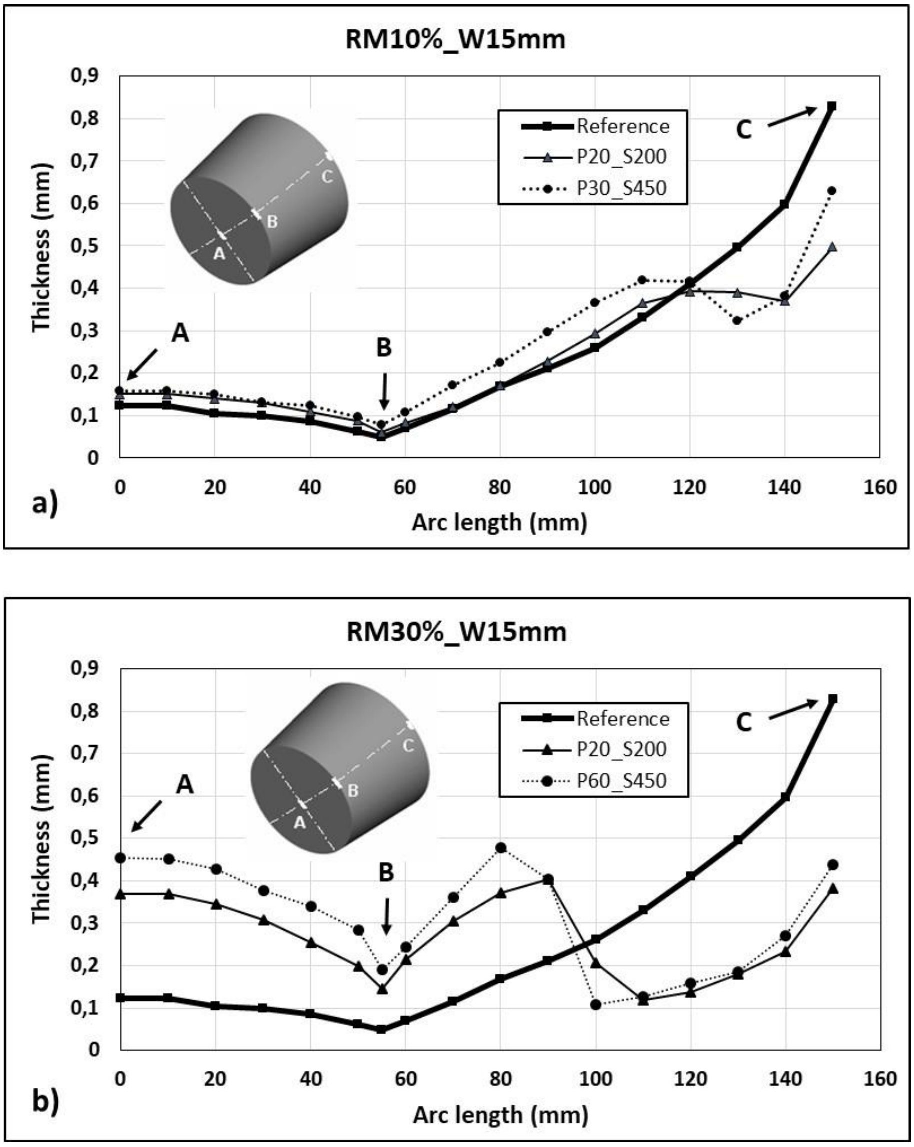

Fig. 8. Thickness distribution of a vacuum-formed part from a sheet containing a thinner annulus with a width of 15 mm with a) a removed material depth of 10%. b) a removed material depth of 30%. The reference line represents the thickness distribution along the arc length of a vacuum thermoformed part from a sheet with uniform thickness of 1mm. The thinner lines represent the thickness distribution using different laser conditions producing the same depth removal

Furthermore, the thickness distribution profiles produced by different laser operating conditions leading to the same removal depths are coincident, although the actual thickness values are somewhat dissimilar. This may be associated with experimental errors, to limits in the reproducibility of laser ablation, or to changes in the sheet surface/thermal properties caused by the energy of the laser.

Finally, the hybridization strategy can also be used to allocate a specific thickness in a particular region of the part. For the same cup, Figure 9 displays a thickness distribution similar to that occurring when using plug-assisted thermoforming, i.e., the base is thicker than the lateral wall. This was achieved by adequately setting the ablation program (power and laser velocity), as well as the removed material width. Specifically, two concentric annuli, with a width of 15 mm, were removed, one with a removal depth of 30%, the other with a depth of 20%.

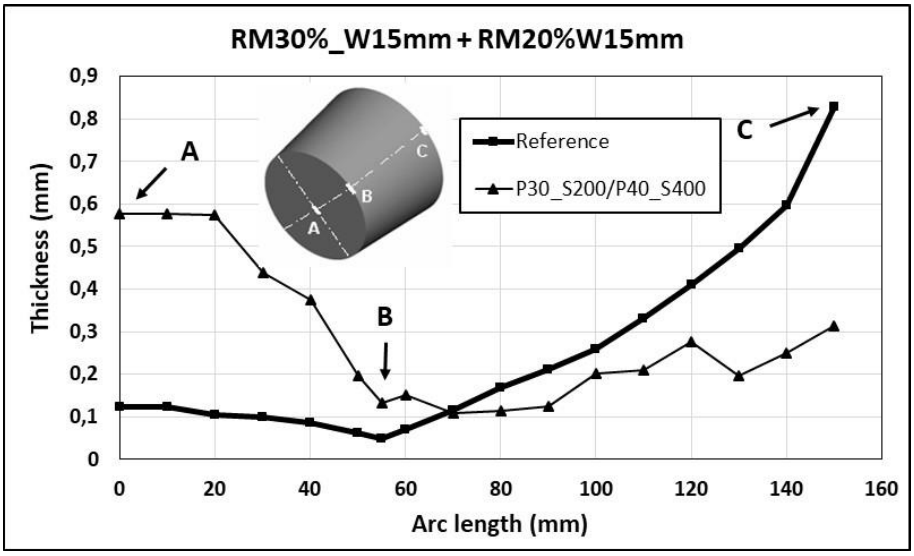

Fig. 9. Thickness distribution of a vacuum-formed part from a sheet containing two concentric annuli with a width of 15 mm, and removal depths of 30% and 20%. The reference line represents the thickness distribution along the arc length of a vacuum thermoformed part from a sheet with uniform thickness of 1mm

5. Adding material approach

5.1 Fused Filament Fabrication

Hybridizing thermoforming with 3D printing was achieved using a FFF Raised3d Pro2 3D printer and the IdeaMaker slicer software (version 3.3.0). HIPS filament with a diameter of 1.75 mm was supplied by Orbi-Tech (Leichlingen, Germany). A preliminary calibration of the printing equipment, namely of the printing base (Z axis offset), was carried out in order to consider the presence of the 1mm sheet of HIPS/PS. The latter was fixed to the printing bed of the 3D printer using double-sided adhesive tape. The printing conditions are as listed in Table 2. Disks with diameters of 40, 60 and 80mm, and heights of 0.05, 0.1, 0.2 and 0.4 mm were printed as sheet over-thickness. At least 3 sheets were produced and tested for each condition. Samples were coded in terms of the existing over-thickness: for example, D80/T0.2 denotes a part/sheet with an over-thickness with a diameter of 80mm and a height of 0.2 mm.

It was important to check whether the printed disks and the sheet exhibited good bonding, or whether they would detach during vacuum forming. Figure 10 presents cross-sections of the sheet and over-thickness before (Fig.10a) and after forming (fig.10b), as observed with optical microscopy. The good bonding of the individual filaments to the extruded sheet throughout printing and forming is evident.

Figure 11 displays vacuum formed cups obtained from a sheet with uniform thickness (Fig.11 top) and D80/T0.2 (fig. 11 bottom). The thicker regions are easily identifiable. As before, the cups were sliced into 4 equal parts and the thickness was measured along each arc length.

Table 2. 3D printing parameters

Geometry	Circular
Pattern type	Concentric
Infill (%)	100
Nozzle diameter (mm)	0.4
Printing velocity (mm/s)	20
Extrusion temperature (ºC)	245
Printing bed temperature (ºC)	60

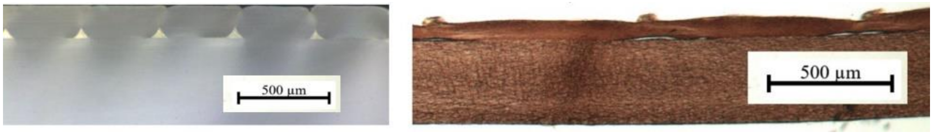

Fig. 10. Bonding between the printed filaments and the extruded sheet. a) after 3D printing, b) after vacuum forming

5.2 Thickness distribution

Figure 12 shows the thickness distribution along the arc-length of the thermoformed part under study, obtained from a uniform sheet thickness of 1 mm (D0/T0) and from sheets with an over-thickness with a diameter of 40 mm (Figure 12a) and a diameter of 80 mm (Figure 12b), for heights of 0.05, 0.1, 0.2 and 0. 4mm. The thicker extent of the various experimental lines corresponds to the arc length where the over-thickness is present. For each over-thickness diameter, the length changes with the height of the printed layer.

As anticipated (see Fig.2), the over-thickness of sheet located at its center affects significantly the thickness distribution and average value at the base of the cup. Moreover, and also logically, as the diameter of the over-thickness increases from 40 to 80mm, the effect of the latter extends to the bottom corner and lateral wal

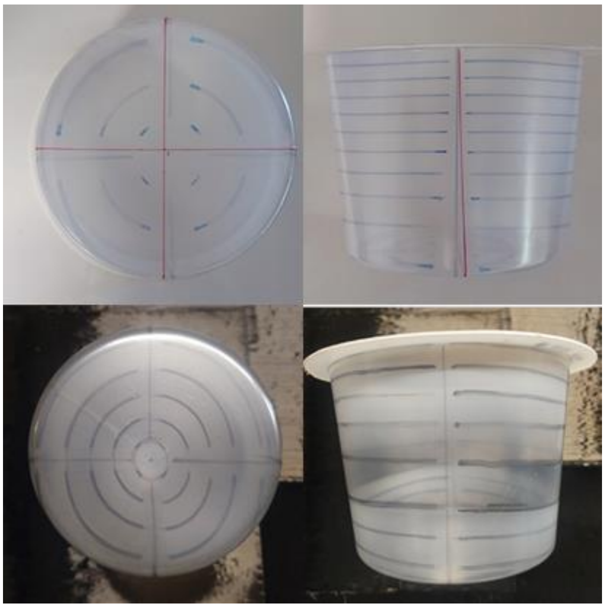

Fig.11 Thermoformed parts made from extruded sheets with uniform thickness (top) and D80/T0.2 (bottom). The existence of the over-thickness could be readily identified both visually and performing wall thickness measurements. Red lines were used to cut slices. Dark lines show differences in local deformation

Fig.12 also shows that for over-thicknesses of 0.05mm or less, their presence has little influence on the final thickness distribution. Conversely, a height of 0.4mm has a very significant effect, especially on the cup base.

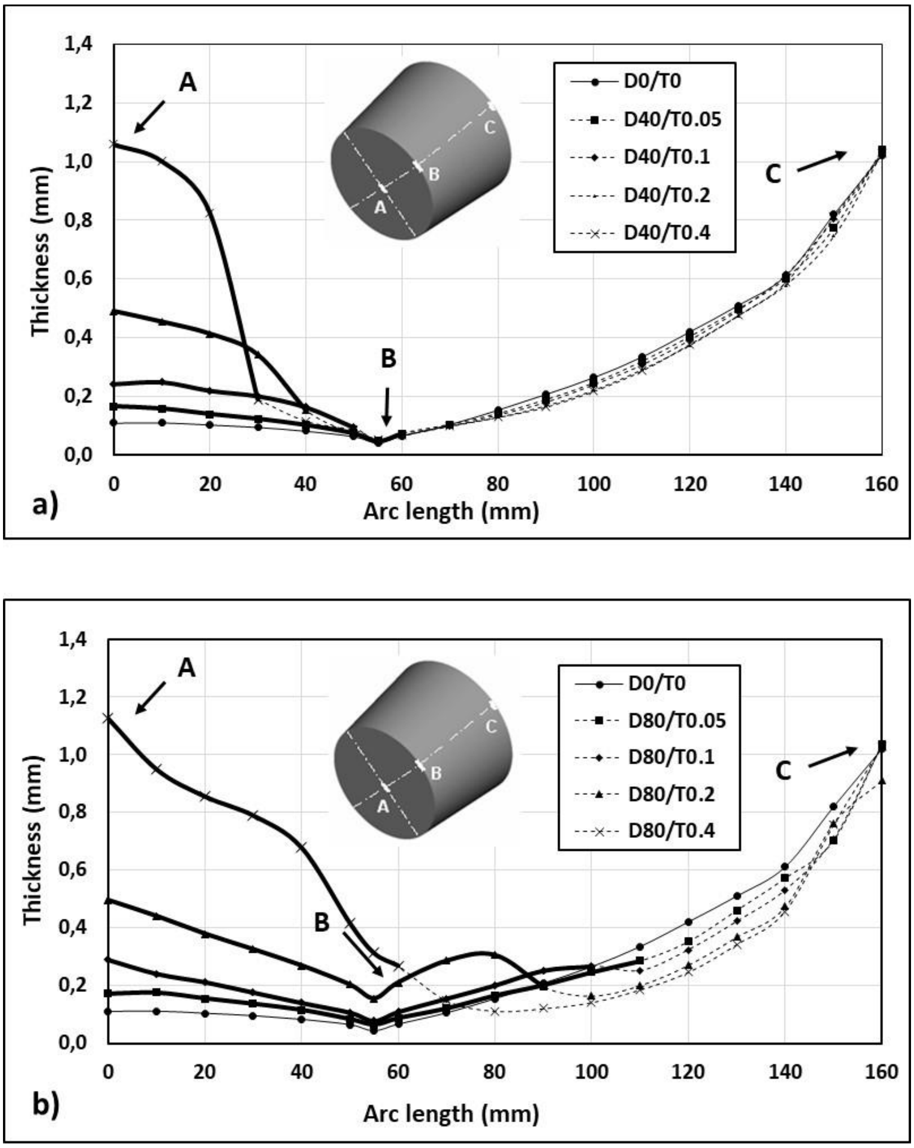

Fig. 12. Thickness distribution of a vacuum-formed part from a sheet containing an over-thickness a) with a diameter of 40 mm b) with a diameter of 80 mm, with different heights (from 0.05 to 0.4mm). The thin continuous line represents the thickness distribution along the arc length of a vacuum thermoformed part from a sheet with uniform thickness of 1mm. The thicker length of each line corresponds to the length of the arc where the over-thickness is present

Contrarily to the approach of removing material, which caused a higher temperature of the thinner regions of the sheet, the over-thickness strategy generates a lower local sheet temperature at the end of the heating stage, hence a lower deformation capacity. When the diameter of the over-thickness is 80 mm and its height is at least 0.2mm (Figure 12b), the thickness distribution becomes quite favorable, as the base of the cup, including its corner, becomes significantly thicker in relation to conventional thermoforming (an increase of 10 times for a height of 0.4mm).

6. Conclusions

Thermoforming produces parts with a thickness gradient, which may affect their performance under service conditions. To reduce this drawback, several variant techniques have been developed, and operating strategies have been proposed. However, the problem persists, in the sense that although the local thickness differences can be made more favorable, a far from optimal thickness gradient is inherent to the process.

This chapter proposed new approach to the process, which could achieve control of the thickness distribution of the manufactured parts. It involves the hybridization of thermoforming with techniques yielding extruded sheets with localized non-uniform thickness. Two routes were explored. The first consisted in reducing the thickness of the sheet in the areas where it will undergo less stretching during forming, by means of CO_2 laser ablation. The second involved adding material in the zones of the sheet that will be subjected to higher stretch during forming, using Fused Filament Fabrication, an additive manufacturing technique.

These two methodologies were evaluated experimentally for a practical case study. The results obtained demonstrated that both thermoforming hybridization with CO_2 laser or with FFF produce the expected significant effects on thickness distribution, and thus have the potential to be used for controlling purposes.

Further work is required to explore the effects of all the parameters involved in these hybridization techniques, as well as establishing an optimization methodology to set the operating conditions of hybrid thermoforming leading to a specific thickness distribution.

Acknowledgements

This project has received funding from the European Union's Horizon 2020 research and innovation programme under the Marie Skłodowska-Curie grant agreement No. 734205 – H2020-MSCA-RISE-2016.

References

[1] Throne J.L., Technology of Thermoforming, Hanser Publishers, Germany, 1996.

[2] Ayadi A., Lacrampe, M.F., Krawczak, P., Bubble assisted vacuum thermoforming: considerations to extend the use of in-situ stereo-DIC measurements to stretching of sagged thermoplastic sheets. Int. J. Mater. Form., 13, 59–76, 2020.

[3] Sasimowski E., A pressure-bubble vacuum forming process for polystyrene sheet. Advan. Sci. Tech. Res. J., 11 (2), 180-186, 2017.

[4] Martin P., Duncan P., The role of plug design in determining wall thickness distribution in thermoforming. Polym. Eng. Sci., 47, 804-813, 2007.

[5] Duarte F. M., Covas, J. A., Multilayer plug concept to enhance thickness distribution control of deep thermoformed parts, Plastics, Rubber and Composites, 37:7, 293-300, 2008.

[6] McCool R., Martin P.J., The role of process parameters in determining wall thickness distribution in plug-assisted thermoforming. Polym. Eng. Sci., 50, 1923-1934, 2010.

[7] Marathe D., Rokade D., Busher A. L., Jadhav K., Mahajan S., Ahmad Z., Gupta S., Kulkarni S., Juvekar V., Lele A., Effect of Plug Temperature on the Strain and Thickness Distribution of Components Made by Plug Assist Thermoforming. International Polymer Processing, 31:2, 166-178, 2016.

[8] Wang C., Nied H.F., Temperature optimization for improved thickness control in thermoforming. J. Mater. Process. Manuf. Sci., 8, 113-126, 1999.

[9] DiRaddo R.W., Meddad A., Sensitivity of operating conditions and material properties for thermoforming process. Plast. Rubber Compos., 29:4, 163-167, 2000.

[10] Duarte F.M., Covas J.A., IR sheet heating in roll fed thermoforming: Part 1 - Solving direct and inverse heating problems. Plast., Rubb. Compo., 31, 307-317, 2002.

[11] Schmidt F.M., Le Maoult Y., Monteix S., Modelling of infrared heating of thermoplastic sheet used in thermoforming process. J. Mater. Process. Technol.,143, 225-231, 2003.

[12] Duarte F.M., Covas J.A., On the use of the heating stage to control the thickness distribution in thermoformed parts, International Polymer Processing, 19, 186-198, 2004.

[13] Bordival M., Andrieu S., Schmidt F., Maoult Y.L., Monteix S., Optimization of infrared heating system for the thermoforming process. ESAFORM 2005 -8th ESAFORM conference on material forming, Cluj-Napoca, Romania, hal-01788422, 925-928, 2005.

[14] Chy M. M., Boulet B., A conjugate gradient method for the solution of the inverse heating problem in thermoforming, IEEE Industry Applications Society Annual Meeting, Houston, TX, USA, 1-8, 2010.

[15] Li ZZ., Ma G., Xuan D.J., Seol S.Y., Shen, Y.D., A study on control of heater power and heating time for thermoforming. Int. J. Precis. Eng. Manuf., 11, 873–878, 2010.

[16] Gaspar-Cunha A., Costa P., Galuppo W.C., Nóbrega J.M., Duarte F., Costa L., Multi-Objective Optimization of Plastics Thermoforming. Mathematics, 9, 1760-2021.

Volodymyr Krasinskyi[1], **Ivan Gajdoš**[2], **Tomasz Jachowicz**[3]

REVIEW ON THE PROCESSING AND PROPERTIES OF NANOCOMPOSITES BASED ON POLYVINYL ALCOHOL AND INTERCALATED MONTMORILLONITE

Abstract: *The work is devoted to developing a method for producing nanocomposite based on polyvinyl alcohol (PVA) and montmorillonite intercalated with polyvinylpyrrolidone. The structure and thermal characteristics of nanocomposites were investigated by X-ray diffraction analysis and differential scanning calorimetry. The modification of PVA with intercalated montmorillonite reduces the degree of crystallinity of the resulting nanocomposites but significantly increases their thermal stability. Under ultrasound, the intercalated montmorillonite was completely distributed in a PVA solution and formed a monocrystalline structure. The method of obtaining structured, water-insoluble nanocomposite films based on PVA is also developed in work. Films based on PVA with modified montmorillonite were cross-linked at 110 ºC in the presence of 5 wt.% acrylic acid and 0.5 wt.% Ferrous (II) sulfate as an initiator. The formed films have a homogeneous cross-linked structure. The influence of borax, the content of intercalated MMT, and solution pH on the rheological properties of PVA-based compositions have been established.*

Keywords: *Polyvinyl alcohol, montmorillonite, polyvinylpyrrolidone, X-ray diffraction analysis, differential scanning calorimetry, structure, viscosity, water absorption.*

1. Introduction

Nanocomposites are a new class of alternative materials in which nanosized fillers are dispersed into a polymer matrix, resulting in improved elasticity, strength, thermal stability, fire resistance, and barrier properties [1,2]. In this regard, nanocomposites are an attractive alternative to polymer-filled disperse powders for use in the packaging, medical, automotive and other industries [3,4].

Intercalation inorganic polymers in laminated materials such as clay minerals – a promising new method of obtaining organic-inorganic nanostructures – supramolecular structures with specific molecular structure [4,5]. Such an approach causing multifaceted interest. Firstly, there is the practical ability to create layered nanocomposites. Secondly, it is important specificity intercalation and its manifestation in acquiring systems improved physical and chemical properties.

---

[1] *Lviv Polytechnic National University, Department of Chemical Technology of Plastics Processing, 12 Bandera Str., Lviv, 79013, Ukraine, vkrasinsky82@gmail.com.*

[2] *Technical University of Košice, Faculty of Mechanical Engineering, Department of Technologies, Materials and Computer Aided Production, Masiarska 74, 040 01, Košice, Slovakia, ivan.gajdos@tuke.sk.*

[3] *Lublin University of Technology, Faculty of Mechanical Engineering, Department of Technology and Polymer Processing, ul. Nadbystrzycka 36, 20-618 Lublin, Poland, t.jachowicz@pollub.pl.*

Furthermore, the study of these products can provide important information about the nature of chemical interactions in them, specific adsorption of polymers on nanoscale particles and so on.

Currently, layered silicates, in particular montmorillonite (MMT), hectorite, and saponite, are the most used nanofillers [5]. Polymer molecules can intercalate in a gallery of layered silicates, pushing the layers and creating a nanocomposite [6,7,8]. The most common methods for producing aluminosilicate nanocomposites are polymer modification during polymerization, mixing with a polymer in the viscous-fluid state at high shear stress, or mixing in solution [9]. To achieve a high dispersion of nanofiller in a polymer matrix, high-pressure mixing, centrifugation, and ultrasonic treatment are used. Ultrasonic treatment is one of the most important methods for increasing the gallery interval between silicate layers in nanoclay, which considerably improves their dispersion in polymers [9,10]. In addition, ultrasonic treatment also affects the polymer matrix, resulting in the formation of a material with a new structure and altered properties [11].

Polyvinyl alcohol (PVA) is used in the industrial, commercial, medical, and food sectors to produce many products, such as varnishes, resins, surgical yarns, and food packaging, that are often in contact with food [12]. Therefore, improving the mechanical and chemical stability of PVA is an urgent problem that can be successfully solved by combining PVA with layered silicates.

Nanocomposites on a PVA and layered silicate base have improved characteristics, explained by the formation of a new crystalline structure. Strawhecker et al. [13] examined the structure of PVA based nanocomposite with a 20 wt.% MMT content using a transmitted electron microscope. In the intercalated structures, inorganic layers with parallel to each other orientation, characteristic of natural silicates, were separated by superfine (1.3–5 nm) layers of PVA. Due to the orderly parallel orientation of the silicate layers, the intercalated structures have clearly expressed peaks in the X-ray diffraction curves. In layered structures, the silicate layers are much further apart (>> 5 nm). In this case, the orientation of the layers is chaotic, and there is no parallel aggregation [14].

Aslam et al. [15] used XRD to show that with the increase in MMT content from 40 to 90 wt.% in PVA, the height of the interlayer space in the nanocomposite is uniformly reduced. At low concentrations of layered silicate, the diffraction peak, corresponding to the magnitude of the MMT interlayer space, moves to the $2\theta < 3^{\circ}$ area. At these concentrations, the structure of MMT intercalated silicate layers, which are characterized by a more than 5 nm interlayer space, remains ordered.

By using the DSC method [13,16,17], it was established that with the increasing MMT content in PVA, the intensity of peaks corresponding to the glass-transition and melting points decrease. With a more than 60 wt.% MMT content in the composite, the peaks completely disappear [13]. This suggests that in such materials, the polymer is under the influence of inorganic layers. At lower MMT concentrations (up to 20 wt.%), two clear peaks, referring to the melting point, appear on the DSC curves. One of them is in the region of the unfilled polymer's melting point, and the second one is at a higher temperature. The double (dual) melting point corresponds to two crystalline phases, one phase is formed predominantly by syndiotactic molecular chains and the second phase by atactic ones. The difference between the melting points is 15–22 °C. Rajeswari et al. [18] melted polymer nanocomposites using polyvinyl alcohol (PVA) with the different weight percentages of calcined clays in a twin-screw extruder. Scanning electron microscopy confirmed the degree of exfoliated nanocomposites. The polymer and functionalized nanoclay interactions were reflected in the enhanced thermal stability and mechanical properties.

Fang et al. [19] further improved and enhanced the performances and properties of polyvinyl acetate (PVAc); MMT and N-hydroxymethyl acrylamide (NMA) were simultaneously introduced to polymerize with vinyl acetate (VAc). Linear macromolecular chains of PVAc–NMA were formed in MMT layers. MMT was exfoliated into layers or sheets of nanoparticles and dispersed randomly in the PVAc–NMA matrix. PVAc–NMA–MMT had good dispersion, excellent storage stability, and high static tensile strength (6.47–6.85 MPa).

Bee et al. [20] investigated the effect of calcined eggshell and MMT on the physicomechanical properties and thermal characteristics of PVA blends. The addition of MMT particles significantly reduced the tensile strength and elongation at break of PVA blends. This indicates that the MMT particles did not provide a reinforcement effect to polymer matrix of PVA blends due to the poor dispersion and intercalation effect of MMT particles in PVA, as evidenced by shifting 2θ to higher values in the XRD analysis. However, the effective intercalated MMT particles in the PVA matrix were only observed in a polymer matrix with 2 phr calcined eggshell added PVA/MMT blends with the increased d-spacing of deflection peak (002). The incorporation of low calcined eggshell loading levels (≤ 2 phr) showed a significant increase in the optimum melting temperature and enthalpy of melting for PVOH and PVA/MMT blends. Additionally, there are known studies [21] in which the thermal stability of PVA is increased by adding ZnO nanoparticles.

The physicomechanical properties of PVA depend differently on the MMT content. The Young's module of a nanocomposite with 4 wt.% MMT is 3 times higher than that of unfilled PVA. The increase in MMT content decreases the dependence of the elasticity modulus on the MMT concentration [22]. The maximum tensile stress of PVA/MMT composites depends slightly on the MMT concentration. The higher the MMT concentration, the less fracture load is observed [23,24].

Stratified nanocomposites based on polymer and layered silicate have a higher thermal stability, resistance to solvents and resistance to different environments permeability compared to conventional filled materials. Due dispersion of the filler at the nanoscale they are able to maintain light transmission of the polymer. In nanocomposites PVA/MMT, especially at low concentrations layered silicate (< 10%) suitable for industrial use, transmission electron microscopy and the number of simultaneous RPDA show intercalated simultaneously reveal the number and stratified silicate layers [25].

Nanocomposites PVA/MMT has a high light transmission even in the filler content, sufficient for the formation of layered nanocomposites. This is due to the dispersion of particles in a matrix layered silicate cover the nanoscale. Good light transmission allows using nanocomposite materials PVA/MMT for manufacturing paper coating simultaneously with unfilled PVA (which is used now). The presence of MMT particles does not affect the permeability of the composite for the visible spectrum (wavelength 400-700 nm), so there is a high light transmission characteristic of unfilled PVA [15], but significantly increases atmospheric stability.

A method for obtaining nanocomposite films based on PVA and MMT intercalated with polyvinylpyrrolidone (PVP) was previously developed [26]. Polyvinylpyrrolidone initiates the polymerization of hydroxyalkylene methacrylates as an active complexing agent [27], forms new polymeric random cross-linked matrices [28,29], and contributes to the formation of homogeneous polymer mixtures based on amphipolar polymers [30]. In this work [31], the formation of the intercalated structure of MMT during PVP modification in aqueous solution by ultrasound is substantiated by X-ray and DTA analyses. Intercalated PVP MMT is easily distributed into PVA aqueous solutions without agglomerate formation.

The objective of this work was to investigate the influence of composition and production conditions on the structure and thermal characteristics of the developed nanocomposites using XRD and DSC analyses. And also create a method of producing structured water-resistant films based on PVA and intercalated MMT, investigate the impact of borax, MMT content, and pH on the rheological properties of PVA solutions.

2. Results and Discussion

2.1. Study of rheological properties of compositions based on modified PVA and intercalated MMT

PVA SUNDY 088-20 by Chinese company "Sinopec Sichuan Vinylon Works" (PVA 088-20 – 23 mPa·s) used for obtaining films. Prepared 8% solution of PVA in water and buffer solution with pH 4.4 and 7.9. Dissolution was performed at 60 °C using a magnetic stirrer. To the PVA resulting solution was added MPM in an amount that the ratio of elementary units of PVA to elementary parts PVP system was 16:1, 12:1, 8:1. The resulting mixture was treated with ultrasonic waves of a frequency of 22 kHz on the machine "Volna UZTA 0.4/22 OM" for 3 minutes. Then the mixture was poured into special molds to produce films with plastic lining (to facilitate removal of the finished films form) and air-dried at room temperature. Finished films separated from the form and subjected to heat treatment strove at a temperature of 150 °C for 30 minutes (fig. 1).

Viscosimaterial study of aqueous solutions of PVA was performed using capillary viscometer (capillary diameter – 0.56 mm). Research performed at 25±0,1 °C.

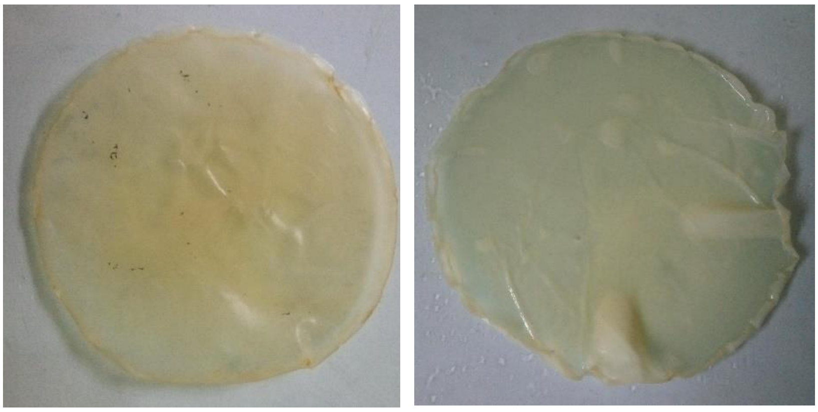

a) b)

Fig. 1. Samples of films PVA: MPM =12:1
a – after heat treatment at 150 ^{0}C; b – after the extracts in water for 24 hours

For research were used compositions based on PVA and MPM (PVP:MMT = 5:1) ratio of the number of elementary units of PVA to the number of PVP elementary units in and montmorillonite-polyvinylpyrrolidone mixture as 12:1.

The introduction of modifiers delivered in the processing solutions ultrasonic waves for 3 minutes because this method of mixing ensures satisfactory distribution of particles in the composition. Comparative results of research of the effect of pH and sodium tetraborate developed on the rheological properties of compositions presented in Tables 1-3.

As we see, the lowest values of intrinsic viscosity regardless of environment marked by pure PVA solutions. The introduction of MPM to PVA solution leads to higher viscosity of compositions which can be explained by physical interaction of montmorillonite-polyvinylpyrrolidone mixture of polymer macromolecules in solution under the influence of ultrasound (evidenced by a slight change of color compositions).

It is logical that the highest viscosity solutions are characterized by compositions with traces of sodium tetraborate resulting from the formation of intermolecular chelate compounds by interaction of the -hydroxyl of PVA groups with borate-ions.

Evaluating the results presented in Tables 1-3, can be concluded significant effect of pH on the viscosity of the solution of compositions. The lowest values observed intrinsic viscosity of the composition obtained in a neutral environment. Viscosity similar solution compositions in alkaline and acidic environments, virtually the same and is significantly higher.

Table 1. Rheological properties of solutions of compositions (pH = 7)

№ s/n	C, g/ml	T, s	η_{rel}	η_{spec}	[η]
PVA					
1	1	198,25	2,05	1,05	0,585
2	0,5	139,75	1,42	0,42	
3	0,25	113,44	1,17	0,17	
PVA:MPM = 12:1					
1	1	221,5	2,29	1,29	0,625
2	0,5	144,1	1,49	0,49	
3	0,25	115,56	1,2	0,2	
PVA:MPM= 12:1 of sodium tetraborate					
1	1	226,3	2,34	1,34	0,695
2	0,5	146,51	1,52	0,52	
3	0,25	117,26	1,22	0,22	

*MPM – PVP:MMT = 5:1, while the net outflow of solvent (water) – 96.71 sec.

C – concentration of polymer in the solution, g/ml;
t – time leakage of the solution through capillary viscometer with capillary diameter of 0.56 mm, sec;
η_{rel} – relative viscosity of polymer solution;
η_{spec} – specific viscosity of polymer solution;
[η] – intrinsic viscosity.

Table 2. Rheological properties of solutions of compositions (pH =4,4)

№ s/n	C, g/ml	T, s	η_{rel}	η_{spec}	[η]
PVA					
1	1	222,14	2,15	1,15	0,59
2	0,5	148,84	1,445	0,445	
3	0,25	122,21	1,18	0,18	
PVA:MPM = 12:1					
1	1	236,25	2,29	1,29	0,91
2	0,5	160,17	1,555	0,555	
3	0,25	128,9	1,25	0,25	
PVA:MPM= 12:1 of sodium tetraborate					
1	1	243,2	2,36	1,36	0,98
2	0,5	166,34	1,615	0,615	
3	0,25	131,85	1,28	0,28	

* Time outflow of pure solvent (acid buffer solution) – 103 sec.

With aim to determine the permeability and degree of structuring films based on modified PVA investigated their water absorption in cold water. The research results are presented in Table 4.

Table 3. Rheological properties of solutions of compositions (pH =7,9)

№ s/n	C, g/ml	T, s	η_{rel}	η_{spec}	[η]
PVA					
1	1	236,17	2,26	1,26	0,645
2	0,5	153,62	1,47	0,47	
3	0,25	146,3	1,4	0,4	
PVA:MPM = 12:1					
1	1	247,67	2,37	1,37	0,97
2	0,5	167,2	1,6	0,6	
3	0,25	131,6	1,26	0,26	
PVA:MPM= 12:1 of sodium tetraborate					
1	1	256,03	2,45	1,45	0,106
2	0,5	169,3	1,62	0,62	
3	0,25	132,72	1,27	0,27	

* Time outflow of pure solvent (alkaline buffer solution) – 104.5 sec.

Table 4. The water absorption of films based on modified PVA depending on the pH environment (heat treatment at 150 °C)

The composition structure	The water absorption for 24 hours,% by weight.		
	pH=7	pH=4.4	pH=7.9
PVA: MPM =16:1	219,66	82,56	86,15
PVA: MPM =12:1	**186,26**	**76,23**	**83,23**
PVA: MPM =8:1	196,85	80,51	90,17
PVA:MMT=16:1	185,03	136,24	208,71
PVA:MMT=12:1	292,84	120,07	269,56
PVA:MMT=8:1	**130,69**	**105,72**	**124,66**

Without treating all the films based on modified PVA dissolved in water independently of pH in which they are received. After heat treatment at 150°C for 30 minutes film based on modified PVA only swell in water but not dissolved. From Table 4 we see that the lowest water absorption of film observed PVA:MPM = 12:1, produced in an acidic environment, which correlates well with the results of the mechanical strength of the films [14]. Thus, water absorption of films obtained in acidic medium, 2.5 times lower than the films obtained in a neutral environment. The films-based compositions obtained in an alkaline environment also characterized by reduced water absorption, but after treating they slightly yellow, which may indicate partial destruction of PVA. It is also worth noting that films based on PVA modified MPM characterized by lower water absorption than films based on PVA modified pure MMT. So, the best environment to produce structured films based on modified PVA is acidic buffer solution, a modifier – MPM ratio PVA:MPM = 12:1 (the number of elementary units of PVA to PVP).

2.2. Study of the structure and thermal characteristics of nanocomposites based on PVA and intercalated MMT

SUNDY PVA 088-20 from the Chinese firm "Sinopec Sichuan Vinylon Works" (PVA 088-20, 23 mPa·s) was used for producing films. 8% (by weight) solutions of PVA in water were used. Dissolution was carried by stirring out at 60°C with a magnetic stirrer for 2–3 hours. MPM was added to the prepared PVA solutions in the amount such that the ratio of PVA:PVP elementary links should be 12:1. At the same time compositions based on PVA with similar amounts of unmodified MMT were prepared. The resulting mixtures were treated for 3 minutes with 22 kHz ultrasound using a "Wave UZTA-0.4/22-OM". To obtain films, the mixture was poured into special forms with a polyethylene lining. After formation, the film was dried in air at room temperature. The resulting films were separated from the form and subjected to heat treatment in an oven at 110°C for 30 minutes. To obtain water-insoluble films, 5 wt.% acrylic acid and 0.5 wt.% polymerization initiator ($FeSO_4$) were added to these solutions. $FeSO_4$ initiates the cross-linking reaction due to the formation of an active complex with charge transfer in the presence of PVP.[27] The behavior of the obtained films in water was investigated. Only a heat-treated film containing acrylic acid is water-insoluble.

The research objects were: sample 1 – PVA based film; sample 2 – PVA/MPM based film (PVA:MPM = 12:1) dried at room temperature; sample 3 – PVA/MPM based film (PVA:MPM = 12:1) heat-treated at 110 ºC; sample 4 – PVA/MMT based film (PVA:MMT = 12:1) dried at room temperature; sample 5 – PVA/MMT based film (PVA:MMT = 12:1) heat-treated at 110 ºC; sample 6 – PVA/MPM based film (PVA:MPM = 12:1) cross-linked at 110 °C in the presence of acrylic acid (5 wt.%) and $FeSO_4$ (0.5 wt.%) as the initiator.

X-ray studies were performed on a Dron-4-07 diffractometer. Illuminating lamps with a copper anode and Ni-filter were used. The research was carried out in the 4 to 60° 2θ range, the step size was 0.1, and the pulse measurement time was 8 s.

Thermal research was carried out on a differential scanning calorimeter SDT Q600 (TA Instruments, USA). The changes in sample weight (thermogravimetric analysis) were registered simultaneously with the processes accompanied by release or absorption of heat (differential scanning calorimetry/differential thermal analysis) in the temperature range from room temperature to 1500ºC. Samples of nanocomposite films (3-4 mg) were investigated in an argon atmosphere at a 10 °C/min heating to 20–450°C. According to the measured heat of melting ΔH_p and PVA crystallites heat of melting ΔH_k = 156.8 J/g [33] the degree of crystallinity was calculated according to the formula:

$$S_k = \frac{\Delta H_p}{\Delta H_k} 100,\% \qquad (1)$$

The thermolysis of samples 1–5 took place according to similar mechanisms, passing five stages (Table 5, fig. 2). At the first stage, in the 44–46 ºC range, the composites' glassy state transits to a highly elastic physical state, which is accompanied by insignificant endothermic effects on the DSC curves. It should be noted that the composites compositions and the conditions for obtaining films practically do not affect the samples' glass transition temperatures.

In the 70–167ºC range, at the second stage of thermolysis, the separation of physically bound water occurs. This process is accompanied by a slight weight loss (4–5%) and the appearance of insignificant endothermic effects on the DSC curves. Samples 2 and 3 are characterized by higher moisture content (5%) due to the presence of hygroscopic PVP in their composition.

In the 172–218°C range, during the third stage of thermolysis, an endothermic effect without weight loss is observed on the DSC curves, corresponding to composite melting (fig. 2). This effect is the most acute and deep for samples 1, 4, 5, which do not contain amorphous PVP. Additionally, these samples have higher values of melting heat and, accordingly, degree of crystallinity (Table 5). Samples with unmodified MMT, which were heat-treated at 110ºC, have the highest degree of crystallinity. The addition of PVP modified MMT to PVA reduces the degree of crystallinity of the resulting composites. Heat treatment increases the degree of crystallinity by 2%, but it remains lower than that of the initial PVA. The absence of double melting peaks on the DSC curves of the created nanocomposites, in contrast to the endotherms obtained for PVA/MMT based nanocomposites [13,16,17], indicates a complete distribution of MMT in PVA and the formation of a single crystal structure. This fact also confirms the correctness of the chosen technology for PVA based nanocomposites.

In the 237–295ºC range (4th stage of thermolysis), PVA cross-linking and the hydrolytic and oxidative composite degradation occur simultaneously. These processes are accompanied by weight loss and the appearance of endothermic effects on the DSC curves. The heat resistance of the composites containing intercalated MMT was 21ºC higher and their weight loss was lower compared to the initial PVA (PVA thermal-oxidative degradation temperature is 237ºC) and the composites containing nonintercalated MMT. The temperature of thermal-oxidative degradation beginning is about 258ºC for the composites with modified MMT (Table 5, Fig. 2(b,c)).

Table 5. Results of thermal analysis

Sample	Thermolysis stage	Temperature range, ºC	Weight loss, %	Enthalpy, J/g	Degree of crystallinity, %
1	I	44–46	–	–	–
	II	75–163	4.0	–	–
	III	172–217	–	19.51	12.4
	IV	237–292	10.0	358.2	–
	V	292–450	74.0	–	–
2	I	44–46	–	–	–
	II	75–162	5.0	–	–
	III	172–215	–	15.55	9.9
	IV	258–291	8.0	326.0	–
	V	291–450	71.0	–	–
3	I	44–46	–	–	–
	II	70–167	5.0	–	–
	III	175–208	–	13.53	8.6
	IV	258–289	8.0	296.1	–
	V	289–450	74.0	–	–
4	I	44–46	–	–	–
	II	75–167	4.0	–	–
	III	176–218	–	16.97	10.8
	IV	237–293	9.0	313.6	–
	V	293–450	72.0	–	–
5	I	44–46	–	–	–
	II	75–166	4.0	–	–
	III	172–204	–	20.04	12.8
	IV	240–295	9.0	358.8	–
	V	295–450	71.0	–	–
6	I	44–46	–	–	–
	II	63–163	4.5	–	–
	III	169–181	–	188.5	–
	IV	181–286	27.0	–	–
	V	286–450	48.0	–	–

Thermal treatment of these samples at 110ºC did not affect their thermal stability. Samples with unmodified MMT had a thermal-oxidative degradation temperature beginning at about 237 ºC, which increases to 240ºC after heat treatment. Composites with intercalated MMT have the highest temperatures at the beginning of intense weight loss, i.e. for the PVA:MPM = 12:1 composition, the temperature is 282ºC, which decreases to 280 ºC after heat treatment. The intense weight loss of the PVA:MMT = 12:1 composite begins at 276ºC, and decreases to 268ºC after heat treatment. The initial PVA intensively loses weight at 273ºC.

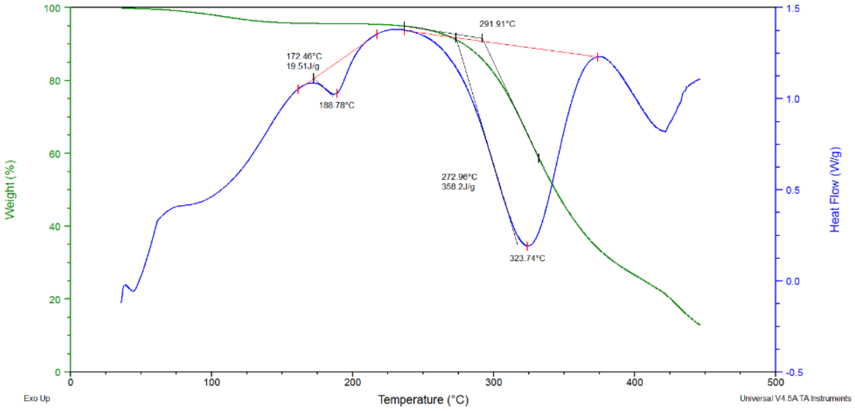
Weight (%)
100
80
60
40
20
0
0
100
200
300
400
500
Temperature (°C)
Heat Flow (W/g)
1.5
1.0
0.5
0.0
-0.5
Exo Up
Universal V4.5A TA Instruments
291.91°C
172.46°C
19.51J/g
188.78°C
272.96°C
358.2J/g
323.74°C

a)

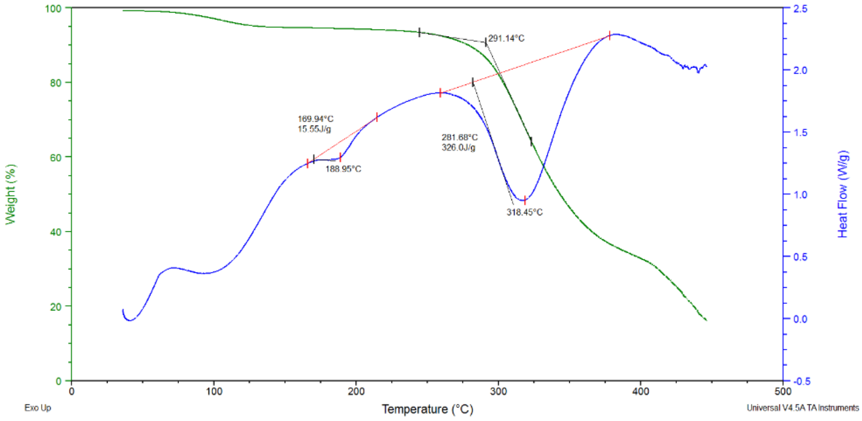
Weight (%)
100
80
60
40
20
0
0
100
200
300
400
500
Temperature (°C)
Heat Flow (W/g)
2.5
2.0
1.5
1.0
0.5
0.0
-0.5
Exo Up
Universal V4.5A TA Instruments
291.14°C
169.94°C
15.55J/g
188.95°C
281.68°C
326.0J/g
318.45°C

b)

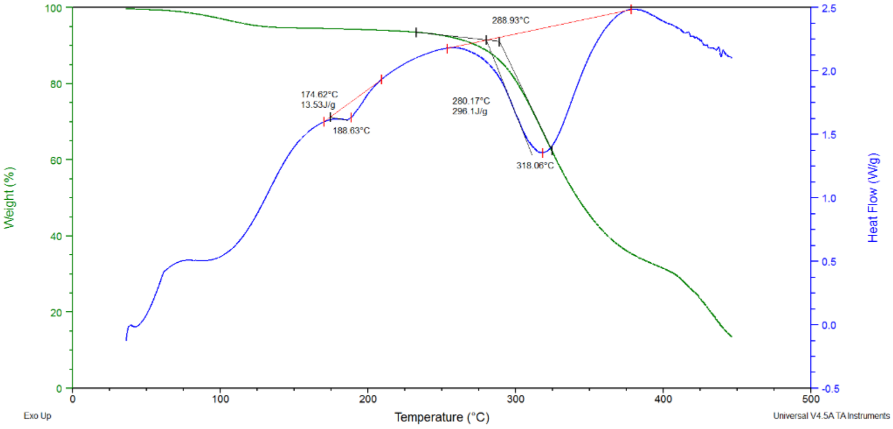
Weight (%)
100
80
60
40
20
0
0
100
200
300
400
500
Temperature (°C)
Heat Flow (W/g)
2.5
2.0
1.5
1.0
0.5
0.0
-0.5
Exo Up
Universal V4.5A TA Instruments
288.93°C
174.62°C
13.53J/g
188.63°C
280.17°C
296.1J/g
318.06°C

c)

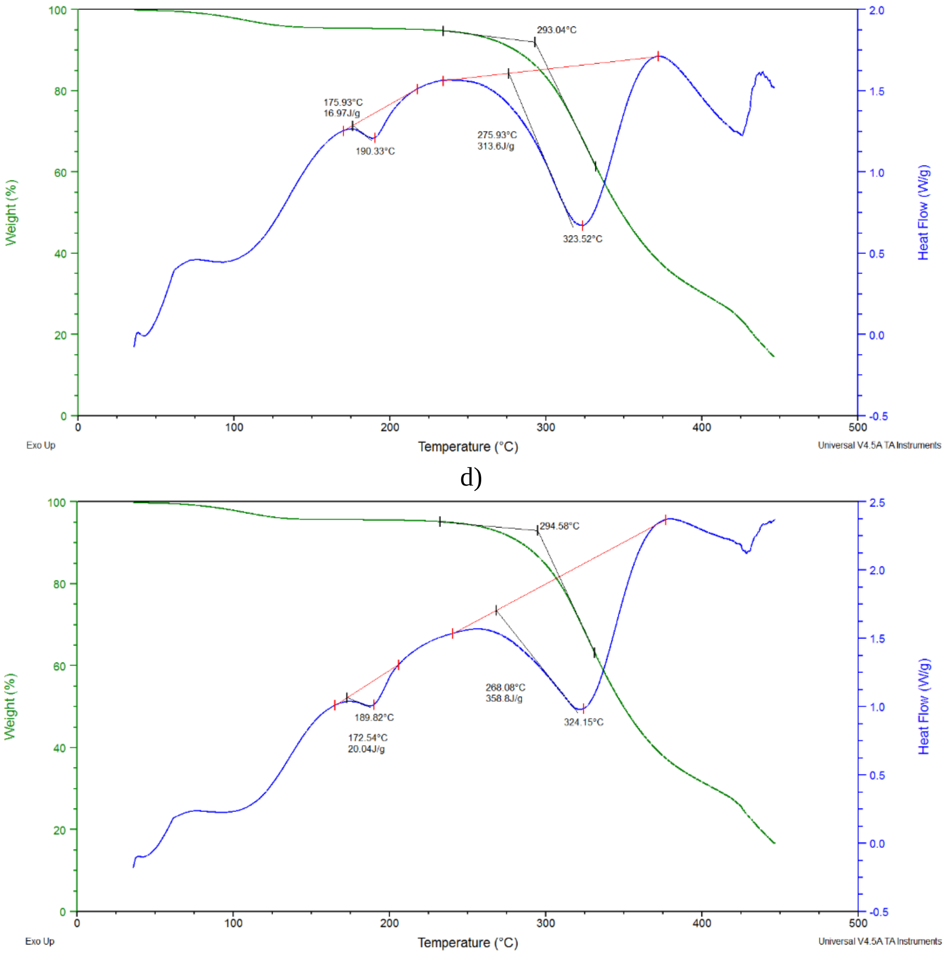

e)

Fig. 2. DSC curves of the composites based on modified PVA: a) sample 1 – a film based on the initial PVA; b) sample 2 – a film based on the PVA:MPM = 12:1 composition, dried at room temperature; c) sample 3 – a film based on the PVA:MPM = 12:1 composition, heat-treated at 110 ºC; d) sample 4 – a film based on the PVA:MMT = 12:1 composition, dried at room temperature; e) sample 5 – a film based on the PVA:MMT = 12:1composition, heat-treated at 110 ºC

During the 5th stage of thermolysis, in the 289–450ºC range, thermal-oxidative degradation of hydrolysis and combustion products, accompanied by intense weight loss, takes place. The weight loss at this stage is more than 70% for all samples, but the weight loss of the resulting composites is lower compared to the initial PVA. Moreover, the degradation processes occurring in the composites were less deep than in the initial PVA, as evidenced by significantly lower endopics in this area.

Thus, it has been established that composites based on PVA with PVP intercalated MMT (ratio of 12:1) have higher thermal stability than the initial PVA or composites with unmodified MMT. There are studies [20] in which the thermal and mechanical properties of the PVA/MMT mixture were increased by the addition of calcined eggshells to the composite. The authors explain the improvement of the properties by blocking hydrogen atoms in the PVA hydroxyl groups. While in our studies, we can increase the heat resistance of the PVA/MMT composite using MMT intercalated by PVP. However, previous studies found that films of this composition were not completely cross-linked even after heat treatment at 110 °C, which results in high water absorption [22]. Therefore, using DSC, we investigated an insoluble film based on the PVA:MPM = 12:1 composition, cross-linked at 110 °C in the presence of 5 wt.% acrylic acid and 0.5 wt.% $FeSO_4$ initiator (Fig. 3, Table 5, Sample 6).

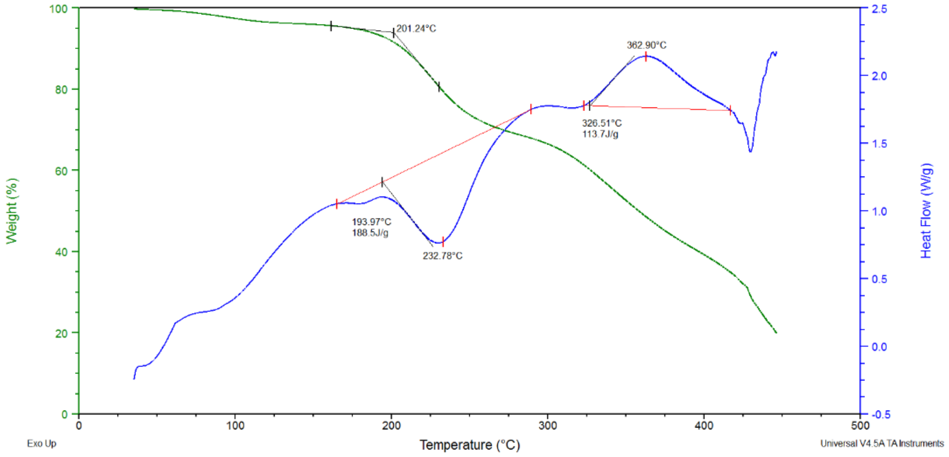

Fig. 3. Thermal analysis of a film based on the PVA:MPM = 12:1 composition, cross-linked at 110 ºC in the presence of 5 wt.% acrylic acid and 0.5 wt.% $FeSO_4$ initiator

The thermolysis of the cross-linked composite also has 5 stages. At the first two stages, the processes are similar to those occurring in samples 1–5. In the 44–46ºC range, the transition from glassy to a highly elastic physical state occurs, and in the 63–163ºC range, the evaporation of physically bound water with a weight loss of 4.5% is observed. At the third stage of thermolysis, in the 169–181ºC temperature range, sample softening occurs with the appearance of a slight endothermic effect on the DSC curve. This process is accompanied by a significant 188.5 J/g absorption of heat (the melting heat of the initial PVA is 19.51 J/g), which confirms the high degree of composite cross-linking. In the 181–286ºC range (4th stage of thermolysis), additional PVA cross-linking, acrylic acid evaporation, and oxidative degradation of the composite occur simultaneously. These processes are accompanied by a 27% weight loss and a clear endothermic effect on the DSC curve. The effect of PVA physical and chemical cross-linking is expected in this temperature range. Physical cross-linking occurs due to the formation of hydrogen bonds between PVA hydroxyl groups and acrylic acid. At the same time, chemical structuring of PVA through the formation of inter macromolecular bridges occurs due to polymerization with respect to double bonds under the influence of temperature and MMT as a catalyst. These processes lead to the formation of a homogeneous cross-linked structure. This is confirmed by X-ray diffraction analysis (Fig. 4) and the low depth of the destructive processes at the 5th stage of thermolysis in the 286–363°C range (Fig. 3). In this range, a fuzzy and insignificant endothermic effect is observed on the DSC curve. Only one intensive crystalline reflex is observed in the 2θ~16–23° region of diffraction angles (Fig. 4). PVA has crystalline reflexes of 100, 101', 101, and 200 at the diffraction angles 2θ = 16.0, 19.4, 20.1, and 22.7°, respectively. This indicates the formation of a homogeneous cross-linked structure in sample 6.

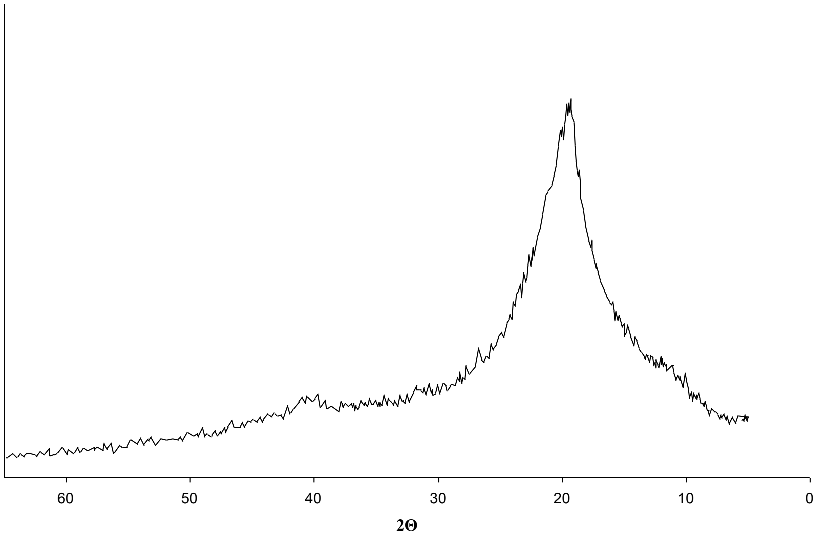

Fig. 4. The diffractogram of the composite based on the PVA:MPM = 12:1 composition, cross-linked at 110 ºC in the presence of 5 wt.% acrylic acid and 0.5 wt.% $FeSO_4$ initiator

3. Conclusions

1. Thus, experimental studies have shown that the montmorillonite-polyvinylpyrrolidone mixture significantly affects the viscosity characteristics of a solution of polyvinyl alcohol when mixed in an ultrasonic field. Compositions with traces of sodium tetraborate in an aqueous solution have the highest viscosity. The viscosity of the developed compositions is also significantly affected by the pH of the medium. In particular, the compositions obtained in a slightly alkaline medium have higher values of relative viscosity than the compositions obtained in neutral and acidic media. At the same time, the mechanical properties and water resistance of the films obtained in an acidic environment are the best. Optimal from the point of view of strength and water resistance is the composition of PVA: MPM = 12: 1. Depending on

the content of MPS and pH of the medium, characteristics of PVA-based films can be adjusted widely, it involves expanding the scope.

2. Depending on composition and reaction conditions, the structure and thermal characteristics of nanocomposites based on PVA and MMT intercalated with PVP were investigated using X-ray diffraction analysis and differential scanning calorimetry. It was established that the modification of PVA by intercalated MMT reduces the degree of crystallinity of the resulting nanocomposites but significantly increases their thermal stability. The composites with unmodified MMT, heat-treated at 110ºC, have the highest degree of crystallinity. Under an ultrasound, intercalated MMT is completely distributed in a PVA solution to form a monocrystalline structure, as evidenced by the absence of double melting peaks on the DSC curves. The composites with intercalated MMT are characterized by a 21ºC higher heat resistance and a lower weight loss compared to the initial PVA (temperature of PVA thermal-oxidative degradation is 237ºC) and to composites containing nonintercalated MMT. Nanocomposite thermal treatment at 110ºC does not have a practical effect on their thermal stability.

Films based on PVA with modified MMT, cross-linked at 110°C in the presence of 5 wt.% of acrylic acid and 0.5 wt.% of initiator, have a homogeneous cross-linked structure formed due to the chemical and physical cross-linking.

References

[1] Shokrieh M., Esmkhani M., Taheri-Behrooz F., A novel model to predict the fatigue life of thermoplastic nanocomposites. Journal of Thermoplastic Composite Materials, 2015.

[2] Gaaz, T., Sulong, A., Akhtar, M., et al., Properties and applications of polyvinyl alcohol, halloysite nanotubes and their nanocomposites. Molecules 2015.

[3] Pinnavaia T., Beall G., Polymer-Clay-Nanocomposites. 1st ed. New York: Wiley, 2000.

[4] Krasinskyi V., Suberlyak. O., Kochubei V., et al., Effect of small additives of polyamide modified by polyvinylpyrrolidone and montmorillonite on polypropylene technological properties and heat resistance. Advances in Science and Technology Research Journal, 2018.

[5] Aranda P., Mosqueda Y., Pérez-Cappe E., et al., Electrical characterization of poly(ethylene oxide)-clay nanocomposites prepared by microwave irradiation. Journal of Polymer Science Part B: Polymer Physics, 2003.

[6] Elbokl T., Detellier C., Aluminosilicate nanohybrid materials. Intercalation of polystyrene in kaolinite. Journal of Physics and Chemistry of Solids, 2006.

[7] Attaran S. A., Hassan A., Wahit M. U., Materials for food packaging applications based on bio-based polymer nanocomposites: A review. Journal of Thermoplastic Composite Materials, 2017.

[8] Dulebová Ľ., Greškovič F., Sikora J., et al., Analysis of the mechanical properties change of PA6/MMT nanocomposite system after aging. Key Engineering Materials, 2017.

[9] Alexander M., Dubois P., Polymer nanocomposites: Synthesis, characterization, and modeling. Materials Science and Engineering, 2000.

[10] Mohamed W., Nasr H., Sobh R., et al., Study the ultrasonic assisted for polymeric nanocomposite. Egyptian Journal of Chemistry, 2017.

[11] Mirsafaei R., Kolahdoozan M., Preparation and characterization of poly (amide-ester-imide)/Na+-MMT nanocomposite via ultrasonic method. Journal of Polymer Engineering, 2017.

[12] Qu L., Preparation and properties of polyvinyl alcohol/polyvinyl pyrrolidone blend films. Applied Mechanics and Materials, 2010.

[13] Strawhecker K., Manias E., Structure and properties of poly(vinyl alcohol)/na montmorillonite nanocomposites. Chemistry of Materials, 2000.

[14] Strawhecker K., Manias E., AFM of poly(vinyl alcohol) crystals next to an inorganic surface. Macromolecules, 2001.

[15] Aslam M., Kalyar M., Raza Z., Polyvinyl alcohol: A review of research status and use of polyvinyl alcohol based nanocomposites. Polymer Engineering & Science, 2018.

[16] Suzuki K., Mori T., Thermal and catalytic properties of alumina-pillared montmorillonite prepared in the presence of polyvinyl alcohol. Applied Catalysis, 1990.

[17] Părpăriță E., Cheaburu C., Pațachia S., et al., Polyvinyl alcohol/chitosan/montmorillonite nanocomposites preparation by freeze/thaw cycles and characterization. Acta Chemica Iasi, 2014.

[18] Rajeswari B., Malarvizhi N., Prakash D., et al., Viscoelastic, thermal, and morphological properties of nanocomposites based on modified PVA using a twin-screw melt extrusion process. Journal of Thermoplastic Composite Materials, 2019.

[19] Fang Q., Cui H-W., Du G-B., Preparation and characterization of PVAc–NMA–MMT. Journal of Thermoplastic Composite Materials, 2013.

[20] Bee S-T., Liew S-Q., Ang W., et al., Interactive effect of calcined eggshell and montmorillonite on the characteristics of polyvinyl alcohol blends. Journal of Vinyl and Additive Technology, 2018.

[21] Abd-Elrahman M., Enhancement of thermal stability and degradation kinetics study of poly(vinyl alcohol)/zinc oxide nanoparticles composite. Journal of Thermoplastic Composite Materials, 2014.

[22] Biswas M., Ray S., Recent progress in synthesis and evaluation of polymer-montmorillonite nanocomposites. Advances in Polymer Science, 2001.

[23] Sapalidis A., Katsaros F., Kanellopoulos N., PVA / montmorillonite nanocomposites: Development and properties. In: Cuppoletti J Nanocomposites and polymers with analytical methods. London: InTech, 2001.

[24] Kotal M., Bhowmick A., Polymer nanocomposites from modified clays: Recent advances and challenges. Progress in Polymer Science, 2015.

[25] Tayser Sumer G., Abu Bakar S., Majid Niaz A., Properties and Applications of Polyvinyl Alcohol, Halloysite Nanotubes and Their Nanocomposites. Molecules, 2015.

[26] Khamula N., Antoniuk V., Krasinskyi V., et al., Investigation of the impact of modified montmorillonite on the viscosity of the solutions of polyvinyl alcohol. In: 2017 IEEE 7th International Conference Nanomaterials: Application & Properties (NAP), Zatoka, Ukraine, September 10–15, 2017.

[27] Suberlyak O., Grytsenko O., Kochubei V., The Role of FeSO4 in the obtaining of polyvinylpirrolidone co-polymers. Chemistry and Chemical Technology, 2015.

[28] Suberlyak O., Krasinskiy V., Sikora J., et al., Ammonia-free, low-toxic press-materials with improved electroinsulating properties based on modified novolak phenol-formaldehyde resin. Chemistry and Chemical Technology, 2012.

[29] Suberlyak O., Krasins'kyi V., Shapoval I., et al., Influence of the mechanism and parameters of hardening of modified novolac phenol-formaldehyde resins on the physicomechanical properties of the composite. Material Science, 2011.

[30] Krasinskyi V., Kochubei V., Klym Y., et al., Thermogravimetric research into composites based on the mixtures of polypropylene and modified polyamide. Eastern-European Journal of Enterprise Technologies, 2017.

[31] Krasinskyi V., Suberlyak O., Dulebová Ľ., et al., Nanocomposites on the basis of thermoplastics and montmorillonite modified by polyvinylpyrrolidone. Key Engineering Materials, 2017.

[32] Krasinskyi V., Suberlyak O., Zemke V., et al., The role of polyvinylpyrrolidone in the formation of nanocomposites based on a compatible polycaproamide and polypropylene. Chemistry and Chemical Technology, 2019.

[33] Cho J., Lyoo W., Chvalun S., et al., X-ray analysis and molecular modeling of poly(vinyl alcohol)s with different stereoregularities. Macromolecules, 1999.

Anastasia Kucherenko[1], **Ludmila Dulebova** [2],**Volodymyr Moravskyi**[1]

ANALYSIS OF PROCESSES OCCURRING DURING PROCESSING OF METALLIZED POLYMER GRANULES

Abstract: *The processes of destruction of a copper shell formed on a spherical polypropylene granule by the method of chemical deposition are considered. A method for calculating the characteristics of metallized polymer granules is proposed and the main factors influencing the destruction of the metal shell during the processing of metallized polymer granules are identified. It is shown that the proposed technology of obtaining metal-filled polymer composites by processing metallized polymer granules can be used to obtain materials intended for protection against electromagnetic radiation.*

Keywords: *metal-filled polymer composites, metallization, metal coating, shell, polypropylene, copper*

1. Introduction

The significant demand of modern society for high-tech materials stimulates the development and production of new polymeric materials and especially composite polymeric materials. Due to their high manufacturability and chemical resistance, good physical and mechanical properties, polymers and composites based on them are widely used in various industries.

Conventional polymers, in comparison with metals, have lower mechanical properties, but the process of obtaining products from them is less time consuming. Typically, the improvement of the mechanical properties of polymers is achieved by adding various fillers. The mechanical properties of composites can be changed by selecting fillers of different shapes and sizes, as well as changing their content in the polymer matrix [1]. The combination of the polymer matrix and the filler leads to the formation of a mixture that has new properties, while maintaining the properties of both the filler and the polymer.

Many methods of obtaining polymer composites are known. The most common method can be considered to obtain composites by introducing a filler into the polymer melt. This method involves heating the polymer matrix to the melting point, adding the filler and then mixing them to obtain a uniform distribution of the filler in the polymer matrix. This method, along with the simplicity of implementation has one significant disadvantage, namely the difficulty of ensuring a uniform distribution of the filler in the polymer matrix [2]. Interesting in terms of obtaining polymer composites, which allow to ensure better distribution of the filler in the polymer matrix

---

[1] *Lviv Polytechnic National University, Department of Chemical Technology of Plastics Processing, 12 Bandera Str., Lviv, 79013, Ukraine, vmoravsky@gmail.com.*

[2] *Technical University of Kosice, Faculty of Mechanical Engineering, Department of Technologies, Materials and Computer Aided Production, Masiarska 74, 040 01 Košice, Slovakia, ludmila.dulebova@tuke.sk.*

can be considered in situ methods (polymerization in the presence of filler or synthesis of filler in the matrix), sol-gel technology, ultrasonic cavitation, etc. [3-5].

The introduction of fillers into the polymer matrix, as a rule, leads to improved mechanical properties. In this case, the filler binds to the polymer matrix due to weak intermolecular and in some cases chemical bonds. Thus, the formation of various relationships leads to an increase in the physico-mechanical properties of polymer composites. Fillers are introduced into the polymer matrix not only to increase the physico-mechanical properties or reduce the cost of the material, more interesting in terms of creating new materials is the use of fillers that give composites new unique and uncharacteristic properties of polymers. Such fillers can be a variety of metals, which allows to obtain polymer composites characterized by the presence of electrical and thermal conductivity, magnetic properties, fungicidal and antimicrobial properties, etc. Another promising area of use of metal-filled composites can be considered the field of protection against electromagnetic radiation.

The rapid development and widespread use of electronic devices, the introduction of high-speed information transmission systems has led to a significant increase in electromagnetic radiation, which can already be considered as one of the harmful factors [6]. In particular, electromagnetic and radio frequency radiation can affect the malfunction of electronic devices, as well as have a harmful effect on humans. Metals and their alloys are effective materials for protection against electromagnetic radiation. However, their high weight and cost, low corrosion resistance and manufacturability make them an undesirable choice for many modern electronic devices. Thus, there is a question of development of effective means of reduction of negative influence of electromagnetic radiation and creation of easy, strong, technological and economic materials for protection against various types of radiation.

The development of new polymer composites will replace materials for protection against electromagnetic radiation based on metals. This will be possible as a result of the use of inherent properties of polymers, namely low weight, high corrosion resistance, good dielectric, thermal and mechanical properties. The disadvantage of polymers as materials for protection against electromagnetic radiation is their low density. It is known that with increasing density of the material, the probability of interaction of the absorbing material with the photon of radiation increases [7]. In addition, the elements of which mostly consist of polymers (C, H, O, Si) are characterized by low effective atomic and electronic number, which also reduces their efficiency of use as an absorbent material [8].

The low efficiency of the use of polymers for protection against electromagnetic radiation can be increased by creating composite materials based on them, which contain metal particles as a filler. Such materials are widely used and studied for protection against electromagnetic radiation [9].

Traditionally, polymeric composite materials are used to protect against low-energy electromagnetic radiation. However, polymer composites can be used to protect against ionizing high-energy radiation [10]. Such composites can be created on the basis of various polymer matrices and fillers: composites based on polymethyl methacrylate and filler bismuth oxide (Bi_2O_3); high density polyethylene composite filled with tungsten (W), molybdenum sulfide (MoS_2) and boron carbide (B_4C); polymer composites based on emulsion polyvinyl chloride and tungsten oxide (WO_3); composites based on isophthalic resin filled with lead oxide; silicone rubber composites containing bismuth; polyester composites filled with zinc [11-24]. The use of metal-filled polymer composites is also widely used in the textile industry to obtain highly efficient shielding fabric materials [25].

Attenuation of electromagnetic radiation in the material occurs by three mechanisms [9]: reflection, absorption and multiple reflection and in general is the sum of all three components. For materials with high conductivity (metals) reflection is the main mechanism of attenuation of electromagnetic radiation. Such materials have free charge carriers (electrons) that can interact with electromagnetic radiation. In addition, the formation in the protective material of a metal filler in the form of spatially extended structures (plates) will contribute to the attenuation of electromagnetic radiation by the mechanism of multiple reflection.

2. Description of the developed technology for obtaining metal-filled polymer composites

We are developing a technology for obtaining metal-filled polymer composites [26-30], which can be used to obtain materials suitable for protection against electromagnetic radiation. The main advantage of the proposed technology is the ability to form elongated structures of the metal filler (plates) in the polymer matrix, which is the optimal form for protection against electromagnetic radiation [9]. Copper is used as a filler metal in the proposed technology, which will allow to obtain high values of protection against electromagnetic radiation. The main idea underlying the creation of protective composites is the destruction of the metal shell formed on the polymer granules during their processing into products.

The proposed technology of obtaining metal-filled products is three-stage (Fig. 1). The first stage involves obtaining an activated polymeric raw material. Activation of the polymer surface occurs as a result of joint processing of polymer granules and fine metal activator in a ball mill. This treatment fixes the activator metal on the surface of the polymer granules, which is necessary for the second stage of the process - metallization.

Metallization of activated polymer granules occurs in solutions of chemical precipitation, the main component of which is copper sulfate. The use of such solutions provides fast and high-quality metallization of the surface to obtain polymer granules evenly covered with a layer of metal.

The final stage is the processing of metallized polymer raw materials to obtain metal-filled products.

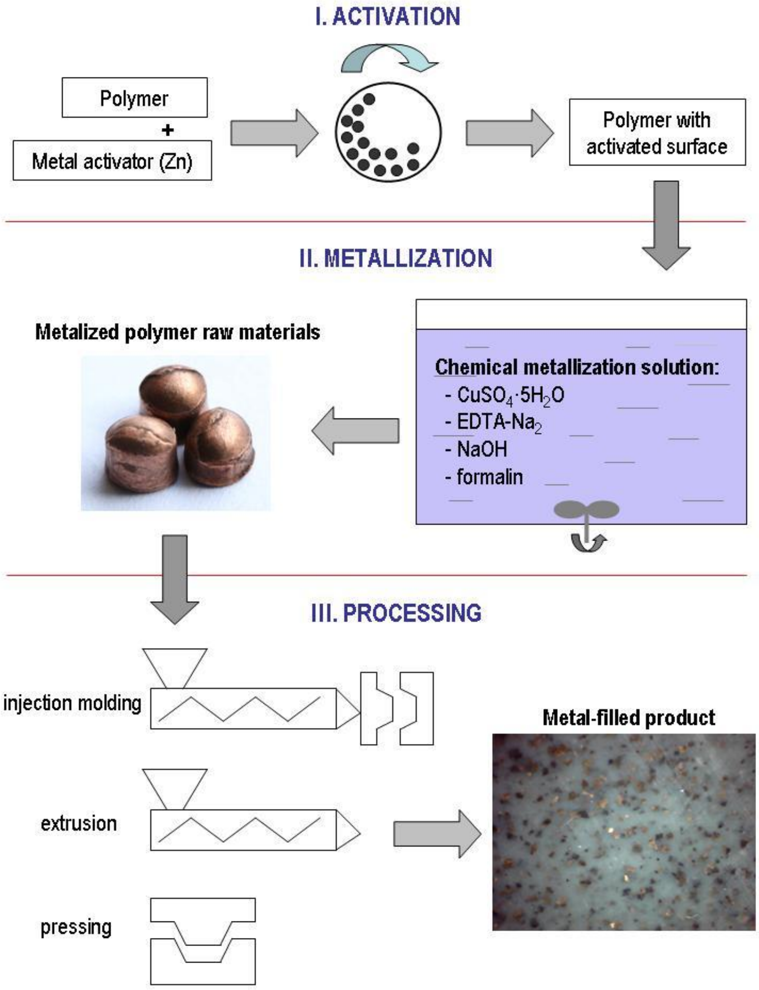
I. ACTIVATION
Polymer
+
Metal activator (Zn)
Polymer with activated surface
II. METALLIZATION
Metalized polymer raw materials
Chemical metallization solution:
- CuSO4·5H2O
- EDTA-Na2
- NaOH
- formalin
III. PROCESSING
injection molding
extrusion
pressing
Metal-filled product

Fig. 1. Scheme of obtaining metal-filled polymer composites

The mechanism of destruction of the metal shell formed on the polymer granule will depend on its thickness, as well as the method of processing. The characteristics of the metal filler obtained by processing metallized raw materials by extrusion and injection molding methods will differ significantly from the material obtained by pressing. During extrusion processing and injection molding, the material is subjected to significant shear stresses, which will contribute to the grinding of the metal. Predicting the properties of the obtained metal filler in this case is a difficult task.

In the case of obtaining metal-filled polymer products by pressing metallized polymer granules, it is possible to predict to some extent the characteristics of the obtained metal filler.

3. Calculation of characteristics of metallized polymeric raw materials

In order to assess the characteristics of metallized raw materials obtained by the developed technology and to understand the processes occurring during the destruction of the metal shell during its processing, the calculation of the geometric dimensions of the metal filler depending on the size of the polymer granule were made. The thickness of the formed metal layer on the polymer granule was calculated for a spherical particle, which is evenly covered with a layer of metal (Fig. 2).

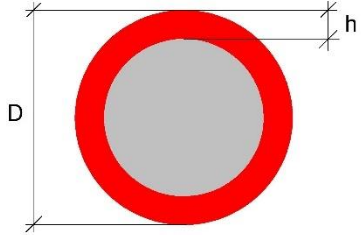

Fig. 2. Metallized spherical polymer particle

The calculation algorithm is as follows:

1 for a given diameter of the polymer particle, calculate its volume and mass (1, 2);

2 according to the obtained value of the mass of the polymer particle and the set value of the metal content, we calculate the mass of the metal, its volume and the diameter of the metallized particle (2, 3).

Volume of polymer particle:

$$\mathrm{V} = \frac{4}{3} \cdot \pi \cdot r^3, \tag{1}$$

where *r* is the radius of the polymer particle.

The mass of the polymer particle and the volume of the metal depending on:

$$\rho = \frac{m}{V}, \tag{2}$$

where ρ is the density, *V* is the volume and *m* is the mass of the polymer and metal.

The diameter of the metallized particle is calculated using the value of the volume of the metal forming the shell:

$$V = \frac{4}{3} \cdot \pi \cdot \left(R^3 - r^3\right),$$

where *r* is the radius of the inner sphere (given the radius of the polymer particle), *R* is the radius of the outer sphere (the radius of the metal shell);

whence:

$$\mathrm{D} = 2 \cdot \sqrt[3]{\frac{3\mathrm{V}}{4\pi} + r^3}\ . \tag{3}$$

The thickness of the metal layer obtained on the metallized particle was determined by the difference between the calculated value of the diameter of the metallized particle and the set value of the diameter of the polymer particle.

Initial data for calculation:

The diameter of the polymer particle (mm) – 1, 3, 5;
Metal content (wt.%) – 1, 5, 10;
Polymer - polypropylene (ρ=0,9 g/cm^3);
Metal - copper (ρ=8,96 g/cm^3).

The calculation of the thickness of the formed copper layer on the spherical granule of polypropylene shows that the thickness significantly depends on both the size of the initial granule and the metal content (Table 1). This difference in the thickness of the formed copper coating is explained by a significant increase in the specific surface area of polymer particles with a decrease in their diameter (with a decrease in the diameter of a spherical polypropylene particle from 5 mm to 1 mm specific surface area increases from 1.3 to 6.7).

Table 1. The results of calculating the thickness of the copper layer obtained on a spherical polypropylene granule

The diameter of the spherical granule $d\cdot10^3$, m	Copper content wt.%	The thickness of the obtained copper layer $h\cdot10^6$, m	Specific surface area S_{SSA}, m^2/kg	(R/h>10)
1	1	0.17	6.7	2994
	5	0.84		598
	10	1.67		300
3	1	0.5	2.2	2988
	5	2.51		598
	10	5.01		300
5	1	0.84	1.3	2988
	5	4.18		598
	10	8.34		300

It is clear that such a significant difference in the thickness of the copper layer will significantly affect the properties of the obtained composites and in addition the behavior of the copper layer during the processing of such raw materials will be different.

4. The mechanism of destruction of the metal shell formed on the polypropylene granule

The main processes that occur during the processing of polymers by pressing are melting and plastic deformation of the material. Plastic deformation occurs without significant shear rates and in the simplest case can be represented by a variable shape of the initial sphere to the shape of a cube. The effect of temperature on the polymer material affects its thermal expansion, which, given the different coefficients of thermal expansion of metals and polymers will have some effect on the destruction of the metal shell.

To calculate the change in the volume of a spherical particle of polypropylene during its heating, use the formula:

$$V^{/} = V \cdot (1 + \alpha_V \cdot \Delta t), \qquad (4)$$

where V is the initial volume of the polymer; α_V - coefficient of volume expansion; Δt - temperature variable.

Using the assumption that the thermal coefficient of linear expansion in the temperature range below the temperature of the phase transitions is linear [31], we can calculate the thermal coefficient of volumetric expansion ($\alpha_V \approx 3 \cdot \alpha_L$). Which will allow to calculate the variable volume of the spherical polypropylene granule when heated (Fig. 3).

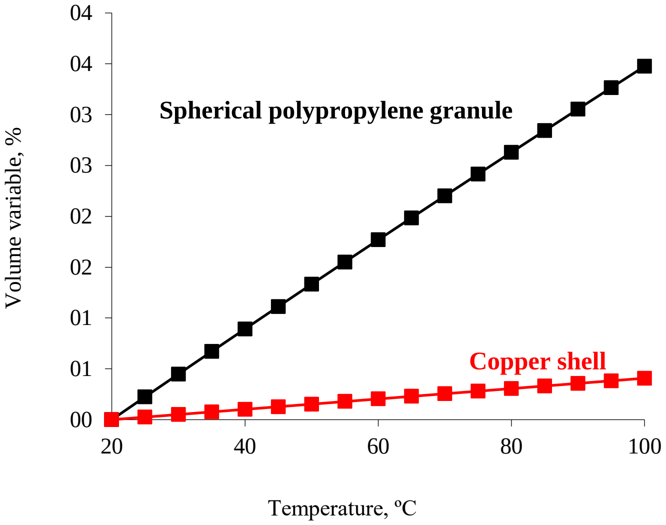

Fig. 3. Variable volume of spherical granules of polypropylene and copper shell during heating. (For polypropylene $\alpha_L = 1{,}5 \cdot 10^{-4}\ K^{-1}$*, for copper* $\alpha_L = 17 \cdot 10^{-6}\ K^{-1}$*)*

The variable volume of a spherical polypropylene particle in the considered temperature range, as well as the coefficient of linear thermal expansion has a linear dependence. However, in this case, it is necessary to pay attention to the significant difference in the values of the change in volume for polypropylene and copper shell, which is formed on its surface. The heating of polypropylene, which is in a closed volume of the copper shell, is accompanied by its thermal expansion, which will cause an increase in stress in the copper layer and as a result will lead to its destruction. In this case, the destruction of the copper shell will be caused by a significant increase in the tic acting on the shell.

To calculate the process of increasing the pressure in a closed volume during heating, you can use a formula that allows you to set the maximum pressure of the substance [32]:

$$P^{(M)} = P_0 + \frac{\alpha_{\mathrm{L}}}{\alpha^{(P)}} \cdot \Delta t , \qquad (5)$$

where P_0 – initial pressure, Pa; $\alpha^{(P)}$ – compressibility factor, Pa^{-1}.

Thermoplastic melts are a low-compressibility medium and the average values of the compressibility coefficients and thermal linear expansion for polypropylenes of different brands are respectively 10^{-9} Pa^{-1} i 10^{-4} K^{-1}. Such values of coefficients are very small. Thus, we can assume that the assumptions about the constancy of the properties of polypropylene and the independence of the values of the coefficients from pressure and temperature will make a small error in the calculations.

Formula (5) allows to set the maximum pressure that will create polypropylene in an enclosed space, but it does not take into account the thermal expansion of the metal shell. Simultaneous thermal expansion of the metal shell during the heating of the polymer will affect slightly lower values of the maximum pressure acting on the shell. The value of the maximum pressure taking into account the thermal expansion of the metal shell can be obtained using the formula:

$$P^{(M)} = P_0 + \left(\frac{\alpha_{\mathrm{LPP}}}{\alpha_{\mathrm{PP}}^{(P)}} - \frac{\alpha_{\mathrm{LCu}}}{\alpha_{\mathrm{Cu}}^{(P)}} \right) \cdot \Delta t , \qquad (6)$$

here the coefficients for polypropylene and copper are denoted by indices, respectively PP and Cu.

Based on formula (6), the calculation of the maximum pressure in a closed volume, which takes place during thermal expansion of polypropylene (Table 2). The following parameters were used in the calculations: $\alpha_{\mathrm{LPP}} = 1{,}5 \cdot 10^{-4}$ K^{-1}; $\alpha_{\mathrm{PP}}^{(P)} = 1{,}5 \cdot 10^{-9}$ Pa^{-1}; $\alpha_{\mathrm{LCu}} = 1{,}7 \cdot 10^{-5}$ K^{-1}; $\alpha_{\mathrm{Cu}}^{(P)} = 7{,}3 \cdot 10^{-9}$ Pa^{-1}. Initial conditions: $P_0 = 0{,}1$ MPa; $t_0 = 20$ºC.

The results of the calculations show that when polypropylene is heated in a closed volume, which prevents its expansion, the pressure acting on the walls of the sphere increases, which can lead to its destruction. These calculations do not take into account the initial geometric dimensions of the polymer granule and the processes of heat transfer in it. The obtained values show the maximum pressure at the set thermal mode.

Table 2. The results of the calculation of the maximum pressure acting on the copper shell formed on a spherical granule of polypropylene

T, ºC	$P^{(M)}$, Pa	T, ºC	$P^{(M)}$, Pa
20	0.10	60	4.01
25	0.59	65	4.50
30	1.08	70	4.98
35	1.57	75	5.47
40	2.05	80	5.96
45	2.54	85	6.45
50	3.03	90	6.94
55	3.52	95	7.43

The pressure created by polypropylene during thermal expansion in a closed volume will act on the copper shell. In this case, stresses will occur in the copper shell, the value of which can be established using the calculation of spherical shells according to the theory of momentless shells [33]. The use of this theory is possible because the metal shell formed on a spherical polymer granule can be considered as a body of rotation with a small wall thickness (Fig. 4). In this case, it can be assumed with high accuracy that there are only normal stresses (stretches) in the walls, which are evenly distributed over the wall thickness. Calculations based on such assumptions agree well with experimental data only in the case of thin-walled shells. For such shells, the ratio of the smallest radius of curvature at this point to the wall thickness of the shell exceeds 10 $\left(\frac{R}{h} > 10\right)$. In accordance with the accepted restrictions on the size of the granules and the metal content, the copper shell formed on spherical polypropylene granules in all cases can be considered thin-walled (Table 1).

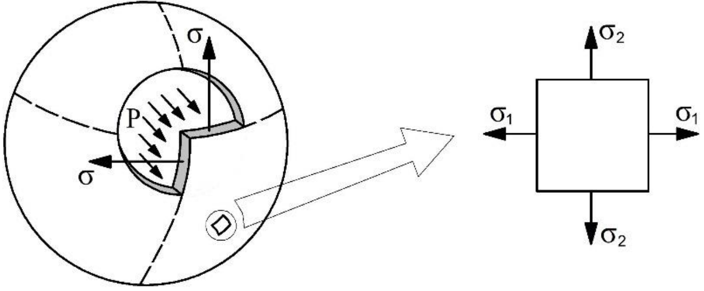

Fig. 4. Scheme of stress formation in a copper shell

The stresses acting on the shell have the properties of axial symmetry, the central symmetry also has the shell itself. The consequence of this is $\sigma_1=\sigma_2=\sigma$, and $\rho_1=\rho_2=d/2$, where *d* is the diameter of the sphere. For this case, the Laplace formula takes the form [33]:

$$\sigma = \sigma_1 = \sigma_2 = \frac{P \cdot d}{4 \cdot h}.$$

Since in this case there is a flat stress state, to calculate the strength, you can use the third hypothesis of strength and the assumption of no pressure between the layers of the shell, ie $\sigma_3=0$. The main stresses in this case matter: $\sigma_1=\sigma$; $\sigma_2=\sigma$; $\sigma_3=0$ and in accordance with the third hypothesis of strength, the calculation of stresses is carried out as in the case of uniaxial stress:

$$\sigma = \frac{P \cdot d}{4 \cdot h}, \tag{7}$$

where P – internal pressure acting on the shell; d – shell diameter; h – shell wall thickness.

Analysis of the formula used to calculate the stress in the shell shows that the amount of stress depends on the ratio of the shell diameter and the thickness of its wall. Since this ratio is the same for granules of different diameters with the same metal content (Table 1), the calculation can be performed only for granules of the same size. Thus, the initial data for calculating the stresses occurring in the spherical shell are the pressure and thickness of the shell. Based on the condition that the metal layer on the polymer surface is formed at a pressure of 0.1 MPa, the excess pressure generated during the thermal expansion of the polypropylene granules will be $P = 0{,}1 - P^{(M)}$ (Table 3).

The obtained results show that the increase in temperature affects a significant increase in stresses occurring in the shell. Moreover, its thickness has a significant effect on the stress in the shell.

Literature data [34] and our microscopic studies of copper coatings obtained by the developed method (Fig. 5) show that such coatings have a microcrystalline structure. The microcrystalline structure of the copper coating obtained by the method of chemical deposition affects the fact that such coatings have higher values of the yield strength compared to the strength of technical copper and its value reaches 400 MPa [34, 35]. For technical copper - 225 MPa [36]. Thus, in accordance with the stress results from table. 3 destruction of the copper shell, depending on its thickness, will begin at a temperature of 23ºC for a shell with a thickness of $0.17 \cdot 10^{-6}$ m, 34ºC for a shell with a thickness of $0.84 \cdot 10^{-6}$ m and 48ºC for a shell with a thickness of $1.67 \cdot 10^{-6}$ m. These findings do not take into account the fact that with increasing temperature there is a decrease in the yield strength of copper. Although the temperatures at which the destruction of the copper shell begins are low and a significant decrease in strength in the range of such temperatures will not be observed. Plastic deformation of copper with microcrystalline structure is in the range of 2-3% [35]. This value of plastic deformation of the copper shell allows to predict its destruction at a temperature of 95°C, regardless of the thickness of the shell.

Table 3. Calculation of stresses occurring in a copper shell formed on a spherical polypropylene granule

T, ºC	P, MPa	The thickness of the copper layer, 10^6, m		
		0.17	0.84	1.67
		Stress in the shell, MPa		
20	0.00	0.0	0.0	0.0
25	0.49	731.1	146.0	73.2
30	0.98	1462.1	292.1	146.3
35	1.47	2193.2	438.1	219.5
40	1.95	2924.3	584.2	292.6
45	2.44	3655.4	730.2	365.8
50	2.93	4386.4	876.2	438.9
55	3.42	5117.5	1022.3	512.1
60	3.91	5848.6	1168.3	585.2
65	4.40	6579.6	1314.4	658.4
70	4.88	7310.7	1460.4	731.5
75	5.37	8041.8	1606.4	804.7
80	5.86	8772.9	1752.5	877.8
85	6.35	9503.9	1898.5	951.0
90	6.84	10235.0	2044.6	1024.1
95	7.33	10966.1	2190.6	1097.3

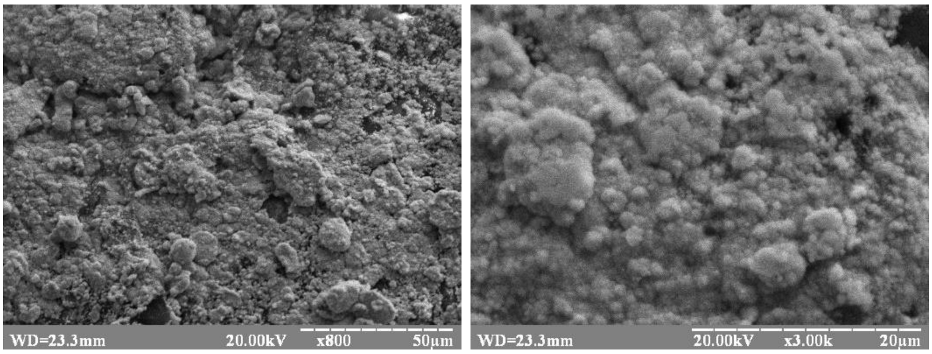

Fig. 5. Electron microscopy of copper coating obtained on polypropylene granules

During pressing, the granules of the original polymer are exposed to external loads, which causes their deformation. Consider the option when the spherical particle is subjected to evenly directed loads that cause its deformation to a cubic shape (Fig. 6).

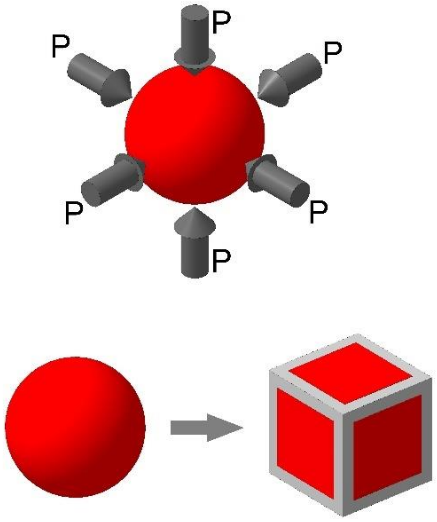

Fig. 6. Scheme of deformation of a spherical granule

Deformation of a spherical particle to a cubic shape, provided that its volume is preserved, affects the increase in its surface area. The magnitude of the increase in surface area in this case does not depend on the initial diameter of the spherical particle and is 24%. The result of increasing the surface area of the particle during its deformation will be the destruction of the metal shell and obtaining a particle, which, in contrast to the original granule, partially has a surface that is not covered with metal. In this case, the destruction of the metal shell, which is formed on the spherical polymer granule during its processing by pressing will ensure the placement of metal particles in the contact nodes of the initial metallized granules. Thus, it can be expected that in the resulting composite will be formed a spatial structure of the metal filler, which is evenly distributed in the polymer matrix.

It is clear that the considered assumptions of destruction of the metal shell on the polymer granule are far from real conditions. The granules of industrial polymers have an irregular shape and, accordingly, the shape of the metal shell formed on their surface will be far from spherical. Such shells will be destroyed by other mechanisms and in this case the decisive factor will be the presence of stress concentration zones. In the case of processing polymers by pressing also has a more complex mechanism of deformation of the granules, which will form a completely different structure of the distribution of the filler in the polymer matrix.

However, the considered factors of destruction of the metal shell are interesting in terms of establishing the main factors that affect the process of destruction of the metal shell formed on the polymer granule. Such information is necessary to understand the processes that occur in the production of metal-filled composites by processing metallized polymer raw materials and the possibility of influencing the properties of the final product.

5. Conclusion

Thus, the theoretical studies of the process of processing metallized polymer granules allowed to identify the main factors influencing the destruction of the metal shell during processing. It is shown that the proposed technology for obtaining metal-filled polymer composites can be used to obtain materials designed to protect against electromagnetic radiation. The use of copper in the developed technologies in the form of a coating on polymer granules allows to obtain a composite material which is predicted to have high values of protection against electromagnetic radiation due to the formation of metal filler in the form of elongated structures (plates) and the use of conductive filler (copper).

Acknowledgments

This paper is the result the work was carried out within the framework of the National Scholarship Program of the Slovak Republic and KEGA 036TUKE-4/2021.

References

[1] Bhattacharya M., Polymer nanocomposites - a comparison between carbon nanotubes, graphene, and clay as nanofillers. Materials, 2016, 9(4), 262.

[2] Zeng Q., Wang D., Yu A., Lu G., Synthesis of polymer–montmorillonite nanocomposites by in situ intercalative polymerization. Nanotechnology, 2002, 13 (5), 549-553.

[3] Grytsenko O., Gajdoš I., Spišák E., Krasinskyi V., Suberlyak O., Novel Ni/pHEMA-gr-PVP composites obtained by polymerization with simultaneous metal deposition: Structure and properties, Materials, 2019, 12(12), 1956.

[4] Ameen S., Akhtar M.S., Shin H.S., Hydrazine chemical sensing by modified electrode based on in situ electrochemically synthesized polyaniline/graphene composite thin film. Sens Actuators B Chem, 2012, 173, 177-183.

[5] Camargo P.H.C., Satyanarayana K.G., Wypych F., Nanocomposites: synthesis, structure, properties and new application opportunities. Mater Res, 2009, 12(1), 1-39.

[6] Barsukov V., Senyk I., Kryukova O., Butenko O., Composite Carbon-Polymer Materials for Electromagnetic Radiation Shielding. Materials Today Proceedings, 2018, 5(8), 15909-15914.

[7] Hellström K., Dioszegi A., Diaconu L., A broad literature review of density measurements of liquid cast iron. Metals, 2017, 7(5), 165.

[8] Vahabi S.M., Bahreinipour M., Shamsaie Zafarghandi M., Determining the mass attenuation coefficients for some polymers using MCNP code: a comparison study. Vacuum, 2017, 136, 73-76.

[9] Kumar P., Maiti U. N., Sikdar A., Kumar Das T., Kumar A., Sudarsan V., Recent Advances in Polymer and Polymer Composites for Electromagnetic

Interference Shielding: Review and Future Prospects. Polymer Reviews, 2019, 59(4), 687-738.

[10] More, C.V., Alsayed, Z., Badawi, M.S. et al., Polymeric composite materials for radiation shielding: a review. Environ Chem Lett, 2021, 19, 2057-2090.

[11] Plionis A.A., Garcia S.R., Gonzales E.R., Porterfield D.R., Peterson D.S., Replacement of lead bricks with non-hazardous polymer-bismuth for low-energy gamma shielding. J Radioanal Nucl Chem, 2009, 282(1), 239.

[12] El-Fiki S., El Kameesy S.U., Nashar D.E., Abou-Leila M.A., El-Mansy M.K., Ahmed M., Influence of bismuth contents on mechanical and gamma ray attenuation properties of silicone rubber composite. Int J Adv Res, 2015, 3(6), 1035-1041.

[13] Aghaz A., Faghihi R., Mortazavi S.M.J., Haghparast A., Mehdizadeh S., Sina S., Radiation attenuation properties of shields containing micro and Nano WO_3 in diagnostic X-ray energy range. Int J Radiat-Res, 2016, 14(2), 127-131.

[14] Mahmoud M.E., El-Khatib A.M., Badawi M.S., Rashad A.R., El-Sharkawy R.M., Thabet A.A., Fabrication, characterization and gamma rays shielding properties of nano and micro lead oxide-dispersed-high density polyethylene composites. Radiat Phys Chem, 2018, 145, 160-173.

[15] Mahmoud M.E., El-Khatib A.M., Badawi M.S., Rashad A.R., El-Sharkawy R.M., Thabet A.A., Recycled high-density polyethylene plastics added with lead oxide nanoparticles as sustainable radiation shielding materials. J Clean Prod, 2018, 176, 276-287.

[16] Afshar M., Morshedian J., Ahmadi S., Radiation attenuation capability and flow characteristics of HDPE composite loaded with W, MoS_2, and B_4C. Polym Compos, 2019, 40(1), 149-158.

[17] Alsayed Z., Badawi M., Awad R., Thabet A., El-Khatib A., Study of some γ-ray attenuation parameters for new shielding materials composed of nano ZnO blended with high density polyethylene. Nucl Technol Radiat Prot, 2019, 34, 33-33.

[18] Alsayed Z., Badawi M., Awad R., Elkhatib A., Thabet A., Investigation of γ-ray attenuation coefficients, effective atomic number and electron density for ZnO/HDPE composite. Phys Scr, 2020, 95(8), 085301.

[19] El-Khatib A.M., Abbas M.I., Elzaher M.A., Badawi M.S., Alabsy M.T., Alharshan G.A., Aloraini D.A., Gamma attenuation coefficients of nano cadmium oxide/high density polyethylene composites. Sci Rep, 2019, 9(1), 16012.

[20] Cao D., Yang G., Bourham M., Moneghan D., Gamma radiation shielding properties of poly(methyl methacrylate)/Bi_2O_3 composites. Nucl Eng Technol, 2020, 52(11), 2613-2619.

[21] Kaçal M.R., Polat H., Oltulu M., Akman F., Agar O., Tekin H.O., Gamma shielding and compressive strength analyses of polyester composites reinforced with zinc: an experiment, theoretical, and simulation based study.

Appl Phys A, 2020, 126(3), 205.

[22] Ambika M.R., Nagaiah N., Suman S.K., Role of bismuth oxide as a reinforcer on gamma shielding ability of unsaturated polyester based polymer composites. J Appl Polym Sci, 2017, 134, 44657.

[23] Alavian H., Tavakoli-Anbaran H., Comparative study of mass attenuation coefficients for LDPE/metal oxide composites by Monte Carlo simulations. Eur Phys J Plus, 2020, 135(1), 82.

[24] Atashi P., Rahmani S., Ahadi B., Rahmati A., Efficient, flexible and lead-free composite based on room temperature vulcanizing silicone rubber/W/Bi_2O_3 for gamma ray shielding application. J Mater Sci Mater Electron, 2018, 29, 10.

[25] Subhankar M., Kunal S., Pulak D., Mrinal S., Textiles in Electromagnetic Radiation Protection. Journal of Safety Engineering, 2013, 2(2), 11-19.

[26] Moravskyi V., Dziaman I., Suberliak S., Grytsenko O., Kuznetsova M., Features of the production of metal-filled composites by metallization of polymeric raw materials, IEEE 7th Inter. Conf. Nanomaterials: Applications and Properties (NAP-2017), 2017, Sumy: Sumy State University.

[27] Moravskyi V., Dziaman I., Suberliak S., Kuznetsova M., Tsimbalista T., Dulebova L., Research into kinetic patterns of chemical metallization of powder-like polyvinylchloride. East-Eur. Jour. Enterp. Technol., 2017, 4(12), 50-57.

[28] Moravskyi V., Kucherenko A., Kuznetsova M., Dziaman I., Grytsenko O., Dulebova L., Studying the effect of concentration factors on the process of chemical metallization of powdered polyvinylchloride. East-Eur. Jour. Enterp. Technol., 2018, 3(12), 40-47.

[29] Moravskyi V., Kucherenko A., Kuznetsova M., Dulebova L., Spišák E., Majerníková J., Utilization of polypropylene in the production of metal-filled polymer composites: development and characteristics. Materials, 2020, 13, 2856.

[30] Kucherenko A., Moravskyi V., Kuznetsova M., Grytsenko O., Masyuk A., Dulebova L., Regularities of obtaining metal-filled polymer composites. Springer Proceedings Phys., 2020, 244, 59-66.

[31] Heinle, M., Drummer, D., Temperature-dependent coefficient of thermal expansion (CTE) of injection molded, short-glass-fiber-reinforced polymers. Polym Eng Sci, 2015, 55, 2661-2668.

[32] Shahapov V., Yumahulova Y., Povysheniye davleniya zhidkosti v zamknutom obyeme pri teplovom vozdeystvii cherez stenki. Teplofizika i aeromekhanika, 2013, 20(4), 505-512.

[33] Zaslavskiy B.V., Kratkiy kurs soprotivleniya materialov. Moskva: Mashinostroyeniye, 1986.

[34] Shalkauskas M., Vashkyalis A., Chemical metallization of plastics. Leningrad: Khimiya, 1985.

[35] Tyumentsev A.N., Panin V.Ye., Ditenberg I.A., Pinzhin YU.P., Korotayev

A.D., Derevyagina L.S., Shuba YA.V., Valiyev R.Z., Osobennosti plasticheskoy deformatsii ul'tramelkozernistoy medi pri raznykh temperaturakh. Fizicheskaya mezomekhanika, 2001, 4(6), 77-85.

[36] Bobylev A.V., Mekhanicheskiye i tekhnologicheskiye svoystva metallov: Spravochnik. Moskva: Metallurgiya, 19

Oleksandr Grytsenko[1], **Natalia Baran**[1], **Bohdan Berezhnyy**[1]

DEVELOPMENT OF A NEW TECHNOLOGY OF OBTAINING OF TUBULAR PRODUCTS BASED ON COMPOSITE HYDROGELS

Abstract: *The method for obtaining composite hydrogel tubular products with the increased strength on the basis of copolymers of 2-hydroxyethylmethacrylate with polyvinylpyrrolidone has been developed. The method consists in the formation of hydrogel tubes with a subsequent precipitation from the solution into their outer surface of the reinforced layer based on polyamide, modified with polyvinylpyrrolidone. The obtained composite hydrogel tubes are characterized by the sufficient strength, resilience, elasticity, as well as the ability to withstand an internal pressure within 24–43 kPa (180–320 mm Hg).*

Keywords: *hydrogels, composite materials, composite hydrogels, polyamide, polyvinylpyrrolidone, vascular prostheses*

1. Introduction

Blood vessel prostheses are implanted devices, which function in the human body in constant contact with the blood. Preferably, the patient's own vessels removed from other parts of the body are used for this purpose. Creation of synthetic materials for the production of samples of vascular prostheses and implants with improved properties is an urgent task, which is caused by the deficiency of healthy vessels to replace the affected areas of arteries and veins [1].

Unlike most synthetic products, which are used in medicine, blood vessel prostheses are developing to be as close to natural vessels as possible by its characteristics. It should be noted that nowadays, none of the synthetic prostheses is perfect and has a number of disadvantages. For the purpose of use, a large variety of synthetic textile fibers including Ivalon, Orlon, Nylon and Dacron, as well as non-textile materials (Teflon) have been tested for prosthetic applications [2]. However, studies have shown that vessels based on these materials lead to occur various complications, associated with structural defects such as lack of compliance, dilatation and resistance to the blood and obstruction. Nowadays, the textile watertight implants of polyethylene terephthalate (PET) share the market of vascular prostheses with those one-piece implants, moulded from polytetrafluoroethylene (PTFE) [2]. Biocompatibility, biostability and high tensile strength of prostheses based on PET, used for a long time during exploitation have long-been well documented [3]. In medical practice, polyurethane prostheses are used as well [4]. However, synthetic prostheses of synthetic materials are non-durable during the exploitation due to thrombosis and insufficient healing process [5].

Therefore, the question of developing new vascular prostheses and simple

---

1) *Lviv Polytechnic National University, Department of Chemical Technology of Plastics Processing, 12 Bandera Str., Lviv, 79013, Ukraine, ogryts@gmail.com.*

technologies for their production remains open, and researches related to its solution need to be continued. This task is in the area of interests not only of vascular surgeons, but also of researchers in the field of chemistry, mechanics, biotechnology, *etc*.

Due to their unique properties [6-8], polymer hydrogels are seen as perspective materials for the production of vascular protheses. Polymer hydrogels are obtained through high hydrophilic cross-linked polymers saturation by water. As a rule during swelling the physical transfer from glassy state into high elasticity one is observed. As a result of this hydrogels are characterized by a high sorption ability relative to low-molecular substances, penetrability for liquids and gases, and this is the main reason for their usage in different branches of science and industry.

Due to their structure, which resembles the structure of living tissues, hydrogels are characterized by good biocompatibility, which allows them to be used in direct contact with a living organism.

The performance properties of hydrogel materials depend on the nature of the components of the original composition. Besides, the technological obtaining features of hydrogel material play the final role in the selection of such type of material for the purpose of manufacturing products for the specific practical use.

Materials based on copolymers of 2-hydroxyethylmethacrylate (HEMA) with polyvinylpyrrolidone (PVP), developed at Lviv Polytechnic National University in the Department of Chemical Technology of Plastics Processing [9-12] are particularly noteworthy. HEMA was selected as the main component of the hydrogel network due to its solubility in water, as well as the presence of a carbonyl group that is able to coordinate various compounds [13]. Poly(2-hydroxyethyl methacrylate) (pHEMA) and its copolymers are characterized by a high degree of water-absorption, ability to adsorb low molecular weight substances, high biocompatibility and low thrombogenicity [14-16]. PVP has drawn a great attention due to its unique properties such as biocompatibility, non-toxicity, solubility in water and in many organic solvents, pH stability, affinity for both hydrophobic and hydrophilic complex substances, as well as chemical inertness in physiological reactions [17]. The use of PVP opens additional opportunities during the obtaining and stabilizing nanopowders of metals [18, 19], modifying various substances and materials [20-22], improving modern technologies [23], obtaining new functional materials [24-26] and, accordingly, expanding areas of their use.

The obtained hydrogels based on copolymers of HEMA with PVP (pHEMA-gr-PVP) draw attention by elasticity, resilience, sufficient porosity, high chemical and biological inertness, antithrombogenicity [9], which provides a perspective for their use as materials for vascular protheses. However, the disadvantage, which limits the use of the obtained materials for the production of vascular prostheses is their insufficient strength characteristics, as well as the lack of technology production of protheses.

It has been established that one of the methods of increasing the strength characteristics of the products based on polymer hydrogels is to modify their surface by applying additional reinforced layers, for example, on the basis of interpolymer complex PA-6/PVP by using the method of diffusion precipitation from a formate solution [10].

2. Purpose and objectives

The purpose of this work is to develop a formation method of tubular products from composite hydrogels based on copolymers pHEMA-gr-PVP of increased strength, which could be used as vascular prostheses.

To achieve the purpose, the following objectives were set:

- to develop the obtaining technology of hydrogel tubular products and the method of their research;
- to develop and design the equipment and facilities for the manufacture and research of hydrogel tubular products;
- to establish the possibility of obtaining hydrogel tubular products by the developed technology and to investigate their operational characteristics.

3. Results and Discussion

In order to combine the stages of synthesis of the hydrophilic polymer and its subsequent swelling, the polymerization was carried out in water. The initial HEMA/PVP/H_2O compositions are characterized by a high fluidity, which ensures the ability for them to be processed into tubes by the casting method (Fig. 1). The synthesis of the hydrogel with the simultaneous formation of the tubular product occurred in a polymerization form.

To obtain the hydrogel tubular products 2-hydroxyethylmethacrylate (Sigma Chemical Co), purified and distilled in vacuum (residual pressure 130 N/m^2, T_B = 351 K) was used; polyvinylpyrrolidone (AppliChem GmbH) of high purity with MM 12000 was dried at 338 K in vacuum for 2-3 h before use; inorganic salts (iron(II) sulfate, silver nitrate) were of P.A. grade. Polycaproamide (PA-6) of trade mark “Tarnamid-27” and formic acid of pure grade containing the main substance of 90 % were used to obtain a modifying solution. The composition of the modifying solution is as follows: (PA-6/PVP):HCOOH = 7:93 mass parts, PA-6:PVP = 95:5 mass parts.

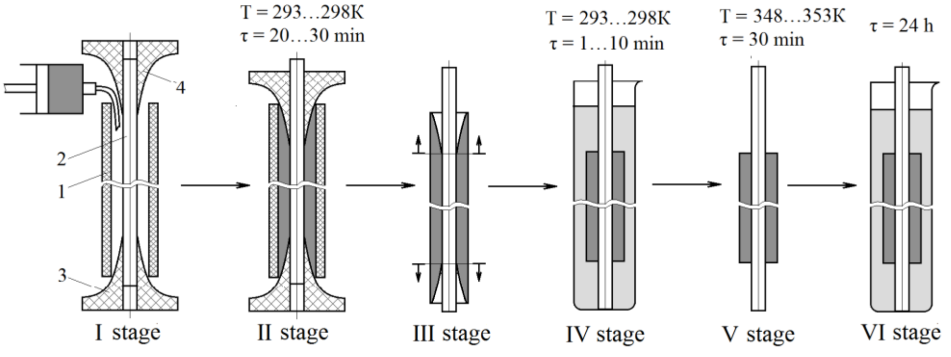

Fig. 1. Schematic diagram of two-layer hydrogel tubes obtaining. Stages: I – dosage of the composition (1 – matrix; 2 – punch; 3, 4 – calibration insert); II – polymerization; III – trimming the edges; IV – application of the modifying layer; V – evaporation of the solvent; VI – hydration

Hydrogel tubular products were obtained in a polymerization form, the main elements of which are the matrix *1* and the punch *2* (Fig. 2).

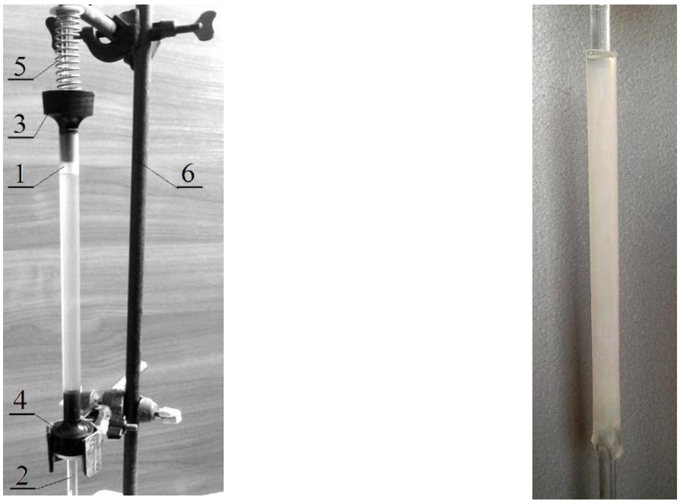

a) b)

Fig. 2. Laboratory installation for obtaining hydrogel tubes (a) and hydrogel tube on the punch (b): 1 – matrix; 2 – punch; 3, 4 – calibration insert; 5 – compression spring; 6 – stand rod

In order to facilitate a product removal from the mold, the outer molding surface (matrix) was made of polypropylene, because of the adhesion of pHEMA-gr-PVP copolymers to it was the lowest. The use of the developed mold with changeable molding elements ensures an obtainment of tubular products (Fig. 3) with geometric dimensions: length – from 100 to 400 mm, inner diameter – from 3 to 10 mm, wall thickness – from 0.2 to 2 mm.

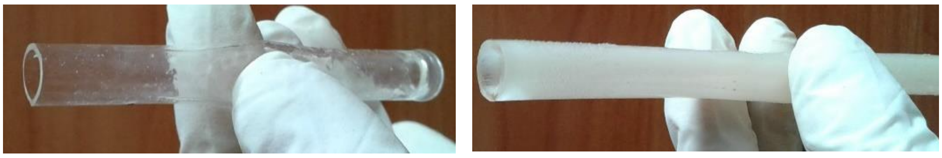

a) b)

Fig. 3. Tubular products based on hydrogel pHEMA-gr-PVP (a) and hydrogel pHEMA-gr-PVP +(PA-6/PVP) composite (b)

On the basis of previous studies [9, 27], HEMA with PVP copolymerization in the presence of iron(II) sulfate was used to obtain hydrogel tubes. Synthesis of pHEMA-gr-PVP copolymers was carried out at the temperatures of 293–298 K without additional vacuumization of the initial composition [27]. Polymerization occurs with a high speed at room temperature, in the air, which makes it possible to significantly simplify and reduce the cost of the process, shorten its duration and extend its abilities of usage.

The compositions of the structure HEMA:PVP = (90–60):(10–40) mass parts using from 50 till 200 mass parts of the solvent (H_2O) were studied. The lower limit of the PVP content is caused by the fact that with the less content of it, the hardening time of the compositions significantly increases (up to 24h). The upper limit is caused by technological complications – the higher the PVP content, the duration of its dissolution in HEMA increases, the viscosity of the composition, which is difficult to dispense and deaerate, increases as well.

The main performance properties of hydrogel materials are the ability to swell in solvents and diffusion-transfer properties. The paramount importance is the ability to swell in solvents, because this particular property determines the properties of the material, such as elasticity, biotolerance and permeability for low molecular weight compounds. Copolymers of pHEMA-gr-PVP are characterized by a porous structure and contain hydrophilic groups: hydroxyl and carbonyl HEMA, as well as peptide PVP. Precisely the number of such groups in the structure of the copolymer, as well as the porosity of the hydrogel determine its sorption capacity. The porous structure promotes rapid sorption of the solvent due to capillary forces, which causes swelling of the copolymers. The ability to swell was characterized by parameters such as boundary water absorption (W, %) and hydrogel swelling factor (k). Boundary water absorption (W, wt.%) was determined by the weight method as the difference between dry (m_0, g) and swollen (m_1, g) samples:

$$W = \frac{m_1 - m_0}{m_1} \cdot 100\%, \tag{1}$$

Hydrogel swelling factor was determined as a ratio of sizes of dry (d_d, mm) and swollen (d_s, mm) samples:

$$k = d_s / d_d \tag{2}$$

Samples of 1.3±0.1mm thick were used for the studies.

With increasing PVP content in the composition, the water content and swelling coefficient of the synthesized copolymer increase (Fig. 4a), which is explained by the hydrophilization of the network due to the introduction into its composition of chemically bound hydrophilic PVP chains, as well as the growth of intermacromolecular free volume in copolymer, due to outwashing the part of PVP, which did not enter into reaction of grafting.

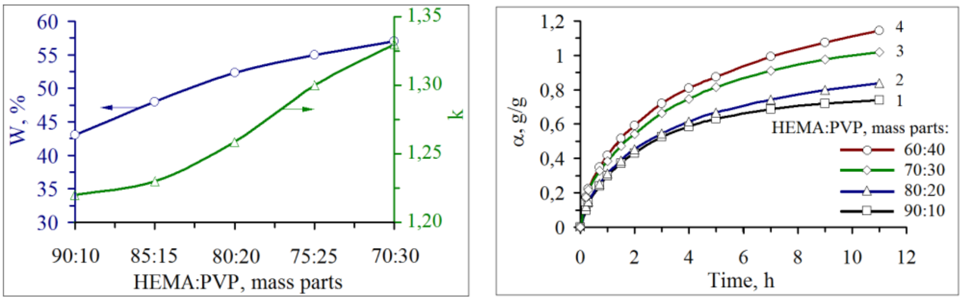

a) b)

Fig. 4. The effect of the initial composition formulation on the water content, the coefficient of swelling (a) and the kinetics of changes in the swelling degree (b) of the copolymers

Since the synthesized polymers are operated mainly in the swollen state, it is necessary to know the time of achievement of equilibrium swollen state by the material. In order to this, the kinetics of swelling of copolymers with different composition in water was studied.

The kinetics of swelling were characterized by the degree of water absorption α, g(H_2O)/g(polymer). α at time t was determined by the ratio of the mass of absorbed liquid by the polymer during swelling (m_t) to the mass of dry polymer (m_0):

$$\alpha_t = (m_t - m_0)/m_0 , \qquad (3)$$

It is established that the maximum swelling degree of samples with different composition formulation under normal conditions occurs after 24 h (Fig. 4b). As follows from the obtained dependences, the rate of swelling increases with increasing PVP content in the original composition.

The main physico-mechanical properties that determine the suitability of the polymer material for the production of vascular prostheses are strength, elasticity and resilience [1-5]. Samples in the form of blocks, films and tubes in the hydrated state were used to investigate the physico-mechanical characteristics of the obtained products. The strength of the hydrogel samples was characterized on the basis of the study results of their tensile strength during the bursting (σ, MPa) and the hardness number. Resilience was estimated by the resilience index, and elasticity by a percentage elongation at bursting (ε, %).

The bursting strength (σ, MPa) and the percentage elongation at bursting (ε, %) of the synthesized materials were determined by a breakthrough method using the film sample fixed in a ring-shaped clip, under the action of a pin indenter, by using a tensile testing machine "Kimura" of 050/RT-6010 type with the sample strain rate of 25 mm/min [10].

The bursting strength and percentage elongation at bursting for hydrated films have been calculated according to the following formulas:

$$\sigma = \frac{F}{D \cdot h} \cdot 10^{-6}; \qquad \varepsilon = 257 \cdot \frac{l}{D} - 25 \tag{4}$$

where F is stress, under which the sample is destroying, N; D is a diameter of ring-shaped clamp hole, m; h is a film thickness, m; l is a pin transposition from moment of contact with the sample till the moment of rupture, m (Fig. 5).

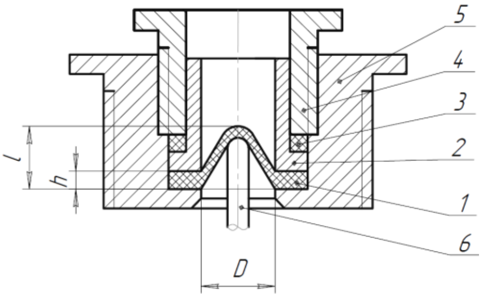

Fig. 5. Scheme of device for film materials physico-mechanical characteristics determination by bursting: 1 – film; 2 – ring-shaped clamp; 3 – fluoroplastic seal; 4 – clamping nut; 5 – holder; 6 – pin

Deformation and elastic characteristics – the hardness number (H, MPa) and the resilience index (E, %) – were determined using hardness meter TShR-320 by measuring the difference between the immersion depth of the indenter in the sample under the action of pre- and total load:

$$H = \frac{0.1F}{\pi \cdot d \cdot h}; \qquad E = \frac{h - h_1}{h} \cdot 100, \tag{5}$$

where F is an applied load, N; d is a diameter of indenter ball, mm ($d = 5$ mm); h is a depth of ball penetration into the sample under the load F, mm; h_1 is a residual deformation after removing the load, mm.

In order to determine the composition formulation, which would provide optimal characteristics of the hydrogel tubular products, the effect of PVP and solvent content (Figs. 6, 7) in the initial composition on the physico-mechanical properties of the hydrogels was studied.

The results showed that if the PVP content of the initial composition increases, the strength and resilience of the hydrogel samples decrease, while their elasticity increases, which is caused by the formation of a polymeric network with a less crosslinking degree, as well as outwashing of chemically unbound PVP, which promote an increasing of the free volume [28].

At the same time, it was found [10] that with increasing porosity of the hydrogel, the adsorption value of the modifying layer to the hydrogel substrate improves.

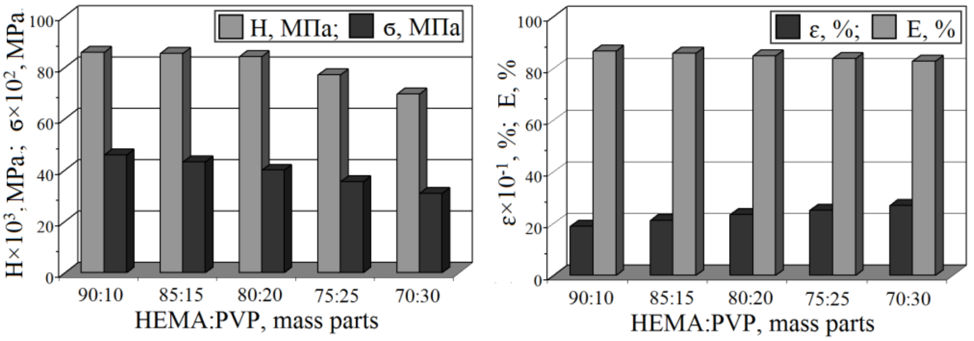

a) b)

Fig. 6. Dependence of hardness number (H, MPa) and tensile strength during breakthrough (σ, MPa) (a), as well as elasticity index (E, %) and relative elongation during breakthrough (ε, %) (b) of hydrogels (based on pHEMA-gr-PVP copolymers) on the content of initial composition HEMA:PVP (Composition:H_2O=1:1)

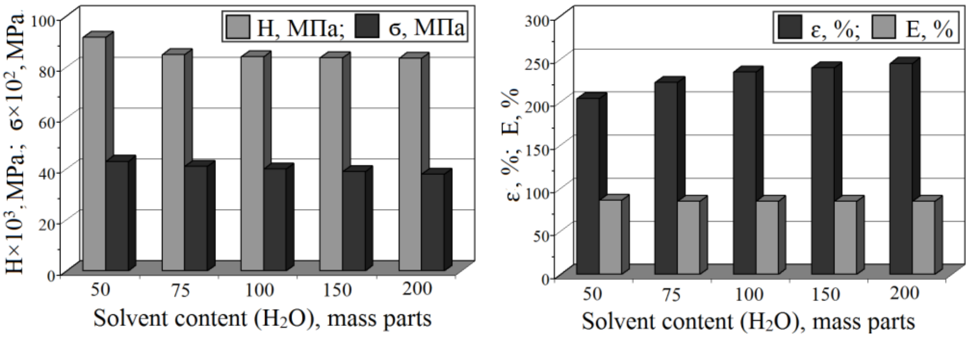

a) b)

Fig. 7. Dependence of hardness number (H, MPa) and tensile strength during breakthrough (σ, MPa) (a), as well as elasticity index (E, %) and relative elongation during breakthrough (ε, %) (b) of hydrogels (based on pHEMA-gr-PVP copolymers) on the solvent content (HEMA:PVP = 80:20 mass parts)

The relatively high strength and resilience properties with the retention of sufficiently high elasticity and surface adsorption, are characteristic for the polymer-monomer composition of the formula HEMA:PVP = 80:20 mass parts (Fig. 8). Therefore, the optimal properties of the hydrogels are ensured by the water content in the initial composition within 75 mass parts. Thus, the hydrogel tubes were formed by using the initial polymer-monomer composition of the formula HEMA:PVP:H_2O = 80:20:75 mass parts and an initiation system based on iron(II) sulfate.

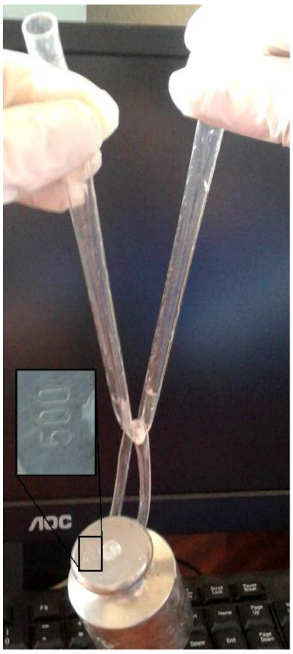

Fig. 8. Demonstration of hydrogel tube strength (δ=0,5mm, inner diameter – 4mm, load weight – 0,5 kg). Composition formulation: HEMA:PVP:H_2O=80:20:75 mass parts

To increase physico-mechanical properties of the tubular products based on the pHEMA-gr-PVP hydrogels, they were modified with a thin layer of the PA-6/PVP mixture, which was obtained from the formate solution by the precipitation of hydrogel free water [23]. The studies were carried out by using film samples. The film thickness was measured with a TR 10-60 thickness gauge with an accuracy of ±0.01 mm. Certainly, the holding time of the sample in the modifying solution will affect the characteristics of the modifying layer and the composite in total. It was established [10] that holding the samples in the modifying solution positively affects the strength of the composite hydrogel. However, after 5 min of modification, the resilience and elasticity of the composites deteriorate sharply. At the same time, it was investigated that the holding duration of the hydrogel film samples in the modifying solution has a positive effect on the surface adsorption value of the mixture PA-6 with PVP (Fig. 9). The value of surface adsorption (A, kg/m^2) was determined as the ratio of the formed modifying layer weight to the area of the modified surface:

$$A = (m_0 - m_1)/S \tag{6}$$

where m_0 is the initial weight of hydrogel film, kg; m_1 is the weight of the hydrogel film after application of the modifying layer, kg; S is the area of the modified surface, m^2.

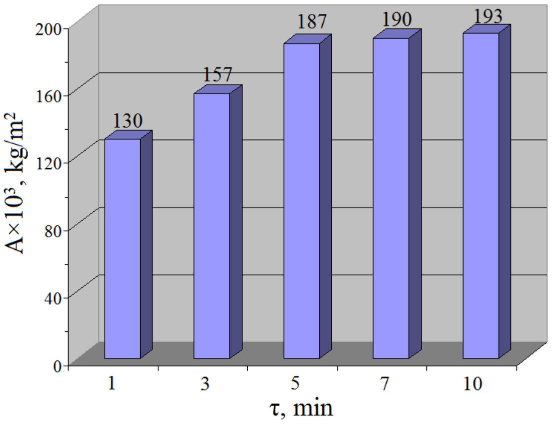

Fig. 9. Surface adsorption of PA-6/PVP mixture from formic acid solution on modification time of hydrogel films (HEMA:PVP:H2O = 80:20:75 mass parts)

It was found that the adsorption of the reinforced layer to the hydrogel substrate increases straight-linearly during the first 5 min of holding the hydrogel sample in the modifying solution, after which the value of adsorption changes slightly. Consequently, for the subsequent studies, we establish the duration of the holding stage of the hydrogel tubes in a modifying solution for 5 min.

Accordingly, on the basis of the conducted researches it is possible to distinguish the following main stages of the forming process of composite two-layer hydrogel tubular products (Fig. 1): dosage of the composition; polymerization; mechanical processing (trimming the edges); application of the modifying layer; evaporation of the solvent; hydration of the hydrogel tube.

On the basis of the obtained results, and by the use of the designed laboratory equipment, tubular hydrogel samples with different formulation of the initial polymer-monomer composition were formed. The strength of tubular products suitable for use as vascular prostheses, further characterize the ability to withstand internal pressure. For this purpose, the studies of the resistance of the obtained hydrogel tubes to the internal pressure were carried out.

To study the resistance to the internal pressure of the hydrogel tubular samples, a laboratory unit was constructed (Fig. 10) and a method was developed, the essence of which is the liquid pressure fixation under which the sample is bursting. The internal pressure, fixed by using a manometer 2, is created in a tubular sample 1 by the force of water supplied through a through-hole in the conical fitting 3.

The results (Fig. 11) showed that the resistance to breakthrough from the internal pressure of the modified samples is almost two times higher than the strength of the unmodified ones and is within the permissible limits of blood vessel exploitation.

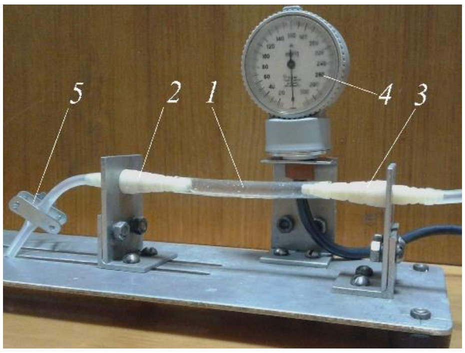

Fig. 10. Laboratory setup for investigation the resistance of hydrogel tubes to the internal pressure: 1 – tubular hydrogel sample; 2, 3 – conical fittings for fixation of a research sample; 4 – manometer; 5 – clip

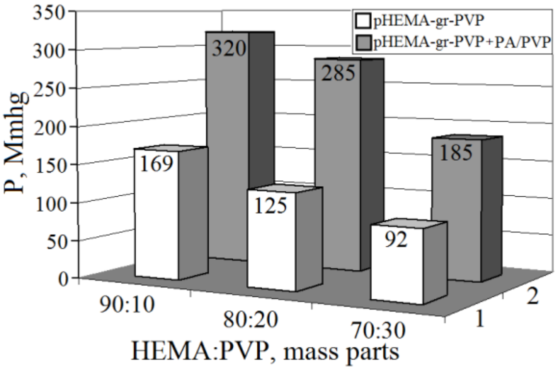

Fig. 11. Dependence of maximum bursting pressure on the composition of initial HEMA:PVP (composition:water = 1:1 mass parts): hydrogel tubular sample based on a copolymer pHEMA-gr-PVP (1) and hydrogel tubular sample based on a copolymer pHEMA-gr-PVP +(PA/PVP) (2)

At the same time, there is information [29] that prosthetic graft infection is one of the main complications of vascular surgery associated with high morbidity rate. The leading cause of the infection of vascular graft is contamination during the initial surgical procedure. The most common bacteria cultured from infected grafts include *Staphylococcus aureus*, *Staphylococcus epidermidis*, diphtheroids, and gram-negative enteric organisms [29].

The combination in the developed method processes of obtaining tubular products and reduction process of metal ions at the stage of polymerization [12], ensured the possibility of obtaining composite silver-filled tubular hydrogels with bactericidal and antifungal properties, which is confirmed by medico-biological studies on the examples of tested bacterial cultures: *Escherichia* coli (*E. coli*), *Staphylococcus aureus* (*S. aureus*), *Staphylococcus epidermidis* (*S. epidermidis*), *Streptococcus viridans* (*Str. viridans*) and diploid fungus *Candida albicans* (*C. albicans*).

Due to the comparative analysis of bactericidal and antifungal properties of unfilled and Ag(0)-filled hydrogels concerning the microorganisms usage, it was found that unfilled hydrogels do not exhibit bactericidal and antifungal properties. At the same time, materials containing Ag(0) block the growth of bacteria and fungi (Table).

Table. Bactericidal and antifungal activity of silver-filled hydrogel tubes, obtained on the basis of HEMA copolymers with PVP

Magnitude of the zone of inhibition of microorganism growth, mm				
S. aureus	*S. epidermidis*	*Str. viridans*	*E. coli*	*C. albicans*
12, 10, 9	12, 8, 9	11, 11, 9	3, 3, 0	11, 11, 7

4. Conclusions

The peculiarities of the forming technology of composite double-layer hydrogel tubes on the basis of liquid-structured copolymers of 2-hydroxyethylmethacrylate with polyvinylpyrrolidone, which were strengthened with a layer of polymer mixture of polycaproamide/polyvinylpyrrolidone, have been studied. Tubular hydrogel products with the increased strength and with the ability to provide bactericidal and antifungal properties were obtained.

The proposed technology is easy to implement into production and does not require sophisticated hardware design. Such technology is a priority and needs the development, considering the perspective of the obtained products.

The obtained composite double-layer hydrogel tubes with the increased strength are recommended for further preclinical studies for the possibility of use as blood vessel prostheses.

References

[1] Popova I., Stepanova A., Sergeevichev D., Akulov A., Zakharova I., Pokushalov A., Laktionov P., Karpenko A., Comparative study of three vascular grafts produced by electrospinning in vitro and in vivo // Patologiya krovoobrashcheniya i kardiokhirurgiya. 2015. V. 19(4). P. 63-71.

[2] Khlif H., Abdessalem S., Dhouib S., Sakli F., Contribution to the Improvement of Textile Vascular Prostheses Crimping // Trends in Applied Sciences Research. 2011. V. 6. P. 1019-1027.

[3] Marzougui S., Abdessalem S., Sakli F., Viscoelastic behavior of textile artificial ligaments // J. Applied Sci. 2009. V. 9. P. 2794-2800.

[4] Grasl C., Bergmeister H., Stoiber M., Schima H., Weigel G., Electrospun polyurethane vascular grafts: In vitro mechanical behavior and endothelial adhesion molecule expression // Journal of Biomedical Materials Research. 2010. V. 93A. P. 716-723.

[5] Chlupác J., Filová E., Bacáková L., Vascular prostheses: 50 years of advancement from synthetic towards tissue engineering and cell therapy // Rozhledy. 2010. V. 89. P. 85–94.

[6] Khan S., Ullah A., Ullah K., Rehman N., Insight into hydrogels // Designed Monomers and Polymers. 2016. V. 19(5). P. 456-478.

[7] Jumadilov T., Abilov Z.et al., Influence of Hydrogels Initial State on their Electrochemical and Volume-Gravimetric Properties in Intergel System Polyacrylic Acid Hydrogel and Poly-4-vinylpyridine Hydrogel // Chemistry & Chemical Technology. 2015. V. 9(4). P. 459-462.

[8] Gibas I., Janik H., Review: Synthetic Polymer Hydrogels for Biomedical Applications // Chemistry & Chemical Technology. 2010. V. 4(4). P. 297-304.

[9] Suberlyak O., Skorokhoda, V., Hydrogels based on polyvinylpyrrolidone copolymers. In S. Haider, A. Haider (Ed.) // Hydrogels. Monography. London: IntechOpen. 2018. P. 136–214.

[10] Suberlyak O., Baran N., Melnyk Y., Yatsulchak G., Formation of composite hydrogel membranes // Voprosy khimii i khimicheskoi tekhnologii. 2018. № 3 (118). P. 121–126.

[11] Skorokhoda V., Matrix polymerization of 2-Hydroxyethylmethacrylate in the presence of polyvinylpyrrolidone in permanent magnetic field // Chemistry & Chemical Technology. 2010. V. 4. P. 191–196.

[12] Grytsenko O., Pokhmurska A., Suberliak S., Kushnirchuk M., Panas M., Moravskyi V., Kovalchuk R., Technological features in obtaining highly effective hydrogel dressings for medical purposes // Eastern-European Journal of Enterprise Technologies. 2018. № 6/6 (96). P. 6–13.

[13] Montheard J., Chatzopoulos M., Chappard, D., 2-Hydroxyethyl Methacrylate (HEMA): chemical properties and applications in biomedical fields // Journal of Macromolecular Science. 1992. V. 32. P. 1-34.

[14] Yanez F., Concheiro A., Alvarez-Lorenzo C., Macromolecule release and smoothness of semiinterpenetrating PVP–pHEMA networks for comfortable soft contact lenses // European Journal of Pharmaceutics and Biopharmaceutics. 2008. V. 69(3). P. 1094-1103.

[15] Malešić N., Rusmirović, J., Jovašević, J., Antimicrobial Hydrogels Based on 2-hydroxyethylmethacrylate and Itaconic Acid Containing Silver (I) Ion. Tehnika. 2014. V. 69. P. 563-568.

[16] Prasitsilp M., Siriwittayakorn T., Molloy R., Suebsanit N., Siriwittayakorn P., Veeranondha S. ,Cytotoxicity study of homopolymers and copolymers of 2-hydroxyethyl methacrylate and some alkyl acrylates for potential use as temporary skin substitutes // Journal of Materials Science: Materials in Medicine. 2003. V. 14. P. 595–600.

[17] Teodorescu M., Bercea M., Poly(vinylpyrrolidone) – a versatile polymer for biomedical and beyond medical applications // Polymer-Plastics Technology and Engineering. 2015. V. 54. P. 923-943.

[18] Reverberi A., Salerno M., Lauciello S., Fabiano B., Synthesis of copper nanoparticles in ethylene glycol by chemical reduction with vanadium (+2) salts // Materials. 2016. V. 9. P. 809-820.

[19] Koczkur K., Mourdikoudis S., Polavarapu L., Skrabalak S., Polyvinylpyrrolidone (PVP) in nanoparticle synthesis // Dalton Transactions. 2015. V. 44(41). P. 17883–17905.

[20] Fan M., Zhang L., Wang R., Guo H., Jia, S., Facile and controllable synthesis of iron nanoparticles directed by montmorillonite and polyvinylpyrrolidone // Applied Clay Science. 2017. V. 144. P. 1-8.

[21] Suberlyak O. V., Krasins'kyi V., Shapoval I., Hrytsenko O., Influence of the mechanism and parameters of hardening of modified novolac phenol-formaldehyde resins on the physicomechanical properties of the composite // Materials Science. 2011. V. 46. P. 669–678.

[22] Suberlyak O., Volodymyr K., Sikora J., Krzyzak A., Ammonia-free, low-toxic press-materials with improved electroinsulating properties based on modified novolak phenol-formaldehyde resin / Chemistry & Chemical Technology. 2012. V. 6, No. 2. P. 199-202.

[23] Suberlyak O., Baran N., Yatsul’chak H., Physicomechanical properties of the films based on polyamide–polyvinylpyrrolidone mixtures // Materials Science. 2017. V.53. P. 392–397.

[24] Suberlyak O., Grytsenko O., Hischak K., Hnatchuk N., Researching influence the nature of metal on mechanism of synthesis polyvinilpyrrolidone metal copolymers// Chemistry & chem. tecnology. 2013. Vol. 7, No. 3. P. 289-294.

[25] Roy N., Saha N., PVP-based hydrogels: synthesis, properties and applications [in:] F. V. Câmara and L. J. Ferreira (Ed.) // Hydrogels: Synthesis, Characterization and Applications. Monography. Hauppauge, NY, USA. 2012. P. 227-252.

[26] Grytsenko O., Naumenko O., Suberlyak O., Dulebova L., Berezhnyy B. ,The technological parameters optimization of the graft copolymerization 2-hydroxyethyl methacrylate with polyvinylpyrrolidone for nickel deposition from salts // Voprosy Khimii i Khimicheskoi Tekhnologii. 2020. V. 1. P. 25-32.

[27] Suberlyak O., Grytsenko, O., Kochubei, V., The role of $FeSO_4$ in the obtaining of polyvinylpirolidone copolymers // Chemistry & Chemical Technology. 2015. V.9. P. 429-434.

[28] Suberlyak O., Grytsenko O., Hischak Kh., Influence of the metal surface of powder filler on the structure and properties of composite materials based on the co-polymers of methacrylates with polyvinylpyrrolidone // Materials Science. 2016. V. 52(2). P. 155-164.

[29] Sousa J., Antunes L., Mendes C., Marinho A., Gonçalves A., Gonçalves Ó., Matos, A., Prosthetic vascular graft infections: A center experience // Angiologia e Cirurgia Vascular. 2014. V.10(2). P. 52-57.

Andrii Masyuk[1], **Bozhena Kulish**[1], **Khrystyna Kysil**[1],
Volodymyr Levytskyi[1], **Diana Katruk**[1], **Dmytro Ketchur** [1]

FEATURES OF TECHNOLOGY, MORPHOLOGY AND PROPERTIES OF HEAT-RESISTANT POLYLACTIDE COMPOSITES

Abstract. *Extrusion-filled polylactide composites were obtained***.** *The influence of talc filler, its content as well as an additional heat treatment and temperature on the regularities of polylactide materials water-absorption has been researched. Based on the obtained data, the water diffusion coefficient in polylactide materials and the activation energy of the diffusion process was determined. It was found that the process of water absorption by the filled and heat-treated materials based on polylactide proceeds slower and requires more activation energy of the process. Stability of the developed polylactide materials to acidic and alkaline media has been determined. A change in the morphology of the obtained materials was revealed, in particular, an increase in the degree of crystallinity of filled and heat-treated polylactide materials was noted. Based on the modular-deformation method of calculation, the elastic-plastic properties of the developed polylactide materials and the structure coefficient are determined. The change of modulus of deformation, modulus of elasticity, surface hardness and thermomechanical characteristics of polylactide composites is revealed.*

Keywords: *polylactide, talc, water absorption, chemical resistance, heat treatment, elastoplastic properties, thermal treatment*

1. Introduction

At present, polymers and composites based on polymers are among the most widespread materials in all spheres of human activity [1, 2]. The processes of manufacturing of polymeric products are characterized by the availability of raw materials, low power intensity and labor input, and simplicity of the technologies. At the same time, polymeric materials are rarely used repeatedly because secondary polymeric raw materials have numerous significant disadvantages: incompatibility with each other, high degrees of contamination of the secondary raw materials, noticeable degradation of the operating and technological characteristics after repeated processing, wide range of colors, etc. Therefore, polymers and polymer-based materials exert an increasingly harmful influence on the ambient medium. This is why the application of biodegradable polymers capable of regulated decomposition in the environment under the action of external factors (humidity, heat, microorganisms, ultraviolet radiation, etc.) realized with the possibility of recovery of their initial raw materials is currently regarded as the most acceptable and generally recognized direction in the development of the chemistry and technology of polymeric materials [3, 4]. As the most promising among these polymers, we can mention polylactide (PLA), i.e., a biocompatible biodegradable thermoplastic polymeric material obtained from recoverable raw materials [5, 6]. Moreover, there exist wide possibilities of

---

1) *Lviv Polytechnic National University, Department of Chemical Technology of Plastics Processing, 12 Bandera Str., Lviv, 79013, Ukraine,* *masyukas@gmail.com.*

modifying PLA and creation of composites based on this material, which makes it possible to obtain materials with required properties for specific applications. In particular, as a result of the development of new materials based on PLA and finely divided fillers, it becomes possible to guarantee their improved operating properties and the possibility of regulated biodegradation, as well as to substantially decrease the cost of the final products [7, 8]. At the same time, for polylactide materials, parallel with the strength and thermal characteristics, it is also important to know the characteristics of their elasticity, flexibility, and plasticity, which are used to determine various physical, rheological, and (partially) technological properties of the material, its homogeneity, and the changes caused by the conditions of processing and operation. The investigations of the deformation properties of polymeric materials are required to understand their behavior under loads of various types (static or dynamic, instantaneous, or sustained, etc.) and morphological characteristics [9, 10].

It should be noted that the technologies of extrusion of products based on PLA and its composites are insufficiently studied. They are marked by a number of features that require further research: - study of the processes of degradation and depolymerization of polylactide in processing on standard extrusion equipment; - the influence of fillers of different nature on the features of polylactide extrusion; - technological compatibility of the filler and the polymer matrix; features of the extrudate cooling process, etc.

Along with that the hydrolytic degradation of polylactide is influenced by such physical and chemical factors as temperature, pH, molecular weight of the polymer, crystallinity degree, fillers content and so on [11, 12]. Therefore, there is a need to study the characteristics of water absorption of polylactide and materials based on it depending on environmental conditions, to predict both the areas of application of such materials and methods of their further utilization.

At the same time, among the methods of directed influence on morphology and properties of polylactides there are their blending with fine dispersed fillers [13] and additional heat treatment [6]. So, it would be expedient to study the influence of the mentioned factors on the regularities of polylactide water-absorption and its chemical resistance to alkaline and acidic mediums.

2. Materials and methods

In the presented work for the obtaining of polylactide composites the polylactide of Ingeo 2500 HP brand (manufactured by NatureWorks LLC) has been applied. Algol Chemicals Finntalc M05 natural talc mineral with a density of 2.7–2.85 g/cm^3 was applied as a fine dispersed filler. The components were pre-mixed in the desired ratio using a drum type mixer (powdering a granular thermoplastic with talc) for 15–20 min. After obtaining the mechanical blend, it was dried for 1.5–2 h in an air vacuum dryer of 2B-131 type at 343 K. Further homogenization of the blend was conducted via mixing in a viscous state of components on a Cellier extruder, which is equipped with a screw having a length of 700 mm and diameter of 25 mm. The rotation velocity of the extruder screw is 10–15 rpm. The temperatures of the extruder zones are 438–443, 448–453 and 458–463 K. The obtained extrudate in the form of a tube was used for further studies. The filler content was 0–7 wt %. Additional heat treatment of the obtained materials was conducted in a thermal furnace at 393 K for 10 min.

Water absorption of polylactide composites was determined according to ISO 62:2008. The change in a mass was recorded by the periodic removal of samples from water and by weighing on scales with the preciseness to 1 mg. The change in the mass (W_t) as a percentage at any time moment t, due to water absorption was determined by Eq. (1):

$$W_t = \frac{M_{\text{в}} - M_c}{M_c} \cdot 100\% \qquad (1)$$

where M_d and M_w are the mass of the dry sample (initial) and the mass of the sample after staying in the water, respectively, g.

The values of maximum water absorption (W_m) were calculated as the average value of several consecutive measurements which did not show appreciable changes in the water absorption values. The mass increase which is caused by the water absorption can be expressed in two parameters: the diffusion coefficient D and the maximum water absorption W_m using Eq. (2):

$$\frac{W_t}{W_{\text{М}}} = 1 - \frac{8}{\pi^2} exp\left[-\left(\frac{Dt}{h^2}\right)\pi^2\right] \qquad (2)$$

where h is the thickness of the samples, m.

The value of the diffusion coefficient D was calculated according to Eq. (3):

$$D = \frac{\pi h^2 (W_2 - W_1)^2}{16 M_{\text{М}}^2 (t_2^{1/2} - t_1^{1/2})^2} \qquad (3)$$

where $\frac{(W_2 - W_1)^2}{(t_2^{1/2} - t_1^{1/2})^2}$ – is the sine of α angle in the graph of the dependence M_t on $t^{1/2}$.

The diffusion activation energies (E_a) of water for the PL composites were determined through the Arrhenius equation (4) making the dependency graph of lnD on 1/T:

$$\ln D = -\frac{E_a}{RT} + \ln D_0 \qquad (4)$$

where D is the diffusion coefficient of the sample; D_0 is an initial diffusion coefficient; E_a is an activation energy of the water diffusion; R is the gas constant (8.314 J/K·mol) and T is the temperature.

The chemical resistance of polylactide materials to the action of 5% H_2SO_4 solution and 0.5–5% NaOH solution was estimated according to ISO 2812-1: 2007.

The SPECORD 70 spectrograph was applied for FTIR spectroscopy; the spectra were recorded within the range of 400–4000 cm^{-1}. Samples were prepared by pressing the tablets with KBr.

Thermomechanical investigations were carried out in order to determine the level of strains in a specimen in the form of a pellet 5 mm in thickness caused by the variations of temperature and the action of a load of 5.0 kg upon a rod with an area of 23.7 mm^2. The initial temperature of the tests was equal to 20°C. The results of measurements (the changes in the depth of indentation of the rod into the specimen, mm) were recorded every 0.5°C. The tests were carried out according to the ISO 11359-1:1999.

The elastoplastic properties were determined by using a procedure [15, 16] based on the modular deformation method of calculations (a conic indenter was pressed under a load into the investigated polymeric specimen). According to the procedure, the initial load was equal to 120 N, the residual load to 30 N, and the thickness of specimens was not smaller than 5 mm. The readings of the indicator (the depth of penetration of the indenter) were recorded in 1 sec and 5 sec and also in 1, 3, 12, and 15 min after the application of the load, as well as in 1 and 3 min after the removal of the main load. For each specimen, we carried out at least five measurements.

3. Results and discussion

3.1. Features of extrusion of polylactide composites

To establish the features of the technological process of manufacturing products by extrusion from polylactide, an extrusion head is designed and manufactured. The main design feature of the extrusion head is the use of an elongated mandrel.

The design was carried out taking into account the rheological patterns of the flow of molten raw materials in the channels of the forming tool of different diameters and configurations (cylindrical or conical). For this purpose, empirical dependences were used to determine the pressure change in individual sections of the extrusion head in order to calculate the geometric parameters of these sections (to minimize pressure losses in the head and reduce the melting pulsation of the polymeric material).

The outer diameter of the product was formed by passing the molten polymer through the sleeve (matrix) of the housing of additional cooling, as well as changing the productivity of the extruder and the speed of rotation of the traction rolls.

According to the research results, the cooling parameters (intensity, temperature and angle and trajectory of the cooled air) have a significant influence on the melting characteristics of the polymer. To cool the molten polymer after leaving the extrusion head according to the results of a set of experimental studies, the use of simultaneous annular compressor and cooler air cooling is justified.

Based on experimental studies with a rational combination of different types of cooling, it is determined that the optimal parameters of extrusion are: temperature in the zones:

zone 1 of loading - 170 °C;
zone 2 of plasticization - 180 °C;
zone 3 dosage - 190 °C;
extrusion head - 150 °C.
Screw speed of 7-8 rpm

As the temperature rises both in the areas of the material cylinder and in the extrusion head, the melt of the polylactide lost the viscosity characteristics necessary to form a product with the required properties. At the same time, the decrease in temperature in the material cylinder of the extruder led to an increase in the load on the drive of the extruder and the occurrence of local overheating due to friction of molten polymer between the auger and the walls of the material cylinder (due to energy dissipation). The decrease in temperature in the extrusion head led to a partial premature transition of the polylactide to a highly elastic state inside the head and the adhesion of material to the mandrel, which in turn led to a significant increase in pressure in the head and deterioration of melt supply stability.

It should be noted that the use of only cooler cooling directly at the end of the mandrel led to local supercooling of both the mandrel and the matrix (insert), which made it impossible to optimally supply the melt with the required properties from the extrusion head. Due to that, in this laboratory extrusion line point ring compressor cooling was used. In this case, the use of water cooling without a calibrator led to a sharp fixation of the internal stresses of the polylactide after the transition to the vitreous state. The negative effect of such cooling was manifested after additional heat treatment of finished products - the products were deformed and completely lost their shape.

The obtained products were further directed to the study of physical and mechanical, thermophysical properties and water absorption and resistance to aggressive environments.

3.2. Resistance of polylactide materials to water mediums of the various natures

Interest to the problem of interaction of water with polymers, as well as the polymer materials, especially which are biodegradable ones, is conditioned by the number of factors. One of them is the practical importance of information concerning the interaction of water and the polymers. Polylactide materials, due to their ability to biodegrade are beginning to be widely applied as packaging materials, disposable and so on. In this case, water and moist air are the environment which most often polymer materials and the products based on them contact with. The same conditions are usually in landfills, where the polymeric products are stored after utilization. Therefore, the data concerning the sorption properties of material [17] and water diffusion [18] are needed to predict the behavior of mentioned materials in the humid mediums as well as to assess their working ability and the water impact on polymer degradation.

To provide polylactide materials with necessary operational and technological properties they are being modified with the fillers of different nature and the directed change in their morphology, in particular via additional heat treatment which promotes a significant increase in the crystallinity degree of the polymer [10]. For the determination of the impact of filler (talc) content and heat treatment conditions, the studies concerning water absorption of obtained polylactide materials were conducted. The kinetic dependencies of polylactide water absorption on the talc content and the heat treatment are shown in Fig. 1.

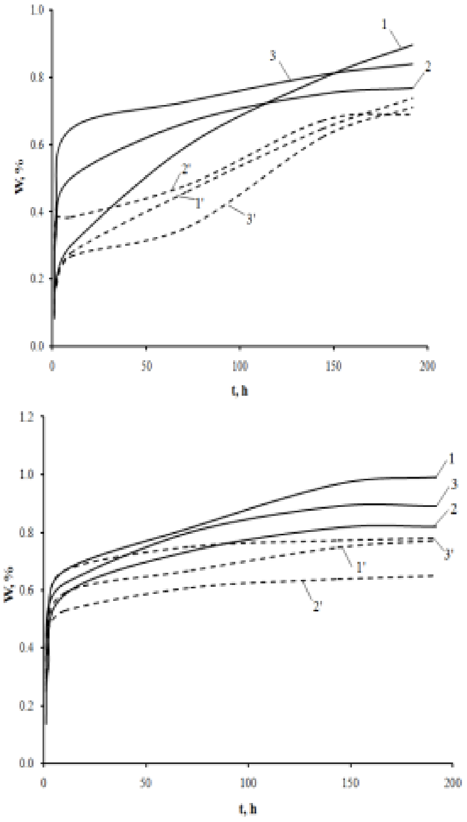

a) *b)*

Fig. 1. Dependence of water absorption of polylactide materials on time at water temperature of 276 K (a) and 333 K (b). Talc content: 0 wt % (1, 1'); 2 wt % (2, 2'); 7 wt % (3, 3'). 1, 2, 3 – not heat-treated samples, 1', 2', 3' – heat-treated samples

The water absorption of polylactide materials occurs by stages. At the first stage when keeping in water up to 10 h, the rate of water absorption is quite high where upon we can observe a slowdown in water absorption and equilibrium values reaching.

It should be noted that adding of talc into polylactide slightly accelerates the water absorption at the initial stage. The above mentioned obviously occurs due to the flabby polymer structure and the formation of transitional adsorption layers around the filler particles. Probably, at the initial stage, the swelling degree of hydrophobic polymers is as higher as more additives are in their composition. At the same time, an additional heat treatment of polylactide materials leads to a decrease in both the water absorption rate and the equilibrium value of water absorption. Such regularities of the heat treatment influence are associated with a significant compaction of the PLA materials structure owing to the increase of the crystallinity degree of the polymer. It should be noted that the increase in water temperature promotes faster establishment of equilibrium water absorption.

Hereby there is a minor increase in water absorption values during long-term staying of polylactide in the water due to the plasticizing effect of the water leading to increased flexibility and easier orientation of PLA macromolecules [20].

To define the possible changes in the polylactide supramolecular structure under the heat treatment, as well as to determine the nature of intermolecular interactions between the functional groups of the hydrophobic polymer, the IR spectroscopic studies were conducted (Fig. 2).

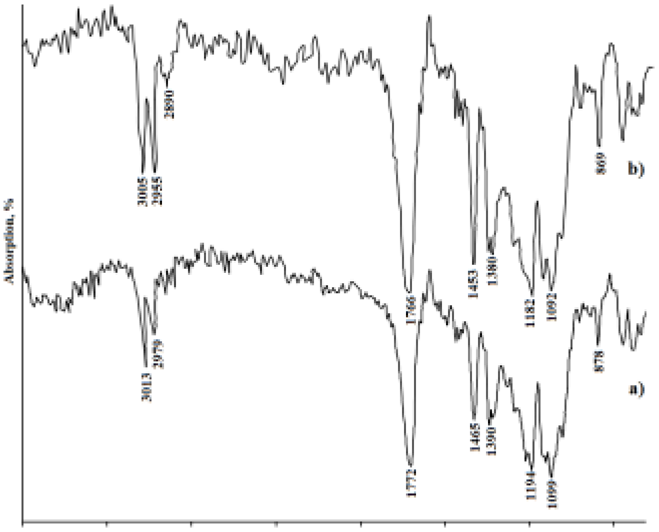

Fig. 2. IR absorption spectra of initial (a) and heat-treated polylactide (b)

For polylactide, independently of its thermal prehistory and crystallinity degree, the absorption bands within the area of 1050–1200 cm^{-1} with the highest intensity due to the valence symmetric and antisymmetric oscillations of –C–O–C– ester group are typical. For all the samples, absorption bands corresponding to the valence symmetric and antisymmetric oscillations of the CH bond of the methylene group within the area of 2900– 3100 cm^{-1} are definite as well as the deformation symmetric and antisymmetric oscillations of methylene group in the range of 1380–1400 and 1450–1470 cm^{-1} were also noted. The intensive absorption band observed in the range of 1760–1780 cm^{-1} can concern to the valence vibrations of C=O carbonyl group in polylactide [21].

It should be emphasized that for the heat-treated polylactide a change in the intensity of characteristic bands and their insignificant shift are observed if compared to the original polylactide. The presence of a crystalline structure in the heat-treated sample being confirmed by both higher absorption intensities and the appearance of an additional absorption band within the range of 920 cm^{-1} which corresponds to the bending oscillations of CH bonds and, in our opinion, indicates intermolecular interactions in the system as well as crystallization of polylactide under the heat treatment impact. Mentioned interactions are obviously accompanied by the formation of macrochains in supramolecular structures [22].

Since the peaks of the absorption bands of the deformation oscillations for the C=O group and the deformation symmetric and antisymmetric oscillations for the CH bond are shifted toward the lower values of the wave number for the initial PLA, it can be assumed that weak C–H…O=C hydrogen bonds are formed in the amorphous PLA.

The influence of water temperature, talc concentration and additional heat treatment on the value of equilibrium water absorption was studied (Table 1).

Table 1. Equilibrium water absorption of PLA-based composites at different temperatures

Talc content, wt %	Equilibrium water absorption $W_{м}$, %			
	276 K	290 K	323 K	333 K
0	0,87 / 0,68*	0,91 / 0,72	0,93 / 0,74	0,99 / 0,77
2	0,76 / 0,69	0,73 / 0,66	0,75 / 0,63	0,82 / 0,65
7	0,81 / 0,71	0,84 / 0,73	0,82 / 0,76	0,89 / 0,78

* values for the heat-treated samples

Based on the research conducted, it is determined that the maximum water absorption of polylactide materials is insignificant and belongs to diapason of 0.6– 1.0 wt %.

Based on the data obtained, the diffusion coefficients of water in the polylactide materials were determined depending on the temperature, talc content and additional heat treatment (Table 2).

Table 2. Water diffusion coefficient in PLA-based materials at different temperatures

Water temperature, K	Diffusion coefficient $D \cdot 10^{12}$, m^2/s					
	Pure PLA	+ 2 % of talc	+ 7 % of talc	Heat-treated pure PLA	+ 2 % of talc, heat-treated	+ 7 % of talc, heat-treated
276	2.45	1.18	2.43	1.91	0.81	1.34
290	2.99	1.51	3.02	2.31	1.12	1.72
323	3.18	2.09	3.27	2.59	1.32	2.01
333	3.36	2.14	3.42	2.85	1.46	2.07

It is known that the mass transfer of water in nonporous (in kinetic and sorption regard) polymer materials is varied in two features [23]: (i) diffusion of molecules in the material consisting of amorphous and crystalline phases with different diffusion properties is carried out mainly through the amorphous part of the polymer, while the diffusion conductivity of the crystallites can be neglected; (ii) the migration of water molecules proceeds by its diffusion not through the rigidly fixed pores, but through "cavities" in the polymer matrix. Mentioned "cavities" disorderly appear and disappear due to the thermal movement of macromolecule segments according to the probability laws.

The polymer polarity significantly affects the process of water diffusion into the polymer. The greater polymer polarity, the stronger internally molecular and intermolecular interactions, and more difficult to overcome them with polar water molecules [24]. Therefore, the polar polymers, in particular PLA, are characterized by high barrier properties in relation to the water.

It was found that the diffusion coefficient, regardless of the filler content and additional heat treatment increases with the increasing of water temperature. The temperature dependence of the diffusion coefficient in polymer materials is well approximated by the Arrhenius equation (4).

Based on the data obtained, the activation energy of the process of diffusion water-absorption by PLA has been calculated. Fig. 3 presents the value of activation energy of the water absorption process of PLA-based composites depending on the filler content and heat treatment.

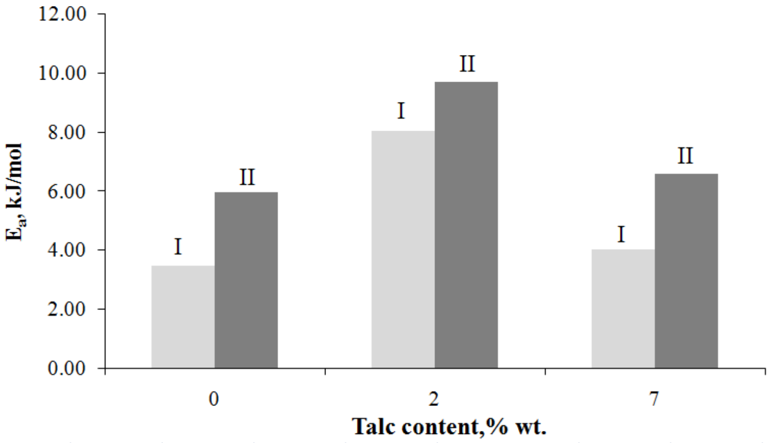

Fig. 3. The influence of filler content and heat treatment (I – without heat treatment, II – with heat treatment) on activation energy of water diffusion processes in the PLA

It is determined that the adding of talc causes an increase in the activation energy of the water absorption process, at the same time, additional heat treatment also increases the E_a value of the process. Such regularities are connected, first of all, with the compaction of the PLA structure under the action of both the inorganic nucleator filler and the crystallization process that takes place during the heat treatment. The E_a values increase indicates the need for an additional energy to water molecules for the diffusion into the matrix due to the barrier effect of talc particles and PLA crystallites.

During their operation, the polymer composite materials are exposed not only to water, but also to aqueous solutions of acids or alkalis which are chemically active media consisting of various types of kinetic units: water and electrolyte molecules, hydrated molecules and ions, etc. Such multicomponent medium transfer through a polymer material has a complicated physico-chemical nature and depends on the nature, concentration and temperature of the medium, as well as the composition of the composite. In this case, the pH value of the medium significantly affects the proceeding of hydrolytic degradation of polylactide.

Thereby, the aggressive medium interaction with the polymer matrix and the filler should be taken into account when developing the polymer composite materials [25]. It is also advisable to study the effect of filler on chemical resistance of the obtained composites.

First of all, it should be noted that polylactide can be destroyed by the hydrolysis mechanism: water breaks the ester bonds. In this case two modes of degradation could be presented: 1) If the hydrolysis rate is higher than the diffusion rate, the surface or heterogeneous degradation occurs and only the polymer surface undergoes degradation and erosion (namely the weight loss), and the bulk remains undamaged. The shape of the sample remains the same, but its volume decreases over time; 2) If the water penetration occurs much faster than the water consumption, the uniform or volumetric degradation takes place: the rate of degradation is almost the same at each point of the matrix and the volume is not changed significantly over time. Weight losses are observed after a certain period of time, when the stratification of the chains has led to the oligomeric products formation. Mentioned products are mobile enough to diffuse through the matrix into the environment. During hydrolysis, there is an initial increase in the crystallinity degree which can be explained by two main reasons: better degradation of the amorphous phase and the forming of new crystalline formations transformed from amorphous chains. The described phenomenon is probably accelerated by neighboring water molecules, oligomers or monomers which can facilitate the chain mobility.

The results of fine-dispersed filler and heat treatment influence on the polylactide composites resistance to the action of 5% H_2SO_4 solution are shown in Fig. 4.

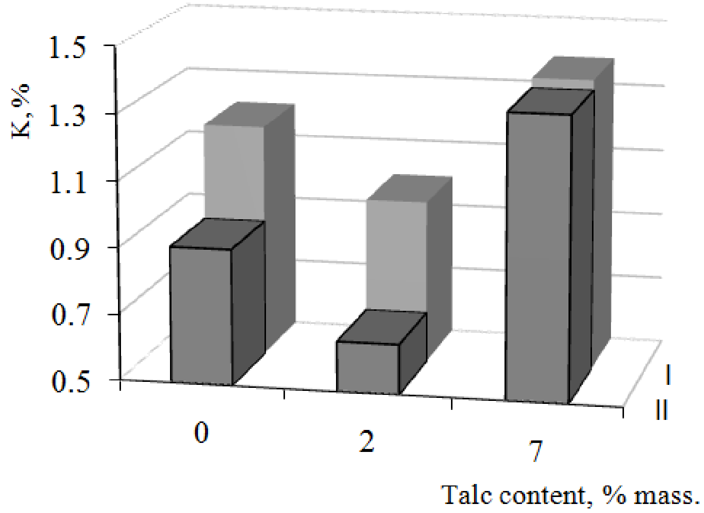

Fig. 4. Influence of talc content and heat treatment (I – without heat treatment; II – with heat treatment) on the swelling coefficient of PLA composites in 5% H_2SO_4 *solution*

The pH value has a significant impact on the hydrolytic degradation of PLA because it affects both the reaction mechanism and the kinetics of the reaction. Certainly, the polylactide degradation reactions can occur via hydrolytic degradation of ester groups in various ways: acid catalyzation, basic catalyzation and catalyzation free. The research has shown that the end ester groups break down faster than the ester groups of the main chain.

It should be noted that the composites after 12 days of exposure in a 5% solution of H_2SO_4 are characterized by the high mixed diffusion behavior and the swelling coefficient (K) of the samples is 0.7–1.6 %. Talc addition, as well as an additional heat treatment of PLA composites leads to an increase in chemical resistance of an acidic medium. It was found that the mechanism of hydrolysis at acidic pH occurs through the chain splitting.

In this case, the splitting of end ester groups promotes the faster weight loss of the polymer as a result of obtaining soluble low molecular weight polylactide oligomers. The reaction does not depend on the chain length and proceeds through the final –OH group. The influence of alkaline medium on the chemical resistance of the developed polylactide materials was defined (Figs. 5 and 6).

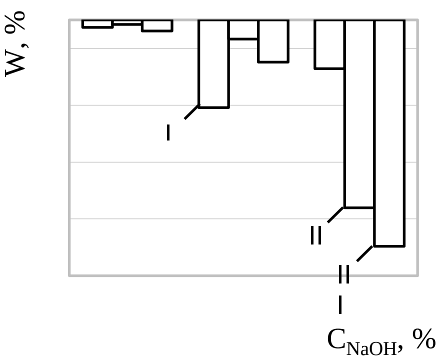

Fig. 5. Chemical resistance of PLA composites (10th day). Filler content (wt %): 0 (I); 2 (II) and 7 (III)

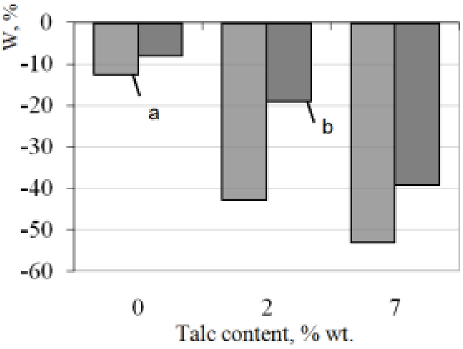

Fig. 6. Chemical resistance of PLA composites to the action of 5% NaOH depending on heat treatment (14th day): without heat treatment (a); with heat treatment (b)

Based on the research results it was found that independently of filler amount and the heat treatment during the exposure of composites in an alkaline medium all samples are characterized by a significant weight loss. Described loss relates to the leaching of the filler and water-soluble products, mainly lactic acid and probably low molecular weight oligomers from the composite during PLA degradation in the water. Visual observations also showed that polylactide composites which were immersed in alkali solutions, irrespective of their concentration, have lost transparency and became brittle. Thus, it was found that the pH value significantly influences the degradation velocity of polylactide.

3.3. Elastoplastic properties of polylactide composites with finely divided fillers

It is worth noting that the mechanical and elastoplastic behaviors of the actual polymeric materials and, first of all, of polymeric composites, cannot be described by a single simple scheme because numerous materials may be both in the plastic state and in the viscoplastic state depending on the testing conditions (duration of loading and temperature). In fact, the physicomechanical and elastoplastic properties of the polymers can be clearly illustrated by using different mechanical models. Thus, the Maxwell and Voigt–Kelvin models are regarded as generally accepted. However, they cannot give a complete description of the viscoelastic properties of polymeric materials. Indeed, if an actual material is represented in the form of the Maxwell model, then the deformation of a viscosity element does not find any resistance and continues infinitely. Parallel with the instantaneous elasticity and yield, the polymers have some properties caused by the highly elastic state and the retarded response of the material to the external force field. This is taken into account in the Voigt–Kelvin mechanical model. If the actual material is represented with the help of this model in which the stress is characterized by the determined strain connected with a spring, then the viscosity element cannot continue motion and play the role of a delaying mechanism. This is why it is better to represent the relaxation processes running in the polymeric material under the action of certain forces by using various combinations of elements of the Voigt–Kelvin and Maxwell models (Fig. 7).

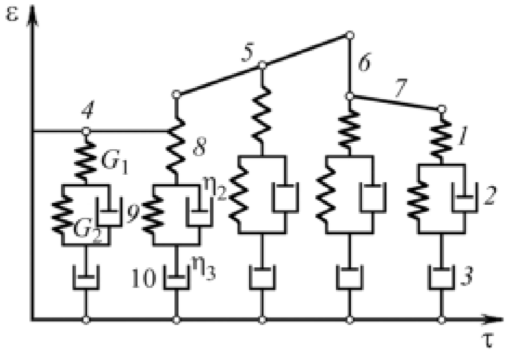

Fig. 7. Combined Voigt–Kelvin–Maxwell model: (1)–(3) elements; (4) strain-free specimen; (5) deformed specimen under stresses; (6) weakened stress; (7) reversible elastic strain; (8) elastic component of strain; (9) retarded flexibility; (10) irreversible strain

According to the displayed combined model, the behavior of the actual polymeric material can be described as follows: At the time of appearance of stresses in the element, the elastic element with modulus G_1 undergoes instantaneous stretching, whereas the element with modulus G_2 begins to deform with a certain rate controlled by a damper with viscosity η_2 . At the same time, a damper with viscosity η_3 begins to deform. After the relaxation of stresses, the elastic element with modulus G_1, instantaneously takes its initial value, the element with modulus G_2 starts its slow relaxation, whereas the deformation of the damper with viscosity η_3 is terminated and it remains in the deformed state.

If the behavior of the polymer under the action of the external force is described by this mixed model, then the level of strains in it changes as a function of time as follows: First, we observe instantaneous elastic deformation up to the level of strains equal to σ/G_1. Then the specimen undergoes retarded deformation and asymptotically attains the equilibrium value σ/G_2 , which corresponds to the onset of yield. First, the yield is determined by the ratio σ/η_3 . If, after a certain time, the specimen is rapidly unloaded, then the first strain disappears instantaneously, while the retarded strain gradually vanishes. At the same time, the strains caused by flow remain irreversible. Thus, the combined mechanical model simulates all three types of deformation: instantaneous elastic deformation, retarded (configuration) deformation, and yield.

An analytic expression of the time dependence of strains under the action of constant stresses has the form by Eq. (5):

$$\varepsilon = \sigma \frac{1}{G_1} + \sigma \frac{1}{G_2}(1 - e^{-t/\tau}) + \sigma \frac{1}{\eta_3} t \, . \tag{5}$$

On the basis of the described model, by using the procedure described in [11, 12], we determined the deformation and elasticity module of the obtained polylactide materials (Fig. 8).

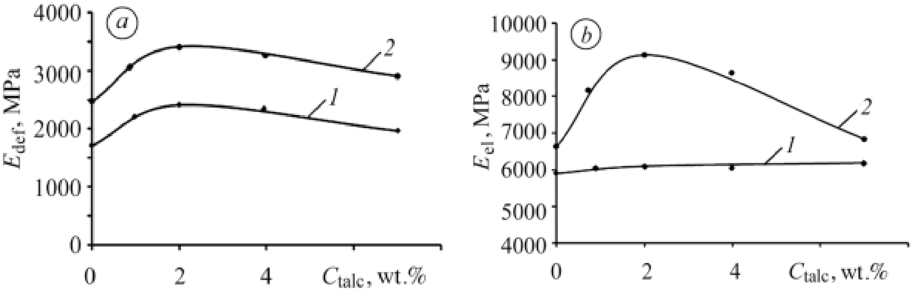

Fig. 8. Deformation (a) and elasticity (b) module of polylactide materials as functions of the talc content: (1) without heat treatment; (2) after heat treatment

According to the established values of the deformation modulus, the developed polylactide composite materials belong to the class of low deformable materials characterized by reversible strains and a strong elastic aftereffect. It is easy to see that, as compared with talc-containing materials, the unfilled PLA is characterized by the lowest values of the deformation modulus. This regularity is observed both for thermally treated specimens and for specimens without thermal treatment. This is obviously explained by the influence of talc as an active filler, which plays the role of nucleator of PLA [26], which also increases the degree of crystallinity. The obtained crystalline formations of PLA (mainly of spherulitic type) almost do not fail under static loads and make the motion of sufficiently large segments of free polylactide macromolecules impossible. This is why, in these materials, the only possible relaxation phenomena are connected with the slow reconstruction of supramolecular structures observed after the removal of static loading. It should be noted that the maximum influence of the filler (talc) is attained for its concentration equal to 2 wt.%, which is obviously explained by an increase in the fraction of heterophase structures in the system for higher concentrations and stronger interactions between the filler particles.

The elasticity modulus characterizes the ability of the material to restore its shape and sizes after the removal of the action of external forces. In the case of equilibrium deformation of the elastic bodies, the entire work of external forces is reversibly accumulated in the material and the time factor is absent in the relationship between the stresses and strains. The elastic deformations of polymers are caused by the mutual displacements of atoms. This leads to changes in the distances between valence-unbound atoms and valence angles between these atoms [27]. The equilibrium elasticity modulus remains almost invariable for the materials without thermal treatment but strongly increases after thermal treatment. These specific features are obviously explained by the intense formation of crystalline areas and a decrease in the mobility of supramolecular PLA formations, especially in the transient layer around talc particles.

On the basis of the modular-deformation method of calculations, we determined the components of the total strains under loading (see Table 3).

Table 3. Influence of Talc and Thermal Treatment on the Components of Total Strains of PLA

Specimen	Elastic component, ε_{el}, %	Highly elastic component, ε_{hel}, %	Plastic component, ε_{pl}, %
Unfilled PLA	23,5	6,0	70,5
Unfilled heat-treated PLA	36,6	5,7	57,7
PLA + 2 wt.% talc	32,6	6,8	60,6
Heat-treated PLA + 2 wt.% talc	33,5	5,8	60,7
PLA + 7 wt.% talc	27,5	4,5	68,0
Heat-treated PLA + 7 wt.% talc	36,8	5,5	57,7

It is easy to see that the fraction of elastic strains (ε_{el}) (characterized by small displacements of atoms, changes in the interatomic and intermolecular distances, and insignificant variations of the valence angles) increases for the thermally treated specimens and, especially, for the unfilled PLA. The indicated features of the influence of the active filler and thermal treatment can be explained by changes in the supramolecular structure of PLA and, first of all, by an increase in the degree of crystallinity, which is accompanied by the fixation of segments of macromolecules in spherulite-type structures. It is clear that the development of deformation corresponding to the action of the instantaneous force is realized for a certain time.

If the duration of transition is small and the development of deformation is practically instantaneous, then, in the course of variations (increase and decrease) of the force, the polymeric body is permanently in the equilibrium state as a result of continuous transitions through a sequence of equilibrium deformation states corresponding to instantaneous values of the force. The direction of the process (increase or decrease in the force) is of no importance in this case. If the process of elongation requires significant amounts of time, i.e., deformation occurs for the time equal to the period of variations of the force, then process of deformation is significantly complicated for both filled and thermally treated polylactide systems. At the same time, the level of strains depends not only on the instantaneous values of the force but also on the direction of the process and its rate.

At the same time, the fraction of highly elastic strains (ε_{hel}), which is primarily connected with the conformation changes of the macromolecules, decreases for thermally treated specimens as a result of compactification of the structure caused by the denser packing of macrochains and changes in the intermolecular interactions under the action of filler particles and additional thermal treatment. It is worth noting that the nonequilibrium highly elastic state of polymers is connected with the fact that the system of linear chain molecules cannot be simultaneously in the state of complete equilibrium and in the stressed state. Any stresses acting in system cause either irreversible strains or the phenomenon of flow. As a result, these stresses inevitably decrease and disappear. However, due to the large sizes of PLA macromolecules [28], the viscosity of the material can be sufficiently high to cause yield of the material hardly detectable even for relatively large periods of time. Then the applied stress does not disappear and induces irreversible highly elastic strains. Hence, the effect of high elasticity manifests itself in full measure when the irreversible strains can be neglected. Thus, even in the presence of steady-state equilibrium highly flexible deformation of a linear polymer, we observe the realization of the state of incomplete equilibrium.

A substantial decrease in the fraction of plastic strains (ε_{pl}) caused by the irreversible displacements of macromolecules in the total strains observed for thermally treated and filled specimens also serves as a confirmation of the appearance of a rigid structure of polymeric material characterized by a much lower susceptibility to reversible deformations. We also mention a significant influence of finely divided filler and additional thermal treatment on the coefficient K_{str} and the hardness of polylactide materials (Fig. 9).

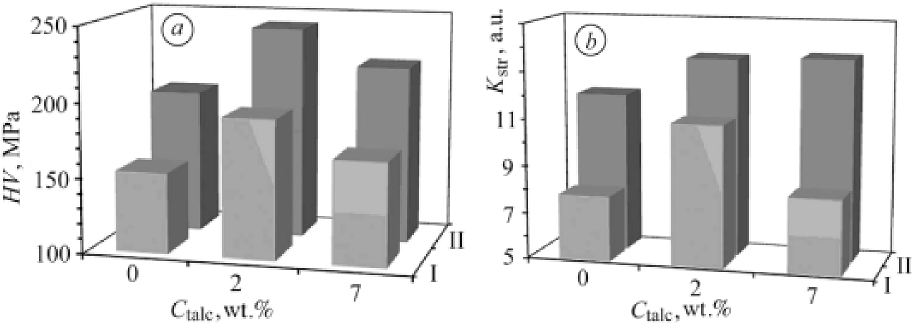

Fig. 9. Hardness (a) and structure factor (b) of polylactide materials as functions of the talc content: (I) without thermal treatment; (II) after treatment

It is easy to see that, both the introduction of the finely divided filler and the procedure of additional thermal treatment promote an increase in the hardness of polylactide materials. In this case, the highest hardness is observed for a heat-treated material with 2 wt.% of talc. At the same time, the increase in the level of hardness for filled composites is caused by the fact that a part of the external load is applied to rigid particles of the filler and, moreover, we observe the formation of a "polymeric matrix–filler" transient layer in which macromolecules are characterized by shorter statistical segments of the polymeric chain.

For the thermally treated specimens, we observe an increase in the structure factor characterizing a spatial fluctuation network, which corresponds to strengthening of the structure of polymer caused by the denser packing of macromolecules and the formation of additional physical bonds. In particular, among the materials not subjected to thermal treatment, a material containing 2 wt.% of talc is characterized by the highest value of the analyzed parameter and, clearly, an additional increase in the filler content would result in the interaction between its particles and, hence, in a decrease in the nodes of spatial fluctuation network. At the same time, the procedure of additional thermal treatment facilitates the attainment of the maximum values of structure factors in the material, which substantiates the formation of the ordered structures of polymers, i.e., an increase in crystallinity.

As an important characteristic of polymeric composite materials, we can mention the variations of their properties under the action of temperature. The exact data on temperature transitions in polylactide materials and, in particular, on the vitrification temperature and melting point, enables us to establish the required temperature range in which the material has a sufficiently high mechanical strength and can be used in practice. To study the molecular mobility and relaxation processes in polymers, it is customary to use the thermomechanical method. The thermomechanical properties of the polymers and composite materials based on polymers are closely connected with their operating characteristics and enable us to determine both the temperature ranges of operation of the material and the temperature ranges of the physical states of polymers required for the proper choice of the rational conditions of their processing and operation. It is convenient to describe these properties with the help of a thermomechanical curve, which characterizes the evolution of strains for a certain time period at different temperatures and under the conditions of given static stresses (Fig. 10).

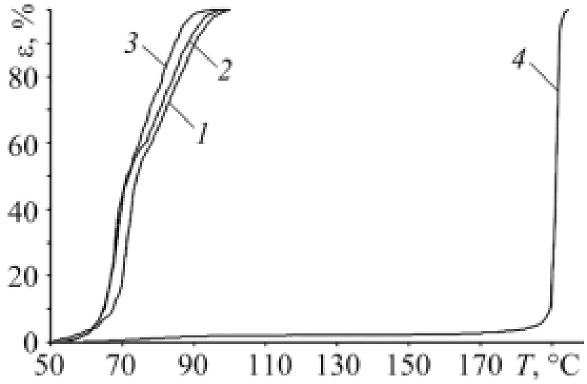

Fig. 10. Thermomechanical curves of polylactide materials: (1) PLA without fillers; (2) PLA with 2 wt.% of talc; (3) polylactide with 7 wt.% of talc; (4) thermally treated PLA without fillers

It should be emphasized that the introduction of fillers leads to changes in the slope of the curve in the course of transition into the viscous-flow state. In particular, the application of talc facilitates a decrease in the indicated slope and leads to a certain shift of the melting point into the region of lower temperatures, which is obviously caused by its active participation in the redistribution of intermolecular interactions between the components of the system. It is clear that, in this case, highly elastic deformation manifests itself due to changes in the free volume of the system rather than as a result of segmental mobility of the macromolecules.

The procedure of thermal treatment of polylactide specimens strongly affects the character of the thermomechanical curves. Thus, for the treated PLA, the curve is identical to the curves obtained for classical partially crystalline polymers, which is explained by significant changes in the supramolecular structure and, in particular, by the increase in the degree of crystallinity and changes in the average size of crystallites. It is worth noting that thermally treated PLA has the highest melting point among all developed composites.

4. Conclusions

Based on the research results obtained it the influence of filler-talc amount, its content, as well as the heat treatment and temperature of the water medium on the regularities of water absorption of polylactide materials were revealed. It was established that the equilibrium water absorption of PLA materials is insignificant and makes 0.6–1 wt %. As the result the process of water absorption occurs in two stages. In this case, the adding of talc in the amount of 2–7 wt % in PLA, and an additional heat treatment promote the reduction of polylactide equilibrium water absorption.

It was found that with the increasing temperature the diffusion coefficient of water through the polymer being raised. The addition of talc and a heat treatment of composites lead to the decrease in the diffusion coefficient and the increase in the activation energy of the water absorption process. In this case, the highest values of activation energy and the lowest diffusion coefficient are typical for the heat-treated materials with 2 wt % of the talc.

It was found that PLA composites after 12 days of exposure in a 5% solution of H_2SO_4 are characterized by a two-stage diffusion behavior and the swelling coefficient of the samples is 0.7–1.6 wt %. The adding of talc and additional heat treatment of samples promote the increase of chemical resistance in an acidic medium which is probably due to the following changes in the morphology of polylactide: an increase in the degree of its crystallinity and the structure compaction.

On the basis of the results of investigations, we discovered a significant influence of the finely divided filler (talc) and additional thermal treatment on the elastoplastic and thermomechanical characteristics of polylactide materials caused by the changes in the supramolecular structure of PLA. We detected an increase both in the deformation module of polylactide materials (by 45–95%) and in their elasticity module (by 15–50%) under the action of the filler and thermal treatment. In particular, the highest values of these module were recorded for thermally treated specimens with a talc content of 2 wt.%. It was shown that the introduction of the filler and additional thermal treatment lead to an increase in the fraction of elastic component and a decrease in the fraction of plastic component, whereas the fraction of highly elastic component remains practically invariable.

Studied the hardness of the obtained polylactide materials and, in particular, revealed an increase in hardness caused by the introduction of the filler and additional thermal treatment. Its highest value (240 MPa) was obtained for the heat-treated material with 2 wt.% of talc. The introduction of talc into PLA and the procedure of additional heat treatment promote an increase in the structure factor of the material, which characterizes the spatial fluctuation network of the polymer. In this case, additional thermal treatment exerts the strongest influence of the structure factor. On the basis of the results of thermomechanical analysis, it was shown that the addition of the filler exerts almost no influence on the character of thermomechanical curves but, at the same time, the procedure of thermal treatment promotes a substantial increase in the degree of crystallinity of PLA and, hence, shifts its melting point into the region of higher temperatures.

References

[1] Yiu-Wing Mai, Zhong-Zhen Yu Polymer Nanocomposites. Boca Raton: Woodhead Publishing, 2006 – 608.

[2] Thakur V. K., Thakur M. K., Pappu A., Hybrid Polymer Composite Materials, Cambridge: Woodhead Publishing Limited, 2017- 430.

[3] Niaounakis M., Biopolymers: Applications and Trends. Oxford:William Andrew, 2015 - 604.

[4] Tokiwa Y., Calabia B. P. Biodegradability and biodegradation of poly(lactide). Appl Microbiol Biotechnol 20,06, 72. 244–251.

[5] Sin L. T., Tueen B. S., Polylactic Acid 2nd Edition. A Practical Guide for the Processing, Manufacturing, and Applications of PLA. Oxford: William Andrew, 2019 - 422.

[6] Laura M., Lorenzo D., Androsch R., Industrial Applications of Poly(lactic acid). Cham:Springer, 2018 - 228.

[7] Murariu M., Dubois P., PLA composites: From production to properties. Advanced Drug Delivery Reviews 2016, 107, 17–46.

[8] Carrasco F., Pages P., Gamez-Perez J., Santana O.O., Maspoch M.L., Processing of poly (lactic acid): characterization of chemical structure, thermal stability and mechanical properties. Polym. Degrad. Stab. 2010, 95, 116–125.

[9] Levyts'kyi V., Masyuk A., Bialopiotrowicz T., Bilyi L., Humenets'kyi T., Morphology and properties of thermoplastic composites with modified silicate fillers. Materials Science 2018 – 54, 1. 48-54.

[10] Levytskyj V., Laruk Y., Humenetsky T., Sikora J., The influence of polystyrene modifier and plasticizer nature on the properties of poly(vinyl chloride). Chemistry and Chemical Technology 2015, 9, 2, 199-203.

[11] Stloukal P., Kalendova A., Mattausch H., Laske S., Holzer C., Koutny M., The influence of a hydrolysis-inhibiting additive on the degradation and biodegradation of PLA and its nanocomposites. Polym. Test. 2015, 41, 124-132.

[12] Xu L., Crawford K., Gorman C.B., Effects of Temperature and pH on the Degradation of Poly(lactic acid) Brushes. Macromolecules 2011, 44, 4777-4782.

[13] Levytskyi V. E., Masyuk A. S., Bilyi L. M., Bialopiotrowicz T., Humenetskyi T. V., Shybanova A. M., Influence of Silicate Nucleation Agent Modified with Polyvinylpyrrolidone on the Morphology and Properties of Polypropylene. Mater. Sci., 2020, 55, 555-562.

[14] Laura M., Lorenzo D., Androsch R., Industrial Applications of Poly(lactic acid). New York City: Springer, 2018 - 228.

[15] Liyv E., Metodika opredeleniya fiziko-mehanicheskih svoystv polimernyih kompozitov putem vnedreniya konusoobraznogo indentora. Tallyn:estNYYNTY, 1983 - 27.

[16] Levytskyi V., Masyuk A., Samoiliuk D., Bilyi L., Humenetskyi T., Morphology and properties of polymer-silicate composites and polyester materials based on them. Materials Science, 2016, 52, 1, 17-24.

[17] Moravskyi V., Levytskyi V., Bratychak M. Jr., Khromyak U., Kuznetsova M., Chopyk N., Physico-Chemical and Technological Regularities of Foam Polystyrene Degazation in the Liquid Medium. Chem. Chem. Technol 2019, 14, 347-351.

[18] Saha S.K, Tsuji H., Effects of molecular weight and small amounts of D-lactide units on hydrolytic degradation of poly(L-lactic acid)s. Polym. Degrad. Stab 2006, 91,1665–1673. doi: 10.1016/j.polymdegra009.

[19] Androsch R., Schick C., Lorenzo D., Kinetics of Nucleation and Growth of Crystals of Poly(l-lactic acid). Adv Polym Sci. 2016, 279, 235-272. doi:10.1007/12_2016_13.

[20] Koenig J. L., Spectroscopy of Polymers 2nd Edition. New York: Elsevier Science. 1999 - 491.

[21] Levytskyj V., Kochubei V., Gancho A., Influence of the silicate modifier nature on the structure and properties of polycaproamide. Chem. Chem. Technol. 2013, 7, 169-173.

[22] Faghri, A., Zhang Y., Transport Phenomena in Multiphase Systems. Cambridge: Academic Press, 2006 -1030.

[23] Suberlyak O.V., Levitskij V.E., Skorokhoda, V.Y., Godij, A.B., Physical-chemical fenomena on phase boundary vinyl monomer-water solution of polyvinylpyrrolidone. Ukrainskij Khimicheskij Zhurnal, 1998, 5-6, 122-125.

[24] Katruk D., Levytskyi V., Khromyak U., Moravskyi V., Masyuk A., Physicochemical Principles of Synthesis and Modification of Unsaturated Polyester-Polyvinyl Chloride Composites and the Properties of Materials Derived from Them. Intern. J. of Polym. Sci. 2019, 2019, 1-9.

[25] Jiménez A., Peltzer M., Ruseckaite R., Poly(lactic acid) Science and Technology: Processing, Properties, Additives and Applications. – Cambridge: Royal Society of Chemistry, 2014 – 372.

[26] Levyts’kyi V. E., Katruk D. S., Shybanova A. M., Bilyi L. M.,. Humenets’kyi T. V., Physicochemical properties of modified polyester-polyvinylchloride compositions Fiz.-Khim. Mekh. Mater, 2016, 52, 4, 100–105.

[27] Hamada K., Kaseemb M., Ayyoobd M., Jooa J., Deric F., Polylactic acid blends: The future of green, light, and tough. Progr. Polymer. Sci. 2018, 85, 83–127.

Edited by: Assoc. Prof. Ľudmila Dulebová, Ph.D., D.Sc.
prof. Janusz W. Sikora, Ph.D., D.Sc.

Reviewed by: prof. Janette Brezinová, Ph.D., D.Sc.
Assoc. Prof. Tomasz Rydzkowski, Ph.D, D.Sc.
Assoc. Prof. Mykola Brailo, Ph.D., D.Sc.

Title: **Technological and design aspects of the processing of composites and nanocomposites**
Volume IV

Publisher: Technical University of Kosice, Faculty of Mechanical Engineering,
Letna 1/9 Str., 040 01 Kosice, Slovakia, First Edition, 2021, 280 pages

Print: 50 pieces

Printed by: Technical University of Kosice, Letna 1/9 Str., 040 01 Kosice

ISBN 978-80-553-3817-0

978-80-553-3817-0